ISSN 0915-6348

NATIONAL INSTITUTE FOR FUSION SCIENCE

Summary Report of Japan-US Joint Project (JUPITER-II) (FuY 2001-2006)

(Eds.) K. Abe, A. Kohyama, S. Tanaka, T. Muroga, C. Namba, S.J. Zinkle and D.K. Sze

(Received - Feb. 19, 2008)

NIFS-PROC-71 Mar. 2008

RESEARCH REPORT
NIFS-PROC Series

TOKI, JAPAN

Summary Report of Japan-US Joint Project (JUPITER-II)
(FuY 2001-2006)

Edited by
K. Abe, A. Kohyama, S. Tanaka, T. Muroga, C. Namba, S.J. Zinkle, D.K. Sze

Summary Report of Japan-US Joint Project (JUPITER-II)
(FuY 2001-2006)

Edited by
K. Abe, A. Kohyama, S. Tanaka, T. Muroga, C. Namba, S.J. Zinkle, D.K. Sze

This report summarizes the scientific accomplishments achieved through the JUPITER-II Japan-US Collaboration Program. The JUPITER-II collaboration (**J**apan-**U**SA **P**rogram of **I**rradiation/**I**ntegration **Te**st for Fusion **R**esearch –**II**) has been carried out through six years (2001-2006) under Phase 4 of the collaboration implemented by Amendment 4 of Annex I to the MEXT (Ministry of Education, Culture, Sports, Science and Technology)-DOE (United States Department of Energy) Cooperation. This program followed the RTNS-II Program (Phase 1: 1982-1986), the FFTF/MOTA Program (Phase 2: 1987-1994) and the JUPITER Program (Phase 3: 1995-2000).

The JUPITER-II collaboration was established to provide the scientific foundations for understanding the integrated behavior of blanket materials combinations operating under conditions characteristic of fusion reactors, including interactive neutron irradiation effects, high temperature coolant flow phenomena, heat and mass transport in blanket materials, and coolant chemistry and its interactions with surrounding materials. The scientific concept of this program is to study the key technology in macroscopic system integration for advanced blanket based on an understanding of the relevant mechanics at the microscopic level.

Key words: Japan-US Collaboration, fusion reactors, blanket material, coolant chemistry, advanced blanket system, self-cooled liquid blanket, Flibe system, V alloy, MHD coatings, high-temperature gas-cooled blanket, SiC/SiC composites, blanket system modeling, multi-scale modeling

Table of Contents

1. Summary of the JUPITER-II Project

(K. Abe)

1-1 Introduction

The JUPITER-II collaboration (**J**apan-**U**SA **P**rogram of **I**rradiation/**I**ntegration **Te**st for Fusion **R**esearch –**II**) has been carried out through six years (2001-2006) under Phase 4 of the collaboration implemented by Amendment 4 of Annex I to the MEXT (Ministry of Education, Culture, Sports, Science and Technology)-DOE (United States Department of Energy) Cooperation. This program followed the RTNS-II Program (Phase 1: 1982-1986), the FFTF/MOTA Program (Phase 2: 1987-1994) and the JUPITER Program (Phase 3: 1995-2000) [1].

In the RTNS-II Program the fundamental mechanism of radiation damage was emphasized and "cascade effects" of neutron irradiation were clarified at low fluence levels by using a fusion relevant 14 MeV neutron source. In the FFTF/MOTA Program, on the other hand, the microstructural development and property changes caused by relatively high dose levels up to about 100 dpa were studied using materials irradiation capsules in the fast reactor.

In the JUPITER Program, in order to study the dynamic behavior of fusion reactor materials under irradiation and their response to variable and complex irradiation conditions, a program of systematic irradiation experiments utilizing fission neutrons at HFIR and ATR reactors has been performed. The irradiation experiments in this program included low activation structural materials, functional ceramics and other innovative materials

Throughout these programs, the irradiation resistance of various structural and functional materials were surveyed during and after neutron irradiation. These basic understandings of irradiation performance, as well as new developments in alloy technology, led to the prospect that ferritic steels, vanadium alloys and SiC/SiC composite are strong candidates for low activation structural materials and led naturally to a new research theme of materials system integration for advanced fusion blankets.

The JUPITER-II collaboration was established to provide the scientific foundations for understanding the integrated behavior of blanket materials combinations operating under conditions characteristic of fusion reactors, including interactive neutron irradiation effects, high temperature coolant flow phenomena, heat and mass transport in blanket materials, and coolant chemistry and its interactions with surrounding materials. The scientific concept of this program is to study the elemental technology in macroscopic system integration for advanced blanket based on an understanding of the relevant mechanics at the microscopic level, as schematically illustrated in Fig.1 [2].

Fig.1 Schematic concept of JUPITER-II Program.

Outcomes from this program have been presented at international fusion oriented meetings, such as ICFRM and ISFNT, and published in related articles. Technical results of each research subjects in detail and full lists of publication will be summarized in the latter sections. The overall perspective of the program and typical references are described in this section.

1-2 Objectives and Tasks

1.2.1 Advanced Blanket System and Integration Issues

Fusion reactor blankets must successfully generate and recover tritium, function as radiation shielding, and convert the kinetic energy of fast neutrons to usable heat. Advanced blankets are also required to satisfy requirements for high thremodynamic efficiency and low induced radioactivity. There are several advanced blanket concepts that combine various breeding/cooling materials and low activation structural materials [3,4]. Structural materials considered are ferritic steels, vanadium alloys and SiC/SiC composite instead of austenitic steels. Breeding materials studied are Li ceramics, liquid metals (Li, Li-Pb), and molten salt (LiF-BeF2, Flibe). Coolant materials considered are water, He gas, liquid metal and molten salt. The advanced blanket systems studied in this program are (a) Flibe molten salt system, (b) Vanadium alloys with Li, (c) SiC/SiC with He.

The Flibe system design avoids MHD problems due to its low electrical conductivity and it has

relatively low reactivity with oxygen and water. However, the low thermal conductivity of Flibe limits the power density, and its low tritium breeding ratio requires a neutron multiplier such as Be. Reduction-oxidation (Redox) control and corrosion problems involving the structural materials must also be solved.

The liquid lithium breeder concept has high thermal conductivity and a high tritium breeding ratio. If lithium is combined with vanadium alloys, relatively simple blanket design with high thermal efficiency and low induced radioactivity is possible. However, MHD problems must be solved, and liquid lithium and vanadium alloy technology must be further developed.

The SiC/SiC composite as structural material has relatively lower induced radioactivity and can be used at very high temperatures with He gas cooling. Using solid breeding materials, a blanket design with high thermal efficiency and low induced radioactivity is proposed. Issues to be solved are irradiation performance with thermal conductivity degradation under high concentration of He in the composite, and thermomechanics of the combination with breeding materials.

Table 1 summarizes the characteristics and issues for these three types of blanket systems [5-7]. Irradiation performance of materials system and related tritium issues are common to all systems.

Table 1 Characteristics of advanced blanket systems studied in JUPITER-II Program [5-7]

System	FLiBe system	Vanadium Alloys/Li	SiC/SiC /He
Candidate Structural Material	Ferritic, ODS (Vanadium Alloy)	Vanadium Alloy V-4Cr-4Ti	SiC/SiC Composite
Coolant	FLiBe (He)	Liquid Li	He
Breeding Materials	FLiBe	Li	Li2O etc
Typical Blanket Design	FFHR Liquid Blanket	ARIES-RS Liquid Blanket	DREAM Gas Cooled Blanket
Activation	Medium Low	Low	Very Low
Inlet / Outlet Temperature & Heat Flux	450/550(700) °C Medium	330/610°C High	500/800°C High/Medium
Thermal Efficiency	37%	45%	50%
Issues for Power Reactor	FLiBe Technology Redox Control	MHD Drop Li Technology	Thermal Conductivity Hermeticity
Materials System Issues	Corrosion	Ceramic Coating Fabrication	H, He Production Fabrication

1.2.2 Tasks and Objectives

In the program, research themes were categorized and research objectives are clarified as summarized below.

Task 1. Self-Cooled Liquid Blanket

1-1. Flibe system

1-1 A. Flibe Handling/Tritium Chemistry

Technical requirements necessary to apply Flibe to a self-cooled liquid blanket of a fusion reactor were surveyed. Maintaining Flibe under a reducing atmosphere is a key issue to transform TF to T_2 with a faster reaction rate compared with the residence time in blanket. The purpose of the task is to clarify whether or not the Redox control of Flibe can be achieved with Be through the following reaction.

$$Be + 2\ TF \rightarrow BeF_2 + T_2$$

1-1 B. Flibe Thermofluid Flow Simulation

The thermal conductivity of Flibe is low, and its kinematic viscosity is high compared to other lithium-containing metal alloys. The high viscosity and low thermal conductivity put Flibe in the class of high Prandtl number fluids. In order to obtain sufficiently large heat transfer for such a fluid coolant, high turbulence is required under magnetic field. The effects of magnetic field on the turbulence is an important issue for heat transfer.

1-2. Lithium Cooled with V Alloy Structure

1-2 A. Coatings for MHD Reduction

In order to reduce the pressure drop from the magneto-hydrodynamic force assisted with liquid lithium coolant flowing through magnetic fields, conductive structural materials must be coated with insulating ceramics. The purpose of the task is to find stable ceramics in high-temperature lithium, to coat the layer on to vanadium alloys and to evaluate its stability including radiation effects.

1-2 B. V Alloy Capsule Irradiation

The candidate vanadium alloy is V-4Ti-4Cr, whose irradiation creep properties and compatibility with lithium are important for high-temperature applications. Related mechanical properties and their improvement by alloy modification and heat treatment are also important. The purpose of the task is to obtain information on property changes caused by neutron irradiation in the lithium

capsule.

Task 2. High-Temperature Gas-Cooled Blanket

2-1. SiC Fundamental Issues, Fabrication, and Materials Supply

2-2. SiC System Thermomechanics

2-3. SiC Capsule Irradiation

The purpose of task 2 is to demonstrate the feasibility of high efficiency gas cooling blanket systems using advanced SiC/SiC composites based on new material development strategy and thermo-mechanical properties and irradiation resistance of the materials system. Three subtasks are arranged systematically. In subtask 2-1, the research subjects are fundamental issues, fabrication, and materials supply of SiC/SiC composites. The combination of mechanical integrity and thermal properties is focused. In subtask 2-2, thermomechanics, compatibility and heat transfer performance of gas blanket system were studied. The thermomechanical interaction between the lithium-oxide pebble bed and SiC materials must be known. Radiation behavior of the advanced SiC/SiC composites and solid breeding system in high temperature environment were studied in subtask 2-3. The properties of composite and also the behavior of matrix, fiber and interface after high-temperature irradiation and effects of H and He are important.

Task 3. Blanket System Modeling

3-1. Design-based Integration Modeling

The main purpose of this task is to develop the integrated engineering model of blanket systems and to make clear key issues in each task in this project from the point of view of blanket systems based on fusion reactor designs. For this purpose, it is essential to optimize the blanket system not as a single component but as an integrated system device under the boundary conditions of burning core plasmas and out-vessel environments. Therefore, collaboration to connection to each task is very important.

3-2. Materials System Modeling

In order to understand the microscopic behavior of materials under fusion relevant irradiation conditions, multiscale modeling of microstructural evolution including He and interface effects must be studies. Extension to macroscopic behavior will require combination with Finite Element Method analysis.

1-3. Managing structure and Facilities

1.3.1 Managing System

Table 2 Research tasks and coordinators in JUPITER-II Program

Representative			K. Abe		S. Berk/G. Nardella	
Program Coordinator			A. Kohyama & S. Tanaka		S.J. Zinkle and D.K. Sze	
Task			Japan		US	
			Task Coordinators	Deputy	Task Coordinators	Deputy
Task1: Self-Cooled Liquid Blanket	1-1: FLiBe Cooled	1-1-A: FLiBe Handling /Tritium Chemistry/Safety	T. Terai	K. Okuno/ M. Nishikawa	D.A. Petti	R.A. Anderl
		1-1-B: FLiBe Termofluid Flow Simulation	T. Kunugi	T. Kunugi	M.A. Abdou	N. Morley
	1-2: Li Cooled with V Alloy Structure	1-2-A: Coatings for MHD Reduction	T. Muroga	T. Muroga	R.J. Kurtz	B.A. Pint
		1-2-B: V Alloy Capsule Irradiation		H. Matsui		G.R. Odette
Task2: High-Temperature Gas-Cooled Blanket		2-1: SiC Fundamental Issues, Fabrication, and Material Supply	A. Hasegawa	T. Hinoki	L.L. Snead	Y. Katoh
		2-2: SiC System Themomechanics		A. Shimizu		A. Ying
		2-3: SiC Capsule Irradiation		A. Hasegawa		L.L. Snead
Task3: Blanket System Modeling		3-1: Design-based Integration Modeling	A. Sagara	H. Hashizume	N.M. Ghoniem	D. Sze
		3-2: Material Systems Modeling		N. Sekimura		R.E. Stoller
Liaisons	S.J.Zinkle (ORNL), D.A. Petti (INL), M.A. Abdou (UCLA), C. Namba (NIFS) H. Matsui (IMR Oarai), S. Ohnuki, A. Kimura, J. Robertson (PIE)					

The management structure continued with a Steering Committee consisting of a Representative (Japan: K. Abe, US: S. Berk/G. Nardella) and two Program Coordinators (Japan: A. Kohyama, S. Tanaka, US: S. J. Zinkle, D.-K. Sze) for each side, with five Task Coordinators for each side, and with nine Subtask Coordinators for each side. In addition, there were six Liaison Officers for the U.S. side and four for the Japanese side, their purpose being to facilitate communications and assist in the coordination of collaboration activities. Tasks and coordinators are shown in Table 2. The whole program plan and research schedule were discussed at the annual Steering Committee Meetings. Research assignments and appropriate workshops were arranged for each tasks. The Personnel Assignment Guidelines for the JUPITER-II Collaboration, developed by the Steering Committee in the second year, continued to contribute toward the fruitfulness and productivity of assignments from both sides.

In Japanese side, Research Planning Committee of Japan-USA Fusion Collaboration Program has been organized by national Institute for Fusion Science to decide the annual plan of assignments and workshops for JUPITER-II Program as well as other fusion-related collaboration programs. Technical issues and priorities in JUPITER-II Program were discussed at Domestic Researchers Meetings in spring and fall annually.

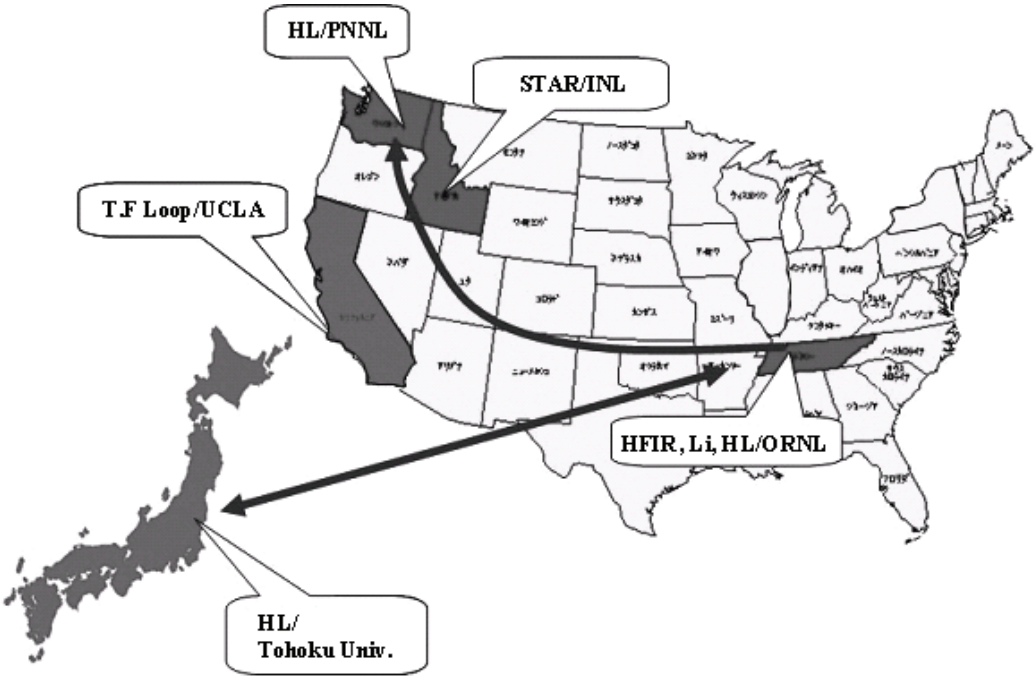

Fig.2 Facilities used in JUPITER-II Program. (HL: Hot Laboratory)

1.3.2 Facilities

Fig.2 shows the main facilities used and flows of test specimens in this program. Flibe experiments under the JUPITER-II Program were performed in the Safety and Tritium Applied Research Facility (STAR) at the Idaho National Laboratory (INL). These experiments included production, purification, sampling, analysis and Redox control of Flibe. STAR is a unique facility for systematic experiments using Flibe and related tritium work.

Thermofluid simulation experiments of Flibe were done using the FLiHy Loop with and without magnetic field at University of California, Los Angeles (UCLA). Simulation experiments using High Temperature Salt were done using the TNT (Tohoku-NIFS-Thermofluid) loop at Tohoku University.

Neutron irradiation experiments were done using the High Flux Isotope Reactor (HFIR) at Oak Ridge National Laboratory (ORNL). The HFIR provides both a high flux of fast neutrons to produce displacement damage and a high flux of thermal neutrons to produce helium and hydrogen through (n,a) and (n,p) reaction. Complementary irradiation tests were done using the JOYO (fast experimental reactor) and Japan Materials Test Reactor (JMTR) at Japan Atomic Energy Agency (JAEA) in Japan. Post Irradiation Experiments (PIE) were performed at the hot laboratories at ORNL, and also at Pacific Northwest National Laboratory (PNNL) in the early stages of the program. Subsidiary tests were

performed at hot cells of Oarai Branch of Institute of Materials Research (IMR), Tohoku University. Lithium experiments for ceramic coating of vanadium were performed at ORNL.

Fabrication and testing of SiC/SiC composite were done using the High Temperature Materials Laboratory (HTML) at ORNL and at the Institute of Advanced Energy of Kyoto University. Thermomechanics experiments of SiC and breeding materials were done at UCLA.

Other facilities used for experiments in Japan were the DUET facility at Kyoto University, the Cyclotron and Dynamitron accelerators at Tohoku University, the creep apparatus at NIFS, the molten salt apparatus at the University of Tokyo, etc.

1-4 Concluding remarks

The Japan-USA collaborative program, JUPITER-II, has made significant progress in a six-year research program titled “The irradiation performance and system integration of advanced blanket” through a six-year plan for 2001-2006. The scientific concept of this program is to study the elemental technology in macroscopic system integration for advanced fusion blankets based on an understanding of the relevant mechanics at the microscopic level.. The types of systematic experimental and theoretical studies of blanket materials conducted under JUPITER-II are important and essential elements toward realizing attractive fusion energy options.

For the three blanket systems studied, technical feasibility was shown from the viewpoint of their original issues. Remaining issues are tritium behavior and related irradiation performance of materials system in advanced blankets. Some of these issues are being studied now in Phase 5 of the Japan-USA Collaboration, called the TITAN Program.

Through this program, many young scientists including doctoral students contributed to the success of the task research work. It is expected that fusion research and developments for the future will be strengthened by these researchers.

References:

[1] K. Abe a,, A. Kohyama, C. Namba, F.W. Wiffen, R.H. Jones, Neutron irradiation experiments for fusion reactor materials through JUPITER program, J. Nucl. Mater. 258-263(1998)2075.

[2] Intermediate report on Japan-USA Collaboration Progrram JUPITER-II, “The irradiation performance and system integration of advanced blanket”, NIFS report in Japanese (2004)

[3] K.Abe, Materials System Integration for Fusion Blanket, “Introduction to Fusion Engineering” edited by Y.Katoh et al. Atomic energy Society of Japan(2001),pp.113

[4] T.Terai, Advanced Blanket Concepts and Their R&D Issues Materials, “Introduction to Fusion Engineering” edited by Y.Katoh et al. Atomic Energy Society of Japan(2001),pp123.
[5] A. Sagara, et al., Studies on flibe blanket designs in helical reactor FFHR, Fusion Tech. 39 (2001) 753-757.
[6] ARIES-Team, D.K. Sze, The Aries-RS power core-recent development in Li/V design, Fusion Eng. Des. 41 (1998) 371-376.
[7] S. Nishio, S. Ueda, I. Aoki, R. Kurihara, T. Kuroda, Improved tokamak concept focusing on easy maintenance, Fusion Eng. Des. 41 (1998) 357-364.

2. Highlights of Accomplishments

(A. Kohyama, S. Tanaka, S.J. Zinkle and D.K. Sze)

2.1 Flibe System

Flibe Chemistry [1-4]

Flibe handling and purification method was tested and an experimental apparatus to investigate the Be Redox control of Flibe was prepared. The Redox control of Flibe by Be was proved experimentally, and the prompt transformation of HF to H_2 was completed in the Flibe crucible. Related results are summarized below.

For the subtask on molten salt handling and tritium/chemistry control, hydro-fluorination was demonstrated for reducing impurities in Flibe to acceptable levels with the resulting fluorides either precipitating or remaining stable in the salt. Many practical lessons were learned while operating systems using Flibe, such as the need for in-line filtration to remove large carbon particles, splatter shields to prevent vapor species transport which tends to plug gas purge exhaust lines, and coating of all system components with Ni to minimize corrosion from salt or salt vapor contact.

Mobilization studies were performed to quantify salt vapor species at temperatures lower than those of previous studies, producing results in the appropriate temperature range of a fusion blanket system. The predominant vapor species was verified to be BeF_2, however the quantity observed was 3-5 times less than values expected from extrapolated high temperature data or model predictions. Concentrations of Li components also increased with temperature, reflecting a possible change in the vaporizing gas species.

Permeation studies performed with deuterium or tritium in Flibe provided data on mass transport parameters of solubility and diffusivity – key parameters required for the selection and design of blanket tritium extraction techniques. Two different experiment systems were developed, varying the contact surface of the salt and container with the permeating species. Diffusivity of deuterium in liquid Flibe was measured to be marginally larger than that for solid Flibe, whereas the activation energy of diffusion was similar in value to F^+ diffusion.

A major objective of this subtask was to demonstrate Redox control with excess Be introduced into the flibe, allowing the energetically preferred formation of BeF^2 and recombination of molecular tritium. Experiments were performed allowing introduction of HF into salt exposed to metallic Be samples, followed by quantifying the rate of HF conversion. Rapid and effective reduction of HF occurred at the concentrations much higher compared to those expected in a blanket system; without neutrons to

generate T+, low F- concentrations are practically unachievable. However, modeling of the chemical system assisted in calculating rate coefficients that can be used to predict system behavior at the very low concentrations applicable to the blanket. An unexpected result obtained from the experiment series concerns the mechanism of Be transport into the salt. Rather than dissolution of Be metal, which is known to have very low solubility in flibe, the transport appears driven by galvanic action. This discovery can potentially influence the design of the chemical control system for a blanket.

Corrosion tests were also performed with and without Redox control for samples of the advanced ferritic steel JLF-1. Exposures of up to 500 hours in the non-flowing molten salt indicate a corrosion rate of 0.1 μm/hr, with a Cr-rich oxide layer forming at the sample interface. Corrosion was effectively halted during periods of REDOX control using Be.

Flibe Thermofluid [5,6]

In the first half of the program, thermofluid flow experiment without magnetic field was performed. Selection of stimulant fluid (30 to 40% KOH aqueous solution) and reconstruction of FLiHy loop with enough length test section were completed. Development of Particle Image Velocimetry (PIV) for non-MHD pipe flow was performed. Direct Numerical Simulation (DNS) code was improved and MHD turbulence model was developed.

In the second half of the program, the thermofluid flow experiment was extended to the condition with magnetic field. Velocity profile and turbulence quantities are measured under magnetic field. Heat transfer and temperature profile measurement was performed by developing thermocouple tower. Heat transfer tests at high parameter range were performed successfully to establish a database for MHD flow and heat transfer and to validate the MHD turbulence model.

As for flow characteristics, DNS results and PIV measurement regarding the mean velocity and the turbulent statistics of turbulent pipe flows showed very good agreement, and the laminarization of turbulent flow due to the Lorentz force was clearly observed in both DNS and PIV experiments. Therefore, a large database for turbulent flow with and without magnetic field was established and can be used for developing the non-MHD and MHD turbulence models.

As for heat transfer characteristics, temperature profiles with conducting wall were measured for lower Re number flow, and the effect of a magnetic field on temperature fluctuation was clearly observed. Effect of thermal stratification on heat transfer performance was examined and temperature profile was generated by interaction between laminarization due to B effect and thermal stratification. It was found that the degradation of heat transfer performance due to B-field is larger than the

conventional prediction regarding low Pr number fluid.

2.2 Vanadium/Li System

MHD Coating [7,8]

For the subtask on coatings for vanadium alloys to reduce the pressure drop from the magneto-hydrodynamic force associated with liquid lithium coolant flowing through magnetic fields, four important results were obtained. (1) Identification of leading candidate ceramics: Exploration of MHD coating candidates was carried out by Li exposure tests of bulk ceramics. Ceramics of Er_2O_3 and Y_2O_3 showed good stability in Li. Later, reaction layer was observed in Y_2O_3. Er_2O_3 is shown to be the promising new candidates. (2) Development of coating with sufficient stability in static Li: Various coating technologies were applied for fabrication of Er_2O_3 coating on V-4Cr-4Ti substrate. High crystalline Er_2O_3 coating showed good stability in Li to 973K at 1000hr. (3) Development of two-layer coatings, i.e. to coat the V-alloy with insulator and then have another thin V-alloy coating outside the insulator to protect the insulating coating from Li corrosion, with sufficient stability in static Li: In-situ resistivity measurements in Li for V/Er2O3/V alloy substrates systems showed satisfactory resisitivity in molen Li to 873K. This two-layer coating showed good performance in static Li. (4) Compatibility in flowing Li: Using a stainless steel loop at 873K for 1000hr, no significant damage was observed for Er_2O_3 bulk specimens and weight loss was small. Compatibility of the two-layer coating in flowing Li at 973K were tested in ORNL using a loop made of vanadium alloy.

The electrical resistance of the coated specimens in contact with Li was acceptable up to 600°C and was not degraded by repeated temperature cycling between the room temperature to 600°C in static Li. Bulk specimens of Er_2O_3, Y_2O_3 and AlN irradiated at 450°C in Li environment in HFIR-RB-17J were examined and no signification corrosion was observed.

Li Capsule Irradiation [9-11]

Performance of V-alloy components in Li and irradiation environments up to 3-5 dpa at 450 and 600 °C was clarified as follows. (1) Regarding the effect of Li environment on thermal creep performance of V-4Cr-4Ti, creep rate was lower in Li than in vacuum. (2) Regarding irradiation creep in Li, comparison with Na capsule irradiation in JOYO reactor showed insignificant difference in irradiation creep between Li and Na environments. (3) Regarding improvement of irradiation properties of V-4Cr-4Ti by doping with Si, Al, and Y, relatively higher ductility after irradiation was confirmed for

specimens in irradiated in HFIR-17J at 450C to 5 dpa. Microstructures showed retarded dislocation evolution by the addition of Si, Al, and Y.

Recent results are as follows: Measurement of diametral strains of pressurized creep tubes irradiated at 425°C was completed. The results showed moderate irradiation creep strain with only small differences between specimens prepared from the US-Heat and NIFS-Heat of V-4Cr-4Ti. The results are also consistent with those obtained for specimens irradiated in a Na environment in the JOYO reactor. Measurement and analysis of the creep tubes irradiated at 600°C has almost been completed.

The effect of Y, Al, and Si additions on microstructure and tensile properties was investigated. Suppression of irradiation-induced hardening and loss of ductility by addition of Y, Al, and Si was confirmed. Charpy impact tests are planned for an identical set of specimens. Shipping of the specimens irradiated at 425°C to Japan was aonost complete.

Research activity continued to study enhancement of technology for testing small fracture and deformation specimens at variable loading rates for application to HFIR-RB-17J irradiated specimens. The PIE of HFIR RB-17J specimens includes the effect of trace elements on the microstructure and properties of vanadium alloys, characterization of laser weld joints and advanced alloys, measurement of radiation-induced fracture transition temperature shifts using disc compact tension and pre-cracked bend bar specimens, and determination of stress-state effects on flow localization in V-4Cr-4Ti.

2-3 SiC/He System

SiC Fabrication [12-14]

Extensive efforts for development and characterization of advanced SiC/SiC composites for fusion have been successfully carried out in Task 2-1. Advanced small specimen test technologies and procedures for mechanical properties of SiC/SiC were developed. Joining and hermetic sealing using (a) (NITE) SiC/SiC and (b) (CVI) / NITE hybrid process has been explored. The robust joining technique using NITE joint was successfully developed and evaluated. The optimized composite samples were produced and supplied to irradiation experiments. Guidance was provided for selection of appropriate materials for the pebble-bed thermo-mechanics experiments.

Recently, progress has been achieved in the areas of fracture toughness evaluation and interfacial shear properties characterization for advanced SiC/SiC composites, and chemical compatibility of SiC in dual-cooled blankets. The fracture behavior of advanced SiC fiber composites with (a) CVI and (b) NITE SiC matrices were successfully evaluated by bend testing of single edge notched beam (SENB)

specimens. Based on that, J-integral analysis of SENB fracture was selected as a standard test method for post-irradiation examination of 18J specimens. For the interfacial characterization, methods to explicitly determine debond and frictional shear stresses at fiber/matrix interfaces by single fiber push-out experiments were developed. Additionally, static compatibility testing of high purity monolithic SiC and advanced SiC/SiC composite materials in liquid lead-lithium was performed in support of dual-cooled blanket R&D, providing another promise of those materials systems.

Thermomechanics [15]

For the subtask on helium-cooled SiC/SiC composite and solid breeder pebble bed blanket system thermomechanics, experiments were performed for the Li_2TiO_3 pebble bed using a batch of Li2TiO3 pebbles not previously investigated. Specifically, CVD-SiC clad deformation-time histories were recorded using a laser position sensor. The thermo-mechanical interaction between this batch of pebbles and CVD-SiC clad appeared less significant as compared to what happened to the previous beds of Li_4SiO_4 pebbles, where hundreds of micrometers deformations have been recorded. Here the deformation dropped below twenty micronmeters because of a lower thermal expansion coefficient of metatitanate pebbles, and therefore a lower differential thermal stress at the pebble/SiC interface. A lower differential thermal stress is preferable for blanket operations, and thus Li_2TiO_3 pebbles are more compatible for use in high temperature SiC/SiC blankets. Stress relaxation of the bed was found to be fast even when initially applied stresses were low such as around 0.2MPa.

To understand and develop predictive capability of thermomechanics concerning a structure/ceramic breeder pebble bed material system, experimental data from Task 2.2 confirmed that a different set of consecutive equations other than those obtained from the uni-axial experimental results was needed to better describe ceramic breeder thermomechanical properties under prototypical loading conditions. The design based on the DREAM concept reduces the above concern, where heat generated inside the breeder bed is removed by the forced convection (rather than conduction as in the ARIES-I case.) However, a cost-effective tritium extraction technology from the high temperature helium stream is needed in order to make this concept attractive.

He capsule irradiation [16,17]

In subtask 2-3, various PIE and analysis of HFIR-14J experiment was carried out to establish radiation resistant design strategy of SiC/SiC composites. Screening irradiation in HFIR rabbit was carried out on the new developed SiC/SiC composited to confirm the material selection. Supporting

experiments in JMTR and JOYO reactors, and accelerator irradiation were conducted to ensure He/H effect on microstructure development, mechanical properties of the advanced composites and monolithic SiC. Results of the rabbit and supporting irradiation experiments showed the advanced SiC/SiC composite was expected to have enough radiation resistance at high temperature region. The HFIR-18J irradiation rig for high temperature irradiation experiments was fabricated and irradiation experiment will be completed in early 2008.

Other accomplishments include the completion of post irradiation examination of tensile specimens from the screening rabbit irradiation campaign. Results confirmed the strength retention of advanced SiC fiber, CVI SiC matrix composites after irradiation at below 1000ºC, and also implied potential degradation in ultimate tensile strength after irradiation above about 1100ºC.

2.4 Design and Modeling

Design-based Integration Modeling [18-20]

The main works performed in this task are as follows:

(1) Flibe Blanket system (Task 1-1-A):

Design and revelop code, MCNP-4C, which has been newly improved for a non-axisymmetric helical system in order to enable frequent modification of blanket designs and to quickly check neutronics performance requirements on tritium recovery system

Proposal and key issues on tritium permeation

Design and evaluation of Flibe / V blanket

(2) Thermofluid of Flibe (Task 1-1-B)Requirements on the first wall condition for FFHR

Modeling of MHD effects on heat-transfer

Enhancement of heat-transfer efficiency

(3) Li-V Blanket (Task 1-2-A):

Evaluation and requirements on MHD coating

Design and evaluation of Self-cooled Be-free Li/V blanket

(4) All tasks:

Improvement of neutronics calculation system for helical structure.

Recent results for the subtask on design-based integration modeling are as follows. The peaking factor of neutron wall loading in helical reactor designs such as FFHR has been evaluated using the 3D

Monte-Carlo neutron transpmance. The peaking factor evaluated is fairly low, estimated as 1.2 on a simplified model with a helical neutron source with typical profiles of plasma density and temperature. A new concept for a Flibe cooled vanadium-alloy blanket has been proposed to increase the outlet operation temperature and ΔT. Thermodynamics analysis has revealed that, although the conventional redox control with Be (TF to T2) results in an unacceptably high T inventory in V-alloy, another redox control (T2 to TF) by MoF6 or WF6 doping works well with a corrosion protective Mo or W coating on V-alloy. However, tritium recovery in the form of TF is the key issue. As for the conventional Be in flibe, the thermodynamic analysis proves that the redox control can be achieved even under the TF concentration of 10 Pa expected in a steady-state fusion power of 1 GW in such as FFHR2. Regarding T recovery using flibe-He counter-current extraction tower of 5 m height, the T decontamination factor estimated is sufficiently high around 10^6 at the outlet. T permeation through tube walls in a heat exchanger is the key issue.

Materials systems Modeling [21,22]

The topics studied were as follows: (1) code development for evaluating atomic displacements due to neutron irradiations, (2) multiscale modeling of helium effects in irradiated materials, (3) interface damage modeling in irradiated alloys and compounds, (4) modeling of microstructural evolution of vanadium alloys under irradiation, (5) modeling of radiation damage in advanced SiC/SiC composites, (6) modeling of mechanical deformation through multiscale simulations, (7) the development of MD-FEM combination methodology, (8) calculation of ideal interfacial strength between vanadium and oxide ceramics, and (9) information technology for modeling and integration of experimental data with computer models.

Recent results for the subtask on materials systems modeling were as follows. Multiscale modeling of microstructural evolution in reduced activation ferritic-martensitic steels during irradiation was done using molecular dynamics (MD) and kinetic Monte Carlo (KMC) simulation techniques. The nucleation path of He bubbles in metals under wide irradiation conditions was clarified. This effort can clearly explain a difference in formation mechanisms between He bubbles in fusion first wall materials where He is produced by (n, α) nuclear transmutation reactions and those in fusion divertor materials where He is directly implanted. Energetics of lattice defects in β-SiC was investigated using an MD technique with empirical interatomic potentials, which will be used to evaluate the formation kinetics of defect clusters in ceramics during irradiation. A new modeling method linking different size-scales with MD and the finite element method (FEM) was developed to investigate dislocation movements and crack

initiation and propagation in materials. This effort can be applied to clarify the mechanism of radiation-induced mechanical property changes of irradiated materials. A detailed Kinetic Rate Theory based Helium bubble evolution code (HEROS) was developed to describe bubble growth and gas release from helium implanted tungsten. A knowledge-based fusion materials database, Fusion NET, was developed for automated archiving of materials property data and rendering it in a web-based interactive form that is convenient for structural designers and analysts. For example, data and properties for F82H have been assembled and stored in the database. This is being applied to the design and analysis of test blanket modules for ITER.

2.5 Summary and Conclusion

The program completed its six-year plan with important progress toward its objectives and with significant scientific accomplishments that address key issues for several attractive blanket systems of common international interest. The program had four main research emphases, as follows:

1) Flibe system: It was shown that redox(reduction-oxidation) control of Flibe by Be is feasible. Thermofluid flow simulation and experiment and numerical demonstrated the MHD effects on turbulence and heat transfer. This will provide database for thermal analysis for a Flibe based fusion blanket.
2) Vanadium/Li system: MHD ceramics coating of vanadium alloys and compatibility with Li was verified successfully. Neutron irradiation experiments in Li capsule and radiation creep experiments showed the radiation resistance of the candidate alloys.
3) SiC/He system: Fabrication of advanced composites with high thermal conductivity was performed successfully and used for neutron irradiation experiment in He capsule at high temperatures to show good radiation resistance.
4) Blanket system modeling: Design-based integration modeling of Flibe system and V/Li system improved substantially. Multi-scale materials system modeling including He effect progressed.

References

[1] S. Fukada, M.F. Simpson, R.A. Anderl, J.P. Sharpe, K. Katayama,G.R. Smolik, Y. Oya, T. Terai, K. Okuno, M. Hara, D.A. Petti, S. Tanaka, D.-K. Sze, A. Sagara, Reaction rate of beryllium with fluorine ion for Flibe redox control Journal of Nuclear Materials 367–370 (2007) 1190

[2] David A. Petti , G.R. Smolik, Michael F. Simpson, John P. Sharpe, R.A. Anderl, S. Fukada, Y. Hatano, M. Hara, Y. Oya, T. Terai, D.-K. Sze, S. Tanaka, JUPITER-II molten salt Flibe research: An update on tritium, mobilization and redox chemistry experimentsFusion Engineering and Design 81 (2006) 1439

[3] M. Hara, Y. Hatano, M.F. Simpson, G.R. Smolik, J.P. Sharp, Y. Oya, K. Okuno, M. Nishikawa, T. Terai, S. Tanaka, R.A. Anderl, D.A. Petti, D.-K. Sze, Interactions between molten Flibe and metallic Be, Fusion Engineering and Design 81 (2006) 561

[4] Michael F. Simpson, Galen R. Smolik, John P. Sharpe, Robert A. Anderl, David A. Petti, Yuji Hatano, Masanori Hara, Yasuhisa Oya, Satoshi Fukada, Satoru Tanaka, Takayuki Terai, Dai-Kai Sze, Quantitative measurement of beryllium-controlled redox of hydrogen fluoride in molten Flibe, Fusion Engineering and Design 81 (2006) 541

[5] J.Takeuchi, S.Satake, T.Kunugi, T.Yokomine, N.B.Morley, M.A.Abdou, Development of PIV Technique under Magnetic Fields and Measurement of Turbulent Pipe Flow of Flibe Simulant Fluid, Fusion Scinence and Technology, 52(2007)860

[6] T.Yokomine, J.Takeuchi, H.Nakaharai, S.Satake, T.Kunugi, N.B.Morley, M.A.Abdou, Experimental Investigation of Turbulent Heat Transfer of High Prandtl Number Fluid Flow Under Strong Magnetic Field, Fusion Science and Technology, 52(2007)625

[7] B. A. Pint, P. F. Tortorelli, A. Jankowski, J. Hayes, T. Muroga, A. Suzuki, O. I. Yeliseyeva and V. M. Chernov,"Recent progress in the development of electrically insulating coatings for a liquid lithium blanket",Journal of Nuclear Materials, Volumes 329-333, Part 1, 1 August 2004, Pages 119-124

[8] K. Fukumoto, S. Takahashi, R.J. Kurtz, D.L. Smith and H. Matsui, Microstructural examination of V-(Fe or Cr)-Ti alloys after thermal-creep or irradiation-creep tests, Journal of Nuclear Materials, Volume 341, Issue 1, 1 May 2005, Pages 83-89

[9] T. Muroga, J.M. Chen, V.M. Chernov, K. Fukumoto, D.T. Hoelzer, R.J. Kurtz, T. Nagasaka, B.A. Pint, M. Satou, A. Suzuki and H. Watanabe, "Review of advances in development of vanadium alloys and MHD insulator coatings", Journal of Nuclear Materials, Volumes 367-370, Part 1, 1 August 2007, Pages 780-787

[10] M. Li, T. Nagasaka, D.T. Hoelzer, M.L. Grossbeck, S.J. Zinkle, T. Muroga, K. Fukumoto, H. Matsui and M. Narui,"Biaxial thermal creep of two heats of V4Cr4Ti at 700 and 800 °C in a liquid lithium environment", Journal of Nuclear Materials, Volumes 367-370, Part 1, 1 August 2007, Pages 788-793

[11] Satou.M.,Nagasaka.T.,Hino.T.,Fujiwara.M.,Muroga.T., Iikubo.T.,Abe.K ,Development of V-Cr-Ti Type Alloys with Small Additives for Advanced Fusion Applications.[21th IAEA Fusion Energy Conference, (2006) FT/P5-34]

[12] T. Nozawa, K. Ozawa, S. Kondo, T. Hinoki, Y. Katoh, L.L. Snead and A.Kohyama, "Tensile, Flexural, and Shear Properties of Neutron Irradiated SiC/SiC Composites with Different F/M Interfaces," Journal of ASTM International, 2[2] (2005)

[13]Y. Katoh, T. Nozawa, L.L. Snead, T. Hinoki and A. Kohyama, "Property tailorability for advanced CVI silicon carbide composites for fusion," Fusion Engineering and Design, 81 (2006) 937-944.

[14]S. Nogami, N. Otake, A. Hasegawa, Y. Katoh, A. Yoshikawa, M. Satou, Y. Oya, K. Okuno Oxidation Behavior of SiC/SiC Composites for Helium Cooled Solid Breeder Blanket Fusion Engineering and Design (submitted ISFNT-8 Heidelberg, Germany 2007)

[15]Ying, A., Yokomine, T. Shimizu, A., Abdou, M., Kohyama, A., "Impact of Material System Thermomechanics Performance on He-Cooled Ceramic Breeder Blanket Designs with SiCf/Sic" Journal of Nuclear Materials, 329-333(Part 2):1605 - 1609 (August 2004)

[16]T. Hinoki, L.L. Snead, Y. Katoh, A. Hasegawa, T. Nozawa and A. Kohyama, "The effect of high dose/high temperature irradiation on high purity fibers and their silicon carbide composites," Journal of Nuclear Materials, 307-311 (2002) 1157-1162.

[17]K. Ozawa, T. Nozawa, Y. Katoh, T. Hinoki, A. Kohyama, Mechanical Properties and Microstructure of Advanced SiC/SiC composites after Neutron Irradiation, J. Nucl. Mater.. 367-370 (2007) 713-718.

[18] A. Sagara, S. Imagawa, O. Mitarai, T. Dolan, T. Tanaka, Y. Kubota, K. Yamazaki, K.Y. Watanabe, N. Mizuguchi, T. Muroga, N. Noda, O. Kaneko, H. Yamada, N. Ohyabu, T. Uda, A. Komori, S. Sudo and O. Motojima, Improved structure and long-life blanket concepts for heliotron reactors, Nuclear Fusion, 45 (2005) 258-263.

[19] T. Muroga, T. Tanaka, Zaixin Li, A. Sagara and Da-Kai Sze, Tritium control for Flibe/V-alloy blanket system, in this conference.

[20] Teruya Tanaka, Akio Sagara, Takeo Muroga, Maumoud Z. Youssef, Neutronics Investigation of Advanced Self-Cooled Liquid Blanket Systems in Helical Reactor, 21th IAEA Fusion Energy Conf. Chengdu, 2006.

[21] K. Morishita, R. Sugano, B.D. Wirth, T. Diaz De La Rubia, ‘Thermal Stability of Helium-Vacancy Clusters in Iron’, Nuclear Instruments and Methods in Physics Research B, **202**, 76 (2003).

[22] M. Satou, N. Komatsu, T. Sawada, K. Abe, ‘Calculation of electronic structure at bonding interface

between vanadium and oxide ceramics for insulator coating applications', Journal of Nuclear Materials, **329-333**, 1571 (2004).

3. Task Summaries

3-1 Task 1-1-A: Flibe Handling/Tritium Chemistry

(T. Terai, K. Okuno, M. Nishikawa, D.A. Petti, R.A. Anderl)

3-1-1 Objectives of the Task

Based on the key issues associated with the use of Flibe as a coolant in a fusion blanket, the objectives of our work are:

- to develop the capability to purify Flibe at the liter scale for use in the experiments;
- to characterize tritium/deuterium behavior (e.g., solubility and diffusivity) in REDOX-controlled and non-REDOX controlled Flibe;
- to characterize the magnitude and physio-chemical forms of material mobilized during an accidental spill of Flibe and to develop safe handling practices;
- to develop a redox agent for use in Flibe in a fusion blanket;
- to demonstrate the effectiveness of the redox agent in terms of structural material corrosion for fusion materials of interest using a simple dip specimens in small scale pot type experiments.

3-1-2 Participants to the Task

T. Terai, S. Tanaka, A. Suzuki, H. Nishimura (U. Tokyo), M. Nishikawa, S. Fukada, K. Katayama (Kyushu U.), K. Okuno, Y. Oya (Shizuoka U.), Y. Hatano, M. Hara (Toyama U.), A. Sagara (NIFS)
D. A. Petti, G.R. Smolik, Michael F. Simpson, John P. Sharpe, R.A. Anderl (INL)
Da-Kai Sze (UCSD)

3-1-3 Research Highlights

(a) Flibe purification

The Flibe used in the JUPITER-II collaboration was prepared from reagent grade chemicals. Both the Be_2F and LiF were listed as 99.9% pure based upon the metals

Table 1 Impurities in ingredients and final salt

		O (ppm)	C (ppm)	N (ppm)	Fe (ppm)	Ni (ppm)	Cr (ppm)
BeF_2	5700		<20	58	295	20	18
LiF	60		<2	78	100	30	4
Flibe	560		10	32	260	15	16

content. The powders were dried and weighed to provide the mole ratio of 2:1 and then purged with helium and melted. The salt was then purged with gas mixtures of He, H_2 and HF at 520 ◦C to reduce inherent oxides in a pot.

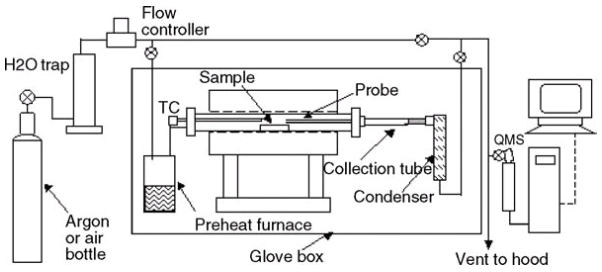

Fig. 1. Transpiration test setup.

The salt was then filtered through a 60μm metal mesh frit during a transfer to another vessel. The impurities in the final product are given in Table 1. Measurements of beryllium and lithium in the final product ranged from 8.3 to 8.5 and 13.06 to 13.2 wt%, respectively. Although these are lower than the theoretical values of 9.04 and 14.14 wt%, the lithium to beryllium mole ratios of 2.01–2.06 are close to the targeted composition. This suggests that the weight-based discrepancies might be due to absorbed water or analytical biases.

(b) Flibe mobilization experiment

A key safety issue associated with Flibe is the mobilization of vapors and aerosols from accidental introduction of air, moist air, or steam to the molten salt. Mobilization tests were performed with argon, air and moist air using a classical transpiration apparatus designed for vapor pressure determinations.

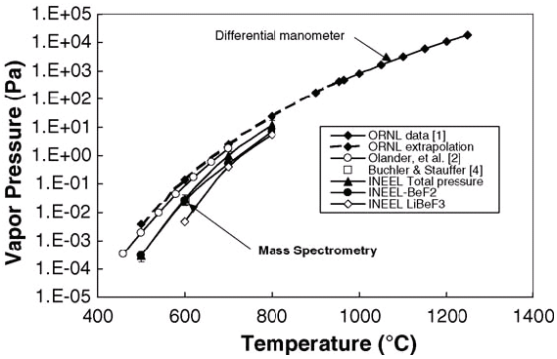

Fig. 2. Total pressure over Flibe.

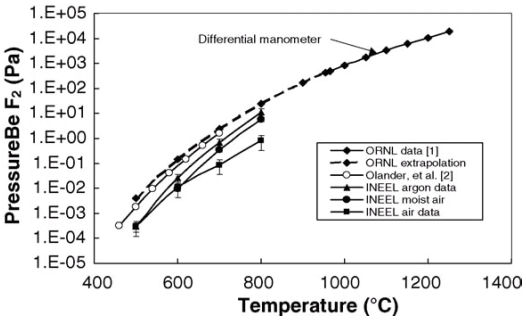

Fig. 3. BeF_2 pressure in various environments.

A schematic of the test system setup in an inert gas glove box is shown in Fig. 1. Flibe salt was tested in argon at temperatures of 500, 600, 700 and 800 ◦C at flow rates of 25, 50 and 100 sccm. Nickel crucibles were used for most tests; however, some tests were also run in glassy carbon crucibles. Tests with dry air were run at these four temperatures with flow rates of 25 and 50 sccm. Tests in moist air were run at 600, 700 and 800 ◦C with flow rates of 25 and 50 sccm.

The BeF_2 and $LiBeF_3$ partial pressures that were derived from the mobilized material

chemical analyses for the argon tests are plotted in Fig. 2 along with those from the previous studies and models. Total measured pressures for BeF_2 and $LiBeF_3$ are two to three times lower than predicted values. The increasing contribution from the lithium species in the INEEL data is apparent at 700 and 800C.

Partial pressures calculated for BeF_2 for all three test gases are shown in Fig. 3. The data for moist air parallels and are about one-half of those measured for the argon tests. The reason for the lower datum points in the dry air tests at 700 and 800 ◦C is not known. This trend is based upon limited tests and some repeated tests would be needed to confirm this trend. The data did not show any markedly different volatilization rates in dry and moist air compared to those in argon.

Mass comparisons using probe interior ICP-AES measurements and sample loss for the argon test series in the nickel crucibles showed that about 22% of the material was deposited in the probe. The remainder was deposited on the probe exterior and the walls of the test chamber. This reflects the diffusion and re-deposition of material down the temperature gradient. Mass flux calculation (kg/m h) obtained by adjusting ICP-AES measurements for the 22% factor generally agreed within a factor of two of the mass based determinations for individual tests.

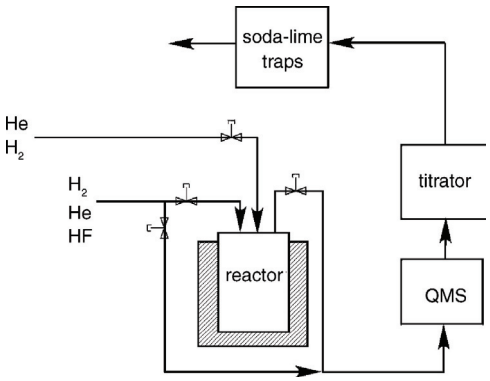

Fig. 4. test system for measureing redox kinetics

(c) REDOX control and corrosion

A series of experiments was performed in which HF was bubbled through Flibe with varying concentrations of dissolved Be to investigate the viability of using Be as a redox agent in a molten Flibe ($2LiF–BeF_2$) blanket. The objective of this work was to perform such measurements with the goal of obtaining useful kinetic data that could be used to quantitatively validate the feasibility of using Be as a redox agent in Flibe.

A simplified diagram of the system used for

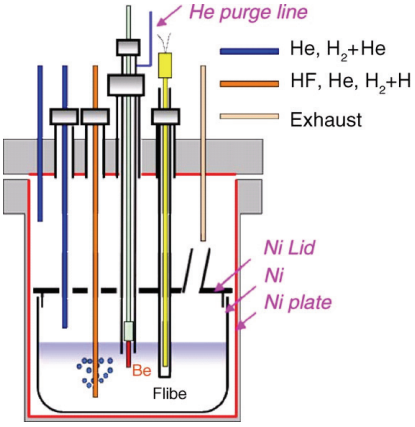

Fig. 5. Reactor for measuring redox

observing the HF–Be redox reaction is shown in Fig. 4. A mixture of H_2, He and HF gases was introduced into the test reactor, while the effluent passed through a quadrupole mass spectrometer (QMS) followed by an autotitrator. The reactor, shown in more detail in Fig. 5, was designed to provide a controlled reaction between Be and HF in the molten salt phase. The HF was introduced into the system via bubbling into the salt in a gas mixture that also contains H_2 and He. The H_2 is intended to minimize the likelihood of HF reacting with metal components in the system hardware. The He is a carrier gas so that the total actual flow rate was about 300 cm^3/min to minimize transport time to the QMS and titrator. A cylindrical beryllium rod, 0.76 cm in diameter and 3 cm in length was introduced into the salt for a specified period of time. A nickel tube containing a slow flow of He (~2–5 sccm) acted as a sheath to protect the Be specimen from contact with HF or salt (via capillary action) during times when it was not in the salt. All non-nickel metal surfaces inside of the reactor were spray coated with nickel to prevent HF from participating in corrosion-type side reactions.

Each experiment started with the HF–H_2–He feed gas bubbled into the salt with the Be specimen pulled out of the salt. Once the HF concentration in the effluent stabilized close to the expected level, the Be specimen was inserted into the salt. After 10–60 min, the Be was lifted out of the salt and into its protective housing while HF in the effluent was continually monitored for times ranging from several hours up to a few days. Once the HF concentration in the effluent had again stabilized, the next experiment was run by re-inserting the Be into the salt for a different duration. As shown in Fig. 6, the effluent HF concentration as measured by the QMS dropped rapidly usually within a matter of minutes after the Be

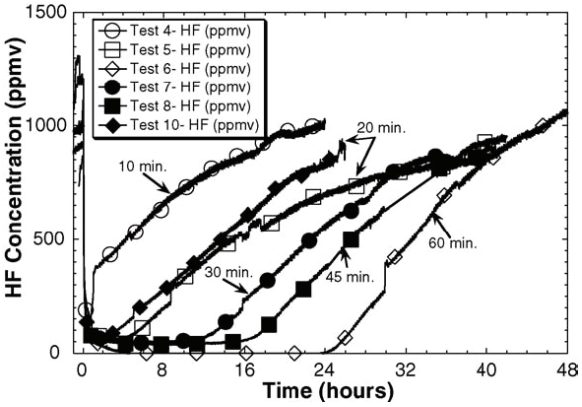

Fig. 6. HF concentration measured by QMS on the outlet of the REDOX experiment for several Be immersion times.

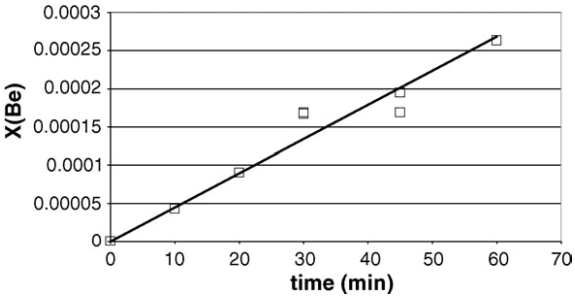

Fig. 7. Effects of immersion time on the initial mole fraction of Be in the salt

was initially inserted into the salt. The slow recovery of the effluent HF concentration after the Be was removed is believed to be the result of continued reaction of Be dissolved in the salt with HF added by ongoing gas injection.

The autotitrator data from the redox experiments were used to estimate the amount of Be that dissolved into the salt for each experiment. The results of the analysis are shown in Fig. 7, where mole fraction of Be in the salt is plotted versus immersion time. The linearity of the plot in Fig. 7 suggests a simple mass transfer mechanism with a high saturated concentration.

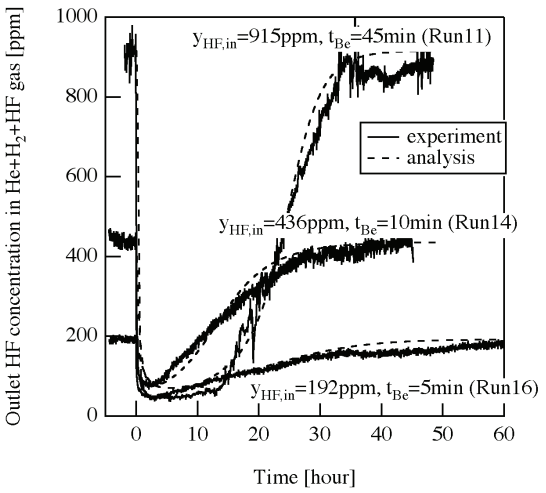

Fig. 8 Comparison between experiment and calculation for Flibe redox control

Fig. 8 shows the comparison of HF effluent curves from Flibe pot between experiment and caculation. Close agreement was obtained between them with use of proper values of a Be dissolution rate, the saturated Be solubility in Flibe, a reaction rate coefficient of $Be + 2HF = BeF_2 + H_2$.

Corrosion tests were also performed with and without REDOX control for samples of the advanced ferritic steel JLF-1 as seen in Fig. 9. The dissolution rates of Fe and Cr were suppressed by dipping Be into Flibe. However, their rates were increased when the Be rod was withdrawn from Flibe. Exposures of up to 500 hours in the non-flowing molten salt indicate a corrosion rate of 0.1μm/hr, with a Cr-rich oxide layer forming at the sample interface. Corrosion is effectively halted during periods of REDOX control using Be.

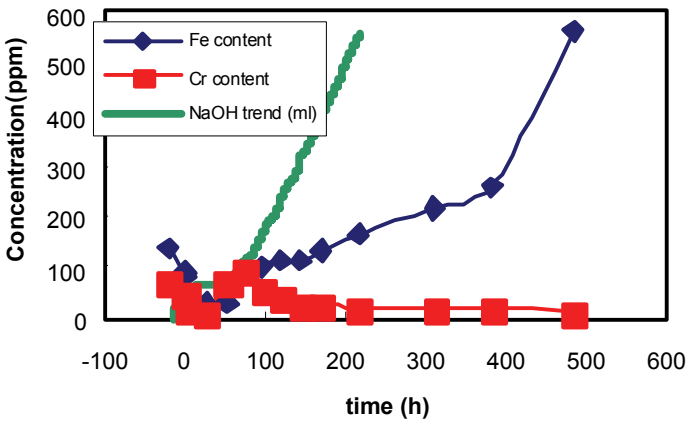

Fig. 9 Dissolution of JLF-1 to Flibe

(d) Deuterium/tritium behavior

In this study, deuterium transport experiments were

conducted in a cylindrically symmetric, dual probe permeation pot setup illustrated in Fig. 10. The assembly consisted of a type-316 stainless-steel pot, a nickel crucible for containing Flibe, two permeation probes of thin-walled nickel, a gas-manifold to enable Ar purge gas flow through assembly volumes, and a quadrupole mass spectrometer (QMS) for on-line measurements of the flow stream gas transport between the probes and the cover gas above the molten salt. Typically, with the pot at test temperature, probe-1 was pressurized with deuterium and QMS analysis of Ar gas from probe-2 provided a measure of the deuterium that permeated through the walls of probe-1, the molten Flibe and the walls of probe-2. The barrier volumes and the volumes above the salt were purged with separate Ar gas streams that were analyzed sequentially with the QMS.

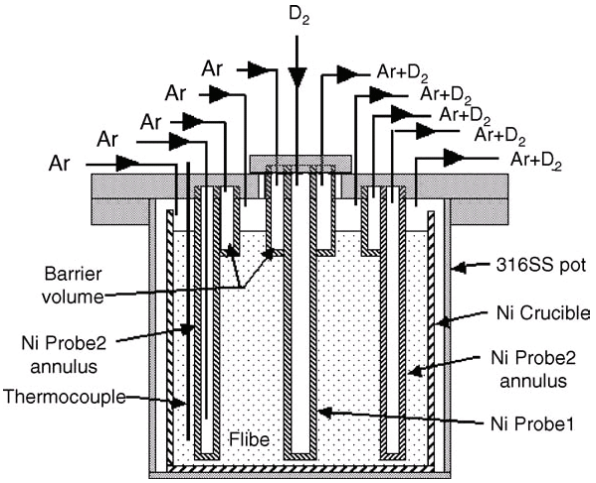

Fig. 10. Schematic illustration of cylindrically symmetric, permeation probe assembly.

Several deuterium permeation experiments were made with the system at temperatures of 600 and 650 ◦C and with a deuterium pressure of around 9.0×10^4 Pa in probe-1. TMAP-4 simulation calculations were used to evaluate the overall deuterium permeation rates in the Flibe/Ni/D_2 system using previous literature transport data for these materials. These analyses showed that diffusion in Flibe was rate-determining for our experimental conditions. Results of the analytical fit (by adjustment of diffusivity and solubility values) were compared to experimental data measured at 600 and 650 ◦C. Diffusion coefficients derived from

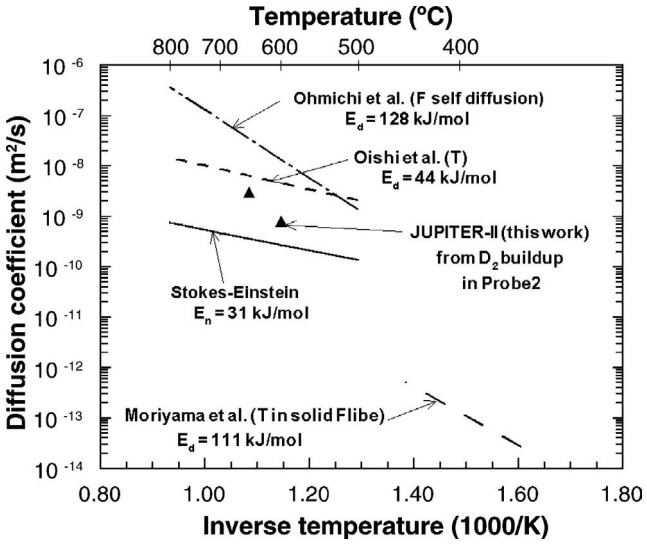

Fig. 11. Diffusion coefficients for Flibe.

these experiments are compared to previously published data in Fig. 11.

Solubility coefficients derived from these experiments were comparable to those for DF in Flibe, as reported by Field and Shaffer, rather than to those for H_2, D_2, reported by Malinauskas et al. These results suggest that the chemical potential of deuterium in the Flibe for the current experiments was greater than the chemical potential of D solute when the dominant species of deuterium in Flibe was D_2. This interpretation is consistent with previous experiments in which a significant overpressure of hydrogen was required to promote exchange reactions with TF in the salt and facilitate transport of tritium in the Flibe as HT. Thus, these results suggest that deuterium transport in the present experiments was mediated by the presence of a bond between D^+ and F^- in the molten salt.

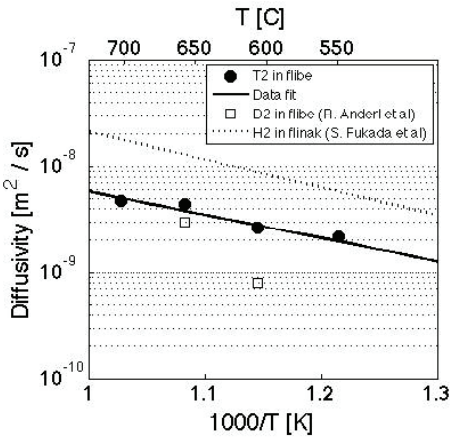

Fig. 12 Diffusivity of T_2 in Flibe

Diffusivity of T_2 in Flibe which redox condition is sufficiently controlled was determined for the first time. The result is shown in Fig. 12. The activation energy of T_2 in the redox-controlled Flibe was smaller than that of D_2 in the non-redoxcontrolled Flibe. This is because T_2 is the dominant species in the redox-controlled Flibe while DF is that in the non-redox-controlled Flibe.

3-1-4. Summary

The experimental program has been focused on addressing the key feasibility issues associated with the use of Flibe. Data have been gathered on purification of Flibe, deuterium transport in non-REDOX controlled Flibe, and Flibe mobilization under accident conditions. Most importantly, our REDOX experiments have indicated that Be is a good redox agent to control HF and suppress corrosion, and the kinetics at fairly high concentrations are rapid. The solubility and diffusivity of D_2 and T_2 in Flibe were successfully determined.

3-2 Task 1-1-B: Thermofluid Characteristics of Flibe Simulant

(T. Kunugi, T. Yokomine, M. A. Abdou, N. B. Morley)

3-2-1 Objectives of the Task

A molten salt coolant, Flibe, has attracted attention because high temperature stability and low magneto-hydro-dynamics (MHD) pressure drop are special concerns. However, there are some issues making Flibe-based blanket design challenging. The main issues include 1) low thermal conductivity of Flibe (1.0 W/mK), 2) high kinematic viscosity at temperatures close to the melting point (11.5 mm^2/s at 500 °C) and 3) to need an additional neutron multiplier because of the limitation of the tritium breeding capability of Flibe, and 4) the requirement of the structural material with temperature range over 650 °C. The high viscosity and low thermal conductivity put Flibe in the class of high Prandtl number fluids. In order to obtain sufficiently large heat transfer using high Prandtl number fluid coolant, high turbulence is required under a high magnetic field. Thus, it is important to investigate the effect of magnetic fields on the flow and heat transfer characteristics of the high Prandtl number fluids.

3-2-2 Participants to the Task

T. Kunugi, Z. Kawara (Kyoto U.)
T. Yokomine, S. Ebara (Kyushu U.)
S. Satake (Tokyo U. of Science)
S. Toda, H. Hashizume, K. Yuki (Tohoku U.)
Y. Yamamoto (Nagoya U.)
M. A. Abdou, N. B. Morley, J. Takeuchi, R. Miraghaie, S. Smolentsev, H. Huang, Y. Tajima, , T. Sketchley, J. Burris (UCLA)

3-2-3 Research Highlights

A pipe flow experimental facility called “FLiHy” (FLibe Hydrodynamics) was constructed at UCLA as shown in Fig. 1. The experimental facility consisted of a pipe flow loop with a transparent visualization section by using a Particle Image Velocimetry (PIV) system. Pure water and 30% aqueous solution of potassium hydroxide (KOH hereafter) were used as a working fluid for Non-MHD flow and MHD flow, respectively. The experimental approaches include flow and heat transfer measurements

using a Flibe simulant fluid along with a direct numerical simulation (DNS) by Satake et al. in *J. Turbulence* (2002) and the modeling by Smolentsev et al. in *Int. J. Eng. Sci.* (2002).

The flow facility utilizing water and electrically conducting fluid as a Flibe simulant was constructed, and turbulent flow field measurements using PIV and heat transfer measurements by Takeuchi et al. in *Fusion Eng Design* (2006) were carried out without magnetic field using water as a working fluid to establish the experimental techniques. The performance of this FLiHy facility for the non-MHD flows in pipe was verified with high accuracy compared with the existing experimental results by Eggels et al. in *J. Fluid Mechanics* (1994) and the DNS data by Satake et al. in *Lecture Notes in Computer Science 1940* (2000) as shown in Fig. 2.

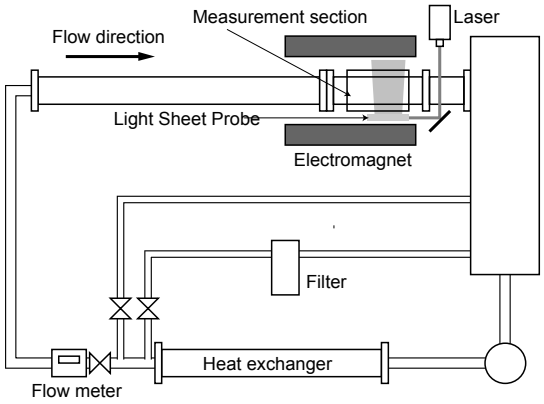

Fig. 1. Schematic drawing of FLiHy facility

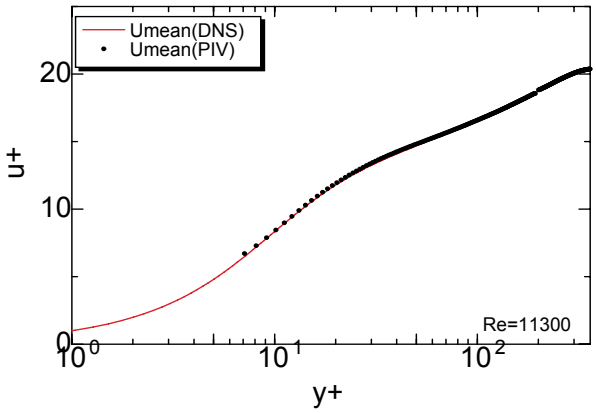

Fig. 2 Mean velocity distribution in case of Re=11300

As for MHD flow experiments, a magnet used for the current experiments produces maximum 2.0 Tesla magnetic fields in a narrow gap of the iron core at 3000 A of applied electric current. The pipe flow test section was placed in the gap which was 1.4 m in the streamwise direction, 25 cm in height, and 15 cm in width. The B field has uniform distribution within 5% variation for 1.0 m in the streamwise direction. The mean velocity measurements were performed for five different Hartmann numbers: Ha = 0, 5, 10, 15 and 20 (based on pipe radius) as shown in Fig. 3. The mean velocity profiles show that it becomes flatter as the Hartmann number increases in the core region of the flow, and that the near-wall velocity gradient increases with increasing of the Hartmann number: this shows the typical characteristics of the Hartmann flow. Figure 4 shows the streamwise-velocity fluctuation distribution in the radial direction for Re=5300. The intensity of the velocity fluctuation decreases with increasing of the Hartmann number. Thus, the application of the magnetic filed leads the turbulent flow to the laminar flow: this phenomenon usually calls a “Laminarization due to the Lorentz force.”

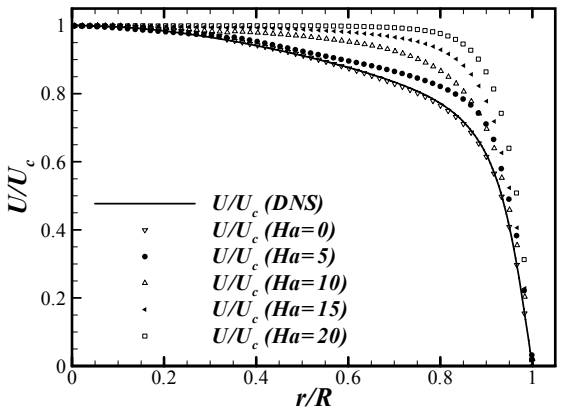

Fig. 3 Mean velocity distritution at Re = 5300

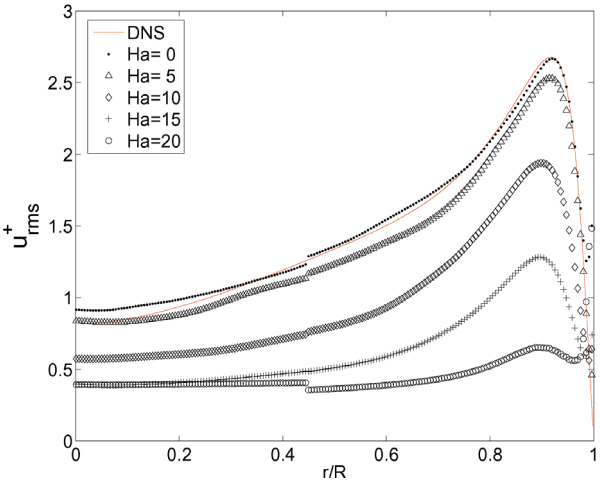

Fig. 4 Streamwise velocity fluctuation at Re=5300

As for the heat transfer experiments, a part of the test section of FLiHy loop was heated uniformly by heating tape under the constant magnetic field up to 2.0 Tesla. Forty T-type thermocouples with a diameter of 0.75 mm were fixed with high thermal conductivity grease (15 W/mK) in the holes of 1mm diameter at five axial stations and eight angles from the horizontal magnetic field. The depths of holes and the tube wall thickness were 4 mm and 5 mm respectively, i.e., the length from the inner tube surface to measuring point was 1mm. Temperature of KOH was monitored at both the inlet and the outlet of test section using thermocouples. The bulk mixing temperature of arbitrary cross section was estimated by the linear interpolation from the inlet and the outlet temperature. The radial temperature distribution of the fluid flow in the pipe was measured by means of thermocouples tower (TC tower) which was consisted of the Inconel sheathed K-type thermocouples with a diameter of 0.13mm arranged from the inner wall surface to the centre of the pipe as shown in Fig. 5. The 63% response time of this thermocouple was 2 ms. The angle of TC tower and magnetic field was set to 0 degree and 90 degrees. The Reynolds number based on bulk velocity and pipe diameter was set to 5000 and 20000 for Ha=0, 5, 10 and 15, and Pr=6 and 10. Figure 6 shows a non-dimensional mean temperature (T^+) distribution from the wall (y^+) in case of Re=9000. The solid line shows the existing correlation by Kader and the plots along the correlation corresponds to Ha=0, i.e., non-MHD flow. Other plots for Ha=5 and 10 are away from the correlation curve. This means that the temperature inside the pipe increases in case of MHD flows, i.e., this is another evidence of the laminarization of turbulent flow under the magnetic fields. Influence of the transverse magnetic field on the heat transfer is also to suppress as shown in Fig. 7.

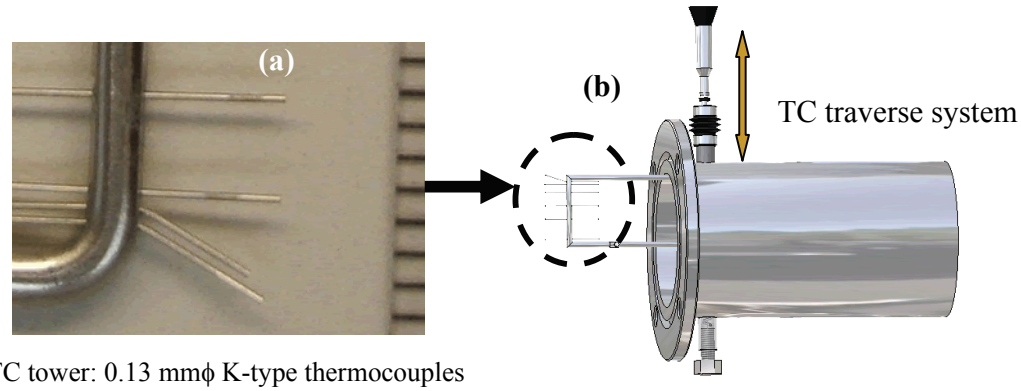

TC tower: 0.13 mmϕ K-type thermocouples

Fig. 5 Temperature measurement system inside the pipe: (a) TC tower equipment (b) Traverse system

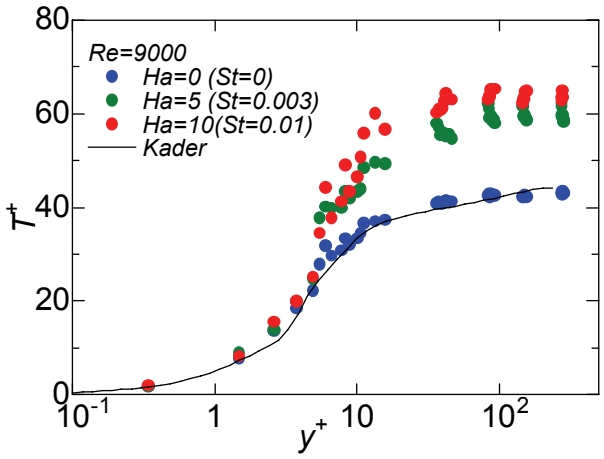

Fig. 6 Non-dimensional temperature distribution

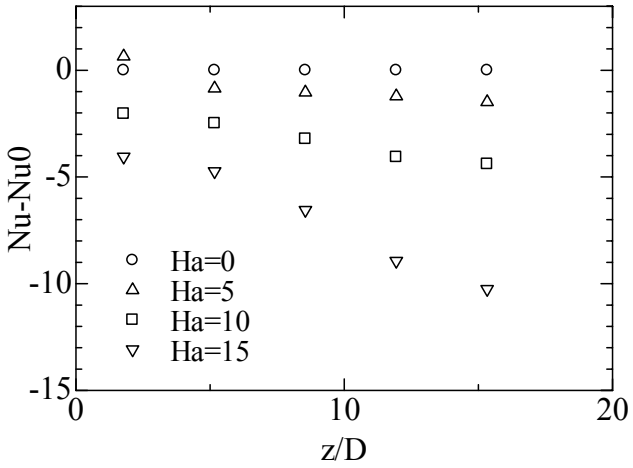

Fig. 7 Heat transfer deterioration in the case of Re=20000 and Pr=6.2

3-2- 4 Summary

The PIV measurement technique for non-MHD/MHD turbulent flows of Flibe simulant fluid was developed. The non-MHD turbulent flow measurements showed in very good agreement with the well established DNS database, so that the FLIHY loop was confirmed as a fluid dynamic experimental facility with high accuracy. By obtaining the two-dimensional two-component vectors map from the measurement of the MHD turbulent pipe flow, the change of the mean flow profile and the suppression of turbulence by MHD effects were shown. The heat transfer results showed its deterioration due to the magnetic field. The current MHD turbulent flow models will be able to revise based on these data.

3-3 Task 1-2A : MHD coating for V/Li systems

(T. Muroga and B.A. Pint)

3-3-1 Objectives of the Task

The objective of this task is to develop coatings to reduce the pressure drop associated with the magneto-hydrodynamic (MHD) effect that were compatible with Li at ~700°C. A strategy was laid out to evaluate bulk ceramics in static Li compatibility tests followed by development of coatings and evaluations in static Li and in flowing Li with a temperature gradient. Also carried out in this task were preliminary evaluation of irradiation effects of the coating and fundamental investigation on the interface structure and strength and mass-transfer in V-alloy substrate/coating/Li system.

3-3-2 Participants to the Task

T. Muroga, T. Nagasaka, T. Tanaka (NIFS), T. Terai, A. Suzuki, A. Sawada, Z. Yao (U. Tokyo), K. Abe, M. Satou, M. Fujiwara (Tohoku U.)
B.A. Pint, M. Li, P. F. Tortorelli (ORNL), A. Jankowski (LLNL)

3-3-3 Research Highlights

(a) Static immersion tests of candidate bulk ceramics

Figure 1 summarizes the bulk ceramic testing in static Li. The mass losses shown after 1000h exposures in Li reflect the degree of dissolution. The dissolution of CaO was observed. Calculations showed that the equilibrium solubility of Ca in Li increased dramatically with temperature, which was consistent with the high dissolution rates observed experimentally. Thus, the task focused efforts on Y_2O_3 and Er_2O_3.

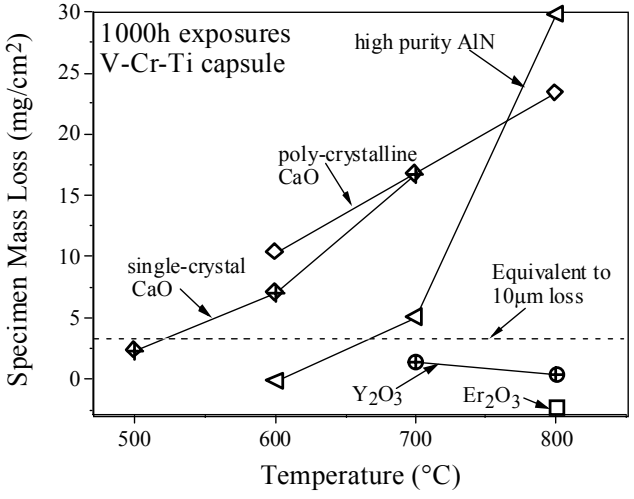

Figure 1. Mass losses after 1000h in a static Li capsule test as a function of temperature for candidate oxide and nitride materials. The dashed line shows the mass loss associated with the loss of ~10μm of coating in a 1000h exposure.

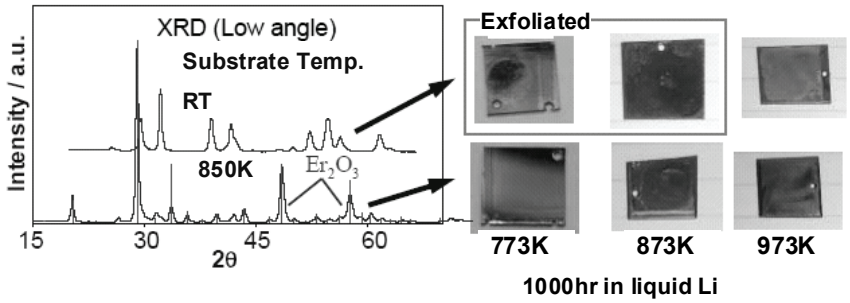

Figure 2. Change of Er_2O_3 coating on V-4Cr-4Ti by exposure to Li at 773, 873 and 973K for 1000 hr. The coating was made using Arc Source Plasma Deposition method with substrate temperature at RT and 850K. Crystalline structure of Er_2O_3 was observed only in the case of the high substrate temperature. Remarkable change was not observed in the coating at high substrate temperature after exposure to Li.

(b) Long term compatibility of single layer coating

The static Li immersion tests of bulk specimens identified Y_2O_3 and Er_2O_3 as promising candidate ceramics. Feasibility of the coating with Y_2O_3 and Er_2O_3 on V-4Cr-4Ti was demonstrated by EB-PVD, Arc Source Plasma Deposition and RF sputtering. Especially, Er_2O_3 fabricated with Arc Source Plasma Deposition showed good corrosion resistance as shown in Figure 2. By deposition on a substrate at higher temperature, high crystalline Er_2O_3 coating was produced, which were shown to be stable in Li to 1000hr at 973K.

(c) In-situ resistivity of two-layer coatings

Coating development focused on Y_2O_3 and Er_2O_3 and then on these coatings with a vanadium overlayer. While mass loss is one measure of performance, the principal figure of merit is resistivity. Therefore, the resistivity of bulk materials and coatings also was measured, Figure 3. For the coatings, an in-situ test was developed to measure the resistivity of the coating in contact with Li. These tests, along with static Li

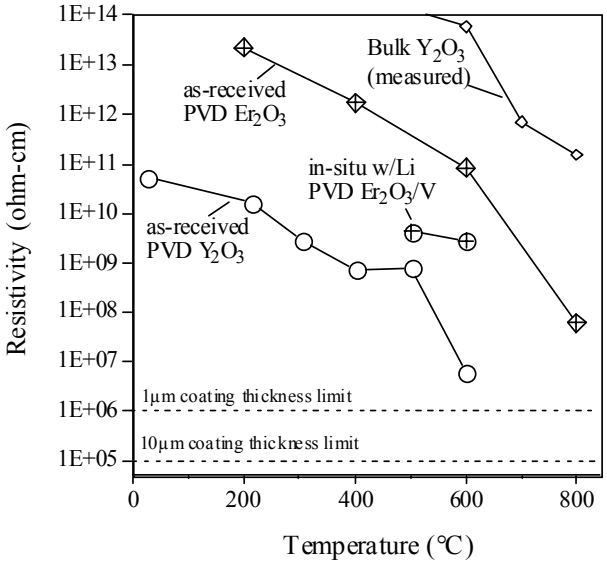

Figure 3. Resistivity as a function of temperature for as-received EB-PVD Er2O3 and Y2O3 coatings, in-situ Er2O3/V coatings and literature and measured values for bulk Y2O3 and bulk Y2Ti2O7. Minimum required coating values are shown for reference.

exposures, revealed that a single-layer oxide coating was not performing well and that multi-layer coatings showed superior performance.

(d) Impurity transfer of V-4Cr-4Ti alloy during liquid lithium exposure

Figure 4 shows impurity contents, tensile stress and elongation of US (US-832665) and Japanese (NIFS-HEAT-2) heats of V-4Cr-4Ti as a function of exposure time to Li at 1073K. Remarkable difference in the rate of N enrichment and O depletion is seen between the two alloys.

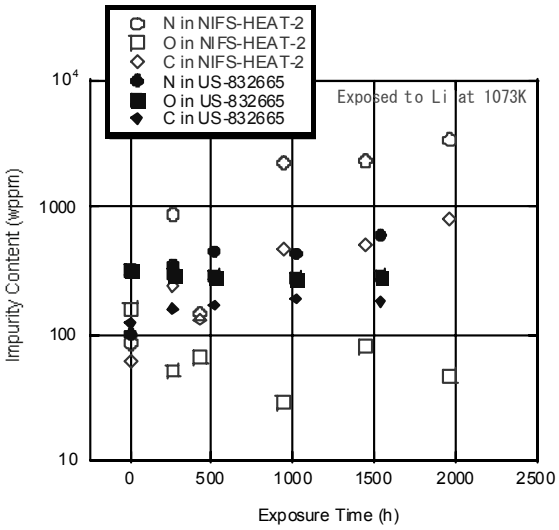

Figure 4. Impurity contents, (b) tensile stress and (c) elongation of US (US-832665) and Japanese (NIFS-HEAT-2) reference V-4Cr-4Ti alloys as a function of exposure time to molten Li at 1073K

However, the total and the uniform elongation of the both alloys saturated around 20% and 10%, respectively. The difference in the impurity transfer of the two alloys may be attributed to the difference in the sample thickness, 3 mm for US-832665 and 0.25 mm for NIFS-HEAT-2.

(e) Thermal convection tests

Monometallic, thermal convection loop test with flowing Li (~2cm/s) and a thermal gradient (~400°-700°C) was carried out. The loop was constructed of V-4Cr-4Ti tubing and contained specimens of V-4Cr-4Ti including several with Y_2O_3 /V MHD coatings. The loop operated for 2,350h in a vacuum chamber with a pressure of $<10^{-5}$Pa during operation. The experiment required the development of specialized control and temperature monitoring systems.

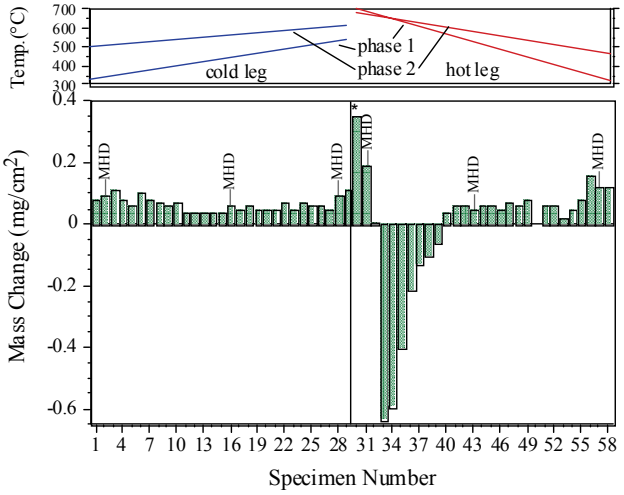

Figure 5. Specimen mass gain for V-4Cr-4Ti specimens in the hot and cold leg of the mono-metallic loop along with the nominal temperature that the specimens saw during the two phases of operation. In the hottest section of the loop, mass losses were observed, elsewhere, small mass gains were measured.

The initial results of the loop test showed no significant thickness loss from the MHD coatings and limited (<1μm) mass transfer of vanadium, Figure 5. Interstitial mass transfer was observed with O being removed in the hottest section and C and N increase in the rest of the specimens. (This explains the small mass gains in most of the specimens, Figure 5.) Further characterization of the MHD coatings and V-4Cr-4Ti specimens will be conducted.

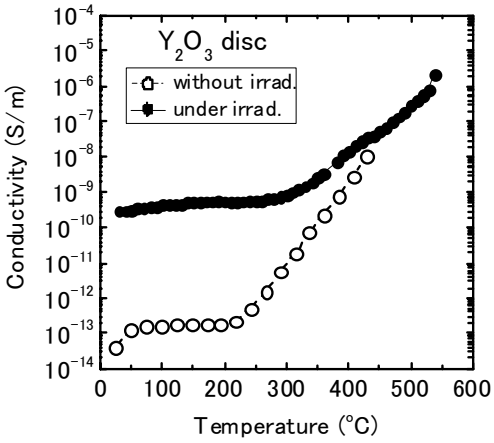

Figure 6. Temperature dependence of conductivities without and under gamma-ray irradiations for bulk specimens.

(f) Evaluation of adhesive property of the MHD coating

Y_2O_3 coating was successfully made on vanadium alloys by means of DC-sputter coating. To evaluate reliability of the coating, adhesive property was measured by scratch test. The Weibull analysis of the shear strength of the interface between yttrium oxide coating and vanadium alloys made by DC-sputter coating indicated that small additions of yttrium to V-4Cr-4Ti would improve adhesive property of the interface between yttrium oxide coating and vanadium alloys.

(g) Radiation effects

Radiation-induces conductivity of bulk and coating of Y_2O_3 and Er_2O_3 was evaluated by irradiations with D-T neutrons (FNS), fission neutrons (JMTR) and gamma-rays. Relative to the temperature effects of the resistivity, the irradiation effects were shown to be negligible as shown in Figure 6. Neutron irradiation of bulk Y_2O_3 and Er_2O_3 specimens in Li environments was carried out in HFIR-17J. No significant corrosion loss was observed at 425°C.

3-3-4 Summary

For the purpose of developing MHD coating for V/Li system, evaluations of a wide range of ceramic candidate materials were carried out and several were selected for coating development: Y2O3, Er2O3 etc. Technology for single and double coating fabrication was developed. Characterization of the coating by static and loop tests showed superior performance of the double layer coating.

3-4 Task 1-2-B: Vanadium Alloy Capsule Irradiation

(T. Muroga, H. Matsui, R.J. Kurtz, G.R. Odette)

3-4-1 Objectives of the Task

In this task, irradiations of vanadium alloys and MHD coating candidates in Li-filled capsules were carried out in HFIR for the purpose of studying the irradiation performance of structural components of V/Li blankets. The experimental objectives are to a) investigate the effect of trace elements C, O, and N and minor alloying elements Y, Al, Si on the properties of vanadium alloys irradiated at 425 and 600°C, b) study general aspects of deformation, fracture, and irradiation creep at irradiation temperatures of 425 and 600°C, c) examine the irradiation performance of weld joints of vanadium alloys mostly at 425°C, d) explore the fundamental effects of neutron irradiation on bulk ceramics relevant to MHD insulator coatings associated with Subtask 1-2-A, and e) perform a limited investigation of helium effects on mechanical properties of vanadium alloys using B-doping simulation techniques. Also carried out were out-of pile thermal and environmental control tests.

3-4-2 Participants to the Task

T. Muroga, T. Nagasaka (NIFS), K. Fukumoto (Fukui U.), H. Matsui, K. Abe, M. Satou, H. Kurishita (Tohoku U.), H. Watanabe, N. Yoshida, (Kyushu U.) S. Ohnuki (Hokkaido U.)
R.J. Kurtz, D.S. Gelles, M.B. Toloczko (PNNL) D.T. Hoelzer, M. Li, S.J. Zinkle (ORNL), G..R. Odette, T. Yamamoto (UCSB)

3-4-3 Research Highlights

(a) Environmental effects on irradiation creep of V-4Cr-4Ti irradiated by neutrons

The objective of this study is to investigate the effect of environment on irradiation creep properties of high-purified V-4Cr-4Ti alloys, NIFS-HEAT2 irradiated by neutrons. In order to examine the effect of environment on irradiation creep pressurized creep tubes (PCTs) were enclosed in Li-filled capsules and irradiated in HFIR to 3.7 dpa at 425 and 600°C. The results were compared to similar specimens enclosed in Na-filled capsules irradiated in JOYO.

It was found that the creep strain rate exhibited a linear relationship with the effective stress up to 150 MPa at 425°C as shown in Fig. 1. At 600°C the data were scattered but the creep strain was much larger than that at 425°C.

The activation energy of irradiation creep was estimated to be 46kJ/mol·K. No significant difference in irradiation creep behavior between liquid sodium and liquid lithium environments was observed.

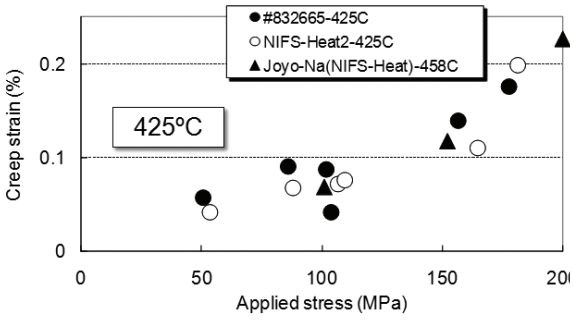

Figure. 1 Creep strain vs. applied stress for US832665 and NIFS-Heat 2 in HFIR Li capsule and Joyo Ba-capsule

(b) Compression Testing of Un-irradiated and Irradiated V-4Cr-4Ti

To understand the effect of stress state on the propensity for localized deformation in vanadium alloys, compression specimens, fabricated from Heat 832665 and NIFS-1 heats of V-4Cr-4Ti, have been tested before and after irradiation in the High Flux Isotope Reactor at 425°C and 600°C to ~3.7 dpa. Specimens were tested before and after irradiation at temperatures of 25°C, ~250°C, and ~425°C. Unirradiated yield strength values in compression are similar to uniaxial tensile yield strength values found in the literature, see Figure 2. Irradiation at 425°C to ~3.7 dpa more than doubles the compressive yield strength of both alloys at test temperatures of 25°C and 425°C. The increase in yield strength is due primarily to production of unshearable defect clusters and precipitates. Microstructural studies on interrupted compression tests are underway to determine the effect of stress state on deformation behavior as a function of compressive strain.

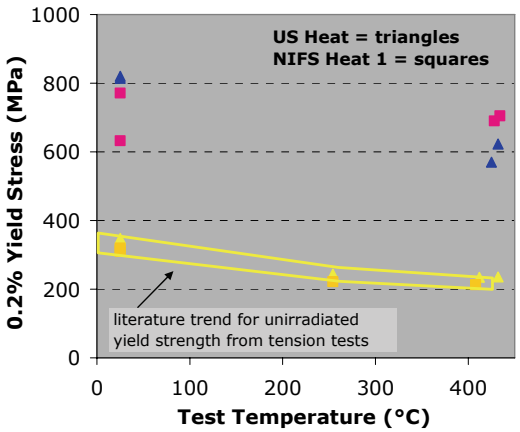

Figure 2. Comparison of compressive and tensile yield strengths for two heats of unirradiated V-4Cr-4Ti. Irradiation to ~3.7 dpa at 425°C increased the compressive yield strength by more than a factor of two.

(c) Self-Consistent Constitutive Laws for Flow Localization-Ductility Loss in Irradiated Vanadium Alloys

A self-consistent approach to derive constitutive properties [σ(ε)] and corresponding plasticity rules of vanadium alloys over a strain range beyond the low-uniform ductility limit, especially after the irradiation, has been developed.

The basic approach is to simultaneously measure load (P)-displacment (Δ) curves and large geometry changes (LGC) in subsized flat dogbone tensile specimens (both with and without side notches and center holes), in cone indentation tests, and three or four point bending tests. Confocal microscope/ topological mapping and/or surface microimage analysis/strain mapping techniques are used to observe LGC. An example of LGC measurements for a flat tensile specimen at various points in the load-elongation curve is shown in Figure 3. Experimental measurements of LGC are compared to corresponding predictions obtained from finite element models, iterating to arrive at an optimally self-consistent input σ(ε) and corresponding plasticity rules. The technique has been successfully applied to irradiated flat tensile specimens of V-4Cr-4Ti and F82H steel. An experimental setup to map strains around a center hole or a side notch in a specially designed tensile specimen has also been developed.

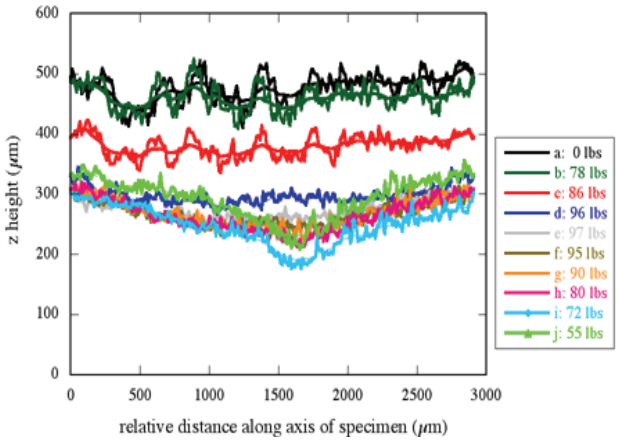

Figure 3. Large geometry change mapped on a flat tensile specimen under various loading conditions.

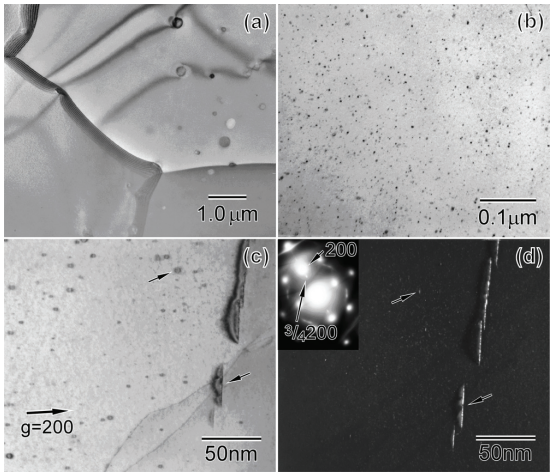

Figure 4. TEM micrographs showing Ti(CON) precipitates that formed in V-4Cr-4Ti following a final anneal at (a) 1000ºC for 2 h and (b-d) 1300ºC for 1 h.

(d) Improved Thermo-mechanical Treatment Developed

The determination of ~1300ºC as the solvus temperature for Ti(CON) precipitates in V-4Cr-4Ti resulted in the establishment of a thermal-mechanical treatment (TMT) that redistributes the Ti solute atoms and O, N, and C interstitial atoms from an

inhomogeneous distribution of a low number density of coarse globular-shaped Ti(CON) precipitates to a more homogeneous distribution of a high number density of nano-size plate-shaped Ti(CON) precipitates as shown in the TEM micrographs in Figure 4. The plate-shaped Ti(CON) precipitates have a {100} habit with the matrix and obey the diffraction imaging contrast that is characteristic of dislocation loops that have a Burgers vector of b = a<100> with large stresses normal to the plate in the matrix. The modified TMT that produces the high number density of plate-shaped Ti(CON) precipitates and cold-work induced dislocations also improves the high temperature strength properties of V-4Cr-4Ti compared to the conventional TMT that consists of a final annealing at 1000ºC for 1 to 2 hours and produces an inhomogeneous distribution of larger globular Ti(CON) precipitates as shown in Figure 5.

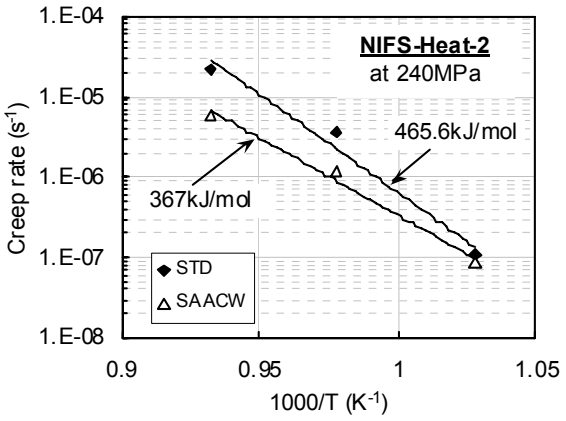

Figure 5. The reciprocal temperature dependence of creep rate for NIFS-Heat-2 tested at 240 MPa using different TMT. Standard (STD): 1000 ºC 2h; Solution-annealed, aged and cold-worked (SAACW): 1100 ºC 1h+600ºC 20h+20%CW.

(e) Development of V-Cr-Ti Type Alloys with Small Additives for Fusion Applications

Results from oxidation experiments with controlled oxygen partial pressures in helium gas flow at elevated temperatures indicated that addition of 0.2 wt.% of yttrium to the V-4Cr-4Ti alloy decreased the diffusion coefficient of oxygen by an order of magnitude. Yttrium in solution aids the formation of a protective layer against oxidation. Results from indentation fracture toughness tests showed that the oxidation layer formed on a V-4Cr-4Ti-0.2Y alloy had more than five times greater fracture toughness (K_{Ic}) compared to that of the V-4Cr-4Ti alloy. The depth profile of the hardness and weight change after oxidation indicated that the oxidation layer of the V-4Cr-4Ti-0.2Y alloy was denser and thinner than that of the V-4Cr-4Ti alloy. The results suggest that yttrium improves oxidation resistance of the alloy by reducing oxygen diffusion and by forming a tough protective layer. Improvement of compatibility with various environments including oxidation should reduce the effects of gaseous impurity pick-up during fabrication, thermo-mechanical treatment and reactor operations.

The tensile properties of V-4Cr-4Ti and V-4Cr-4Ti -0.1SiAlY irradiated in HFIR at 425°C to ~3.7 dpa are shown in Figure 6.

In the case of V-4Cr-4Ti-Si-Al-Y type alloys, the uniform elongation is larger and the yield stress is lower than for the V-4Cr-4Ti alloy.

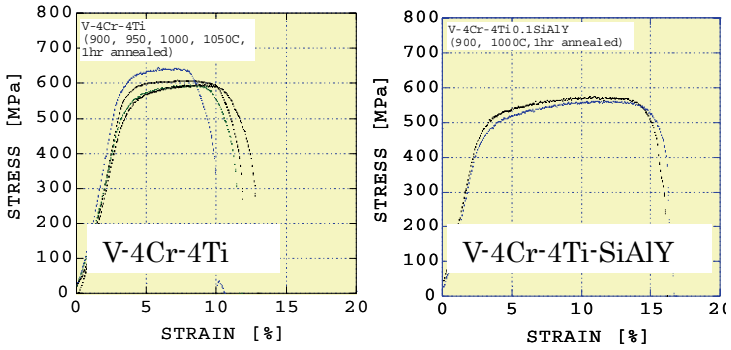

Figure 6. Tensile properties of V-4Cr-4Ti and V-4Cr-4Ti-0.1SiAlY irradiated in HFIR at 425°C to ~3.7 dpa.

The differences probably represent scavenging of interstitial impurities (C,O, and N) by small amounts of Si,Al, and Y. It is possible that the differences correspond to microstructural evolution during irradiation, such as irradiation-enhanced precipitation.

(f) Development of a Semi-Automated Small Specimen Fracture Testing Instrument

A semi-automated device for performing fracture tests on small pre-cracked bend bars has been developed. The overall test device consists of. a) an indexed specimen cartridge positioning stage, b) two types of test fixtures for dynamic and static loading, c) a loading device for easy specimen insertion, d) a gas blanket temperature control system, and e) a load-time-displacement instrumentation and data acquisition system. The dynamic loading station consists of a high-power, high-speed stepper motor driving an instrumented TUP on a lever arm. Nine bend bars with allowable dimensions ranging from ≈1.65x1.65x8mm to 3.3x3.3x18 mm are loaded in a testing cartridge with the long specimen axis vertical so that the loading resembles an IZOD impact test. The instrument has been extensively calibrated and validated by comparison to data from tests from drop tower instruments both in the U.S. and in Japan.

3-4-4 Summary

The Li-capsule irradiations on vanadium alloys in HFIR were carried out. Radiation effects on candidate vanadium alloys with respect to mechanical properties including creep properties and compression properties, trace and minor alloying effects were clarified, enhancing the feasibility of vanadium alloys for V/Li blankets. PIE of irradiated specimens are being continues both in the US and Japan by their domestic programs.

3-5 Task 2-1 : SiC/SiC Fundamentals and Material Processing

(T. Hinoki and Y. Katoh)

3-5-1 Objectives of the Task

The objectives of Task 2 is to demonstrate feasibility of high efficiency gas cooling blanket system using advanced SiC/SiC composites based on new material design and development strategies and by evaluating thermo-mechanical properties and irradiation resistance of the material system. Materials design and fabrication, fundamental properties evaluation, and micromechanical constitutive modeling of materials behavior were studied in Subtask 2-1. In aid of other subtasks, design, fabrication, and supply of adequate SiC/SiC composites were also performed in Subtask 2-1. Thermo mechanics, compatibility and heat transfer performance of the model gas blanket systems, comprising SiC/SiC structure and ceramic breeder pebbles were studied in Subtask 2-2. Based on the material development and the thermo-mechanical analysis, radiation behavior of the advanced SiC/SiC composites and elements of solid breeding blanket systems in high temperature environment were studies in Subtask 2-3.

The scope of Task 2-1 is followed;

- Baseline properties
  - Perform thermal conductivity assessment and modeling
  - Develop high thermal conductivity CVI composites
  - Develop appropriate test techniques
- Joining and hermetic sealing
  - Design hermetic materials
  - Develop robust joining technique
- Process development / optimization
  - Optimize FCVI Process
  - Develop alternate processes
- Materials supply
  - Supply composite materials to other subtasks

3-5-2 Participants to the Task

T. Hinoki, A. Kohyama, T. Nozawa, S. Kondo, H. Kishimoto (Kyoto U.) A. Hasegawa, (Tohoku University), T. Shibayama (Hokkaido U.)

Y.Katoh, L.L.Snead, B.A. Pint, S.J. Zinkle, E. Lara-Curzio, H-T. Lin, R.A. Lowden, G.C. McLaughlin (ORNL) C.H. Henager, Jr., G.E. Youngblood, R.H. Jones, C.A. Lewinsohn (PNNL)

3-5-3 Research Highlights

Extensive R&D efforts for development and characterization of advanced SiC/SiC composites for fusion have been successfully carried out in Task 2-1. The FCVI process using high purity SiC fibers was optimized and density, mechanical properties and uniformity were improved significantly. Figure 1 shows multilayer fiber/matrix interphase of reduced C and SiC and fracture surface of the composites. Complicated fracture at the fiber/matrix interphase increased utimate tensile strength. Advanced small specimen test technologies and procedures for mechanical properties of SiC/SiC were developed. Joining and hermetic sealing using of NITE SiC/SiC and CVI / NITE hybrid process has been explored. The robust joining technique using NITE joint was successfully developed and evaluated. The optimized composite samples were produced and supplied to irradiation experiments. Refractory coating technique for SiC and SiC/SiC composites was also developed by infrared transient liquid phase processing. The tungsten armored silicon carbide samples proved uniform, strong, and capable of withstanding thermal fatigue testing. Guidance was provided for selection of appropriate materials for the pebble-bed thermo-mechanics experiments.

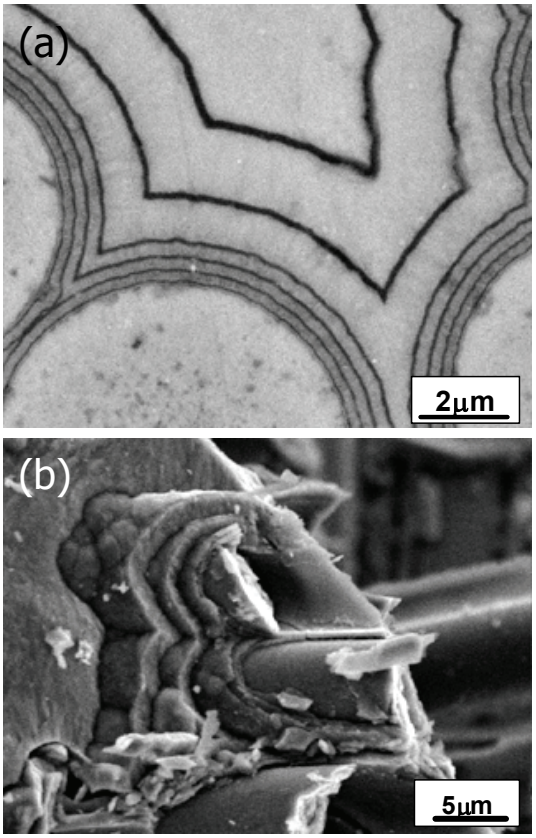

Figure 1: A SEM image of multilayer (C/SiC) fiber/matrix interphase (a) and fracture surface of the composites (b)

Anisotropy of SiC/SiC composites was characterized by transthickness tensile test, diametral compression test and shear test using double-notched specimens in adition to basic tensile test. The diametral compression experiment for SiC/SiC composites was newly developed as shown in Figure 2 and size effect was also evaluated. Progress has been achieved in the areas of fracture toughness evaluation and

interfacial shear properties characterization for advanced SiC/SiC composites, and chemical compatibility of SiC in dual-cooled blankets. The fracture behavior of advanced SiC fiber composites with chemically vapor-infiltrated (CVI) and nano-infiltration and transient eutectic-phase (NITE) SiC matrices were successfully evaluated by bend testing of single edge notched beam (SENB) specimens. Based on that, J-integral analysis of SENB fracture was selected as a standard test method for post-irradiation examination of 18J specimens. For the interfacial characterization, methods to explicitly determine debond and frictional shear stresses at fiber/matrix interfaces by single fiber push-out experiments were developed. Additionally, static compatibility testing of high purity monolithic SiC and advanced SiC/SiC composite materials in liquid lead-lithium was performed in support of dual-cooled blanket R&D, providing another promise of those materials systems.

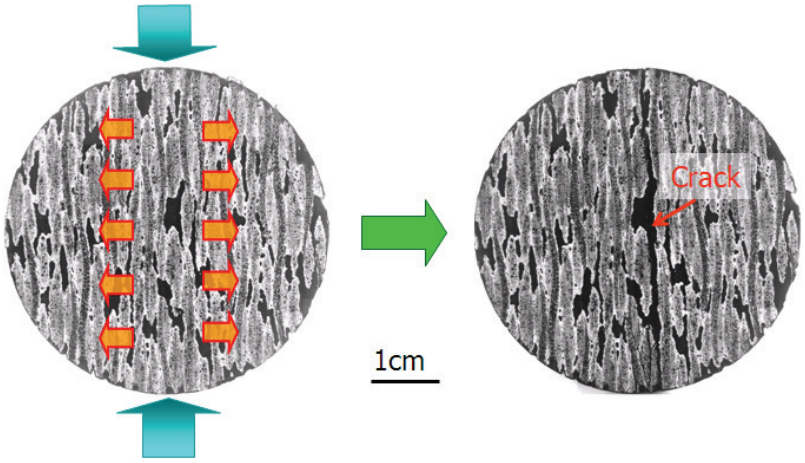

Figure 2: Procedure of diametral compression test with SEM images of SiC/SiC composites before and after the experiment

Following is achivement overview of Task 2-1;

- Extensive R&D for development and characterization of advanced SiC/SiC composites for fusion have been successfully carried out in JUPITER-II Task 2-1.
- Developed radiation-resistant CVI SiC/SiC composites
  - ☑ Optimized FCVI process was developed.
  - ☑ Advanced radiation resistant interphase was developed.
  - ☑ Advanced high thermal conductivity composite was demonstrated.
- Pursued advanced joining, coating and hermetic materials
  - ☑ Robust joint of SiC/SiC by NITE process was studied.
  - ☑ Tungsten coating technique for SiC materials were developed by infrared transient liquid phase processing.
  - ☑ Hermetic, high performance CVI / NITE hybrid composite was

developed.

- Developed advanced evaluation methods and test procedures
  - ☑ Small specimen test technologies were developed to generate engineering property data for advanced SiC/SiC.
  - ☑ Anisotropic mechanical properties were characterized.
  - ☑ Predictive capability for anisotropic thermal conductivity of woven fabric, CVI SiC/SiC composites was developed.
  - ☑ Enabled advanced interactions with design activities
- SiC - breeding materials compatibility
  - ☑ Chemical compatibility of SiC with various lithium oxide ceramics was studied.
  - ☑ Static compatibility of SiC and SiC/SiC with Pb-Li was studied.
  - ☑ Chemical compatibility of SiC with ceramic and liquid metal breeders was positively addressed.
- Materials supply and guidance
  - ☑ Guidance was provided for the maximized value of irradiation and thermo-mechanics experiments.
  - ☑ Various composite materials were designed, produced, and supplied to irradiation experiments.
- Academic and educational impact
  - ☑ Greater than 35 peer-reviewed papers were published.
  - ☑ ~10 PhD and MS students were involved.

3-5-4 Summary

Task 2-1 functioned as a utility vehicle for entire Task 2 very effectively. Moreover, Task 2-1 represented ideal collaboration between two countries.

3-6 Task 2-2 : SiC System Thermomechanics

(A.Shimizu and A.Ying)

3-6-1 Objectives of the Task

The high temperature gas cooled solid blanket concept aims to obtain the outlet coolant temperature equivalent to or higher than HTGR. There exist two typical designs for it, namely DREAM and ARIES-I. In the former, both heat and tritium generated in the blanket are extracted by a single helium flow while they are, in the latter, recovered separately by flows for each. Although the DREAM design can simplify the blanket structure, the problem of how to recover the low partial pressure tritium from high temperature/pressure helium has not been solved yet.

Meanwhile, the purge gas in the ARIES-I design must be of low pressure and velocity in order to ensure higher tritium exit density so that generated heat must be transported to the coolant only by thermal conduction and radiation through the packed layer. Each candidate breeder material has limited operating temperature window, for instance between 673 and 1193 K for Li_2TiO_3, so that allowable temperature difference within the blanket is only of 100 K order. Meanwhile, the packed pebble layer has essentially poor apparent thermal conductivity due to small pebble-to-pebble contact area so that overall heat transfer performance between breeding zone and coolant is affected strongly by thermomechanical interactions between pebbles as well as between SiC_f/SiC clad and pebbles. In addition, the stresses generated from differential thermal expansion between pebbles and SiC/SiC_f containment structure, and/or the irradiation swelling of pebbles may break the particles and endanger safe blanket operation.

Based on these, main efforts of the task 2-2 were directed towards clarification of thermomechanical characteristics of the pebble bed layer cladded within SiC plates.

3-6-2 Participants to the Task

A. Ying, M. Abdou, A. Abou-Sena, J. An and T. Sketchley (UCLA), Y. Katoh (ORNL), A. Shimizu and T. Yokomine (Kyushu Univ.), A. Hasegawa (Tohoku Univ.), A. Kohyama (Kyoto University)

3-6-3 Research Highlights

In the first stage, thermal hydraulic analysis was performed for the DREAM type blanket in which 10 MPa helium enters the module of single size pebble bed with a

typical packing density of 62%. The distinct feature of velocity overshooting near the containing wall was well simulated by adapted simulation code. Although the helium flow becomes slightly stagnant behind the partition membrane plate, it does not cause a significant increase in the temperature so that the calculated maximum temperature of 1191 K at the outlet was kept well below the allowable level.. It was concluded, therefore, that the thermal-hydraulic design of the DREAM type blanket is easy compared to that of ARIES-I type blanket.

The second subject was the thermomechanical characteristics of the pebble bed layer. A cylindrical pebble bed test assembly was constructed for that purpose in which ceramic lithium orthosilicate pebbles were enclosed between two CVD SiC plates that were fixed at their circumference. The deformations of the top SiC plate, with respect to temperature rise, were measured and the results reflected the amount of bending of the SiC plate under the effect of differential thermal stress and the applied constrained mechanical boundary. Main observations are as follows.

•Even the small thermal stress was significantly magnified at the particle/wall and particle/particle contacts as a result of small contact areas. This caused a thermal creep to occur as the deformation decreased as the bed temperature was kept at a constant value. As the creep was initiated, both the stress magnitude and the creep rate were reduced. The creep evolution process was found to depend significantly on the temperature level.

•The numerical simulation by DEM was able to capture the trend of the experimental data concerning thermal creep characteristics. However, the absolute values would still need to be resolved by finding the correct material properties.

•Experimental data confirmed that a different set of consecutive equations other than those obtained from the uni-axial experimental results is needed to better describe ceramic breeder thermomechanical properties under prototypical thermo-mechanical loading conditions.

3-6-4 Summary

The task 2-2 has broadened the understanding of pebble bed material system thermomechanics and its impact on the use of SiC/SiC structure in a helium-cooled ceramic breeder blanket concept. The interface conductance was found not to be a fixed value but varies according to pebble bed thermomechanical state and design associated mechanical boundary conditions. The thermal stress induced by the differential thermal expansion between the SiC structural clad and the ceramic breeder pebble bed may

crack the pebbles and cause the clad to be separated away from the pebble bed. This can form a gap at the interface and increase the breeder temperature even more. This makes a design that based on the ARIES-I concept more challenging.

The design based on the DREAM concept reduces the above concern, where heat generated inside the breeder bed is removed by the forced convection (rather than conduction as in the ARIES-I case.) However, a cost-effective tritium extraction technology from the high temperature helium stream is needed in order to make this concept attractive.

SiC/pebble bed thermomechanics test set-up with Keyence laser position system for displacement measurement

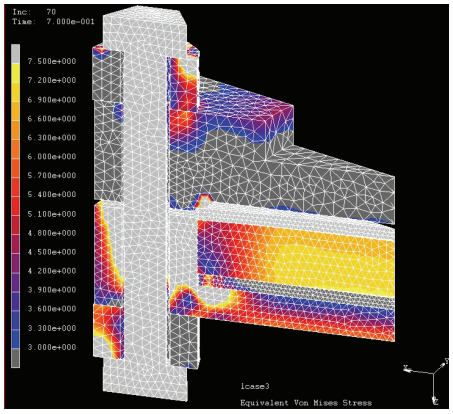

FEM simulation of SiC/Li_2TiO_3 pebble bed thermomechanics at 800C. Calculated differential stress

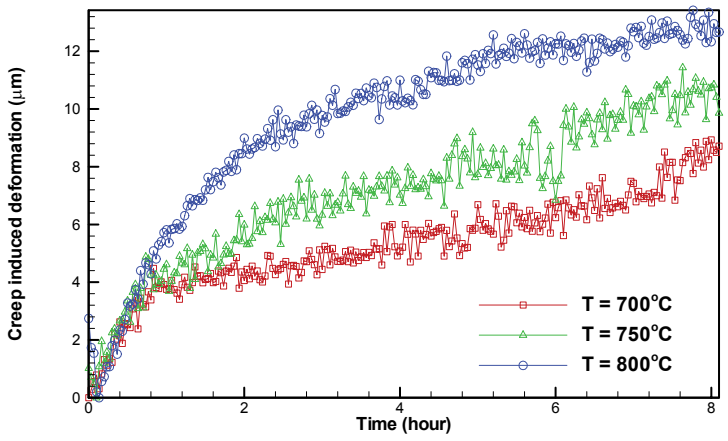

Temperature effects on SiC/Li_4SiO_4 pebble bed thermal creep characteristics

Figure 1 Example Task 2-2 SiC/pebble bed thermomechanics activities/results

3-7 Task 2-3 : SiC Capsule Irradiation

(A.Hasegawa and Y.Katoh)

3-7-1 Objectives of the Task

The objectives of Task 2 is to demonstrate feasibility of high efficiency gas cooling blanket system using advanced SiC/SiC composites based on new material design and development strategies and by evaluating thermo-mechanical properties and irradiation resistance of the material system. Materials design and fabrication, fundamental properties evaluation, and micromechanical constitutive modeling of materials behavior were studied in Subtask 2-1. In aid of other subtasks, design, fabrication, and supply of adequate SiC/SiC composites were also performed in Subtask 2-1. Thermo mechanics, compatibility and heat transfer performance of the model gas blanket systems, comprising SiC/SiC structure and ceramic breeder pebbles were studied in Subtask 2-2. Based on the material development and the thermo-mechanical analysis, radiation behavior of the advanced SiC/SiC composites and elements of solid breeding blanket systems in high temperature environment were studies in Subtask 2-3.

In order to clarify radiation behavior of the solid blanket system using SiC/SiC composites, irradiation experiments in high temperature (800-1300ºC) conditions were planed to address the important scientific issues, including;

(a) dimensional stability, thermal conductivity and strength change due to irradiation,

(b) radiation resistance of newly developed SiC/SiC composites, joints, and hermetic coating,

(c) chemical compatibility between SiC/SiC composites and ceramic breeding materials or neutron multiplier under neutron irradiation,

(d) He effects on mechanical properties and dimensional stability of SiC/SiC composites and constituents, and

(e) irradiation performance of the key elements of SiC/SiC-based ceramic-breeding blanket systems.

3-7-2 Participants to the Task

A.Hasegawa, S.Nogami(Tohoku University), T.Hinoki, A.Kohyama, T.Nozawa, S.Kondou (Kyoto U.) , T.Shibayama(Hokkaido U.)

Y.Katoh, L.L.Snead, B.A. Pint, S.J. Zinkle, J.L. McDuffee (ORNL), C.H. Henager, Jr., G.E. Youngblood (PNNL), N.B. Morley (UCLA)

3-7-3 Research Highlights

In the first half of the program period, PIE of HFIR-14J and rabbit irradiation expeirnents were conducted to examine fundamental irradiation behavior of near-stoihciometric SiC fiber composites and to identify adequate SiC/SiC composites for irradiation in more extensive and severe conditions in the HFIR-18J campaign. The PIE of HFIR-14J have successfully been completed and the knowledge acquired were utilized in Subtask 2-1 for design and fabrication of SiC/SiC composites with improved irradiation stability. The results showed:

(a) Newly developed SiC fibers, with low oxygen content, high crystallinity and near-stoichiometric composition, possess very substantially improved resistance to neutron irradiation at elevated temperatures compared to the older generation SiC fibers.

(b) He implanted prior to neutron irradiation exerts only negligible effects on post-irradiation mechanical properties of SiC and SiC/SiC composites.

Based on the results, several types of SiC/SiC composites, including those with interphases specifically designed for improved radiation stability and those produced through novel processing techniques newly developed in Japan, were fabricated and examined for irradiation performance using rabbit irradiation facility of HFIR. The low dose, high temperature irradiation performance was positively addressed for most of the composites tested. The results were utilized to identify appropriate materials, irradiation conditions, and properties for evaluation for the planned HFIR-18J irradiation campaign. The following results were obtained.

(c) Rabbit capsule irradiation (1000C, 4dpa) was completed. The developmental composite fabricated through Nano-Infiltration and Transient Eutectic-phase (NITE) process demonstrated the excellent radiation stability, whereas the developmental near-stoichiometric polymer -impregnation and pyrolysis (PIP) composites lost mechanical integrity. A figure shows stress-strain curves of unirradiated and irradiated SiC/SiC composites fabricated by NITE process. No degradation (strength, modulus) in NITE SiC was confirmed. Irradiation-toughening was apparent.

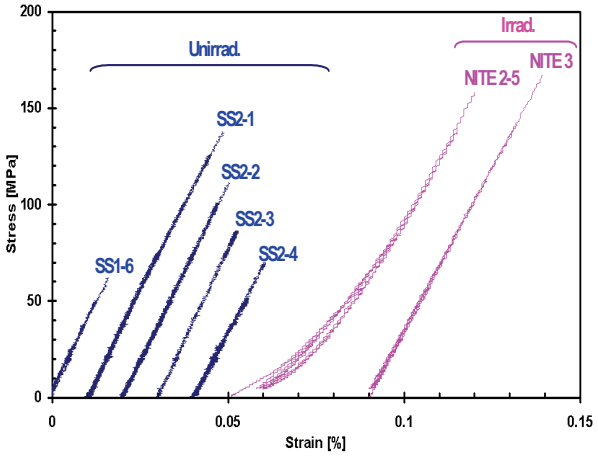

Figure: Stress-strain curves of NITE composites

In the second half of the program period, neutron irradiation experiment using an instrumented capsule in the Large Removable Beryllium (RB*) Facility of HFIR was designed, developed, and performed as a core irradiation program of Subtask 2-3. Objectives of the experiment were 1) to gain understanding of irradiation effects in SiC/SiC composites and constituents in aggressive domains of fusion-relevant irradiation conditions, 2) to determine neutron irradiation effects in the new generations SiC/SiC composites, joints, and SiC-ceramic breeder systems, 3) to aid constitutive modeling of irradiation effects on mechanical and transport properties of SiC/SiC, and 4) to acquire irradiation effect data in support of blanket system R&D. The irradiation capsule designated RB-18J was developed to irradiate large quantity of specimens of various types to a medium dose (~6 dpa) at 800, 1100 and 1300ºC. In parallel with the development of the irradiation matrix and the capsule, novel techniques for studying irradiation creep and in-pile compatibility experiments were developed. The irradiation experiments started from the summer of 2007 and the PIE is anticipated to start from the summer of 2008. Figures show a schematic view of irradiation capsule of 18J and specimens of SiC/SiC composites.

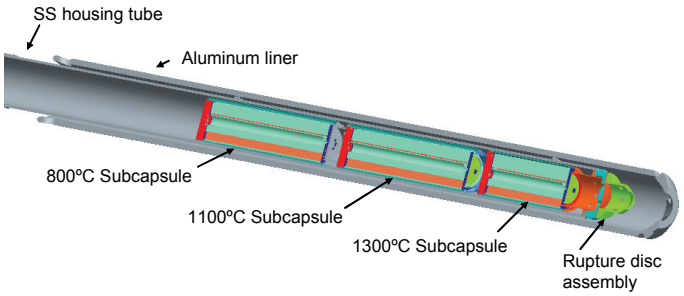

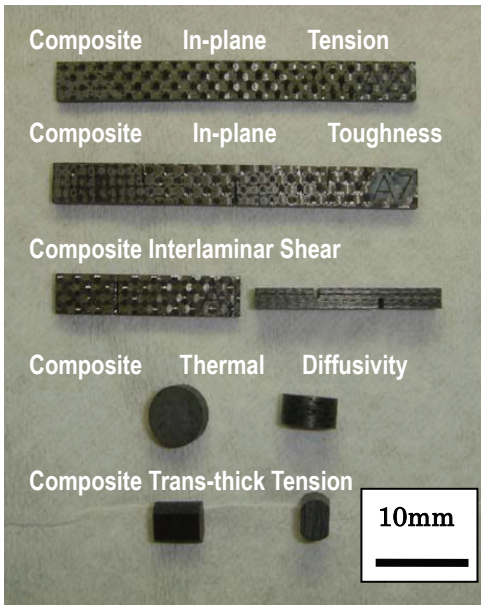

The RB-18J is the first-ever experiment that examines the mechanical properties of SiC-based ceramics and composites of current interest to fusion energy development after irradiation in a very high temperature regime (>~1000ºC). Below are the examples of scientific issues which are expected to be addressed by the 18J experiment.

(d) Responses of high-purity, ideal-grade SiC and advanced SiC/SiC composites and constituents (matrix materials, fibers, interphase) to neutron irradiation at very high temperatures.

(e) Upper temperature limit due to irradiation for advanced SiC/SiC in terms of

baseline properties.

(f) Some of the critical yet controversial questions regarding irradiation effects in advanced SiC/SiC such as potential benefit of advanced composite design factors (advanced interphases, hybrid composites, etc.) developed through recent fusion SiC/SiC R&D efforts, irradiation effect on fracture toughness, and potentially expedited interfacial degradation at very high temperatures.

(g) Fundamental irradiation response of various breeding ceramics and reactivity with SiC under irradiation.

In order to support the irradiation experiment in HFIR, irradiation experiments in Japanese reactors were also conducted using JMTR and JOYO using the same SiC/SiC composites fabricated in subtask2-1. Helium effects and supporting fundamental studies were conducted by neutron and charged particle irradiation using DuET(Kyoto University), Dynamitorn(Tohoku University) and TIARA(JAERI). Following results were obtained.

(h) irradiation resistance to high temperature and lower fluence of SiC/SiC composites

(i) map of irradiation microstructure evolution of SiC

(j)synergistic effect of Heliun, Hydrogen and displacement damage on SiC/SiC composites.

3-7-4 Summary

In order to demonstrate feasibility of high efficiency gas cooling blanket system using advanced SiC/SiC composites based on new material development strategy and irradiation resistance of the material system were examined.

Evaluation of radiation resistance of SiC and advanced SiC/SiC developed and fabricated JUPITER-II program were performed using HFIR irradiation (rabbit capsule and HFIR-18J RB* capsule irradiation). Additional irradiation data of the advanced SiC/SiC and SiC was also collected by alternative irradiation facilitates such as JMTR, JOYO and charged particle irradiation facilities.

Radiation resistance of advanced SiC/SiC composite was demonstrated. Gide line of radiation resistance of SiC/SiC composites was confirmed. Engineering data of advanced SiC/SiC composites at high temperature irradiation conditions was collected. The data shows feasibility of the high temperature gas cooling system made of SiC/SiC composites.

3-8 Task 3-1: Design-based Integration Modeling

(A. Sagara, H. Hashizume, N.M. Ghoniem, D.K. Sze)

3-8-1 Objectives of the Task

The main purpose of this task is to develop integrated engineering models of blanket systems based on fusion reactor designs. The constraints imposed by one area of research must be considered in solving problems in another area. Integration has been accomplished in the areas of tritium transport and permeation, thermofluids, materials, and neutronics. For this purpose, it is essential to optimize the blanket system not as a single component but as an integrated system device under the boundary conditions of burning core plasmas and out-vessel environments. Therefore, collaboration works with connecting each task are basically quite important.

3-8-2 Participants to the Task

A. Sagara, T. Muroga, T. Tanaka (NIFS),
S. Fukada, M. Nishikawa (kyusyu U.),
S. Tanaka, T. Terai, A. Suzuki (U. Tokyo),
S. Toda, H. Hashizume, K. Yuki, S. Chiba (Tohoku U.),
S. Satake (Tokyo U of Science), T. Kunugi (Kyoto U.),
N.M. Ghoniem, S. Sharafat, M.Z. Youssef (UCLA),
Da-Kai Sze (UCSD)

3-8-3 Research Highlights

Fukada et al., have revealed that, for the FFHR blanket system, tritium permeation windows in a realistic-scale (lower than a few 100 m^2) are usable for tritium disengager systems. It is found that the diffusion process of tritium in Flibe or the surface process at the boundary is the critical rate limiting process to be investigated. From the safety point of view, they have proposed that a small amount of Flibe or He gas flow in the double tube are good as permeation barriers to reduce the tritium leakage rate below 10 Ci/day. However, it is pointed out that the most serious problem is permeation leak of about 34 kCi/day through the heat exchanger to the He loop.

Muroga et al., have evaluated the V-alloy/Flibe blanket system for FFHR to increase the operation temperature. For this system, thermodynamic analysis has been carried out for another REDOX control (T_2 to TF) with MoF_6 or WF_6, which can form corrosion protective Mo or W coating on V-alloy surfaces with self-healing capability, resulting in reduction of T inventory in the blanket below 100 g by doping of 1ppm MoF_6 or WF_6. Among the issues of this concept is recovery of tritium in the form of TF and Mo or W out of the blanket.

Sagara et al., have newly proposed the STB (Spectral-shifter and Tritium breeder Blanket) for replacement-free blankets in the reactor life of 30 years in FFHR. For this STB, they have evaluated the first wall condition for FFHR, and have proposed enhancement of Flibe cooling capability on one-side heating over 1MW/m^2. Regarding this request, the Task 1-1-B group has investigated modeling of MHD effects on heat-transfer.

Hashizume et al., have investigated flow structures in sphere-packed pipes to enhance heat-transfer efficiency in the TNT (Tohoku-NIFS Thermofluid) loop experiments using HTS (Heat Transfer Salt, T_m= 142°C). Same performance as turbulent flow has been obtained at one order lower flow rate. This is a big advantage for reducing MHD effects and the pumping power. They have also investigated MHD suppression coating on the Li/V-alloy blanket system. They have proposed a three-layered wall system, where the inner thin metal layer protects permeation of lithium into cracks in the coated layer. The performance required to the insulator has been evaluated. Based on this coating concept, they designed and evaluated a self-cooled Be-free Li/V blanket resulting in good tritium breeding. However, improving shielding efficiency is the major key issue.

Tanaka et al., have started a new challenge to construct an interface code between the Monte-Carlo neutron transport code MCNP-4C

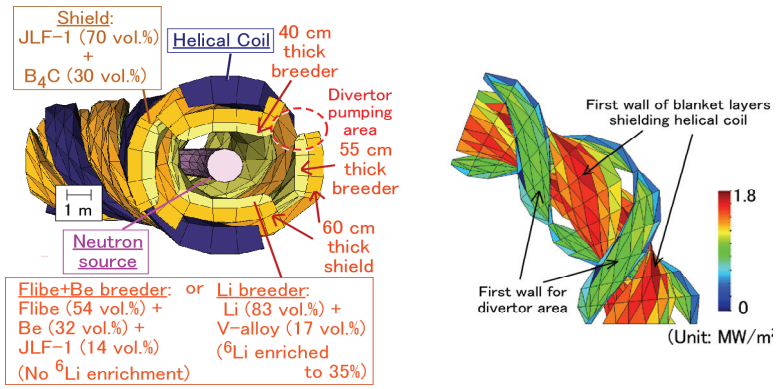

Fig.1. Example of 3-D geometry data with MCNP (~3,000 cells) and helical neutron wall loading

and a complicated blanket design such as in helical systems in order to enable us to frequently modify blanket designs and quickly check neutronics performance. The examples are shown in Fig. 1. Using this easy-feedback code system, both of the Flibe cooled reduced-activation ferritic steel (RAFS) and Li/V-alloy blanket systems have be optimized in the feasibility of tritium breeding ratio higher than 1.0 and nuclear shielding in the FFHR2m helical design.

3-8-4 Summary

The main research performed in this task as collaboration works with connecting each task are as follows:

(1) Flibe Blanket system (Task 1-1-A),

- Design and requirements on tritium recovery system,
- Proposal and key issues on tritium permeation,
- Design and evaluation of Flibe / V blanket,

(2) Thermofluid of Flibe (Task 1-1-B),

- Requirements on the first wall condition for FFHR,
- Modeling of MHD effects on heat-transfer,
- Enhancement of heat-transfer efficiency,

(3) Li-V Blanket (Task 1-2-A),

- Evaluation and requirements on MHD coating,
- Design and evaluation of Self-cooled Be-free Li/V blanket,

(4) All tasks,

- Improvement of neutronics calculation system for helical structure.

3-9 Task 3-2: Materials Modeling

(A. Sagara, N. Sekimura, N.M. Ghoniem, R.E. Stoller)

3-9-1 Objectives of the Task

The goal of task 3.2 at the beginning of the JUPITER-II project was to establish the methodology of "Multiscale Modeling of Mechanical Deformation (M3D)" for contributions to the research and development of fusion materials, which may cover a broad range of fundamental issues, including: primary radiation damage formation, extended defect formation and evolution, dislocation-defect interactions, dislocation dynamics, the development of constitutive relationships for irradiated materials, and predictions of engineering properties of materials needed for component design. For this purpose, a wide variety of evaluation techniques should be used, because a solid material has essentially a hierarchical structure from atoms to continuum bodies, and in addition, a radiation damage process is essentially a multi-time, -length and -energy scale phenomenon.

3-9-2 Participants to the Task

K. Morishita (Kyoto University), M. Satou (Tohoku University), N. Nita, H. Matsui (Tohoku University), T. Okita, N. Sekimura, H. Abe (University of Tokyo)
B.D. Wirth (UC Berkeley), T. Diaz de la Rubia, W.G. Wolfer (LLNL), N.M. Ghoniem, S. Sharafat (UCLA), H.L. Heinisch, F. Gao, R.J. Kurtz (PNNL), G.R. Odette (UCSB), R.E. Stoller (ORNL)

3-9-3 Research Highlights

Morishita et al. have investigated the nucleation and growth process of helium bubbles in Fe. They employed molecular dynamics and molecular statics calculation techniques as well as continuum theory to determine the formation energy of helium bubbles. Furthermore, they introduced these results as input parameters in kinetic Monte-Carlo simulations, thus enabling us to study the nucleation kinetics of helium bubbles as a function of temperature and point defect concentrations in an Fe matrix. An Arrhenius plot of bubble growth rates shows two different activation energies clearly,

depending on helium concentrations in the matrix: one is 0.74 eV and the other is 0.078 eV, as shown in Fig. 1, which are in good agreement with the vacancy and interstitial helium migration energies, respectively. It indicates that the growth of helium bubbles is controlled by vacancy migration when the helium concentration is relatively low, while it is controlled by interstitial helium migration when the helium concentration is relatively high. These results respectively correspond to the fusion first wall environment where helium is created by (n, α) transmutation reactions and the fusion divertor material environment where helium is directly implanted. This work was performed in collaboration with LLNL, PNNL, UC Berkeley and UCLA.

Abe et al. performed molecular dynamics calculations to investigate dynamical interactions between an SFT and a dislocation, and they estimated the effects of the interaction on radiation-induced hardening. Also, they investigated the migration behavior of a crowdion bundle (i.e., a small self-interstitial atom loop) using a molecular dynamics technique. They compared the calculation results with in situ TEM observations. This work was performed in collaboration with ORNL.

Fundamental understanding of metal/ceramics bonding will provide useful guideline to develop a robust coating technique. Satou et al. performed ab-initio calculations to investigate bonding states between vanadium and coated CaO. Ideal peak interfacial strength between vanadium and CaO was evaluated using universal binding energy relation to be 6.4 GPa. Evaluation of other combinations of metals/ceramics and the effect of crystal orientation showed that atomistic configuration at the interface strongly related the ideal strength of the interface. This work was done in collaboration with UCLA and CSUN.

SiC/SiC composite materials are proposed candidates for fusion structures, but the formation mechanisms of defect clusters in the material are not well understood. Watanabe et al. are now

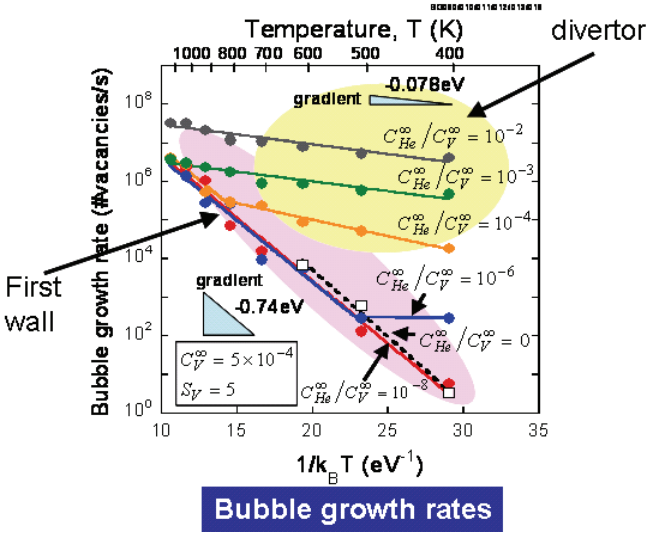

Fig. 1. Arrhenium plot of bubble growth rate.

investigating formation energy of small self-interstitial atom loops in SiC, using a molecular static calculation technique.

Each of these studies is really important for fusion materials science and technology. Further efforts to achieve the final goal “M3D” should be made using findings obtained from these studies.

Sharafat et al. investigated the transport of helium in irradiated materials driven by spatially dependent fields, such as temperature and stress gradients. To this end modeling of helium transport through finite geometries thus requires a spatially dependent helium transport model. A spatially resolved rate-theory based helium bubble evolution code was developed at UCLA, called HEROS (Helium Bubble Evolution and ResOlution Code). The HEROS bubble evolution model is based on a simplification of hierarchical kinetic rate equations for the clustering of helium bubbles, immobile vacancy clusters, glissile interstitial clusters, sessile dislocation loops, as well as precipitates and grain boundaries. The HEROS code models helium transport through a finite media allowing for space and time inhomogeneities caused by spatially dependent temperature- and stress fields, as well as inhomogeneous production or implantation rates. The HEROS was applied to model low energy helium implantation data in tungsten. Space and time dependent helium bubble size distributions in helium implanted tungsten were developed. The HEROS code uses the helium implantation test characteristics and shows that the transport of helium bubbles is a strong function of temporal and spatial temperatures, and temperature gradients. Helium recycling rates determined by the HEROS code also compared well with experimental data.

The primary goal of this research is to extend the “M3D” findings on radiation damage and defect formation and evolution, to predict engineering properties and performance of materials, particularly due to the formation of helium during fusion neutron exposure of metals.

3-9-4 Information technology for modeling and integration of data and model:

Improved accessibility to the latest and up-to-date material properties for fusion scientists and engineers is being addressed by Sharafat et al. through an effort to develop an online, interactive, scalable, and highly automated fusion materials properties database. Internet technology is providing the means to develop an efficient on-line fusion

materials database. By combining advanced Internet programming with Relational Database Management Software (RDBMS) an effective technology for online and interactive materials property database web site with Internet efficiency is being developed for the fusion research community. The database is called "FusionNET©" and can be accessed at http://fusionnet.seas.ucla.edu. Key features of the FusionNET database are that publishing and updating of content is performed with the involvement of the fusion materials property data community: (1) data is presented with a uniform standard in both graphical and tabular format; (2) original publications of hosted data is available in PDF format; (3) search engines can readily locate available data upon request; (4) the materials database is automatically expandable; (5) older data is never removed, new data is simply added to the database; (6) new data can be submitted over the Internet directly to the site; (7) quality assurance can be performed with direct involvement of the data's author. Another advantage of the FusionNET material property database is that equivalent design equations can be generated for all tabulated data. A link is provided to choose from a large number of empirical and/or physical based design equations of materials property data. The materials data is categorized into thermo-physical, mechanical, chemical, and microstructural properties, which are readily accessed using both textual information and thumbnail sketches. The database is currently hosting data on a number of structural metallic and ceramic materials, breeder materials, refractory alloys, and SiC.

3-9-5 Summary

The topics that we have devoted ourselves for this project were as follows:

(1) code development for evaluating atomic displacements due to neutron irradiations,
(2) multiscale modeling of helium effects in irradiated materials,
(3) interface damage modeling in irradiated alloys and compounds,
(4) modeling of microstructural evolution of vanadium alloys under irradiation,
(5) modeling of radiation damage in advanced SiC/SiC composites,
(6) modeling of mechanical deformation through multiscale simulations,
(7) the development of MD-FEM combination methodology,
(8) calculation of ideal interfacial strength between vanadium and oxide ceramics,
(9) information technology for modeling and integration of data and model.

4. Research report

Task 1-1-A

(1) Initial studies of tritium behavior in flibe and flibe-facing material
(2) Quantitative measurement of beryllium-controlled redox of hydrogen fluoride in molten Flibe
(3) Interactions between molten Flibe and metallic Be
(4) JUPITER-II molten salt Flibe research: An update on tritium, mobilization and redox chemistry experiments
(5) Reaction Rate of Beryllium with Fluorine Ion for Flibe Redox Control

Task 1-1-B

(1) PIV Technique for measurement of turbulent flow under magnetic fields
(2) The influence of a magnetic field on turbulent heat transfer od a high Prandtl number fluid
(3) Direct numerical simulation of MHD flow with electrically conducting wall
(4) DNS and K-epsiron model simulation of MHD turbulent channel flows with heat transfer
(5) Experimental research on molten salt thermofluid technology using a high temperature molten salt loop applied for a fusion reactor Flibe blanket
(6) Experimental investigation of turbulent heat transfer of high Prandtl number fluid flow under strong magnetic field
(7) Heat transfer performance for high Prandtl and high temperature molten salt flow in sphere-packed pipes
(8) Experimental study of MHD effects on heat transfer characteristics on turbulent pipe of flibe stimulant fluid

Task 1-2-A

(1) Advances in development of vanadium alloys and MHD insulator coatings
(2) Recent progress in the development of electrically insulating coatings for a liquid lithium blanket
(3) Initial characterization of V-4Cr-4Ti and MHD coatings exposed to flowing Li
(4) Tensile property of V-4Cr-4Ti alloy after liquid lithium exposure
(5) Biaxial thermal creep of two heats of V4Cr4Ti at 700 and 800oC in a liquid lithium environment

Task 1-2-B

(1) Recent progress on development of vanadium alloys for fusion
(2) Effects of doping elements on oxidation properties of V–Cr–Ti type alloys in several environments
(3) Microstructural examination of V- (Fe or Cr)-Ti alloys after thermal-creep or irradiation-creep tests
(4) Manufacturing pressurized creep tubes from highly purified V-4Cr-4Ti alloys, NIFS-Heat2
(5) Creep mechanism of highly purified V-4Cr-4Ti alloys during thermal creep in a vacuum
(6) Tungsten coating on low activation vanadium alloys by plasma splay process
(7) The microstructure of laser-welded V-4Cr-4TI alloy after neutron irradiation
(8) Modeling the multiscale mechanics of flow localization-ductility loss in irradiation damaged BCC alloys using hysteresis loop analysis of tensile test

Task 2-1

(1) Optimization and characterization of chemical vapor infiltrated SiC/SiC Composites
(2) Tensile strength of chemical vapor infiltrated advanced SiC fiber composites at elevated temperatures
(3) Tensile and thermal properties of chemically vapor-infiltrated silicon carbide composites of various high-modulus fiber reinforcements

Task 2-2

(1) Impact of material system thermomechanics and thermofluid performance on He-cooled ceramic breeder blanket designs with SiCf/SiC
(2) Experimental study of the interaction of ceramic breeder pebble beds with structural materials under thermo-mechanical loads
(3) Numerical characterization of thermo-mechanical performance of breeder pebble beds

Task 2-3

(1) The effect of high dose/high temperature irradiation on high purity fibers and their silicon carbide composites
(2) Neutron irradiation effects on high-crystallinity and near-stoichiometry SiC fibers and their composites
(3) Effect of He pre-implantation and neutron irradiation on mechanical properties of SiC/SiC composite
(4) Mechanical properties of advanced SiC/SiC composites after neutron Irradiation
(5) Current status and critical issues for development of SiC composites for fusion applications
(6) Evaluation of Fiber/Matrix Interfacial Strength of Neutron Irradiated SiC/SiC Composites
(7) Mechanical properties of advanced SiC/SiC composites after neutron Irradiation

Task 3-1

(1) Innovative liquid breeder blanket design activities in Japan
(2) Neutronics investigation of advanced self-cooled liquid blanket systems in helical reactor
(3) Tritium control for Flibe/V-alloy blanket system

Task 3-2

(1) MD and KMC modeling of the growth and shrinkage mechanisms of helium-vacancy clusters in Fe
(2) Nucleation path of helium bubbles in metals during irradiation

Initial studies of tritium behavior in flibe and flibe-facing material

S. Fukada [a], R.A. Anderl [b], Y. Hatano [c], S.T. Schuetz [b], R.J. Pawelko [b], D.A. Petti [b], G.R. Smolik [b], T. Terai [d], M. Nishikawa [a], S. Tanaka [d], A. Sagara e

[a] *Kyushu University, Hakozaki, Higashi-ku, Fukuoka, 812-8581, Japan*
[b] *Idaho National Engineering and Environmental Laboratory, INEEL, Idaho Falls, ID 83415, USA*
[c] *Toyama University, Gofuku, Toyama 930-8555, Japan*
[d] *The University of Tokyo, Hongo, Bunkyo-ku, Tokyo 113-8656, Japan*
[e] *National Institute for Fusion Sciences, Shitaishi-cho, Toki 509-5292, Japan*

Flibe-tritium experiment in the Japan−US joint project (JUPITER-II) was initiated in 2001. H/D isotopic exchange experiments were conducted to select a Flibe-facing material. Because of hydrogen isotope interactions with carbon, Ni crucibles were selected for Flibe/tritium behavior experiments. A Flib-tritium pot with two Ni (or Cu) permeable probes was designed. The rate of the overall tritium permeation through the Flibe-facing Ni or Cu was estimated by numerical simulation using TMAP4 code. Diffusion in bulk Flibe was found to be the rate-determining step for purified Flibe.

1. Introduction

Flibe (LiF-BeF_2 molten salt) has been considered a promising blanket material of a fusion reactor [1], because of low electron conductivity, i.e. low MHD effect, low tritium solubility, i.e. low tritium inventory, low reactivity with water and oxygen and so on. Flibe was also known as a heat transfer fluid for a molten salt reactor that was intensively investigated in ORNL [2]. Although a lot of physical or chemical properties were determined previously, tritium behavior in Flibe is less well understood. For example, there are few data available on diffusivity or the mass-transfer coefficient of hydrogen isotopes including tritium in Flibe except for Japanese researchers [3,4]. Thus, a Flibe-tritium chemistry study was initiated in 2001 as part of the Japan-US joint project (JUPITER-II) [5]. In the first year of the project, experiments of Flibe handling, purification and tritium behavior in Flibe are being carried out. A purpose of our research is to determine tritium behavior in Flibe that is purified by He and then HF/H_2 gas bubbling. As an initial study, results of preliminary research of tritium behavior in a Flibefacing material are presented here.

2. Blank experiment

Experiments were conducted to select a Flibe facing material to be used for our Flibe-tritium experiment. Graphite with a glassy carbon impregnation on surfaces was considered one of the most promising candidate materials for the experiment because of high resistance to corrosive Flibe and HF [5]. Highly purified H_2 or D_2 mixed with He of a constant flow rate ($100cm^3$(STP)/min) was introduced into a stainless-steel 316 pot with or without a glassy carbon crucible and Flibe. The residual gas exhausted from the pot system was analyzed by a closed-ion-source-type quadrupole mass spectrometer that has a very low background. Fig. 1 shows a comparison of the residual gas under the following three experimental conditions: (a) only stainless-steel 316 pot, (b) stainless steel 316 pot-glassy carbon crucible and (c) stainless-steel 316 pot-glassy carbon crucible-Flibe. Temperature is 600C. No appreciable release of hydrocarbons was observed in the stainless-steel 316 pot test. On the other hand, a small amount of hydrocarbons was released in the experiment with the carbon crucible. The release of hydrocarbons was strongly enhanced by the presence of Flibe. Fig. 2 shows variations of mass-spectrum peaks from m/e=15-20 with time when D_2 was supplied to the stainless-steel pot and the glassy carbon crucible without Flibe. Glassy carbon at 600C was found to hold a certain amount of H atoms even after sufficient (around 2 days)

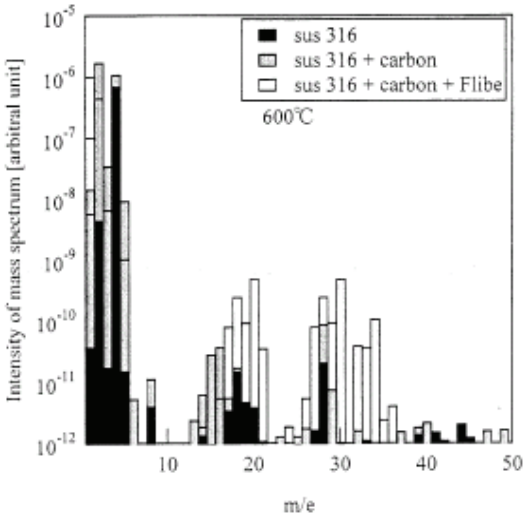

Fig. 1. Comparison of mass-spectrum peaks of residual gas; (a)stainless steel 316 pot, (b) stainless-steel pot and carbon crucible, (c) stainless-steel pot, carbon crucible and Flibe.

He purge before the D_2 supply. The H amount trapped in the carbon crucible was evaluated to be 54 ml (STP) from the experiment of the isotopic exchange of D with H atoms. The hydrogen amount dissolved in Flibe was observed to be much less than that trapped in the carbon crucible [6,7]. The H atoms also exchanged with D in deuterocarbons, as seen in the respective peaks of m/e=15-20 in Fig. 2. The peak of m/e=15 may correspond to CH_3^+, m/e=16 to CH_2D^+ and CH_4^+, m/e=17 to CHD_2^+ and CH_3D^+, m/e=18 to CD_3^+ and CH_2D^{2+}, m/e=19 to CHD^{3+} and m/e=20 to CD_4^+ and HF^+. The slope of the mass-spectrum curves of m/e=15-17 decreases, while those of m/e=18-20 are almost constant or even increasing. This means that deuterided methane was generated by the interaction of carbon with D exchanged with H atoms trapped in the glassy carbon. Thus the use of glassy carbon was considered not appropriate for our Flibe-tritium experiment. Carbon is known as a compatible material with Flibe and was used in the molten salt reactor experiment [2]. Generation of methane in the present experiment may be related to interaction between hydrogen and carbon impurities in Flibe. To ensure that our Flibe/tritium behavior experiments are not influenced by tritium interaction with carbon, we decided Ni to be the most reliable candidate as a crucible material for experiment under a very low impurity level.

3. Flibe-tritium permeation pot

3.1. Design of flibe┐ /tritium permeation pot

Tritium behavior in Flibe and Flibe-facing materials is being investigated using a Flibe pot system containing Ni crucible and two permeation probes. The pot system was designed based on the following considerations: (1) one (or quasi-one) dimensional permeation, (2) easy operation, (3) low tritium leak to the glove-box atmosphere, and (4) low tritium inventory. Fig. 3 shows a schematic illustration of the Flibe-tritium permeation pot system. The pot has two cylindrical probes fabricated from Ni or Cu. A central Ni probe is maintained at a constant tritium pressure. Another outer probe is swept by purified He. The cover gas over Flibe is He. Permeated tritium is detected by ionization chambers. Thus the two probes can detect an overall permeation rate from the upstream probe through fluid Flibe to the downstream He purge gas. Comparison of the transient and steady-state permeation rates between experiment and analysis gives information on tritium diffusion coefficient in Flibe or permeation coefficient in metal. In the present paper, the analytical calculation results are presented below.

3.2. Diffusion equations and solubility relations

We considered more general situations where the diffusion process in a fluid film is different from that in bulk Flibe. This condition also includes a case where migration process on metal surfaces affects the diffusion process in the fluid film [8]. A one-dimensional overall tritium diffusion rate was calculated from the upstream probe through Flibe to the downstream probe. Mass transfer steps taken into consideration are six diffusion processes; (1) through the upstream Ni probe wall, (2) in the upstream surface film, (3) in bulk Flibe, (4) in the downstream surface film, (5) through the downstream probe wall, and (6) in the downstream He purge gas. The recombination process on the metal surfaces was assumed to be very fast. The diffusion equation for respective layers is described as follows:

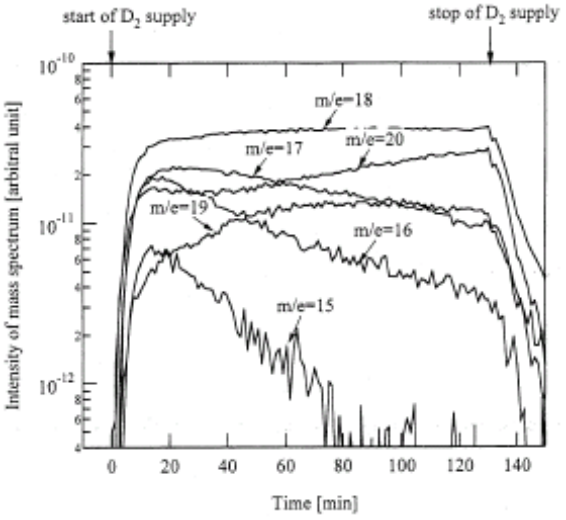

Fig. 2. Variations of mass-spectrum peaks of m/e=15-20 with time.

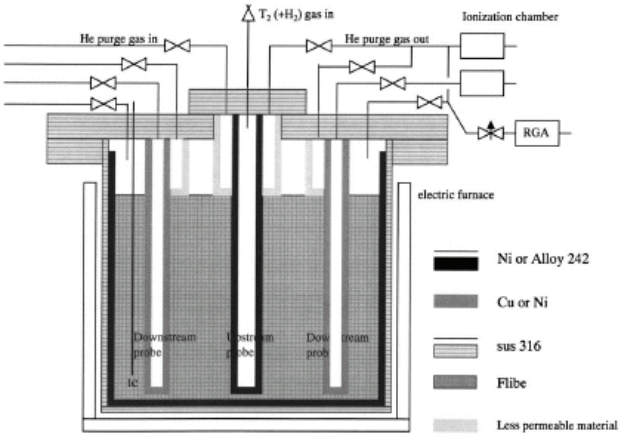

Fig. 3. A schematic diagram of the two-probe pot.

$$\frac{\partial c_j}{\partial t} = D_j \nabla^2 c_j \quad j = \text{metal, Flibe and fluid film}$$

The tritium diffusion equations were simultaneously solved using the TMAP4 code [9]. The diffusion coefficients in Ni and Cu were given by a previous paper [10]. That in Flibe was reported in previous work [5,11]. Since tritium solubility is described by the Sieverts' law in Ni and Cu [10] and the Henry law in Flibe [7,10], the boundary conditions are given for each interface as follows:

$$p = \frac{c_j}{H_j} = \left(\frac{c_k}{S_k}\right)^2 \quad \text{on Flibe–metal interface}$$

$$p^{0.5} = \frac{c_j}{S_j} \quad \text{on metal–gas interface}$$

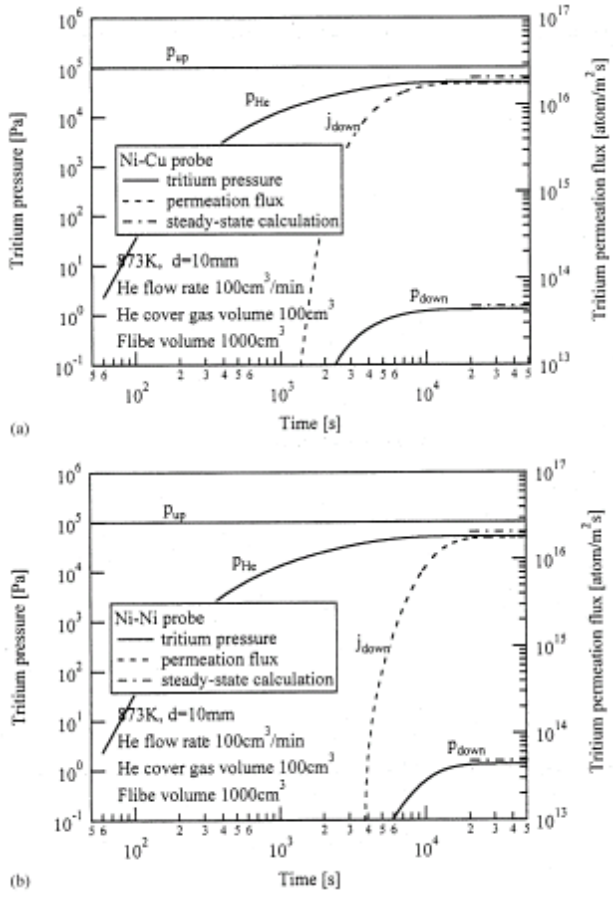

Fig. 4. Rate of transient tritium permeation through Ni upstream and Cu downstream probes. (b) Rate of transient tritium permeation through Ni upstream and Ni downstream probes.

3.3. Calculation of tritium permeation

Fig. 4a, b are examples of the calculational results. The tritium pressure in the upstream probe, pup, that in He cover gas, pHe, and that in the downstream probe, p_{down}, are shown by a solid line. The downstream overall tritium permeation rate, j_{down}, is depicted by a dotted line. The steady state values of p_{down} and j_{down} that can be calculated in analytical way are also shown in the figure by short horizontal chain lines extending from the right y-axis. The calculations of p_{down} and j_{down} by the TMAP4 code are almost coincident with those by the analytical one.

Several things were found from the two calculations.

(1) The rate-determining step is diffusion in bulk Flibe. (2) The steady-state tritium permeation rate is almost unchanged regardless of the downstream Ni and Cu probes. (3) The time to reach the steady-state permeation for the Cu probe is smaller than that for the Ni probe. This is because the tritium diffusion coefficient in Cu is about ten times larger than that in Ni. (4) The tritium pressure in the He cover gas is about half of that in the upstream Ni probe.

Fig. 5 shows the rate-determining step for various tritium pressures in the upstream probe and for various Flibe-metal interface conditions. The reciprocal of the value on the vertical axis corresponds to the mass-transfer resistance of migration through a film formed on Ni surfaces. It is assumed that both probes are made of Ni.

Several things were also found from calculations of different diffusion coefficients in film, different probe distances and so on. (1) Diffusion in fluid Flibe is the rate-determining step under a usual tritium pressure if the migration resistance is ignored. (2) The steady-state permeation rate is almost in proportion to D_{Flibe}/d. (3) Time to reach the steady-state permeation is almost in proportion to d^2/D_{Flibe}. (4) If He gas is bubbled into bulk

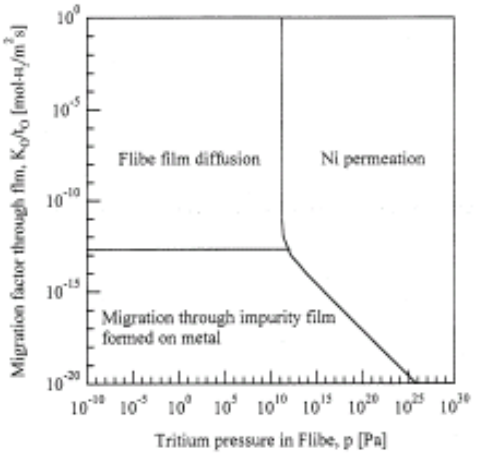

Fig. 5. Rate-determining step of overall tritium permeation through Flibe-facing Ni.

Flibe, transient time can be made very short.

The present system was analyzed under a static Flibe condition. The calculation is still applicable to a Flibe system under a turbulent flowing condition. Then, the characteristic distance d in the above discussion is replaced by the boundary layer thickness, d, or the D_{Flibe}/d is replaced by the mass-transfer coefficient, k_{Flibe}.

4. Conclusions

H/D isotopic exchange experiments were conducted to select a Flibe-facing material. Because of hydrogen isotope interactions with carbon, Ni crucibles were selected for Flibe/tritium behavior experiment. The overall transient tritium permeation rate between the upstream and downstream probes was evaluated well by the TMAP4 code. The rate-determining step was the diffusion in Flibe in usual cases.

5. Nomenclature

c_j : tritium concentration in Flibe (molecule per m^3) or tritium concentration in metal (atom per m^3)
d : distance between two probe surfaces
D_j : tritium diffusion coefficient in Flibe or metal (m^2/s)
H_j : Henry constant (atom per m^3 Pa)
K_o : tritium migration factor through film formedon metal surfaces (mol/ms)
p : tritium pressure (Pa)
S_j : Sieverts constant (atom per m^3 $Pa^{0.5}$)
t : time
t_o : thickness of film formed on metal surfaces (m)

REFERENCES

[1] A. Sagara, H. Yamanishi, T. Uda, O. Motojima, T. Kunugi, Y. Matsumoto, Y. Wu, H. Matsui, S. Takahashi, T. Yamamoto, S. Toda, O. Mitarai, S. Satake, T. Terai, S. Tanaka, S. Fukada, M. Nishikawa, A. Shimizu, N. Yoshida, Studies of Flibe blanket designs in helical reactor FFHR, Fusion. Technol. 39 (2001) 753-757.

[2] J.H. Shaffer, Preparation and handling of salt mixtures for the molten salt reactor experiment, ORNL-4616 (1971).

[3] H. Moriyama, et al., Chemical behaviors of tritium formed in a LiF-BeF_2 mixture, J. Nucl. Mater. 148 (1987) 211-216.

[4] A. Suzuki, T. Terai, S. Tanaka, Change of tritium species in Li_2BeF_4 molten salt breeder under neutron irradiation at elevated temperature, J. Nucl. Mater. 258-263 (1998) 519-524.

[5] D.A. Petti, G.R. Smolik, R.A. Anderl, D.K. Sze, S. Tanaka, T. Terai, A program plan for molten salt experiments being performed as part of the Second Japan/US program on irradiation tests for fusion energy research (JUPITER-II) collaboration, INEEL/EXT-01-00796, 2001.

[6] Y. Hatano, et al., Release of hydrogen containing impurities from Flibe (in Japanese), Proceedings of the 2002 Spring Meeting of the Atomic Energy Society of Japan, 2002.

[7] A.P. Malinauskas, D.M. Richardson, The solubility of hydrogen, deuterium and helium in molten Li_2BeF_4, Ind. Eng. Chem. Fundam. 13 (1974) 242-245.

[8] S. Fukada, M. Nishikawa, A. Sagara, Calculation of recovery of tritium from a flibe blanket, Fusion. Technol. 39 (2001) 1073-1077.

[9] G.R. Longhurst, D.F. Holland, J.L. Jones, B.J. Merrill, TMAP4 users manual, EGG-FSP-10315, 1998.

[10] F. Reiter, K.S. Forcey, G. Gervasint, A compilation of tritium-material interaction parameters in fusion reactor materials, EUR 15217 EN, 1993.

[11] J. Oishi, H. Moriyama, S. Maeda, Y. Asaoka, Tritium recovery from molten LiF-BeF_2 salt, Fus. Eng. Des. 8 (1989) 317-321.

Quantitative measurement of beryllium-controlled redox of hydrogen fluoride in molten Flibe

Michael F. Simpson [a,*], Galen R. Smolik [a], John P. Sharpe [a], Robert A. Anderl [a], David A. Petti [a], Yuji Hatano [b], Masanori Hara [b], Yasuhisa Oya [c], Satoshi Fukada [d], Satoru Tanaka [c], Takayuki Terai [c], Dai-Kai Sze [e]

[a] *Idaho National Laboratory, P.O. Box 2528, Idaho Falls, ID 83403, United States* [b] *Hydrogen Isotope Research Center, Toyama University, Japan* [c] *University of Tokyo, Japan* [d] *Department of Applied Quantum Physics and Nuclear Engineering, Kyushu University, Japan* [e] *University of California at San Diego, United States*

Abstract

In order to investigate the viability of using Be as a redox agent in a molten Flibe ($2LiF–BeF_2$) blanket, a series of kinetics experiments were performed in which HF was bubbled through Flibe with varying concentrations of dissolved Be. The feed gas consisted of 910–1800 ppm HF and 0.1–0.2 vol.% H2, with the balance comprised of He. A cylindrical rod of Be was contacted with the salt for periods of time ranging from 600 to 3600 s, resulting in mole fractions in the salt ranging from 4.3×10^{-5} to 2.6×10^{-4}. Initially, high HF conversion levels in excess of 90% were observed. As HF reacted with the Be, the conversion levels slowly dropped over a period of several hours to a few days. A simple kinetic model, which is first order in both HF and Be concentration has been coupled with a non-mixed reactor model to yield a good fit to the data. Application of this model indicates that Be should be suitable for keeping the TF concentration in the salt below 0.02 ppb.

1. Introduction

Molten Flibe (BeF2–2LiF) is currently under consideration as a blanket and coolant for both magnetic and inertial fusion systems [1,2]. This is because Flibe is very stable chemically and is an excellent attenuator of neutrons. One matter of concern for this application of Flibe, however, is the potential for generating corrosive TF molecules as a consequence of the reaction of neutrons with both Li-6 and Li-7. A redox agent is, thus, needed to reduce the T in TF to T_2.

A number of different redox agents have been considered, including Be, Ce, and Eu. Be is a more attractive candidate than Ce or Eu due to the fact that BeF_2 is already a major component in the salt. The gradual accumulation of CeF_3 or EuF_3 in the salt would eventually necessitate salt purification or disposal and replacement. Both of these options would be costly. On the other hand, the rising BeF_2 concentration in the salt would only require addition of LiF to keep the salt near the eutectic composition.

Some previous work has been reported that indicates Be is capable of serving as a redox agent in Flibe, keeping the TF concentrations low [3]. But no quantitative measurement of the rate of the Be–TF redox reaction is known to have been made. The objective of this study was to perform such measurements with the goal of obtaining useful kinetic data that could be used to rigorously validate the feasibility of using Be as a redox agent in Flibe. Of particular interest is whether the inclusion of Be in the salt can keep the TF concentrations below a level which would prevent the corrosion of structural materials.

2. Kinetic model development

It has been estimated that more than 90% of the T bred in the blanket will form TF, with the formation rate ranging from 1.2×10^{18} to 1.33×10^{18} atoms TF per m^3 per second in the blanket [4]. For the experiments reported in this paper, the mass of salt was approximately 0.55 kg. In order for

experiments to be run under the appropriate conditions, the HF feed rate would need to be 5.5 x10^{-10} mol/s. Due to the volume of the test reactor, the total gas flow rate needed to be on the order of 100 cm^3/min (1.7x10^{-6} m^3/s) or higher, assuming standard conditions. The HF feed concentration would need to be about 8 ppm. Due to reaction, the HF concentration in the effluent would be considerably less. This concentration level would be virtually undetectable using the measurement methods available. Thus, it was necessary to run experiments with an HF flow rate two orders of magnitude higher than would be typical for a fusion system. A model was then developed to facilitate extrapolation to lower HF concentrations. This section of the paper covers the development of this model. The next section will show how the measured data fit the model. It will then be demonstrated how extrapolation of the model predicts redox performance under actual fusion blanket conditions.

A kinetic model has to first consider the relative importance of homogenous versus heterogeneous reactions. HF can be either in the gas phase or dissolved in the molten salt phase. Beryllium can be either in the solid phase or dissolved in the molten salt phase. Since early experiments indicated that Be had a high solubility in Flibe at the temperature of interest [5], it was decided to run the experiments in such a way as to minimize the extent of HF reaction with the Be surface. So, the model could then ignore this mechanism. As for the state of HF, it was assumed that equilibrium is rapidly reached for HF between the molten salt and vapor phases. Henry's Law could then be used to relate the concentration of HF in the vapor phase to its concentration in the liquid phase. And it was assumed that the actual redox reaction occurred solely in the molten salt phase.

The model itself consists of an intrinsic kinetics model as well as a reactor model. The intrinsic model neglects heat and mass transfer resistances and simply states the reaction rate as a function of species concentrations. The chosen intrinsic reaction rate ($\Re$)is given below. The unknown kinetic rate parameter is k. The mole fraction of HF in the gas phase is yHF. The mole fraction of Be in the liquid phase is xBe. The mole fraction in the salt phase is based on total moles of salt using 33 g/mol as the molar weight rather than 98.9 g/mol, which is representative of 2LiF–BeF2 being considered to be one molecule.

$$\Re = k y_{HF} x_{Be} \qquad (1)$$

A Henry's Law constant is essentially embedded into the value for k, since the above equation is written in terms of the gas phase concentration of HF, not the liquid phase concentration. Assuming the gas bubbles containing HF traverse a fixed-length path through the salt without any backflow or mixing, the following differential equation can be used to determine the spatial dependence of the HF concentration in the gas phase. The distance along the path is l, the cross-sectional area of the path is A, and the total molar flow rate of gas through the path is $\dot{n}_{tot}$.

$$= \frac{dy_{HF}}{dl} = -\frac{k x_{Be} y_{HF} A}{\dot{n}_{tot}} \qquad (2)$$

Integrating over the path length yields a relationship between conversion of HF (f) and xBe. The effective volume of the bubble's path is V_R, defined by the total distance times the cross-sectional area (A). This reactor model is mathematically equivalent to a plug flow reactor (PFR).

$$f = 1 - e^{-(kV_R/\dot{n}_{tot})x_{Be}} \qquad (3)$$

Conversion is a function of time, because xBe decreases with time. Assuming that the HF consumption is only due to Be consumption, Eq. (4) canbe derived which is a Be material balance. The moles of salt in the system is represented by ns, the initial mole fraction of Be in the salt is x_{Be}^0, and the initial mole fraction of HF in the gas phase is y_{HF}^0

$$x_{Be} = x_{Be}^0 - \frac{y_{HF}^0 \dot{n}_{tot}}{2n_s} \int_0^t f \, dt \qquad (4)$$

Simultaneously solving Eqs. (3) and (4) resultsin Eq. (5) inwhich xBe is implicitly defined as a function of time.

$$t = \frac{2n_s}{\dot{n}_{tot} y_{HF}^0} \left((x_{Be}^0 - x_{Be}) + \frac{\dot{n}_{tot}}{kV_R} \ln \times \left(\frac{1 - e^{-(kV_R/\dot{n}_{tot})x_{Be}^0}}{1 - e^{-(kV_R/\dot{n}_{tot})x_{Be}}} \right) \right) \qquad (5)$$

To determine the conversion of HF at any time, the initial Be concentration in the salt is first needed. Then, Eq. (5) isused to calculate the Be concentration at time *t*. This information is then plugged into Eq. (3) to yield the conversion.

3. Experimental results and discussion

3.1. Description of experimental system and procedure

A simplified diagram of the system used forobserving the HF–Be redox reaction is shown in Fig. 1.Amixture of H2, He, and HF gases was flowed into the

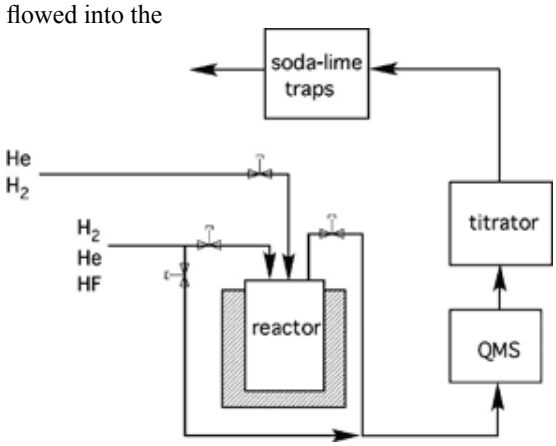

Fig. 1. Test system for measuring redox kinetics.

test reactor containing molten Flibe at 803 K, while the effluent was channeled through a mass spectrometer (VG Quadrupole) followed by an autotitrator (Schott Titronic Universal). The preparation and purification of the Flibe used in this study is described in detail elsewhere [5–7]. The autotitrator used 0.1N NaOH to maintain the pH constant while gas containing HF was bubbled through a stirred titration cell. Effluent from the titration cell was directed into soda lime beds to react any residual HF that may be present in the gas. Experiments with two titration cells placed in series verified that virtually all of the HF was neutralized in the first titration cell.

A more detailed drawing of the reactor is shown in Fig. 2. Its design was intended to support controlled reaction between Be and HF in the molten salt phase. The HF was introduced into the system via bubbling into the salt in a gas mixture that also contains H_2 and He. The H_2 was intended to minimize the likelihood of HF reacting with metal components in the system hardware. The He was a carrier gas so that the total actual flow rate was about 7.5×10^{-6} m^3/s (2.2×10^{-6} m^3/s at STP). The free volume inside of the reactor is estimated to be about 10^{-3} m^3, so the gas residence time is about 130 s. Beryllium could be introduced into the salt via dunking a cylindrical Be rod into the salt for a specified period of time. This rod had a diameter of 0.0076 m and a length of 0.003 m. About 0.0019 m of the specimen was actually exposed to the salt. The rest was nestled within the mounting fixture. A nickel tube acted as a sheath for protecting the Be specimen from

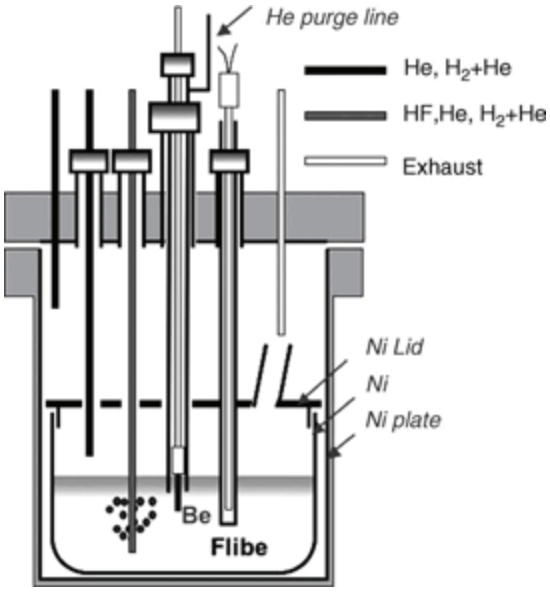

Fig. 2. Reactor for measuring redox kinetics.

contact with HF or salt during times in which the Be was supposed to be isolated. A slow flow of He down through this sheath was used to prevent salt from rising up and coming in contact with the Be specimen. All other internal surfaces of 300 series stainless steel in the reactor were coated with nickel using a high velocity oxyfuel (HVOF) spray process to prevent HF from participating in corrosion-type side reactions.

Each experiment started with the HF–H_2–He feed gas being bubbled into the salt with the Be

specimen retracted. Once the HF concentration in the effluent stabilized at the expected level, the Be specimen was immersed into the salt. After 600–3600 s, the Be was retracted while HF in the effluent was continually monitored for several hours up to a few days. Once the HF concentration in the effluent had again stabilized, the next experiment was run by re-immersing the Be into the salt for a different duration. The same Be specimen was used for each experiment reported in this paper, since the amount of material lost during each experiment was estimated to be very low.

3.2. Be dissolution

The autotitrator data from the redox experiments were used to estimate the amount of Be that dissolved into the salt for each experiment. In each case,

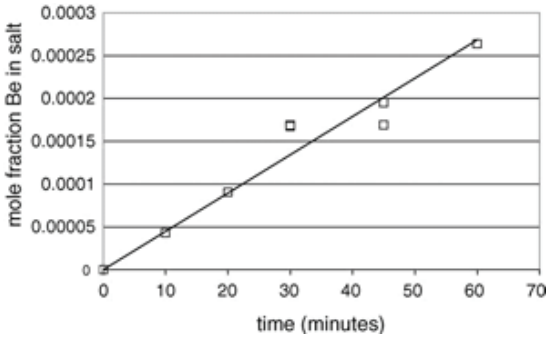

Fig. 3. Effect of dunk time on the initial mole fraction of beryllium in the salt.

the difference in the moles of HF, which would have titrated without any reaction occurring and the moles of HF, which were actually titrated was calculated. Some experiments were not included in this analysis due to evidence that either the Be was not completely consumed in the experiment or the initial HF concentration had not stabilized prior to dunking Be into the salt. The results of the analysis are shown in Fig. 3, where mole fraction of Be in the salt is plotted versus time. The symbol at the origin is not a data point in the literal sense. It is an assumed initial condition.

The linearity of the plot in Fig. 3 suggests a simple mass transfer model of the form shown in Eq. (6), with the saturated concentration term being very high compared to the measured concentrations. The fact that the saturated Be concentration is very high is supported by saturation experiments which were performed and reported elsewhere [5].

$$\frac{dx_{Be}}{dt} = \frac{hA_{Be}(C_{Be}^{sat} - C_{Be}(t))}{n_s}, \quad x_{Be}(0) = 0 \tag{6}$$

Since C_{Be}^{sat} is much greater than CBe, this equation simplifies to Eq. (7).

$$\frac{dx_{Be}}{dt} = \frac{hA_{Be}C_{Be}^{sat}}{n_s}, \quad x_{Be}(0) = 0 \tag{7}$$

The approximate area of exposed surface, ABe,is 5.0×10^{-4} m^2. The saturated concentration of Be in the salt has been estimated to be 21 mol/m^3 based on results published elsewhere [5]. And the total moles of salt, ns, is about 16.7. Thus, h is calculated to be 1.1×10^{-4} m/s, based on these given assumptions.

3.3. Redox reaction kinetics

Table 1 gives a summary of conditions for each redox experiment reported in this paper. Previous experiments ran but not included in this table appearedto be affected by the presence of reactive impurities in the salt or on metal surfaces. As expected, the HF concentration in the effluent dropped rapidly within a matter of minutes after the Be was initially dunked into the salt. As shown in Fig. 4, the conversion of HF peaked above 90% for

Table 1
Summary of HF–Be redox experiments in Flibe

Test	HF concentration (ppm)	Total flow (standard $\times 10^{-6}$ m^3/s)	Be dunk time (s)
REDOX-6	1000	1.8	3600
REDOX-7	910	2.1	1800
REDOX-8	910	2.1	2700
REDOX-9	1800	2.2	1800
REDOX-10	910	2.1	1200
REDOX-11	910	2.1	2700

All tests run at a temperature of 803 K.

each run and then required as much as 60 h to return t o zero. The curve fits shown in Fig. 4 were based on the model from Section 2 of this paper and appear to be reasonably representative of the data.

The decrease in HF conversion was attributed to the slow consumption of dissolved Be in the salt. The integrated moles of HF converted was used to estimate the mole fraction of Be in the salt (xBe) as a function of time. In Fig. 5, conversion is plotted versus xBe. The model based on Eq. (3) predicts difference is not very large. Intuitively, it was expected that the order of the HF concentration dependence in the intrinsic rate equation should be 2. But fits involving such a model were poor in comparison to the ones that assumed an order of 1 for the HF dependence. More experiments are needed with a larger variation in conditions to develop confidence in the order of the HF concentration dependence. Assuming that the given model is close enough to be useful, it is impressive that the curves generated in Figs. 4 and 5 are based on a single kinetic parameter (k). However, since the volume of the reactor in the model (VR) is an artificial construct based on the path traversed by the bubbles, k cannot be definitively separated from kVR. The best fit value of kVR was estimated to be 2.25 mol/s.

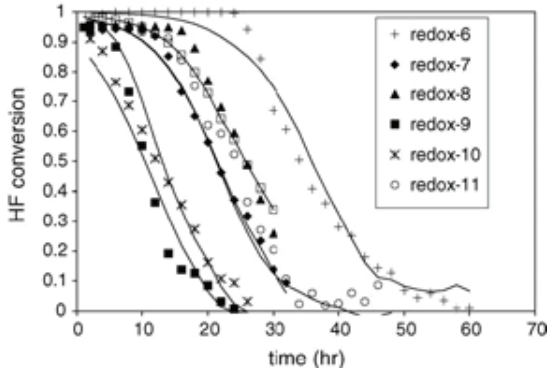

Fig. 4. HF conversion vs. time for redox experiments.

nearly a single curve for all of these experiments, since ṅtot is close to identical for all runs. Interestingly, Eq. (3) predicts no dependence on initial HF concentration. And Fig. 5 shows that the one experiment with an appreciably higher HF feed concentration relative to the rest (REDOX-9) demonstrated results very close to the rest. There may be a slight HF concentration dependence, since the conversion data points from REDOX-9 are a little lower than the rest. But the magnitude of the

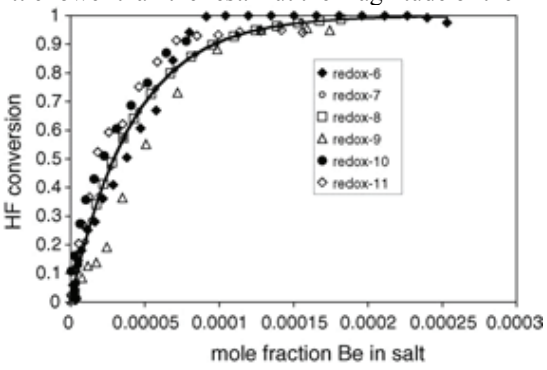

Fig. 5. HF conversion vs. mole fraction of beryllium in the salt.

3.4. Extrapolation of kinetics to blanket conditions

As mentioned previously, it is assumed that there would be a TF generation rate of $1.2\text{x}10^{18}$ molecules/m^3s($2\text{x}10^{-6}$ mol/m^3s) in the Flibe in a real fusion system. This must necessarily be balanced by the rate of redox with Be. Eq. (8) represents this relationship.

$$2 \times 10^{-6}\ \text{mole/m}^3\text{s} = k x_{\text{Be}} y_{\text{HF}} \qquad (8)$$

Unfortunately, the kinetic model was only solved so that the combined product kV_R is known. V_R is an artificial construct, as mentioned previously. While neither V_R nor k can be individually specified from the available experimental data, it is possible to place a lower bound on k by placing an upper bound on V_R. Assume V_R is the entire volume of salt used in the experiment ($2.75\text{x}10^{-4}$ m^3). This is expected to be a gross over-estimation of V_R and thus a gross underestimation of k. But if k is still large enough to keep the TF concentration in the salt low, then the feasibility of Be-controlled redox will be convincingly supported.

It is also necessary to convert from yHF to xHF, since it is the TF concentration in the salt, not the

vapor phase, which is critical with respect to corrosion. For low concentrations of HF in Flibe, Henry's Law has been found to be valid [8]. The Henry's Law constant at 773 K is 3.3×10^{-9} mol HF/mol salt Pa [8]. Assuming the total pressure for the experiments was 8.5×10^{4} Pa, the following equation should satisfy the requirement for consuming TF as fast as it is produced.

$$x_{Be} x_{HF} \leq 6.9 \times 10^{-14} \quad (9)$$

Experiments have indicated that Be solubility in the Flibe at 803 K is about 0.087 wt.% ($x_{Be} = 0.0032$) [5]. At this level, the TF concentration in the salt could be maintained at a level well below 0.02 ppb. This is expected to keep the corrosion rate acceptably low

4. Conclusions

The Be–TF redox reaction has been quantitatively studied using HF in molten Flibe at 803 K. A series of kinetics experiments were run with HF feed concentrations ranging from 910 to 1800 ppm. Though this is too concentrated to be representative of conditions for a Flibe-based fusion system blanket, a kinetic model was derived and fit to the data. This kinetic model was used to estimate how low the TF concentration could be controlled by Be. That level appears to be no higher than 0.02 ppb, a magnitude well below that which is expected to lead to high rates of corrosion in the system. However, the initial HF concentration dependence in the kinetics model has not been well tested. Thus, more experiments with widely varying initial HF concentrations are necessary to develop confidence in the model and its extrapolation to realistic process conditions

References

[1] A. Sagara, H. Yamanishi, T. Uda, O. Motojima, O. Mitarai, T. Kunugi, Y. Matsumoto, S. Satake, W. Yican, T. Terai, S. Tanaka,
H. Matsui, S. Takahasi, T. Yamamoto, S. Toda, S. Fukada, M. Nishikawa, A. Shimizu, N. Yoshida, Studies on Flibe blanket designs in helical reactor FFTR, Fusion Technol. 39 (2001) 753–757.

[2] R.W. Moir, R.L. Bieri, X.M. Chen, T.J. Dolan, M.A. Hoffman, P.A. House, R.L. Leber, J.D. Lee, Y.T. Lee, J.C. Liu, G.R. Longhurst, W.R. Meier, P.F. Peterson, R.W. Petzoldt, V.E. Schrock, M.T. Tobin, W.H. Williams, HYLIFE-II: a molten-salt inertial fusion energy power plant design-final report, Fusion Technol. 25 (1994) 5–25.

[3] T. Terai, A. Suzuki, S. Tanaka, Tritium release from Li2BeF4 molten salt breeder under neutron irradiation at elevated temperature, Fusion Technol. 39 (2001) 768–772.

[4] M. Sawan, Transmutation and production rates for elements in Flibe, in: Proceedings of the APEX Meeting, San Diego, April 17–19, 2002.

[5] M. Hara, Y. Hatano, M.F. Simpson, G.R. Smolik, J.P. Sharp, Y. Oya, K. Okuno, M. Nishikawa, T. Terai, S. Tanaka, R.A. Anderl, D.A. Petti, D.-K. Sze, Interactions between molten Flibe and metallic Be, Fusion Eng. Design 81 (2006) 561–566.

[6] G. Smolik, R. Pawelko, Y. Morimoto, K. Okuno, R. Anderl, D. Petti, T. Terai, Mobilization measurements from Flibe under M.F. Simpson et al. / Fusion Engineering and Design 81 (2006) 541–547 argon and air flow, J. Nucl. Mater. 329–333 (2004) 1322– Flibe-facing materials, J. Nucl. Mater. 329–333 (2004) 1327– 1326. 1331.

[7] R.A. Anderl, S. Fukada, G.R. Smolik, R.J. Pawelko, S.T. Schuetz, J.P. Sharpe, B.J. Merrill, D.A. Petti, H. Nishimura, T. Terai, S. Tanaka, Deuterium/tritium behavior in Flibe and 3218–3222

[8] P.E. Field, J.H. Shaffer, The solubilities of hydrogen fluoride and deuterium fluoride in molten fluorides, J. Phys. Chem. 71 (1967)

Interactions between molten Flibe and metallic Be

M. Hara [a], Y. Hatano [a], M.F. Simpson [b], G.R. Smolik [c], J.P. Sharp [c], Y. Oya[d], K. Okuno[e], M. Nishikawa [f], T. Terai [d], S. Tanaka [d], R.A. Anderl [c], D.A. Petti c, D.-K. Sze g

[a] *Hydrogen Isotope Research Center, Toyama University, Gofuku 3190, Toyama 930-8555, Japan*
[b] *Argonne National Laboratory - West, P.O. Box 2528, Idaho Falls, ID 83403-2528, USA*
[c] *Idaho National Engineering and Environmental Laboratory (INEEL), P. O. Box 1625, Idaho Falls, ID 83415-2218, USA*
[d] *The University of Tokyo, Hongo 7-3-1, Bunkyo-ku, Tokyo 113-8656, Japan*
[e] *Shizuoka University, Ohya 836, Shizuoka 422-8529, Japan*
[f] *Kyushu University, Hakozaki, Higashi-ku, Fukuoka 812-8581, Japan*
[g] *University of California, San Diego, La Jolla, CA 92093-0427, USA*

To understand the interactions between molten Flibe and Be, a metallic Be rod was immersed in molten Flibe at 803K under He atmosphere for 210 h. The Be rod was significantly eroded during immersion in molten Flibe, and the Flibe changed from a clear crystal to a brownish-gray marble-like appearance. The concentration of Be0 in Flibe was evaluated by dissolving salt samples in acid solutions. This dissolution test is based on the reaction of Be0 with proton ions in the acid solutions to generate H2. Hydrogen gas was generated from Flibe contacted with Be under flowing He. The amounts of gas generated corresponded to mole fractions of [Be0]/[Flibe] ranging from 9.9×10^{-4} to 7.6×10^{-3}. On the other hand, no H2 was generated from Flibe that was not exposed to Be or which was exposed to Be and then given significant H_2–HF–He bubbling. These observations showed that Be does, indeed, dissolve in Flibe as Be0. The fact that no Be0 was detected after bubbling H_2–HF–He into the salt indicates that Be0 is an effective redox agent for reacting HF.

1. Introduction

Molten Flibe ($2LiF–BeF_2$) is one of the candidate materials for liquid blanket breeding components for fusion reactors [1]. Flibe has many advantages as a liquid blanket material such as low electrical conductivity and low reactivity with air. On the other hand, Flibe generates tritium fluoride (TF) gas under neutron irradiation [2,3]. Since TF is a strongly corrosive gas, the pressure ratio of TF/T_2 in the system has to be strictly controlled at low levels to prevent the corrosion of structural materials. Metallic Be has been proposed as a reductant for TF in molten Flibe [4–6]. It is the most suitable reductant, because Be acts also as a neutron multiplier. In addition, it is expected that this Be is made up the lost Be in Flibe during the neutron irradiation. The interaction between molten Flibe and metallic Be, however, has been scarcely investigated. From these viewpoints, the interaction between Be and Flibe and tritium behavior in Flibe have been extensively studied under the framework of the second Japan-US Program on Irradiation Tests for Fusion Research (JUPITER-II) [7–11].

In the present paper, the results of Be immersion tests are described. Metallic Be rods were immersed in molten Flibe at 803 K, and then the erosion of the Be and color changes to the Flibe were visually determined. The chemical state of Be in Flibe (Be^{2+} or Be0) was examined by observing H2 generation during acid dissolution. The analysis by means of Auger electron pectroscopy was also carried out.

2. Experimental

2-1. Immersion of Be rod in molten Flibe

The Flibe was prepared from BeF_2 (Alfa Aeasar) and LiF (Aldrich) powders, where the purities of both regents were above 99.9%. Several impurities concentrations are shown in Table 1. The molar ratio BeF_2 to LiF was adjusted to be 2:1 in a glove box and then the mixed powder was put into a nickel crucible. Then the crucible was installed in a stainless steel pot and heated to 798K to melt the powders under He flow.

To remove oxides in molten Flibe, HF gas was bubbled at 798K [10,11]. Then the Flibe was filtered to remove precipitates with a 60-┌ m sintered stainless steel filter. The purity of Flibe finally obtained is shown Table 1. Details of the Flibe preparation have been described in previous work [10,11].

The initial test (BeDis1) involved 20.6 g of prepared Flibe and a Be rod (0.525 g) in a nickel crucible. The

Table 1
Chemical analyses of original regents and Flibe

	O (ppm)	C (ppm)	Fe (ppm)	Ni (ppm)	Cr (ppm)
BeF_2	4800	<20	230	40	7
LiF	60	<20	100	30	4
Flibe	560	<5 to 35	260	15	4

crucible was placed into a stainless steel pot. The stainless steel pot was equipped with gas ports to control the atmosphere in the pot. An electric heater surrounding the pot was used to control the temperature of the Flibe [7]. The temperature of the Flibe was raised to 803K and maintained for 210 h, while the plenum space in the pot was purged with He at 50 sccm. After cooling to room temperature, the pot was opened in a glove box. The Be rod and the Flibe were taken out from the nickel crucible and visually examined. An analysis by means of Auger electron spectroscopy was also carried out. Another similar test (BeDis2) was run for 74 h in a glassy carbon crucible.

Also, a similar Be immersion test (BeDisHF1) was carried out while bubbling of H_2–HF–He gas mixture through the salt.

2-2. Dissolution of Flibe in acid solution

To determine the chemical state and the concentration of neutral Be incorporated in Flibe by the immersion of the Be rods, samples of the salt were dissolved in acid (Table 2). This test is based on a reaction of reducing reagents with the proton ions in the acidic solution to generate hydrogen gas. For instance, if the reducing regent is Be, the reaction would be as follows:

$$Be + 2H^{+} -> Be^{2+} + H2. \quad (1)$$

Namely, Be present in the zero valence state (Be0) should generate hydrogen corresponding to its concentration in Flibe. On the other hand, the divalent form of Be (Be^{2+}) would not generate hydrogen according to Eq. (1).

Three types of Flibe specimens were examined by dissolution tests: (a) salt from BeDis1 and BeDis2 obtained by the immersion tests under He atmosphere, (b) salt, identified as BeDisHF1, that had experienced Be immersions followed by significant H_2–HF–He exposure, and (c) salt from hydrogen permeation experiments [8], PermH, which had never contacted metallic Be.

These Flibe specimens were dissolved in H_2SO_4 solutions, and any generated gas was collected using an inverted funnel attached to a burette.

3. Results and discussion

3.1. Appearance of Be rod and Flibe after immersion test

Fig. 1 shows a picture of the Flibe and the Be rod after the immersion test under He atmosphere. The appearance of Flibe (BeDis1) changed from clear crystals to a marble-like appearance. The top surface was cloudy white, and various locations appeared black or reddish-brown.

To observe the cross section of BeDis1 and the shape of the Be rod, the BeDis1 salt was broken into several pieces by a wedge and a hammer and removed from the crucible. Fig. 2 shows the shape of the Be rod and the cross section of Flibe. Black matter was observed around the Be rod and at the interface between the Flibe and the nickel crucible. The color of the immersed Be rod changed from metallic silver to black. The shape of the Be rod was also changed significantly. Namely, the portion of the Be rod immersed in Flibe was severely eroded by molten Flibe. The top portion of the Be rod not immersed in Flibe retained its original shape. Since the immersed Be rod could not be completely removed from the Flibe matrix, its weight could not be measured accurately. The amount of Be lost to the Flibe was approximated by the change in the area of the cross section of the Be rod, where the length of the Be rod was assumed to be unchanged. This estimation from the Be

Table 2
Summary of dissolution of Flibe in acid solution

Sample	Salt samples		Amount of generated hydrogen or Be equivalent (mol)	$[Be^0]/[Flibe]$
	Weight (g)	Mole (mol) MW of Flibe assumed as 33.0 g/mol		
BeDis1-1	0.3946	1.20E-2	1.7E-5	1.4E-3
BeDis1-2	0.5713	1.73E-2	1.7E-5	9.9E-4
BeDis1-3	0.3515	1.07E-2	4.5E-5	4.2E-3
BeDis1-4	0.3568	1.08E-2	2.1E-5	1.9E-3
BeDis2-1	1.5540	4.71E-2	2.8E-4	5.8E-3
BeDis2-3	1.0548	3.20E-2	4.6E-5	1.5E-3
BeDis2-4	0.4419	1.34E-2	3.1E-5	2.3E-3
BeDis2-6	0.3950	1.20E-2	9.1E-5	7.6E-3
PermH	0.5679	1.72E-2	None	–
BeDisHF1-1	0.3003	9.10E-3	None	–
BeDisHF1-2	0.4363	1.32E-2	None	–
BeDisHF1-3	0.8158	2.47E-2	None	–
BeDisHF1-4	0.7180	2.17E-2	None	–

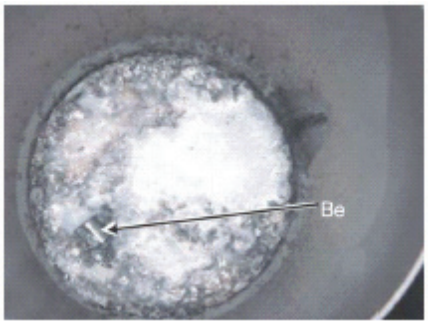

Fig. 1. Top view of Flibe (BeDis1) and Be rod after heating at 803K for 210 h under He atmosphere.

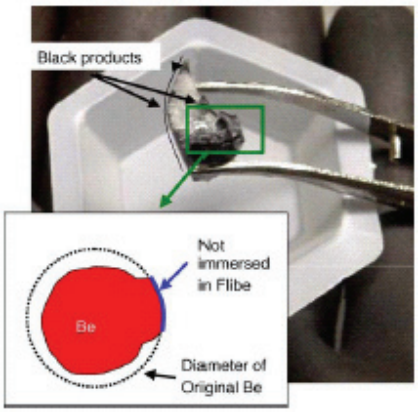

Fig. 2. Shape of Be rod and cross section of Flibe.

rod in Fig. 2 indicated a 25% decrease during the immersion test. The loss of weight of approximately 25% corresponded to a mole fraction of [Be0]/[Flibe] of 0.023. This calculation uses 33 g as the molar weight (denoted as MW) of the salt rather than the 98.9 g/mole which represents the MW of the $2LiF{\cdot}BeF_2$ compound.

3.2. Chemical state of Be incorporate Flibe

Flibe specimens were readily dissolved in sulfuric acid solutions. Only BeDis1 and BeDis2 salt samples generated H2, and this gas appeared to be mainly generated from the black matter. No gas was generated from the PermH and BeDisHF samples. These observations indicated that Be was incorporated as Be0 into the BeDis1 and BeDis2 salts and that the concentration of Be0 was highest in the black matter. The H2 generated by dissolving BeDis1 salts samples provided [Be0]/[Flibe] mole ratios ranging from 9.9×10^{-4} to 4.2×10^{-3}. The mean concentration of Be0 in BeDis1 was calculated to be 2.1×10^{-3} by assuming that all H2 was generated by Be0. The ratios, however, represent only from 4 to 23 percent of the 0.023 mole fraction indicated by the sample loss reported in the previous section. This and possible consumption by oxidizing reagents such as H+ or other impurities in the Flibe may be reasons for the low Be0 accountability. Considering the scatter obtained from the acid dissolution tests, it seems likely that significant Be0 partitioned or segregated to surfaces probably during solidification. Sampling of the hot molten salt will be done in the future. The dissolving BeDis2 salts gave [Be0]/[Flibe] ranging from 1.5×10^{-3} to 7.6×10^{-3}. The mean concentration in BeDis2 was 4.3×10^{-3}. Since these values are almost same as the result of the dissolving BeDis1, the concentration of Be0 in Flibe appeared not to be affected by the difference between the nickel crucible and the glassy carbon crucible. The mean concentration of Be0 in Flibe was estimated to be 3.2×10^{-3}.

It should be noted that BeDisHF1 specimens did not generate H_2. This observation suggests that Be proportioned to the salt was completely consumed by the reaction withHFduring the subsequent treatments with the H_2–HF–He gas mixtures. Namely, Be incorporated in Flibe acted as a reductant of HF. This is very encouraging with regard to the use of Be in the blanket of a fusion reactor to control fluorine potential [12].

3.3. Auger spectra of BeDis1

The differentiated Auger spectrum of BeDis1

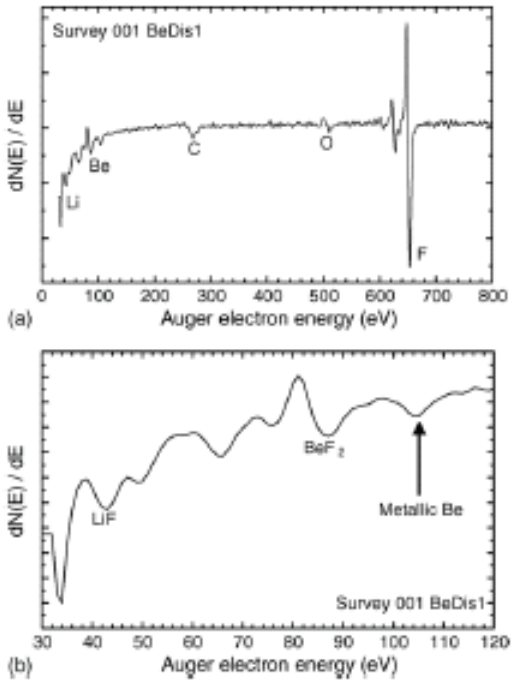

Fig. 3. Auger spectrum of BeDis1.

specimen is shown in Fig. 3(a). Peaks for F, Li and Be were observed along with those for O and C. The detailed spectrum in low energy region is given in Fig. 3(b). Although the origins of several peaks have not been identified, the peak at 43 eV was assigned to Li in the state of LiF [13]. And the peak at 104 eV was assigned to Be in the metallic state [14,15]. The peak at 87 eV was assigned to Be in the state of BeF_2. By assuming that the Auger electron was emitted by inter-atomic transition between Be 1 s electrons and F 2p electrons, the kinetic energy of Auger electron is described as: $Ek=E_{Be1s}-E_{F2p}-E_{F2p}-\varphi$. Here, the binding energy of Be 1 s electron (E_{Be1s}) in BeF2 is 115.3–116.1 eV [16]. The kinetic energy Ek of Auger electrons corresponding to the peak at 87 eV was determined as 83.3 eV from non-differentiated spectrum. If the work function of the specimen (φ) is 0-4 eV as BeO and LiF prepared on metal substrates [17,18], the binding energy of F 2p electrons is evaluated to be 14.0–16.4 eV. These values are very close to the binding energy of F 2p electrons (EF2p) in BeF2 [19]. It should be emphasized that Be in the metallic state was present along with Be in the state of BeF2 as expected from the results of the dissolution tests by acid solution.

4. Conclusions

Interaction between Be and Flibe was studied by immersing a Be rod in molten Flibe under He atmosphere. The Be rod was significantly eroded during immersion of Be in molten Flibe, and the appearance of Flibe was also changed. The dissolution of Be immersed Flibe in acid solution led to the generation of H_2 gas. This observation indicates that Be was incorporated in Flibe as Be0 and not as Be^{2+}. Similar immersion tests were also carried out and then subjected to HF bubbling. In these cases, however, H_2 gas was not generated during the dissolution of the Flibe in acid solution, indicating that incorporated Be0 was consumed by the reaction with HF. Namely, Be incorporated in Flibe acted as reductant against HF.

Acknowledgement

This study was carried out as part of the second Japan-US Program on Irradiation Tests for Fusion Research, JUPITER-II.

References

[1] A. Sagara, H. Yamanishi, T. Uda, O. Motojima, T. Kunugi, Y. Matsumoto, Y. Wu, H. Matsui, S. Takahashi, T. Yamamoto, S. Toda, O. Mitarai, S. Satake, T. Terai, S. Tanaka, S. Fukada, M. Nishikawa, Studies of Flibe blanket designs in helical reactor FFHR, Fusion Technol. 39 (2001) 753–757.
[2] D.-K. Sze, M.E. Sawan, E.T. Cheng, Impact of transmutations in fusion environment on flibe chemistry, Fusion Technol. 39 (2001) 789–792.
[3] A. Suzuki, T. Terai, S. Tanaka, Change of tritium species in Li2BeF4 molten salt breeder under neutron irradiation at elevated temperature, J. Nucl. Mater. 258–263 (1998) 519–524.
[4] R.W. Moir, R.L. Bieri, X.M. Chen, T.J. Dolan, M.A. Hoffman, P.A. House, R.L. Leber, J.D. Lee, T.C. Liu, G.R. Longhurst, W.R. Meier, P.F. Peterson, R.W. Petzoldt, V.E. Schrock, M.T. Tobin, W.H. Williamas, HYLIFE-II: a molten-salt inertial fusion energy power plant design-final report, Fusion Technol. 25 (1994) 5–25.
[5] T. Terai, A. Suzuki, S. Tanaka, Tritium release from Li2BeF4 molten salt breeder under neutron irradiation at elevated temperature, Fusion Technol. 39 (2001) 768–772.
[6] H. Nishimura, A. Suzuki, T. Terai, M. Yamawaki, S. Tanaka, A. Sagara, O. Motojima, Chemical behavior of Li2BeF4 molten salt as a liquid tritium breeder, Fusion Eng. Des. 58–89 (2001) 667–672.
[7] D.A. Petti, R.A. Anderl, G.R. Smolik, D.-K. Sze, T. Terai, S. Tanaka, JUPITER-II Flibe tritium/chemistry and safety experimental program, Fusion Sci. Technol. 41 (2002) 807–811.
[8] S. Fukada, R.A. Anderl, Y. Hatano, S.T. Schuetz, R.J. Pawelko, D.A. Petti, G.R. Smolik, T. Terai, M. Nishikawa, S. Tanaka, A. Sagara, Initial studies of tritium behavior in flibe and flibefacing material, Fusion Eng. Des. 61–62 (2002) 783–788.
[9] S. Fukada, R.A. Anderl, R.J. Pawelko, G.R. Smolik, S.T. Schuetz, J.E. O'Brien, H. Nishimura, Y. Hatano, T. Terai, D.A. Petti, D.-K. Sze, S. Tanaka, Flibe-D2 permeation experiment and analysis, Fusion Sci. Technol. 44 (2003) 410–414.
[10] G. Smolik, R. Pawelko, Y. Morimoto, K. Okuno, R. Anderl, D. Petti, T. Terai, Mobilization measurements from Flibe under argon and air flow, J. Nucl. Mater. 329–333 (2004) 1322–1326.
[11] R.A. Anderl, S. Fukada, G.R. Smolik, R.J. Pawelko, S.T. Schuetz, J.P. Sharpe, B.J. Merrill, D.A. Petti, H. Nishimura, T. Terai, S. Tanaka, Deuterium/tritium behavior in Flibe and Flibefacing materials, J. Nucl. Mater. 329–333 (2004) 1327–1331.
[12] M. F. Simpson, G. R. Smolik, J. P. Sharpe, R. A. Anderl, D. A. Petti, Y. Hatano, M. Hara, Y. Oya, S. Tanaka, T. Terai and D.-K. Sze, Quantitative measurement of beryllium-controlled redox of hydrogen fluoride in molten Flibe, in press.
[13] L.E. Davis, Handbook of auger electron spectroscopy: a reference book of standard data for identification and interpretation of auger electron spectroscopy data, Phys. Electron. (1996).
[14] R.G. Musket, R.J. Fortner, Observation and interpretation of the auger electron spectrum from clean beryllium, Phys. Rev. Lett. 26 (1971) 80–82.
[15] D.E. Fowler, J.M. Blakely, An auger electron spectroscopy (AES) study of the initial states of oxidation of the single crystal Be (0001) surface, J. Vac. Sci. Technol. 20 (1982) 930–933.

[16] J.F. Moulder, W.F. Stickle, P.E. Sobol, K.D. Bomben, Handbook of X-ray photoelectron spectroscopy: a reference book of standard spectra for identification and interpretation of Xps data, Phys. Electron. (1995).
[17] E.J. LeJeune Jr., R.D. Dixon, Interpretation of the Auger electron spectrum from oxidized beryllium, J. Appl. Phys. 43 (1972) 1998–1999.
[18] R. Schlaf, B.A. Parkinson, P.A. Lee, K.W. Nebesny, G. Jabbour, B. Kippelen, N. Peyghambarian, N.R. Armstrong, Photoemission spectroscopy of LiF coated Al and Pt electrodes, J. Appl. Phys. 84 (1998) 6729–6736.
[19] K.L. Bedford, R.T. Williams, W.R. Hunter, J.C. Rife, Electronic structure of beryllium fluoride, Phys. Rev. B 27 (1983) 2446–2457.

JUPITER-II molten salt Flibe research: An update on tritium, mobilization and redox chemistry experiments

David A. Petti [a,*], G.R. Smolik [a], Michael F. Simpson [a], John P. Sharpe [a], R.A. Anderl [a], S. Fukada [b], Y. Hatano [c], M. Hara [c], Y. Oya [d], T. Terai [d], D.-K. Sze [e], S. Tanaka [d]

[a] *Fusion Safety Program Idaho National Laboratory, P.O. Box 1625, Idaho Falls, ID 83415, USA* [b] *Kyushu University, Hakozaki, Higashi-ku, Fukuoka 812-8581, Japan* [c] *Hydrogen Isotope Research Center, Toyama University, Gofuku 3190, Toyama 930-8555, Japan* [d] *University of Tokyo, Hongo, Bunkyo-ku, Tokyo 113-8656, Japan* [e] *University of California at San Diego, La Jolla, CA 92093-0427, USA*

Abstract

The second Japan/US Program on Irradiation Tests for Fusion Research (JUPITER-II) began on April 1, 2001. Part of the collaborative research centers on studies of the molten salt $2LiF_2$–BeF_2 (also known as Flibe) for fusion applications. Flibe has been proposed as a self-cooled breeder in both magnetic and inertial fusion power plant designs over the last 25 years. The key feasibility issues associated with the use of Flibe are the corrosion of structural material by the molten salt, tritium behavior and control in the molten salt blanket system, and safe handling practices and releases from Flibe during an accidental spill. These issues are all being addressed under the JUPITER-II program at the Idaho National Laboratory in the Safety and Tritium Applied Research (STAR) facility. In this paper, we review the program to date in the area of tritium/deuterium behavior, Flibe mobilization under accident conditions and testing of Be as a redox agent to control corrosion. Future activities planned through the end of the collaboration are also presented.

1. Background and objectives

A key issue associated with the use of the molten salt, Flibe (Li_2BeF_4), in fusion applications is the control of tritium permeation and structural material corrosion in the blanket. Irradiation of Flibe will produce in-situ tritium and free (or excess) fluorine ions via numerous nuclear reactions. This free fluorine can impact corrosion processes. The fluorine ions can either combine with the triton produced to form TF, combine with other metal impurities in the Flibe, or remain as a fluorine ion. These can react with the structural metal, depending on the kinetics of the competing reactions. The tritium can also permeate through the structural material of the coolant system with eventual release to the environment.

Thermodynamic stability of the fluoride salt components is quite important because molten salt corrosion is usually induced by reduction/oxidation (redox) reactions. Corrosion control is best accomplished by control of the free fluorine in the system, usually by a redox agent via the reaction:

$$xM + F_2 = xMF_{2/x}$$

where M is the redox agent. The redox agent if properly selected would tie up all of the free fluorine generated on each coolant pass in the system and thus prevent it from being available for reaction with the metals in the structural components. The fluoride chemical potential is defined as $-RT\ln p_{F_2}$ and is plotted for a number of different fluoride reactions in Fig. 1. The more negative the fluoride chemical potential the better that redox agent is at controlling free fluorine generated in the system. Based on these results, we have selected Be as the redox agent for our studies. Be has been previ ously proposed as a redox agent for fusion applications such as HYLIFE-II [1]. It is probably the most natural choice of a redox agent in the fusion context since Be is needed for neutron multiplication in a magnetic fusion blanket to ensure adequate tritium breeding [2]. Other agents (Ce, Eu, HF/H_2) do not have a low enough fluoride potential to suppress TF formation to a level where corrosion is not a concern.

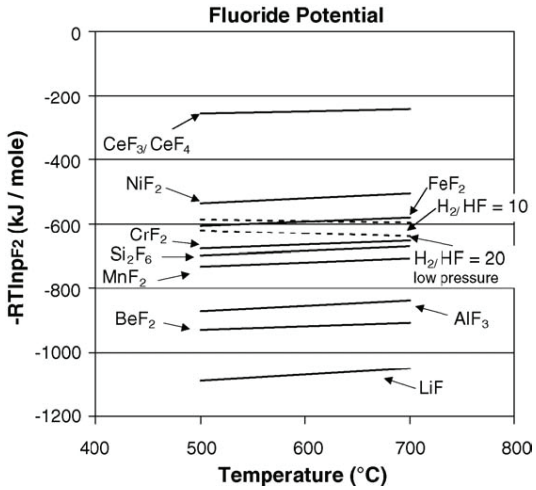

Fig. 1. Fluoride potential for different materials.

The overall tritium behavior in the system will be a function of the REDOX control strategy that is adopted. The low solubility of tritium in Flibe and the strongly reducing conditions expected in a REDOX-controlled Flibe fusion blanket would suggest that tritium would be present primarily as T_2(g). The behavior of tritium with structural materials of interest in a REDOX-controlled Flibe fusion blanket needs to be understood.

Of equal importance are the safety issues associated with the handling of the Flibe and its use as a coolant in a fusion power plant [3]. With the recent tightening of Be standards in the US [4], there is continued attention to the use of all Be containing compounds. There is a need to know the physio-chemical forms of vapors and aerosols produced in a spill of Flibe when it interacts with air or water. Although unirradiated Flibe is not significantly chemically reactive with air or steam, reaction with moist air or water is expected to produce HF and could mobilize tritium, ^{18}F and other radionuclides produced during irradiation.

Based on the key issues associated with the use of Flibe as a coolant in a fusion blanket, the objectives of our work are:

. •to develop the capability to purify Flibe at the liter scale for use in the experiments;
. •to characterize tritium/deuterium behavior (e.g., solubility and diffusivity) in REDOX-controlled and non-REDOX controlled Flibe;
. •to characterize the magnitude and physio-chemical forms of material mobilized during an accidental spill of Flibe and to develop corresponding safe handling practices;
. •to develop a redox agent for use in Flibe in a fusion blanket;
. •to demonstrate the effectiveness of the redox agent in terms of structural material corrosion for fusion materials of interest using a simple dip specimens in small scale pot type experiments.

2. Flibe purification, sampling and analysis

The Flibe used in the JUPITER-II collaboration was prepared from reagent grade chemicals. Both the Be_2F and LiF were listed as 99.9% pure based upon the metals content. Oxygen, nitrogen and carbon were determined by methods utilizing LECO® equipment.

Metals analyses were by inductively coupled plasma-atomic emission spectroscopy (ICP-AES) and mass spectrometry (ICP-MS). The powders were dried and weighed to provide the mole ratio of 2:1 and then purged with helium and melted. The salt was then purged with gas mixtures of He, H_2 and HF at 520 °C to reduce inherent oxides in a pot (see Fig. 2).

The salt was then filtered through a 60-□m metal mesh frit during a transfer to another vessel. The impurities in the final product are given in Table 1. Measurements of beryllium and lithium in the final product ranged from 8.3 to 8.5 and 13.06 to 13.2 wt%, respectively. Although these are lower than the theoretical values of 9.04 and 14.14 wt%, the lithium to beryllium mole ratios of 2.01–2.06 are close to the targeted composition. This suggests that the weight-based dis-crepancies might be due to absorbed water or analytical biases.

Fig. 2. Photograph of Flibe purification setup.

3. Deuterium/tritium behavior

Tritium behavior in molten salts depends strongly on the tritium chemical species in the salt and on the diffusive and solution properties of those species [5]. Several experiments that focused on characterization of tritium species in Flibe under neutron exposure [6–10] indicate that the tritium was borne as T^+ and most likely was bonded to F^- in the salt as TF, unless there was an abundance of hydrogen in solution. Use of hydrogen in purge gas streams over and through the molten salt increased the hydrogen in solution, promoted changes in the tritium chemical species to HT via exchange reactions, enhanced release of tritium from the salt to the gas phase above the salt, and enhanced tritium permeation through metal walls surrounding the molten salt. Only a few studies reported transport properties (diffusivity and solubility). Diffusion coefficients (500–800 °C) were derived in experiments based on T^+ diffusion from a capillary containing irradiated Flibe into a reservoir containing molten Flibe [11]. Tritium diffusion as T^+ was also measured in solid Flibe at temperatures from 350 to 400 °C [12]. Solubility measurements, made for H_2,D_2, HF and DF in Flibe at 500–700 °C, indicated that the solubility of H_2 and D_2 was about a factor of 100 less than that for HF and DF at 600 °C [13,14].

As part of the JUPITER-II program, deu transport experiments were conducted in a cylindrically symmetric, dual probe permeat setup illustrated in Fig. 3 [15]. The assembly consisted of a type-316 stainless-steel pot, a crucible for containing Flibe, two permeation of thin-walled nickel, a gas-manifold to enab purge gas flow through assembly volumes, a quadrupole mass spectrometer (QMS) for on measurements of the flow stream gas

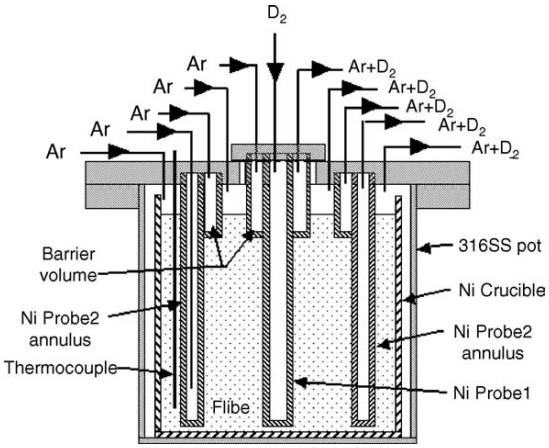

Fig. 3. Schematic illustration of cylindrically symmetric, permeation probe assembly. Overall dimensions of the steel pot were: 178-mm height and a 102-mm o.d. pot wall that was 3-mm thick. Nickel crucible dimensions were: 91.4-mm o.d., 85-mm i.d. and 150-mm height. Probe-2 was a cylindrical annulus with 75-mm o.d., 51-mm i.d., 0.5-mm wall, and 110-mm height. Probe-1 was a 12-mm o.d. cylinder with 0.5-mm wall and a 110-mm height.

transport between the probes and the cover gas above the molten salt. Typically, with the pot at test temperature, probe-1 was pressurized with deuterium and QMS analysis of Ar gas from

Table 1 Impurities in ingredients and final salt

	O (ppm)	C (ppm)	N (ppm)	Fe (ppm)	Ni (ppm)	Cr (ppm)
BeF_2	5700	<20	58	295	20	18
LiF	60	<2	78	100	30	4
Flibe	560	10	32	260	15	16

probe-2 provided a measure of the deuterium that permeated through the walls of probe-1, the molten Flibe and the walls of probe-2. The barrier volumes and the volumes above the salt were purged with separate Ar gas streams that were analyzed sequentially with the QMS.

Several deuterium permeation experiments were made with the system at temperatures of 600 and 650 °C and with a deuterium pressure of around 9.0×10^4 Pa in probe-1. Fig. 4 compares the results of deuterium permeation experiments at 600 °C with no Flibe in the system (Exp A) and with Flibe filling the assembly (Exp B). Probe-2 Ar flow rates were 25 cm^3/min for both experiments. For Exp A, measured D_2 partial pressures in probe-2 (dash–dot line) are plotted relative to the left axis. The Exp A deuterium transient behavior reflects the condition with no Ar flow through the volume between the probes and the case when the flow through the inter-probe volume was changed to 100 cm^3/min. The temporal deuterium behavior followed a traditional permeation transient, and derived permeability coefficients agreed with pre-

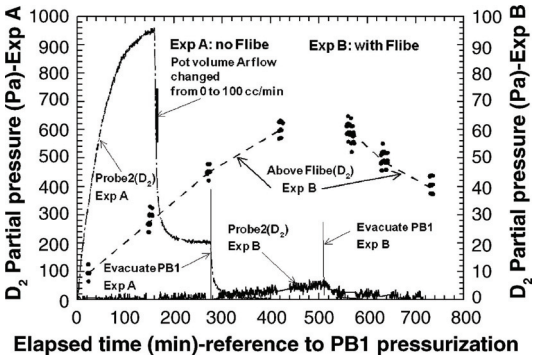

Fig. 4. Comparison of measured deuterium transport data for experiments at 600 °C with (Exp B) and without Flibe (Exp A).

vious work [16,17]. For Exp B, measured D_2 partial pressure data (plotted on the right ordinate) are shown for probe-2 (solid line) and above the Flibe (dash line). Because the QMS was alternately switched to analyze flow streams through probe-2 and above the Flibe, the plotted data show regions with no scatter. Two features of the Exp B data reflect the influence of Flibe on permeation. First, there is significant time delay (on the order of 300 minutes) in the probe-2 D_2 permeation signal and in the buildup of deuterium above the Flibe. Second, the maximum D_2 partial pressures in probe-2 and above the salt are a factor of 200 and 20 less than the partial pressure in probe-2 observed in Exp A. These results are due to the low solubility and low diffusivity of D_2 in Flibe.

TMAP-4 simulation calculations were used to evaluate the overall deuterium permeation rates in the Flibe/Ni/D_2 system using previous literature transport data for these materials. These analyses showed that diffusion in Flibe was rate-determining for our experimental conditions. Results of the analytical fit (by adjustment of diffusivity and solubility values) were compared to experimental data measured at 600 and 650 °C.

Diffusion coefficients derived from these experiments are compared to previously published data in Fig. 5. Our diffusion results are about a factor of 2–5 less than those reported by Oishi et al. [11] for T^+ transport in molten Flibe, suggesting that deuterium was also diffusing as the D^+ species in our experiments. Both of these results are about a factor of 2–5 greater than those derived from the viscosity using the Stokes–Einstein relation, $D = kT/(6\pi R\eta)$, assuming a particle radius, R, of 2 Å and the viscosity of Flibe,

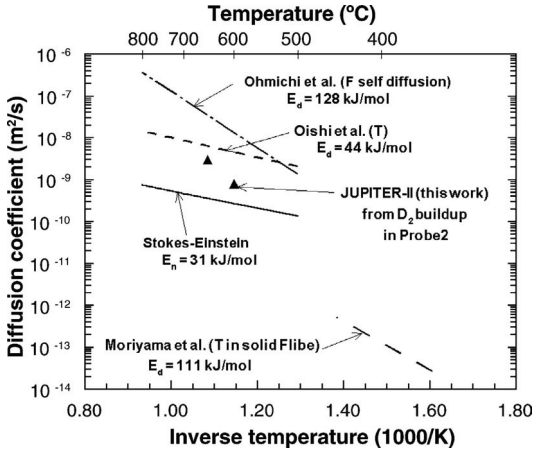

Fig. 5. Diffusion coefficients for Flibe.

reported by Cantor [18] for 2LiF • BeF_2. The diffusion activation energy for the Oishi et al. data is consistent with the viscosity data. However, a two-point fit to our diffusion coefficients (a

dangerous approach with such limited data) yields a diffusion activation energy comparable to that for F^- self diffusion. Such a result would suggest transport mechanisms similar to that postulated by Ohmichi et al. [19], namely ion-pair diffusion or exchange processes that break Be F bonds.

Solubility coefficients derived from these experiments were comparable to those for DF in Flibe, as reported by Field and Shaffer [14], rather than to those for H2,D2, reported by Malinauskas et al. [13]. These results suggest that the chemical potential of deuterium in the Flibe for the current experiments was greater than the chemical potential of D solute when the dominant species of deuterium in Flibe was D2. This interpretation is consistent with previous experiments in which a significant overpressure of hydrogen was required to promote exchange reactions with TF in the salt and facilitate transport of tritium in the Flibe as HT.

Thus, these results suggest that deuterium transport in the present experiments was mediated by the presence of a bond between D^+ and F^- in the molten salt. This could be due to the presence of excess residual HF or free fluorine in the salt following the hydro-fluorination purification process, to ion-pair diffusion processes suggested by Ohmichi et al. [19],or to insufficient concentrations of deuterium in the salt.

Future experiments will examine the solubility of tritium in Flibe at different partial pressures and different REDOX conditions.

4. Flibe mobilization experiments

A key safety issue associated with Flibe is the mobilization of vapors and aerosols from accidental introduction of air, moist air, or steam to the molten salt. Mobilization tests were performed with argon, air and moist air using a classical transpiration apparatus designed for vapor pressure determinations [20]. Whereas previous vapor pressures determined by Oak Ridge National Laboratory (ORNL) studies were conducted at temperatures of above 1000 °C [21], current applications of this salt in fusion energy devices are around 600 °C. Recent models[22,23]have been developed to express vapor pressures for temperatures more applicable to fusion energy applications. Olander et al. [22] compared the extrapolation of ORNL data with a model utilizing selected activity coefficients from various studies and prominent vapor species as identified by mass spectroscopy by Buchler and Stauffer [24]. The latter authors reported BeF2 and LiBeF3 as the dominant vapor species above the LiF–BeF2 system. Above a LiF saturated solution of 74%LiF–26%BeF2 at 600 °C these two species were found to exist in a ratio of 10:1. The two models [22,23] provide essentially the same pressure for BeF2 that is about 60% below the extrapolated ORNL data. The models differ only by the minor contribution attributed to lithium bearing species. Our study for JUPITER-II was undertaken to provide experimental confirmation of vapor pressures at the lower fusion-relevant temperatures and to determine influences of different environments, e.g., argon, dry air and moist air or steam possibly encountered during an accident. Another goal was to obtain mass flux measurements from conditions approximating saturation to provide a basis for comparison with loss of vacuum safety studies addressing blanket design concepts for APEX [25].

Mobilization tests of the salt were performed in a transpiration setup similar to that described by Sense et al. [26] forvapor pressure measurements. A schematic of the test system setup in an inert gas glove box is shown in Fig. 6. The test chamber contained a nickel pipe, 2.09 cm i.d. and 51 cm long, that was heated in

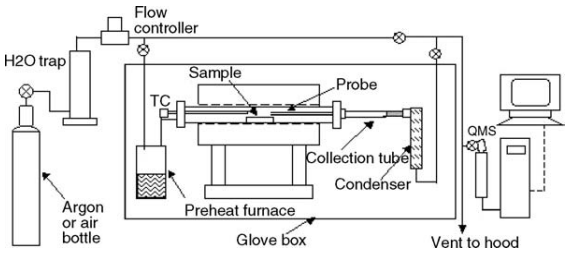

Fig. 6. Transpiration test setup.

a 36 cm long resistance heated muffle furnace. Flibe samples were contained at the center of the hot zone in different types of crucibles depending on the test environment. An Inconel 600 tube was used as a probe through which vapors were transported by the gas flow. A steep thermal gradient existed between

the test region and the ends of the furnace, which forced condensa-tion/deposition of mobilized material onto surfaces of the probe and/or in packed quartz wool attached to the tubing. Tests were performed in argon, dry air and moist air (air saturated with water vapor at 40 °C).

Flibe salt was tested in argon at temperatures of 500, 600, 700 and 800 °C at flow rates of 25, 50 and 100 sccm. Nickel crucibles were used for most tests; however, some tests were also run in glassy carbon crucibles. Tests with dry air were run at these four temperatures with flow rates of 25 and 50 sccm. Tests in moist air were run at 600, 700 and 800 °C with flow rates of 25 and 50 sccm.

The BeF_2 and $LiBeF_3$ partial pressures that were derived from the mobilized material chemical analyses for the argon tests are plotted in Fig. 7 alongwith those from the previous studies and models [21,22,24]. The

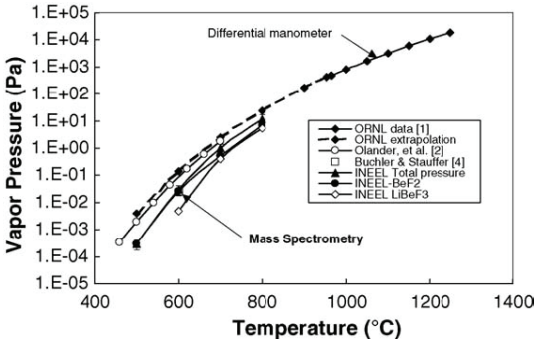

Fig. 7. Total pressure over Flibe.

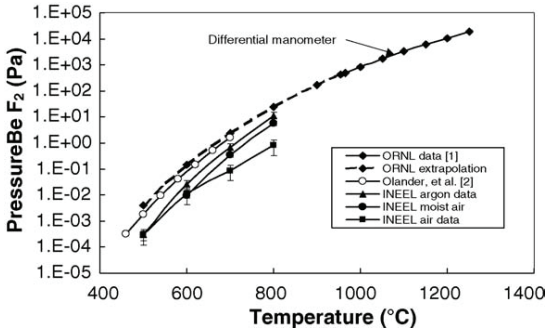

Fig. 8. BeF_2 pressure in various environments.

plot shows the excellent agreement at 600 °C of this study with that of Buchler and Stauffer [24]. The total pressures represented by Olander et al. [22], which are essentially equivalent to those of Zaghloul et al. [23], are about 60% lower than the extrapolated ORNL data [21]. Total measured pressures for BeF_2 and $LiBeF_3$ are two to three times lower than predicted values. The increasing contribution from the lithium species in the INEEL data is apparent at 700 and 800C.

Partial pressures calculated for BeF_2 for all three test gases are shown in Fig. 8. The data for moist air parallels and are about one-half of those measured for the argon tests. The reason for the lower datum points in the dry air tests at 700 and 800 °C is not known. This trend is based upon limited tests and some repeated tests would be needed to confirm this trend. The data did not show any markedly different volatilization rates in dry and moist air compared to those in argon.

Vapor pressures calculated for lithium bearing species, assuming one lithium atom per molecule, are plotted for the various test gases in Fig. 9. No

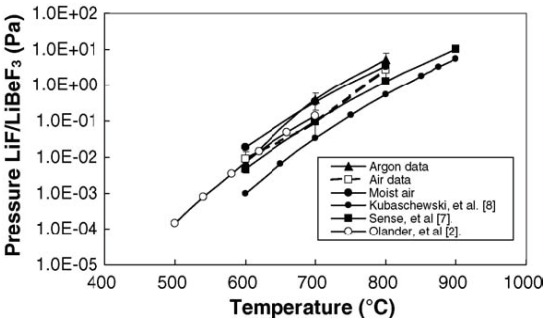

Fig. 9. Pressure of Li bearing vapor over Flibe.

differences in the results can be seen between the environments considering the scatter within the data. The data are slightly higher than pressure of $LiBeF_3$ indicated by Olander et al. [22] and that based on an extrapolation of the LiF data by Sense et al. [26] multiplied by 0.66 the mole fraction in Flibe to simulate ideal solution behavior. The latter extrapolation was from above the 845 °C melting point of LiF.

Mass comparisons using probe interior ICP-AES measurements and sample loss for the argon test series in the nickel crucibles showed that about 22% of the material was deposited in the probe. The

remainder was deposited on the probe exterior and the walls of the test chamber. This reflects the diffusion and re-deposition of material down the temperature gradient. Mass flux calculation (kg/m^2 h) obtained by adjusting ICP-AES measurements for the 22% factor generally agreed within a factor of two of the mass based determinations for individual tests. The model for safety assessments [25] assumes that in a spill of Flibe, the evaporation process from the surface becomes rate limiting by diffusion through the boundary layer. The boundary layer mass transport coefficient K_m of 0.01–0.03 m/s derived for Flibe from this study was applied along with measured vapor pressures and mass based flux determinations to show that the vapor pressures for the argon tests were likely within 70% of saturation. This is in line with the comparison made with vapor pressures from the LiF study by Sense et al. [26]. Although the flow conditions within the test system are not specifically representative to the relatively placid conditions for a LOVA accident [25], the mass based flux values of 2.6×10^{-2} g/m^2 hat500 $^\circ$C, 7.7×10^{-2} g/m^2 hat 600 $^\circ$C, 3.1×10^{-1} g/m^2 hat700 $^\circ$C and 2.4 g/m^2 hat 800 $^\circ$C could be used as first order approximations of evaporation rates.

5. REDOX control

A series of experiments was performed in which HF was bubbled through Flibe with varying concentrations of dissolved Be to investigate the viability of using Be as a redox agent in a molten Flibe (2LiF–BeF2) blanket. Although some previous work has been reported that indicates Be is capable of serving as a redox agent and keeping the TF concentrations low[27], no quantitative measurement of the rate of the Be–TF redox reaction is known to have been made. The objective of this work in the JUPITER-II collaboration was to perform such measurements with the goal of obtaining useful kinetic data that could be used to quantitatively validate the feasibility of using Be as a redox agent in Flibe. Of particular interest is whether the inclusion of Be in the salt can keep the TF concentrations below a level which would lead to structural materials corrosion.

A simplified diagram of the system used for observing the HF–Be redox reaction is shown in Fig. 10. A mixture of H2, He and HF gases was introduced into the test reactor, while the effluent passed through a quadrupole mass spectrometer (QMS) followed by an autotitrator. Our initial experiments used HF gas concentrations between ~ 900 and 1800 ppm in the gas phase. This corresponds to HF solubilities in the Flibe that are ~ 100–200 times higher than expected in a fusion blanket. The autotitrator used 0.1 N NaOH to maintain the pH constant while gas containing HF was bubbled through a stirred titration cell. The autotitrator and QMS yielded both consistent and complimentary results. The QMS directly measures concentration of HF in the effluent, while the autotitrator directly measures cumulative moles of HF that have been collected.

The reactor, shown in more detail in Fig. 11,was designed to provide a controlled reaction between Be and HF in the molten salt phase. The HF was introduced into the system via bubbling into the salt in a gas mixture that also contains H2 and He. The H2 is intended to minimize the likelihood of HF reacting with metal components in the system hardware. The He is a carrier gas so that the total actual flow rate was about 300 cm^3/min to minimize transport time to the QMS and titrator. A cylindrical beryllium rod, 0.76 cm in diameter and 3 cm in length was introduced into the

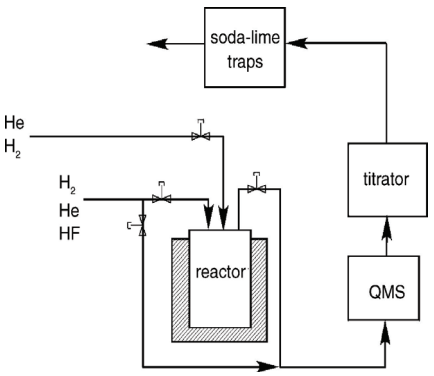

Fig. 10. test system for measureing redox kinetics

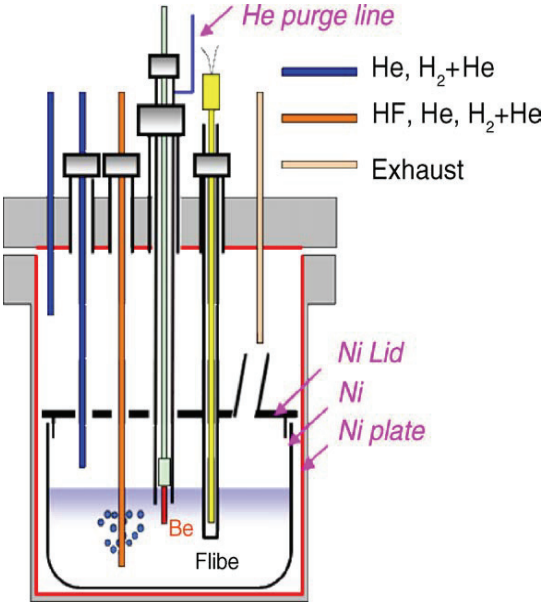

Fig. 11. Reactor for measuring redox

salt for a specified period of time. It is estimated that 1.9 cm of length was actually exposed to the salt, with the rest remaining within the mounting fixture. A nickel tube containing a slow flow of He (~ 2–5 sccm) acted as a sheath to protect the Be specimen from contact with HF or salt (via capillary action) during times when it was not in the salt. All non-nickel metal surfaces inside of the reactor were spray coated with nickel to prevent HF from participating in corrosion-type side reactions.

Each experiment started with the HF–H2–He feed gas bubbled into the salt with the Be specimen pulled out of the salt. Once the HF concentration in the effluent stabilized close to the expected level, the Be specimen was inserted into the salt. After 10–60 min, the Be was lifted out of the salt and into its protective housing while HF in the effluent was continually monitored for times ranging from several hours up to a few days. Once the HF concentration in the effluent had again stabilized, the next experiment was run by re-inserting the Be into the salt for a different duration. The same Be specimen was used for each experiment because the amount of material lost during each experiment was estimated to be very low. As shown in Fig. 12, the effluent HF concentration as measured by the QMS dropped rapidly usually within a matter of minutes after the Be was initially inserted into the salt. The slow recovery of the effluent HF concentration after the Be was removed is

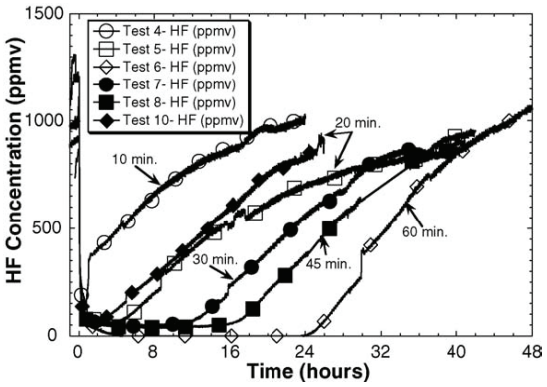

Fig. 12. HF concentration measured by QMS on the outlet of the REDOX experiment for several Be immersion times.

believed to be the result of continued reaction of Be dissolved in the salt with HF added by ongoing gas injection.

The autotitrator data from the redox experiments were used to estimate the amount of Be that dissolved into the salt for each experiment. The results of the analysis are shown in Fig. 13, where mole fraction of Be in the salt is plotted versus immersion time.

The linearity of the plot in Fig. 13 suggestsa simple mass transfer mechanism with a high saturated concentration. This conclusion is supported by the results of our recent Be dissolution experiments [28] inwhich the saturated concentration of Be in the salt has been estimated to be 0.0022 mol/cm^3.

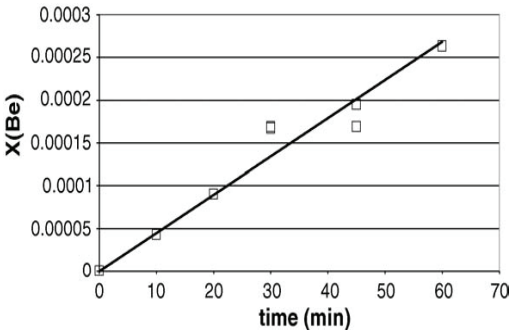

Fig. 13. Effects of immersion time on the initial mole fraction of Be in the salt

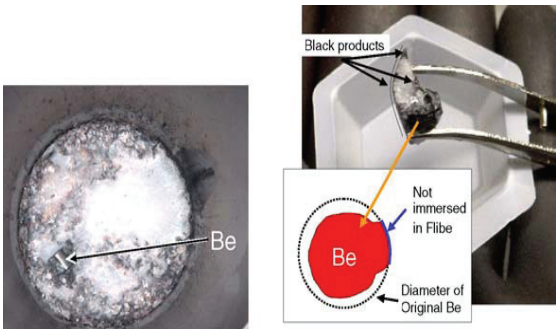

Fig. 14. Photographs of samples from Flibe/Be dissolution tests

To further understand the interactions between molten Flibe and Be, a series of Be dissolution experiments was performed in which a metallic Be rod was immersed in molten Flibe at 803 K under He atmosphere for 210 h [28]. The Be rod was significantly eroded during immersion in molten Flibe, and the Flibe changed from a clear crystal to a brownish-gray marble-like appearance (see Fig. 14). The concentration of Be^0 in Flibe was evaluated by dissolving salt samples in acid solutions. This dissolution test is based on the reaction of Be^0 with proton ions in the acid solutions to generate H2. Hydrogen gas was generated and collected from Flibe contacted with Be under flowing He. The amounts of gas generated corresponded to mole fractions of $[Be^0]/[Flibe]$ ranging from 9.9×10^{-4} to 7.6×10^{-3}. On the other hand, no H2 was generated from Flibe that was not exposed to Be, or Flibe exposed to Be and then given significant He–H2–He bubbling. These observations showed that Be does, indeed, dissolve in Flibe as Be^0. The fact that no Be^0 was detected after bubbling H2–HF–He into the salt indicates that Be^0 is an effective redox agent for reacting HF. Auger analysis of the deposits confirms this inference from these experiments. Additional understanding about the behavior occurring in the salt can be obtained by converting the data in Fig. 13 tofractional conversion of HF (defined as one minus the ratio of the HF QMS data to the HF concentration being added to the pot). The results shown in Fig. 15 allillustrate similar behavior but differ in their time response because of the difference in Be exposure time in the salt (given in parentheses in the legend of Fig. 15). The fractional conversion of HF peaked above 0.9 for each run and then required as much as 60 h to return to zero. A simple first order kinetics model, shown as the curve fits in Fig. 15 and described in reference [29] appear to be reasonably representative of the data.

The integrated moles of HF reacted was used to estimate the mole fraction of Be in the salt (xBe)as a function of time. In Fig. 16, the fractional conversion of HF is plotted versus the time varying mole fraction of beryllium in the salt, xBe. The results show a remarkable similarity over a range of Be exposure times (Be mole fraction dissolved in the salt). Also shown inFig. 16isa single line that is based on the kinetics model developed in Ref. [29]. The results indicate that the model in this dimensionless form does a very good job of predicting the conversion of HF as a function of Be dissolved in the salt over a broad range of Be exposure times and HF gas concentrations between ~ 900 and 1800 ppm.

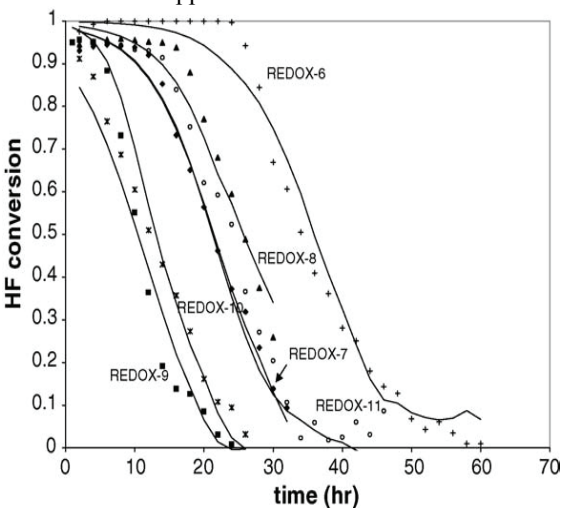

Fig. 15. HF cpnversion versus time for redox experiments (solid lines are kinetic model fits to the data)

These experiments have indicated that Be solubility in the Flibe at 530 °C is about 0.1 wt% (xBe = 0.0036) [5]. At this level, the TF

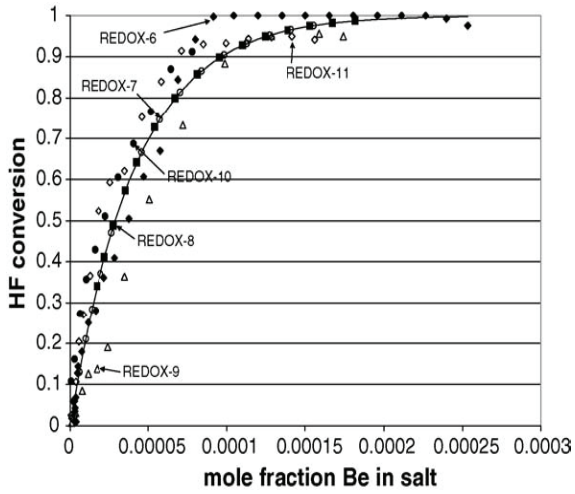

Fig. 16. HF cpnversion versus mole fraction of Be in the salt for all REDOX teasts (solid line is kinetic model fit to data).

concentration in the salt could be maintained at a level well below 0.019 ppb. This is expected to keep the corrosion rate acceptably low.

Thus, our results to date have demonstrated the REDOX process in a laboratory scale experiment by using Be as the REDOX agent. The experiments used HF concentrations that were ~ 100 times higher than that expected in a fusion blanket. The kinetics of the REDOX process was rapid in converting HF to H_2. Continued reaction of HF following removal of the Be from the Flibe indicates that dissolved Be is acting to reduce the HF. A simple kinetics model has been developed to predict the expected HF concentration as a function of Be dissolved in the salt. Future work includes improving the kinetics model to incorporate the uncertainty and impurity effects and performing additional experiments at lower HF concentrations (~ 100–250 ppm) that are closer to those expected in a fusion reactor. Measurement limitations prevent us from performing experiments at typical fusion blanket conditions. Our modeling will be used to extrapolate down to blanket conditions to make preliminary assessments of the use of Be as a redox agent in a fusion blanket. Following the lower concentration experiments, simple dip tests of fusion structural materials are planned with and without Be to demonstrate the reduction in corrosion with Be as a redox agent

6. Summary and conclusions

This document presents an update on the Flibe experiments that have conducted under the US/Japan JUPITER-II collaboration. The experimental program has been focused on addressing the key feasibility issues associated with the use of Flibe. To date, data have been gathered on purification of Flibe, deuterium transport in non-REDOX controlled Flibe, and Flibe mobilization under accident conditions. Most importantly, our initial REDOX experiments have indicated that Be is a good redox agent to control HF and the kinetics at fairly high concentrations are rapid. In the final two years of the collaboration, experiments are planned to study tritium behavior in Flibe with and without REDOX control and to study reduction in the corrosion of fusion structural materials in the presence of Be as a REDOX agent.

References

[1] R.W. Moir, HYLIFE-II: a molten-salt inertial fusion energy power plant design-final report, Fusion Technol. 25 (January 1994).

[2] D.-K. Sze, M. Sawan, E.T. Cheng, Impact of transmutations in fusion environment on flibe chemistry, Fusion Technol. 39 (2) (March 2001) (Part 2).

[3] L. Cadwallader, G. Longhurst, Flibe use in fusion reactors: an initial safety assessment, INEEL/EXT-99-00331, May 1999.

[4] 10CFR850, Chronic Beryllium Disease Prevention Program, January 2001.

[5] H. Moriyama, Chemical behaviors of tritium formed in LiF–BeF2 mixtures, J. Nucl. Mater. 148 (1987) 211–216.

[6] T. Terai, Tritium release from Li2BeF4 molten salt breeder under neutron irradiation at elevated temperature, Fusion Technol. 39 (2001) 768.

[7] A. Suzuki, In-situ HT release behavior from molten Li2BeF4 salt, Fusion Eng. Des. 39–40 (1998) 781–785.

[8] A. Suzuki, Change of tritium species in Li2BeF4 molten salt breeder under neutron irradiation at elevated temperature, J. Nucl. Mater. 258–263 (1998) 519–524.

[9] A. Suzuki, Change of tritium species in Li2BeF4 molten salt breeder under neutron irradiation at elevated temperature, Fusion

Technol. 34 (1998) 526–530.
[10] T. Terai, In-situ tritium release experiment from molten Li2BeF4 salt under neutron irradiation at elevated temperature (INTREXFLIBE), Fusion Technol. 30 (1996) 911.
[11] J. Oishi, Tritium recovery from molten LiF–BeF2 salt, Fusion Eng. Des. 8 (1989) 317.
[12] H. Moriyama, The effect of fusion neutron irradiation on tritium recovery from lithium salts, J. Nucl. Mater. 161 (1989) 197.
[13] A.P. Malinauskas, The solubilities of hydrogen, deuterium, and helium in molten Li2BeF4, Ind. Eng. Chem. Fundam. 13 (3) (1974) 242.
[14] P.E. Field, J.H. Shaffer, The solubilities of hydrogen fluoride and deuterium fluoride in molten fluorides, J. Phys. Chem. 71 (10) (1967) 3218.
[15] R.A. Anderl, Deuterium/tritium behavior in Flibe and Flibefacing materials, J. Nucl. Mater. 329–333 (2004) 1327–1331.
[16] S. Fukada, Initial studies of tritium behavior in Flibe and Flibefacing materials, Fusion Eng. Des. 61–62 (2002) 78.
[17] S. Fukada, Flibe-D2 permeation experiments and analysis, Fusion Sci. Technol. 44 (2003) 410.
[18] S. Cantor, Physical properties of molten-salt reactor fuel, coolant and flush salts, ORNL-TM-2316, August 1968.
[19] T. Ohmichi, J. Phys. Chem. 80 (1976) 1628.
[20] G.R. Smolik, Mobilization measurements from Flibe under argon and air flow, J. Nucl. Mater. 329–333 (2004) 1322–1326.
[21] S. Cantor, D.S. Hsu, W.T. Ward, Vapor pressures of fluoride salts, in: W.R., Grimes (ed.), Reactor Chemistry Division Annual Progress Report, ORNL-3913, ORNL, 1966, pp. 24–26.
[22] D.R. Olander, Equilibrium pressures over BeF2/LiF (Flibe) molten mixtures, Fusion Sci. Technol. 41 (2002) 141–150.
[23] M.R. Zaghloul, D.K. Sze, A.R. Raffray, Thermo-physical properties and equilibrium vapor-composition of lithium fluoride-beryllium fluoride (2LiF/BeF2) molten salt, Fusion Sci. Technol. 44 (2003) 344.
[24] A. B¨uchler, J.L. Stauffer, Vaporization in the lithium fluoride–beryllium fluoride system, in: Symposium on Thermodynamics of Nuclear Materials, International Atomic Energy Agency, 1966, pp. 271–290.
[25] B.J. Merrill, Safety assessment of two advanced ferritic steel molten salt blanket design concepts, Fusion Eng. Des. 72 (1–3) (2004) 277–306.
[26] K.A. Sense, C.A. Alexander, R.E. Bowman, R.B. Filbert Jr., Vapor pressure and derived information of the sodium fluoride-zirconium fluoride system, J. Phys. Chem. 61 (1957) 337–344.
[27] T. Terai, A. Suzuki, S. Tanaka, Tritium release from Li2BeF4 molten salt breeder under neutron irradiation at elevated temperature, Fusion Technol. 39 (March 2001) 768– 772.
[28] M. Hara, Y. Hatano, M.F. Simpson, G.R. Smolik, J.P. Sharpe, Y. Oya, K. Okuno, M. Nishikawa, T. Terai, S. Tanaka, R.A. Anderl, D.A. Petti, D.-K. Sze, Interactions between molten Flibe and metallic Be, Fusion Eng. Des. 81 (2006) 561– 566.
[29] M.F. Simpson, G.R. Smolik, J.P. Sharpe, R.A. Anderl, D.A. Petti, Y. Hatano, M. Hara, Y. Oya, S. Tanaka, T. Terai, D.-K. Sze, Quantitative measurement of beryllium-controlled redox of hydrogen fluoride in molten Flibe, Fusion Eng. Des. 81 (2006) 541–547.

Reaction Rate of Beryllium with Fluorine Ion for Flibe Redox Control

S. Fukada[a)*], M. F. Simpson[b)], R. A. Anderl[b)], J. P. Sharpe[b)], K. Katayama[a)], G. R. Smolik[b)], Y. Oya[c)], T. Terai[c)], K. Okuno[d)], M. Hara[g)], D. A. Petti[b)], S. Tanaka[c)], D.-K. Sze[e)], A. Sagara[f)]

a) Kyushu University, Fukuoka 812-8581, Japan
b) Idaho National Laboratory, Idaho Falls 83415-7113, USA
c) University of Tokyo, Tokyo 113-8656, Japan
d) Shizuoka University, Shizuoka 422-8529, Japan
e) San Diego College of University of California, San Diego, USA
f) National Institute of Fusion Sciences, Toki 509-5292, Japan
g) *Toyama University, Toyama 930-8555, Japan*

Abstract

An experimental effort to apply Flibe (a mixed molten salt of 2LiF + BeF_2) to a self-cooled liquid blanket of a fusion reactor was carried out under a Japan-US collaboration called JUPITER-II. Maintaining Flibe under a reducing atmosphere is a key issue to transform TF to T_2 with a faster reaction rate compared with the residence time in blanket. One of the tasks was to clarify whether or not the redox control of Flibe can be achieved with Be. The dissolution rate of a Be rod and the reaction rate of Be + 2HF = BeF_2 + H_2 in Flibe were experimentally determined. Sufficiently fast rates of the Be dissolution and the reduction reaction of HF to H_2 were clarified by our redox-control experiment. Close agreement was obtained between experiments and our simplified complete-mixing model. In particular, the reaction between Be and a F^- ion immediately after their contact was found to be limited by diffusion of the F^- ion.

1. Introduction

As a promising advanced liquid blanket material, Flibe (a mixed molten salt of 2LiF + BeF_2) has several advantages: low reactivity with oxygen and water even at 600°C and lower electric conductivity. Consequently, it has a lower magneto-hydrodynamic (MHD) effect than other liquid blanket materials such as Li and Li-Pb eutectic alloy. Therefore, Flibe was adopted into a Japanese conceptual design of Force-Free Helical Reactor, FFHR-2 [1,2]. Previously, some physical or chemical properties were determined in the molten-salt fission reactor experiment at ORNL [3], and afterwards tritium release from irradiated Flibe was measured by Japanese researchers [4,5]. However, the chemical behavior of tritium in Flibe was not clarified sufficiently. The largest problem to overcome in a self-cooled Flibe blanket is to control the generation of TF. This is because TF is not only very corrosive to structural materials but also the reduced product T_2 is permeable through the materials. Previously, it was proved that the corrosion rate of 316 stainless-steel was reduced to a negligible level by the addition of Be to Flibe [6]. However, quantitative evaluation has not been performed on the Be dissolution rate and the reduction reaction between Be and F^- ions. In order to control the redox (reduction-oxidation) condition of Flibe, dissolution of Be and transformation of TF (or HF) to T_2 (or H_2) is being investigated at INL as one of the most important tasks of a Japan-US joint study program called JUPITER-II [7-12]. Metallic Be was considered one of the most promising redox-control agents through the reaction of Be + 2TF = BeF_2 + T_2. When the redox reaction is successfully controlled by metallic Be, the tritium chemical form in Flibe will be T_2. Then, tritium permeation through structural materials becomes crucial because of its low solubility and, therefore, its high equilibrium pressure. In order to reduce the tritium permeation, the condition of the extremely low T_2 concentration should be realized and, therefore, high tritium recovery is demanded in the Flibe self-cooled system [13]. Tritium leak rate is estimated huge unless the tritium concentration dissolved in Flibe is extremely low and a proper coating material is developed to suppress tritium permeation. Consequently, the transformation of TF to T_2 by redox control demands not only the high tritium recovery but also the control of T_2 permeation down to an acceptable rate. Unfortunately, there was no information on the TF concentration dependence of the above redox-control reaction and the rate and amount of Be dissolution before starting our study. In the present paper, several reaction-rate constants on the redox control by Be are quantitatively determined in our collaboration experiment of JUPITER-II.

2. Experimental results of redox control by Be

(1) Experimental conditions

An experimental apparatus to investigate the Be redox control of Flibe was already shown in previous papers [8,9]. A powder mixture of BeF_2 and 2LiF with 540 g in weight was melted in a Ni crucible. After purification of Flibe by various HF + H_2 + He mixtures for a sufficient time, a mixture of HF (0 or 500 – 2000 ppm) + H_2 (the H_2/HF ratio of 10, 20 or ∞) in He was introduced into the molten Flibe with a constant flow rate of 110 to 130 cm^3(NTP)/min at 530°C. The compositions of Li, Be, F and other metallic impurities in the mixed molten salt were determined by an ICP-mass spectrometer after sampling a small piece of Flibe. After immersing a Be rod with 5.1 mm in diameter

and 5.0 cm^2 in exposed surface area in Flibe during a specified period from 5 to 60 min, variations of the effluent HF and H_2 concentrations with time were determined by an auto-titrator and a quadrupole mass-spectrometer. The dissolution or absorption rates of Be, HF and H_2 and the reaction rate between Be and F^- ions dissolved in Flibe were determined based on comparison between experimental HF and H_2 effluent curves and numerical simulation curves.

(2) H_2 and HF absorption rate into Flibe

Fig. 1 shows typical effluent curves of H_2 or HF when constant concentrations of H_2 or HF were bubbled through the molten Flibe. All the notations in the figure are listed in Nomenclature. A fast response for H_2 and a delayed one for HF were observed in their respective H_2 and HF curves. The differences in response are due to the rates and amounts of absorption of H_2 and HF into the Flibe. The lines in the figure were expressed in terms of respective linear absorption rate-constants, $k_{abs,H2}A_g$ and $k_{abs,HF}A_g$ and saturated concentrations of H_2 and HF dissolved in Flibe, $x_{H2,sat}$ and $x_{HF,sat}$. In addition, A_g is the surface area that includes bubble surfaces and the overlayer of Flibe.

When the solubilities of H_2 and HF are low and Flibe-gas interaction is expected small, their solubilities should obey the Henry's law. Previous solubility data also supported the Henry law [14,15]. It was considered that the solubilities of H_2 and HF in Flibe obey the Henry law also in the present experiment. Their values were determined as follows: $K_{Henry,H2}$ = 1.24x10^{-3} mol-H_2/m^3Pa and $k_{abs,H2}A_g$ = 1x10^{-5} m^3/s for H_2 absorption, and $K_{Henry,HF}$ = 6.61x10^{-2} mol-HF/m^3Pa and $k_{abs,HF}A_g$ = 1x10^{-7} m^3/s for HF absorption. The $K_{Henry,H2}$ value determined here agreed with our data determined by the D_2 permeability through Flibe [10-12]. However, the fact of $K_{Henry,H2}$ being consistent with our D_2 permeability data does not mean that hydrogen isotopes always exist as a bi-molecular form in Flibe. The values of $K_{Henry,H2}$ and $K_{Henry,HF}$ were about ten times higher than data published in ORNL previously [14,15]. This may be because the chemical form of hydrogen atoms in Flibe is strongly related to the redox-control condition as will be shown below.

(3) Be dissolution rate into Flibe

A proper Be dissolution rate (not too fast or too slow) is a key for the redox control. Fig. 2 shows the molar fraction of Be dissolved in Flibe, x_{Be}, determined from HF effluent curves as a function of the Be immersion period, t_{Be}. Although the Be concentration in Flibe was measured directly by ICP-mass spectrometry, the difference in concentration between a small mount of dissolved Be and the major component of BeF_2 composing Flibe was too small to distinguish the Be dissolution rate. The value of x_{Be} on the vertical axis was determined from the equivalent amount of reacted HF in that introduced into the pot by HF + H_2 + He gas bubbling.

As seen in the figure, the dissolution rate was correlated to a linear equation, and its rate constant was $k_{dis,Be}A_{Be}$ = 8.9x10^{-8} (Be/Li_2BeF_4)/s. The saturated

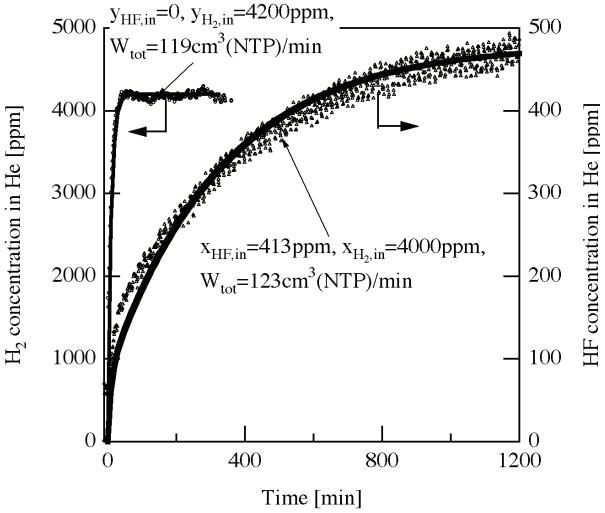

Fig. 1 H_2 or HF concentration curve after gas introduction into Flibe

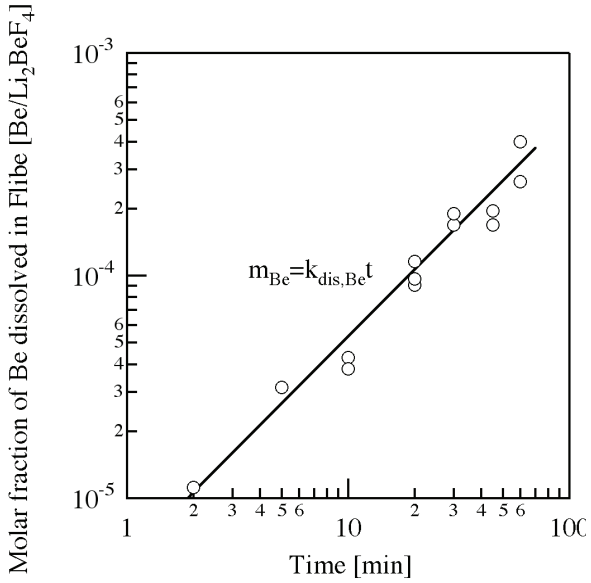

Fig. 2 Be dissolution amount as a function of immersion time

concentration of Be, $x_{Be,sat}$, was estimated as 2.7x10^{-4} in molar ratio of Be/Li_2BeF_4 without a galvanic-coupling effect between Ni and Be [7,16]. When the galvanic-coupling effect was present, $x_{Be,sat}$ became around 6x10^{-3}. The value of $x_{Be,sat}$ was such that the use of Be as a neutron multiplier as well as a redox-control agent in Flibe flowing through a self-cooled blanket. The line in the figure was calculated from the linear dissolution model. The linearity in the wide range means that Be dissolution reached a steady-state rate immediately after the Be immersion.

(4) Reaction rate between Be and HF dissolved in Flibe

Fig. 3 shows typical results of the HF effluent curves as a function of time after the Be rod was immersed in Flibe at t = 0. Conditions for three different runs are as follows: $y_{HF,in}$ = 915 ppm and t_{Be} = 45 min for Run 11, $y_{HF,in}$ = 436 ppm and t_{Be} = 10 min for Run 14 and $y_{HF,in}$ =

192 ppm and t_{Be} = 5 min for Run 16. The total flow rate was 120 cm^3(NTP)/min throughout the three runs. Before starting each experiment, a H_2/HF gas mixture with He balance was continuously bubbled through the Flibe crucible. When the Be rod was immersed into Flibe during a specified time of t_{Be}, the outlet HF concentration dropped drastically. It should be noted that the Be dissolution is deeply related with the galvanic-coupling effect between Be and Ni. When the Be rod was electrically isolated from others, no redox-control could be achieved [17]. In other words, it is probable that Be was dissolved in Flibe as an ion. After a large time delay, the outlet HF concentration gradually returned to the original inlet HF concentration. The measured HF concentrations for the various values of the Be immersion time and the inlet HF concentration were reproduced with good agreement by calculations (dashed lines) using a complete-mixing model described in the next section. Close agreement in the HF effluent curves was obtained between experiment and calculation.

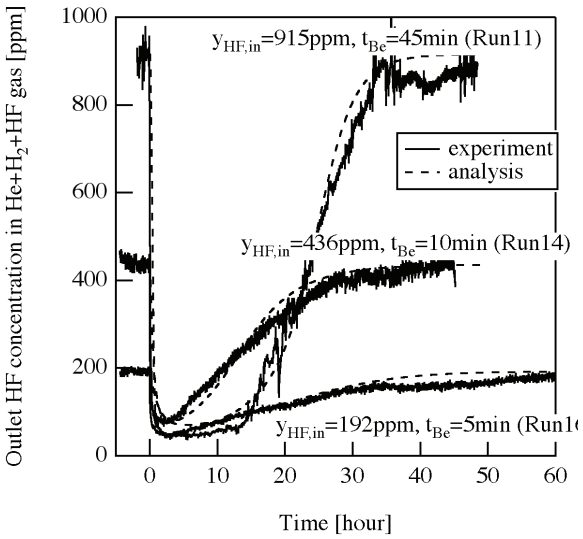

Fig. 3 Comparison between experiment and calculation for Flibe redox control

3. Analysis of reaction between Be and HF dissolved in Flibe

(1) Overall reaction-rate equation

We focused on the overall material balance of Be and HF dissolved in Flibe and HF in He bubbled through a Ni crucible. Calculation was carried out under the assumption of a complete-mixing model, where the HF concentrations in the gas phase and molten Flibe, y_{HF} and x_{HF}, and the Be concentration dissolved in Flibe, x_{Be}, are uniform because of sufficient bubbling rates. Then, variations of y_{HF}, x_{HF} and x_{Be} with time are expressed as follows:

$$V_g c_g \frac{dy_{HF}}{dt} = W\left(y_{HF,in} - y_{HF}\right) - k_{abs,HF} A_g c_g \left(y_{HF} - K_{Henry,HF} R_g T x_{HF}\right) \quad (1)$$

$$V_{Flibe} c_{Flibe} \frac{dx_{HF}}{dt} = k_{abs,HF} A_g c_g \left(y_{HF} - K_{Henry,HF} R_g T x_{HF}\right) - 2V_{Flibe} m_{HF\to H_2} \quad (2)$$

$$V_{Flibe} c_{Flibe} \frac{dx_{Be}}{dt} = V_{Flibe} c_{Flibe} k_{dis,Be} A_{Be} - V_{Flibe} m_{HF\to H_2} \quad (3).$$

All the notations in the equations are listed in Nomenclature. The transformation rate of HF to H_2, $m_{HF\text{-}H2}$, in Eqs. (2) and (3) was expressed in terms of the apparent reaction-rate constants, k_{BeF2} and k_{MF2}, as follows:

$$m_{HF\to H_2} = k_{BeF_2}\left(x_{Be} x_{HF}^2 - K_{Be-BeF_2} x_{BeF_2} x_{H_2}\right) + \sum_i k_{MF_2}\left(x_M x_{HF}^2 - K_{M-MF_2} x_{MF_2} x_{H_2}\right) \quad (4).$$

Here, $K_{M\text{-}MF2}$ is the thermodynamic equilibrium constant of the following reaction:

$$MF_2 + T_2 = M + 2TF \quad (5).$$

Since BeF_2 is very stable thermodynamically, the reverse reaction in the first term on the right-hand side of Eq. (4) can be ignored. The second term in Eq. (4) is an impurity effect and will be discussed in the next section. The word "apparent" means that k_{BeF2} can depend on x_{Be} and x_{HF}. Based on the comparison in the HF and Be concentrations between the experiment and simulation, k_{BeF2} was found to be independent of x_{Be}. On the other hand, two cases of the dependence of k_{BeF2} on x_{HF} were investigated as follows; (i) k_{BeF2} is independent of x_{HF} (*i.e.*, the second-order reaction rate on x_{HF}) and (ii) k_{BeF2} is in reverse proportion to x_{HF} (*i.e.*, the first-order reaction rate on x_{HF}). After simulating HF curves under a wide-range of experimental conditions, the case (ii) assuming the first-order reaction rate gave better fitting. Consequently, Eq. (4) was reduced to the following simplified equation in terms of a modified reaction rate constant, k_{BeF2}*, that includes the contribution of impurity metals:

$$m_{HF\to H_2} = k^*_{BeF_2} x_{Be} x_{HF} \quad (6)$$

The k_{BeF2}^* value determined from the comparison between experiment and calculation was 1.5x10^6 mol/m^{3}s. The deviation between experiment and calculation defined as $\{(y_{HF})_{exp} - (y_{HF})_{cal}\}/(y_{HF,in})_{exp}$ was within 10% for the three runs.

Lines in Fig. 4 in the logarithmic scale as well as Fig. 3 in the linear scale are calculated by Eqs. (1)-(3) and (6) under the assumption of the first-order reaction rate. Good agreement was obtained between the experiment and calculation. Therefore, it was found that the present results can provide the quantitative prediction of the redox control of Flibe by Be in a Flibe blanket. However, there seemed to be appreciable difference between experiment and calculation immediately after or during the Be immersion that will be discussed in Section 4.

(2) Impurity effect on redox control

Effects of metallic impurities included in Flibe are inevitable. Impurities in molten Flibe after HF purification were detected by the ICP-mass spectrometry

and were Cr 12 ppm, Fe 100 ppm, Mn 3 ppm and Ni 6 ppm. The compositions were near to the impurity level of Flibe used in ORNL previously (Fe 21 ppm, Ni 8 ppm, Cr 61 ppm and S 3ppm) [15]. If Flibe contacts Reduced Activation Ferritic/Martensitic Steel, Fe, Cr, W and so on are possibly included as impurities in the future self-cooled Flibe blanket. Judging from the Gibbs free-energy change of Eq. (5), Fe was considered the most critical impurity for the redox control. Even if Be particles can change TF (or HF) to T_2 (or H_2), there is possibility in that Fe can affect the TF concentration in the blanket through the second term in Eq. (3). We should mention that the k_{BeF2} value determined here includes contributions of metallic impurities, mainly Fe.

4. Discussion of redox control by Be rod in fusion blanket

Below we address the redox control by Be immediately after or during Be making contact with the molten Flibe. This condition can simulate the circumstance of flowing Flibe that contacts a Be redox controller in a Flibe self-cooled blanket. We don't always assume that the Be neutron multiplier is placed in a position making contact with a Flibe coolant directly. Fig. 5 shows variations of the HF concentration in the gas phase with time immediately after or during the Be immersion into Flibe. Drastic change of the HF concentration was observed regardless of different HF concentrations and immersion periods. Several things were noticed from the figure: (i) the decrease in y_{HF} continued for a certain time even when Be was withdrawn from the Flibe, (ii) the initial HF decrease rate was correlated to the relation of $y_{HF}/y_{HF,in} = kt^{-n}$ regardless of different conditions of $y_{HF,in}$ and t_{Be}, and (iii) since the residence time of supplied gas was less than 0.1 hour, variations of y_{HF} with time were independent of the residence time. Consequently, the behavior should be explained based on the concentration changes of HF and Be dissolved in Flibe immediately after contacting the Be rod. The Be concentration was almost constant immediately after the Be withdrawal as seen in the dashed line of Fig. 4. The experimental results showed that the value of index n in the relation of $y_{HF}/y_{HF,in}$ was around 0.5. This implies that the reaction of Be and HF is controlled by diffusion of the F^- ions in the Flibe molten salt.

Since the partial pressure of TF generated in a self-cooled fusion blanket to maintain a steady-state fusion power of 1 GW [18,19] is around 10 Pa, the condition is near Run 16. Therefore, $m_{TF\text{-}T2}$ will be expressed by the first-order reaction of x_{TF} even in actual blanket conditions. Consequently, the expected rate of the TF to T_2 transformation is so fast that the x_{TF} value is kept low. Then, the transformation ratio of T_2/TF at the blanket outlet is expected high. The present study proved that the redox control by Be can be achieved even under the TF concentration expected in the FFHR-2 Flibe blanket.

It is important to estimate how the physical property of Flibe such as viscosity changes with the addition of

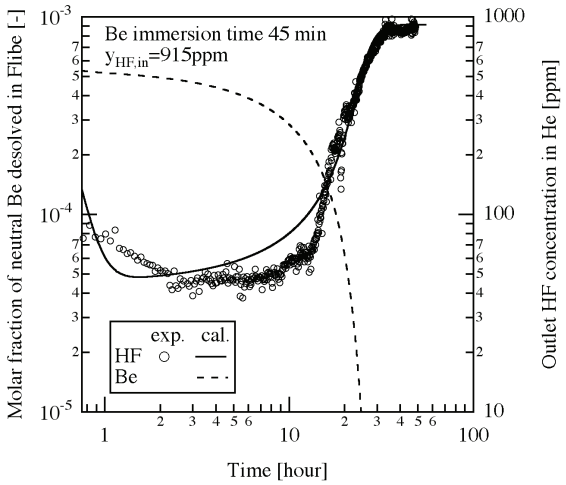

Fig. 4 Typical variations of HF and Be concentrations in Flibe

Be. The consumption rate of LiF in a Flibe blanket for tritium production to maintain a steady-state fusion power of 1GW is 64 mol/day. Therefore, the additional 32 mol/day of Be is necessary for the redox control. In summary, LiF of 96 mol/day should be added to maintain the same blanket composition during the steady-state operation of a fusion reactor. The amount is not large compared with the total Flibe volume of the whole blanket that is estimated as an order of Mmol. However, the constant addition of Be for redox control as well as the Li consumption for tritium generation brings the increase of Flibe viscosity. An increase in the 6% BeF_2 concentration ($2LiF + 1.1BeF_2$) results in an increase in Flibe viscosity from 0.008 Pas to 0.01 Pas at 600°C. Therefore, the proper adjustment of Flibe components is necessary to operate the Flibe blanket in a long range.

5. Conclusions

The redox control of Flibe by Be was successfully proved experimentally, and the prompt transformation of

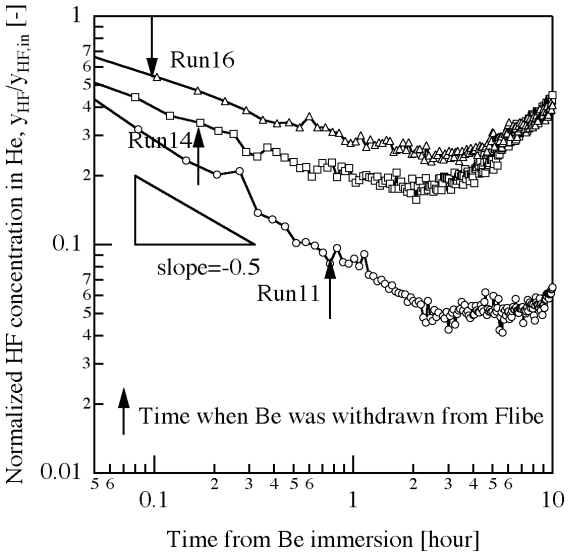

Fig. 5 Initial behavior of HF concentration

HF to H_2 was completed in the Flibe crucible. With the use of the HF solubility ($K_{Henry,HF}$ = 6.61x10^2 mol-HF/m^{3}Pa), the HF absorption rate constant ($k_{abs,HF}A_g$ = 1x10^{-7} m^3/s), and the Be dissolution rate constant ($k_{dis,Be}$ = 8.9x10^{-8} (Be/Li_2BeF_4)/s) determined experimentally, the transformation rate of HF to H_2 in molten Flibe under the assumption of the complete-mixing model could well simulate experimental HF curves. The modified first-order rate constant for Be + 2HF = BeF_2 + H_2 was 1.5x10^6 mol/m^{3}s. In particular, since the decreasing rate of the HF concentration was correlated to $y_{HF}/y_{HF,in} = kt^{-0.5}$ during and immediately after the Be immersion, the rate-determining step of the redox-control reaction was diffusion of F^- ions in Flibe. The expected rate of the TF to T_2 transformation in a Flibe self-cooled blanket system became sufficiently fast to keep the TF concentration low. As a result, a high transformation ratio of T_2/TF at the blanket outlet is expected in a FFHR-2 when Be is used for the redox-control agent material.

Nomenclature

A_{Be} Surface area of Be rod, m^2
A_g Surface area of He bubble and Flibe overlayer, m^2
c Total molar concentration of Flibe or gas phase, mol/m^3
K_{Henry} Henry solubility constant of H_2 or HF in Flibe, mol/m^{3}Pa
k_{abs} Absorption rate constant of H_2 or HF, m/s
$k_{dis,Be}$ Dissolution rate constant of Be, (Be/Li_2BeF_4)/s
k_{BeF2} Reaction rate constant of BeF_2 formation, mol/m^{3}s
m_{TF-T2} Transformation rate from HF to H_2, mol/m^{3}s
R_g Gas law constant, m^{3}Pa/Kmol
T Temperature, K
t Time, s
V Volume of Flibe or gas-phase, m^3
W Molar flow rate of gas, mol/s
x Molar fraction of HF or Be in molten Flibe, -
y_{HF} HF molar fraction in gas phase, -

References

[1] A. Sagara, H. Yamanishi, T. Uda, *et al*., "Studies on Flibe blanket designs in helical reactor FFHR", Fus. Sci. Technol. 39 (2001) 753-757.
[2] A. Sagara, T. Tanaka, T. Muroga, *et al*., "Innovative liquid breeder blanket design activities in Japan", Fus. Sci. Technol. 47 (2005) 524-529.
[3] J. H. Shaffer, "Preparation and handling of salt mixtures for the molten-salt reactor experiment", ORNL-4616 (1971).
[4] H. Moriyama, S. Maeda, T. Ohmura, *et al*., "Chemical behaviors of tritium in a LiF-BeF_2 mixture", J. Nucl. Mater. 148 (1987) 211-216.
[5] A. Suzuki, T. Terai, S. Tanaka, "Change of tritium species in Li_2BeF_4 molten salt breeder under neutron irradiation at elevated temperature", J. Nucl. Mater. 258-261 (1998) 519-524.
[6] J. R. Keiser, J. H. DeVan, E. J. Lawrence, J. Nucl. Mater., 85&86 (1979) 295-298.
[7] M. F. Simpson, G. R. Smolik, J. P. Sharpe, *et al*., "Quantitative measurement of beryllium-controlled redox of hydrogen fluoride in molten Flibe", Fus. Engng. Des., 81 (2006) 541-547.
[8] M. Hara, M. F. Simpson, G. R. Smolik, *et al*., "Interactions between molten Flibe and metallic Be", Fus. Engng Des., 81 (2006) 561-566.
[9] D. A. Petti, G. R. Smolik, M. F. Simpson, *et al*., "JUPITER-II molten salt Flibe research: an update on tritium, mobilization and redox chemistry experiments", Fus. Engng. Des., 81 (2006) 1439-1449.
[10] S. Fukada, R. A. Anderl, Y. Hatano, *et al*., "Initial studies of tritium behavior in Flibe and Flibe-facing material", Fus. Engng. Des., 61-62 (2002) 783-788.
[11] S. Fukada, R. A. Anderl, R. J. Pawelko, *et al*., "Flibe-D_2 permeation experiment and analysis", Fus. Sci. Technol. 44 (2003) 275-286.
[12] R. A. Anderl, S. Fukada, G. R. Smolik, *et al*., "Deuterium/tritium behavior in Flibe and Flibe-facing materials, J. Nucl. Mater., 329-333 (2004) 1327-1331.
[13] S. Fukada, A. Morisaki, A. Sagara, *et al.*, "Control of tritium in FFHR-2 self-cooled Flibe blanket", Fus. Engng. Des., 81 (2006) 477-483.
[14] P. E. Field, J. H. Shaffer, "The solubilities of hydrogen fluoride and deuterium fluoride in molten fluorides", J. Phys. Chem. 71 (1967) 3218-3222.
[15] A. P. Malinauskas, D. M. Dichardson, "The solubilities of hydrogen deuterium and helium in molten Li_2BeF_4", Ind. Eng. Chem. Fundam., 13 (1974) 242-245.
[16] G. R. Smolik, M. F. Simpson, P. J. Pingero, *et al*., "Beryllium interactions in molten Flibe", Proc. ICFRM-12.
[17] M. F. Simpson, G. R. Smolik, S. Fukada, *et al*., "An overview of recent progress in studying redox control in Flibe using dissolved beryllium", Proc. ICFRM-12.
[18] S. Fukada, M. Nishikawa, A. Sagara, *et al*., "Mass-transport properties to estimate rates of tritium recovery from Flibe blanket", Fus. Sci. Technol., 41 (2002) 1054-1058.
[19] S. Fukada, R. A. Anderl, A. Sagara, *et al*., "Diffusion coefficient of tritium through molten salt Flibe and rate of tritium leak from fusion reactor system", Fus. Sci. Technol., 48 (2005) 666-669.
[20] Y. Abe, O. Kosugiyama, A. Nagashima, "Viscosity of LiF-BeF_2 eutectic mixture (X_{BeF2} = 0.328) and LiF single salt at elevated temperatures", J. Nucl. Mater., 99 (1981) 173-183.

PIV TECHNIQUE FOR MEASUREMENT OF TURBULENT FLOW UNDER MAGNETIC FIELDS

J. Takeuchi[1], S. Satake[2], T. Kunugi[3], T. Yokomine[4], N. B. Morley[1], M. A. Abdou[1]

[1]*University of California, Los Angeles, 420 Westwood Plaza, 44-114 Eng. IV, Los Angeles, CA 90095, USA, takeuchi@fusion.ucla.edu, morley@fusion.ucla.edu, abdou@fusion.ucla.edu*
[2]*Tokyo University of Science, 2641 Yamazaki, Noda, Chiba 278-8510 Japan, satake@te.noda.tus.ac.jp*
[3]*Kyoto University, Yoshida, Sakyo, Kyoto, 606-8501 Japan, kunugi@nucleng.kyoto-u.ac.jp*
[4]*Kyushu University, 6-1 Kasuga-koen, Kasuga, Fukuoka 816-8580, Japan, yokomine@ence.kyushu-u.ac.jp*

The investigation of MHD effects on a Flibe (Li_2BeF_4) simulant fluid has been conducted under the U.S.-Japan JUPITER-II collaboration program using "FLIHY" pipe flow facility at UCLA. The present paper reports a development of unique experimental techniques using aqueous solution of potassium hydroxide as a Flibe simulant. In order to apply a particle image velocimetry (PIV) technique for magnetic field condition, special optical devices were developed. The PIV measurements of MHD turbulent pipe flow at Re = 5300 was performed, and modification of the mean flow velocity as well as turbulence suppression were observed. A flat velocity profile in the pipe center and a steep velocity gradient in the near-wall region at Ha = 20 exhibit typical characteristics of Hartmann flow.

I. INTRODUCTION

The design of tritium breeding blankets and plasma facing components is an important field in the R&D activities toward a viable commercial nuclear fusion reactor[1]. The main functions of the blankets for D-T fusion reactors are to breed tritium, to convert the kinetic energy of neutrons and X-rays into heat, and to provide radiation shielding. An essential idea of a liquid breeder concept is that if a liquid containing lithium can be introduced into the blanket, it can be used as both coolant and breeding material. In recent research, a molten salt coolant, Flibe, has attracted attention. Moriyama et al[2] surveyed various design concepts using Flibe and suggested its use in reactor designs where high temperature stability and low MHD pressure drop were special concerns. Among the design concepts utilizing Flibe are HYLIFE-II[3], the APEX thick/thin liquid walls[1], FFHR[4], and a solid first wall design based on advanced nano-composited ferritic steel[5].

Although Flibe has attractive features as coolant and tritium breeding material, there are some issues making Flibe-based blanket design challenging[5]. The main issues include 1) thermal conductivity of Flibe (1W/mK) is low compared to other lithium-containing metal alloys, Pb-17Li (15W/mK) and Li (50W/mK), 2) kinematic viscosity of Flibe is high, especially at temperatures close to the melting point (11.5mm^2/s at 500°C), 3) the tritium breeding capability of Flibe is relatively limited and use of additional neutron multiplier is mandatory, and 4) the high melting point of Flibe requires structural material with temperature range over 650°C. The high viscosity and low thermal conductivity put Flibe in the class of high Prandtl number fluids. The limited temperature window above the high melting point of Flibe requires good heat transfer (low film temperature drop) to cool first wall structures. In order to obtain sufficiently large heat transfer using high Prandtl number fluid coolant, high turbulence is required. On the other hand, Wong et al[5] suggested that the parameter Ha/Re would exceed the critical value of 0.008, especially in large channels, which indicated the suppression of turbulence might be significant[6].

The MHD effects on turbulent flows have been investigated by many researchers, however, most of the experimental efforts were conducted using liquid metals as the working fluid[7][8]. Liquid metals are generally classified as low Prandtl number fluids, and the heat transfer characteristics of low Prandtl number fluids are conduction dominant. Thus it is important to investigate the effect of magnetic fields on the turbulent flow and heat transfer characteristics of the high Prandtl number fluids.

To understand the underlying science and phenomena of fluid mechanics and heat transfer of Flibe, a series of experiments as a part of the U.S.-Japan JUPITER-II collaboration are in progress. The approach includes flow and heat transfer measurements using a Flibe simulant fluid along with numerical simulation[9] and modeling[10]. A flow facility utilizing water and aqueous electrolytes as Flibe simulants has been constructed. Turbulent flow field measurements using PIV[11] and heat transfer measurements[12] have been carried out without magnetic field to establish the experimental techniques and verify the performance of the facility by comparing an existing experimental result[13] and DNS data[14].

The objectives of the present report are to describe the development of the experimental techniques under magnetic fields and introducing some preliminary results of the flow field measurements. In particular, the application of the PIV technique under difficult experimental conditions inside a narrow gap of the magnet is presented. Since most of the existing experimental data of MHD turbulent flows were obtained with liquid metals, flow visualization was impossible. The present work provides unique 2-dimensional 2-velocity-component information of the flow field to enhance understandings of the MHD turbulent flows.

II. DEVELOPMENT OF EXPERIMENTAL TECHNIQUES

An experimental MHD flow facility called "FLIHY" (FLIbe Hydrodynamics) has been constructed at UCLA under the U.S.-Japan collaboration. The experimental facility consists of a flow loop with a pipe flow test section with integrated transparent visualization section, magnet system, and PIV measurement system. A 30% aqueous solution of potassium hydroxide (KOH hereafter) is used as the electrically conducting working fluid.

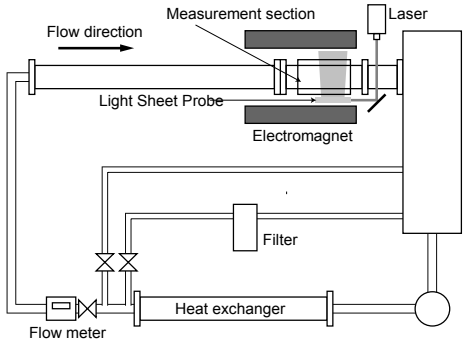

Fig. 1. Schematic drawing of pipe flow facility

II.A. Flow Facility

A schematic drawing of the pipe flow apparatus is shown in Fig. 1. The fluid flow is circulated by a pump and introduced into the horizontal circular pipe test section. Flow passes through a heat exchanger, a flow meter, and a honey comb flow straightener before entering the test section. The temperature of the fluid was monitored by T-type thermocouples and kept constant using the heat exchanger. The test section is a circular pipe made of acrylic with 89 mm inner diameter and 7.0 m in length, which is 79 times the pipe diameter. This length was considered to be sufficient to obtain a fully developed turbulent flow. This relatively large diameter was chosen to allow access to information in near-wall region by making viscous length scale large. Flow rate was controlled by changing the pump output with a variable frequency power controller. A throttle valve in the main loop and a bypass line were also equipped to help flow rate control. Flow rate was measured and monitored by vortex-shedding type flow meter.

The visualization section for the PIV measurement was built 6.8 mm downstream from the inlet. The pipe wall thickness in the visualization section is 1 mm to allow velocity measurement down to very close to the pipe wall. A "water jacket" tank with square cross section was installed surrounding the pipe. The cross section view of the water jacket is shown in Fig. 2. The water jacket is 11 × 11 cm in the cross section and 23 cm long. It was filled with the same fluid as the main flow in order to compensate for the image distortion due to the difference in index of refraction between the inside and outside of the circular pipe. This eliminates the optical distortion to a negligible level, except for the region very close to the wall.

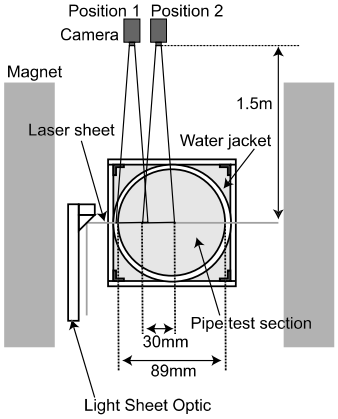

Fig. 2. Cross section view of water jacket and optical configuration

II.B. Magnet

The magnet used for the current experiments produces maximum 2.0 Tesla magnetic fields in a narrow gap of the iron core at 3000 A of applied electric current. The pipe flow test section was placed in the gap which is 1.4 m in the streamwise direction, 25 cm in height, and 15 cm in width.

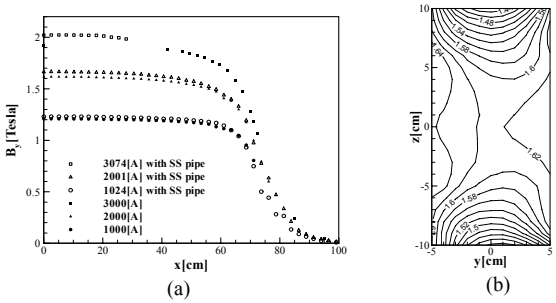

(a) (b)

Fig. 3. B field distribution as function of the streamwise distance from the magnet center (a) and B field distribution at the center cross section (b)

The B field distribution at the center of the streamwise cross section as a function of the distance from the magnet center is shown in Fig. 3. The B field has uniform distribution within 5% variation for 1.0 m in the streamwise direction. Fig. 3 also shows the B field distribution in the center cross section in the streamwise direction.

II.C. PIV SYSTEM

The PIV technique has been developed in last two decades and has become a well established technique for flow field measurements[15][16]. However, there were some difficulties in application of the PIV to the flow measurements in the magnetic fields due to the limited space in the magnet gap, the limited types of the material that can be used under the strong magnetic fields condition and with a corrosive working fluid. Therefore, the PIV system especially tailored for the current experiment was developed by carefully selecting the materials and optical component placement to cope with these difficulties.

II.C.1. Seeding Particles

Seeding particles were selected so that they are compatible with KOH and their density was comparable to that of KOH (1300 kg/m^3). Several materials were immersed in the KOH for several months in order to test compatibility. Methyl methacrylate – ethylene glycol dimethacylate copolymer (Sekisui Plastic Co., Ltd.) turned out to be compatible as well as to have the density close to the solution (about 1200 kg/m^3). It was provided by the company as a sample material. Although it was not specifically tailored for PIV use, its relatively uniform particle diameter was suitable for PIV measurements.

II.C.2. PIV Hardware

The laser sheet was supplied by New Wave mini Solo-III Nd:YAG Laser. A laser beam was introduced into the magnet gap using dielectric coated mirror. A laser sheet was created by light sheet optics specifically designed for this experiment shown in Fig. 4. It equipped with beam collimator and cylindrical lens to create laser sheet, and two dielectric mirrors to introduce the laser sheet horizontally to the test section.

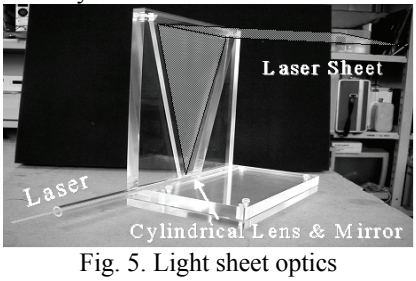

Fig. 5. Light sheet optics

The particle images illuminated by the laser sheet were captured by Phantom v.5.0 camera (Vision Research Inc.). The camera was equipped with 1024×1024 pixels monochrome CMOS array. Tamron SP 35-210 mm lens was used to achieve 90×90 mm field of view on the measurement plane 1.0 m from the lens.

A LabSmith LC880 experiment controller was used for synchronization of the camera and laser. The camera strobe signal was used as a master trigger signal, and the laser firings were controlled by setting delay times from the master signal. The synchronization chart is shown in Fig. 6.

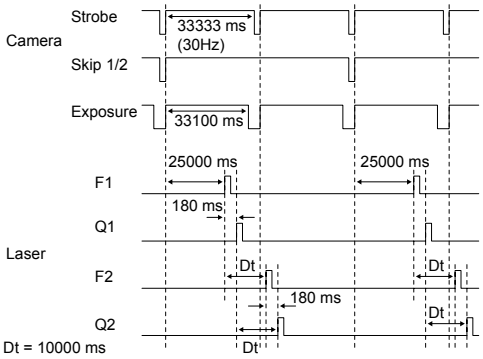

Fig. 6. Synchronization chart

II.C.3. PIV Analysis Software

Dantec FlowManager 3.70 software was used for PIV analysis. It provides analysis method called “adaptive correlation”, which is based on commonly used cross correlation technique[17]. The important feature of the adaptive correlation is a multiple step analysis method[18]. Large interrogation windows are used in the first step and the interrogation windows are successively reduced in the following steps. For this experiment, the reduction of the window size was repeated 4 times. Thus 256 × 128 pixels interrogation windows in the first step were reduced to 32 × 16 pixels in the final step. In each step, cross correlation analysis was performed twice. The first analysis gave a rough estimate of the particle displacement by analyzing exactly the same are of the first and second images, and the location of the interrogation windows in the second analysis determined using the information given by the first analysis in order to minimize loss of particle pairs in the windows[19]. To reduce the possibility of yielding spurious vectors due to mismatch of the particle pairs, local median validation was applied between the steps, and the invalidated vectors were replaced by using information from the vectors in vicinity[20]. The particle displacement was determined down to sup-pixel order. A Dantec 80S33 high accuracy software module was used for this experiment. This module has an advantage over the conventional three-point Gaussian curve fitting method. However, the details of the algorithm are proprietary

II.D. THERMO-PHYSICAL PROPERTIES OF KOH SOLUTION

In order to determine the thermo-physical properties of 30% KOH aqueous solution, measurements were carried out for some of the most critical of them. The kinematic viscosity was measured by U-tube capillary viscometer. The electrical conductivity was measured by conductivity meter. Other properties were quoted from the reference book[21]. TABLE I shows the thermo-physical properties at 33.8°C experimental temperature.

TABLE I. Properties of KOH solution at 33.8°C

ρ	Density	1280 [kg/m^3]
μ	Viscosity	1.431×10^{-3} [Pa·s]
ν	Kinematic viscosity	1.118×10^{-6} [m^2/s]
σ	Electrical conductivity	73.67 [S/m]
λ	Heat conductivity	0.727 [W/(m·K)]
Cp	Heat capacity	3.00 [J/(kg·K)]
Pr	Prandtl number	5.90

III.MHD TURBULENT FLOW MEASUREMENTS

III.A. Experimental Procedures

Experiments were performed by the following procedures. A calibration target was inserted in the test pipe. The camera placement was adjusted so that the field of view encompassed the pipe diameter. The camera focus was focused on the calibration plate at the bisection plane, and calibration images were taken. The correspondence of the pixel length to the physical length was determined by reading the pixel numbers and the physical position of the calibration image on the computer monitor. After the calibration target was removed, flow rate was adjusted to 25 litter per minutes, which corresponds to Re = 5300.

The instantaneous velocity measurements under changing B field strength were performed by starting the measurement without applied B field, and gradually increasing the B field strength during 33 sec measurement time. The field strength reached the maximum around 30 sec after the measurement started.

The mean velocity measurements were performed for five different Hartmann numbers, Ha = 0, 5, 10, 15, 20. 2000 images were taken for each Hartmann number, and the mean velocity profiles were calculated by ensemble averages of 1000 instantaneous velocity vectors and streamwise average of 127 vectors.

III.B. Results

Fig. 7 shows instantaneous velocity vector maps at various instants with increasing Hartmann number. At initial moment (t=0), there was no imposed magnetic field (B=0). After the magnet was turned on (t=10), no significant change in the velocity was observed. At t=20, turbulence fluctuation started to be suppressed, and at t=30, it was completely suppressed.

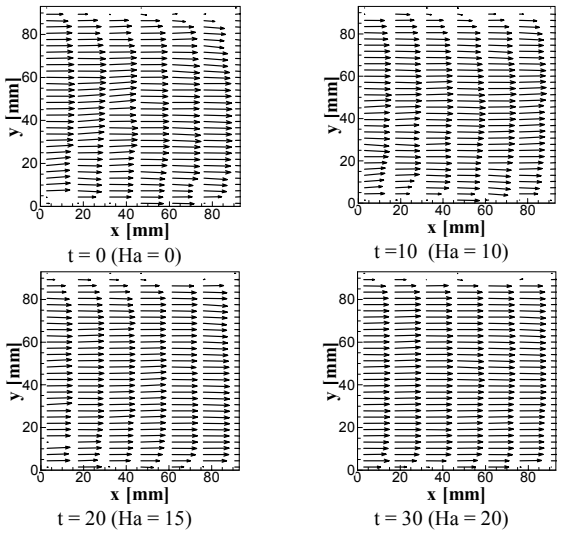

Fig. 7. Velocity vector maps under increasing B field strength

Fig. 8 shows mean velocity distributions at Re = 5300 with variable Hartmann number. The mean velocity profiles are non-dimensionalized by the friction velocity of Ha = 0 case. The actual local friction velocity for higher Hartmann number cases are different from Ha = 0 case. The mean velocity profiles show that it becomes flatter as Hartmann number increases in the core region and that the near-wall velocity gradient increases with increasing Hartmann number, showing typical characteristics of Hartmann flow[7].

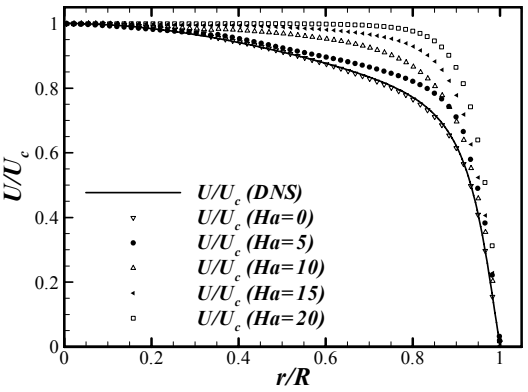

Fig. 8. Mean velocity distritution at Re = 5300

IV.CONCLUSIONS

The PIV measurement technique for MHD turbulent flow of Flibe simulant fluid has been developed. The major difficulties arisen from the limited space in the gap

of the magnet and material limitation due to the strong magnetic field were overcome by specially tailored optical components. The measurement of the MHD turbulent pipe flow yielded unique 2-D 2-component vector maps showing the modification of the mean flow and the suppression of turbulence by MHD effects. Additional experiments are underway to quantify the effect of MHD on fluctuating turbulent velocity components and their subsequent effect on turbulent heat transfer for fusion blankets.

ACKNOWLEDGMENTS

Authors are grateful for the financial support from the U.S. D.O.E., Grant No. DE-FG03-86ER52123, and the Japanese Ministry of Education, Culture, Sports, Science and Technology via JUPITER-II collaboration.

REFERENCES

[1] M. A. ABDOU, THE APEX TEAM and A. YING et al., "On the Exploration of Innovative Concepts for Fusion Chamber Technology," *Fusion Eng Des*, **54**, 181 (2001)

[2] H. MORIYAMA, A. SAGARA and S. TANAKA et al, "Molten Salts in Fusion Nuclear Technology," *Fusion Eng. Des.*, **39-40**, 627, (1998).

[3] R. W. MOIR, R. L. BIERI and X. M. CHEN et al, "HYLIFE-II: A molten-salt inertial fusion energy power plant design - final report," *Fusion Technol.*, **25**, 5, (1994).

[4] A. SAGARA, H. YAMANISHI and S. IMAGAWA et al, "Design and Development of the Flibe Blanket for Helical-Type Fusion Reactor FFHR," *Fusion Eng. Des.*, **49-50**, 661, (2000).

[5] C. P. C. WONG, S. MALANG and M. SAWAN et al, "Molten Salt Self-Cooled Solid First Wall and Blanket Design Based on Advanced Ferritic Steel," *Fusion Eng. Des.*, **72**, 245, (2004).

[6] E. BLUMS, YU. A. MIKHAILOV and R. OZOLS, *Heat and Mass Transfer in MHD Flows*, World Scientific, Singapore, (1987).

[7] R. A. GARDNER and P. S. LYKOUDIS, "Magneto-Fluid Mechanic Pipe Flow in A Transverse Magnetic Field. Part 1. Isothermal Flow," *J. Fluid Mech.*, **47**, 737, (1971).

[8] C. B. REED and P. S. LYKOUDIS, "The Effect of a Transverse Magnetic Field on Shear Turbulence," *J. Fluid Mech.*, **89**, 147, (1978).

[9] S. SATAKE, T. KUNUGI and S. SMOLENTSEV, "Direct Numerical Simulations of Turbulent Pipe Flow in a Transverse Magnetic Field," *J. Turbulence*, **3**, 020, (2002).

[10] S. SMOLENTSEV, M. A. ABDOU and N. B. MORLEY et al, "Application of the K-ε model to open channel flows in a magnetic field," *Int. J. Eng. Sci.*, **40**, 693, (2002).

[11] J. TAKEUCHI, S. SATAKE and N. B. MORLEY et al, "PIV Measurements of Turbulence Statistics and Near-Wall Structure of Fully Developed Pipe Flow at High Reynolds Number," *Proc. 6th International Symposium on Particle Image Velocimetry*, Pasadena, CA, USA, Sept 21-23, (2005).

[12] J. TAKEUCHI, S. SATAKE and R. MIRAGHAIE et al, "Study of Heat Transfer Enhancement / Suppression for Molten Salt Flows in a Large Diameter Circular Pipe: Part One - Benchmarking," *Fusion Eng Design*, 81, 601, (2006).

[13] J. G. M. EGGELS, F. UNGER and J. WEISS et al, "Fully Developed Turbulent Pipe Flow: A Comparison between Direct Numerical Simulation and Experiment," *J. Fluid Mech.*, **268**, 175, (1994).

[14] S. SATAKE, T. KUNUGI and R. HIMENO, "High Reynolds Number Computation for Turbulent Heat Transfer in Pipe Flow," In: M. Valero et al, Ed., *Lecture Notes in Computer Science 1940*, Springer-Verlag, Berlin-Heidelberg, (2000).

[15] R. J. ADRIAN, "Particle-Imaging Techniques for Experimental Fluid Mechanics," *Annu. Rev. Fluid Mech.*, **23**, 261, (1991).

[16] M. RAFFEL, C. E. WILLERT and J. KOMPENHANS, *Particle Image Velocimetry: A Practical Guide*, Springer-Verlag, Berlin-Heidelberg, (1998).

[17] R. D. KEANE and R. J. ADRIAN, "Theory of Cross-Correlation Analysis of PIV Image," In: F. M. T. Nieuwstadt Ed., *Flow Visualization and Image Analysis*, Kluwer Academic Publishers, Netherlands, (1993).

[18] F. SCARANO and M. L. RIETHMULLER, "Iterative Multigrid Approach in PIV Image Processing with Discrete Window Offset," *Exp. Fluids*, **26**, 513, (1999).

[19] J. WESTERWEEL, D. DABIRI and M. GHARIB, "The Effect of a Discrete Window Offset on the Accuracy of Cross-Correlation Analysis pf Digital PIV Recordings," *Exp. Fluids*, **23**, 20, (1997).

[20] J. WESTERWEEL, "Efficient Detection of Spurious Vectors in Particle Image Velocimetry Data," *Exp. Fluids*, **16**, 236, (1994).

[21] A. L. HORVATH, *Handbook of Aqueous Electrolyte solutions*, Ellis Horwood, Chichester, (1985).

THE INFLUENCE OF A MAGNETIC FIELD ON TURBULENT HEAT TRANSFER OF A HIGH PRANDTL NUMBER FLUID

H. Nakaharai[1], J. Takeuchi[2], T. Yokomine[1], T. Kunugi[3], S. Satake[4], N.B. Morley[2], M.A. Abdou[2]

[1]*Kyushu University, 6-1 Kasuga-koen, Kasuga, Fukuoka 816-8580, Japan, nakah@aees.kyushu-u.ac.jp, yokomine@ence.kyushu-u.ac.jp*
[2]*University of California, Los Angeles, 420 Westwood Plaza, 44-114 Eng. IV, Los Angeles, CA 90095, USA, takeuchi@fusion.ucla.edu, morley@fusion.ucla.edu, abdou@fusion.ucla.edu*
[3]*Kyoto University, Yoshida, Sakyo, Kyoto, 606-8501 Japan, kunugi@nucleng.kyoto-u.ac.jp*
[4]*Tokyo University of Science, 2641 Yamazaki, Noda, Chiba 278-8510 Japan, satake@te.noda.tus.ac.jp*

The influence of a transverse magnetic field on the local and average heat transfer of an electrically conducting, turbulent fluid flow with high Prandtl number was studied experimentally. The mechanism of heat transfer modification due to magnetic field is considered with aid of available numerical simulation data for turbulent flow field. The influence of the transverse magnetic field on the heat transfer was to suppress the temperature fluctuation and to steepen the mean temperature gradient in near-wall region in the direction parallel to the magnetic field. The mean temperature gradient is not influenced compared to the temperature fluctuation in the direction vertical to the magnetic field.

I. INTRODUCTION

In the long history of the study of an electrically conducting fluid flow, a great deal of effort has been made on magnetohydrodynamics (MHD) effects in liquid metals, commonly used in many engineering applications. Gardner [1] examined the influence of a transverse magnetic field on the structure of a turbulent flow of mercury and observed that the turbulence intensity decreased to a laminar level over a broad range of Reynolds numbers and magnetic fields. A similar result has been reported by Brouillette [2] and Reed [3]. As for the numerical simulation, the effects of the magnetic field on near-wall turbulence structures were investigated by Satake [4] and Lee [5]. They reported an increase in the skin friction when the strength of the wall-normal magnetic field exceeded a certain value. This increase was attributed to the drag increase due to the Hartmann effect, which was greater than the drag reduction due to turbulence suppression, that is laminarization. Gardner [6] also reported that the influence of a transverse magnetic field on the heat transfer was to inhibit the convective mechanism of heat transfer, resulting in up to 70% reductions in Nusselt number. In another paper [7], Gardner summarized his results of turbulent heat transfer calculations using a curve fit equation representing the average Nusselt number as a function of both Peclet number and Hartmann number. Recently, several studies have been made for a fusion blanket cooled by molten salt [8]. Unlike MHD effects on the flow field, as for the heat transfer the problem becomes more complicated, because the molten salt is a characteristic of a high Prandtl number fluid. In general, for a high Prandtl number fluid, heat transport from a heated wall into the core of the fluid flow is dominated by turbulent motion rather than thermal diffusion. Moreover, near-wall flow structures are especially important, because the thermal boundary layer is much thinner than the momentum boundary layer. In the case of where turbulence suppression due to strong magnetic field occurs, it is expected that the heat transfer performance degradation of high Prandtl number fluid is more sensitive than that of low Prandtl number fluid. Thus, investigation of the fluid mechanics, and the heat transfer of a high Prandtl number fluid is very important from the design point of view compared to low Prandtl number fluid, especially for the high heat flux cooling system such as fusion reactor. In comparison with the studies on heat transfer mechanism of liquid metal, very few attempts have been made on heat transfer mechanism of a high Prandtl number fluid for the design of MHD devices. Blum [9] conducted heat transfer experiment using an electrolyte flowing through a rectangular channel over a wide range of Reynolds number including the transition region from laminar to turbulent and presented an empirical function for the reduction of heat transfer in a turbulent MHD flow by means of an interaction parameter. It is the objective of the present study, to acquire the data for local and average heat transfer and temperature fluctuation of an electrically conducting turbulent fluid round pipe flow with high Prandtl number under the magnetic field, and to understand the interaction between the magnetic field, the fluid turbulence and the heat transfer.

II. EXPERIMENT

A Potassium hydroxide (KOH) 30wt% water solution is used in this experiment, the KOH water solution properties are mentioned in Table 1. A schematic diagram of the experimental closed loop, named ‘‘Fli-Hy (FLiBe-

Table 1 The properties of 30%wt KOH water solution

	T=15[C]	T= 35[C]
Thermal conductivity [W/(m K)]	0.693	0.729
Density [kg/m^3]	1291	1279
Kinematic viscosity [m^2/s]	1.778×10^{-6}	1.189×10^{-6}
Specific heat capacity [J/(kg K)]	2957	2999
Electrical conductivity [1/Ω*m]	51.6	75.2
Prandtl Number	9.8	6.2

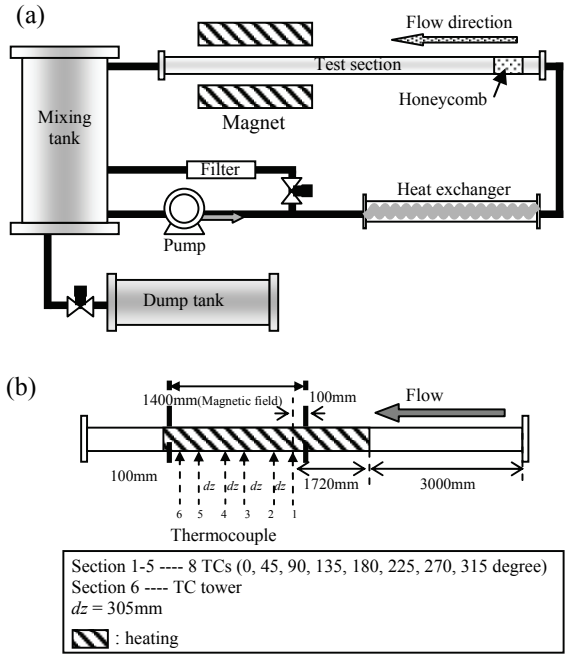

Fig.1 Systems of Fki-Hy closed loops: (a) overall view and (b) detail of test section.

simulant Hydrodynamics) loop'' established at UCLA [10] is shown in Fig.1a. The KOH water solution flow is introduced into the horizontal pipe test section by mechanical pump. The KOH temperature is monitored at both the inlet and the outlet of the test section using thermocouples. The bulk mixing temperature of an arbitrary cross section T_b is estimated by the linear interpolation from the inlet temperature T_{in} and the outlet temperature Tout using Eq.(1) where, x is the downstream position of the measurement and L is the total heating length.

$$T_b = T_{in} + (T_{out} - T_{in})\frac{x}{L} \qquad (1)$$

The details of the test section are shown in Fig.1b. The test section of this loop is made of 8m long SUS pipe, an inner diameter of 89mm. A part of this test section is heated uniformly by heating tape. A constant magnetic field is applied for 1.4m along the pipe up to 2 T. A number (40) T-type thermocouples having a diameter of

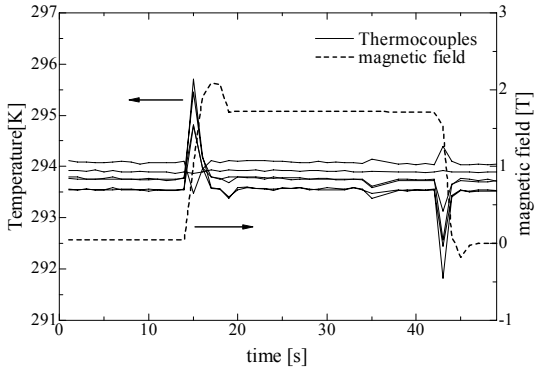

Fig.2 Magnetic field effect on thermocouple.

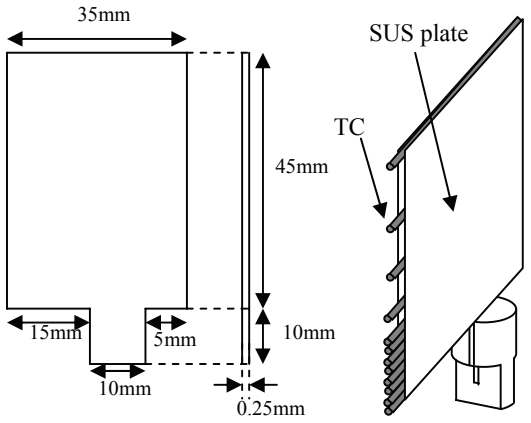

Fig.3 Schematic view of TC tower.

Table 2 Details of experimental condition

Pr (Temp. of KOH[C])	Re	Ha (magnitude of magnetic field [T])
6.2 (35)	5000, 20000	0(0), 5(0.51), 10(1.05), 15(1.60)
9.8 (15)	5000, 20000	0 (0), 5 (0.75), 10 (1.6)

0.5mm are fixed using high thermal conductivity grease (15W/mK) at five axial stations and eight angles from the horizontal magnetic field. The depths of the holes and the tube wall thickness are 4mm and 5mm, respectively, i.e. the length from the inner tube surface to measuring point is 1mm. The location of thermocouples for wall temperature measurement is shown in Fig.1b. The effect of the magnetic field on the thermocouples is shown in Fig.2, where, a significant noise signal appeared at the moment of application and removal of the magnetic field. This noise is not caused by the induction current in the SUS pipe, but due to the effect of changing the magnitude of the magnetic field on the thermoelectric power directly, because the sheathed T-type thermocouples used in this test section is insulated. However, the measured temperature was stable when the magnetic field was constant. The average difference in temperature measured

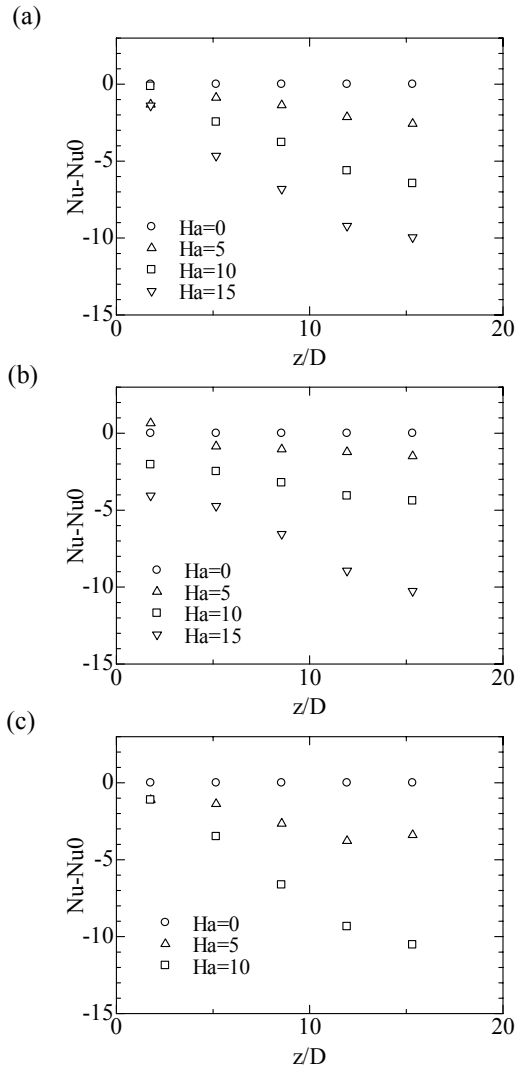

Fig.4 Local heat transfer from magnetic field: (a) *Re*=5000, *Pr*=6.2, (b) *Re*=20000, *Pr*=6.2, and (c) *Re*=5000, *Pr*=9.8.

with and without the magnetic field was about 0.01K on all the thermocouples.

The radial temperature distribution of the fluid flow in the pipe is measured by means of thermocouples tower (TC tower) consisting of inconel sheathed K-type thermocouples having a diameter of 0.13mm arranged from the inner wall surface to the centre of the pipe as shown in Fig.3. The 63% response time of this thermocouple is 2ms. The case when the angle between the TC tower and the magnetic field is 0° and 90° are named case A and case B, respectively.

The Reynolds number based on bulk velocity and pipe diameter is set to 5000 and 20000 for four Hartmann numbers, *Ha*=0, 5, 10, 15, and *Pr*=6.2, 9.8. The bulk

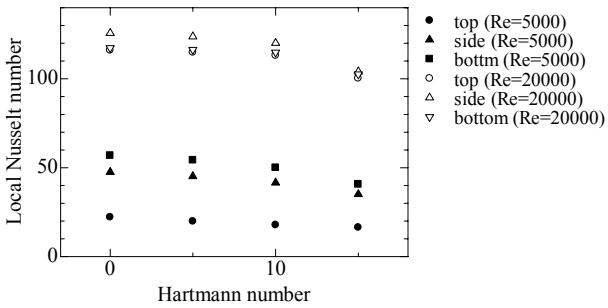

Fig.5 Local Nusselt number *Pr*=6.2.

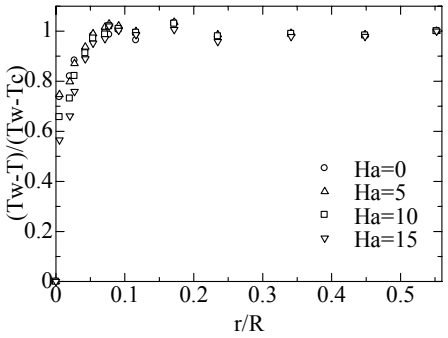

Fig.6 Inner temperature profile *Re*=5000, *Pr*=6.2, case A.

velocity is calculated by the flow rate and the cross section of pipe. The flow rate is measured and monitored using vortex flow sensor which measures the flow rate from the frequency of Karman vortex. Details of the experimental conditions are summarized in Table 2 below. It is to be noted that the maximum Hartman number is 15 in the case that Prandtl number is 6.2. However, in the case of Prandtl number is 9.8, maximum Hartman number is 10, because of low electrical conductivity of KOH solution at low temperature.

III. RESULTS

Fig.4a shows the difference in Nusselt number between *Ha*=0 and *Ha* =5, 10, 15 at *Re*=5000, *Pr*=6.2. The vertical axis, $Nu–Nu_0$, is defined by the difference in Nusselt number with and without magnetic field. In the horizontal axis-z and D are the distance from the starting point of applying the magnetic field and the pipe diameter, respectively. *Nu* is defined as the following,

$$Nu = \frac{q_w D}{(T_w - T_b)\lambda} \qquad (2)$$

where q_w is the heat flux applied to the surface, which is calculated by heater power q_w = 500W/m^2 at *Re*=5000, q_w =3500W/m^2 at *Re*=20000, where T_w and T_b are the wall temperature measured by T.C. directly and the bulk mixing temperature from Eq.(1), respectively. The

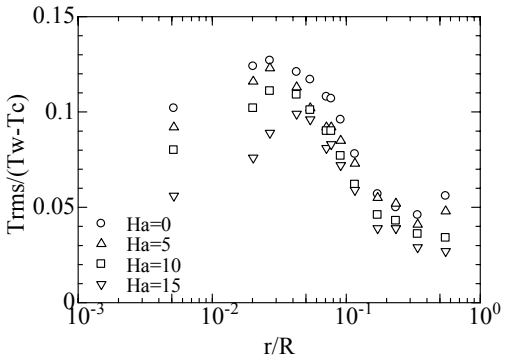

Fig.7 Temperature fluctuation profile, *Re*=5000, *Pr*=6.2, case A

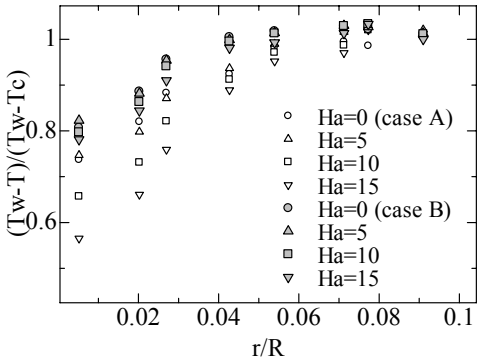

Fig.8 The magnetic field effect on temperature distribution in the pipe (*Re*=5000, *Pr*=6.2).

Nusselt number decreased when the magnetic field was applied. It is reasonable to suppose that the turbulence suppression under the magnetic field causes the decrease in Nusselt number. Gardner [6] showed a qualitatively similar tendency in his experimental result using mercury as a working fluid in spite of its extremely low Prandtl number and high electric conductivity compared with KOH. In addition, the amount of change in Nusselt number increases toward the magnetic field end. This indicates that the turbulent is more suppressed toward downstream.

Fig.4b shows the difference in Nusselt number between *Ha*=0 and *Ha*=5, 10, 15 at *Re*=20000, *Pr*=6.2. The tendency of this figure is the same as the case of *Re*=5000. However, the magnetic field effect on heat transfer is smaller than that at *Re*=5000, because of the decrease in the interaction parameter (Ha^2/Re). More definitely, a ratio of $Nu–Nu_0$ to Nu_0 at *Re*=5000 is 0.25, while it is 0.15 at *Re*=20000.

The change in Nusselt number at *Re*=5000, *Pr*=9.8 is shown in Fig. 4c. The decrease in Nusselt number is large compared with the case of Pr = 6 at the same Hartmann number. The heat transfer of a high Prandtl number fluid is dominated by turbulent diffusion rather than molecular diffusion. Assuming that the temperature is a passive scalar, turbulent diffusion itself is independent of Prandtl number. Therefore, it is reasonable that higher Prandtl number fluid is susceptible to turbulence suppression due to the magnetic field.

Fig. 5 shows the local Nusselt number at the top, side, and bottom of the pipe at the thermocouple Section 5 in Fig.1b. Incidentally, the sidewall of the pipe is perpendicular to the direction of the magnetic field. In the case of *Re*=5000, the Nusselt number at the bottom is the highest. Since this tendency of Nusselt number is similar to that under the mixed convection pipe flow, the effect of natural convection cannot be negligible at *Re*=5000. On the other hand, local Nusselt number does not depend on the angle at *Re*=20000. Therefore, the effect of natural convection can be negligible.

Fig. 6 shows the mean temperature distribution in the pipe measured by the TC tower at *Re*=5000, *Pr*=6. The TC tower is set horizontally i.e. case A. The temperature is normalized with the temperature difference between the wall T_w and the centre of the pipe T_c, where T_c is the measurement value of the T.C. tower top thermocouple. When a transverse magnetic field is applied, the temperature difference between the wall and the fluid is reduced. This means that the temperature of near-wall fluid is raised and a steeper temperature gradient is formed in the near wall region. In this region, heat transfer mechanism is likely dominated by mean temperature gradient and turbulent heat flux. It is clear that the turbulent intensity is suppressed in this region [4,5]. Therefore, it becomes necessary that the mean temperature gradient grow steeper to transport the constant heat flux from the wall. This tendency is similar to the Gardner's results [6] except for thermal boundary layer thickness. Since he used an extremely low Prandtl number fluid, mercury, as a working fluid, the thermal boundary layer was thicker.

Fig. 7 shows the temperature fluctuation normalized with temperature difference between the wall and the centre of the pipe at *Re*=5000, *Pr*=6.2. The TC tower setting was corresponding to case A. It is observed that the temperature fluctuation near the wall is damped when the magnetic field was applied. In order to explain this more exactly, we need to deeply investigate the behavior of turbulent heat flux under the magnetic field, since the production term of temperature fluctuation consists of a turbulent heat flux in its transport equation. However, there has been no study that tried to measure the temperature and velocity simultaneously under the magnetic field with a high accuracy. Therefore, we consider the mechanism of such suppression of temperature fluctuation with the aid of some DNS [4,5] results for the velocity field. In this past work, the suppression of turbulence fluctuation of velocity due to the magnetic field is seen throughout the pipe. This

suppression strengthens our conjecture for the chain of events: first, the magnetic field suppresses the turbulent velocity fluctuation, then the turbulent heat flux is decreased. Because the production term in the transport equation of turbulent heat flux includes the Reynolds stress, finally the production of the temperature fluctuation is decreased.

Fig. 8 shows the temperature profile in the pipe. In case B, the magnitude of the temperature gradient change is smaller than that of case A. As mentioned above, the heat transfer mechanism is likely dominated by the mean temperature gradient and the turbulent heat flux in the near wall region. According to Satake [4], the amount of turbulent suppression in case B is not so large compared with case A. Considering these circumstances, it is reasonable that the amount of change of mean temperature gradient is also smaller than that of case A.

IV. SUMMARY

The local and average heat transfer and temperature fluctuation of a high Prandtl number turbulent pipe flow through a uniformly heated tube are measured in this study. As a result, Nusselt number for turbulent pipe flow decreased 22% at Ha=15, Re=5000, Pr=6.2, 24% at Ha=10, Re=5000, Pr=9.8 and 8% at Ha=15, Re=20000, Pr=6.2.

It is clear that the temperature fluctuation is damping under the magnetic field at Re = 5000. More improvement in the TC tower is needed to measure with a higher degree of accuracy. In this study, however, the errors due to the flow meter, gauss meter, and fluid properties are included in both Reynolds number and Hartman number. Therefore, it is difficult to estimate the error precisely, because the experimental data on a like-for-like basis (same Re, same Ha, and same bulk temperature) is not sufficient. This might be an important future issue.

ACKNOWLEDGMENTS

The authors acknowledge the support by the US DOE and the Japanese Ministry of Education, Culture, Sports, Science and Technology (MEXT) via the JUPITER-II Collaboration.

REFERENCES

[1] R.A. GARDNER, P.S. LYKOUDIS, Magneto-fluid-mechanic pipe flow in a transverse magnetic field part 1. Isothermal flow, J. Fluid Mech. 47 (1) (1971) 737–764.

[2] E.C. BROUILLETTE, P.S. LYKOUDIS, Magneto-fluid-mechanic channel flow. I. Experiment, Phys. Fluids 10 (1967) 5.

[3] C.B. REED, P.S. LYKOUDIS, The effect of a transverse magnetic field on shear turbulence, J. Fluid Mech. 89 (part 1) (1978) 147–171.

[4] S. SATAKE, T. KUNUGI AND S. SMOLENTSEV, Direct numerical simulation of turbulent pipe flow in a transverse magnetic field, J. Turbul. (2002).

[5] D. LEE, H. CHOI, Magnetohydrodynamic turbulent flow in a channel at low magnetic Reynolds number, J. Fluid Mech. 439 (2001) 367–394.

[6] R.A. GARDNER, P.S. LYKOUDIS, Magneto-fluid-mechanic pipe flow in a transverse magnetic field Part 2. Heat transfer, J. Fluid Mech. 48 (1) (1971) 129–141.

[7] H.C. JI, R.A. GARDNER, Numerical analysis of turbulent pipe flow in a transverse magnetic field, Int. J. Heat Mass Trans. 40 (8) (1997) 1839–1851.

[8] C.P.C. WONG, S. MALANG, M. SAWAN, S. SMOLENTSEV, S. MAJUMDAR, B. MERRILL, D.K. SZE, N. MORLEY, S. SHARAFAT, M. DAGHER, P. PETERSON, H. ZHAO, S.J. ZINKLE, M. ABDOU, M. YOUSSEF, Assessment of first wall and blanket options with the use of liquid breeder, Fus. Sci. Technol. 47 (2005) 502–509.

[9] E.YA. BLUM, Effect of a magnetic field on heat transfer in the turbulent flow of conducting liquid, High Temp. 5 (1967) 68–74.

[10] J. TAKEUCHI, S. SATAKE, R. MIRAGHAIE, K. YUKI, T. YOKOMINE, T. KUNUGI, N.B. MORLEY, M.A. ABDOU, Study of heat transfer enhancement /suppression for molten salt flows in a large diameter circular pipe: part one-Benchmarking, Fus. Eng. Des. 81 (2006) 601–606.

DIRECT NUMERICAL SIMULATION OF MHD FLOW WITH ELECTRICALLY CONDUCTIONG WALL

S. Satake[1] , T. Kunugi[2] , N. Naito[1], A. Sagara[3]
[1]*Department of Applied Electronics, Tokyo University of Science, satake@.te.noda.tus.ac.jp*
[2]*Department of Nuclear Engineering, Kyoto University. kunugi@nucleng.kyoto-u.ac.jp*
Yoshida, Sakyo, Kyoto 606-8501 Japan
[3] *National Institute for Fusion Science, Toki, Gifu 509-5292 Japan,sagara.akio@lhd.nifs.ac.jp*

The 2-D vortex problem and 3-D turbulent channel flow are treated numerically to assess the effect of electrically conducting walls on turbulent MHD flow. As a first approximation, the twin vortex pair is considered as a model of a turbulent eddy near the wall. As the eddy approaches and collides with the wall, a high value electrical potential is induced inside the wall. The Lorentz force, associated with the potential distribution, reduces the velocity gradient in the near-wall region. When considering a fully developed turbulent channel flow, a high electrical conductivity wall was chosen to emphasize the effect of electromagnetic coupling between the wall and the flow. The analysis was performed using DNS. The results are compared with a non-MHD flow and MHD flow in the insulated channel. The mean velocity within the logarithmic region in the case of the electrically conducting wall is slightly higher than that in the non-conducting wall case. Thus, the drag is smaller compared to that in the non-conducting wall case due to a reduction of the Reynolds stress in the near wall region through the Lorentz force. This mechanism is explained via reduction of the production term in the Reynolds shear stress budget.

I. INTRODUCTION

In the region of transition Reynolds numbers, the increase or decrease of friction coefficients of a coolant having a low magnetic conductivity (e.g., a molten salt[1][2][3]) is obtained: this is a transition Hartmann number behavior. This behavior also leads to the deterioration of heat transfer. Therefore, the thermo-fluid design of the blanket under magnetic field fluctuation is very important. Since the magnetic field is strongly influenced by mean velocity, when the magnetic field is applied perpendicular to the flow direction, it is necessary to investigate the turbulent MHD flow behaviors for each direction of the applied magnetic field normal to the main flow. Furthermore, considering the the case of a wall with varying electrical conductivity, the flow characteristics of the coolant could be different from the usual turbulent non-MHD flows. In this sense, numerical simulation is very convenient for evaluating changes in flow due to changes in physical properties of the wall materials or in the direction of the applied magnetic field. A previous study for the case with electrical conductivity at the wall is exceeding to low speed velocity, such as laminar flow. In particular, the turbulence case is unknown.

In the present study, numerical analysis of the well-known "Vortex Dipole" problem [4][5] under a magnetic field is first performed in order to evaluate the influence of electrical conductivity of the first wall. This approach, with a turbulence eddy modeled by a two dimensional twin vortex, is evaluated for the numerical scheme before full three dimensional DNS is done by a solver, with consideration of the effect of inner wall materials.
Second, to evaluate the effect of the interaction of the wall and fluid in three dimensions, fully developed turbulent channel flow is carried out with a high-conductivity wall. The difference for turbulence statistics of a conducting wall is clearly observed compared with that of an insulated wall.

II. 2D VORTEX DIPOLE PROBLEM

II.A. Numerical Procedures and Flow Parameters

Table1 Flow parameters

Hartmann number	*Ha*=42
Electrical Conductivity	σ=0.01, 1, 100
Width*D*	δ, 1/5 δ

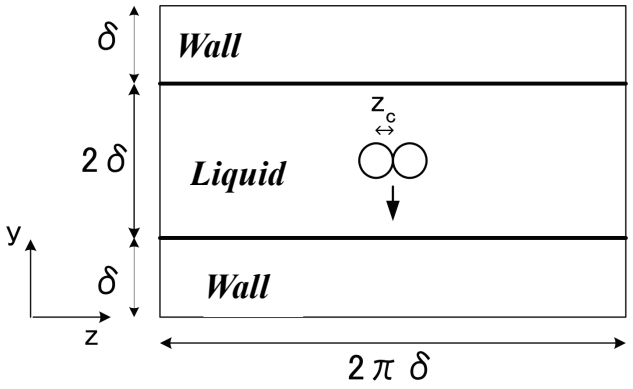

Fig. 1 Computational domain for 2D vortex dipole problem

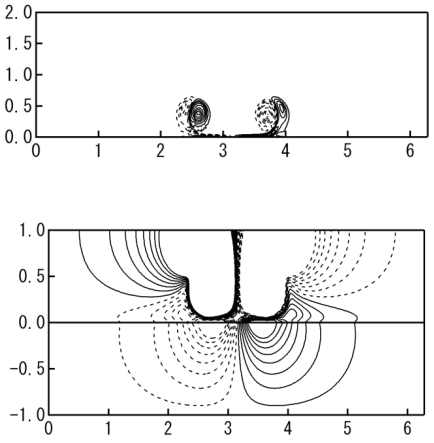

Fig. 2 Vortex and potential distributions at t^*=4 and σ=100: Upper shows the vortex and lower for the

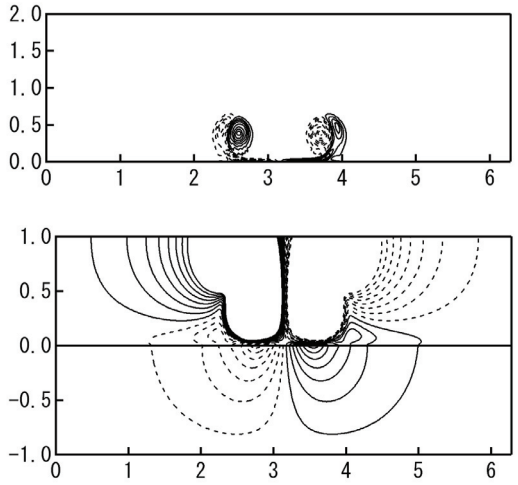

Fig. 3 Vortex and potential distributions at t^*=4 and σ=1: Upper shows the vortex and lower for the potential

The two-dimensional continuity and momentum equations for fluid motion and the potential equation for an electrical field under a low magnetic Reynolds number assumption were solved. Figure 1 shows the MHD fluid in a channel with electrically conductive walls. One pair of vortices with a positive or negative circulation located at the center of the channel is first introduced, and then the vortex motion is traced by numerical simulation. The magnetic orientation is in the streamwise direction. The Reynolds number, based on the circulation Γ and the viscosity ν, is 1800. The relative electrical conductivities of the wall are set to 0.01, 1, and 100. In order to investigate the effect of wall thickness, two cases with different thicknesses, 1 δ and 1/5 δ, were examined in Table 1. The mesh number of (64) + 128 + (64) x 256 is used for the computational domain of ((δ)+2δ+(δ) x 2πδ) in the wall-normal and spanwise directions.

Figure 2 shows the vortex contour, with the vortex pair attached at the wall with σ=100 at t^*= tΓ /δ^2=4, and the 2-D contour for potential distribution inside the wall at the same time. The distribution of vortices for all cases with different electrical conductivities at wall are almost the same. At σ =1 in Fig. 3, the signs of both the primary and secondary vortices are negative. However, the potential distribution over the inside wall with σ=0.01 in Fig. 4 is different from the fluid distribution and the sign of the wall potential distribution is the inverse of that for the vortex in fluid. Thus, the potential distribution disappears incase of the low electrical conductivity.

$$q = \int_0^{\frac{2\pi\delta}{2}} \left. \frac{du_z}{dy} \right|_{y=0} dz \qquad (1)$$

Equation 1 shows the gradient of the velocity in the z direction at the wall. Owing to the symmetry, the

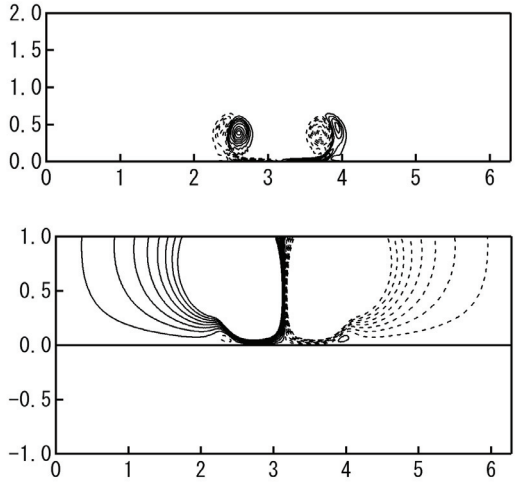

Fig. 4 Vortex and potential distributions at t^*=4 and σ=0.1: Upper shows the vortex and lower for the potential

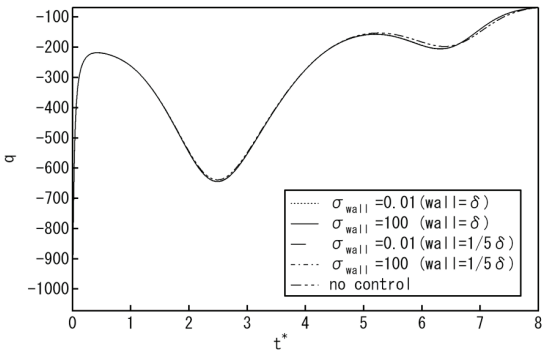

Fig. 5 Time developing of the gradient of the velocity to the z direction

equation is integrated for the half region from the wall. Note that the gradient of the velocity is a part of the vortex definition; the vortex becomes asymptotically the gradient. Time developing of the gradient of the velocity to the z direction is shown in Fig. 5. Although the distribution is the same close to the initial state, the difference between the first twin vortex collision at the wall and the second one is remarkable. In particular, at large conductivity, the difference in the case of the thicker wall becomes large. Therefore, the flow state is not affected by the difference in conductivity. Although the difference appears near the wall region, the current becomes large for the thicker wall. That is, the reduction of wall shear at the wall is necessary to the design of a fusion reactor with conductive walls. As for turbulent flows, many twin vortices must exist near the wall, and the effect of wall conductivity must not be negligible.

III. TURBULENT CHANNEL FLOW WITH ELECTRICAL CONDUCTING WALL

III.A. DNS Code and Flow Parameters

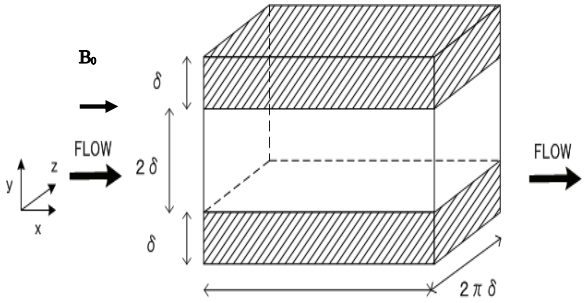

Table2 Friction coefficients

Friction coefficient	C_f	C_f / C_{f0}
Non MHD case	8.5522 x 10^{-3}	1
Conducting wall, Ha =15	8.1848 x 10^{-3}	0.957
Insulated wall, Ha =15	8.289 x 10^{-3}	0.969

The present DNS code is a hybrid spectral finite difference method [6] [7]. The number of grid points, the Reynolds number and grid resolutions are summarized in Table 1. The periodic boundary conditions are applied to the streamwise (x) and the spanwise (z) directions. As for the wall-normal direction (y), non-uniform mesh spacing specified by a hyperbolic tangent function is employed. The mesh number of 128 x (64)+128+(64) x128 is used for the computational domain of $5\pi\delta$ x (δ)+2δ+(δ) x $2\pi\delta$) in the streamwise, the wall-normal, and spanwise directions. The velocity components impose a non-slip condition at the wall. A uniform magnetic field $\boldsymbol{B}_0$ defines that magnetic orientation to be parallel to the axis

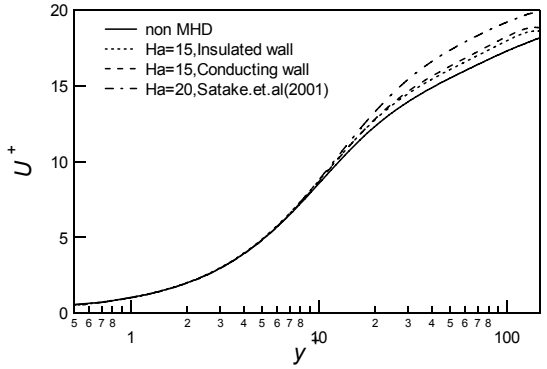

Fig. 7 Mean velocity profiles

of the streamwise direction in Fig.6. The Neumann condition for the electrical potential is adopted outside the wall: this is called the "conducting wall assumption". The Hartmann numbers ($Ha = \boldsymbol{B}_0\,\delta\,(\sigma/\rho\nu)^{1/2}$) based on the magnetic field $\boldsymbol{B}_0$, the kinematic viscosity ν, the electrical conductivity $\sigma$and the channel width δ are set to 15.0. The

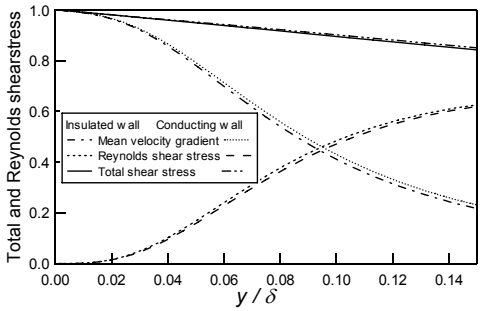

Fig. 8 Reynolds stress distribution near wall region

σ at fluid is 1.0. The σ at solid wall is 62.27. If these parameters are assumed as actual material, the fluid and solid walls are mercury and copper, respectively. The Reynolds number is 4590 based on the bulk velocity. The fluid flows with a constant mass flux condition.

III.B. Statistical Quantities

In Fig.7, the mean velocity profile near the wall is normalized by friction velocity u_τ. The open channel flow with magnetic field is plotted along with the DNS (Direct Numerical Simulation) data by Satake et al. (2002) [8]. The velocity profile in the conducting wall is slightly increased in the logarithmic region compared with that of the insulated wall. Thus, the drag at the conducting wall is reduced compared to that of the insulated wall. As is generally known [8] [9] [10] [11], the drag is reduced by the magnetic field with the orientation of streamwise direction. To confirm the phenomena, the friction coefficients for the both cases and the non-MHD one are examined in Table 2. Although the difference is very

small, the coefficient value of the conducting wall is smaller than that of the insulated wall. When the coefficient is normalized by that of the non-MHD case, the difference is more clearly observed, at a value of 1.2 %. If a body force is caused near the wall region, the velocity gradient on the wall is directly affected by the force. Satake and Kasagi (1996) [12] show the drag reduction is caused by the effect of the artificial spanwise body force $-\alpha w$ which is artificially assumed only near the wall region in the spanwise momentum equation. They also showed that the strength of parameter α and the drag were related. In our case, the difference of 1.2 % for the drag coefficients between the conducting and insulated walls corresponded to α=0.2 by the estimation from their results. Figure 8 shows the Reynolds shear stress, mean velocity gradient and total shear stress. The Reynolds shear stress profile in the conducting wall is slightly decreased near the wall region compared with that of the insulated wall. Thus, this phenomenon is the reason for the drag reduction at the conducting wall. To elucidate this mechanism, we discuss the stress budget level.

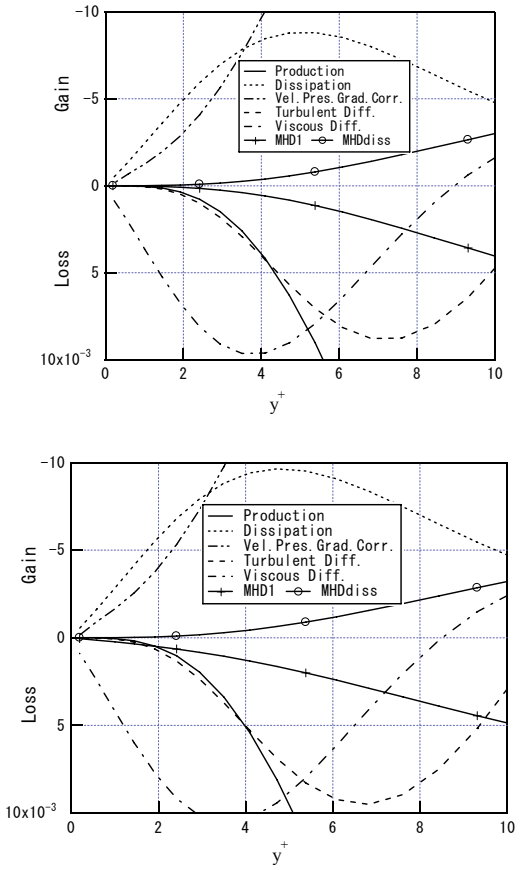

Fig. 9 Reynolds shear stress budget: (a) Conducting wall, (b) Insulated wall

The Reynolds shear stress budget is written as:

$$0 = \underbrace{-\overline{u_y'^+ u_y'^+}\frac{\partial \overline{u}_x^+}{\partial y^+}}_{\text{Production}} \underbrace{-\frac{\partial \overline{u_x'^+ u_y'^+ u_y'^+}}{\partial y^+}}_{\text{Turbulent diffusion}} + \underbrace{\frac{\partial^2 \overline{u_x'^+ u_y'^+}}{\partial y^{+2}}}_{\text{Viscous diffusion}}$$
$$\underbrace{-\left(\overline{u_x'^+ \frac{\partial p'^+}{\partial y^+}} + \overline{u_y'^+ \frac{\partial p'^+}{\partial x^+}}\right)}_{\text{Pressure diffusion}} \underbrace{-2\overline{\frac{\partial u_x'^+}{\partial x_j^+}\frac{\partial u_y'^+}{\partial x_j^+}}}_{\text{Dissipation}}$$
$$\underbrace{+Ha^2 \overline{\frac{\partial \varphi^+}{\partial z^+} u_x'^+}}_{\text{MHD 1}} \underbrace{-Ha^2 \overline{u_x'^+ u_y'^+}}_{\text{MHD Diss.}} \qquad (2)$$

The terms in the above equation for the conducting wall and the insulated wall are shown in Figures 9 (a) and (b). The production terms of the conducting wall decrease at y+<4 compared with those of the insulated wall. The production terms consist of the normal stress and the mean velocity gradient. Although the mean velocity gradient is increased in Fig. 8, the normal stress is further decreased. It is evident that the normal stress (not shown here) of the conducting wall is decreased compared with that of the insulated wall.

III.C. Turbulent Structure

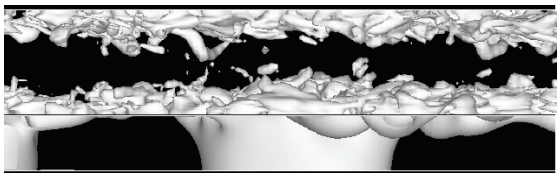

Fig. 10 Second Invariant tensor in fluid and potential surface inside wall

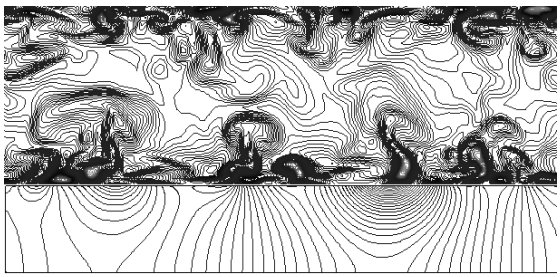

Fig. 11 Streaky structures in fluid and potential inside wall in y-z plane

Figure 10 shows the 3D contour surface for the second invariant tensor and potential value inside wall at the conducting wall. The large potential region is located near the vortical structures. A high shear of the velocity

gradient exists in the region around the vertical structures; it is especially remarkable for the region which has many vortexes adjacent to the wall. The phenomena correspond to the result of the 2D vortex dipole problem. The streaky structures and potential value inside wall in the y-z plane are shown in Fig. 11. The high potential region is located below the streaky structures. A large gradient of potential value gathers between the streaks. It is evident that the potential inside conducting wall is closely related to the mechanism of the production streaks. The streaky structures and the potential value inside the wall in the x-y plane are shown in Fig. 12. Wall shear layers with some alignment against the wall are clearly observed. In generally knowledge, the alignment is due to the vortical motion at the wall surface. The high potential region is located at the wall shear layers. This is also evidence for the relationship between the production of streaks and potential. The second invariant tensor and the potential value inside wall in y-z plane are shown in Fig. 13. The large strength of the second invariant tensor is directly located on the high potential region. Thus, the potential is made of the vertical structures. This phenomenon is in complete agreement with the results of the two dimensional vortex dipole problems as shown in Fig. 2.

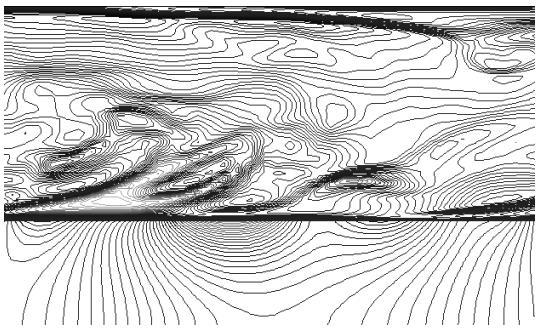

Fig. 12 Streaky structures in fluid and potential inside wall in x-y plane

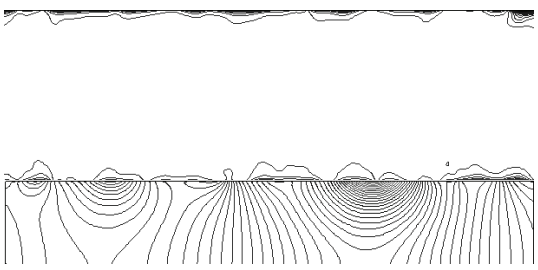

Fig. 13 Second Invariant tensor in fluid and potential inside wall in y-z plane.

IV. CONCLUSIONS

The 2D vortex problem and turbulent channel flow experiments were carried out as an estimation of the electrical conductivity at the wall under magnetic field. In the 2D vortex problem, the large potential region inside the wall is caused by vertical motion, when the electrical conductivity is large. In the visualization from turbulent channel flow with the conducting wall, the turbulent eddy is closely related to the large potential region inside wall. The large region affected the fluid at the wall surface, the drag reduction occurred. This phenomenon is confirmed from the reduction of Reynolds stress and the production term in a part of Reynolds stress budget equations. The Lorentz force causes near wall region from inside large potential, and the velocity gradient on the wall is directly affected by the force.

REFERENCES

1. M. A. Abdou et al. and APEX Team, Exploring novel high power density concepts for attractive fusion systems, Fusion Eng. Design, 45, (1999) 145.
2. R.W., Moir et al., "HYLITE-II: Amoten salt inertial fusion power plant design-final report," Fus. Technol., 25 (1994) 5-25.
3. A. Sagara et al., "Design studies of helical-type fusion reactor FFHR," Fus. Eng. Design, 41, (1998) 349.
4. Orlandi, P., "Vortex dipole rebound from a wall," Phys. Fluid A 2, 1429 (1990)
5. Lim, J., Choi, H. & Kim, J.,"Control of streamwise vortices with uniform magnetic fluxes," Phys. Fluids, 10, 1998, 1997-2005.
6. Satake, S., Kunugi, T.,"DNS of Turbulent Channel and Pipe Flow with High Reynolds Number," Proc. of 3nd Int. Symp. Turb. and Shear Flow Phenomena, Sendai,. June 24-27, Vol., 2003, pp. 479-.481
7. Satake, S., Kunugi, T., Takase, K., Ose, Y., and Naito N., "Large Scale Structures of Turbulent Shear Flow," Lecture Notes in Computer Science 2858 , High Performance Computing, A. Veidenbaum et al. (Eds.), Springer-Verlag Berlin Heidelberg, 2003, pp.468-- 475.
8. Satake, S., Kunugi, T., and Smolentsev, S., "Advances in direct numerical simulation for MHD modeling of free surface flows," Fus. Eng. and Design, Vol. 61-62, 2002, pp. 95-102.
9. H. Noguchi and N. Kasagi, Direct numerical simulation of liquid metal MHD turbulent channel flows, Preprint of JSME, No. 940-53, 1994, 365-366.
10. Lee, D. and Choi, H., Magnetohydrodynamic turbulent flow in a channel at low magnetic Reynolds number, J. Fluid Mech., 439, (2001) 367-394
11. P. Orlandi, Drag reduction in turbulent MHD pipe flows, CTR, Proc of the summer program 1996, (1996) 447-456.
12. Satake , S. and Kasagi , N., "Turbulence Control with a Wall Adjacent Thin Layer Damping Spanwise Velocity Fluctuations," Int. J. Heat & Fluid Flow 17, 1996, pp. 343 - 352.

DNS AND K-EPSION MODEL SIMULATION OF MHD TURBULENT CHANNEL FLOWS WITH HEAT TRANSFER

Y. Yamamoto[1], T. Kunugi[2], S. Satake[3] and S. Smolentsev[4]

[1]*Nagoya University, Chikusa, Nagoya, Aichi 464-8603 Japan, y-yamamoto@nucl.nagoya-u.ac.jp,*
[2]*Kyoto University, Yoshida, Sakyo, Kyoto 606-8501 Japan,kunugi@nucleng.kyoto-u.ac.jp,*
[3] *Tokyo University of Science, Yamazaki, Noda, Chiba 278-8501 Japan, satake@te.noda.tus.ac.jp,*
[4] *University of California at Los Angeles, Los Angeles, CA 90095-1597 USA, sergey@fusion.ucla.edu*

In this study, the MHD pressure loss and heat transfer characteristics of the low-Magnetic Reynolds number and high-Prandtl fluid such as the FLiBe, were investigated by means of DNS and the evaluation of MHD turbulence models was also carried out in high-Reynolds number condition. As the results, the similarity-law between the velocity and the temperature profiles was not satisfied at the near critical Ha condition to maintain turbulent status and anisotropy tendency was remarkable in increase of Ha number. In high-Re number condition, MHD turbulence models coupled with k-ε model can reproduce the MHD pressure loss trend with increase of Ha number but turbulent model which can consider the anisotropy of the Reynolds stresses and the local change of the turbulent Pr number might be required in the view point of quantitative prediction.

I. INTRODUCTION

Molten salt FLiBe is one of the coolant candidates in the first wall and blanket of the fusion reactors and has the advantages in Magneto-Hydro-Dynamics (MHD) pressure loss, chemical stability, solubility of tritium and so on. In the contrast, the low thermal diffusivity and high viscosity are the issues of the FLiBe utilization as the coolant. Moreover, the development of precise MHD turbulence model is highly demanded to predict the MHD pressure loss and the heat transfer for fusion reactor design.

MHD turbulent wall-bounded flows have been investigated extensively both experimentally and numerically (Reed and Lykoudis[1], Simomura[2], Noguchi et al.[3], Orlandi[4], Satake et al.[5], Lee and Choi[6] etc.) and many important information about drag reduction and turbulent modulation have been obtained. Especially, direct numerical simulation (DNS) of turbulent flows is one of the most powerful methods to understand turbulent structures and heat transfer. But, molten salt fluids such as FLiBe are the high-Pr fluids (Pr=20-40), previous DNS studies have conducted at the low-Pr condition. Therefore, MHD turbulent heat transfer on high-Pr fluids hasn't been understood well. One more important problem of DNS studies is low-Reynolds number effects caused from computational resources limitation. However, DNS of MHD channel flow at high-Reynolds number were reported recently by Satake et al.[7] and MHD turbulence model evaluation at high-Reynolds number can be allowed using this DNS database.

In this study, the MHD pressure loss and heat transfer characteristics under medium-high Pr condition (Pr=5.7) were investigated by means of DNS and the evaluation of MHD turbulence model proposed by Kenjeres and Hanjalic[8] and Smolentsev et al.[9] were also carried out at high-Reynolds number corresponding to the DNS database (Bulk-Re=45818)[7].

Table 1 Numerical condition

Re_τ	Ha	Pr	Domain $L_x \times L_y \times L_z$	Grid number $N_x \times N_y \times N_z$	Resolution $\Delta x^+, \Delta y^+, \Delta z^+$
150	0	5.7	$8h \times 2h \times 4h$	80×96×80	15.0, 0.3-6.4, 7.5
150	8	5.7	$8h \times 2h \times 4h$	80×96×80	15.0, 0.3-6.4, 7.5
150	12	5.7	$8h \times 2h \times 4h$	80×96×80	15.0, 0.3-6.4, 7.5
150	16	5.7	$8h \times 2h \times 4h$	80×96×80	15.0, 0.3-6.4, 7.5

$Re_\tau = u_\tau h/\nu$: Turbulent Reynolds number, u_τ: Friction velocity, h: channel half depth (=d/2), ν: Kinetic viscosity, $Ha = B_y d(\sigma/\rho\nu)^{1/2}$, B_y: Wall-normal Magnetic flux density, σ:Electric conductivity, $Pr = \alpha/\nu$: Prandtl number,
α: Thermal diffusivity, $L_x(N_x, \Delta x)$, $L_y(N_y, \Delta y)$, $L_z(N_z, \Delta z)$: Computational domain (Grid number, resolution) for stream (x), vertical (y) and spanwise (z)directions.

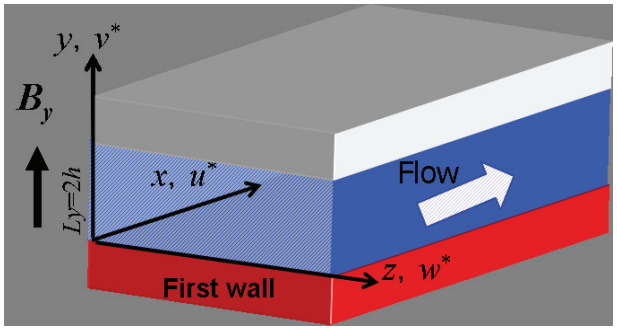

Fig.1 Computational geometry and coordinate system

In this study, the MHD pressure loss and heat transfer characteristics under medium-high Pr condition (Pr=5.7) were investigated by means of DNS and the evaluation of MHD turbulence model proposed by Kenjeres and Hanjalic[8] and Smolentsev et al.[9] were also carried out at high-Reynolds number corresponding to the DNS database (Bulk-Re=45818)[7].

II. DNS OF MHD CHANNEL FLOWS WITH HEAT TRANSFER

II.A. Numerical condition and Numerical procedures

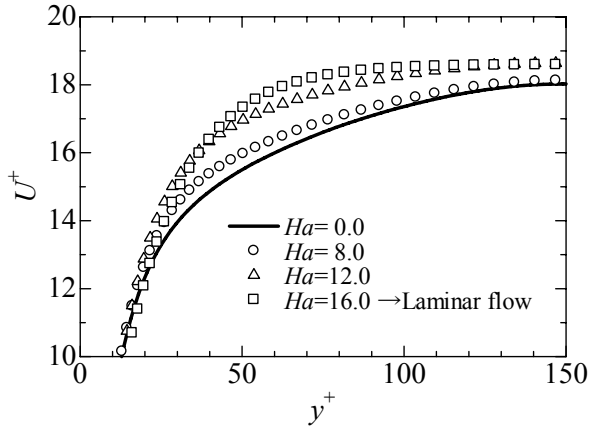

Fig.2 Mean velocity profiles

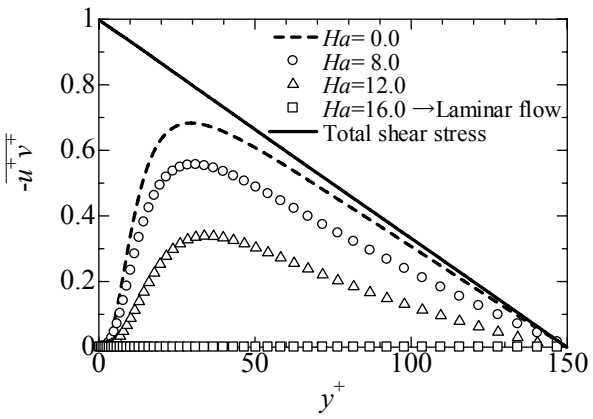

Fig.3 Reynolds shear stress profiles

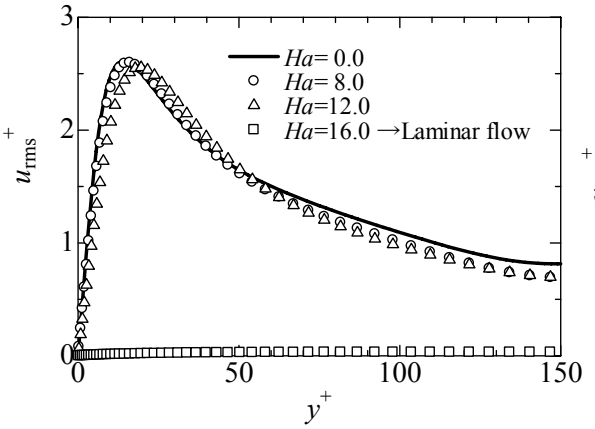

Fig.4 Streamwise turbulent intensity profiles

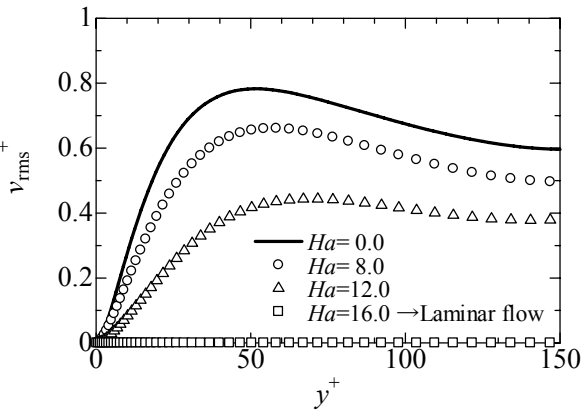

Fig.5 Vertical turbulent intensity profiles

Numerical conditions in DNS of 2D-fully developed turbulent channel flows imposed wall-normal magnetic field, were tabled in Table 1, where super-script + denotes the nondimensional quantities normalized by friction velocity and kinetic viscosity. In the computations, thermal properties of the KOH solution (*Pr* number is 5.7 at 40 deg-C.) were used because the KOH solution instead of FLiBe was used in the JUPITER-2 experiment. Turbulent Reynolds number (Re_τ) was kept on 150 and Hartmann number (*Ha*) was changed from 0 to 16.

The continuity equation, the momentum equations with the electric field described using the electrical potential approach at low magnetic Reynolds number and the energy equation solved by a hybrid Fourier spectral and the second order central differencing method[9]. Nonlinear terms were computed with 1.5 times finger grids in horizontal (*x* and *z*) directions. Time integration method is 3rd order Runge-Kutta scheme for convection terms, Crank-Nicolson scheme for viscous terms and Euler Implicit scheme for Pressure terms, respectively. Non-slip and periodic conditions were imposed for boundary condition of velocity and constant temperature ($T_{top} > T_{bottom}$) and periodic conditions were imposed for passive scalar field, respectively.

II.B. Results and Discussion

Figure 2 and 3 shows mean velocity and Reynolds shear-stress profiles, respectively. In *Ha*=16.0 case, flow is not turbulent but laminar flow. Velocity profile in *Ha*=12.0 is closed to laminar case and velocity profile in *Ha*=8.0 is closed to non-MHD case. To maintain turbulent status, *Ha*=12.0 was the near critical condition. Figure 4 and 5 shows streamwise and vertical turbulent intensity profiles, respectively. Streamwise turbulent intensity was not influenced by MHD effects but vertical and spanwise

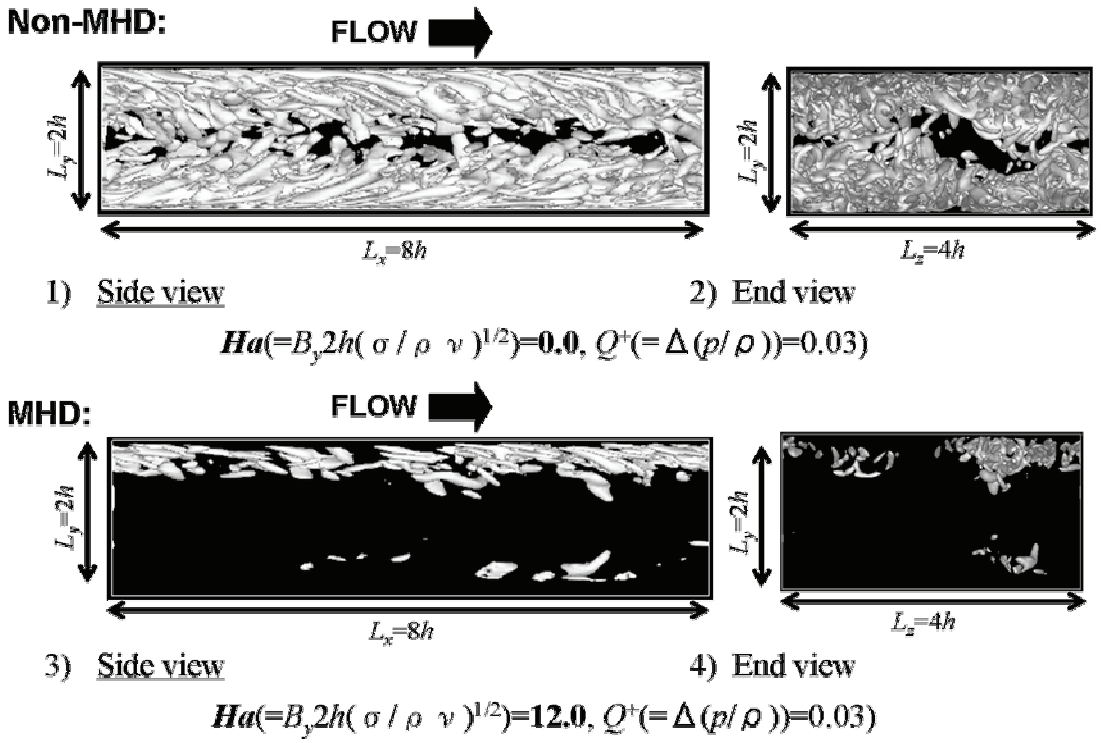

Fig.6 Iso-surfaces of 2nd invariant of velocity gradient tensor

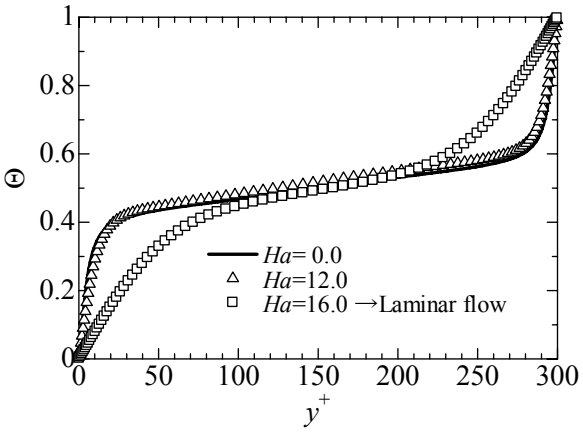

Fig.7 Mean temperature profiles

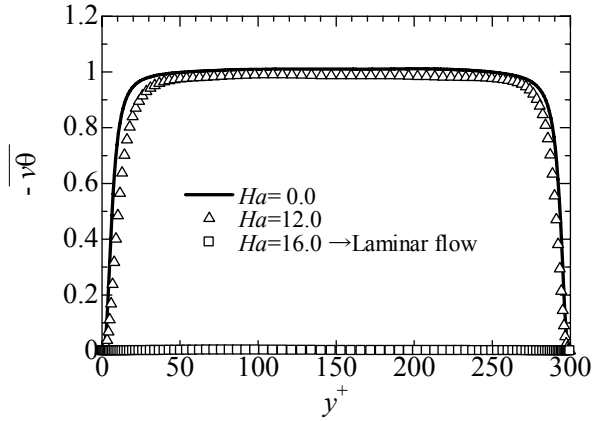

Fig.8 Wall-normal turbulent heat flux profiles

intensity were suppressed by MHD effects. These indicate that MHD force acts on the streamwise vortex reduction and non-isotropic effect is remarkable. The profiles of the turbulent intensity were in good agreement with the previous DNS results[4].

Iso-surfaces of 2nd invariant velocity gradient tensor (Q^+=0.03) are shown in Fig.6, where positive area of 2nd invariant of velocity gradient tensor is corresponded to vortex region. In the MHD case, vortex areas were localized and restricted near wall because of MHD effects. This visualization results are good agreements with turbulent intensities behavior with increase of *Ha* number (MHD effects).

Figure 7 shows mean temperature profiles. Temperature fields were normalized by temperature difference between top and bottom wall. Mean

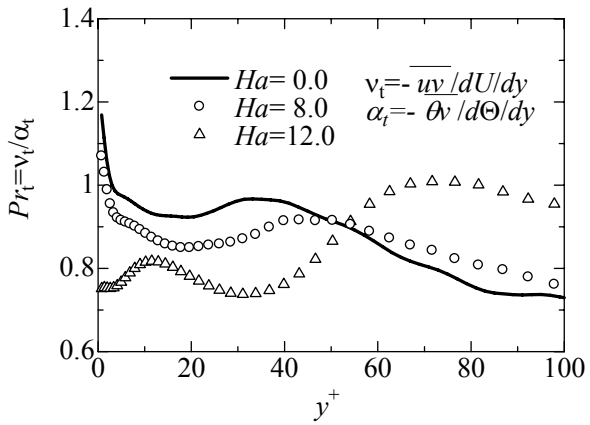

Fig.9 Turbulent Pr number profiles

temperature profile in *Ha*=12.0 is closed to non-MHD case (*Ha*=0.0), though velocity profile is closed to laminar flow's profile. Figure 8 shows wall-normal turbulent heat-flux profiles. As well as temperature profile, wall-normal turbulent heat-flux profile in *Ha*=12.0 is closed to non-MHD case (*Ha*=0.0). These are why velocity profile depended on MHD force but temperature profile depended on wall-normal turbulent heat flux near critical condition and indicate that similarity-law between velocity and temperature fields is not satisfied near critical condition to maintain turbulent status. Figure 9 shows turbulent *Pr* number profiles, where turbulent *Pr* number (Pr_t) was defined by turbulent viscosity ($:\nu_t$) and turbulent diffusivity ($:\alpha_t$). Turbulent *Pr* number profiles are not much difference between in *Ha*=0.0 and 8.0 cases but turbulent Pr number profile tendency in *Ha*=12.0 is the opposite of the others. This indicates that constant turbulent-Pr number can not be used in the zero-equation type turbulent closure model of energy equation. Friction drag coefficient and Nussetl number are tabled in Table 2. Increased in Ha number, Friction drag coefficient changes linearity but Nusselt number jumps at the transition point form turbulence to laminar. Present DNS results indicates that turbulent model which can consider the anisotropy of the Reynolds stresses and the local change of the turbulent *Pr* number might be required in the view point of quantitative prediction.

III. RANS SIMULATION AND COMPARISON WITH HIGH-RE DNS DATABASE

Next, numerical calculations of MHD turbulent channel flow imposed the wall-normal magnetic field were carried out by using the Kenjeres and Hanjalic (KH) model[8] and the Smolentsev et al. (S) model[9] at the same condition as the DNS data[7], Bulk Re = 46000 and Ha= 32.5 and 65. Unfortunately, temperature fields' data don't be reported by Satake et al.[7] and comparison of velocity fields was

Table 2 Friction drag coefficient and Nusselt number

Re	*Ha*	*Pr*	Friction drag coefficient: *Cf*	Nusselt number: *Nu*
150	0	5.7	6.33×10^{-6}	15.73
150	8	5.7	6.20×10^{-6}	14.00
150	12	5.7	5.70×10^{-6}	10.53
150	16	5.7	5.55×10^{-6}	2.47

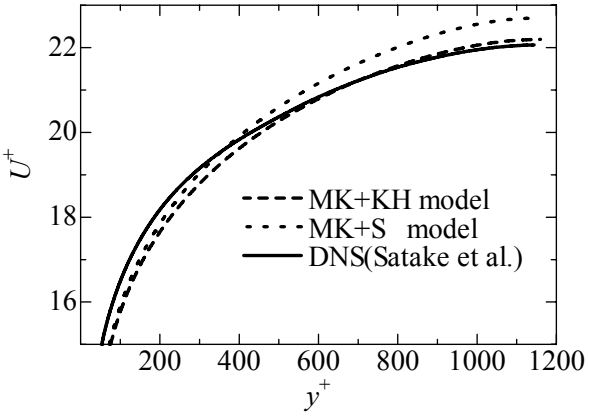

Fig.10-1 Mean velocity profiles (*Ha*=32.5)

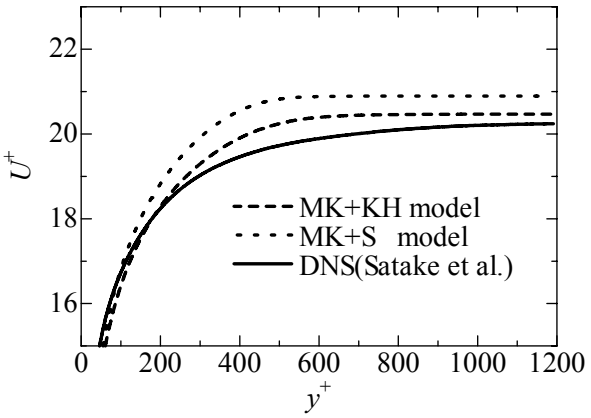

Fig.10-2 Mean velocity profiles (*Ha*=65.0)

conducted in this section. For the k-ε turbulence model, Myong and Kasagi model[10] was adapted with above MHD models.

Figure 10 and 11 show the mean velocity and turbulent kinetic energy profiles in *Ha*=32.5 and 65.0, respectively. Compared with the DNS results, both MHD turbulence models can reproduce the MHD pressure loss trend with increase of Ha number. However, both models

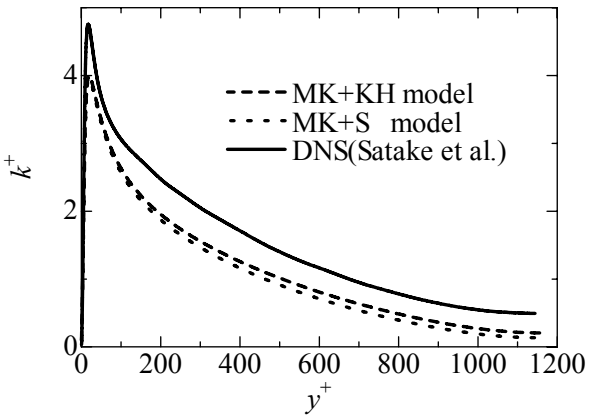

Fig.11-1 Turbulent kinetic energy profiles (*Ha*=32.5)

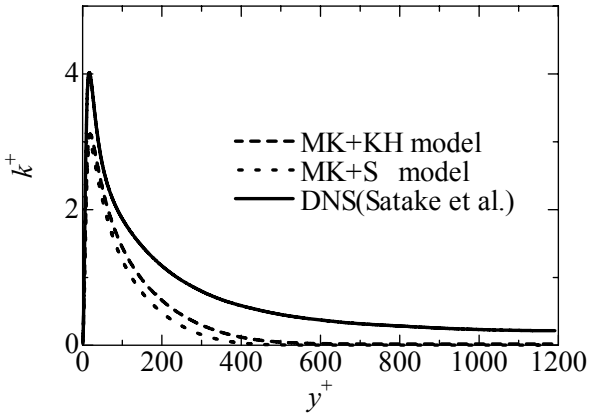

Fig.11-2 Turbulent kinetic energy profiles (*Ha*=65.0)

underestimated the turbulent kinetic energy, and the prediction accuracy was getting worse with increase of Ha number. Compared with the KH model and the S model, the KH model has a little advantage in the prediction accuracy and this result conforms close to a priori test in MHD source terms in k- and epsilon-equation[8]. To improve the prediction accuracy of the k-e turbulent model, some modification of eddy viscosity would be required.

IV. CONCLUSIONS

In this study, the MHD pressure loss and heat transfer characteristics of the low-Magnetic Reynolds number and high-Prandtl fluid, were investigated by means of DNS and the evaluation of MHD turbulence models was also carried out in high-Reynolds number condition. As the results, the possibility of prediction accuracy deterioration for turbulent heat transfer was pointed, especially near critical Ha condition to maintain turbulent status.

REFERENCES

1. C.B. Reed and P.S. Lykoudis, The effects of a transverse magnetic field on shear turbulence, J.Fluid Mech. 89 (1978), 144.
2. Y.Simomura, Large eddy simulation of magnethydrodynamic turbulent channel flows under a uniform magnetic field, Phys. Fluids A 3(1991), pp.3098-3106.
3. P. Orlandi, Drag reduction in turbulent MHD pipe flows, CTR, Proceddings of the Summer Program, 1996, 447.
4. H. Noguchi, Y. Ohtsubo and N. Kasagi, ftp.thtlab.t.u-tokyo.ac.jp/DNS, 1998.
5. S.Satake, T. Kunugi and S. Smolentsv, DND of turbulent pipe flow in a transverse magnetic field, J. Turbulence, 3(2002), 020.
6. D. Lee and H. Choi, Magnetohydrodynamic turbulent flow in a chnnle at low magnetic Reynolds number, J. Fluid Mech. 439(2001), 367.
7. S. Satale, T. Kunugi, K. Takase and Y. Ose, Direct numerical simulation of turbulent flow under a uniform magnetic field for large-scale structures at high Reynolds number, Phys. Fluids 18(2006), 1251 06.
8. S. Kenjeres and K. Hanjalic, On the implementation of effects of Lorentz force in turbulence closure models, In. J. Heat Fluid Flow, 21(2000), 329.
9. S. Smolentsev, M. Abdou, N. Morley, A. Ying and T. Kunugi, Application of K-ε model top open-channel flows in a magnetic field, Int. J. Eng. Sci., 40(2002), 693.
10. H. Myong and N. Kasagi, A new approach to in the improvement of k-ε turbulence model for wall-bounded shear flow, JSME. Int. Fluid Eng., 109(1990), pp.156-160.

EXPERIMENTAL RESEARCH ON MOLTEN SALT THERMOFLUID TECHNOLOGY USING A HIGH-TEMPERATURE MOLTEN SALT LOOP APPLIED FOR A FUSION REACTOR FLIBE BLANKET

S. Toda[1], S. Chiba[1], M. Omae[1], K. Yuki[1], A. Sagara[2]

[1]*Tohoku University, Sendai, Miyagi 980-8579 Japan, saburo.toda@qse.tohoku.ac.jp, schiba@karma.qse.tohoku.ac.jp, moma@karma.qse.tohoku.ac.jp, kyuki@qse.tohoku.ac.jp*
[1]*National Institute for Fusion Science, Toki, Gifu 509-5292 Japan, sagara.akio@lhd.nifs.ac.jp*

Experimental research on molten salt thermofluid technology using a high-temperature molten salt loop (MSL) is described in this paper. The MSL was designed to be able to use Flibe as a coolant, however, a simulant, heat transferr salt (HTS) has to be used alternatively since Flibe is difficult to operate under avoiding a biohazard of Be. Experiment on heat-transfer enhancement, that is required for applying to cool the high heat flux components of fusion reactors, is ongoing. Preliminary experimental results showed that an internal structure of a mixing chamber in the MSL was important to obtain accurate bulk temperatures under severe thermal conditions. For operating the loop, careful handling are needed to proceed how to melt the salt and to circulate it in starting the operation of the MSL. It is concluded that several improvements proposed from the present experiences should be applied for the future Flibe operation.

I. INTRODUCTION

In recent designs of a fusion-reactor blanket, the molten salt Flibe is recommended to be an alternative candidate material for blanket from the viewpoint of avoiding MHD effects[3]. The typical characteristics of Flibe are explained in the reference[1]. Molten salt Flibe is a high Pr-number fluid, which generally has the low heat-transfer on inner heated walls in pipes. Therefore, we have to develop new methods to enhance the heat transfer in a closed channel when Flibe is used. The authors reported that a packed-bed channel is applicable as the heat transfer promoter[1]. In addition, other promoters are also examined as generally used by twisted-tape inserted tube, fins and other turbulent heat-transfer enhancers. Molten salts are conventionally used as medium for chemical heating and metal quench hardening in many industries. Also, Flibe was used as a secondary coolant in MSER. However, there is a few precedential experiments for heat transfer of molten salts under such high heat-flux and high flow-rate conditions as required in fusion power reactors. Especially for such severe conditions, we have less knowledge of handling the molten-salt closed channel loop.

In this paper, the high-temperature molten salt loop (MSL) to investigate heat transfer enhancments of molten salt Flibe and the experimental results using heat transfer salt (HTS) under such severe conditions will be reported.

II. MOLTEN SALT FORCED CIRCULATING LOOP

The MSL (designed by IHI Co., Ltd., Japan) was built at Tohoku University, Japan in 1998 (Fig. 1). It was designed to be able to use Flibe as a working fluid. Because of the high melting point of Flibe (732 K), all components of the MSL and all pipes have to be heated up above this melting temperature. The main components of this loop are: (1) Dump Tank, (2) Circulation Pump, (3) Test Section, (4) Upper Tank and (5) Air Cooler. The inert gas was chosen to be Ar gas so as to keep the experiment under safe and stable conditions.

The flow rate of the working fluid is measured by a differential pressure instrument with orifice flanges. All connections of pipes were welded except for portions needed with flanges. These pipes were constructed with inclinations in order to dump easily the fluid into the Dump Tank when a shutdown of electric power line or a deficiency of inert gas might be caused.

The Dump Tank is the storage of a working fluid. In circulating, the Dump Tank also functions as a buffering tank to keep the circulating line filled with fluid. The

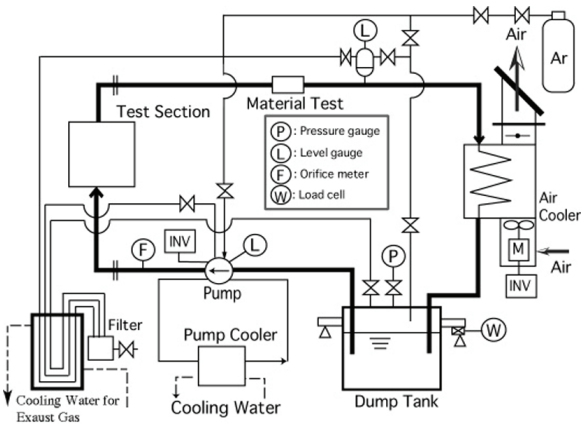

Fig. 1. System diagram of MSL

volume is $130x10^{-3}$ m^3. The procedure to fill up the molten salt in the MSL is as follows; at first, the Dump Tank is heated up in order to melt the salt. Then, the surface of the melted salt in Dump Tank is pressurized by Ar gas, and the Upper Tank is degassed. As a result, the loop of the MSL is filled up with the molten salt.

The Forced Circulation Pump is a centrifugal mechanical pump for high-temperature molten salt manufactured by Teikoku Electric MFG. Co., Ltd., Japan. The pump has a high-pressure head enough. However, the maximum flow rate is limited to be $3.33x10^{-4}m^3/s$ due to large pressure drop through the Air Cooler.

The test section is provided to investigate heat transfer enhancements for high-temperature molten salt. The overall length of the heated section is $5.0x/10^{-1}$m. In order to obtain the heat transfer coefficient, a mixing zone is set so as to measure a bulk temperature. So, the net effective length of the test section for heat transfer measurements is reduced to about $4.5x10^{-1}$m.

The Upper Tank is to keep the surface liquid level at the top of the loop. The tank has three level gauges, the high, middle and low-level gauges. In experiments, the surface level is adjusted between the high and the middle gauges, which is controlled with supplying or degassing Ar gas.

The Air Cooler is applied in order to cool down the fluid heated at the test section. Heat exchanger tubes of the Air Cooler are arrayed in zigzag. The heat transfer area of the tubes with fin is about 5.4 m^2.

III. EXPERIENCES OF HANDLING MOLTEN SALTS

The MSL has been designed on the basis that Flibe can be used. However, it has the too high melting point of 732 K and its vapor includes Be, which might cause the biohazard in the accident of vapor leakage. From consideration of these difficulties, we chose HTS as a simulant of Flibe. HTS is a eutectic mixed salt; KNO_3:$NaNO_2$:$NaNO_3$=53:40:7. Its melting point is 415 K, and it is considerably easy and safe to be handled in experiments. And also, it has the benefit not to contain any noxious materials. HTS is a simulant to obtain the similarity of Pr number for Flibe. The Pr number of the referred Flibe (LiF:BeF_2=66:34) is about 30 at 793 K, and HTS can be adjusted at the same value at 443 K (Fig. 2(a)). In this section, several technological experiences and topics through operating the MSL will be introduced.

III.A. A Big Sound in Melting the Salt in the Dump Tank

At first, the salt is melted at the Dump Tank where the salt is stored as a solid phase ordinarily. As the heater for the Dump Tank was installed around its outside wall, melting of the salt proceeds like a 'whiskey on the rock.'

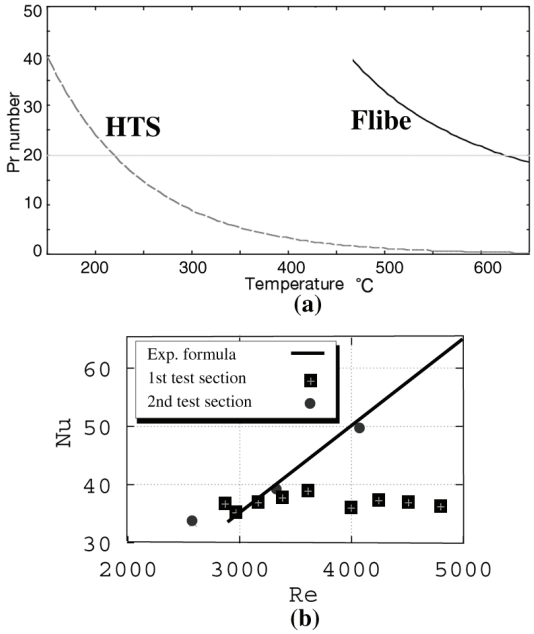

Fig. 2. (a) Temperature vs. Pr number.
(b) Experimental data of Re vs. Nu.

The salt starts to melt from the region adjacent to the wall and pipes, which brings a normal 'cracking sound.

However, there happened some cases where the melting process makes an extraordinary big sound with 'a shock.' Although the inside of the Dump Tank cannot be inspected visibly, it may be supposed to be caused by buoyancy of the molten salt, or by a difference of thermal expansion between the SUS316 and the molten salt. It should be afraid that this shock and sound might destroy the Dump Tank, thus we are on going to grasp this phenomenon more clearly.

III.B. Molten Salt Invades into Gas Pipes

As mentioned above, the liquid level is controlled by the pressure of inert Ar gas at the Upper Tank. Since Ar gas does not need to be preheated, any of preheater and thermal insulation are not attached on the gas lines. However, if the flow rate is over the designed limitation, molten salt might quickly invade into the fine gas pipes and be frozen there.

Such the abnormal situation has to be prevented by installing some hazard equipment. One way is proposed to install one more gauge (the highest level gauge) above the position of the high level gauge in the Upper Tank. The pump should be shut down as quickly as liquid touches the highest gauge. The another way is to install the buffering chamber preventing overflowed molten salt at the entrance of the gas line connecting to the Upper Tank. As the gas pipes are so fine, the buffering chamber

can store overflowing liquid and prevent it flow into gas lines furthermore. In the MSL, the latter way is recommended to be more realistic than the former.

III.C. Others

It is found that small amount of HTS is left behind at some of welding points of the loop due to less fluidity with high viscosity, when the whole working fluid is dumped into the Dump Tank after shutdown. And, in the present loop, airtightness of the loop was found to be broken not from the connections but from some of solenoid valves to intake and exhaust Ar gas for controlling the surface level. These small leak problems should be avoided carefully when we will use Flibe in future, of which vapor involves Be.

After the salt is melted in the tank, the loop has to be entirely preheated above its melting point. Although the preheater was installed all over the present loop, the temperature rise at the parts of flanges is very slow compared with another parts of the loop. Because heaters around flanges are controlled together with the neighboring 'easy heated' parts of the pipes, the molten salt near the flanges might be solidified again due to low temperature at flanges with their large heat capacity, which leads to preventing their smooth temperature rise. From these experiences, heaters of flanges should be controlled separately in order to avoid such solidification.

IV. PRELIMINARY EXPERIMENT AND EXPERIMENTAL PLANNING

Preliminary experiments using HTS have been performed to measure Nu number through a smooth pipe (Fig. 2(b)). From these experiments, the following important experiences have been obtained.

It is needed to use a mixing chamber where the bulk temperatures are measured. Firstly, the first test section was experimented, which we had constructed by applying a mixing method proposed in the reference[2], however, the result could not give the accurate bulk temperatures at outlet of heating area. It was shown in the report[4] that, due to high viscosity, molten-salt flow had to be stirred by other ways different from the above mixing method applied for usual fluids like water.

Secondly, as the present experiments are performed under high-temperature and high Pr-number conditions, we developed the more efficient structure of the test section containing the new type of mixing chamber. The packed-beds mixing chamber (Fig. 3(a)) of the first test section had too high heat capacity because of too large volume of the flanges at the mixing chamber. Although the temperature profile of the wall at the heated area had to be a monotonous increase along flow direction, the temperature at a center point of the heated area was higher than that at an end point, that made it difficult to

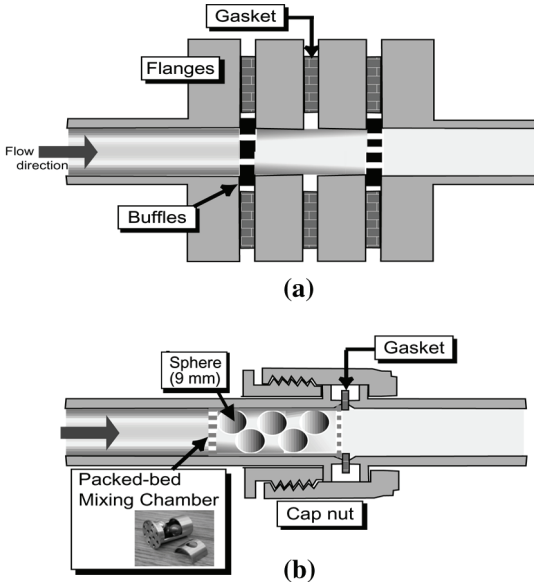

Fig. 3. Schematics of the mixing chamber for: (a) first test section; (b) second test section.

measure heat transfer coefficients. For improving these problems, the second test section was developed (Fig. 3(b)). It is possible to obtain accurate Nu number compared with an experimental formula[5] as shown in Fig. 2(b) because the second test section has smaller heat capacity and compactness.

The experimental planning with this second test section are as follows: the first is to find out the most suitable method for the fluid mixing by considering the effects of the mixing area and the size of the packed bed particles. Thereafter, heat transfer enhancements will be researched by applying the packed-bed tubes, twisted-tape inserted tubes and another possible turbulence promoter.

V. CONCLUSIONS

The main purpose with theMSL is to investigate the heat transfer enhancement for molten salt. From the preliminary experiments using the MSL, several experiences in handling molten salts have been obtained. The important experiences were reported. For avoiding any troubles in a fusion power plant, these experiences should be considered in designs of the fusion-reactor blanket or heat exchanger using Flibe with high melting-point fluid.

From the fundamental experiments for heat transfer of molten salts under such severe conditions with a large forced circulation loop, we could indicate several problems to be solved. The heat capacity of a mixing area should be smaller from the viewpoint of thermal loss and making the temperature distribution uniform. Since the MSL experiments are performed under high-temperature,

high heat-flux and high flow-rate conditions, it is necessary to apply the suitable structure of a test section with the suitable mixing chamber. The experiments are now on going with the improved Test Section. By these experiments, several methods of heat transfer enhancement will be developed. A promising enhancer for molten-salt heat transfer in fusion reactors will be found probably from our future experiments using the MSL.

REFERENCES

1. S. Chiba, S. Toda, K. Yuki, Heat Transfer Enhancement for a molten salt Flibe channel, Fusion Technol., **39**, 779-783 (2001).
2. Y. Shimizu, et al., Measurement of mixing-cup temperature, Trans. JSME (in Japanese), 53, 86-0601B (1987).
3. A. Sagara, et al., Blanket and divertor design for force free helical reactor (FFHR), Fusion Eng. Des. **29**, 51-56 (1995).
4. S. Toda, et al., Molten salt experimental loop, NIFS Annual Report 2001.
5. V. Gnielinski, et al., New equations for heat and mass transfer in turbulent pipe and channel flow, Int. Chem. Eng. 16-2, 359-368 (1976).

EXPERIMENTAL INVESTIGATION OF TURBULENT HEAT TRANSFER OF HIGH PRANDTL NUMBER FLUID FLOW UNDER STRONG MAGNETIC FIELD

T. Yokomine[1], J. Takeuchi[2], H. Nakaharai[1], S. Satake[3], T. Kunugi[4], N. B. Morley[2], M. A. Abdou[2]

[1]*Kyushu University, 6-1 Kasuga-koen, Kasuga, Fukuoka 816-8580, Japan, yokomine@ence.kyushu-u.ac.jp, nakah@aees.kyushu-u.ac.jp*
[2]*University of California, Los Angeles, 420 Westwood Plaza, 44-114 Eng. IV, Los Angeles, CA 90095, USA, takeuchi@fusion.ucla.edu, morley@fusion.ucla.edu, abdou@fusion.ucla.edu*
[3]*Tokyo University of Science, 2641 Yamazaki, Noda, Chiba 278-8510 Japan, satake@te.noda.tus.ac.jp*
[4]*Kyoto University, Yoshida, Sakyo, Kyoto, 606-8501 Japan, kunugi@nucleng.kyoto-u.ac.jp*

An investigation of MHD effects on Flibe simulant fluid (aqueous potassium hydroxide solution) flows has been conducted under the U.S.-Japan JUPITER-II collaboration program using "FLIHY" pipe flow facility at UCLA. Mean and fluctuating temperature profiles in a conducting wall pipe were measured for low Reynolds number turbulent flows using a thermocouples probe at constant heat flux condition. It is suggested that the temperature profiles are characterized by interaction between turbulence production, turbulence suppression due to magnetic field and thermal stratification occurred even under the situation where quite small temperature difference exists in the pipe cross-section.

I. INTRODUCTION

Flibe is one of the possible candidates for coolant/breeding materials for fusion applications. It has very low activation, low tritium solubility, low chemical reactivity, and low electrical conductivity, which relieve the problems associated with MHD pressure drop. In recent research, several design concepts utilizing Flibe have been proposed. Some of the examples are HYLIFE-II,[1] the APEX thick/thin liquid walls[2] and FFHR.[3] Furthermore, Flibe has a crucial difference from liquid metals with respect to the heat transfer characteristic: Flibe is a high Prandtl number fluid. For high Prandtl number fluid, in general, heat transport from a heated wall into the core of the fluid flow is dominated by turbulent motion rather than thermal diffusion. Near-wall flow structures are especially important because thermal boundary layer is much thinner than the momentum boundary layer. In the fusion blanket application of Flibe, there is a severe limitation of temperature window due to its high melting point. The turbulent heat transfer is, therefore, decisive in designing Flibe-based blanket. On the other hand, it is well known that the strong magnetic fields suppress the turbulence even for the flows of low conducting fluids. In the case of occurrence of turbulence suppression, it is concerned that the degradation of the heat transfer performance for high Prandtl number fluid becomes more severe than that for low Prandtl number fluid.

MHD turbulent flows have been extensively studied using liquid metals as working fluids. As far as the MHD effects on the heat transfer characteristics are concerned, Gardner[4] reported that the influence of the transverse magnetic field on the heat transfer was to inhibit the convective mechanism of heat transfer, resulting in reduction of Nusselt number up to 70%. In another paper,[5] Gardner summarized his results of turbulent heat transfer calculations using a curve fit equation representing the average Nusselt number as function of Peclet number and Hartmann number (Ha). However, the MHD turbulent heat transfer characteristics for high Prandtl number fluids are not well understood. Blum[6] conducted heat transfer experiment using an electrolyte flowing through a rectangular channel over a wide range of Reynolds number (Re) including the transition region from laminar to turbulent and presented an empirical correlation for degradation of heat transfer in a turbulent MHD flow as a function of interaction parameter ($N= Ha^2/Re$). Since his correlation was constructed from two different experimental data with completely different experimental conditions and parameter range, more reliable data will be required.

From FY2001, JUPITER-II (Japan-US Program for Irradiation Test of Fusion Materials) collaboration is in progress. As one on the important task of this collaborative program, a series of experiments on fluid mechanics and heat transfer of Flibe-simulants have been performed by means of an experimental MHD flow facility called "FLIHY" (FLIbe HYdrodynamics) at UCLA. Turbulent flow field measurements using PIV[7] and heat transfer measurements[8] have so far been carried out without magnetic field to establish the experimental techniques and verify the performance of the facility by comparing an existing experimental results[9] and DNS data.[10]

The objective of the present investigation is to improve understandings of MHD effects on turbulent heat

transfer on high Prandtl number fluid by acquiring experimental data for local and average heat transfer and mean and fluctuation fluid temperature distributions for turbulent flow of electrically conducting fluid in a electrically conducting wall pipe under magnetic fields using high Prandtl number fluid as a Flibe simulant.

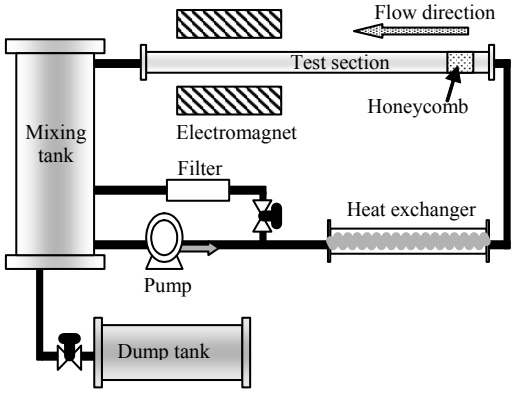

Fig.1 Schematic drawing of the pipe flow facility

II. EXPERIMENTAL SETUP

Fig.1 shows a schematic drawing of the experimental pipe flow loop "FLIHY" in UCLA. The 30%wt aqueous potassium hydroxide (KOH) solution is used as a Flibe-simulant fluid. The fluid flow is introduced into a horizontal pipe test section by a mechanical pump. The inlet and outlet temperature is monitored by thermocouples. The bulk mixing temperature of arbitrary cross section T_b is estimated by linear interpolation from the inlet temperature T_{in} and the outlet temperature T_{out} using equation (1), where x is the length of the heated section at the measurement position and L is the total length of the heated section.

$$T_b = T_{in} + (T_{out} - T_{in})\frac{x}{L} \qquad (1)$$

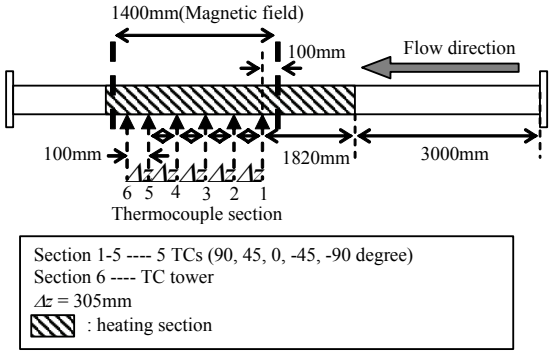

Fig.2 Details of Test Section

The magnet used for the present experiments produces maximum 2.0 Tesla magnetic fields in a narrow gap of the iron core at 3000 A of applied electric current. The test section was placed in the gap which is 1400 mm length in the streamwise direction, 250 mm in height, and 150 mm in width. The generated B field has uniform distribution within 5% variation for 1000 mm in the streamwise direction.

Fig.2 gives details of the test section. The test section is an 8000 mm long stainless steel pipe with 50 mm inner diameter. A part of the pipe is heated uniformly by heating tapes. The magnetic field is applied for 1400 mm along the pipe. Twenty-five T-type sheathed thermocouples with 0.5 mm diameter are installed in drilled holes with 1 mm diameter on the outer surface of the pipe and affixed with high thermal conductivity (15W/mK) adhesive at five axial positions and five angles from the horizontal magnetic field. The distance from the pipe inner surface to the thermocouple junctions is 1mm.

The effect of the magnetic field on the output signals

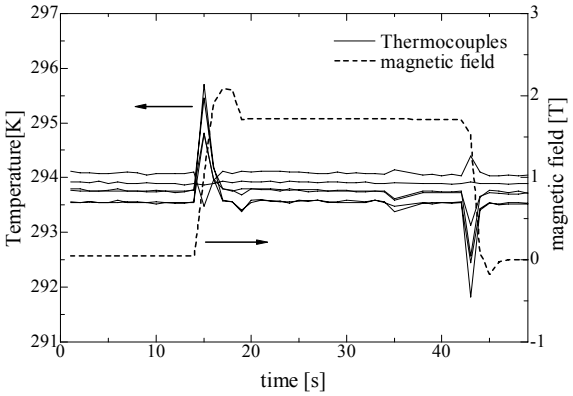

Fig.3 Magnetic field effect on thermocouples

of the wall thermocouples is shown in Fig.3. Large spikes in the thermocouple output signals were observed when the magnitude of the magnetic field was changed; however, the output signals were stable when the magnetic field was kept constant. Since the thermocouples are sheathed and insulated from the test pipe, the effect of induction current in the stainless steel pipe should be negligible, and the spikes are caused by EMF induced in the thermocouple wires. The temperature difference between with and without magnetic field is less than 0.01K for all the thermocouples. Therefore, the effect of the magnetic field on the thermocouple measurements is negligible for steady state.

The radial temperature distributions of the fluid flow in the pipe are measured by means of thermocouples (TC) probe, which consists of six Inconel-sheathed K-type thermocouples with 0.13 mm diameter. The schematic view of TC probe is shown in Fig.4. The TC probe can be moved by a micrometer with the spatial resolution of

0.02mm. Measurable minimum distance from the inner pipe wall is 0.05mm. The 63% response time of these thermocouples is 2ms. It is confirmed that the effect of TC probe on the upstream temperature field and the effect of vibration of TC probe on the temperature measurement are both negligible. Although the angle of the TC probe to the B filed can be changed freely, the angle is fixed in the horizontal plane which is parallel to the B field in present study.

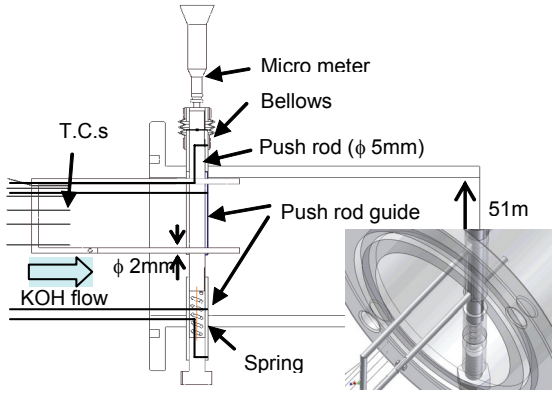

Fig.4 Schematic view of TC probe

The Reynolds number based on the bulk mean velocity and the pipe diameter is varied from 7400 to 20000 for three Hartmann numbers based on a pipe diameter, Ha=0, 10, 20. The bulk mean velocity is calculated from the flow rate. The flow rate is measured and monitored by vortex flow sensor which measures flow rate from frequency of Karman vortex. TABLE I shows the property of KOH solution in the present experimental conditions.

TABLE I. Properties of KOH solution

Temperature [℃]	40.0	42.5	44.0
Density[kg/m^3]	1275.6	1274.0	1272.8
Thermal conductivity[W/(m K)]	0.737	0.741	0.743
Viscosity[10^{-3}Pa*s]	1.280	1.231	1.193
Specific Heat Capacity [J/(kg K)]	3010	3014	3018
Electrical conductivity[1/ohm*m]	81.7	84.7	87.1
Prandtl number	5.23	5.01	4.85

III. EXPERIMENTAL RESULTS

Fig.5 shows the mean temperature distributions. The non-dimensional temperature T^+ is defined as below.

$$T^+ = \frac{T_w - T}{T^*}, \quad T^* = \frac{q_w}{\rho c_p u_\tau} \tag{2}$$

Here T^* is the friction temperature determined by the wall heat flux q_w, fluid density ρ, heat capacity c_p, and the friction velocity u_τ. The wall temperature T_w is measured by thermocouple installed in the pipe wall at the probe location. In each figure, the equation of temperature profiles in fully developed turbulent boundary layer proposed by Kader[11] shown in Eqs. (3) and (4) are plotted along with the experimental data.

$$T^+ = \mathrm{Pr}\, y^+ \exp(-\Gamma) + \left\{ 2.12 \ln\left[\left(1+y^+\right) \frac{1.5\left(2 - y/R\right)}{1 + 2\left(1 - y/R\right)^2} \right] + \beta(\mathrm{Pr}) \right\} \times \exp(-1/\Gamma) \tag{3}$$

$$\left.\begin{aligned} \beta(\mathrm{Pr}) &= \left(3.85\,\mathrm{Pr}^{1/3} - 1.3\right)^2 + 2.12 \ln \mathrm{Pr} \\ \Gamma &= \frac{10^{-2}\left(\mathrm{Pr}\, y^+\right)^4}{1 + 5\,\mathrm{Pr}^3\, y^+} \end{aligned}\right\} \tag{4}$$

Here y is the coordinate normal to the wall, y^+ dimensionless coordinate defined by friction velocity, and R the pipe radius. In all cases, the temperature profiles without magnetic field give close agreement with Kader's equation. From the agreement, it is confirmed that the effect of natural convection is not significant. Indeed, the typical feature of natural convection appeared up to Re=5000. Common trend among these profiles is that the temperature difference between wall and fluid becomes larger in the near-wall region with increase of Ha. Heat transfer to the non-MHD turbulent flows is generally dominated by turbulent transport. For MHD flows, however, it is well known that the turbulence is significantly suppressed especially for the flows in conducting wall ducts. This results in prohibiting the turbulent transport mechanism. Therefore, the increase of the temperature difference can be explained by degradation of heat transfer due to the prohibition of turbulent transport mechanism. It is noted that for Ha = 10, the increase of the temperature difference is obvious only for Re = 9000, and no noticeable change is observed for higher Reynolds number cases. Although Gardner et al.[4] reported that significant natural convection was observed in their experiments, no evidence for natural convection was obtained in this experiments. Meanwhile, large temperature difference between top and bottom (large temperature rise in the top) of the pipe suggests that the thermal stratification occurs in the flow. This is observed even when the temperature difference between wall and bulk fluid is as small as 0.5 K at Re = 11000.

As shown above, the MHD effects on turbulent heat transfer for low Reynolds number flows are characterized by competition between turbulence production, turbulence suppression and thermal stratification. Therefore, the

MHD effects are more prominent for lower Reynolds number cases in which turbulence production is weaker.

The temperature fluctuation profiles are shown in Fig.6. The r.m.s. (root-mean-square) value of the fluid temperature is normalized by the friction temperature T^*. In the case of Re=7400, the temperature fluctuation is declined with increase of Ha in the entire region, which is rather straightforward consequence of the turbulence

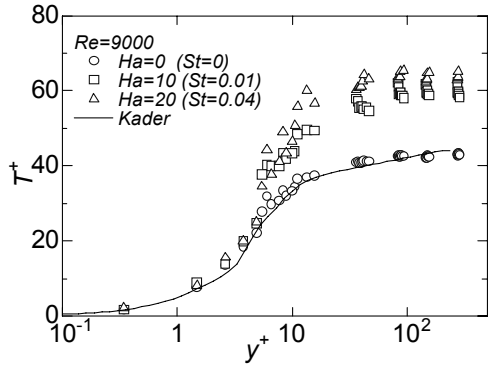

(a) Re=9000

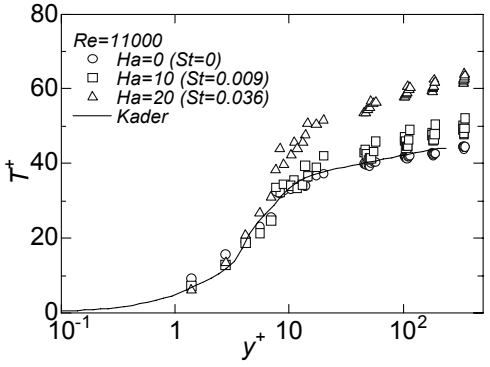

(b) Re=11000

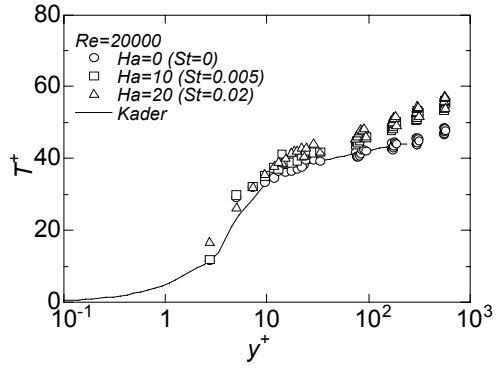

(c) Re=20000

Fig.5 Temperature profile under magnetic field

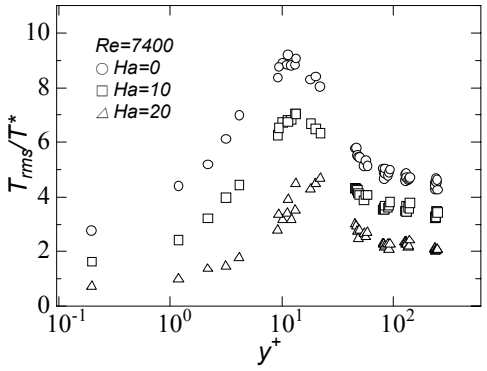

(a) Re=7400

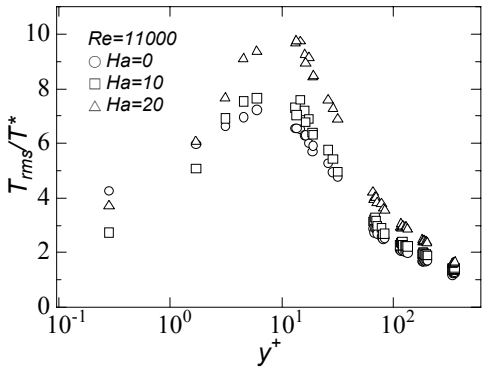

(b) Re=11000

Fig.6 Change of temperature fluctuation profile under magnetic field

suppression. On the other hand, the contradictory result can be seen for Re=11000. The same tendency appears in higher Reynolds number cases. As mentioned above, the mean temperature field is governed by synergetic interaction between turbulence production, turbulence suppression and thermal stratification; therefore, it is conjectured that the fluctuating temperature profiles also depend on the balance between these effects. There is no numerical result as well as experimental investigation about the effect of magnetic field on the temperature field where the thermal stratification is significant, so the additional experiments and DNS are underway to clarify the complicated interaction.

Fig.7 shows the decrease in Nusselt number as a function of interaction parameter. The longitudinal axis is the ratio of Nusselt number with magnetic field (Nu_M) to the one at the same flow condition without magnetic field (Nu). The correlation proposed by Blum[3] and Garder[1] is also plotted on the same figure even the flow configuration and Prandtl number are quite different from present experiment. The MHD effect on the degradation

of heat transfer is much larger than Blums' correlation, which is based on a non-conducting wall duct experiment. Furthermore, it seems that there are two trend lines on reaching value of the interaction parameter 0.01 for present data. As underlaying premise, the original experimental data used to reduce Blum's equation is quite scattered at the small interaction parameter range in his paper. So that, the reason of difference between present data and Blum's one is not cleared yet. In the region above the interaction parameter 0.01, it can be expected that the bulk temperature field is more susceptible to the thermal stratification effect from the above explanation. Therefore, it is suggested that the balance of laminarization and thermal stratification is changed around the value of interaction parameter.

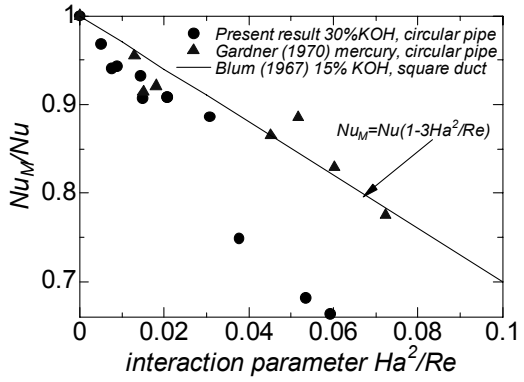

Fig.7 Degradation of heat transfer as a function of interaction parameter

IV. CONCLUDING REMARKS

The mean and fluctuating temperature profiles in the conducting wall pipe were measured for low Reynolds region with variable Hartmann numbers. It is suggested that the shift in the mean temperature profile is a result of interaction between turbulence suppression due to MHD effect and thermal stratification occurred with the temperature difference between wall and bulk fluid as small as 0.5 °C.

According to present investigation, it can be concluded that treatment of temperature field as a passive scalar in traditional numerical simulation becomes unreasonable assumption under magnetic field.

ACKNOWLEDGMENTS

The authors wish to acknowledge support by the US DOE and the Japanese MEXT via the JUPITER-II Collaboration.

REFERENCES

1. R. W. MOIR, R. L. BIERI and X. M. CHEN et al, "HYLIFE-II: A molten-salt inertial fusion energy power plant design - final report," *Fusion Technol.*, 25, 5, (1994).
2. M. A. ABDOU, THE APEX TEAM and A. YING et al., "On the Exploration of Innovative Concepts for Fusion Chamber Technology," *Fusion Eng Des*, 54, 181 (2001).
3. A. SAGARA, H. YAMANISHI and S. IMAGAWA et al, "Design and Development of the Flibe Blanket for Helical-Type Fusion Reactor FFHR," *Fusion Eng. Des.*, 49-50, 661, (2000).
4. R. A. GARDNER and P. S. LYKOUDIS, Magneto-fluid-mechanic pipe flow in a transverse magnetic field Part 2. Heat transfer, *J. Fluid Mech.* 48, 129 (1971).
5. H. C. JI and R. A. GARDNER, Numerical analysis of turbulent pipe flow in a transverse magnetic field, *Int. J. Heat Mass Transfer*, 40, No.8, 1839 (1997).
6. E. YA. BLUM, Effect of a magnetic field on heat transfer in the turbulent flow of conducting liquid, *High Temperature*, 5, 68 (1967).
7. J. TAKEUCHI, S. SATAKE and N. B. MORLEY et al, "PIV Measurements of Turbulence Statistics and Near-Wall Structure of Fully Developed Pipe Flow at High Reynolds Number," *Proc. 6th International Symposium on Particle Image Velocimetry*, Pasadena, CA, USA, Sept 21-23, (2005).
8. J. TAKEUCHI, S. SATAKE and R. MIRAGHAIE et al, "Study of Heat Transfer Enhancement / Suppression for Molten Salt Flows in a Large Diameter Circular Pipe: Part One - Benchmarking," *Fusion Eng Design*, 81, 601, (2006).
9. J. G. M. EGGELS, F. UNGER and J. WEISS et al, "Fully Developed Turbulent Pipe Flow: A Comparison between Direct Numerical Simulation and Experiment," *J. Fluid Mech.*, 268, 175, (1994).
10. S. SATAKE, T. KUNUGI and R. HIMENO, "High Reynolds Number Computation for Turbulent Heat Transfer in Pipe Flow," In: M. Valero et al, Ed., *Lecture Notes in Computer Science 1940*, Springer-Verlag, Berlin-Heidelberg, (2000).
11. B. A. KADER, "Temperature and Concentration Profiles in Fully Turbulent Boundary Layers," *Int. J. Heat Mass Transfer*, 24, No.9, 1541 (1981).

HEAT TRANSFER PERFORMANCE FOR HIGH PRANDTL AND HIGH TEMPERATURE MOLTEN SALT FLOW IN SPHERE-PACKED PIPES

Tomoaki Satoh[1], Kazuhisa Yuki[1], Shin-ya Chiba[1], Hidetoshi Hashizume[1], Akio Sagara[2]

[1]*Tohoku University, Sendai, Miyagi, Japan, tsato@karma.qse.tohoku.ac.jp*
kyuki@qse.tohoku.ac.jp, schiba@karma.qse.tohoku.ac.jp, hidetoshi.hashizume@qse.tohoku.ac.jp,
[2] *National Institute for Fusion Science, Toki, Gifu, Japan, sagara.akio@lhd.nifs.ac.jp*

Heat transfer performance for high Prandtl number and high temperature molten salt flow in a circular pipe and in sphere-packed pipes are evaluated with modified Tohoku-NIFS Thermofluid Loop (TNT loop) using high-temperature molten salt HTS (KNO_3 : $NaNO_2$: $NaNO_3$ = 53 : 40 : 7), as a stimulant of Flibe (LiF : BeF_2 = 66 : 34). The modified TNT loop has much longer entrance region to develop a thermal boundary layer, which enable us to obtain more precise heat transfer data.

In the modified TNT loop experiments, the heat transfer characteristics in a circular pipe flow have good agreements with the representative correlations. It is obvious that the analogy for heat and momentum transfer is also valid for high-temperature and high-Prandtl-number molten salt flow. It is also confirmed that the heat transfer performance of sphere-packed pipes increases up to about 4 times higher than that of circular pipe, in case of relatively low flow rate. This can be effective in the Flibe blanket system from the viewpoints of moderating MHD effect and electrolysis.

I. INTRODUCTION

Molten salt Flibe is recommended as a blanket material in the design of a force-free helical reactor (FFHR), since liquid Flibe can work as both tritium breeder and neutron multiplier with low MHD effects due to low electric conductivity.[1] Flibe, however, has several disadvantages such as low heat transfer performance resulted from its being high-Prandtl (Pr)-number fluid. In the design of the spectral-shifter, [1] it is considered that heat transfer coefficient of at least 20000 W/m^2K is necessary to remove heat flux at the first wall. Therefore, it is necessary to clarify fundamental heat-transfer characteristics for Flibe and to enhance heat-transfer performance. For these reasons, Tohoku-NIFS Thermofluid Loop (TNT loop) was built at Tohoku University, Japan.[2] The design of the TNT loop was based on the presupposition that molten salt Flibe can be used. However, its melting point, 459 °C, is too high and vapor of Flibe includes toxic beryllium. Therefore, Heat Transfer Salt (HTS), which is a mixture of KNO_3, $NaNO_2$ and $NaNO_3$, has been used as a alternate. The melting point of HTS is low (142 °C) in comparison with that of Flibe, and it doesn't contain toxic substances. In addition, the Pr number of the HTS is equivalent to that of Flibe under lower temperature conditions. The Pr number of Flibe is about 30 at 520 °C, while the HTS has the same Pr number at about 170 °C.

In designing the Flibe blanket system, a pressure drop due to its high viscosity and the MHD effect have to be considered since the Flibe is a highly viscous and a electrically conducting fluid, so that it must be better to enhance the heat-transfer performance under low flow rate conditions. From this point of view, the experiments with heat transfer promoter, sphere-packed pipes (SPP), were performed in the previous study using the TNT loop and enhancement of heat-transfer performance was proven.[3] However, the heat-transfer characteristics of the circular pipe flow that were employed as a reference data, didn't agree with some representative empirical formulas such as Sieder-Tate's correlation etc.. As the cause of this disagreement, it was considered that the length of entrance region wasn't long enough to develop a thermal boundary layer. It is, therefore, needed to reinvestigate whether the heat-transfer characteristics of the circular pipe flow also satisfy with well-known representative correlations. For this background, a test section of the loop was redesigned and modified in order to obtain more accurate data. After the modification, the length of entrance region is almost 30 times longer than an inner diameter of pipe.

The present paper reports the experimental results of heat-transfer characteristics for such high-Pr and high-temperature molten salt flow in a circular pipe using the modified TNT loop with more optimal test section. Furthermore, the enhancement of heat-transfer performance with SPP is also reexamined.

II. EXPERIMENTAL

II.A. Experimental Systems

The system diagram of the TNT loop used to investigate the heat-transfer characteristics of molten salt flow is shown schematically in Fig.1, and the birds-eye view of the loop is shown in Fig. 2. The main components of the loop are a dump tank, a circulation pump (a centrifugal pump), a test section, an upper tank and an air

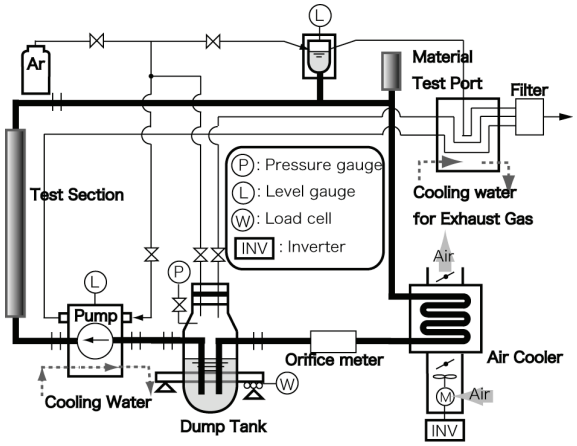

Fig. 1 System diagram of the TNT loop

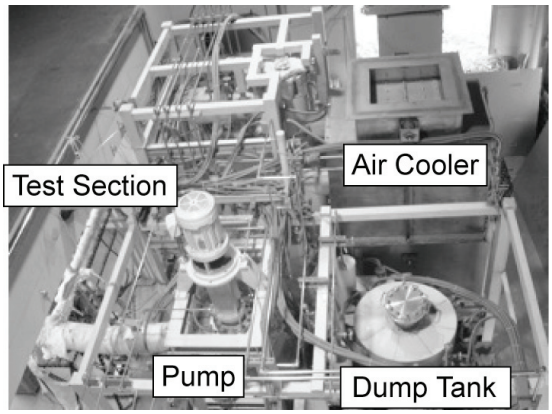

Fig. 2 Birds-eye view of the TNT loop

cooler. More details of the loop are described in the references.[2, 3]

II.B. New Modified Test Section

The modified section is shown schematically in Fig. 3, and flow direction is also shown in the figure with arrows. To alleviate the effect of thermal stress, flexible tubes are used in the modified section.

As shown in Fig. 3, the modified section, which is made of SUS304 and SUS306, mainly consists of (a) Flow straightener, (b) Entrance region, (c) Heated test section, and (d) Mixing chamber. Firstly, HTS flows into the flow straightener through the flexible tube. A shape of the flow straightener is a box 75 mm on a side, and its size is large enough in comparison with the tube diameter. Therefore, the HTS can be completely mixed once in the box. Then temperatures of the mixed HTS are measured here with four K-type thermocouples. An average of the measured temperatures is used as an inlet bulk temperature T_{in} to calculate heat flux. At the outlet of the box, two stainless steel meshes having different grid sizes are fixed in piles. The mixed HTS can be a uniform flow through these meshes. Effectiveness of this flow straightener was confirmed in a water circulation loop by using a flow visualization system. The length of the entrance region is about 630 mm, which is almost 30 times longer than the inner tube diameter d = 19 mm. Before flowing into the heated test section, the velocity distribution of HTS could be fully developed thorough the entrance region. A straight SUS304 tube with 19 mm inner diameter, 20 mm outer diameter, and 1050 mm length was used as a heated test section. In order to measure the accurate outlet bulk temperature, the mixing chamber is attached behind the heated test section. In the mixing area, stainless steel spheres are packed to stir the fluid flow

With the modification of the loop, a heating method was also completely changed from use of a sheathed heater to a direct electrical heating method, which makes measurements of outer wall temperatures easier. Therefore, electrodes are fixed on the both ends of the heated test section. On the outer wall of the heated test section, K-type thermocouples were fixed by aluminum tape to measure outer wall temperatures. These thermocouples, whose wire diameters are 0.1 mm, are all handmade with a spot welder, and they are calibrated certainly before experiment.

Detailed specifications of the TNT loop and experimental procedure are also described in the reference.[2, 3]

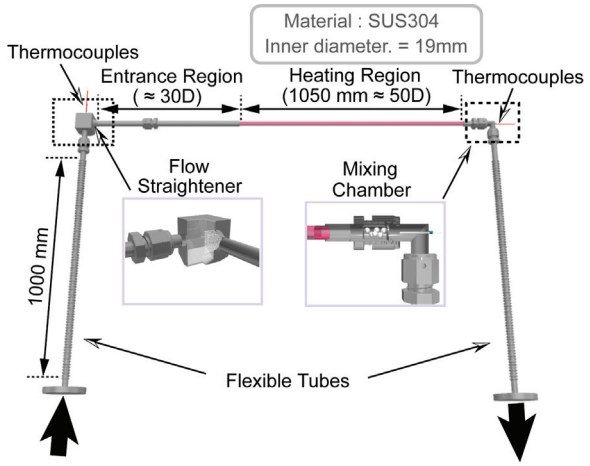

Fig. 3 Modified section of the TNT loop

III. PROCEDURE AND DATA ANALYSIS

The Nusselt numbers calculated from obtained heat-transfer coefficients are compared with representative heat-transfer correlations, which are modified Hausen correlation, Sieder-Tate correlation and modified Petukhov correlation[4] given by,

Modified Hausen correlation:
$(3.5\text{x}10^3 \le \text{Re} \le 10^4)$

$$\text{Nu} = 0.116\left(\text{Re}^{\frac{2}{3}} - 125\right)\text{Pr}^{\frac{1}{3}}\left(\frac{\mu_\text{b}}{\mu_\text{wi}}\right)^{0.14} \tag{1}$$

Sieder-Tate correlation:
$(10^4 \le \text{Re},\ 0.5 \le \text{Pr} \le 10^6)$

$$\text{Nu} = 0.027\text{Re}^{0.8}\,\text{Pr}^{\frac{1}{3}}\left(\frac{\mu_\text{b}}{\mu_\text{wi}}\right)^{0.14} \tag{2}$$

Modified Petukhov correlation:
$(3000 \le \text{Re} \le 5\text{x}10^6,\ 0.5 \le \text{Pr} \le 2000)$

$$\text{Nu} = \frac{(f/2)(\text{Re}-1000)\text{Pr}}{1+12.7\sqrt{(f/2)}\left(\text{Pr}^{2/3}-1\right)} \tag{3}$$

where,

$$K = \left(\text{Pr}/\text{Pr}_\text{wi}\right)^{0.11} . \tag{4}$$

Fanning friction factor f for the circular pipe is calculated from the equation given by G. K. Filonenko.[5]

$$f = \left(3.64\log_{10}\text{Re} - 3.28\right)^{-2} \quad (3000<\text{Re}<10^6) \tag{5}$$

Then heat transfer coefficients are calculated as follows.

$$h_\text{cal} = \frac{\text{Nu}k_\text{f}}{d} \tag{6}$$

In the experiment, heat-transfer coefficients are calculated from the input heat flux, the bulk fluid temperature and the inside wall temperature. The input heat flux is obtained from the enthalpy increase of the fluid;

$$q = \frac{\rho c_\text{p} V\left(T_\text{out} - T_\text{in}\right)}{\pi d L} . \tag{7}$$

The temperatures on the inside wall, T_wi, are calculated from the outside wall temperatures, T_wo, by the following equation,

$$T_\text{wi} = T_\text{wo} - \frac{W_\text{total}}{2\pi L k_\text{s}}\left\{\frac{r_\text{wo}^2}{r_\text{wo}^2 - r_\text{wi}^2}\left(\ln\frac{r_\text{wi}}{r_\text{wo}} - \frac{1}{2}\right)\right\} - \frac{W_\text{loss}}{2\pi L k_\text{s}}\ln\frac{r_\text{wo}}{r_\text{wi}} . \tag{8}$$

The above equation is derived from the heat conduction equation in consideration of the external heat loss and the heat generation in the tube. The total heat generation in the tube, W_total, is given by voltage applied on the test section and current passing through the test section as follows.

$$W_\text{total} = EI \tag{9}$$

Then the external heat loss, W_loss, is assumed to be the difference between the total heat loss and the enthalpy increase;

$$W_\text{loss} = W_\text{total} - \rho c_\text{p} V\left(T_\text{out} - T_\text{in}\right) . \tag{10}$$

Local heat transfer coefficient is calculated by the following equation;

$$q = h_\text{exp}\left(T_\text{wi} - T_\text{b}\right) . \tag{11}$$

IV. RESULTS AND DISCUSSION

IV.A. Heat Transfer in a Circular Pipe

In the heat transfer experiment with the circular pipe, nine K-type thermocouples were fixed on only topside along the flow direction to measure the outside wall temperatures, since it was confirmed that the effect of natural convection was negligible under this experimental condition. Therefore, the heat-transfer performance is evaluated with these temperature data.

IV.A.1. Chemical Effect for Heat Transfer Experiment

According to the study on the thermal stability of HTS, the HTS is very stable at temperature up to 450 °C and can be expected to give excellent performance for many years. Above 450 °C HTS is thermally decomposed by the following reaction.

$$5\text{NaNO}_2 \rightarrow 3\text{NaNO}_3 + \text{Na}_2\text{O} + \text{N}_2 \tag{12}$$

If the thermal decomposition occurs, the reaction products would disturb the heat transfer to the fluid. The experiments were carried out under HTS temperature from 200 °C to 350 °C in this study. Thus, it seems that the thermal decomposition doesn't occur. For confirmation of the effect, we observed the inner surfaces of the tube after the experiments. In the result, any reaction product couldn't be observed on the surface. Therefore, we can conclude that thermal decomposition doesn't occur in this experiment, and the effect for the heat transfer experiment is negligible.

IV.A.2. Heat Transfer Characteristics of HTS Circular Pipe Flow

Fig. 4 shows a typical outside-wall-temperature profile along the test section at the inlet temperature of 200 °C. The temperature increases rapidly near at 400 mm from the inlet of the test section. After this position, the temperatures increase almost linearly. This behavior indicates that the thermal boundary layer and velocity boundary layer can be fully developed in this region even

at the highest Prandtl number. Therefore, the temperatures measured in this region are always used to evaluate the heat transfer.

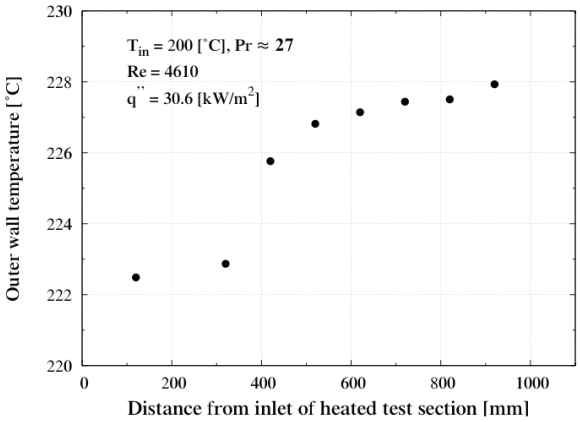

Fig. 4 Typical distribution of outer wall temperatures

The relationship between Nusselt number and Reynolds number is shown in Fig. 5. For references, modified Hausen correlation (Eq. (1)) and Sieder-Tate correlation (Eq. (2)) are also shown in the figure. It can be seen that measured Nusselt numbers in this experiment give close agreement with the well-known representative correlations in comparison with the results obtained in the previous studies. The maximum error rate is less than 10 %. This results show that new test section is suitable for the heat transfer experiment. Especially, the agreements are remarkable around at low Reynolds number. At Reynolds number from 6000 to 9000, differences become slightly large. One reason of this tendency may result from the limitation of applicable range of the correlations. In this Reynolds number-region, the heat transfer is closer to the Sieder-Tate correlation than the modified Hausen correlation.

Then, we compared the results with modified Petukhov correlation (Gnielinski correlation: Eq. (3)) given by V. Gnielinski. This correlation is valid for wide Reynolds numbers and Prandtl numbers. Fig. 6 shows the relationship between Nusselt number and Reynolds number. As shown in the figure, every result shows good agreement with the modified Petukhov correlation. From the results, it is obvious that the analogy of heat and momentum transfer is also effective for the high-temperature and high-Pr molten salt flow. Moreover, it is also shown that some other general fluids having the same Pr as Flibe can be used to evaluate heat-transfer characteristics of Flibe. This definitely makes the experiments for the heat transfer enhancement with/without a magnetic field easier. In the design of FFHR blanket, more than 20000 W/m^{2}K heat transfer

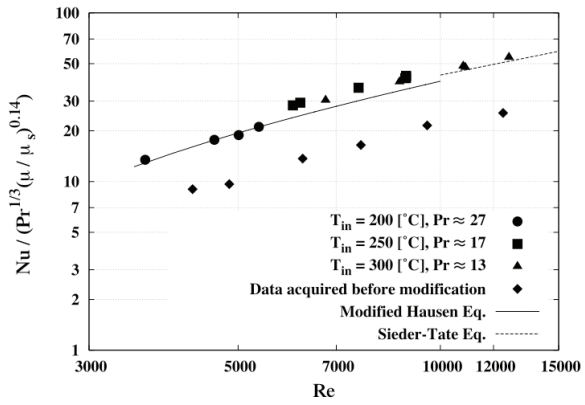

Fig. 5 Comparison between the acquired Nusselt number and the empirical correlations Eq. (1), Eq. (2)

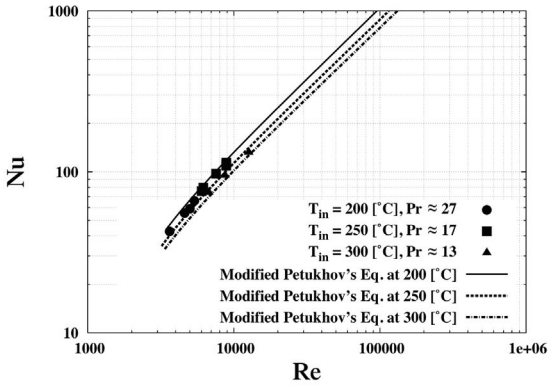

Fig. 6 Comparison between the acquired Nusselt number and modified Petukhov correlation (Eq. (3))

coefficient is necessary to remove high heat flux, 1MW/m^2. Fig. 7 shows the comparison between the obtained heat transfer coefficients and the heat transfer coefficients calculated by modified Petukhov correlation under same flow velocity conditions. The values from modified Petukhov correlation are obtained by iterative calculation. Although this correlation has to be calculated with measured bulk temperature by rights, it is assumed that the bulk temperature is 200 °C, 250 °C and 300 °C in this calculations. Moreover, heat flux used for this calculation is assumed 30 kW/m^2. As shown in the figure, the obtained heat transfer coefficients also give close agreement with the heat transfer coefficient calculated from the modified Petukhov correlations. The maximum error rate is less than 15 %. In the case of using circular pipe, it is evaluated that the flow velocity to achieve h = 20000 W/m^{2}K is 17.3 m/sec (Re ≈ 86300). This fast flow can be a problem in a fusion reactor, because MHD pressure drop is proportional to flow velocity. Besides, the fast flow leads to erosion of a flow channel. Thus, it is

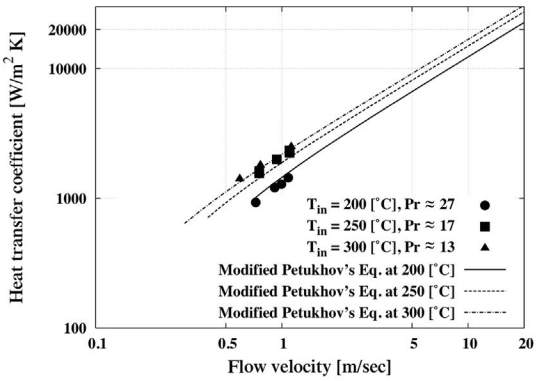

Fig. 7 Comparison between the measured heat transfer coefficient and that calculated from modified Petukhov correlation

need to enhance heat-transfer performance under low flow velocity conditions.

IV.A. Heat Transfer Performance of SPP Flow

In the heat transfer experiment with SPP, twelve K-type thermocouples were used to measure the outside wall temperature, and they were fixed at 3 axial positions, 710 mm, 730 mm and 750 mm from the inlet of the heated test section, and fixed at 4 circumferential positions. The packed spheres used in this experiment have half the size of the tube diameter (D/2 = 9.5 mm) and their material is aluminum oxide.

Fig. 8 shows the comparison of heat-transfer performance between the circular pipe flow, a swirl tube flow and the SPP flow. The line show the performance calculated by Eq. (3) and empirical correlations for the swirl tube with the twisted ratio of 3.0 as shown in the following equations.[6,7]

Manglik correlation for swirl tube flow in turbulent regime

$$\left(\mathrm{Nu}/\mathrm{Nu}_{y=\infty}\right)=1+0.769/y$$

$$\mathrm{Nu}_{y=\infty}=0.023\,\mathrm{Re}^{0.8}\,\mathrm{Pr}^{0.4}\left(\frac{\pi}{\pi-4\delta/d}\right)^{0.8}\left(\frac{\pi+2-2\delta/d}{\pi-4\delta/d}\right)^{0.2}\phi \tag{12}$$

where

$$\phi=\left(\mu_b/\mu_{wi}\right)^{0.18} . \tag{13}$$

Fand correlation for SPP flow

$$\mathrm{Nu}=C\,\mathrm{Re}^{m}\left(\mathrm{Pr}^{p}\right)\left(f_w\,\mathrm{Re}_w\right)^{q}\left[\arctan\left(D/d\right)^{n}\right]^{r} \tag{14}$$

where m = 0.25, n = 1, p = 0.4054, q = 0.5260 and r = -0.6511. The coefficient, C, is decided by fitting the experimental results to the correlation. It can be seen that the heat-transfer performance of the SPP flow is substantially high under the same flow velocity conditions. This tendency is, especially, significant at lower flow velocity. For example, around at V = 0.6 m/sec, the heat-transfer performance of SPP flow is about 4 times higher than that of the circular pipe flow. This result shows that the MHD effect will be sufficiently suppressed by using SPP as a heat transfer promoter, since the MHD pressure drop is proportional to the flow velocity. Also, the electrolysis of Flibe can be moderated since the electromotive force is also proportional to the velocity. As a consequent, SPP can be the effective heat-transfer promoter for the fusion blanket.

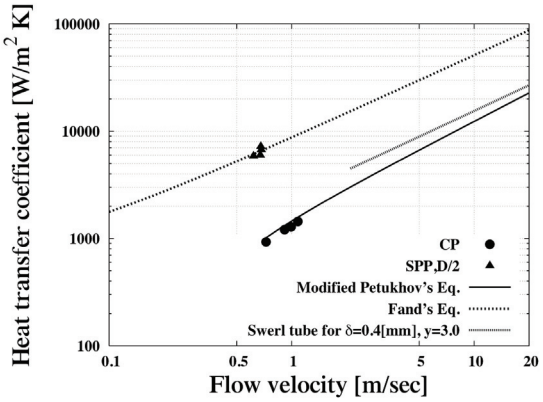

Fig. 8 Results of heat transfer with packed bed

Next, the relationship between pumping power and heat transfer coefficient was compared shown in Fig. 9. At the present system of the TNT loop, pressure drop cannot be measured directly. However in the case of the SPP with D/2 spheres, it has been reported that the pressure drop is good agreements with a drag model [8]. Therefore the drag model is used to evaluate the pressure drop in this study. The result obtained for a smooth tube and SPP can't be compared directly, because the experimental conditions are different. Therefore, empirical correlations mentioned above are used to evaluate the performance for wide range of pumping power.

There is not big difference between the pumping power of SPP and that of the other pipe within the results measured in this study. However this result shows the pumping power through only the test section. In the case of considering the total piping system, the SPP can be a better promoter because low flow velocity can be achieved by using SPP.

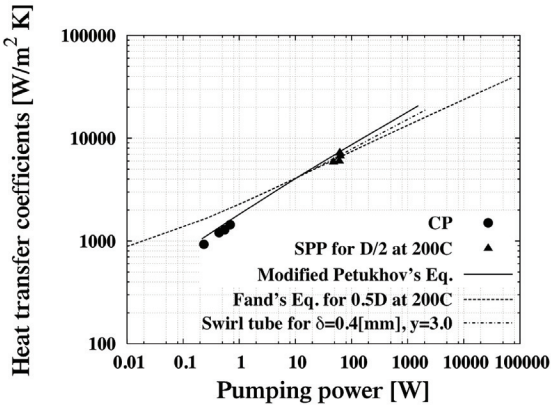

Fig. 9 Results of heat transfer with packed bed

V. CONCLUSIONS

The heat-transfer characteristics in a circular pipe and in sphere-packed pipe have been investigated. The results can be summarized as below.

1. It was confirmed that the thermal decomposition didn't occur in this experiment. Therefore, chemical effect of HTS for heat transfer characteristics was negligible in this study.
2. Heat transfer characteristics of molten salt HTS in a circular pipe were well accorded with some empirical correlations given for some general fluids such as oil, water etc.. The maximum error between the results and the empirical correlations were less than 15% in this experiments.
3. Sphere-packed pipe flow showed greater heat transfer enhancement. The performance of SPP was especially remarkable at low flow velocity under the same flow velocity conditions, and then the performance was about 4 times higher than that of turbulent heat transfer in a circular pipe.
4. Under the same pumping power conditions, the performance of SPP was almost equivalent to or a little lower than that of other promoters. However, in the case of using sphere-packed pipe, high heat flux removal can be achieved with low flow velocity. This indicates that using sphere-packed pipe moderates the MHD pressure drop and electrolysis.

In the present study, pumping power to achieve h = 20000 W/m^{2}K using D/2 sized sphere-packed pipe was a little higher than that of circular pipe flow. In addition, in the case of using D/2 spheres, outer wall temperatures increase locally at the contact spot with spheres. [9] However, in the case of using smaller spheres, it has been reported that the temperatures at the contact spot with spheres are not so high compared with the case of using D/2 spheres, and the heat-transfer performance of sphere-packed pipes can overcome circulate pipe flow, which enables lower pumping power condition. [9]

ACKNOWLEDGMENTS

This work was performed with the support and under the auspices of the NIFS collaborative research program.

REFERENCES

1. A. SAGARA et al., "Innovative Liquid Breeder Blanket Design activities in Japan", *Fusion Sci. Technol.*., **47**, 3, pp. 524-529, (2005).
2. S. TODA et al., "Experimental Research on Molten-Salt Thermofluid Technology Using a High-Temperature Molten-Salt Loop Applied for a Fusion Reactor Flibe Blanket", *Fusion Eng. Des.*, **63-64**, pp. 405-409, (2002)
3. S. CHIBA et al., "Experimental research on Heat Transfer Enhancement for High Prandtl-Number Fluid", *Fusion Sci. Tech.* **47**, 3, pp. 569-573, (2005)
4. V.GNIELINSKI, "New equation for heat and mass transfer in turbulent pipe and channel flow", *Int. Chem. Eng.* **16**, 2, pp. 359-368, (1976)
5. G. K. FILONENKO, Hydraulic Resistance in Pipes, *(in Russian) Teploenergetika* **1**, **No. 4**, pp. 40-44 (1954)
6. R. M. MANGLIK, "Heat Transfer and Pressure Drop Correlations for Twisted-Tape Inserts in Isothermal Tubes: Part II –Transition and Turbulent Flows", *J. Heat Transfer*, **115**, pp. 890-896, (1993)
7. M. VARAHASAMY and R. M. FAND, "Heat transfer by forced convection in pipes packed with porous media whose matrices are composed of spheres", *Int. J. Heat Mass Transfer*, **39**, 18, pp. 3931-3947, (1996)
8. M. OKUMURA et al., "Evaluation of flow structure in packed-bed tube by visualization experiment", *Fusion Sci. Technol.*, **47**, 4, pp. 1089-1093, (2005).
9. K. YUKI et al., "Flow visualization and heat transfer characteristics for sphere-packed pipes", *9th AIAA/ASME Joint Thermophysics and Heat Transfer Conference*, Tracking No. 54264, (2006).

EXPERIMENTAL STUDY OF MHD EFFECTS ON HEAT TRANSFER CHARACTERISTICS ON TURBULENT PIPE FLOW OF FLIBE SIMULANT FLUID

T. Yokomine[1], J. Takeuchi[2], H. Nakaharai[1], S. Satake[3], T. Kunugi[4], N. B. Morley[2], M. A. Abdou[2]

[1]*Kyushu University, 6-1 Kasuga-koen, Kasuga, Fukuoka 816-8580, Japan, yokomine@ence.kyushu-u.ac.jp, nakah@aees.kyushu-u.ac.jp*
[2]*University of California, Los Angeles, 420 Westwood Plaza, 44-114 Eng. IV, Los Angeles, CA 90095, USA, takeuchi@fusion.ucla.edu, morley@fusion.ucla.edu, abdou@fusion.ucla.edu*
[3]*Tokyo University of Science, 2641 Yamazaki, Noda, Chiba 278-8510 Japan, satake@te.noda.tus.ac.jp*
[4]*Kyoto University, Yoshida, Sakyo, Kyoto, 606-8501 Japan, kunugi@nucleng.kyoto-u.ac.jp*

An investigation of MHD effects on Flibe simulant fluid (aqueous potassium hydroxide solution) flows has been conducted under the U.S.-Japan JUPITER-II collaboration program using "FLIHY" pipe flow facility at UCLA. Mean and fluctuating temperature profiles in a conducting wall pipe were measured for turbulent flows using a thermocouples probe at constant heat flux condition. It is suggested that the temperature profiles are characterized by interaction between turbulence production, turbulence suppression due to magnetic field and thermal stratification occurred even under the situation where quite small temperature difference exists in the pipe cross-section.

I. INTRODUCTION

Flibe is one of the possible candidates for coolant/breeding materials for fusion applications. It has very low activation, low tritium solubility, low chemical reactivity, and low electrical conductivity, which relieve the problems associated with MHD pressure drop. In recent research, several design concepts utilizing Flibe have been proposed. Some of the examples are HYLIFE-II,[1] the APEX thick/thin liquid walls[2] and FFHR.[3] Furthermore, Flibe has a crucial difference from liquid metals with respect to the heat transfer characteristic: Flibe is a high Prandtl number fluid. For high Prandtl number fluid, in general, heat transport from a heated wall into the core of the fluid flow is dominated by turbulent motion rather than thermal diffusion. Near-wall flow structures are especially important because thermal boundary layer is much thinner than the momentum boundary layer. In the fusion blanket application of Flibe, there is a severe limitation of temperature window due to its high melting point. The turbulent heat transfer is, therefore, decisive in designing Flibe-based blanket. On the other hand, it is well known that the strong magnetic fields suppress the turbulence even for the flows of low conducting fluids. In the case of occurrence of turbulence suppression, it is concerned that the degradation of the heat transfer performance for high Prandtl number fluid becomes more severe than that for low Prandtl number fluid.

MHD turbulent flows have been extensively studied using liquid metals as working fluids. As far as the MHD effects on the heat transfer characteristics are concerned, Gardner[4] reported that the influence of the transverse magnetic field on the heat transfer was to inhibit the convective mechanism of heat transfer, resulting in reduction of Nusselt number up to 70%. In another paper[5], Gardner summarized his results of turbulent heat transfer calculations using a curve fit equation representing the average Nusselt number as function of Peclet number and Hartmann number (*Ha*). However, the MHD turbulent heat transfer characteristics for high Prandtl number fluids are not well understood. Blum[6] conducted heat transfer experiment using an electrolyte flowing through a rectangular channel over a wide range of Reynolds number (*Re*) including the transition region from laminar to turbulent and presented an empirical correlation for degradation of heat transfer in a turbulent MHD flow as a function of interaction parameter. Since his correlation was constructed from two different experimental data with completely different experimental conditions and parameter range, more reliable data will be required.

From FY2001, JUPITER-II (Japan-US Program for Irradiation Test of Fusion Materials) collaboration is in progress. As one on the important task of this collaborative program, a series of experiments on fluid mechanics and heat transfer of Flibe-simulants have been performed by means of an experimental MHD flow facility called "FLIHY" (FLIbe HYdrodynamics) at UCLA. Turbulent flow field measurements using PIV[7] and heat transfer measurements[8] have so far been carried out without magnetic field to establish the experimental techniques and verify the performance of the facility by comparing an existing experimental results[9] and DNS data[10]. Using aqueous potassium hydroxide as a Flibe simulant, modification of heat transfer characteristic due to the magnetic field has been investigated for turbulent flow by authors[11,12], in which the local temperature profile of fluid parallel to B field and mean Nusselt number have been measured. Nusselt number degradation due to the MHD effect is much larger than both Blums' and Garder's correlations. The objective of the present

investigation is to improve understandings of MHD effects on turbulent heat transfer on high Prandtl number fluid by acquiring experimental data for mean and fluctuation fluid temperature distributions for turbulent flow of electrically conducting fluid in an electrically conducting wall pipe under magnetic fields using high Prandtl number fluid as a Flibe simulant.

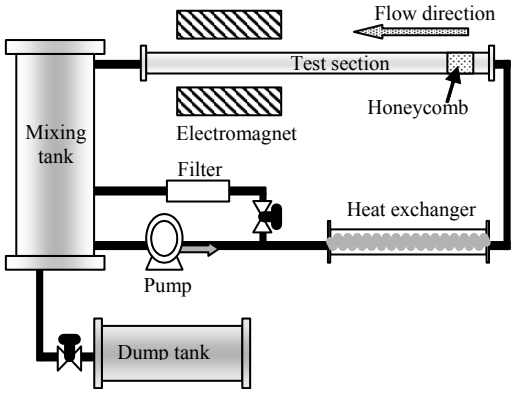

Fig.1 Schematic drawing of the pipe flow facility

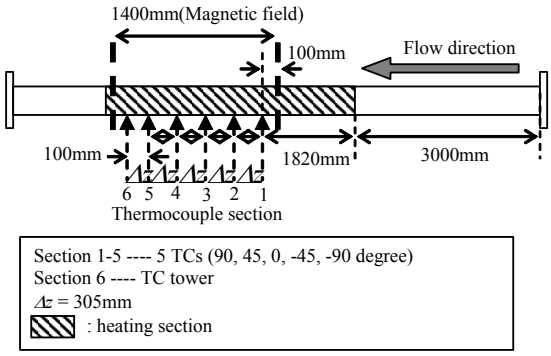

Fig.2 Details of Test Section

II. EXPERIMENTAL SETUP

Figure 1 shows a schematic drawing of the experimental pipe flow loop "FLIHY" in UCLA. The 30%wt aqueous potassium hydroxide (KOH) solution is used as a Flibe-simulant fluid having the same interaction factor as high temperature Flibe. The fluid flow is introduced into a horizontal pipe test section by a centrifugal pump. The inlet and outlet temperature is monitored by thermocouples. The bulk mixing temperature of arbitrary cross section is estimated by linear interpolation from the inlet temperature and the outlet temperature.

The magnet used for the present experiments produces maximum 2.0 Tesla magnetic fields in a narrow gap of the iron core at 3000 A of applied electric current. The test section was placed in the gap which is 1400 mm

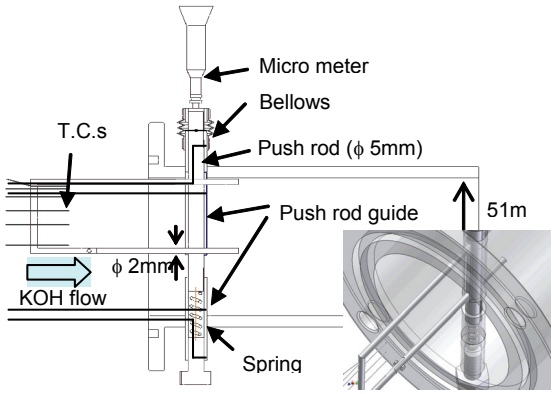

Fig.3 Schematic view of TC probe

TABLE I. Properties of KOH solution

Temperature [℃]	40.0	42.5	44.0
Density[kg/m^3]	1275.6	1274.0	1272.8
Thermal conductivity[W/(m K)]	0.737	0.741	0.743
Viscosity[10^{-3}Pa*s]	1.280	1.231	1.193
Specific Heat Capacity [J/(kg K)]	3010	3014	3018
Electrical conductivity[1/ohm*m]	81.7	84.7	87.1
Prandtl number	5.23	5.01	4.85

length in the streamwise direction, 250 mm in height, and 150 mm in width. The generated B field has uniform horizontal distribution within 5% variation for 1000 mm in the streamwise direction.

Figure 2 gives details of the test section. The test section is an 8000 mm long stainless steel pipe with 50 mm inner diameter. A part of the pipe is heated uniformly by heating tapes. The magnetic field is applied for 1400 mm along the pipe. Twenty-five T-type sheathed thermocouples with 0.5 mm diameter are installed in drilled holes with 1 mm diameter on the outer surface of the pipe and affixed with high thermal conductivity (15W/mK) and high electrical resistivity adhesive at five axial positions and five angles from the horizontal magnetic field. The distance from the pipe inner surface to the thermocouple junctions is 1mm.

The radial temperature distributions of the fluid flow in the pipe are measured by means of thermocouples (TC) probe, which consists of six Inconel-sheathed K-type thermocouples with 0.13 mm diameter. The schematic view of TC probe is shown in Fig.3. The TC probe can be moved by a micrometer with the spatial resolution of 0.02mm. The angle of the TC probe to the B field can be changed freely. Measurable minimum distance from the inner pipe wall is 0.05mm. The 63% response time of these thermocouples is 2ms. It is confirmed that the effect of TC probe on the upstream temperature field and the

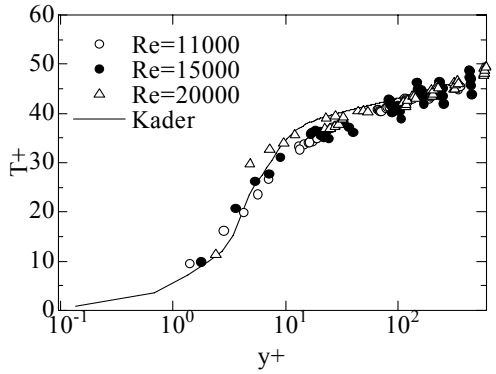

Fig.4 Mean temperature profile without magnetic field.

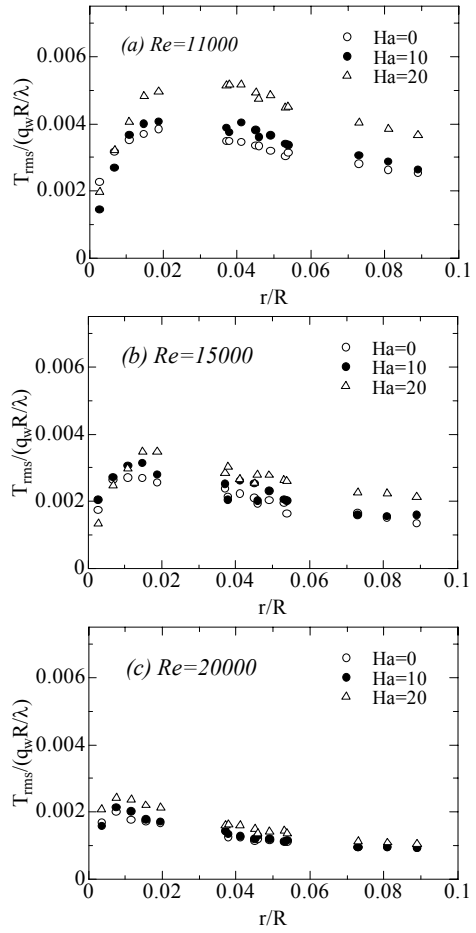

Fig.5 Mean temperature profile under magnetic field (Hartmann wall).

effect of vibration of TC probe on the temperature measurement are both negligible. It is also confirmed that the effect of the magnetic field on the thermocouple measurements is negligible for steady state.

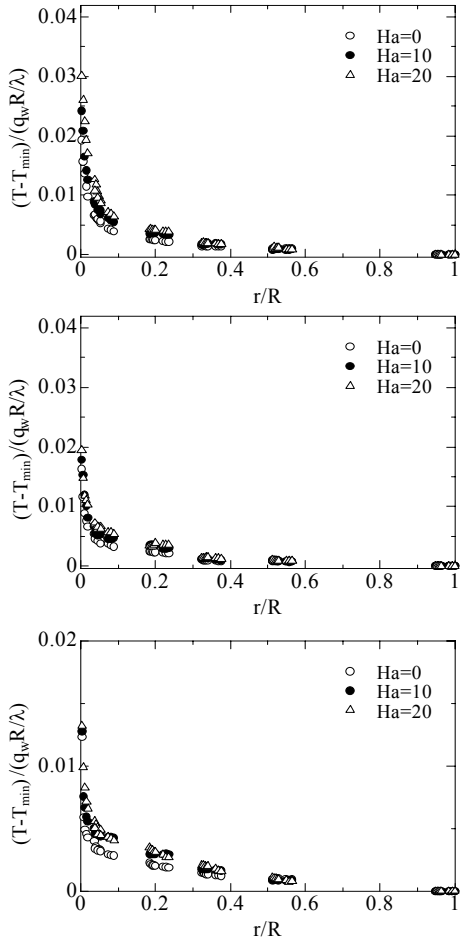

Fig.6 Temperature fluctuation profile under magnetic field (Hartmann wall).

The Reynolds number based on the bulk mean velocity and the pipe diameter is varied from 7400 to 20000 for three Hartmann numbers based on a pipe diameter, *Ha*=0, 10, 20. The bulk mean velocity is calculated from the flow rate which is measured and monitored by vortex flow sensor. Table I shows the property of KOH solution in the present experimental conditions.

III. EXPERIMENTAL RESULTS

Figure 4 shows the mean temperature distributions without magnetic field. The non-dimensional temperature T^+ is defined as below.

$$T^+ = \frac{T_w - T}{T^*}, \quad T^* = \frac{q_w}{\rho c_p u_\tau} \qquad (1)$$

Here T^* is the friction temperature determined by the wall heat flux q_w, fluid density ρ, heat capacity c_p, and the friction velocity u_τ. The wall temperature T_w is measured

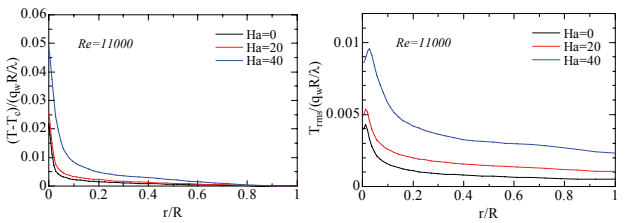

(a) LES results

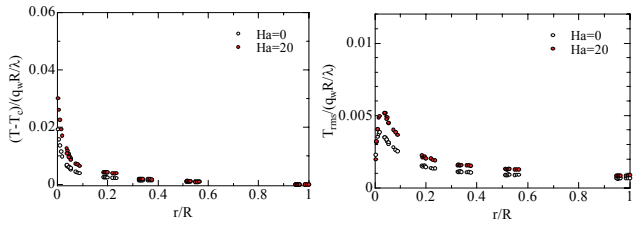

(b) Experimental data

Fig.7 Comparison between experimental data and LES (Hartmann wall).

by thermocouple installed in the pipe wall at the probe location. The abscissa axis y^+ is dimensionless coordinate normal to the wall defined by friction velocity, and R the pipe radius. The equation of temperature profiles in fully developed turbulent boundary layer proposed by Kader[13] is plotted along with the experimental data. In all cases, the temperature profiles without magnetic field give close agreement with Kader's equation because the Kader's equation does not include Reynolds number. From the agreement, it is confirmed that the effect of natural convection is not significant. Indeed, the typical feature of natural convection appeared up to Re=5000. It is confirmed that the temperature field has been fully developed at the TC probe location even under magnetic field Reynolds number flow.

Figure 5 shows the effect of magnetic field on the mean temperature profile. The profiles are measured parallel to B field. The non-dimensional temperature is defined by the difference between measured local temperature and their minimum value. Temperatures near wall increase with increase in *Ha* number, which leads the increase of the temperature gradient (absolute value) in all cases. The heat transfer normal to the wall can be described as following relation, that is, heat transfer due to the molecular diffusion and turbulent heat flux.

$$q = -\lambda \frac{\partial T}{\partial y} + \rho C_p (\overline{u_r' t'}) \qquad (2),$$

where t' and u_r' are fluctuation values of temperature and velocity component in the radial direction, respectively.

When the magnetic field is imposed on the turbulent flow, turbulence intensity decreases (laminarization), so that the turbulent heat flux decreases. It means the heat transfer from the wall to the pipe central region is degraded and the temperature near the wall is raised. It is,

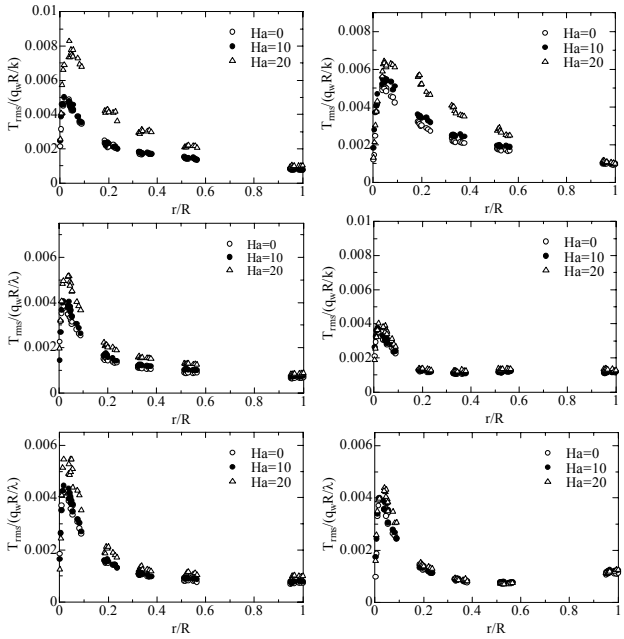

(a) 2026W/m^2 (b) 5315 W/m^2

Fig.8 Directional effect of B field on temperature fluctuation.

therefore, considered that because the decrease of the amount of second term of R.H.S. of eq.(2) induced the increase in the temperature gradient of first term as the result of balance of eq.(2) under the constant wall heat flux. The larger Reynolds number is, the larger the turbulent heat flux is generated and the smaller the suppression of turbulence due to the magnetic field is. Therefore, comparing between different Reynolds numbers, the non-dimensional temperature value is decreased with increasing Reynolds number. It is also found that the region with large temperature gradient spreads with increasing *Ha* number.

The temperature fluctuation profiles parallel to the B field are shown in Fig.6. The r.m.s. (root-mean-square) value of the fluid temperature is normalized by the wall heat flux. In previous study[11], the temperature fluctuation is declined with increase of *Ha* in the entire region in the case that Reynolds number is less than 9000, which is rather straightforward consequence of the turbulence suppression due to the magnetic field. On the other hand, the contradictory result can be seen for high Reynolds number cases; temperature fluctuations with B field become larger than those without B filed in spite that the flow turbulence is suppressed. In order to confirm such an inverted phenomena in respect of the effect of magnetic field on the temperature fluctuation, LES (Large Eddy Simulation) is performed. The detail of numerical procedure can be referred in authors' paper[14]. Comparing between the experimental data and LES result for

Hartmann wall in the case of *Re*=11000 in Fig.7, both of mean temperature profile and temperature fluctuation profile well agree. For LES, it is assumed that the temperature filed can be treated as a passive scalar as well as traditional numerical simulation scheme. Therefore, the effect of magnetic field on the temperature fluctuation can be explained as follows; the increase of mean temperature gradient near the wall exceeds the decrease of turbulent heat flux in $-2\overline{u_r' t'}\left(\partial T/\partial r\right)$ which contributes to the generation of temperature fluctuation $\overline{t'^2}$.

The directional effects of B field on the temperature fluctuation are presented in Fig.8. Reynolds number is 11000 and the wall heat flux is changed in each direction. The temperature difference between top and bottom wall 0.5K, 0.9K and 2.0K correspond to 2026W/m^2 and 5315 W/m^2 of applied wall heat flux, respectively. According to DNS results[10] under isothermal condition, turbulence suppression in vertical direction to B field is not so much as that in Hartmann wall direction. However, present results show that most sensitive to increase of wall heat flux near top wall region, that cannot be explained using abovementioned story on the assumption that the temperature is a passive scalar. It can be deduced that the thermal field in the top region is governed by synergetic interaction between turbulence production, turbulence suppression and thermal stratification because natural convection cannot be observed in all case.

IV. CONCLUDING REMARKS

The mean and fluctuating temperature profiles in the conducting wall pipe were measured for low Reynolds region with variable Hartmann numbers. It is suggested that the shift in the mean temperature profile is a result of interaction between turbulence suppression due to MHD effect and thermal stratification occurred even with the small temperature difference which is not considered in traditional numerical simulation. According to present investigation, it can be concluded that treatment of temperature field as a passive scalar becomes unreasonable assumption under magnetic field.

ACKNOWLEDGMENTS

The authors wish to acknowledge support by the US DOE and the Japanese MEXT via the JUPITER-II Collaboration.

REFERENCES

1. R. W. MOIR, R. L. BIERI and X. M. CHEN et al, "HYLIFE-II: A molten-salt inertial fusion energy power plant design - final report," *Fusion Technol.*, 25, 5, (1994).
2. M. A. ABDOU, THE APEX TEAM and A. YING et al., "On the Exploration of Innovative Concepts for Fusion Chamber Technology," *Fusion Eng Des*, 54, 181 (2001).
3. A. SAGARA, H. YAMANISHI and S. IMAGAWA et al, "Design and Development of the Flibe Blanket for Helical-Type Fusion Reactor FFHR," *Fusion Eng. Des.*, 49-50, 661, (2000).
4. R. A. GARDNER and P. S. LYKOUDIS, Magneto-fluid-mechanic pipe flow in a transverse magnetic field Part 2. Heat transfer, *J. Fluid Mech.* 48, 129 (1971).
5. H. C. JI and R. A. GARDNER, Numerical analysis of turbulent pipe flow in a transverse magnetic field, *Int. J. Heat Mass Transfer*, 40, No.8, 1839 (1997).
6. E. YA. BLUM, Effect of a magnetic field on heat transfer in the turbulent flow of conducting liquid, *High Temperature*, 5, 68 (1967).
7. J. TAKEUCHI, S. SATAKE and N. B. MORLEY et al, "PIV Measurements of Turbulence Statistics and Near-Wall Structure of Fully Developed Pipe Flow at High Reynolds Number," *Proc. 6th International Symposium on Particle Image Velocimetry*, Pasadena, CA, USA, Sept 21-23, (2005).
8. J. TAKEUCHI, S. SATAKE and R. MIRAGHAIE et al, "Study of Heat Transfer Enhancement / Suppression for Molten Salt Flows in a Large Diameter Circular Pipe: Part One - Benchmarking," *Fusion Eng Design*, 81, 601, (2006).
9. J. G. M. EGGELS, F. UNGER and J. WEISS et al, "Fully Developed Turbulent Pipe Flow: A Comparison between Direct Numerical Simulation and Experiment," *J. Fluid Mech.*, 268, 175, (1994).
10. S. SATAKE, T. KUNUGI and R. HIMENO, "High Reynolds Number Computation for Turbulent Heat Transfer in Pipe Flow," In: M. Valero et al, Ed., *Lecture Notes in Computer Science 1940*, Springer-Verlag, Berlin-Heidelberg, (2000).
11. H. NAKAHARAI, J. TAKEUCH and T. YOKOMINE et al. "The Influence of a Magnetic Field on Turbulent Heat Transfer of a High Prandtl Number Fluid," *Experimental Thermal and Fluid Science*, (2007), to be published.
12. T. YOKOMINE, J. TAKEUCH and H. NAKAHARAI et al., "Experimental Investigation of Turbulent Heat Transfer of High Prandtl Number Fluid Flow Under the Strong Magnetic Field," *Fusion Eng. Des.*, (2007), to be published.
13. B. A. KADER, "Temperature and Concentration Profiles in Fully Turbulent Boundary Layers," *Int. J. Heat Mass Transfer*, 24, No.9, 1541 (1981).
14. T. YOKOMINE, S. TAKAMI and H. NAKAHARAI et al., "Turbulent Heat Transfer in a Tube with Twisted Tape Under a Magnetic Field," *Proc. APCOM 2007*, Kyoto, Japan, (2007).

Advances in Development of Vanadium Alloys and MHD Insulator Coatings

T. Muroga[1], J.M. Chen[2], V.M. Chernov[3], K. Fukumoto[4], D.T. Hoelzer[5],
R.J. Kurtz[6], T. Nagasaka[1], B.A. Pint[5], M. Satou[7], A. Suzuki[8] and H. Watanabe[9]

[1]National Institute for Fusion Science, Oroshi, Toki, Gifu 509-5292, Japan
[2]Southwestern Institute of Physics, P.O. Box 432, Chengdu 610041, China
[3] Bochvar Research Institute of Inorganic Materials, P.O. Box 369, Moscow, RF
[4]Graduate School of Nuclear Power and Energy Safety Engineering, University of Fukui, Fukui 910-8507, Japan
[5]Metals and Ceramics Division, Oak Ridge National Laboratory, P.O. Box 2008, Oak Ridge, TN 37831, USA
[6] Pacific Northwest National Laboratory, Richland, WA 99352, USA
[7]Graduate School of Engineering, Tohoku University, Aoba-ku, Sendai 980-8579, Japan
[8]Nuclear Engineering Research Laboratory, University of Tokyo, 2-22 Shirakata-Shirane, Tokai, Naka, Ibaraki 319-1188, Japan
[9]Research Institute for Applied Mechanics, Kyushu University, Kasuga, Fukuoka 816-8580, Japan

Recent progress in the development of low activation vanadium alloys and MHD insulator coatings for Li-self cooled blanket is overviewed. The research progress in vanadium alloys is highlighted by technology of fabricating creep tubes, comparison of thermal creep in vacuum and Li, understanding on impurity transfer between vanadium alloys and Li and its impact on mechanical properties, low dose irradiation effects on weld joints. Major remaining issues of vanadium alloys are thermal and irradiation creep, helium effects on high temperature mechanical properties and radiation effects on low temperature fracture properties.

A new promising candidate of Er_2O_3, which showed good compatibility with Li, was identified for MHD insulator coating on vanadium alloys. The coating technology has made significant progresses for the new candidate material. Recent efforts are being focused on multi-layer coating and in-situ coating. Tests in flowing lithium conditions with temperature gradient are necessary for quantitative examination of the performance.

1. Introduction

Vanadium alloys are known as attractive blanket structural materials for fusion power systems because of their low induced activation characteristics, high temperature strength and high thermal stress factors [1,2]. Recent efforts were focused on developing V-4Cr-4Ti alloy as a reference composition. Many of the critical issues of the vanadium alloys have been resolved by the recent researches. As a result, the feasibility of vanadium alloys as fusion blanket structural materials has been largely enhanced.

The leading blanket concept using vanadium alloys as structural materials is the Li-self cooled system. One of the critical materials issues for the Li-self cooled with vanadium alloy structure is the development of insulator coating for mitigating Magneto-Hydrodynamic (MHD) pressure drop [3,4]. Significant progress has been made in the MHD coating development in recent years including identification of new candidate materials, improvement of the coating technology on vanadium alloy substrate, demonstration of long-term stability in Li and so on.

This paper highlights the recent progress in vanadium alloys and MHD coatings for use in Li-self cooled blanket with vanadium alloy structure. Remaining critical issues are also discussed.

2. Recent progress in the development of vanadium alloys

2.1. Fabrication technology

In recent years, several large heats of V-4Cr-4Ti were produced in the US [5], Japan [6] and Russia [7], followed by fabrication of products such as thin and thick plates, rods and wires, tubes and weld joints [2,8]. Through these efforts, manufacturing technology for vanadium alloys were largely advanced. The examination on microstructural changes during the processing of V-4Cr-4Ti ingots into various products showed that optimization of size and distribution of Ti-CON precipitates is crucial for good mechanical properties of the V-4Cr-4Ti products [9]. Plates, sheets, rods and wires were fabricated minimizing the impurity pickup and maintaining grain and precipitate sizes.

Recent highlight of this area is the effort to fabricate pressurized creep tubes in Japan [10] and the US [11]. Thin pipes, including those for pressurized creep tube specimens, were successfully fabricated maintaining the impurity level, fine grain size and straight band distribution of precipitates by maintaining a constant reduction ratio between the intermediate heat treatments [12]. Through the efforts for fabricating the creep tubes including plugging of end caps, the fine-scale EB welding technology was enhanced [10]. In the US, the increase in the oxygen level during the commercial scale cold

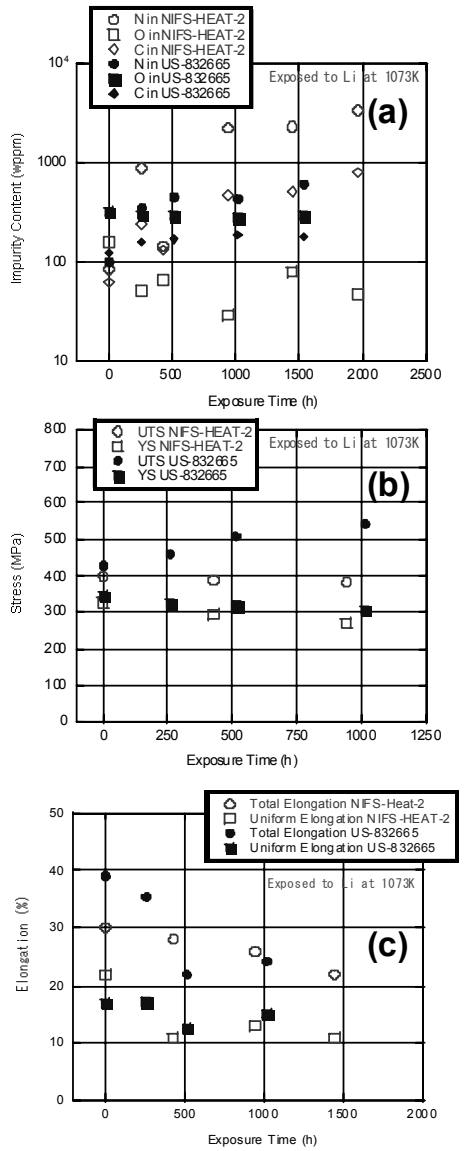

Figure 1 (a) Impurity contents, (b) tensile stress and (c) elongation of US (US-832665) and Japanese (NIFS-HEAT-2) reference V-4Cr-4Ti alloys as a function of exposure time to molten Li at 1073K [18,19].

drawing to fabricate thin-walled tubing of V-4Cr-4Ti has been investigated as a function of the vacuum level in the intermediate annealing [11].

Successful joining of V-4Cr-4Ti by Gus Tungsten Arc (GTA) [13] and laser welding [14] methods was demonstrated without necessity of the Post Weld Heat Treatment (PWHT). A low pressure plasma-spraying method was applied for coating W on V-4Cr-4Ti for the use on the plasma-facing surfaces [15].

2.2 Interactions with Li environment

The properties of vanadium alloys may be changed in Li environment via transfer of impurities across the interface between Li and the vanadium alloys. This might not be any concern if all inner surface of the alloy is covered with insulating MHD ceramic coating. However, it is necessary to evaluate this effect to analyze data such as reactor irradiation or thermal creep in Li environment. Moreover, an idea to cover the MHD coating again with a thin vanadium or vanadium alloy layer was presented, for the purpose of preventing liquid lithium from intruding into the cracks in the ceramics coating. For this case the interaction of vanadium alloys with liquid lithium attracts attention.

It is known that the corrosion of vanadium alloys in liquid lithium is highly dependent on the alloy composition and lithium chemistry [16,17]. Recent thermal creep experiments, to be shown in the following section, provided opportunities to examine the change in chemistry and properties of V-4Cr-4Ti alloys by exposing coupon specimens to Li together with the creep tubes. Fig. 1 shows impurity contents, tensile stress and elongation of US (US-832665) and Japanese (NIFS-HEAT-2) heats of V-4Cr-4Ti as a function of exposure time to Li at 1073K [18,19]. Remarkable difference in the rate of N enrichment and O depletion is seen between the two alloys. However, the total and the uniform elongation of the both alloys seem to saturate around 20% and 10%, respectively. The difference in the impurity transfer of the two alloys may be attributed to the difference in the sample thickness, 3 mm for US-832665 and 0.25 mm for NIFS-HEAT-2. However, precipitate structure or initial impurity distribution could also be factors. Both alloys

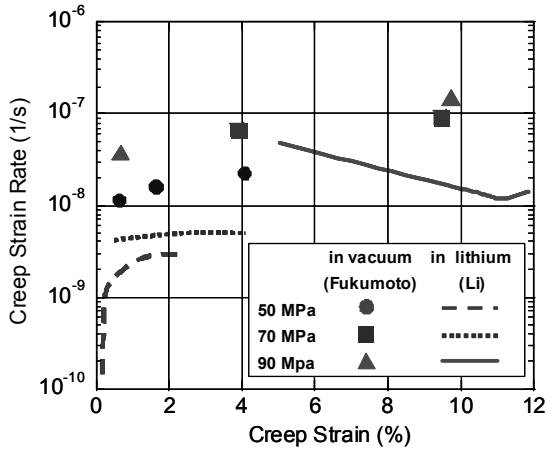

Figure 2 Comparison of creep deformation in vacuum [22] and lithium [18] using the same batch of pressurized creep tubes fabricated with NIFS-HEAT-2 (V-4Cr-4Ti).

were heat treated at 1000C, where precipitation was maximized for US-832665 but significant fraction of the fine precipitates (mostly Ti-O) was dissolved in NIFS-HEAT-2 [20]. The increased level of solid solution oxygen is considered to result in the enhanced depletion of oxygen in NIFS-HEAT-2 by exposure to Li.

Compositional dependence of the corrosion of V-xCr-yTi in Li was examined previously [16,17]. A new effort including optimization of the Li removal technique after the exposure showed that V-(4-7)Cr-4Ti had a good performance [21].

2.3 Thermal creep

The progress in technology for manufacturing high quality V-4Cr-4Ti creep tubes enhanced research on thermal creep performance of V-4Cr-4Ti alloys, including the effects of heat-to-heat variation, thermal and mechanical treatments, uni-axial (tensile) and bi-axial (creep tube) tests, and the test environments. Previous data on thermal creep tests in vacuum was summarized in ref. [1]. A new apparatus for testing bi-axial creep in Li provided opportunities for examining the creep deformation in vacuum and in Li [18]. However, the correlation of creep data is subject to the alloy heat and manufacturing processes as well as test methods and environments. Fig. 2 shows the comparison of the NIFS-HEAT-2 for creep stain rate vs. creep strain tested in vacuum and Li environments, for the same batch of NIFS-HEAT-2 creep tubes [18,22]. The figure clearly shows reduced strain rate in Li environments. The increased resistance to creep deformation in Li may be attributed to increased level of N. However, as shown in Fig. 1, NIFS-HEAT-2 samples eventually softened by exposure to Li. Further investigation is necessary for understanding the environmental effects on impurity redistribution and creep performance. A possible factor could be the surface hardening after exposure to Li [19], which is thought to be induced by N pick-up and could influence the creep processes.

Microstructural observations of the creep tube specimens tested at 1123K showed free dislocations and dislocation cell at 100MPa and in 150MPa, respectively [23]. This change of dislocation structure is pointed out as causing the change in power law creep behavior [24].Another aspect of V alloy metallurgy that has received increased attention in recent years is the interaction of V with interstitial impurities such as C, O and N. Several recent studies [20-22] have shown that most precipitates result from reaction of V or solute atoms with these impurities. These precipitates impede dislocation motion increasing the strength of the alloy. Ti lowers the mobility of the interstitials and reacts to form precipitates at > ~600°C under thermal annealing and > ~300°C under neutron irradiation. Globular Ti- (CON) precipitates appear above ~1000°C. The solvus temperature for globular precipitates is between 1200°C and 1300°C. Following dissolution the interstitial content can be redistributed into a high number density of nano-size {100} plates by controlled precipitation. The precipitate crystal structure is FCC for both {100} plate and globular morphologies. The interstitial concentration varies considerably for {100} plate type precipitates. A conclusion of these investigations is that a better understanding of precipitate nucleation and growth is needed along with an increased knowledge of the range of interstitial solubility. To gain a better understanding of the effects of interstitial impurities on irradiated properties a special set of V alloys [23] with carefully controlled levels of C, O and N has been included in an upcoming JUPITER irradiation experiment.

2.4 Diffusion, retention and desorption of hydrogen and its isotopes

The behavior of hydrogen and its isotopes in vanadium alloys is a concern from tritium retention in the first wall and inventory in blanket. Deuterium ion implantation followed by thermal desorption showed that deuterium retention of V-4Cr-4Ti is much higher than and comparable to those of other PFC candidate materials (graphite and tungsten) at 380K and 773K, respectively [25]. A hydrogen absorption study showed that the rate of absorption is highly influenced by prior heat treatment inducing Ti surface segregation. The formation of Ti oxide on the surface suppressed significantly the absorption rate [26].

Recent progress in detecting tritium by mean of Imaging Plate (IP) enhanced the understanding on the tritium behavior in vanadium alloys. The imaging of tritium-rich area with IP showed that tritium is preferentially absorbed in Ti-rich precipitates[27]. The tritium distribution profile of a specimen after diffusion annealing measured with IP showed the tritium diffusion coefficient of V-4Cr-4Ti [28].

2.5. Irradiation effects

Neutron irradiation can significantly influence the performance of vanadium alloys during operation in fusion reactors. Void swelling is known to be small if alloyed with Ti. Among the feasibility issues of radiation effects of vanadium alloys are loss of ductility at lower temperature, embrittlement enhanced by transmutant helium at high temperature, and irradiation creep at intermediate to high temperature.

The loss of uniform elongation of vanadium alloys irradiated at relatively low temperature (<673K) was accompanied by dislocation channel microstructure, implying flow localization during the deformation [29]. Although the mechanism of the flow localization is not well understood, it is inferred that interaction of

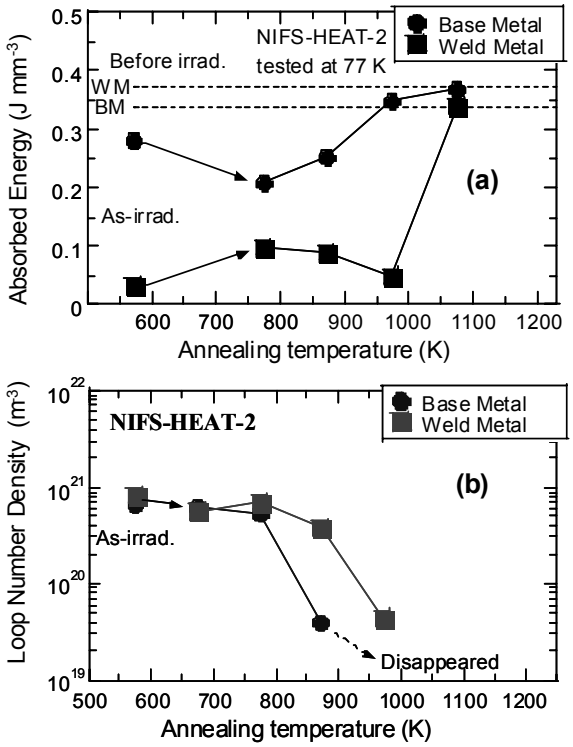

Figure 3 (a) absorbed energy in the impact test at 77K and (b) number density of dislocation loops, for NIFS-HEAT-2 after neutron irradiation to 0.08 dpa and post-irradiation annealing for 1hr at each temperature [32]. DBTT of the as-irradiated weld metal was 113K.

dislocations with high densities of fine radiation-induced defect clusters is responsible. The defects were commonly observed with black-dots by TEM in V-4Cr-4Ti irradiated with neutrons below 673K. Recent elemental analysis of the clusters by Atom Probe Elemental Analysis showed that they are enriched with Ti, O and TiO [30].

Helium embrittlement is a critical issue which may determine the upper temperature limit for vanadium alloys. The past experimental evaluation of the helium effects varied from weak to very strong [1]. Since the technique to generate helium and displacement damage simultaneously is limited, recent progress in experimental evaluation of the helium effect is also limited. Clearly a 14 MeV neutron source is essential to evaluate the helium effects in fusion conditions.

The irradiation creep data are also very sparse. The data are limited to relatively low temperature and low dose. However, irradiation creep tests are making progress partly because of the progress in fabricating high quality pressurized creep tube specimens with reduced impurity levels. The data on irradiation creep at high temperature will be available from HFIR and JOYO.

Only low fluence irradiation data are available on the weld joint. It should be noted that the welding results in resolution of the most precipitates enhancing the level of solid solution impurities. An enhanced defect cluster density and heterogeneous precipitate distribution in the weld metals by irradiation were reported [31]. The effects of post-irradiation annealing are shown in Fig. 3 [32]. Post-irradiation annealing experiment showed a higher recovery temperature of the absorbed energy in the impact tests for the weld metal than that for the base metal. Microstructural observation during post-irradiation annealing showed that the dislocation loops formed by the irradiation were stable to higher temperature in the weld metal, which can be attributed to the increased decoration of impurities to the loops in the weld metal

The results show that the normalized secondary creep rate is power-law dependent on stress with a stress exponent of ~4 at normalized stresses greater than 0.002. The activation energy for creep between 700 and 800°C is about 300 kJ/mole, which is similar to the activation energy for self diffusion in pure V suggesting that in this regime of temperature and stress the predominant creep mechanism appears to be climb-assisted dislocation motion. Limited data at the same temperatures but lower stresses indicates that the creep mechanism may change since the stress exponent appears to decrease to about unity, Figure 1.

2.6 Improvement of alloy properties

Generally larger windows for operation temperature of structural materials allow us to design compact blanket systems with higher efficiency. Therefore, efforts have been made to develop advanced vanadium alloys which have larger operation temperature windows, especially for potential use at higher temperature.

Increase in Cr level in V-Cr-Ti is known to increase high temperature strength, bartering with loss of ductility at low temperature. Recent detailed survey in V-xCr-4Ti alloys showed that the strength at high temperature increases with small change in the DBTT with the Cr level to ~7%[33].

Addition of Y to V-4Cr-4Ti has been investigated for potential reduction of oxygen level in matrix and resulting increase in radiation resistance. Systematic fabrication of V-4Cr-4Ti-xY followed by impact tests showed optimum level of 0.15% for Y [34,35]. Based on the results, a 15 kg ingot of V-4Cr-4Ti-1.5Y was made by levitation melting followed by characterizations [36]

Mechanically alloyed V-Y alloys were fabricated and their irradiation response was examined. Fine grain and oxide dispersion increased high temperature strength and inhibited formation of interstitial loops in the matrix by neutron irradiation, because of the enhanced defect sinks [37]. Recent results showed that further addition of Ti on V-Y enhance the strength [38].

Other efforts to explore new alloying elements include W addition for suppressing hydrogen

embrittlement susceptibility [39], and Zr addition for enhancing impurity gettering by co-precipitation [40]. Also carried out is the exploration of thermal and mechanical treatment conditions for forming high density of fine precipitates [41] or oxides [42] for the purpose of enhancing high temperature strength of the conventional V-4Cr-4Ti alloys

3. MHD coating development

Previously, CaO was regarded as the leading candidate of MHD coating material. However, the following examination showed that it has a problem in the stability in liquid lithium at high temperature [43]. Thus efforts in recent years were focused on identifying new candidate materials which withstand corrosion by Li at high temperature and developing coating technology of the new candidates.

By the recent Li immersion tests of bulk specimens, promising candidate ceramics of Er_2O_3 and Y_2O_3, which were stable to 1073K in liquid lithium, were identified [3]. The feasibility of fabricating Er_2O_3 and Y_2O_3 coatings on V-4Cr-4Ti was demonstrated by EB-PVD [3], Arc Source Plasma Deposition [44] and RF sputtering [45]. Especially, Er_2O_3 fabricated with Arc Source Plasma Deposition showed promising results as shown in Fig.3. By deposition on a substrate at higher temperature, high crystalline Er_2O_3 coating was produced, which were shown to be stable in Li to 1000hr at 973K as shown in Fig. 4 [46].

Recent numerical estimates showed that tolerable crack density of the coating could be very low [47]. The result encouraged the development of double-layer coatings and revisiting of the in-situ healing concept. Double layers with V on Er_2O_3 produced by EB-PVD showed satisfactory resistivity in molten Li to 873K [48]. The composition of the alloys for the surface layer is being investigated for maximizing the compatibility with Li as is introduced in Sec. 2.2.

The in-situ coating method is a quite attractive technology because it will enable coating on complex surfaces after fabrication of components and have the potential to heal cracks in the coating without disassembling the component. In addition to the physical deposition methods, in-situ coating with Er_2O_3 on V-4Cr-4Ti is being developed [49]. In this process, a Er_2O_3 thin insulating layer is formed on V-4Cr-4Ti during its exposure to liquid lithium by reaction of pre-charged oxygen in the vanadium alloy substrate and pre-doped Er in Li. Also demonstrated was the self-healing capability. The results showed significantly higher stability of the coating compared with the CaO in-situ coating [50]. In the optimum condition for oxygen pre-charging to V-4Cr-4Ti a net-structure of Ti-O precipitates oriented to <100> directions was formed, which is the storage of oxygen reserved for formation of the oxide coating. The

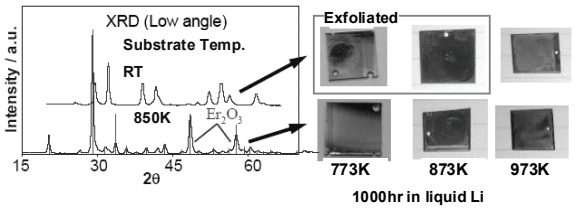

Figure 4 Change of Er_2O_3 coating on V-4Cr-4Ti by exposure to Li at 773, 873 and 973K for 1000 hr. The coating was made using Arc Source Plasma Deposition method with substrate temperature at RT and 850K. Crystalline structure of Er_2O_3 was observed only in the case of the high substrate temperature. Remarkable change was not observed in the coating at high substrate temperature after exposure to Li [44,46].

mechanisms and kinetics for the formation of the structure were analyzed [51].

The degradation of electrical resistivity of the coating during irradiation can potentially deteriorate performance of the coating as the insulator. Radiation-Induced Conductivity of the candidate bulk ceramics and coated samples of Er_2O_3, Y_2O_3 and $CaZrO_3$ on V-4Cr-4Ti were carried out with D-T neutrons[52], fission neutrons[53] at ambient temperature and with χ-rays at high temperature [54], and showed that the change in the resistivity is not an issue for application to fusion blanket.

Most of the recent corrosion characterizations of the coatings have been made by static immersion tests. The static tests are valuable for identifying potentiality of the candidates but not sufficient for verifying their function in the blanket condition. For example, erosion rate of the candidate coating ceramics in liquid lithium could be significantly different between in static and flowing conditions. Thus experiments in flowing Li with temperature gradient and impurity control are essential for characterizing the performance of MHD coating in fusion blanket conditions.

4. Remaining critical issues and future directions

As a result of the recent progress in developing vanadium alloys, limited number of critical issues is remaining for the future researches. As to the available data, thermal and irradiation creep, helium effects on high temperature mechanical properties and radiation effects on fracture properties are insufficient. Especially for the helium effects, conclusive evaluation of the irradiation properties is possible only with the use of 14MeV neutrons, motivating the construction of the 14MeV neutron source.

The thermal creep tests in various conditions suggest that the current reference V-4Cr-4Ti alloys could allow the maximum operation temperature of around 973K [1]. Potential ways to improve the creep performance of V-

4Cr-4Ti for increasing the operation temperature would include increase in Cr level to a level not deteriorating manufacturing ability and low temperature ductility, applying thermal and mechanical treatments by which high density of fine precipitates are formed and addition of new elements. Controlling impurity (C, O, N) levels and optimizing precipitate (Ti-CON) size and distribution are crucial for the mechanical properties of the alloy products and weldments in low and high temperatures. Systematic studies to optimize the microstructure and mechanical properties are necessary for enhancing the performance of vanadium alloys.

The tritium inventory in vanadium alloy structures in the blanket is thought to be a minor issue for Li-self cooled blanket because of low tritium partial pressure in Li. However, this might need to be re-examined taking irradiation effects and impact of potential alloying elements such as Y into account.

Development of MHD insulator coating is a critical feasibility issue for Li-self cooled blanket. Although recent progress in MHD coating is large, further intensive efforts are necessary for validating the performance of the current leading candidates, multi-layer coatings and in-situ coating concepts. Tests in flowing lithium conditions with temperature gradient are necessary for quantitative examination of the performance.

5. Summary

Vanadium alloys are attractive candidate structural materials for Li-self cooled breeding blankets of fusion reactors. The efforts of developing vanadium alloys have been focused on V-4Cr-4Ti alloys as reference materials. Recent researches have successfully resolved many of the critical issues and enhanced feasibility of the alloys as fusion blanket structural materials. Research progress is highlighted by technology of fabricating creep tubes, joints and W-coating, comparison of thermal creep in vacuum and Li environments, understanding on impurity transfer between vanadium alloys and Li and its impact on mechanical properties, behavior of hydrogen and hydrogen isotopes, and exploration for advanced vanadium alloys for enhancing further high temperature strength, low temperature ductility or radiation resistance. Major remaining issues of vanadium alloys are thermal and irradiation creep, helium effects on high temperature mechanical properties and radiation effects on low temperature fracture properties. For conclusive characterization of the irradiation properties, use of IFMIF is essential as well as continuous use of fission reactors.

A new promising candidate of Er2O3 was identified for MHD insulator coating on vanadium alloys, which showed good compatibility with Li. The coating technology has been progressed for the new candidate. Verification of the performance of the candidates, multi-layer coatings with a metallic overlayer, and in-situ coating have been made by static immersion tests. Tests in flowing Li conditions with temperature gradient are necessary for quantitative examination of the performance.

Acknowledgments

This research was partly supported by NIFS-Budget Code NIFS06UCFF003, Japan-USA Fusion Cooperation Program (JUPITER-II), Japan-China Core University Program and the U.S. Department of Energy, Office of Fusion Energy Sciences, under contract DE-AC06-76RLO1830 and DE-AC05-00OR22725.

References

[1] R.J. Kurtz, K. Abe, V.M. Chernov, D.T. Hoelzer, H. Matsui, T. Muroga and G.R Odette, J. Nucl. Mater. 329-333 (2004) 47-55.
[2] T. Muroga, T. Nagasaka, K. Abe, V.M. Chernov, H. Matsui, D.L. Smith, Z.-Y. Xu, S.J. Zinkle, J. Nucl. Mater. 307-311 (2002) 547-554.
[3] B. Pint, P.F. Tortorelli, A. Jankowski, J. Hayes, T. Muroga, A. Suzuki, O.I. Yeliseyeva, V. M. Chernov, J. Nucl . Mater. 329-333 (2004) 119-124.
[4] D.L.Smith, J. Konys and T. Muroga, J. Nucl. Mater. 307-311 (2002) 1314-1322.
[5] W.R. Johnson, J.P. Smith, J. Nucl. Mater. 256-263 (1998) 1425-1429.
[6] T. Muroga, T. Nagasaka, A. Iiyoshi, A. Kawabata, S. Sakurai, M. Sakata, J. Nucl. Mater. 283-287 (2000) 711-715.
[7] M.M. Potapenko et al. Proc. IEA/JUPITER-II Workshop on Critical Issues of Vanadium Alloy Development for Fusion Reactor Applications, Dec 15-16, 2003, NIFS, Japan
[8] T. Nagasaka, T. Muroga, M. Imamura, S. Tomiyama, M. Sakata, Fusion Technology, 39 (2001) 659-663.
[9] T. Nagasaka, N.J. Heo, T. Muroga and M. Imamura, Fusion Engineering and Design, 61-62 (2002) 757-762.
[10] K. Fukumoto, H. Matsui, M. Narui, T. Nagasaka and T. Muroga, J. Nucl. Mater. 335 (2004) 103-107.
[11] A. Rowcliffe, D. Hoelzer, C. Young and R. Kurtz, "Oxidation behavior of a V-4Cr-4Ti alloy during the commercial processing of thin-wall tubing" presented at ICFRM-12.
[12] T. Nagasaka, T. Muroga and T. Iikubo, Fusion Science and Technology, 44 (2003) 465-469.
[13] T. Nagasaka, M.L. Grossbeck, T. Muroga and J.F. King, Fusion Technology 39 (2001) 664-668.
[14] N.J. Heo, T. Nagasaka, T. Muroga, A. Nishimura, K. Shinozaki and N. Takeshita, Fusion Engineering and Design, 61-62 (2002) 749-755.
[15] T. Nagasaka, T. Muroga, N. Noda, M. Kawamura, H. Ise and H. Kurishita, Fusion Science and Technology, 47 (2005) 876-880.
[16] V.A. Evtikhin, I.E. Lyublinski and A.V. Vertkov, J. Nucl. Mater. 258-263 (1998) 1487-1491.

[17] O.I. Yeliseyeva, V.N. Fedirko, V.M. Chernov and L.P. Zavialsky, J. Nucl. Mater. 283-287 (2000) 1282-1286.
[18] M. Li, T. Nagasaka, D. Hoelzer, M. Grossbeck, S. Zinkle, T. Muroga, K. Fukumoto, H. Matsui and M. Narui, "Biaxial thermal creep of V-4Cr-4Ti at 700 and 800□C in a liquid lithium environment" presented at ICFRM-12.
[19] T. Nagasaka, T. Muroga, M. Li, D.T. Hoelzer, S.J. Zinkle, M.L. Grossbeck and H. Masui, Fusion Engineering and Design, to be published.
[20] N. J. Heo, T. Nagasaka and T. Muroga, J. of Nucl. Mater. 325 (2004) 53-60.
[21] M. Fujiwara, B. Pint, T. Muroga, M. Satou, A. Hasegawa and K. Abe, "Influence of Cr and Ti content on compatibility of V-Cr-Ti type alloys" presented at ICFRM-12.
[22] K. Fukumoto, T. Nagasaka, T. Muroga, N. Nita, H. Matsui, "Creep mechanism of V-4Cr-4Ti alloys after thermal creep in a vacuum" presented at ICFRM-12
[23] K. Fukumoto, M. Sugiyama and H. Matsui, "Inner structure of dislocation channels in neutron-irradiated V-Cr-Ti alloys" presented at ICFRM-12.
[24] D.S. Gelles and R. J. Kurtz, "Creep of V-4Cr-4Ti pressurized tube specimens" presented at ICFRM-12.
[25] Y. Yamauchi, T. Yamada, Y. Hirohata, T. Hino and T. Muroga, J. Nucl. Mater. 329-333 (2004) 397-400.
[26]R. Hayakawa, Y. Hatano, K. Fukumoto, H. Matsui, K. Watanabe, J. Nucl. Mater. 329-333 (2004) 411-415.
[27] Y. Hatano, R. Hayakawa, L.Wan, M. Matsuyama, T. Nagasaka, T. Muroga, Y. Nakamura and K. Watanabe, "Dissolution of hydrogen isotopes into V-4Cr-4Ti alloy" presented at ICFRM-12.
[28] K. Hashizume, J. Matsuda, T. Otsuka, T. Tanabe, Y. Hatano, Y. Nakamura, T. Nagasaka and T. Muroga, "Diffusional behavior of tritium in V-4Ti-4Cr alloy" presented at ICFRM-12.
[29] P.M. Rice and S.J. Zinkle, J. Nucl. Mater. 258-263 (1998) 1414-1418.
[30] N. Nita, Y. Anma, H. Matsui, T. Ohkubo and K. Hono, "Irradiation induced precipitates in vanadium alloys studied by atom probe microanalysis" presented at ICFRM-12.
[31] H. Watanabe, K. Yamasaki, A. Higashida, N. Yoshida, T. Nagasaka and T. Muroga, "The microstructure of laser welded V-4Cr-4Ti alloy after neutron irradiation" presented at ICFRM-12.
[32] T. Nagasaka, T. Muroga, H. Watanabe, K. Yamasaki, N.J. Heo, K. Shinozaki and M. Narui, Materials Transactions 46 (2005) 498-502.
[33] K. Sakai, M. Satou, M. Fujiwara, K. Takahashi, A. Hasegawa, K. Abe, J. Nucl. Mater. 329-333 (2004) 457-461.
[34] T. Hino, M. Satou, M. Fujiwara, T. Nagasaka and K. Abe, "Effects of Si, Al and Y addition on neutron irradiation behavior of V-Cr-Ti type alloys", presented at ICFRM-12.
[35] T. Chuto, M. Satou, A. Hasegawa, K. Abe, T. Muroga, N.Yamamoto, J. Nucl. Mater. 326 (2004) 1-8.
[36] T. Nagasaka, T. Hino, T. Muroga, K. Abe, T. Chuto and T. Iikubo, "Impurity behavior in V-4Cr-4Ti-Y alloys produced by levitation melting" presented at ICFRM-12.
[37] S. Kobayashi, Y. Tsuruoka, K. Nakai,and H. Kurishita, J. Nucl. Mater. 329-333 (2004) 447-451.
[38] H. Kurishita, S. Oda, S. Kobayashi, K. Nakai, T. Kuwabara, M. Hasegawa and H. Matsui, "Effects of 2.1%Ti addition on tensile properties and microstructures of an ultra-fine grained V-1.7%Y alloy with nano-sized Y2O3 and YN" presented at ICFRM-12.
[39] J.M. Chen, T. Muroga, S.Y. Qiu, T. Nagasaka, W.G. Huang, M.J. Tu, Y. Chen, Y. Xu, Z.Y. Xu, J. Nucl. Mater. 329-333 (2004) 401-405.
[40] D. T. Hoelzer, A. F. Rowcliffe, and M. Li, Fusion Materials Volume 38, Semiannual Progress Report for Period Ending June 30, 2005, DOE/ER-0313/38, June 30, 2005, 1-10.
[41] T. Muroga, T. Nagasaka, A. Nishimura and J.M. Chen, Materials Science Forum 475-479 (2005) 1449-1454.
[42] A.N. Tyumentsev, V.M. Chernov, A.D. Korotaev, S.V. Ovchinnikov, Yu.P. Pinzhin, M.M. Potapenko and A.K. Shikov, "Effect of internal oxidation on microstructure and mechanical properties of vanadium alloys" presented at ICFRM-12.
[43] B.A. Pint, L.D. Chitwood and J.R. Di Stefano, J. Nucl. Mater. 289 (2001) 52-56.
[44] F. Koch, R. Brill, H. Maier, D. Levchuk, A. Suzuki, T. Muroga and H. Bolt, J. Nucl . Mater. 329-333 (2004) 1403-1407.
[45] A. Sawada, A. Suzuki, H. Maier, F. Koch, T. Terai and T. Muroga, Fusion Engineering and Design, 75-79 (2005) 737-740
[46] A. Sawada, B. Pint, A. Suzuki, F. Koch, H. Maier, T. Terai and T. Muroga, "Long-term stability of erbium oxide coatings" presented at ICFRM-12.
[47] H. Hashizume, S.Chiba, M.Satake, A.Sagara,and T. Muroga, Fusion Engineering and Design, to be published.
[48] B. Pint, J. Moser, A. Jankowski and J. Hayes, "Compatibility of multi-layer electrical insulating coatings for the vanadium-lithium blanket" presented at ICFRM-12
[49] Z. Yao, A. Suzuki, T. Muroga and K. Katahira, J. Nucl . Mater. 329-333 (2004) 1414-1418.
[50] Z. Yao, A. Suzuki, T. Muroga, K. Katahira, Fusion Engineering and Design 75-79 (2005) 1015-1019
[51] O.I. Yeliseyeva, T. Muroga, A. Suzuki, Z. Yao and A. Lukyanenko, "Charging of V-4Cr-4Ti by oxygen to create in-situ insulator coating" presented at ICFRM-12.
[52] T. Tanaka, A. Suzuki, T. Muroga, F. Sato, T. Iida and T. Nishitani, J. of Nucl. Mater., 329-333 (2004) 1434-1437.

[53] T. Tanaka, T. Shikama, M. Narui, B. Tsuchiya, A. Suzuki and T. Muroga, Fusion Engineering and Design 75-79 (2005) 933-937
[54] T. Tanaka, R. Nagayasu, A. Suzuki, A. Sawada, T. Muroga, F. Sato, T. Ikeda and T. Iida, “Electrical insulating property of ceramic coating materials in radiation and high-temperature environment” presented at ICFRM-12.

Recent progress in the development of electrically insulating coatings for a liquid lithium blanket

Bruce A. Pint [a], P.F. Tortorelli [a], A. Jankowski [b], J. Hayes [b],
T. Muroga [c], A. Suzuki [c], O.I. Yeliseyeva [d], V.M. Chernov [e]
[a] Metals and Ceramics Division, Oak Ridge National Laboratory, P.O. Box 2008, 1 Bethel Valley Road, Oak Ridge, TN 37831-6156, USA
[b] Chemistry and Materials Science, Lawrence Livermore National Laboratory, P.O. Box 808, L-352, Livermore, CA 94551, USA
[c] Fusion Engineering Research Center, National Institute for Fusion Science, 322-6 Oroshi, Toki, Gifu 509-5292, Japan
d G.V. Karpenko Physico-Mechanical Institute NASU, L'viv 79601, Ukraine
[e] SSC-RF A.A. Bochvar Institute of Inorganic Materials, 123060, P.O. Box 369, Moscow, Russia

Electrically insulating coatings on the first wall of magnetic confinement reactors are essential to reduce the magnetohydrodynamic (MHD) force that would otherwise inhibit the flow of the lithium coolant. There are very few candidate materials because Li dissolves most oxides and many carbides and nitrides do not have sufficient electrical resistivity for this application. Based on thermodynamic considerations and testing of bulk ceramics, the most promising materials are Y_2O_3, Er_2O_3 and AlN. Coatings of these materials are being fabricated by a variety of processing techniques and their resistivity and microstructure characterized. Electrical resistivity results from Y_2O_3 coatings as-deposited and after exposure to Li are presented. Self-healing and in situ coatings are being investigated based on CaO from Li–Ca and Er_2O_3 from Li–Er. Because there are likely to be cracks in any coatings, a dual-layer system with a thin outer layer of vanadium appears to be a more attractive MHD coating system.s.

1. Introduction

In all alloy–liquid metal (e.g. Li and Pb–Li) blanket concepts for a deuterium/tritium fueled fusion reactor where a strong magnetic field is used to contain the fusion plasma, a magnetohydrodynamic (MHD) pressure drop is developed when the electrically conductive liquid metal flows across the magnetic field lines. To minimize the MHD resistance to flow, it is necessary to have an insulating barrier to decouple the liquid metal and the alloy structure. One possibility is an insulating coating on the structural wall. The coatings must be thin, durable and electrically resistive [1–3]. Perhaps the most difficult material requirement for a Li self-cooled blanket is compatibility with Li at temperatures up to ~700°C [4,5]. Because of the relative stability of Li_2O, most electrically-resistive oxides readily dissolve in Li [6,7]. Therefore, only a few materials are candidates for this application. Over the past few years, there has been a considerable shift in emphasis in this topic as the underlying compatibility issues have been reevaluated and new candidate materials have been tested in bulk form and fabricated as coatings for further experiments. The development of a viable MHD coating is particularly relevant for concepts that use vanadium structural alloys because of the good compatibility of vanadium alloys with liquid lithium and their susceptibility to embrittlement by oxygen and hydrogen in other environments such as helium [8–11].

2. Shift in research emphasis

Both theoretical calculations and experiments over the past 40 years have shown that there are relatively few materials that meet both the Li compatibility and electrical resistance requirements [1,3,6,7,12–16]. Recent reviews have emphasized CaO and AlN as the most attractive candidate materials [2,3]. However, more recent work has shown that the these materials may not be viable [17,18]. Over the past decade, CaO has been extensively investigated as a candidate coating material [2,3,14,19]. One of its noted features is its high solubility in Li which suggested that it might be possible to have a self-healing coating. However, thermodynamic calculations and recent

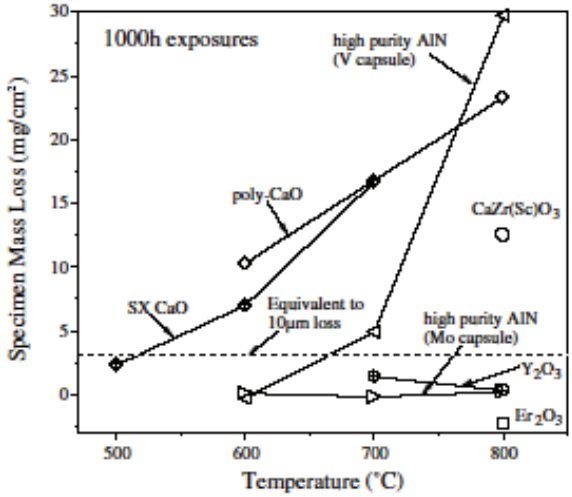

Fig. 1. Mass losses for some candidate oxide and nitride materials after 1000 h at various temperatures. The results for poly-crystalline and single crystal CaO show severe dissolution above 500°C. The dashed line shows the mass loss associated with the loss of ~10 μm of coating in a 1000 h exposure.

experimental work [17] on bulk CaO specimens have proven that CaO cannot perform adequately at 600–800 °C in static Li tests, Fig. 1. A mass loss of ┌ 3 mg/cm2 is equivalent to a 10 lm loss of material. These mass losses at high temperatures are unacceptable for a thin coating. An even higher dissolution rate (0.085 lm/h) was observed for single crystal CaO in Li–2.8 at.% Ca at 600 °C [18]. Results for coatings formed on V–4Cr–4Ti with different oxygen preloading showed a lower dissolution rate when tested under the same conditions at 600°C [18]. However, the dissolution rates were sufficient to remove a significant fraction of the coating after 1000 h and suggested a coating lifetime of <3000 h at 600°C, Fig. 2. Because of its poor high temperature compatibility, the CaO coating development program in the US has recently been concluded.

Screenings studies [6,13,14] initially indicated that CaO was a promising candidate. However, the thermodynamic calculations assumed that the Li was saturated with oxygen. Because CaO has a lower free energy of formation than Li2O, CaO should be stable in Li under these conditions. However, in a flowing system with a temperature gradient this is an unrealistic assumption as the saturation concentration varies considerably with temperature [17] such that if the lithium were saturated at the highest temperature, Li_2O would precipitate out at the lowest temperature and the lithium would no longer be saturated at the highest temperature. A more relevant reaction is for dissolution of the components into lithium until the following equilibrium is reached in solution. Theoretical calculations showed that the equilibrium solubility of Ca in Li increased dramatically with temperature[17], which was consistent with the high dissolution rates observed experimentally.

The other candidate that has been extensively studied

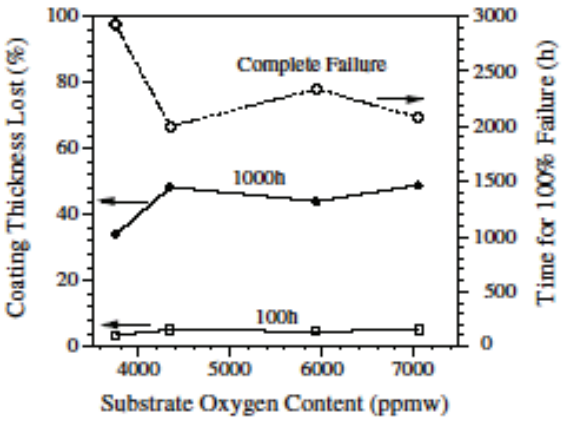

Fig. 2. Performance of CaO coatings in Li–2.8 at.% Ca at 600°C as a function of oxygen in the V–4Cr–4Ti substrate. Basedon the experimentally observed dissolution rate, the percentageof the coating lost with time was calculated as well as the time to complete failure [18].

as a coating is AlN [2,3,20–23]. Nitrides are generally more compatible with Li because nitrides of Li are far less stable than Li_2O. However, AlN is one of only a few nitrides with high electrical resistivity. A number of experiments have shown good Li compatibility up to 600 °C. However, in higher temperatures capsule tests [17,23], the behavior was very sensitive to the capsule material, Fig. 1. With a Mo capsule, very little mass change was noted after 1000 h at 800°C. When a vanadium alloy capsule was used, the mass losses were much higher, Fig. 1. The same behavior was observed for high purity (0.04%Y) and ultra-high purity AlN[17,23]. The effect can be understood based on the dissolution equilibrium equation for AlN. The vanadium alloy capsule gettered N from the Li during the exposure and prevented the Li from becoming saturated with N and thus stopping the dissolution. With capsules made from Mo, which does not form a stable nitride, the Li becomes saturated with N and the dissolution stops. Thus, the use of AlN appears problematic because uncoated vanadium alloy channel walls could getter N from the Li. A further complication is that it is extremely difficult to make AlN without oxygen contamination. Any Al_2O_3 formed during coating fabrication would be readily dissolved by Li. Initial Li exposures of AlN coatings at 500°C have shown poor performance [21]. This combination of experimental results and thermodynamic analyses suggests a new strategy for selecting possible MHD coating materials. Because elements (e.g. Ca) which are highly soluble in Li may be more susceptible to dissolution at high temperature, oxides with cations that have a low solubility in Li will likely have better compatibility. Therefore, more emphasis is now being placed on Y_2O_3 and Er_2O_3 as candidate materials for coating development.

3 In-situ coatings

Despite the observed problems with CaO compatibility at higher temperatures, the concept of a self healing coating is still attractive. An in situ technique would more easily allow coating of complex components. Therefore, the Li–CaO concept as well as Li– Er_2O_3 are currently being examined to develop an understanding of the issues related to the processing and use of in situ coatings. Based on earlier experimental work for vanadium alloys exposed to Li–0.5% Ca at 700°C [24], the process of CaO formation and degradation on vanadium alloys is being modeled [25]. According to the in situ model in Fig. 3, oxygen from the substrate can react with Ca in the Li to form a CaO outer layer. However, this requires balanced fluxes of Ca in the metal and O from the metal which are difficult to achieve. As oxygen is removed from the substrate, Ti rich oxide particles dissolve.

Eventually, some Ca and Li become incorporated into the metal while V and Ti can become incorporated into the oxide. This process degrades the coating and the metal. Another scenario involves the deposition of a CaO layer before exposure to Li–Ca. In this case, similar problems eventually develop as oxygen is removed from the substrate and V and Ti are incorporated into the oxide. Because of the observed problems with CaO, in situ Er_2O_3 coatings also are being explored [26]. Vanadium alloys preloaded with oxygen were exposed to Li–0.006 at.% Er at 600°C. Fig. 4 shows the Er-rich oxide layer formed on the surface. However, the measured O/Er ratio was 2–2.5 due to the incorporation of V, Cr and Ti impurities in the layer. Initial resistance measurements at room temperature showed adequate electrical resistivity when the process was optimized. More work will be required to further optimize this process and characterize the properties and compatibility of coatings made by this process.

4 Result from new coatings

Because of the initial positive results on bulk Y_2O_3 and Er_2O_3, the next step was to fabricate coatings of these materials for further characterization and testing. In the US, Y_2O_3 coatings were deposited by an electronbeam assisted, physical vapor deposition process (EB-PVD) on V–4Cr–4Ti substrates. The coatings were 12.5 lm thick and had a faceted surface microstructure typical of the EBPVD process, Fig. 5(a). For coating evaluations, the figure of merit is the change in coating resistivity at 700°C after exposure to Li. The coating must maintain adequate resistivity in order to warrant further testing. In order to avoid oxidation of the vanadium alloy substrate, the electrical resistance was measured in a vacuum. This initial set of coatings showed relatively low resistivity compared to literature values and values measured on a sintered Y_2O_3 specimen using the same equipment, Fig. 6. Similar to the testing procedure used

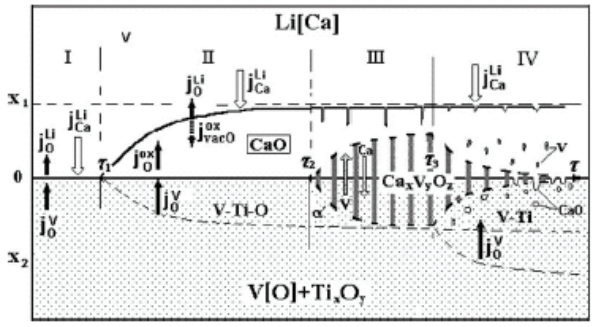

Fig. 3. Schematic of the competing processes for the in situ formation of a CaO layer on a vanadium alloy as a function of time from left to right [25].

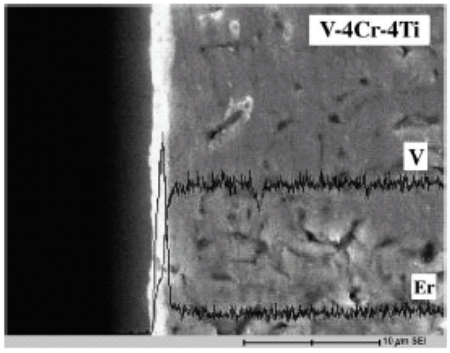

Fig. 4. SEM image and EDS line element scan of a cross section of V–4Cr–4Ti oxidized for 6 h and annealed for 16 h at 700°C, then exposed in Li doped with Er for 300 h at 600°C [26]..

for bulk ceramics [17], the coated specimens were exposed to lithium in sealed vanadium alloy capsules for 100–1000 h at 700 and 800°C. After exposure, performance varied from little change in resistivity and microstructure to complete loss of the coating. The electrical resistance measured after 3, 100 h cycles at 800 °C (cooling to room temperature between each cycle) was higher than the as-received coatings (Fig. 6). However, after 1000 h at 800°C, a degradation in the resistivity was observed. X-ray diffraction results showed an exact match with Y_2O_3 for the as-received coatings. With increasing exposure time and temperature, the Y_2O_3 peaks began to disappear and $LiYO_2$ peaks and unidentified peaks were observed. The surface morphology of the coating changed significantly after exposure, for example, Fig. 5(b). Oxide particles containing Ti and Y were observed on the coating surface using Auger electron spectroscopy. After a 2000 h exposure at 800°C, the coating was destroyed. Exposures at 700°C on a second set of coatings typically showed a complete loss of the coating. Previous work that examined the compatibility of Y_2O_3 and Y_2O_3 coatings in Li found the formation of a $LiYO_2$ layer at the Y_2O_3–Li interface after exposure at 500°C [27,28]. Although the current results on Y_2O_3 coatings show a potential compatibility problem, additional work is needed on coating development to further study the phenomenon as well as the role of coating microstructure on the reaction with Li. In Japan, research programs are characterizing the properties and microstructure of AlN, Y_2O_3 and Er_2O_3 coatings made by RF sputtering and vacuum arc processes [29,30]. Processing issues need to be separated from those associated with compatibility in Li. Therefore, it is important to have high quality, well characterized coatings prior to testing in Li. For example, the crystallinity and purity of AlN coatings is being characterized [29]. Post-fabrication anneals at 400 and 700°C were used to improve the crystallinity. Annealing lowers the resistivity of the coatings but they retain

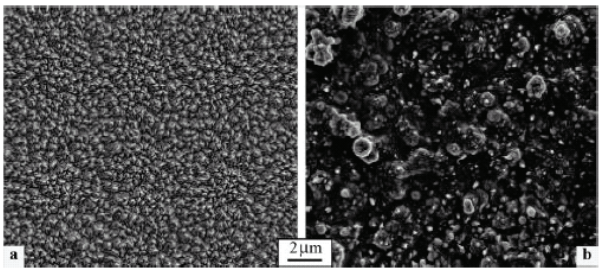

Fig. 5. SEM secondary electron plan view images of EB-PVD Y2O3 coatings (a) as-received and (b) after exposure to Li at 800°C for 1000 h.

sufficient resistance for this application. The coatings contain 3–10 at.% O which probably contributes to their poor performance in Li at 500°C [29]. Radiation-induced conductivity effects are being explored using 14 MeV neutron irradiation of bulk ceramics specimens and AlN and Y_2O_3 coatings [30]. The increases in conductivity were proportional to the neutron flux but were such that the degradation of the resistivity under irradiation were within allowable limits for the V/Li blanket system. Coating compatibility testing has not proceeded beyond static capsule-type testing. In order to truly demonstrate compatibility, testing in a thermal gradient will be necessary in order to evaluate the effects of temperature and mass transfer [31]. For example, previous results for Y_2O_3 showed only limited dissolution in static Li testing at 1100°C [12] but complete dissolution in flowing Li in 109 h at 1143 °C due to mass transfer or erosion [32]. A set of metrics for coating performance has been developed [33]. When coatings are able to meet these metrics in static tests, more extensive thermal convection loop testing will begin.

5 Effects of coating defects

The required properties and effects of defects in MHD coatings have been considered previously [34–36]. A recent analysis of the minimum properties and maximum defect density allowable [37] has caused a reassessment of the MHD coating strategy. Theoretical calculations suggest that only extremely small defect densities of through thickness defects can be tolerated because Li

eadily wets oxides in the temperature range of interest [17]. Therefore, it is expected that any crack will fill with Li and increase the effective conductivity of the coating system. (Even in the absence of a defect, Li has been observed to change the conductivity of oxides by interdiffusion at room temperature [38].) With MHD coating thicknesses expected to be 5–10μm, it is highly unlikely that coatings could be fabricated with virtually no through thickness cracks. High quality bulk ceramics typically will have defects on the order of 10μm[39]. Even

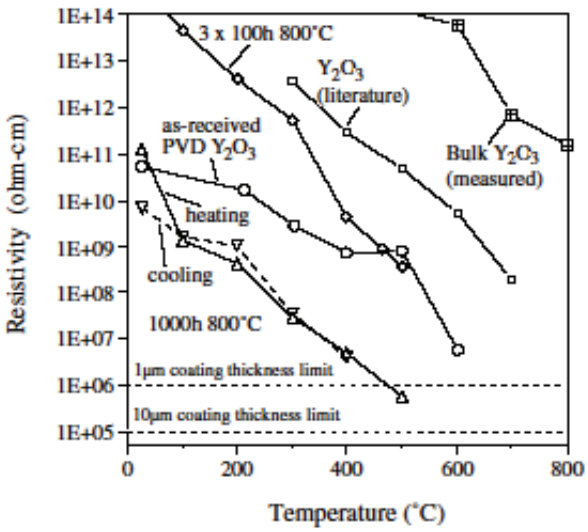

Fig. 6. Resistivity as a function of temperature for EB-PVD Y_2O_3 coatings before and after exposure to Li at 800°C. Literature and measured values for bulk Y_2O_3 were much higher.

if a coating could be fabricated without cracks, tensile loading of the vanadium alloy substrate will cause cracks to form normal to the stress direction with a uniform spacing [40]. Based on data from the literature for standard properties of oxide films [41,42], the tensile crack spacing is generally expected to be 10–100 times the coating thickness. Therefore, unless there are no significant tensile loads on the coated vanadium alloys, through-thickness cracks would be expected every 1 mm or less in a 10 μm thick MHD coating. Lithium should wet these cracks and render the coating virtually useless.

6 Current paradigm

Because of the anticipated defects in the insulating layer, it is suggested that the MHD coating will need to incorporate an outer, protective, metallic layer to prevent Li from entering cracks in the insulating layer. The potential need for an outer layer has been recognized for some time [1]. Most likely, this layer would be vanadium or a vanadium alloy and could be up to 100 μm thick [43].

A dual-layer MHD coating system will need to be carefully assessed. Rather than a deposited coating, the outer layer could be free standing. A dual-layer coating will be more difficult to fabricate but will change the necessary compatibility metrics for the ceramic insulating layer. It also may preclude the in situ or self-healing coating concepts, as lithium will no longer be in direct contact with the ceramic. However, some level of compatibility will be required so that a minor breach in the metallic outer layer will not immediately result in dissolution of the inner layer. For a dual-layer system,

Y_2O_3 may be an adequate insulator candidate since the observed degradation was due to a solid state reaction to form $YLiO_2$. Because the amount of degradation will be limited to the amount of Li able to penetrate the outer layer, a minor leak would only have a limited effect on the ceramic layer. With a thin metallic layer in contact with Li, there is some concern about the compatibility of vanadium and its alloys with Li. Degradation of the relatively thin outer layer by mass transfer or dissolution would have to be minor. There is some conflict about this issue as some investigators have reported rather high dissolution rates for vanadium alloys in flowing Li [44,45]. However, other work has shown good compatibility and low solubility of vanadium in Li [46,47]. As with a single-layer system, this issue will need to be addressed by compatibility studies of a dual-layer system in a temperature gradient.

7 Summary

The past few years have seen great changes in the research emphasis and strategy for MHD coatings. Problems with CaO have led to a focus on new candidates with low cation solubility in Li, such as Y_2O_3 and Er_2O_3. Progress is being made in the development of MHD coatings, but as yet no coatings have shown sufficient compatibility with Li. Anticipated problems with defects in ceramic coatings, either as-fabricated or due to tensile cracking, suggests that the most viable coating strategy will have to be multi-layered. An outer metallic layer will prevent Li from wetting cracks in the inner ceramic insulating layer and also limit interaction between the ceramic and Li. Whether the MHD coating is single- or dual-layered, processing issues will need to be addressed before the issue of compatibility can be answered.

Acknowledgments

The research was sponsored by the Office of Fusion Energy Sciences, US Department of Energy (DOE), under contract DE-AC05-00OR22725 with UT-Battelle, LLC. J.R. DiStefano, D.F.Wilson and S.J. Zinkle at ORNL and N.B. Morley at UCLA provided comments on the manuscript.

References

[1] Y.Y. Liu, D.L. Smith, J. Nucl. Mater. 141–143 (1986) 38.
[2] D.L. Smith, K. Natesan, J.H. Park, C.B. Reed, R.F. Mattas, Fusion Eng. Des. 51&52 (2000) 185.
[3] D.L. Smith, J. Konys, T. Muroga, V. Evitkhin, J. Nucl. Mater. 307–311 (2002) 1314.
[4] E.E. Bloom, J. Nucl. Mater. 258–263 (1998) 7.
[5] D.L. Smith, M.C. Billone, S. Majumdar, R.F. Mattas, D.-K. Sze, J. Nucl. Mater. 258–263 (1998) 65.
[6] J.E. Battles, Int. Mater. Rev. 34 (1989) 1.
[7] R.J. Lauf, J.H. DeVan, J. Electrochem. Soc. 139 (1992)2087.
[8] H.D. R€ohrig, J.R. DiStefano, L.D. Chitwood, J. Nucl. Mater. 258–263 (1998) 1356.
[9] K. Natesan, W.K. Soppet, J. Nucl. Mater. 283–287 (2000)1316.
[10] B.A. Pint, J.R. DiStefano, J. Nucl. Mater. 307–311 (2002)560.
[11] B.A. Pint, J.R. DiStefano, P.F. Tortorelli, Fusion Sci. Technol. 44 (2003) 433.
[12] D. Elliott, D. Cerini, L. Hays, Supporting Research and Advanced Development, Space Programs Summary 37–41,Vol. IV, Jet Propulsion Laboratory, Pasadena, CA October 1966, p. 124.
[13] R.N. Singh, J. Am. Ceram. Soc. 59 (1976) 112.
[14] J.H. Park, T.F. Kassner, J. Nucl. Mater. 233–237 (1996) 476.
[15] P. Hubberstey, J. Nucl. Mater. 247 (1997) 208.
[16] P. Hubberstey, T. Sample, J. Nucl. Mater. 248 (1997) 140.
[17] B.A. Pint, J.H. DeVan, J.R. DiStefano, J. Nucl. Mater. 307–311 (2002) 1344.
[18] J.-H. Park, K. Natesan, R. Mattas, Argonne National Laboratory, unpublished results from teleconference, August 2002.
[19] K. Natesan, M. Uz, S. Wieder, J. Nucl. Mater. 283–287(2000) 1277.
[20] K. Natesan, C.B. Reed, D.L. Rink, R.C. Haglund, J. Nucl. Mater. 258–263 (1998) 488.
[21] T. Terai, A. Suzuki, T. Yoneoka, T. Mitsuyama, J. Nucl. Mater. 283–287 (2000) 1322.
[22] T. Yoneoka, T. Sakurai, T. Sato, S. Tanaka, J. Japan, Inst. Metals 66 (2002) 384.
[23] A. Suzuki, T. Muroga, B.A. Pint, T. Yoneoka, S. Tanaka, Fusion Eng. Des. 69 (2003) 397.
[24] O.I. Yeliseyeva, V.M. Chernov, T.V. Tsaran, J. Nucl. Mater. 307–311 (2002) 1400.
[25] O.I. Yeliseyeva, V.M. Chernov, M.M. Potapenko, T.V. Tsaran, J. Nucl. Mater., these Proceedings. doi:10.1016/j.jnucmat.2004.04.209.
[26] Z. Yao, A. Suzuki, T. Muroga, K. Katahira, J. Nucl. Mater., these Proceedings. doi:10.1016/j.jnucmat.2004. 04.208.
[27] T. Terai, T. Yoneoka, H. Tanaka, A. Suzuki, S. Tanaka,M. Nakamichi, H. Kawamura, K. Miyajima, Y. Harada, J.Nucl. Mater. 233–237 (1996) 421.
[28] T. Mitsuyama, T. Terai, T. Yoneoka, S. Tanaka, Fusion Eng. Des. 39&40 (1998) 811.
[29] A. Sawada, A. Suzuki, T. Terai, T. Muroga, J. Nucl. Mater., these Proceedings. doi:10.1016/j.jnucmat. 2004.04.287.
[30] T. Tanaka, A. Suzuki, T. Muroga, F. Sato, T. Iida, T. Nishitani, J. Nucl. Mater., these Proceedings. doi:10.1016/ j.jnucmat.2004.04.211.
[31] J.H. DeVan, J. Nucl. Mater. 85&86 (1979) 249.

[32] L. Hays, NASA Tech. Report 32-1233, JPL, Pasadena, CA, December 1967.
[33] B.A. Pint, J.R. DiStefano, DOE-ER-0313/32, 2002, p. 87.
[34] L. B€uhler, Fusion Eng. Des. 27 (1995) 650.
[35] S. Malang, H.U. Borgstedt, E.H. Farnum, K. Natesan, I.V. Vitkovski, Fusion Eng. Des. 27 (1995) 570.
[36] A.Y. Ying, A.A. Gaizer, Fusion Eng. Des. 27 (1995) 634.
[37] D.-K. Sze et al., J. Nucl. Mater., these Proceedings.
[38] J.W. Lee, S.I. Pyun, J. Power Sources 119 (2003) 760.
[39] P.F. Becher, private communication, 2003.
[40] D.C. Agrawal, R. Raj, Acta Metall. 37 (1989) 1265.
[41] J.R. Nicholls, D.J. Hall, P.F. Tortorelli, Mater. High Temp. 12 (1994) 141.
[42] M. Sch€utze, Mater. High Temp. 12 (1994) 237.
[43] D.-K. Sze, private communication, 2003.
[44] Ch. Adelhelm, H.U. Borgstedt, J. Konys, Fusion Technol. 8 (1985) 541.
[45] O.K. Chopra, D.L. Smith, J. Nucl. Mater. 155–157 (1988) 683.
[46] V.A. Evtikhin, I.E. Lyublinski, A.V. Vertkov, J. Nucl. Mater. 258–263 (1998) 1487.
[47] S.N. Votinov et al., J. Nucl. Mater. 233–237 (1996) 370. 124 B.A. Pint et al. / Journal of Nuclear Materials 329–333 (2004) 119–124

Initial Characterization of V-4Cr-4Ti and MHD Coatings Exposed to Flowing Li

B. A. Pint, S. J. Pawel, M. Howell, J. L. Moser, G. W. Garner,
M. L. Santella, P. F. Tortorelli, F. W. Wiffen and J. R. DiStefano

Materials Science and Technology Division, Oak Ridge National Laboratory,
P.O. Box 2008, Oak Ridge, TN 37831-6156, USA

A mono-metallic V-4Cr-4Ti thermal convection loop was operated in vacuum (~10-5Pa) at a maximum Li temperature of 700°C for 2,355h and Li flow rate of 2-3cm/s. Two-layer, physical vapor deposited Y2O3-vanadium, electrically-insulating coatings on V-4Cr-4Ti substrates as well as tensile and sheet specimens were located in the flow path in the hot and cold legs. After exposure, specimens at the top of the hot leg showed a maximum mass loss equivalent to ~1μm of metal loss. Elsewhere, small mass gains were observed on the majority of specimens resulting in an increase in hardness and room temperature yield stress and a decrease in ductility consistent with interstitial uptake. Specimens that lost mass showed a decrease in yield stress and hardness. Profilometry showed no significant thickness loss from the coatings.

1. Introduction

One of the critical unresolved issues for the vanadium-lithium blanket concept[1,2] (and any liquid metal concept) in a deuterium/tritium fueled fusion reactor[3,4] is the need to reduce the pressure drop associated with the magnetohydrodynamic (MHD) effect of a conducting liquid flowing across the magnetic field lines One solution to the MHD problem is to decouple the structure wall from the liquid metal with an electrically insulating coating or flow channel insert (FCI).[5] The application requires a thin, crack-free,[6] durable layer with a relatively high electrical resistance.[7] While a "self-healing" layer is possible in corrosion where a re-passivation can occur with the re-formation of a surface oxide, this concept is not applicable to functional (i.e. electrically resistant) coatings because a defect that shorts the coating is unlikely to "heal". Therefore, a robust coating system or a FCI is needed for this application. Due to incompatibility between Li and virtually all candidate insulating oxides,[8-12] the current focus of the U.S. MHD coating program[10-12] is on evaluating the compatibility of durable, multi-layer coatings[7,13] where a vanadium overlayer prevents direct contact between the insulating oxide layer and Li. This concept shifts the compatibility concern from the oxide layer to the thin vanadium overlayer. In order to verify that a thin, ~10μm, V layer is sufficiently compatible with Li to function in a long-term situation, a mono-metallic thermal convection loop was designed and built to expose thin V overlayers to flowing Li. The loop was operated with a peak temperature of ~700°C for 2,355h. Initial characterization of the coatings and V-4Cr-4Ti specimens in the loop are presented. Additional characterization of the coatings will be presented in future publications.

2. Experimental Procedure

A harp-shaped thermal convection loop was constructed of drawn tubing made from the large U.S. heat of V-3.8wt.%Cr-3.9%Ti (Heat#832665 made at Wah Chang, Albany, OR)[14] with an outer diameter of 19mm and a 1.6mm wall thickness. The hot and cold legs were ~85cm long and the top and bottom legs were ~25cm long with a fill/expansion tank at the top of the hot leg. The loop was fabricated using gas tungsten arc welding in an Ar-filled glove box and state-of-the-art expertise.[15] The loop contained four thermal wells that extended ~5mm into the flow path and contained type K thermocouples. The experiment was conducted in a stainless steel vacuum chamber. The loop was heated by three Mo wire furnaces, two on the hot leg and one on the Li tank. A total of 18 type K and 2 type S thermocouples were used to control the furnaces and monitor the temperatures around the loop. Wire and specimens all made from the same V-4Cr-4Ti heat formed ~80cm long chains that were placed in the hot and cold legs. The 29 specimens in each chain consisted of alternating interlocked tabs (31 x 13 x 0.9mm), which held the chain in the center of the tube, and pairs of miniature tensile specimens (type SS-3: 25 x 4 x 0.9mm). Prior to exposure, the tensile specimens were vacuum annealed for 1h at 1050°C. Specimen mass was measured on a microbalance with a ±0.01mg/cm2 error. Six of the exposed tabs had an electron-beam physical vapor deposited (EB-PVD) Y2O3 coating completely covered by an outer layer of unalloyed vanadium.[11,12] The coatings were made in two batches[16] and the unexposed coating thicknesses are shown in Table 1.

Sticks of Li (as-received batch: <100ppmw N, 95ppmw C and 950ppmw O)[12] were loaded into the tank in a glove box and the lid of the tank was welded shut. The loop and tank were then evacuated with a roughing pump, leak checked and valved off. The loop was placed in the vacuum chamber and instrumented using Ta foil to hold the thermocouples and prevent them from direct contact with the V-4Cr-4Ti tubing. After baking for 48h at 150°C, the chamber achieved a base

vacuum of 4x10-6Pa (5x10-8Torr) as measured on a vacuum gauge located on the chamber wall opposite the vacuum pump. The loop was then slowly preheated to ~250°C while maintaining the chamber pressure at ~2x10-4Pa using the hot leg heaters and resistively heating a W wire insulated with ceramic beads on the cold leg. After further heating the hot leg, a drastic increase in cold leg temperatures suggested the start of Li flow. After stabilization, temperature was subsequently controlled by maintaining the thermal well at the top of the hot leg at 700±10°C. Operation continued for a total of 2,355h and stopped due to a weather-related power outage. Temperatures in the four thermal wells are shown in Figure 1. The chamber pressure initially spiked above 5x10-4Pa but then continued to drop during exposure, reaching the desired <10-5Pa by 400h, Figure 1. A much larger than expected temperature gradient was observed during the first 1248h phase of operation. Initially, the difference between the top and bottom of the hot leg was 340°C and slowly increased to almost 400°C, Figure 1. Using thermocouples to measure the movement of a hot spot created by a pair of SiC heating elements, the Li velocity was estimated to be ~2cm/s during the first phase. After an unexplained upset that occurred between 1248-1262h, Figure 1, the cold leg temperatures increased and the gradient was only ~225°C suggesting a faster Li velocity of >3cm/s (based on the lower T gradient) which was similar to the velocity measured in the stainless steel test loop operated at 550° C.[17] However, the higher cold leg temperatures during the second operation phase prevented an accurate velocity measurement. The inability to maintain the peak temperature at 700°C for the second operational phase (Fig. 1) was subsequently attributed to a loose furnace connection. One hypothesis for the high first phase is that the Li flow was restricted by the specimen chain and that specimen movement or the chain breaking (which was not observed during disassembly) allowed more rapid Li flow during the second phase. Additional operational details are provided elsewhere.[18]

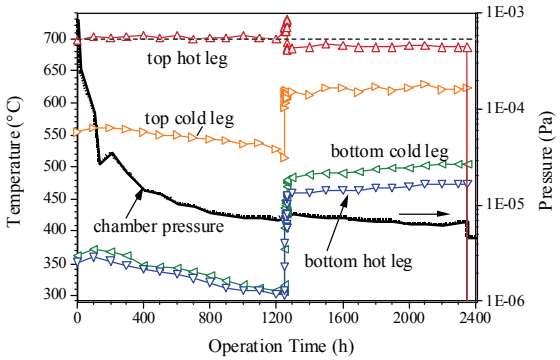

Figure 1. Temperatures and vacuum pressure during the loop operation. Two phases of operation occurred due to an unexplained upset between 1248 and 1262h.

After the experiment ended, the chamber was opened and the loop inverted and re-instrumented. The chamber was then pumped down and the loop was heated to ~400°C allowing the Li to drain back into the tank. The loop was then cut open in an Ar-filled glove box. The top tab specimens were not located below the cross-over joints in the hot and cold leg as designed and therefore could have restricted Li flow. The specimen chains were partially removed from the tubing and residual Li was removed using liquid ammonia followed by soaking in ethanol and then water.

Initial characterization of the specimens and tubing included metallographic cross-sections, hardness (Vickers, 300g) measurements and room temperature tensile testing at 10-3s-1 strain rate. Selected specimens were examined using scanning electron microscopy (SEM) equipped with energy dispersive x-ray (EDX) analysis. The EB-PVD coatings were examined by SEM/EDX, contact profilometry and x-ray diffraction (XRD).

3 Results and Discussion

Figure 2 shows the mass change data for both specimen chains with the nominal temperature profiles in the hot and cold legs. Mass losses in seven specimens from the hot leg were consistent with dissolution of metal (maximum ~0.6mg/cm2 is equivalent to 1µm vanadium) and/or loss of interstitials such as oxygen. Assuming linear kinetics, the maximum observed loss is the equivalent to ~2.5mg/m2h which is similar to the rate reported previously at 538°C for V-15Cr-5Ti with Li+50ppm N in a pumped loop (1 l/min).[19] However, the results in that study were complicated by the use of a stainless steel loop. Prior results in a mono-metallic loop at 700°C reported small mass gains after 1,000h.[20]

Three specimens at the top of the hot leg did not show a mass loss, Figure 2. As mentioned previously, the chain was not positioned in the loop as designed and the first specimen in the chain (* in Figure 1) appeared to be above the Li flow path which may explain its high mass gain. The second and third specimens appeared to be within the Li flow path although they were located above the hot leg furnace about ~2cm from the hot leg thermal well where the 700°C temperature was measured. Elsewhere in both legs, all of the specimens showed a small mass gain, likely due to the uptake of N and/or C. Chemical analyses of specimens are being performed. The location of the six EB-PVD coated specimens are shown in Figure 2,and each had a mass gain comparable to neighboring specimens.

Figure 3 shows results from room temperature tensile tests of specimens from the hot and cold legs as well as average values for unexposed specimens from the same specimen batch which have similar properties to prior studies.[21-23] The 0.2% yield and ultimate tensile

strengths increased in specimens as the exposure temperature decreased, Figure 3a. These specimens all showed a mass gain after exposure and this increase is consistent with interstitial hardening. The specimen from the hot leg with a mass loss showed a large decrease in yield strength. In Figure 3b, modest decreases in the uniform and total elongations also were observed compared to unexposed specimens. These ductility values are somewhat higher than were previously reported.[20] Additional tensile specimens will be tested at room temperature and at 500°C to compare to prior work on Li-exposed material.[24]

Figure 4 shows the change in average hardness and mass for tab specimens as a function of nominal average temperature based on their location in the specimen chain and assuming a linear temperature change across the hot and cold legs. The hardness, but not the mass change, showed a correlation with exposure temperature. Hardness values and standard deviations are based on 7 measurements across the polished ~0.9mm tab cross-section. Figure 5 shows etched metallographic cross-sections of two of the hot leg tab specimens from Figure 4 with the surface at the top of each figure. The specimen exposed at ~655°C (Fig. 5b) showed a much larger re-crystallized grain size and a surface layer which appeared to be depleted in precipitates. A similar layer or recrystallization was not observed in the other five specimens. None of the tab specimens were annealed prior to exposure. The near-surface microhardness has not been investigated yet. Prior work,[19] showed a ~30µm deep microhardness gradient in V-15Cr-5Ti after exposure at 482-538°C.

Finally, Table I shows the profilometry data for the EB-PVD coatings after exposure. Batch 1 coatings

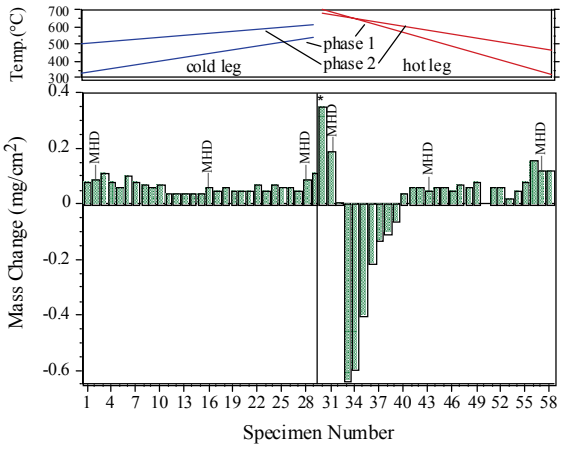

Figure 2. Specimen mass gain for V-4Cr-4Ti specimens in the hot and cold leg of the mono-metallic loop along with the nominal temperature that the specimens saw during the two phases of operation. In the hottest section of the loop, mass losses were observed, elsewhere, small mass gains were measured.

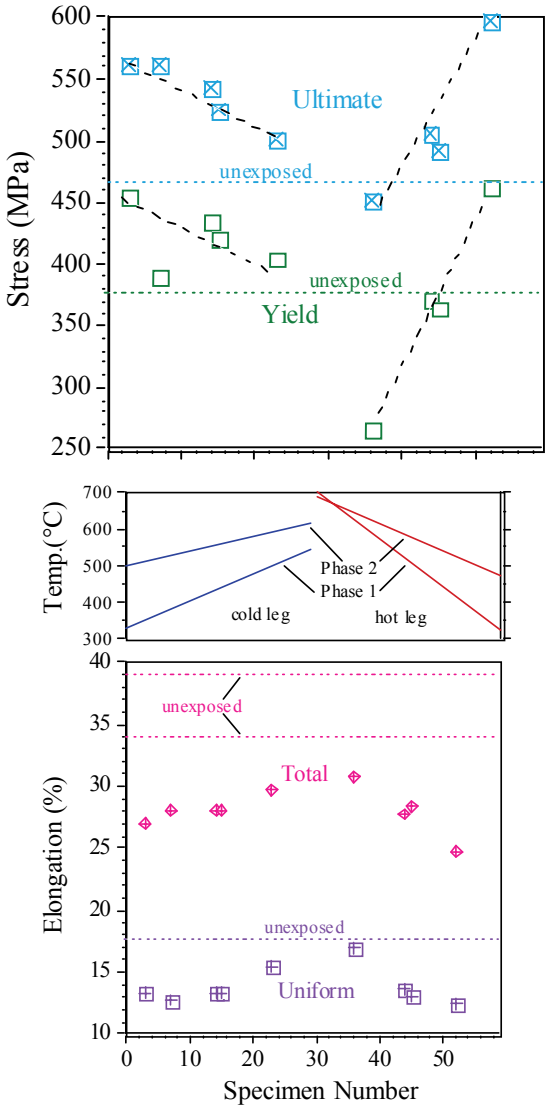

Figure 3. Room temperature tensile properties of a subset of V-4Cr-4Ti specimens after exposure in a mono-metallic loop: (a) 0.2% yield and ultimate tensile stress and (b) uniform and total elongation. The specimen in the hottest locations that lost mass showed a decrease in strength and less loss in ductility than the other specimens that had a mass gain after exposure.

were exposed at the higher temperatures because they were of higher quality.[16] No significant loss in thickness was detected. However, the unexposed coated specimens were concave indicating that the as-deposited coatings were under compression while the coated specimens exposed at the highest temperatures were all convex after exposure which could indicate stress relief or some type of degradation such as cracking or expansion due to reaction with Li.

.

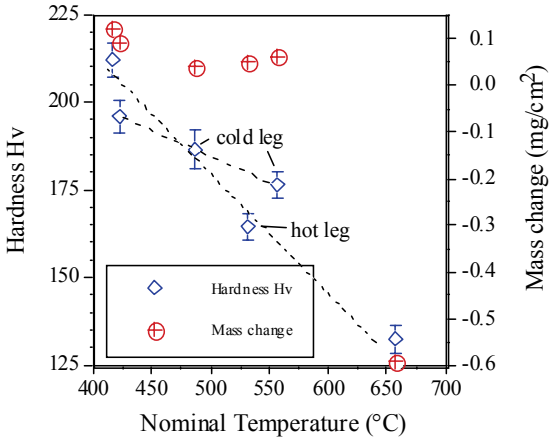

Figure 4. Average hardness measurements as a function of nominal exposure temperature along the hot and cold legs of the mono-metallic loop. The hardness decreased with exposure temperature in both legs.

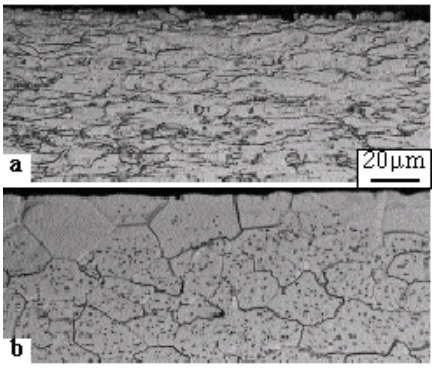

Figure 5. Light microscopy of V-4Cr-4Ti tab specimens after exposure to flowing Li. (a) bottom of the hot leg (~415°C) and (b) top of the hot leg (~655°C) where the surface grains appear depleted in precipitates. These specimens were not annealed prior to exposure

4 Conclusion

A mono-metallic V-4Cr-4Ti thermal convection loop was run for 2,355h with a maximum temperature of 700°±10°C to determine the compatibility of V-4Cr-4Ti and Y2O3/V coatings with flowing (~2-3cm/s) Li. Small mass losses (equivalent to ≤1µm of metal loss) were measured at the top of the hot leg. Elsewhere, small mass gains were measured. Specimens that gained mass also showed an increase in yield stress and modest decrease in ductility consistent with an increase in interstitial content. The EB-PVD Y2O3/V coatings showed no significant loss in thickness, however, further characterization is needed to determine their electrical resistance and microstructure after exposure.

Acknowledgments

This research was sponsored by the Office of Fusion Energy Sciences, U. S. Department of Energy (DOE), under contract DE-AC05-00OR22725 with UT-Battelle, LLC and the JUPITER-II Japan-U.S. collaboration on fusion blanket systems and materials. T. Brummett, R. Parten and H. Longmire assisted with the experimental work. D. F. Wilson, M. Li, S. J. Zinkle and R. Stoller provided comments on the manuscript.

References

[1] R. J. Kurtz, K. Abe, V. M. Chernov, D. T. Hoelzer, H. Matsui, T. Muroga and G. R. Odette, J. Nucl. Mater. 329-333 (2004) 47.
[2] T. Muroga, J. M. Chen, V. M. Chernov, K. Fukumoto, D. T. Hoelzer, R. J. Kurtz, T. Nagasaka, B. A. Pint, M. Satou, A. Suzuki and H. Watanabe, J. Nucl. Mater. 367-370 (2007) 780.
[3] I. R. Kirillov, C. B. Reed, L. Barleon and K. Miyazaki, Fus. Eng. Design 27 (1995) 553.
[4] L. Barleon, V. Casal and L. Lenhart, Fus. Eng. Design

Table 1. Profilometry data of the V/Y2O3 coatings on V-4Cr-4Ti substrates after exposure to flowing Li for 2,355h in a V-4Cr-4Ti loop with a maximum temperature of 700°C.

	Batch 1		Batch 2	
Location	V layer	Y2O3 layer	V layer	Y2O3 layer
Unexposed	9 µm	13 µm	10 µm	17 µm
Top Hot Leg	8	12		
Top Cold Leg	8	11		
Middle Cold Leg	7	12		
Bottom Cold Leg			10	15
Bottom Hot Leg			9	17
Middle Hot Leg			9	16
As-deposited*	7.4±0.3	11.7±0.5	9.9±0.4	15.7±0.9

* Reference 16

14 (1991) 401.
[5] S. Malang, H. U. Borgstedt E. H. Farnum, K. Natesan and I. V. Vitkovski, Fus. Eng. Design 27 (1995) 570.
[6] L. Bühler, Fus. Eng. Design, 27 (1995) 650.
[7] Y. Y. Liu and D. L. Smith, J. Nucl. Mat. 141-143 (1986) 38.
[8] J. E. Battles, Intern. Mater. Rev. 34 (1989) 1.
[9] T. Terai, et al., J. Nucl. Mater. 233-237 (1996) 1421.
[10] B. A. Pint, P. F. Tortorelli, A. Jankowski, J. Hayes, T. Muroga, A. Suzuki, O. I. Yeliseyeva and V. M. Chernov, J. Nucl. Mater. 329-333 (2004) 119.
[11] B. A. Pint J. L. Moser and P. F. Tortorelli, Fus. Eng. Des. 81 (2006) 901.
[12] B. A. Pint, J. L. Moser, A. Jankowski and J. Hayes, J. Nucl. Mater. 367-370 (2007) 1165.
[13] I. V. Vitkovsky, et al., Fus. Eng. Design, 61-62 (2002) 739.
[14] D. L. Smith, H. M. Chung, B. A. Loomis and H.-C. Tsai, J. Nucl. Mater. 233-237 (1996) 356.
[15] M. L. Grossbeck, J. F. King, T. Nagasaka and S. A. David, J. Nucl. Mater. 307-311 (2002) 1590.
[16] A. F. Jankowski and B. A. Pint, unpublished research (2007).
[17] B. A. Pint, et al., DOE-ER-0313/41 (2006) 2.
[18] B. A. Pint, et al., DOE-ER-0313/42 (2007) 2.
[19] O .K. Chopra and D. L. Smith, J. Nucl. Mater. 155-157 (1988) 683.
[20] V. A. Evtikhin, I. E. Lyublinski and A. V. Vertkov, J. Nucl. Mater. 258-263 (1998) 1487.
[21] H. M. Chung, B. A. Loomis and D. L. Smith, Fus. Eng. Des. 29 (1995) 455.
[22] K. Fukumoto, T. Morimura, T. Tanaka, A. Kimura, K. Abe, H. Takahashi and H. Matsui, J. Nucl. Mater. 239 (1996) 170.
[23] B. A. Pint and J. R. DiStefano, Oxid. Met. 63 (2005) 33.
[24] T. Nagasaka, T. Muroga, M. M. Li, D. T. Hoelzer, S. J. Zinkle, M. L. Grossbeck and H. Matsui, Fus. Eng. Des. 81 (2006) 307-313.

TENSILE PROPERTY OF V-4Cr-4Ti ALLOY AFTER LIQUID LITHIUM EXPOSURE

T. Nagasaka[1], T. Muroga[1], M. M. Li[2], D. T. Hoelzer[2], S. J. Zinkle[2], M. L. Grossbeck[3], H. Matsui[4]

[1]*National Institute for Fusion Science, Oroshi 322-6, Toki, Gifu 509-5292, Japan*
[2]*Oak Ridge National Laboratory, Oak Ridge, TN 37831-6376, USA*
[3]*The University of Tennessee, Knoxville, TN 37996-2300, USA*
[4]*Institute for Materials Research, Tohoku University, Katahira 2-1-1, Aoba-ku, Sendai 980-8577, Japan*

A candidate low activation vanadium (V) alloy, V-4Cr-4Ti (NIFS-HEAT-2), was exposed to liquid lithium (Li) at 973 and 1073 K for up to 1963 hr. Contaminations with carbon (C) and nitrogen (N) from Li by thousands of wppm were observed. Oxygen (O) was removed to several 10 wppm level by Li exposure at 1073 K, but not at 973 K. The Li exposure caused strength degradation in tensile tests at 973 and 1073 K. On the other hand, good ductility was demonstrated after the Li exposure even with the significant contamination of C and N. From microstructural observations, C and N are likely to be scavenged by Ti-C-N type precipitates. Reduction of O was attributed to disappearance of Ti-C-O type precipitates.

I. INTRODUCTION

Vanadium alloys are recognized as attractive candidate structural materials for liquid Li cooled blanket for fusion reactor[1, 2]. Transfer of impurities occurs between V alloy and liquid Li. Generally, C and N migrate to V alloy from Li, while O is removed from V alloy by Li[3]. However, the mechanisms of the transfer, distribution of the impurities during Li exposure and the effects on mechanical properties have not been clarified. Recently, some irradiation programs on V alloys with liquid metal (Li or Na) have been initiated by using creep tubes[4], where impurity concentration in the V alloy specimens change during irradiation. In order to understand the creep behavior in liquid Li, impurity effects on the deformation process have to be examined. In the present study, a candidate V-4Cr-4Ti alloy, designated as NIFS-HEAT-2, was exposed to liquid Li for up to 1963 hr. The impurity transfer, impurity distribution and its effect on tensile properties were investigated.

II. EXPERIMENTAL PROCEDURE

The reference low activation V-4Cr-4Ti alloy, designated as NIFS-HEAT-2, was cold-rolled into 0.25 mm-thick sheets, followed by annealing at 1273 K for 2 hr[5]. The sheets were cut into coupon specimens with the size of 0.25 x 5 x 25 mm. The exposure temperature to Li (T_{Li}) was 973 K and 1073 K. The exposure time was 255 to 1963 hr. The detail for exposure tests has been described elsewhere[6]. After the exposure, Li was chemically removed by liquid ammonia. From the coupons, miniature tensile specimens with a size of 0.25 x 4 x 16 mm (gauge: 0.25 x 1.2 x 5 mm), and disks of 0.25 mm in thickness and 3 mm in diameter were punched out. The residual punched-coupons were chemically analyzed for C, N and O.

Tensile tests were conducted by using the punched tensile specimens. Initial strain rate in tensile tests was 6.7 x 10^{-4}. Test temperatures ($T_{Tensile}$) ranged from room temperature (RT) to 1073 K. The atmosphere for the tensile tests at RT and elevated temperature were the air and a vacuum better than 10^{-4} Pa, respectively. Vickers microhardness was measured along the cross section of the coupons with a load of 25 g for 30 s. Microstructural observations were performed with scanning electron microscope (SEM) and transmission electron microscope (TEM) by using the punched disks.

III. RESULTS

Table 1 lists the results of chemical analysis after the Li exposure. The table also shows the liquid Li batch number. Liquid Li was changed after each 1 or 2 sets of exposure. Impurity concentrations in NIFS-HEAT-2 after Li exposures depended on the batch. Better correlation between exposure time and impurity concentrations are given in some batches as shown in Fig. 1. In these batches, C and N impurity levels were increased with exposure time by contamination from the Li, while O was decreased by scavenging by the Li.

Table 1 Impurity concentrations in NIFS-HEAT-2 (V-4Cr-4Ti) before ($t_{Li} = 0$) and after ($t_{Li} > 0$) liquid Li exposure

Exposure temperature, T_{Li} / K	Exposure time, t_{Li} / hr	C, C_C / wppm	N, C_N / wppm	O, C_O / wppm	Li batch ID
	0	62	84	158	
973	255	142	342	142	#5
	499	280	1000	171	#6
1073	260	238	884	51	#2
	428	130	143	66	#1
	943	477	2273	29	#2
	1443	505	2317	79	#3
	1963	797	3420	47	#4

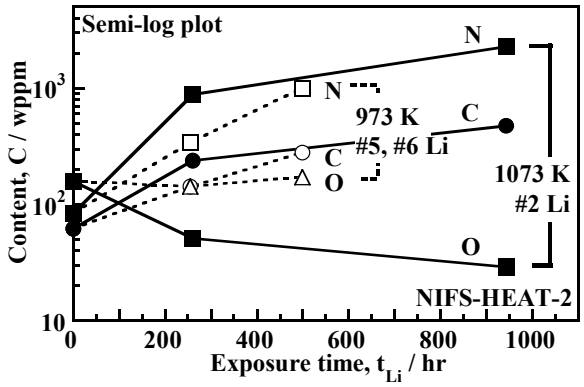

Fig. 1 Change in impurity concentration after the Li exposures at 973 K (Li #5 and 6) and 1073 K (#2).

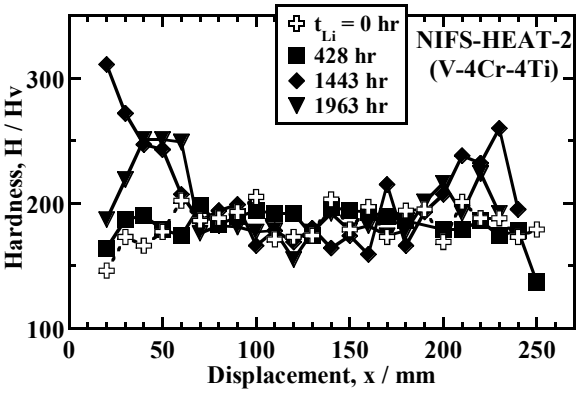

Fig. 2 Hardness distribution in the cross section and along the thickness direction of the coupons after exposure to liquid Li at 1073 K. The surfaces of the coupons are located at 0 mm and 250-270 mm in displacement, x.

Figure 2 shows the hardness distribution in the cross section along the thickness direction of the coupons exposed with liquid Li at 1073 K (T_{Li}). The coupons after Li exposure up to 428 hr exhibited uniform and similar hardness distribution to that before Li exposure. The coupons exposed for 1443 and 1963 hr showed hardening in 60 μm from the surface. Fig. 3 and 4 present the tensile parameters obtained for specimens exposed with liquid Li at 1073 K (T_{Li}). From the previous data[7] and the present data at room temperature (943 hr), miniature tensile tests show data scattering of about 40 MPa in strength (YS, UTS) and 10 % in elongation (UE, TE). Considering these scattering, both strength (YS, UTS) and elongation (UE, TE) before Li exposure were comparable to other V-4Cr-4Ti alloys in the previous study[7, 8]. After Li exposure at 1073 K (T_Li) for 428 and 943 hr, change in UTS was small until 773 K ($T_{Tensile}$), while degradation of UTS at 973 and 1073 K ($T_{Tensile}$), such as 50 and 80 MPa,

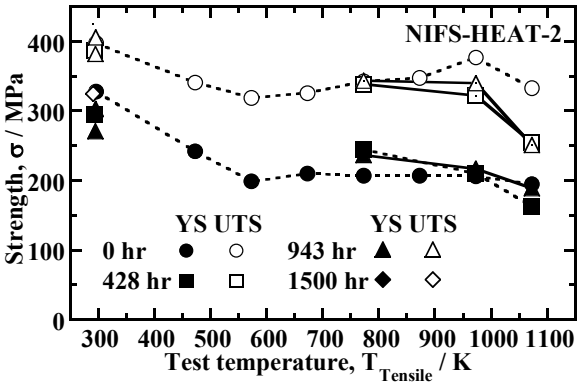

Fig. 3 Tensile test temperature ($T_{Tensile}$) dependence of yield strength (YS, 0.2 % proof stress) and ultimate tensile strength (UTS) of NIFS-HEAT-2 before and after the Li exposures at 1073 K (T_{Li}).

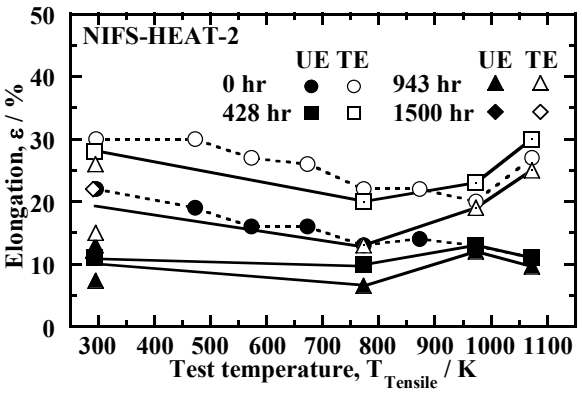

Fig. 4 Tensile test temperature ($T_{Tensile}$) dependence of uniform elongation (UE) and total elongation (TE) of NIFS-HEAT-2 before and after the Li exposures at 1073 K (T_{Li}).

respectively, were considerable. Such clear drop at high temperature was not observed in YS, however YS at 1073 K ($T_{Tensile}$) seems to be lower than that before Li exposure. On the other hand, elongation decrease by Li exposure was observed at RT and 773 K ($T_{Tensile}$), but not at higher temperature. However, all the specimens still keep higher ductility than 6.5 % in UE and 13 % in TE.

Figure 5 shows the microstructures obtained by SEM. Precipitates were observed in all the specimens. Comparing with the specimen before Li exposure, the precipitates increased and grew. The grain boundary was also decorated by precipitates after Li exposure. By energy dispersive X-ray (EDX) analysis, Ti, C, N and O segregations were detected for both precipitates in grain interior and at grain boundary. For the precipitates in grain interior, Ti-C-N is considered to be the main compound, because C and N were introduced in large amount in the present study, and it has been reported that

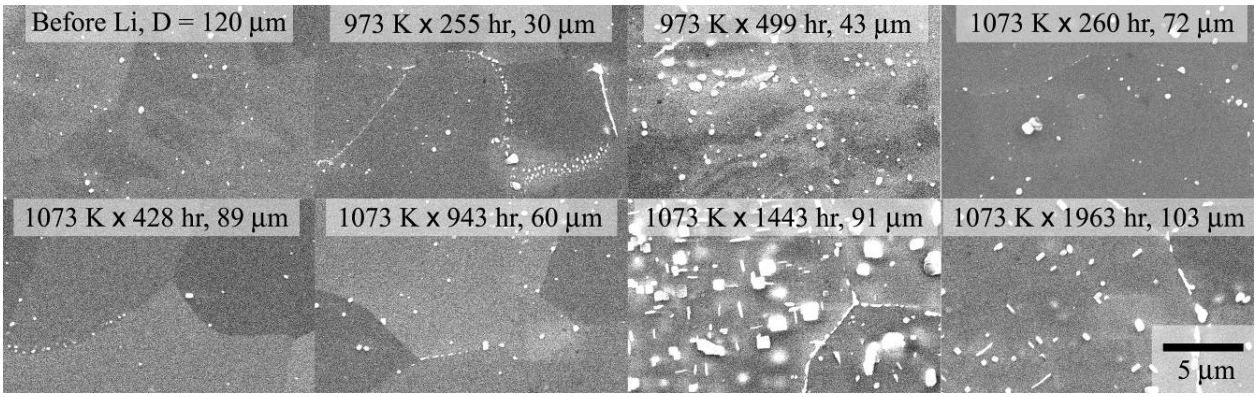

Fig. 5 SEM images before and after the Li exposure. The exposure temperature (T_{Li}) and time are indicated. Observation depth from the coupon surface, D, is also indicated.

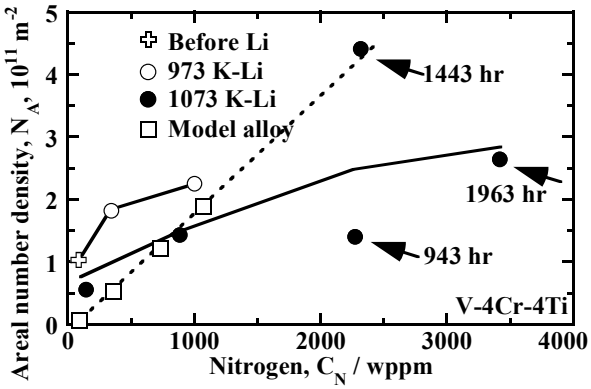

Fig. 6 Correlation between N concentration and areal number density of Ti-C-N type precipitates observed by SEM in NIFS-HEAT-2 and Li-exposed ones. Previous data on V-4Cr-4Ti model alloys with N doping are plotted.

N doping strongly increased the amount of the precipitates compared with O[9]. Fig. 6 presents the areal number density of the Ti-C-N type precipitates in grain interior for Li-exposed specimens compared with the model alloys doped with N. In the Li-exposed specimens, the areal number density is increased with N concentration. The number densities for 973 K (T_{Li}) were higher than the extrapolated (dashed) line by the results on the model alloys. For 1073 K(T_{Li}) exposure, the number densities were consistent with the model alloys until 1000 wppm in N concentration, however the data around 2000 wppm or higher (arrows) were scattered or far from the dashed line. Especially 943 and 1963 hr exposure data were much lower than expected. On the other hand, TEM can detect smaller precipitates than SEM. Fig. 7 shows TEM images before and after Li exposure. Re-precipitation annealing, such as annealing at 1373 K for 1 hr and again at 973 K for 1 hr, was conducted on a part of specimens. The 1373 K annealing dissolves precipitates smaller than about 100 nm observed only in TEM, but does not dissolve the above mentioned Ti-C-N type precipitates observed both in TEM and SEM. The 973 K annealing produces re-precipitation in the matrix. The shape of the precipitates before the re-precipitation was unsettled, whereas disk shape was obtained after the re-precipitation, and the diameter of the disk can be determined as the length of precipitate image. Detailed experimental technique and the impurity behavior have been explained elsewhere[9]. The main compound of the small and unstable precipitates is estimated as Ti-C-O, since C and O were detected in EDX analysis[10], and the number density of the precipitates increased with O concentration in the experiments for model alloys doped with O[9]. Fig. 8 shows the correlation between O concentration and the number density of both the small precipitates (Ti-C-O, < 100 nm) and larger ones (Ti-C-N, > 100 nm) observed by TEM. The Ti-C-O type precipitates decreased with decreasing O concentration by Li exposure. After the re-precipitation annealing, the number density of the Ti-C-O type precipitates after Li exposure was much smaller than that before exposure.

IV. DISCUSSION

IV. A. Impurity transfer

From Fig. 1, C and N were contaminated by Li exposure at both 973 K and 1073 K (T_{Li}). For example, N concentration of Li before melting prior to the exposure was measured as 161 and 171 wppm. During melting of Li prior to the exposure tests, the concentration could change, because melted Li was considered to uptake impurities from the atmosphere. From Table 1, C and N contaminations in batch #1 are much smaller than the other batches. C and N contents in the batch #1 were considered already lower than those in the other batch, because this batch was re-use one and already purified by previous exposure tests by using vanadium alloys. C and N contamination can be controlled by a management of Li

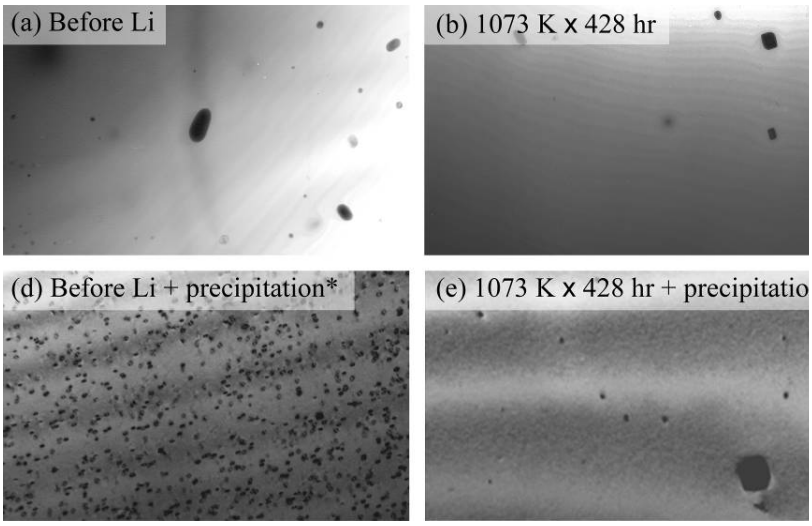

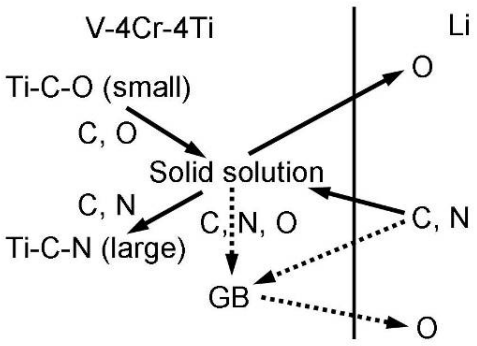

Fig. 9 Impurity transfer between V-4Cr-4Ti alloys and liquid Li. Arrows with solid line are discussed in the present study. Flow to grain boundary is remained to be studied (dashed lines).

Fig. 7 TEM images (a) before and (b), (c) after the Li exposure at 1073 K. Small precipitates were dissolved by an annealing at 1373 K, and then (d), (e) homogeneous re-precipitation was introduced at 973 K. In TEM analysis, observation depth is expected at the center of the specimen, which is about 130 μm from the surface.

purity. C and N are strong hardening agent, if they are dissolved into interstitial positions. From Fig. 2 hardening region was limited around the surface. From SEM observation after the exposure at 1073 K (T_{Li}) for 1443 hr and 1963 hr in Fig. 5, the increase in the amount of Ti-C-N type precipitates was observed at 91 and 103 μm from the surface, where no hardening was detected in Fig. 2. This means that C and N diffused to around the center of the specimens, but scavenged out from solid solution state by producing Ti-C-N precipitates at grain interior and also at grain boundary.

On the other hand, O concentration was reduced by the Li exposure at 1073 K (T_{Li}), but not at 973 K (T_{Li}) up to 500 hr in Fig. 1. Diffusion coefficient of O has been obtained in the previous study on V-4Cr-4Ti alloy[11].

$$D = D_0 \exp (Q / RT) \qquad \text{(Eq. 1)}$$

$D_0 = 4.02 \times 10^{-6}$ m^2 s^{-1}

$Q = 1.30 \times 10^5$ J mol^{-1}

D: Diffusion coefficient, D_0: Constant, R: gas constant = 8.3144 J mol^{-1} K^{-1}, T: temperature

Diffusion range during Li exposure, R_{Li}, can be estimated by following.

$$R_{Li} = D\, t_{Li} \qquad \text{(Eq. 2)}$$

The diffusion ranges at 973 K and 1073 K for 500 hr are calculated as 871 and 1840 μm, respectively. Even 871 μm for 973 K is enough large for O to diffuse out from the specimen with 260 μm in thickness. At 973 K, Ti-C-O type precipitates are considered stable[9] and effective to maintain O. At 1073 K, a part of the Ti-C-O precipitates is thought to be decomposed and dissolved, then O diffused out to Li. Fig. 8 shows an evidence of reduction of small precipitates with decreasing O concentration by Li exposure. The difference in the number density of the precipitates after re-precipitation treatment is clear. Strictly the difference evaluates the sum of impurity in solid solution state and in small precipitates decomposed at 1373 K. However, no softening after the exposure at 1073 K (T_{Li}) for 428 hr in Fig. 2 suggests that the amount of O in solid solution state was not significantly different between before and after Li exposure. Assuming (1) the difference reflects the amount of Ti-C-O precipitates dissolved during the Li exposure and (2) the Ti-C-O precipitates re-produced are disks with d in diameter and the same thickness, tP, the residual O as Ti-C-O precipitates after the 428 hr exposure can be estimated.

$$\frac{(N_P\, \pi\, (d/2)^2\, t_P)_{428\ hr}}{(N_P\, \pi\, (d/2)^2\, t_P)_{Before\ Li}} = \frac{8.0 \times 10^{18}\ \text{m}^{-3} \times (20\ \text{nm})^2}{2.3 \times 10^{20}\ \text{m}^{-3} \times (14\ \text{nm})^2}$$

$$= 7.1\ \% \qquad \text{(Eq. 3)}$$

From this result, the O concentration before Li exposure, 158 wppm, could be decomposed into 99 wppm in the Ti-C-O precipitates and 59 wppm in other states, such as solid solution state, large precipitates or at grain boundary. 7.1 % of the Ti-C-O precipitates, 7 wppm, and the other component, 59 wppm, were remained and resulted in 66 wppm in total.

From the above discussions, a diagram for impurity transfer is suggested as Fig. 9. In the present study, transfer among liquid Li, solid solution state and two types of precipitates (solid lines) was discussed. Impurities are considered to be released or absorbed by the two types of the precipitates in V-4Cr-4Ti alloys. On the other hand, flow to grain boundary (dashed line) could be considerable. The much lower areal number density of 943 and 1963 hr exposure in Fig. 6 can be attributed to migration of impurities to grain boundary and their precipitation. This impurity flow is remained to be studied

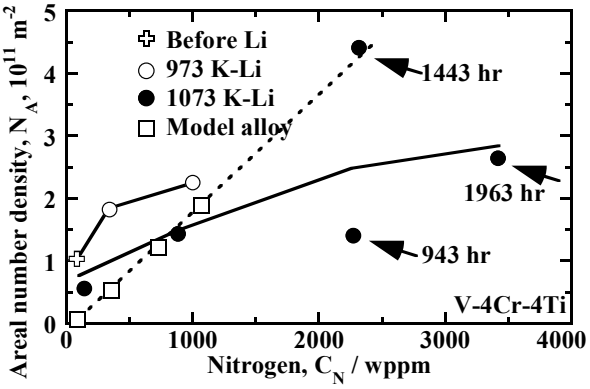

Fig. 8 Correlation between O concentration and number density of the precipitates observed by TEM for the specimens after Li exposure at 1073 K. In order to estimate the amount of the small and unstable precipitates, the precipitates smaller than 100 nm (Ti-C-O type) and larger ones (Ti-C-N type) were counted separately. Here the size, d, means the maximum length of precipitate image. *Re-precipitation heat treatment: 1373 K x 1 hr + 973 K x 1hr

to complete the quantitative analysis for impurity transfers.

IV. B. Effect of Li exposure on tensile property

Ultimate tensile strength at 973 K and 1073 K ($T_{Tensile}$) decreased by the Li exposures. Thousands wppm of C and N contamination indicated in Table 1 did not introduce significant hardening in both hardness and tensile tests. The contaminated C and N were thought not to induce solid solution hardening, since they were, as mentioned above, absorbed by the Ti-C-N precipitates.

Possible mechanisms of 80 MPa softening at 1073 K ($T_{Tensile}$) with impurity reduction are (1) loss of precipitation hardening by Ti-C-O precipitates and (2) loss of solid solution hardening by O. Another mechanism independent of O reduction is (3) change of grain boundary condition. Assuming Orowan type strengthening[12] for (1) case, even the initial contribution to deformation stress of Ti-C-O precipitates before Li exposure is less than 5 MPa. This is maximum estimation by using 1.6 X 1017 in number density in Fig. 8, 100 nm in precipitate size and 1 as interaction coefficient between dislocations and the precipitates. Such small contribution is consistent with no significant softening at room temperature. For (2) case, the softening would be partly explained, if Ti-C-O precipitates before Li exposure release O into the matrix during tensile tests at 1073 K ($T_{Tensile}$). O in pure V is completely in solid solution states. The hardening coefficient of O at RT has been reported as 0.057 Hv / wppm[13]. The estimated amount of O for Ti-C-O is 99 wppm before Li exposure, whereas 7 wppm after the exposure. The reduction of O, 92 wppm is equivalent to 5.2 Hv, which can be roughly converted into about 16 MPa in reduction of deformation stress[12]. This contribution of impurity should be decreased at higher temperature and is still much smaller than UTS decrease at 1073 K ($T_{Tensile}$), therefore another mechanism should be considered. (3) case is the effect of the precipitates covering grain boundaries. Enhancement of grain boundary slip and local fracture of the precipitates are possible. Further investigation on these processes at 1073 K is undergoing.

From Fig. 4, NIFS-HEAT-2 maintained enough large ductility after Li exposure up to 1443 hr, though significant C and N contamination occurred. Li exposure is expected not to induce fatal embrittlement on V-4Cr-4Ti alloys. From the practical viewpoint, the thickness of V alloy plate in fusion blanket is expected as about 5 mm[14]. Scavenging effect is controlled by O diffusion, and gradually reduced in deeper region, therefore the thicker plate probably shows smaller change in tensile properties.

V. CONCLUSIONS

NIFS-HEAT-2 maintained large ductility after Li exposure at 1073 K, while it showed degradation of high temperature tensile strength. Li exposure caused large contamination with C and N. Reduction of O occurred at 1073 K, but not at 973 K up to 500 hr. The C and N contamination lead to the formation of course Ti-C-N type precipitates, but did not cause hardening. O is considered to be released from Ti-C-O type precipitates and scavenged out to the liquid Li.

ACKNOLEDGEMENTS

This study was supported by National Institute for Fusion Science budget code NIFS05UCFF005, JUPITER-II program (Japan-USA Program of Irradiation Test for Fusion Research), and the inter-university cooperative research program of the Irradiation Experimental Facility, Institute for Materials Research, Tohoku University.

REFERENCES

1. Najmabadi et al., Overview of the ARIES-RS reversed-shear tokamak power plant study, Fusion Eng. Des. 38 (1997) 3-25.
2. R. J. Kurtz, K. Abe, V. M. Chernov, D. T. Hoelzer, H. Matsui, T. Muroga and G. R. Odette, Recent progress on development of vanadium alloys for fusion, J. Nucl. Mater., 329-333 (2004) 47-55.
3. R. L. Ammon, Vanadium and vanadium-alloy compatibility behavior with lithium and sodium at elevated temperatures, Metals Reviews, ASTM, 25 (1980) 255-268.
4. K. Fukumoto, H. Matsui, M. Narui, T. Nagasaka, T. Murog, Manufacturing pressurized creep tubes from highly purified V-4Cr-4Ti alloys, NIFS-Heat2, J. Nucl. Mater. 335 (2004) 103-107.

5. T. Nagasaka, N. J. Heo, T. Muroga, M. Imamura, Examination of fabrication process parameters for improvement of low-activation vanadium alloys, Fusion Eng. Des. 61-62 (2002) 757-762.
6. M. L. Grossbeck, Creep of V-4Cr-4Ti in a Li environment, J. Nucl. Mater. 307-311 (2002), 615-619.
7. S. J. Zinkle, A. F. Rowcliffe, C. O. Stevens, High Temperature Tensile Properties of V-4Cr-4Ti, DOE/ER-0313/24, US Department of Energy, 1998, p. 11-14.
8. K. Fukumoto, T. Yamamoto, N. Nakao, S. Takahashi, H. Matsui, High temperature performance of highly purified V-4Cr-4Ti alloy, NIFS-Heat 1, J. Nucl. Mater. 307-311 (2002) 610-614.
9. N. J. Heo, T. Nagasaka, T. Muroga and H. Matsui, Effect of impurity levels on precipitation behavior in the low-activation V-4Cr-4Ti alloys, J. Nucl. Mater., Vol. 307-311 (2002) 620-624.
10. N. J. Heo, T. Nagasaka, T. Muroga, Recrystallization and precipitation behavior of low activation V-Cr-Ti alloys after cold rolling, J. Nucl. Mater., 325 (2004) 53-60.
11. M. Uz, K. Natesan and V. B. Hang, Oxidation kinetics and microstructure of V-(4-5) wt% Cr-(4-5) wt% Ti alloys exposed to air at 300-650°C, J. Nucl. Mater. 245 (1997) 191-200
12. T. Nagasaka, N. J. Heo, T. Muroga, A. Nishimura, H. Watanabe, M. Narui and K. Shinozaki, Impact properties of NIFS-HEAT-2 (V-4Cr-4Ti) after YAG laser welding and neutron irradiation at 563 K, J. Nucl. Mater., 329-333 (2004) 1539-1543.
13. T. Nagasaka, H. Takahashi, T. Muroga, T. Tanabe and H. Matsui, Recovery and Recrystallization Behavior of Vanadium at Various Controlled Nitrogen and Oxygen Levels, J. Nucl. Mater., 283-287 (2000) 816-821.
14. L. A. El-Guebaly, The ARIES Team, Overview of ARIES-RS neutronics and radiation shielding: key issues and main conclusions, Fusion Eng. Des., 38 (1997) 139-158.

Biaxial Thermal Creep of Two Heats of V4Cr4Ti at 700 and 800°C in a Liquid Lithium Environment

Meimei Li[1], T. Nagasaka[2], D. T. Hoelzer[1], M. L. Grossbeck[3], S. J. Zinkle[1], T. Muroga[2], K. Fukumoto[4], H. Matsui[5], M. Narui[6]

[1]Materials Science and Technology Division, Oak Ridge National Laboratory, Oak Ridge, TN 37831, USA
[2]National Institute for Fusion Science, Oroshi, Toki, Gifu 509-5292, Japan
[3]Nuclear Engineering Department, University of Tennessee, Knoxville, TN 37996, USA
[4]NPESE, University of Fukui, Bunkyo, Fukui 910-8507, Japan
[5]Institute for Materials Research, Tohoku University, Katahira, Sendai, 980-8577, Japan
[6]International Research Center for Nuclear Materials Science, Institute for Materials Research, Tohoku University, Oarai, Ibaraki 311-1313, Japan

This paper presents biaxial thermal creep results for the vanadium alloy V4Cr4Ti in liquid lithium using US Heat 832665 and two batches of tubing made from NIFS-Heat-2. The tests were performed at 700 and 800□C over a stress range of 30-120 MPa using pressurized tube specimens. Lithium environments changed C, N and O concentrations in V4Cr4Ti. Oxygen removal from the alloy to lithium was small when there was a significant pickup of nitrogen during exposures. The creep response of V4Cr4Ti was characterized by an inverted primary creep followed by a secondary creep or an accelerating creep up to creep rupture. A normal primary creep was also observed in US Heat 832665 when tested at 700□C and 120 MPa. Improved creep rupture properties were observed in the JP-NIFS-Heat-2 specimens compared to the US-NIFS-Heat-2 specimens. Creep response of V4Cr4Ti is apparently dependent on the heat, tubing production, and stress and temperature conditions

1. Introduction

Vanadium alloys are candidates for lithium cooling and breeding blanket structural applications in advanced fusion systems. V4Cr4Ti is a reference alloy that has been studied extensively by the fusion community. The upper operating temperature limit of vanadium alloys is expected to be in the range of 650-750°C, i.e. 0.43-0.47 Tm [1], where high temperature tensile properties and creep performance are critical for fusion structural applications. Therefore, it is of high importance to evaluate creep performance of V4Cr4Ti alloys in liquid lithium environments.

Vanadium alloys are highly susceptible to contamination by interstitial impurity elements, such as oxygen, nitrogen and carbon. Previous investigations have shown that interstitial impurities can significantly affect tensile properties and load-carrying capacity at high temperatures [2]. The strength is increased and the ductility is decreased by pickup of interstitial solutes. The susceptibility to pickup of interstitial elements is more serious if long exposure times are involved. Interstitial impurities can be introduced during fabrication, welding and joining processes and in service. Liquid lithium creates a unique environment that can substantially change the interstitial concentration (C, N, O) in vanadium alloys. Thermodynamic calculations indicated that oxygen preferentially transfers from vanadium to lithium, and nitrogen and carbon move in the opposite direction [3]. The additions of substitutional solutes such as Cr and Ti do not change the impurity transfer direction, but may alter the kinetics of impurity reactions. There are insufficient data characterizing the interstitial reactions of V4Cr4Ti in liquid lithium and their effects on mechanical behavior, particularly on creep performance.

Preliminary work has been carried out to measure the creep properties of V4Cr4Ti in lithium environments at 665 and 765□C on the US Heat 832665 by Grossbeck [4,5]. Grossbeck's results indicated that the creep strain rate of V4Cr4Ti in liquid lithium was higher than in vacuum due to loss of oxygen from exposure to lithium. Additional data are needed to characterize lithium thermal creep of different heats and tubing batches of V4Cr4Ti. This paper summarizes the experimental results on the creep deformation of pressurized creep tubes made from US Heat 832665 and from two batches of tubing of NIFS-Heat-2 in the stress range of 30-120 MPa while exposed to liquid lithium at 700 (0.45 Tm) and 800□C (0.50 Tm) for up to 2500 h. The creep behavior of V4Cr4Ti is characterized by the curves of creep strain vs. exposure time and creep rate vs. creep strain. The creep response of three batches of V4Cr4Ti tubing in liquid lithium was compared.

2. Experimental Procedure

Pressurized creep tube specimens were fabricated from V4Cr4Ti alloy tubing from the US Heat 832665 and from two batches of tubing of the NIFS-Heat-2. The Japan tubing of NIFS-Heat-2 was fabricated using tube vendors in Japan (designated JP-NIFS-Heat-2) and the US tubing of NIFS-Heat-2 was fabricated using vendors in US (designated US-NIFS-Heat-2). The detailed manufacturing processes of JP-NIFS-Heat-2 creep specimens were reported by Fukumoto et al [6], and the fabrication of US Heat 832665 and US-NIFS-Heat-2 creep tube specimens can be found in the references of

[7,8]. The US Heat 832665 pressurized tubes contained 161 wppm N, 509 wppm C and 700 wppm O for a total impurity content of 1370 wppm. The US-NIFS-Heat-2 creep tube specimens contained 277 wppm N, 586 wppm C and 519 wppm O for a total impurity content of 1382 wppm. The JP-NIFS-Heat-2 creep tube specimens had 120 wppm N, 120 wppm C and 330 wppm O for a total impurity content of 570 wppm. Note that the JP-NIFS-Heat-2 tubing has a higher purity than the other two batches of V4Cr4Ti tubing. All creep specimens were annealed at 1000°C for 1-2 h which produced an average grain size of 20-30 μm. The creep tube specimens have a nominal outer diameter of 4.57 mm and a wall thickness of 0.254 mm with a total length of 25.4 mm.

The US-NIFS-Heat-2 and JP-NIFS-Heat-2 creep tube specimens were tested at 800°C over a stress range of 30-90 MPa. The US Heat 832665 and JP-NIFS-Heat-2 creep tube specimens were tested at 700°C at stresses of 90-120 MPa. All the thermal exposure tests of pressurized creep tubes were performed in static liquid lithium. The details of the experimental setup were described previously [4,9]. Pure lithium (>99.9%) was supplied by Sigma-Aldrich (161 ppm N) or by Chemetall Foote Corp. (65 ppm N). To minimize contamination of lithium metal by nitrogen and carbon, the commercial lithium was either purified by hot-trapping with Zr getters prior to exposure tests, or included Zr or Ti getters during lithium exposure tests. A batch of lithium was used for no more than two exposure tests and then replaced with a new batch of lithium. After exposure, all specimens were removed from lithium and cleaned using liquid anhydrous ammonia. This cleaning method generates very little hydrogen so that hydrogen embrittlement can be minimized. The creep specimens were then measured for creep deformation and reloaded into liquid lithium for further exposure. This process was repeated at exposure intervals of 255, 499, 1019 and 2019 h at 700°C and at intervals of 428, 688, 943, 1443, 1963 and 2580 h for JP-NIFS-Heat-2 creep tube specimens at 800°C and at intervals of 260, 515, 1015, and 1535 h for US-NIFS-Heat-2 creep tube specimens at 800°C.

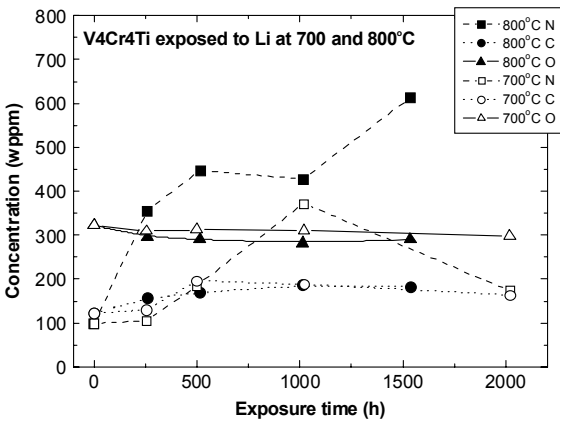

Figure 1. Interstitial impurity contents (O, N, C) in V4Cr4Ti after lithium exposure at 700 and 800°C.

The outer diameters (OD) of pressurized creep tubes were measured at room temperature before and after each exposure using a laser profilometer with a resolution of 0.2 μm. A specimen was loaded vertically into the laser profilometer with the same orientation each time, and the tube profile was obtained by measuring the central 12.7 mm of the tube at 500 unique locations using a standard helical pattern program. The mean OD of a tube was computed by averaging the central 300 measurements to preclude any end effects. A standard gauge pin was periodically measured to compensate for any errors from the laser profilometer and the environment. Each specimen was measured three times in a non-consecutive manner, and the average from these three measurements was used to determine the creep strain. The mid-wall effective creep strain of a pressurized creep tube was determined by assuming that the material is incompressible and the deformation is uniform in plastic flow. The mid-wall von Mises effective stress of a pressurized creep tube was calculated using the analytical solution of stress state for a thick-walled pressured cylinder [10]. The dimensions of the creep specimen at the test temperature were compensated by the linear thermal expansion coefficient of vanadium alloys [11].

Coupon specimens of V4Cr4Ti (nominal dimensions of 25×6×3 mm) were exposed to liquid lithium along with pressurized creep tubes for chemical analysis of O, N and C after each exposure to monitor contamination from lithium environments. Coupon specimens were machined from a 40% cold-rolled R-plate of the US Heat 832665. The initial contents of interstitial impurities in coupon specimens were 322 wppm O, 99 wppm N and 122 wppm C.

3 Results and Discussion

3.1 Chemical Changes

The changes in interstitial impurity (C, N, O) concentration in coupons specimens are shown in Fig. 1 as a function of lithium exposure time at 700 and 800□C. Significant contamination by nitrogen was observed at both temperatures. The source of nitrogen contamination is uncertain. The decrease in nitrogen content in the coupon specimen at 2000 h and 700°C is likely due to stronger chemical affinity of nitrogen with Ti getters that were included during exposure. There was a slight pickup of carbon as exposure time increased. The decrease in oxygen contents in V4Cr4Ti coupon specimens was much smaller than expected. Oxygen concentration dropped only about 30 ppm after 1500 h at 800°C or after 2000 h at 700°C. Grossbeck [5] reported a loss of 600 ppm oxygen and an increase of ~50 ppm nitrogen after ~2500 h at 800°C.

It is possible that the significant pickup of nitrogen in the present tests altered the kinetics of interstitial solute transfer in the V4Cr4Ti-lithium system, leading to reduced oxygen egress (e.g., due to an enhanced formation of Ti (C,O,N) precipitates). It should be mentioned that changes in interstitial impurity contents in creep tube specimens may not be the same as in coupon specimens, due to different volume and area ratios between the two specimen geometries. Note also that creep tubes were under straining during exposure, while coupon specimens were in the stress-free condition. However, the data shown in Fig. 1 demonstrate the general trend of chemical changes in creep tube specimens that were exposed to liquid lithium.

3.2 Creep Curves

The US-NIFS-Heat-2 and JP-NIFS-Heat-2 pressurized creep tubes were tested in liquid lithium at 800°C at stress levels 30-90 MPa. Their creep strain – exposure time curves are shown in Fig. 2(a). To illustrate the change in creep rate during the test, the creep strain – time curves were differentiated to obtain the creep strain rate.

The creep strain rate is plotted as a function of the average strain on a semi-log scale and shown in Fig. 2(b) for the 800□C lithium exposure tests. Creep deformation of V4Cr4Ti was found to be sensitive to the magnitude of the applied stress. The creep of V4Cr4Ti did not follow the classical three-stage creep pattern (primary, secondary and tertiary) under the test conditions shown in Fig. 2. The US-NIFS-Heat-2 specimen tested at 96 MPa exhibited a continuously increasing creep rate with increasing strain up to creep failure. The 30-40 MPa US-NIFS-Heat-2 creep specimens showed an increasing creep rate with creep strain in the primary stage as well. This inverted primary transient behavior is often observed in solid solution strengthened alloys [12]. The creep response of the JP-NIFS-Heat-2 specimens is similar to that of the US-NIFS-Heat-2 specimens, i.e. an inverted primary transient followed by either a steady-state or an accelerating creep up to creep rupture. If a steady-state is observed, it often occurred at about 1-2% creep strain.

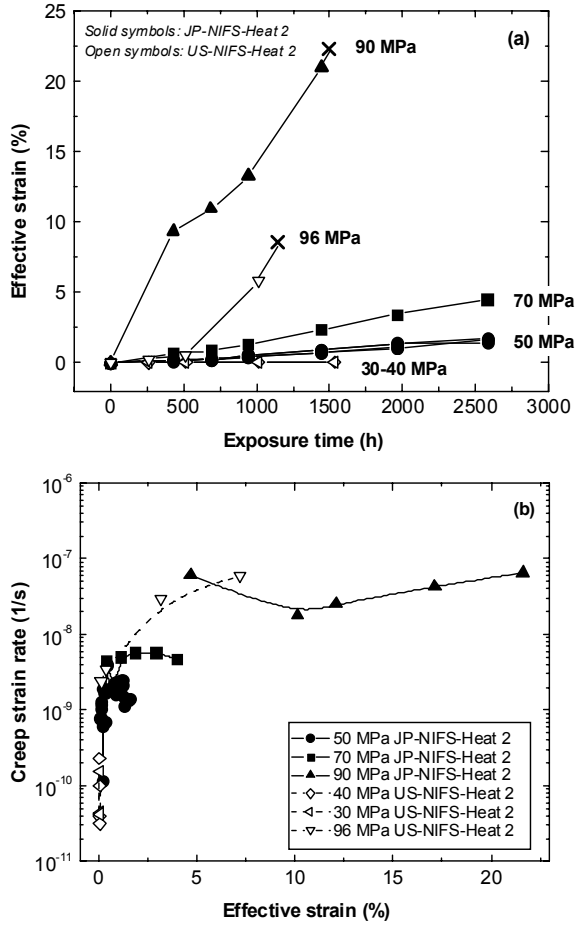

Figure 2. Creep curves of V4Cr4Ti exposed to liquid lithium at 800□C (a) effective strain vs. exposure time, and (b) creep strain rate vs. effective strain.

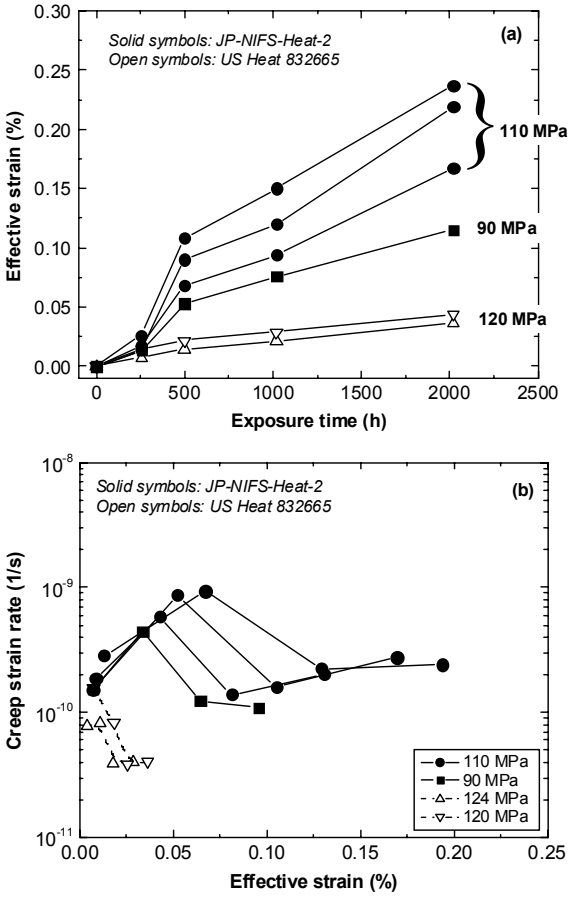

Figure 3. Creep curves of V4Cr4Ti exposed to liquid lithium at 700□C (a) effective strain vs. exposure time, and (b) creep strain rate vs. effective strain.

However, there was a short decelerating creep (creep rate decreasing with increasing strain) in the primary stage that was observed only in the JP-NIFS-Heat-2 specimens but not in the US-NIFS-Heat-2 specimens, as shown in Fig. 2.

Lithium thermal exposure tests were performed at 700°C on the US Heat 832665 and JP-NIFS-Heat-2 pressurized creep tubes in the stress range of 90-120 MPa. The creep strain – time curves and creep rate – strain curves of the 700°C tests are shown in Figs. 3(a) and 3(b), respectively. The JP-NIFS-Heat-2 creep tube specimens exhibited an increasing creep rate followed by a decreasing creep rate and later another increasing creep rate with increasing creep strain, similar to their creep behavior at 800°C. The US Heat 832665 creep tube specimens, however, showed a normal primary transient behavior when tested at ~120 MPa. There were not sufficient data to characterize the secondary and tertiary creep behavior at 700°C.

The method of production of tubing apparently played an important role in the creep response of V4Cr4Ti when exposed to liquid lithium. The JP-NIFS-Heat-2 tubing and the US-NIFS-Heat-2 tubing were made from the same heat (NIFS-Heat-2) but by different vendors. The JP-NIFS-Heat-2 tubing has less interstitial impurity contamination than the US-NIFS-Heat-2 tubing (the total interstitial impurity level in the JP-NIFS-Heat-2 was about 40% of that in the US-NIFS-Heat-2). Both the JP-NIFS-Heat-2 and the US-NIFS-Heat-2 exhibited an inverted primary transient behavior followed by either a steady-state or an acceleration of creep until failure for the stress levels and temperatures examined. The difference in creep character between these two batches of tubing was a deceleration of creep in the early stage of creep that was observed only in the JP-NIFS-Heat-2 specimens. Similar decelerating creep phenomena were reported in the literature for nickel alloys [13,14]. This behavior was explained by strengthening of oxide and nitride formed on specimen surfaces of nickel alloys when tested in air. Visual inspection of creep tube specimens of V4Cr4Ti indicated discoloration of the JP-NIFS-Heat-2 specimens, but no discoloration was observed on the US-NIFS-Heat-2 creep tube specimens. Auger Electron Spectroscopy detected nitrogen in the discolored area of specimen surfaces. The formation of a nitride film on the JP-NIFS-Heat-2 specimen surface was likely associated with the observed deceleration of creep. It is not understood why the discoloration and decelerating creep was observed in JP-NIFS-Heat-2 specimens but not in US-NIFS-Heat-2 creep tube specimens.

The tubing processing affected rupture properties as well. The 96 MPa US-NIFS-Heat-2 creep tube specimen failed at 1148 h at a creep strain of 8.6%, while the 90 MPa JP-NIFS-Heat-2 pressurized tube failed at 1499 h at a creep strain of 22.3%. The more "pure" JP-NIFS-Heat-2 specimen exhibited a higher rupture strain and longer rupture life than the less "pure" US-NIFS-Heat-2. This implies that alloy purity may be important to rupture properties. Small changes in grain size, texture, tubing quality, etc. could also be important factors in controlling creep strength.

4 Conclusion

Thermal creep behavior of three batches of V4Cr4Ti tubing made from NIFS-Heat-2 and US Heat 832665 was investigated in a liquid lithium environment at 700 and 800°C. Significant pickup of nitrogen was observed in both 700 and 800°C lithium exposure tests. The loss of oxygen from V4Cr4Ti to lithium was much smaller than that reported in previous studies. The kinetics of oxygen transfer in a V Alloy-Li system apparently was affected by nitrogen contamination of the V4Cr4Ti. The creep properties of V4Cr4Ti are dependent on alloy heat, tubing production method, stress and test temperature. The creep behavior of V4Cr4Ti in liquid lithium is characterized by an inverted primary transient period followed by a steady-state or an accelerating creep to rupture. Normal primary creep was observed in US Heat 832665 at 700°C. The JP-NIFS-Heat-2 with less initial interstitial impurities showed a higher rupture strain and a longer rupture life than the US-NIFS-Heat-2 at 800°C, a difference due to impurity content and/or material variables introduced in the production process. In addition, a short deceleration in the primary creep stage was observed only in the JP-NIFS-Heat-2 creep specimens, not in the US-NIFS-Heat-2 creep specimens.

Acknowledgments

The research was supported by the US-Japan JUPITER II Program and by the Office of Fusion Energy Sciences, the U.S. Department of Energy under contract DE-AC05-00OR22725 with Oak Ridge National Laboratory, managed and operated by UT-Battelle, LLC. We would like to thank L. T. Gibson and Janie Gardner for their technical support, and Drs. F. W. Wiffen and T. S. Byun for their technical review.

References

[1] D. L. Smith, M. C. Billone, S. Majumdar, R. F. Mattas, D. -K. Sze, J. Nucl. Mater. 258-263 (1998) 65.
[2] R. E. Gold, D. L. Harrod, R. L. Ammon, R. W. Buckman, Jr., R. C. Svedberg, Technical assessment of vanadium–base alloys for fusion reactor applications – final report, Westinghouse Electric Corporation, C00-4540-1, 1978.
[3] K. Natesan, J. Nucl. Mater. 115 (1983) 251.
[4] M. L. Grossbeck, J. Nucl. Mater. 307-311 (2002) 615.
[5] M. L. Grossbeck, Fusion Materials Semiannual Progress Report, DOE/ER-0313/32 (2002) 6.

[6] K. Fukumoto, H. Matsui, M. Narui, T. Nagasaka, T. Muroga, J. Nucl. Mater. 335 (2004) 103.
[7] A. F. Rowcliffe, D. T. Hoelzer, and M. L. Grossbeck, Fusion Materials Semiannual Progress Report, DOE/ER-0313/35 (2003) 2.
[8] A. F. Rowcliffe, D. T. Hoelzer, W. R.Johnson, and C. Young, Fusion Materials Semiannual Progress Report, DOE/ER-0313/34 (2003) 6.
[9] M. L. Grossbeck, Fusion Materials Semiannual Progress Report, DOE/ER-0313/30 (2001) 8.
[10] S. Timoshenko and J.N. Goodier, Theory of Elasticity, McGraw-Hill, 2nd ed., 1951.
[11] W.D. Porter, K. B. Dinwiddie, M. L. Grossbeck, Fusion Materials Semiannual Progress Report, DOE/ER-0313-16 (1994) 260.
[12] H. Oikawa and T. G. Langdon, Creep Behavior of Crystalline Solids, B. Wilshire and R. W. Evans (Ed.), 1985, p. 33.
[13] R. Widmer and N. J Grant, Trans. ASME J. Basic Eng., 82 (1960) 882.
[14] P. Shahinian and M. R. Achter, Joint International Conference on Creep, Institute of Mechanical Engineering, London, 1963, pp. 7-49.

Recent Progress on Development of Vanadium Alloys for Fusion

RJ Kurtz[1*], K Abe[2], VM Chernov[3],
DT Hoelzer[4], H Matsui[5], T Muroga[6] and GR Odette[7]

[1]*Pacific Northwest National Laboratory, P.O. Box 999, Richland, WA 99352, USA*
[2]*Department of Quantum Science and Energy Engineering, Tohoku University, Sendai 980-8579, Japan*
[3]*Bochvar Research Institute of Inorganic Materials, P.O. Box 369, Moscow, Russia*
[4]*Oak Ridge National Laboratory, P.O. Box 2008, Oak Ridge, TN 37831, USA*
[5]*Institute for Materials Research, Tohoku University, Sendai 980-8577, Japan*
[6]*National Institute for Fusion Science, Oroshi, Toki, Gifu 509-5292, Japan*
[7]*University of California at Santa Barbara, Department of Mechanical and Environmental Engineering, Santa Barbara, CA 93106, USA*

Considerable progress has been made toward development of vanadium alloys for fusion. Much of the recent research has focused on vanadium alloys containing 4-5% Cr and 4-5% Ti, but a number of alternative compositions and processing routes have been explored in an effort to achieve improved performance. The goal of this paper is to review significant new results and to highlight critical issues that remain for future research. Progress in understanding the influence of interstitial impurities on microstructural evolution in both thermal and radiation environments are covered. The current state of knowledge of hardening and embrittlement of vanadium alloys in response to neutron irradiation is reviewed. Atomic-scale computer simulations to elucidate fundamental irradiation damage mechanisms are presented. The thermal and irradiation creep behavior of V-4Cr-4Ti is summarized along with an overview of the effects of He on tensile properties.

1. Introduction

It has been long recognized that V alloys are attractive candidate materials for fusion power system structural components due to their low induced activation characteristics coupled with high-temperature strength and high thermal stress factor. As noted in recent reviews [1-3] research over the past several years has successfully resolved many of the significant feasibility issues associated with use of V alloys in fusion first-wall/blanket structures. The emphasis of the worldwide V alloy development effort has been on the V-Cr-Ti system, with an alloy containing 4-5% Cr and 4-5% Ti serving as a reference composition in many research programs. This paper highlights recent progress on V alloys with regard to 1) atomistic studies of point defect behavior, 2) understanding microstructural evolution under variable temperature irradiation conditions, 3) assessing hardening and embrittlement following low-temperature irradiation, 4) determining thermal and irradiation creep rates, 5) evaluating the effects of He on tensile and creep deformation, and 6) exploration of alternative alloy compositions for improved performance. Critical issues that require further research and development are described.

2. Atomistic Studies of Point Defect Behavior

Point defects, such as self-interstitial atoms (SIA) and vacancies, are produced in abundance when V alloys are irradiated with neutrons. Evolution of the microstructure, and therefore the properties of the material, is controlled by how these defects migrate through the lattice and interact with one another or with sinks such as dislocations, grain boundaries and other internal interfaces. Therefore, knowledge of the properties, formation and migration mechanisms of point defects and defect clusters is essential for developing robust models of radiation damage. Atomistic simulations play a key role in developing this information. The reliability of atomistic simulations depends largely on the efficacy of the interatomic potential utilized. Recently two new V potentials [4-6] have been developed in an effort to provide an improved description of the atom interactions in this metal. One of the potentials [4,5] uses the Finnis-Sinclair (FS) formalism. That potential was derived from an extensive set of first-principles calculations of six different SIA geometries and vacancies. The first-principles calculations revealed that the <111> dumbbell is the most stable SIA in V with a formation energy of about 3.1 eV. The other potential [6] uses the modified embedded atom method (MEAM) developed by Baskes [7] to represent V. An important aspect of MEAM is that it attempts to account for the directional bonding characteristics of transition metals with partially filled d-orbitals. Satou et al, [6] refit several of the MEAM parameters derived by Baskes [7] to produce a new potential for V with elevated temperature elastic constants that are in better agreement with experimental values.

Zepeda-Ruiz and coworkers [8, 9] have utilized the new FS V potential to study the temperature and orientation dependence of the threshold displacement

energy (TDE). Molecular dynamics simulations were performed to determine the minimum kinetic energy transferred by a primary knock-on atom to a lattice atom that resulted in the formation of a stable Frenkel pair. They found a minimum TDE of 13 eV corresponding to displacements along a <100> direction. The maximum TDE of 51 eV was observed in a direction close to <110>. The possibility for a larger TDE could not be excluded since the simulations did not span all possible angles. The TDE is essentially independent of temperature since the magnitude of the TDE is much greater than thermal energies. Comparison of the TDE in V with experimental values for Fe and Mo revealed that the directional anisotropy is comparable in Mo but the TDE ordering in <110> and <111> orientations is different in Fe.

Zepeda-Ruiz et al., [10, 11] also investigated the character of SIA loops in V using the new FS potential. Their simulations showed that SIA dislocation loops with Burgers vectors were the lowest energy configuration in V and migrated rapidly along their glide cylinder. Dislocation loops with and Burgers vectors easily rotated into orientations at low temperatures during relaxation of the simulation cell. In contrast to Fe, where a metastable loop is very close in energy to the ground-state orientation, constrained loops in V possess much higher formation energies than loops, and the energy difference increases with the size of the loop. Simulations were also performed to explore the interaction of two mobile clusters in V. The intersection of loops on different glide cylinders has been proposed as a possible mechanism for loop formation in Fe. Similar work carried out on V indicate that junctions form during the intersection of two loops, but the junction has low thermal stability and rotates into a orientation at temperatures between 327 and 527°C.

Finally, Han [12] and Zepeda-Ruiz [13] examined SIA diffusion in V as a function of temperature to determine the predominant mechanisms. Their MD results showed that oriented dumbbells migrate rapidly along directions. The SIA migration mechanism was found to be temperature dependent. At low to intermediate temperatures (-173 – 327°C) the SIA executed a 1D random walk along a direction. Above 427°C the SIA began to make infrequent rotations from one direction to another direction. This resulted in 3D like migration trajectory that consisted of long segments of 1D diffusion punctuated by abrupt reorientations. As the temperature increased the frequency of rotation events increased and the lengths of the 1D segments decreased. The apparent activation energy for SIA diffusion increased with increasing temperature. Detailed study of their simulation results revealed that the intrinsic activation energy for SIA diffusion is not temperature dependent, but that SIA jumps are correlated and the correlation factor is highly temperature dependent below 527°C.

3. Microstructural Evolution

A recent emphasis of microstructural evolution studies has been an exploration of the effects of varying irradiation temperature. It is well known that the irradiation temperature can have a significant impact on microstructural development [14]. Variable irradiation temperature can result in significant changes in the microstructure, especially when the temperature excursion occurs between the nucleation and growth regimes [15]. At lower temperatures nucleation of defect clusters is maximized, while at higher temperatures cluster growth and coarsening is maximized. These effects have been explored in neutron and ion irradiations to low doses but not, until recently, to higher dose levels. One of the major tasks of the Japan-U.S. Fusion Cooperation Program (JUPITER) was to investigate the effects of varying irradiation temperature on V alloys to a dose of 4 dpa [16].

In a recent paper Zinkle et al., [17] showed a moderate enhancement of radiation-induced precipitates and dislocation loops for V-4Cr-4Ti undergoing varying temperature irradiation 360/520°C compared to irradiation at a constant temperature of 520°C. The varying temperature irradiation consisted of eight cycles in which the initial 10% was conducted at 360°C and the remaining 90% at 520°C. Varying temperature conditions produced precipitates of finer size and greater number density than under constant temperature conditions, but overall the quantitative effect of the low-temperature excursions was relatively small. Zinkle et al., [17] suggested that more pronounced differences might have been observed had the low-temperature portion of each cycle been below the recovery Stage V temperature. More recently Watanabe et al., [18] examined pure V and four model V alloys from the same experiment, irradiated under the same conditions. These investigators found that varying temperature enhanced void formation in pure V and V-5Cr compared to isothermal irradiation, and a small number of <100> oriented carbides were observed in pure V. For V-4Cr-4Ti and V-5Ti alloys a higher density of Ti oxides was produced under varying temperature but, as noted by Zinkle et al., [17] the effects of varying temperature were not large. It should be noted that while recent work has not shown substantial microstructural differences between varying temperature and isothermal irradiation conditions, some differences were observed. Such differences may be exacerbated by selection of different temperature extremes or by performing irradiations to higher doses [19]. A better understanding of the effects of varying irradiation temperature will require additional experiments but, more importantly, the development of quantitative models to predict material performance under complex irradiation conditions.

Another aspect of V alloy metallurgy that has received increased attention in recent years is the interaction of V with interstitial impurities such as C, O and N. Several recent studies [20-22] have shown that most precipitates result from reaction of V or solute atoms with these impurities. These precipitates impede dislocation motion increasing the strength of the alloy. Ti lowers the mobility of the interstitials and reacts to form precipitates at > ~600°C under thermal annealing and > ~300°C under neutron irradiation. Globular Ti- (CON) precipitates appear above ~1000°C. The solvus temperature for globular precipitates is between 1200°C and 1300°C. Following dissolution the interstitial content can be redistributed into a high number density of nano-size {100} plates by controlled precipitation. The precipitate crystal structure is FCC for both {100} plate and globular morphologies. The interstitial concentration varies considerably for {100} plate type precipitates. A conclusion of these investigations is that a better understanding of precipitate nucleation and growth is needed along with an increased knowledge of the range of interstitial solubility. To gain a better understanding of the effects of interstitial impurities on irradiated properties a special set of V alloys [23] with carefully controlled levels of C, O and N has been included in an upcoming JUPITER irradiation experiment.

4. Hardening and Embrittlement

Neutron irradiation at temperatures at and below 400°C gives rise to hardening and loss of uniform strain [24]. This temperature limit may increase with increasing dose. Hardening and loss of ductility become more pronounced with increasing dose and decreasing irradiation temperature, and are accompanied by varying degrees of flow localization, as evidenced by the formation of dislocation channels in the irradiated microstructure [25]. However, recent finite element modeling of the deformation of flat tensile specimens has demonstrated that the loss of uniform strain can be affected by both an increase in yield strength as well as a decrease in work hardening [26]. Engineering stress strain curves showing no uniform strain and the onset of necking coincident with yield can be generated with constitutive equations that exhibit a gradual yield drop followed by a strain hardening regime. Moreover, the modeling results show that significant irradiation hardening can persist to high strain. Ongoing modeling work will benefit from calibration against data from new techniques that permit strain mapping in all three dimensions during uniform and localized strain, as well as specimen and test designs that explore stress states other than uniaxial tension [27]. The modeling effort also provides a guide for future experiments to explore and understand the effects and consequences of microscopic flow localization on macroscopic deformation behavior.

While considerable information on irradiation hardening of V alloy base metals is available there is a corresponding lack of data on weld metal. Nagasaka et al., [28] recently completed an exploratory study of the effects of low-dose neutron-irradiation on the impact properties of NIFS Heat-2 weld metal. Miniature Charpy impact specimens of V-4Cr-4Ti base and weld metal were irradiated at 290°C to a dose of 0.08 dpa in the JMTR. Weld metal specimens hardened more than base metal specimens, but the effects of neutron irradiation were reduced if a post-weld heat treatment in the range 600 to 950°C was applied prior to irradiation. The predominant radiation defects found in both base and weld metal microstructures were identified as dislocation loops. The higher density of loops found in weld metal compared to base metal did not account for all of the hardness difference. The authors postulated an additional component of hardening associated with decoration and stabilization of dislocation loops by interstitial impurities released into solution by dissolution of Ti-(CON) precipitates during welding.

In an effort to improve high-temperature strength and oxidation resistance of V-xCr-4Ti alloys, Sakai and coworkers [29] performed a study of the effects of Cr additions on fracture properties. The Cr content varied from 4 to 20%. Changes in the ductile-to-brittle transition temperature (DBTT) were correlated with the Cr content and precipitate microstructures produced during heat treatments following cold working. Their research shows that the DBTT is about -190°C when the Cr content is < 10% but rises sharply to –30°C for alloys with more than 10% Cr. The increased DBTT was associated, in part, to increased flow stress due to solid solution strengthening. The sharp rise in DBTT for Cr > 10% was also related to a substantial increase in large diameter (> 400 nm) Ti-(CON) and TiO2 precipitates. This work nicely illustrates the difficulty of altering the alloy composition to improve high-temperature strength at the expense of degrading fracture resistance. The process of optimizing V alloy composition and heat treatment procedures for best performance in a radiation environment is certainly not simple or straightforward.

5. Thermal and Irradiation Creep

A significant amount of thermal creep data on pure vanadium and various V-Cr-Ti alloys was generated several years ago [30-36]. These data demonstrate that Cr significantly increases the creep resistance of V. More recently, several studies have characterized the thermal creep performance of V-4Cr-4Ti in vacuum and liquid Li [37-44]. Both uniaxial [37-38] and biaxial [41-42] tests were performed in vacuum with different starting concentrations of interstitial O. The results show that the normalized secondary creep rate is power-law dependent on stress with a stress exponent of ~4 at normalized

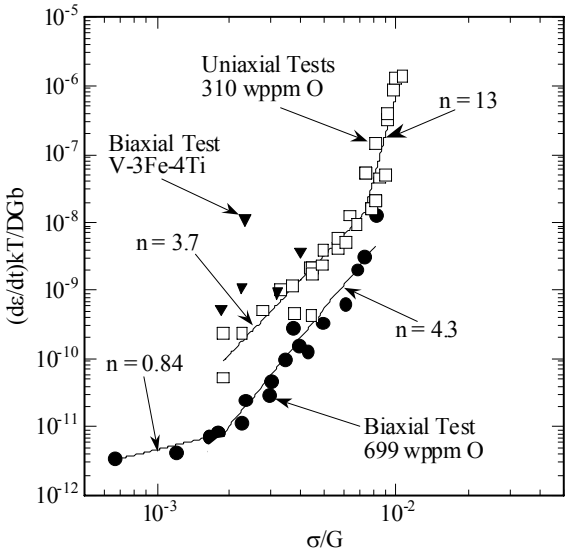

Figure 1. Stress dependence of the normalized effective mid-wall creep strain for unirradiated V-4Cr-4Ti and V-3Fe-4Ti. Normalized stresses are Von Mises effective stresses for biaxial tests. The initial oxygen concentration of the uniaxial and biaxial test specimens was 310 wppm and 699 wppm, respectively.

stresses greater than 0.002. The activation energy for creep between 700 and 800°C is about 300 kJ/mole, which is similar to the activation energy for self diffusion in pure V suggesting that in this regime of temperature and stress the predominant creep mechanism appears to be climb-assisted dislocation motion. Limited data at the same temperatures but lower stresses indicates that the creep mechanism may change since the stress exponent appears to decrease to about unity, Figure 1.

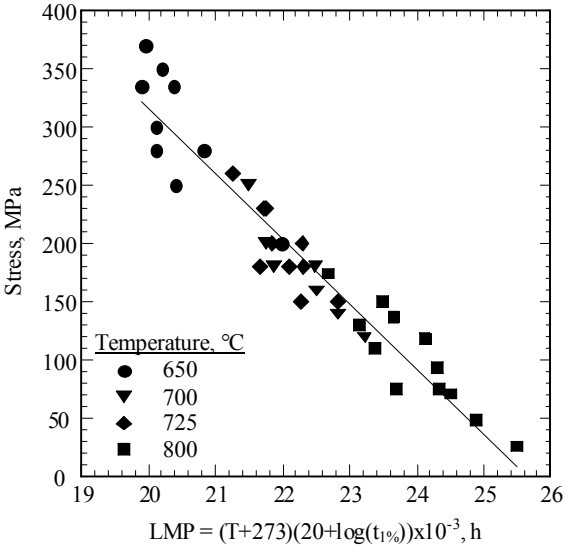

Figure 2. Larsen-Miller Parameter plot (time to reach 1% creep strain) for V-4Cr-4Ti tested in vacuum (uniaxial and biaxial specimens) at the indicated temperatures.

The effect of oxygen on creep strength was convincingly demonstrated in several experiments. The creep rates measured in vacuum with tensile samples [37] containing about 310 wppm O were several times greater than creep rates from pressurized tubes [41,42] with an initial O concentration of about 700 wppm. Similarly, the creep rates measured in Li were higher than those in vacuum [39,40,43]. This is consistent with the vacuum creep data since Li has a higher affinity for O than V and will, after long exposure times, lower the O level in the alloy. Recently Fukumoto et al. [38] and Koyama et al. [44] utilized a novel Zr-foil gettering heat treatment to reduce interstitial O and N concentrations to very low levels in V-4Cr-4Ti and V-10Cr-5Ti sheet stock. Tensile specimens prepared from these highly purified alloys were used to study dynamic strain aging (DSA) and creep properties. The results of these investigations show that high-temperature tensile and creep strengths decrease substantially as interstitial O decreases. Further, DSA was suppressed by O removal as evidenced by a large decrease in the height of post-yield load serrations. Contrary to expectation, the temperature range over which a negative strain rate sensitivity parameter was observed increased rather than decreased suggesting a larger temperature window for heterogeneous deformation. An effort to resolve this inconsistency will be the subject of a future investigation on highly purified unalloyed V.

The maximum operating temperature limit for V alloys in design studies is typically assumed to be about 700°C [45]. Alternately, it has been suggested that V alloys might be capable of operation at 750°C [46]. The thermal creep database may be used to derive an estimate of the limiting stress to avoid creep damage in a structure for a specific time at temperature. A Larsen-Miller Parameter plot of the time to reach 1% creep strain is presented in Figure 2. A creep strain limit of 1% is representative of structural design criteria for first-wall components for a fusion power system [47]. Selecting a first-wall life of 105 h yields limiting stresses of 74 MPa at 700°C and only 4 MPa at 750°C from the curve fit to the data. The coolant pressure for a V/Li system is about 0.5 MPa [47], which should result in relatively low applied loads in the first-wall. It is important to note, however, that detailed stress analyses have not been performed in recent V/Li design studies, therefore all the expected loadings are not well known. The creep data indicates that an attractive design may be feasible at 700°C, but probably not at 750°C. Improving the thermal creep strength would add margin at 700°C to account for uncertainties in anticipated loadings and perhaps expand the design window to higher temperatures.

The irradiation creep database for the V-Cr-Ti alloy system is very sparse. Only a few experiments have been

performed between 300-500°C to damage levels of a few dpa. There is a significant divergence in effective strain rate at effective stresses greater than about 125 MPa. A Russian study suggests a bilinear relationship between the effective irradiation creep strain rate and the effective stress, but such behavior was not observed in more recent experiments carried out under the auspices of the JUPITER program [48]. More data will be forthcoming from experiments recently inserted in the HFIR and JOYO reactors but dose levels will again be on the order of only 5-7 dpa.

For the future additional thermal creep experiments are warranted to examine ways to improve performance through alternative compositions and microstructures without degrading properties such as fracture toughness. More work is needed to define the irradiation creep characteristics of these alloys as there is almost a complete lack of data at any significant dose. Further, the effect of alloy composition and heat treatment on irradiation creep remains to be explored.

6. Helium Embrittlement

The upper temperature limit for V alloys is most probably determined by the effect of gaseous transmutants such as He on creep rupture behavior in the 600-800°C temperature regime. The most realistic studies to perform involve simultaneous creep deformation and introduction of displacement damage and He at fusion relevant rates (~4 appm He/dpa). In the absence of a 14 MeV volumetric neutron source these types of experiments are exceedingly difficult to perform and consequently are seldom done. More often, pre-implanting a tensile specimen with a particular quantity of He and then conducting a tensile test at a strain rate ranging from 10-3 to 10-4 s-1 have been used to characterize the effect of He on elevated temperature mechanical properties. Occasionally pre-implanted tensile specimens have also been neutron-irradiated to explore the concomitant effects of He and radiation damage on tensile properties.

The effect of He on tensile properties has been studied over a broad range of temperatures for a variety of V alloys [49-57]. Figure 3 shows the temperature dependence of the normalized tensile ductility for He concentrations ranging from 14 to 480 appm. The normalized ductility is the total tensile elongation for a He-implanted specimen, ε_{tot}(He), divided by the total tensile elongation of a He free specimen tested at the same temperature, ε_{tot}(ref). In all these experiments He was pre-implanted prior to performing the tensile test by either cyclotron irradiation [49-52, 55-57] or by a modified tritium trick technique [53, 54] where the implantation temperature is typically quite low relative to the tensile test temperature. Matsui et al. [58] have suggested that the He-implantation method can

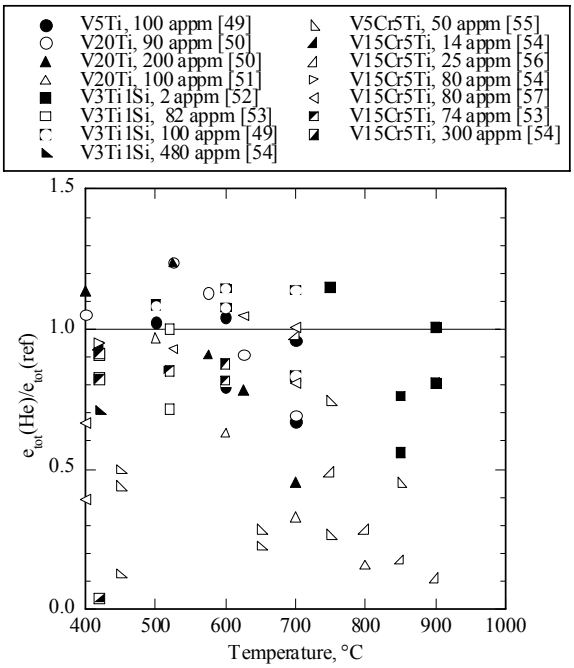

Figure 3. Temperature dependence of the normalized total elongation for several V alloys pre-implanted with He. Implantation was performed by cyclotron injection or a modified tritium trick technique.

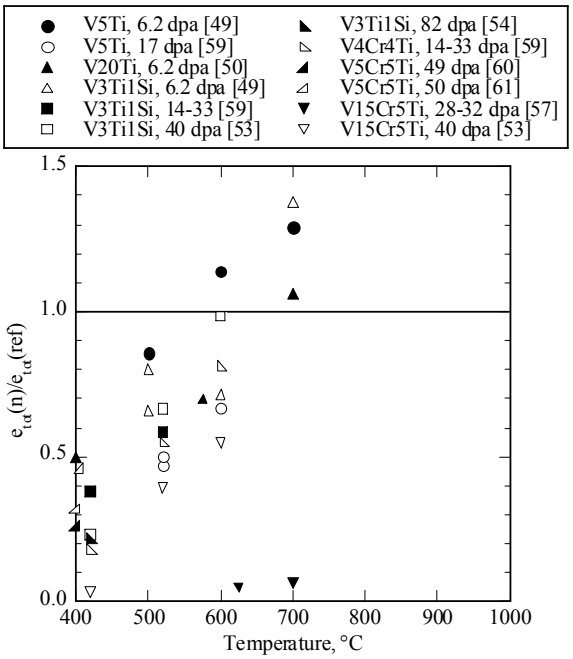

Figure 4. Temperature dependence of the normalized total elongation for several He-free, neutron-irradiated V alloys. The irradiation and tensile test temperatures were the same in all cases.

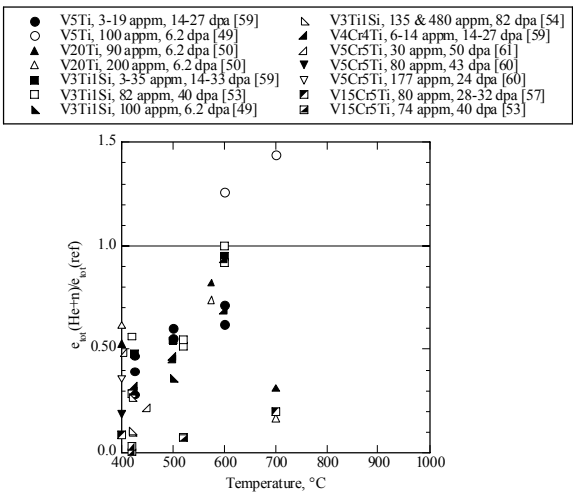

Figure 5. Temperature dependence of the normalized total elongation for several V alloys pre-implanted with He and then neutron-irradiated. Implantation was performed by cyclotron injection or a modified tritium trick technique. The irradiation and tensile test temperatures were the same in all cases.

significantly affect the tensile test results, but the data in Figure 3 do not display a trend indicating that one implantation technique leads to systematically lower ductility than another. Normalized tensile ductilities with values near unity indicate no significant effect of He. Close inspection of the data reveals that He at levels of ≤ 25 appm did not significantly degrade tensile ductility at any test temperature. When the He concentration was ≥ 25 appm tensile ductility was substantially reduced at temperatures ≥ 650°C. A puzzling feature of the data is the apparent effect of He at temperatures around 420 - 450°C. Low normalized tensile ductility in this temperature regime is evident for the Cr bearing V alloys only, suggesting that He may be more deleterious for high strength alloys.

It is instructive to also examine the effect of neutron irradiation on tensile ductility for He free and pre-implanted specimens to determine the relative contributions of He and neutron irradiation on ductility reduction. Figure 4 gives a plot of the temperature dependence of the normalized tensile ductility for He-free V alloys neutron irradiated to doses ranging from about 6 to 82 dpa [49, 50, 53, 54, 57, 59-61]. The data exhibits some scatter but there is a clear trend that the effects of neutron irradiation on tensile ductility are minimal for irradiation temperatures ≥ 650°C. A similar trend is found for specimens pre-implanted with He and then irradiated, Figure 5 [49, 50, 53, 54, 57, 59-61]. These results indicate that He pre-implantation did not further reduce tensile ductility beyond that already caused by neutron irradiation. Results from the Dynamic Helium Charging Experiment (DHCE) [59], which closely simulates the actual fusion environment because He and neutron damage are produced concurrently, displays the same trend. It is clear from the data in Figures 3-5 that over the temperature range 400 to 600°C displacement damage is the largest contributor to loss of ductility. It is important to recognize, however that none of the experiments mentioned above exactly simulated the environment that a structural material will face in a real fusion power system, namely high-temperature, time-dependent deformation in the presence of simultaneous He production and displacement damage so the relative importance of each of these variables may be different for a real power system.

Recently, Chuto and co-workers [62] explored the effect of pre-implanted He on the creep properties of V-4Cr-4Ti. It was anticipated that the effects of He would be more pronounced at strain rates typical of creep deformation, although data by van Witzenburg and Scheurer [63] indicate that V-5Ti pre-implanted with up to 100 appm He and neutron irradiated to 4.5 dpa show little sensitivity of the total elongation to strain rate over the range 10-6 to 10-3 s-1. Helium was cyclotron implanted by Chuto et al. [62] at 700°C followed by creep testing at the same temperature. Creep testing of He-free control samples exposed to the same thermal history as the implanted ones was also performed. Interestingly, the creep strength of the He implanted specimens was significantly better than the He-free samples, even though the fracture surfaces of the implanted specimens were 5 to 15% intergranular. The superior creep performance of the He-implanted specimens was attributed to irradiation strengthening, but this explanation lacks appeal since radiation damage associated with the 700°C implantation should be minimal. Matrix strengthening from a fine dispersion of He clusters seems more likely, but microstructural characterization remains to be performed.

The effect of He on microstructural development still needs to be addressed intensely. Work performed to date has lead to qualitative understanding of basic effects, but accurate quantitative evaluations are not possible due to insufficient data. A 14 MeV fusion neutron source is absolutely essential to acquiring the needed data, but progress may be possible with simulation techniques such as the DHCE.

7. Advanced Alloys

While V alloys offer many attractive properties for fusion applications there is growing recognition that the reference composition, V-4Cr-4Ti, may not be fully adequate to meet the stringent requirements of an advanced power system in terms of resistance to He embrittlement and creep damage. Consequently, alternative compositions are being considered to improve the low-temperature radiation resistance and high-temperature strength. Chen and co-workers [64] have

recently studied the properties of V-based alloys containing 6-8 weight percent W. A broad range of properties were investigated including recovery and recrystallization behavior, the room temperature tensile properties, the solid solution strengthening efficiency of various elements, the susceptibility to H embrittlement, and oxidation kinetics in air from 400 to 600°C. The recovery and recrystallization behavior of V-W alloys not including Ti was similar to unalloyed V, while V-W alloys including Ti gave results similar to V-4Cr-4Ti. The N concentration affected the temperature for onset of recovery in a V-6W-1Ti alloy. Increasing the N concentration from 5 to 30 wppm was sufficient to increase the temperature for onset of recovery by about 100°C. Tungsten, on a per atom basis, was observed to be a more effective strengthener than either Ti or Cr. The room temperature tensile properties of the V-W alloys examined by Chen et al. were equal to or better than a V-4Ti alloy. The addition of W did not influence the H embrittlement behavior. Although Ti tends to enhance H absorption, it appears to be the key element for imparting high resistance to H embrittlement. Parabolic oxidation kinetics were observed for all of the alloys investigated by Chen et al. This result is consistent with an earlier study [65] that demonstrated the oxidation kinetics depend strongly on the O partial pressure. At high O partial pressures parabolic oxidation kinetics are found and low O partial pressures linear kinetics are obeyed. From an operational point of view the most relevant environmental conditions are low O partial pressures and temperatures of about 700°C.

It is well known that V alloys are readily embrittled by neutron irradiation at temperatures below about 400°C [2,3]. Since grain and interphase boundaries act as efficient sinks for point defects produced under irradiation, alloys possessing ultra-fine grains and fine-scale particles may be more resistant to radiation-induced embrittlement. To test this hypothesis, Kobayashi and co-workers [66] examined the effects of neutron irradiation on the microstructure and hardness of V alloys containing small amounts of Y. Two V alloys with 1.6 and 2.6 weight percent Y were prepared by mechanical alloying techniques. The microstructure of the unirradiated materials displayed a mixture of fine grains a few hundred nanometers in diameter along with a small amount of coarse grains a few micrometers in diameter. TEM disks prepared from these materials were irradiated in the JMTR at 290°C to a dose of 0.25 dpa and at 800°C to a dose of 0.7 dpa. The results of this study showed that formation of interstitial loops and voids was suppressed in fine grain regions. Hardness increases associated with low-temperature neutron irradiation (290°C) were relatively modest (3-70 Hv) compared to conventional V alloys processed using ingot metallurgy procedures. Kobayashi et al., found that the ultra-fine grains were stable, only limited particle coarsening occurred at 800°C, and grain miniaturization effectively suppressed formation of radiation-induced defects. Another potential benefit such microstructures may provide is increased resistance to He embrittlement. Higher dose irradiation data is needed to validate the efficacy of this approach for improving radiation resistance.

8. Critical Issues for Future Research

While significant progress has been made toward development of V alloys for fusion applications there remain a number of critical issues that should receive attention in ongoing research programs. The present understanding of the influence of interstitial impurities such as C, O, and N on tensile, creep and fracture properties is not sufficient. Low-temperature ($\leq$ 450°C) properties appear to be improved by removing C, O, and N but high-temperature creep strength is reduced. Ideally, elements such as C, O and N should be considered as alloying elements in V, analogous to C in steel, rather than undesirable impurities. To achieve this state will require much better control of these elements.

Recent atomistic modeling studies have advanced our understanding of fundamental point defect behavior in V alloys, but more needs to be done to develop robust models of material behavior that offer predictive capability. Complex experiments such as variable temperature irradiations need further detailed microstructural characterization coupled with the development of appropriate models that enhance our understanding of the experimental observations.

Although not described in this paper, a lot of progress has been made in development of constitutive laws for unirradiated V alloys [27]. This methodology needs to be extended to irradiated material. Further, the effects of flow localization and the contribution of dynamic strain aging need to be included. Extension of the Master Curve - ΔT and micromechanics approaches to characterize and predict the temperature dependence of fracture toughness for irradiated material should be a high priority. A complete fracture resistance model must also consider the impact of non-hardening embrittlement mechanisms driven by impurity-solute segregation, phase instabilities, and the production of He and H. In addition, subcritical crack growth (fatigue and environmentally assisted) and the realities of actual service such as warm pre-stressing, shallow surface flaws, multiaxial/mixed mode loading, dynamic strain aging, and creep relaxation will also play a role.

The thermal creep performance of V alloys may need improvement. The current reference alloy, V-4Cr-4Ti, may not posses adequate creep strength. There is a need to explore alternative alloying elements for improved creep performance and He management and some steps in this direction have already been taken [64, 66]. Higher dose irradiation creep data and an understanding of the

effects of alloy composition on irradiation creep is required. The effects of He and H on creep resistance, swelling and post-irradiation tensile properties over the range $600 \leq T \leq 800°C$ is needed. Development of an alloy with a multiphase microstructure may be needed for more efficient He management since the sink strength of V-4Cr-4Ti for He trapping may not be adequate.

Acknowledgments

This work was performed, in part, under the auspices of the U. S. Department of Energy, Office of Fusion Energy Sciences, under contract DE-AC06-76RLO1830.

References

[1] T. Muroga, M. Gasparotto, S.J. Zinkle, Fus. Eng. & Design 61-62 (2002) 13.
[2] T. Muroga, T. Nagasaka, K. Abe, V.M. Chernov, H. Matsui, D.L. Smith, Z.-Y. Xu S. J. Zinkle, J. Nucl. Mater. 307-311 (2002) 547.
[3] R.J. Kurtz, K. Abe, V.M. Chernov, V.A. Kazakov, G.E. Lucas, H. Matsui, T. Muroga, G.R. Odette, D.L. Smith, S.J. Zinkle, J. Nucl. Mater. 283-287 (2000) 70.
[4] S. Han, L.A. Zepeda-Ruiz, G.J. Ackland, R. Car, D.J. Srolovitz, Phys Rev B (2002) 220101(R).
[5] S. Han, L.A. Zepeda-Ruiz, G.J. Ackland, R. Car, D.J. Srolovitz, J Appl Phys Vol. 93, No. 6 (2003) 3328.
[6] M. Satou, S. Yip, K. Abe, J Nucl Mater 307-311 (2002) 1007.
[7] M.I. Baskes, Phys Rev B 46 (1992) 2727.
[8] L.A. Zepeda-Ruiz, S. Han, D.J. Srolovitz, R. Car, B.D. Wirth, Fusion Materials Semi-Annual Progress Report, DOE/ER-0313/34, (2003) 32.
[9] L.A. Zepeda-Ruiz, S. Han, D.J. Srolovitz, R. Car, B.D. Wirth, Phys Rev B 67 (2003) 134114.
[10] L.A. Zepeda-Ruiz, J. Marion, B.D. Wirth, D.J. Srolovitz, Fusion Materials Semi-Annual Progress Report, DOE/ER-0313/34, (2003) 31.
[11] L.A. Zepeda-Ruiz, J. Marion, B.D. Wirth, accepted for publication in Phil. Mag.
[12] S. Han, R. Car, D.J. Srolovitz, and L.A. Zepeda-Ruiz, Fusion Materials Semi-Annual Progress Report, DOE/ER-0313/33, (2003) 2.
[13] L.A. Zepeda-Ruiz, S. Han, G.J. Ackland, R. Car, D.J. Srolovitz, Fusion Materials Semi-Annual Progress Report, DOE/ER-0313/34, (2003) 30.
[14] M. Kiritani, J Nucl Mater 160 (1988) 135.
[15] H. Matsui, in Proceedings of the 6th IEA and JUPITER Joint Workshop on Vanadium Alloys for Fusion Energy Applications, Tucson, AZ (2002).
[16] K. Abe, A. Kohyama, C. Namba, F.W. Wiffen, R.H. Jones, J Nucl Mater 258-263 (1998) 2075.
[17] S.J. Zinkle, N. Hashimoto, D.T. Hoelzer, A.L. Qualls, T. Muroga, B.N. Singh, J Nucl Mater 307-311 (2002) 192.
[18] H. Watanabe, T. Muroga, and N. Yoshida, these proceedings.
[19] N. Nita, T. Yamamoto, T. Iwai, K. Yasunaga, K. Fukumoto, H. Matsui, J Nucl Mater 307-311 (2002) 398.
[20] N.J. Heo, T. Nagasaka, T. Muroga, H. Matsui, J Nucl Mater 307-311 (2002) 620.
[21] D. T. Hoelzer, J. Bentley, in Proceedings of the 6th IEA and JUPITER Joint Workshop on Vanadium Alloys for Fusion Energy Applications, Tucson, AZ (2002).
[22] A. Nishimura, A. Iwahori, N.J. Heo, T. Nagasaka, T. Muroga, S.-I. Tanaka, these proceedings.
[23] D.T. Hoelzer, A.F. Rowcliffe, L.T. Gibson, Fusion Materials Semi-Annual Progress Report, DOE/ER-0313/34, (2003) 22.
[24] R.J. Kurtz, R.H. Jones, E.E. Bloom, A.F. Rowcliffe, D.L. Smith, G.R. Odette, F.W. Wiffen, Nucl Fusion Vol. 39, No. 11Y (1999) 2055.
[25] P.M. Rice, S.J. Zinkle, J Nucl Mater 258-263 (1998) 1414.
[26] G.R. Odette, M.Y. He, E.G. Donahue, P. Spaetig, T. Yamamoto, J Nucl Mater 307-311 (2002) 171.
[27] G.E. Lucas, K. Abe, in Proceedings of the 6th IEA and JUPITER Joint Workshop on Vanadium Alloys for Fusion Energy Applications, Tucson, AZ (2002).
[28] T. Nagasaka, N.J. Heo, T. Muroga, A. Nishimura, H. Watanabe, M. Narui and K. Shinozaki, these proceedings.
[29] K.Sakai, M.Satou, M.Fujiwara, K.Takanashi, A.Hasegawa and K.Abe, these proceedings.
[30] K.R. Wheeler, E.R. Gilbert, F.L. Yaggee and S.A. Duran, Acta Metallurgica 19 (1971) 21.
[31] M. Shirra, KfK 2440, Kernforschungszentrum Karlsruhe, (1989).
[32] H. Boehm and M. Schirra, KfK 774, Kernforschungszentrum Karlsruhe, (1968).
[33] W. Pollack, R.W. Buckman, R.T. Begley, K.C. Thomas and E.C. Bishop, WCAP-3487-16, Westinghouse Electric Corporation (1968).
[34] T. Kainuma, N. Iwao, T. Suzuki and R. Watanabe, J. Less Common Metals 86 (1982) 263.
[35] H.M. Chung, B.A. Loomis and D.L. Smith, in U.S. Contribution, 1994 Summary Report, Task T12: Compatibility and Irradiation Testing of Vanadium Alloys, ANL/FPP/TM-287, ITER/US/95/IV MAT 10 (1995) 87.
[36] J. R. Stewart, J.C. LaVake and S.S. Christopher, Data presented at an AEC/RDT Working Group Meeting, Ames, Iowa (1968).
[37] K. Natesan, W.K. Soppet, A. Purohit, J Nucl Mater 307-311 (2002) 585.
[38] K. Fukumoto, T. Yamamoto, N. Nakao, S. Takahashi, H. Matsui, J Nucl Mater 307-311 (2002) 610.
[39] M.L. Grossbeck, J Nucl Mater 307-311 (2002) 615.
[40] M.L. Grossbeck, Fusion Materials Semi-Annual Progress Report, DOE/ER-0313/31, (2001) 2.
[41] R.J Kurtz, A.M. Ermi, H. Matsui, Fusion Materials Semi-Annual Progress Report, DOE/ER-0313/31, (2001) 7.
[42] D.S. Gelles, Fusion Materials Semi-Annual Progress Report, DOE/ER-0313/31, (2001) 17.

[43] M.L. Grossbeck, R.J Kurtz, L.T. Gibson, M.J. Gardner, Fusion Materials Semi-Annual Progress Report, DOE/ER-0313/32, (2002) 6.
[44] M. Koyama, K. Fukumoto, H. Matsui, these proceedings.
[45] H. Matsui et al., Fusion Technology 30 (1996) p. 1293.
[46] D.L. Smith, M.C. Billone, S. Majumdar, R.F. Mattas and D.K. Sze, J. Nucl. Mater. 258-263 (1998) p. 65.
[47] S. Majumdar, Fus. Eng. & Des. 49-50 (2000) p. 19.
[48] H. Tsai, R.V. Strain, M.C. Billone, T.S. Bray, D.L. Smith, M.L. Grossbeck, K. Fukumoto, H. Matsui, Fusion Materials Semi-Annual Progress Report, DOE/ER-0313/27, (2000) 65.
[49] W. van Witzenburg, E. de Vries, ASTM STP 1125 (1992) 915.
[50] M.P. Tanaka, E.E. Bloom, J.A. Horak, J Nucl Mater 103&104 (1981) 895.
[51] A.I. Ryazanov, V.M. Manichev, W. van Witzenburg, J Nucl Mater 227 (1996) 304.
[52] K. Ehrlich, H. Boehm, Proceedings of the IAEA Conference on Radiation Damage in Reactor Materials 2, Vienna, Austria (1969) 349.
[53] D.N. Braski, ASTM STP 956 (1987) 271.
[54] D.N. Braski, ASTM STP 1047 (1990) 161.
[55] M. Satou, H. Koide, A. Hasagawa, K. Abe, Sci Rep RITU A45 (1997) 157.
[56] A.T. Santhanam, A. Taylor, S.D. Harkness, Nucl Metal, Vol 18 (1973) 302.
[57] M.L. Grossbeck, J.A. Horak, ASTM STP 956 (1987) 291.
[58] H. Matsui, M. Tanaka, M. Yamamoto, A. Hasagawa, K. Abe, ASTM STP 1175 (1993) 1215.
[59] M.C. Billone, Fusion Materials Semi-Annual Progress Report, DOE/ER-0313/23, (1997) 3.
[60] M. Satou, H. Koide, A. Hasegawa, K. Abe, H. Kayano, H. Matsui, J Nucl Mater 233-237 (1996) 447.
[61] M. Satou, T. Chuto, H. Koide, A. Hasagawa, K. Abe, Mat Res Soc Symp Proc Vol. 540 (1999) 591.
[62] T. Chuto, N. Yamamoto, J. Nagakawa, Y. Murase, these proceedings.
[63] W. van Witzenburg, H. Scheurer, Proceedings of the Fourteenth Fusion Technology Symposium, Avignon, France (1986) 987.
[64] J.M. Chen, T. Muroga, S.Y. Qiu, T. Nagasaka, W.G. Huang, M.J. Tu, Y. Chen, Y. Xu, Z.Y. Xu, these proceedings.
[65] B.A. Pint, J.R. Distefano, J. Nucl. Mater. 307-311 (2002) 560.
[66] S. Kobayashi, Y. Tsuruoka, K. Nakai and H. Kurishita, these proceedings.

Effects of doping elements on oxidation properties of V–Cr–Ti type alloys in several environments

M. Fujiwara [a], K. Natesan [b], M. Satou [a], A. Hasegawa [a], K. Abe [a]
[a] Department of Quantum Science and Energy Engineering, Graduate School of Engineering, Tohoku University, Aramaki-aza-Aoba 01, Aoba-ku, Sendai 980-8579, Japan
[b] Energy Technology Division, Argonne National Laboratory, 9700 South Cass Avenue, Argonne, IL 60439 USA

The alloys examined in this study include V–4Cr–4Ti–0.5Si, V–4Cr–4Ti–0.5Al, V–4Cr–4Ti–0.5Y and V–4Cr–4Ti.Oxidation experiments were conducted in air. After oxidation, tensile tests, hardness measurements and scanning electron microscopy were performed. Surface oxidation layers were identified by X-ray diffraction (XRD) analysis. Based on this study, the alloy doped with Y was excellent in oxidation resistance at 600 and 700 ┌C. The XRD indicated that V2O5 was the primary oxide phase for the alloys tested at 700 °C, except for the V–4Cr–4Ti–0.5Y alloy. The oxide identified at all temperatures in V–4Cr–4Ti–0.5Y alloy was VO_2, that was also observed for the other alloys after testing at 600 ┌C. It was suggested that the formation of thin and dense VO_2 oxide layers had an important role for superior oxidation properties of the V–4Cr–4Ti–0.5Y alloy. From the results of this study, further optimization of the V–4Cr–4Ti alloy could be possible by controlling the small addition of yttrium.

1. Introduction

The alloys of V–Cr–Ti with and without Si, Al and Y [1] show excellent mechanical properties at high temperature [2–4] and irradiation characteristics [5,6] as low-activation structural materials for nuclear fusion reactors [7,8]. The improvement of the oxidation resistance at high temperature is considered from practical standpoint as one of the important problems [9–11]. In Table 1, the oxidation issues of vanadium alloys for fusion applications are summarized [12–16]. Therefore, it is very important to examine the oxidation behavior (in various atmospheres in high-temperature regions assumed for fusion reactors) of V–4Cr–4Ti and V–4Cr–4Ti–Si–Al–Y alloys regarded as candidates for further development of the practical vanadium alloys. Especially important is to clarify the effect of Si, Al and Y which are the doping elements added to the alloy on the high-temperature oxidation behavior [17–19]. In this study, oxidation experiments were conducted in air at high temperature on the V–4Cr–4Ti type alloys which contained additions of Si, Al and Y. The objectives of this study are to evaluate the oxidation behavior, determine the effect of doping elements of the alloy on the mechanical behavior, and obtain the basic guideline for the development of low-activation oxidation-resistance vanadium alloys for application in fusion reactors.

2. Experimental Procedure

The alloys examined in this study included (in wt%) V–4Cr–4Ti–0.5Si, V–4Cr–4Ti–0.5Al, V–4Cr–4Ti–0.5Y and V–4Cr–4Ti. The alloys were prepared at Tohoku University and V–4Cr–4Ti alloy was developed at the National Institute for Fusion Science (NIFS). In order to reduce the contamination of the interstitial impurity elements (such as C, O and N), high purity V and Ti obtained by electron beam refining were used, and an arc-melting furnace with a contamination reducer was adopted for alloying. The chemical compositions of these alloys are shown in Table 2. Small-size tensile test specimens were punched out from the 0.25 mm thick sheet obtained by cold rolling, and the size of the gauge section was 5 x 1.2mm^2. All the specimens were annealed at 1000°C for 1 h under 1x10^{-3} Pa vacuum to obtain recrystallized microstructures. Oxidation experiments were conducted in dry air for 1 h at 500, 600, 700 and 750 °C. The weight increase measurements were carried out after oxidation. Tensile tests were conducted at room temperature at a strain rate of 6.7x10^{-4} s^{-1}. Secondary electron microscopy was used to characterize the microstructures of oxidized specimens. The surface oxide layers were identified by X-ray diffraction (XRD) and the effect of the doping elements on the oxidation resistance of the alloy was examined.

3. Results and Discussion

Fig. 1 shows the weight increase per surface area of each alloy after oxidation in air for 1 h. None of the alloys showed a significant increase in weight up to 600°C. The V–4Cr–4Ti alloy showed a substantial weight gain after oxidation at 700 ┌C whereas V–4Cr–4Ti–0.5Al and V–4Cr–4Ti–0.5Y alloys did not show negligible weight change after oxidation at 700°C. After oxidation at 750 °C, all the alloys containing dopant elements exhibited substantial weight increase; a similar test could not be conducted on the V–4Cr–4Ti alloy due to melting of the surface oxide (V_2O_5). Among the three alloys, the Y-containing alloy exhibited the maximum weight gain at 750°C.

Fig. 2 presents stress–strain curves of the V–4Cr–4Ti and V–4Cr–4Ti–0.5Y alloys, in as-annealed conditions and after oxidation testing at 500, 600, 700 and 750°C.

The tensile elongation of each alloy was reduced with increasing oxidation temperature. The V–4Cr–4Ti alloy

Table 1 Oxidation issues of vanadium alloys for fusion applications[12–16]

Exposure environment	Applicable component in a fusion system	Typical service condition
Vacuum	Plasma facing component	≈1×10^{-4} Pa [12]
Helium	He-cooled blanket structure	350–650 °C [13]
Lithium	Li-cooled blanket structure with ceramic coating	300–700 °C (for ARIES-RS) [14]
Air	Vacuum component safety under leakage	Operating temperature, ≈600 °C [15]
Water	Component with water cooling	High-temperature pressurized water, 200–300 °C [16]

Table 2 Chemical composition of the vanadium alloys used in the study (in wt%)

	V	Ti	Cr	Si	Al	Y	C	O	N	H
V–4Cr–4Ti	Balance	4.1	4.4	–	–	–	0.0067	0.0181	0.0088	0.0018
V–4Cr–4Ti–0.5Si	Balance	4.01	4.03	0.421	0.02	0.0002	0.0228	0.0161	0.0552	0.0010
V–4Cr–4Ti–0.5Al	Balance	3.85	3.97	0.014	0.44	0.0002	0.0238	0.0140	0.0641	0.0008
V–4Cr–4Ti–0.5Y	Balance	3.95	3.96	0.014	0.02	0.452	0.0230	0.0150	0.0648	0.0012

specimen oxidized at 700°C broke with almost no plasticity whereas the V–4Cr–4Ti–0.5Y alloy specimen broke in a similar mode after oxidation at 750°C. The results of the fracture surface analysis obtained after the tensile test (see Fig. 3) showed three distinct zones namely, a surface oxidized layer, a cleavage fracture area and ductile rupture zone in both V–4Cr–4Ti and in V–4Cr–4Ti–0.5Y alloys after oxidation at 700 and 750°C, respectively. The cleavage crack region and surface oxidized layer were related to the embrittlement of the alloy, and they corresponded to the depth of diffusion of oxygen into the alloys.

In V–4Cr–4Ti–0.5Y that was oxidized at 700°C, the surface oxide layer was thin and dense and the cleavage crack region was thinner than that of other alloys. Therefore, it was considered that the growth of the oxidized layer and the diffusion of oxygen into the alloy were suppressed by the Y addition. Fig. 4 shows the oxide thickness measured in all of the alloys after oxidation at several temperatures. In the V–4Cr–4Ti alloy, a significant growth of the oxide layer was observed at 700 °C. In the V–4Cr–4Ti–0.5Y alloy, the oxide layer did not grow up to 700°C, while the layer grew at 700°C and substantially at 750°C in the V–4Cr–4Ti–0.5Si alloy. The V–4Cr–4Ti–0.5Al alloy showed an intermediate behavior between those of V–4Cr–4Ti–0.5Si and V–4Cr–4Ti–0.5Y alloys.

XRD analysis of the oxide scales on the V–4Cr–4Ti alloy showed predominantly the VO_2 phase after oxidation at 600°C and the V_2O_5 phase after oxidation at 700°C. On the contrary, VO_2 was stable in the Y-containing alloy even after oxidation at 700°C; however, it changed to V_2O_5 after oxidation at 750°C. The superior oxidation resistance of the Y-containing alloy at 700°C can be attributed to the formation and slow growth rate of the VO_2 phase, as evidenced by the thinness and

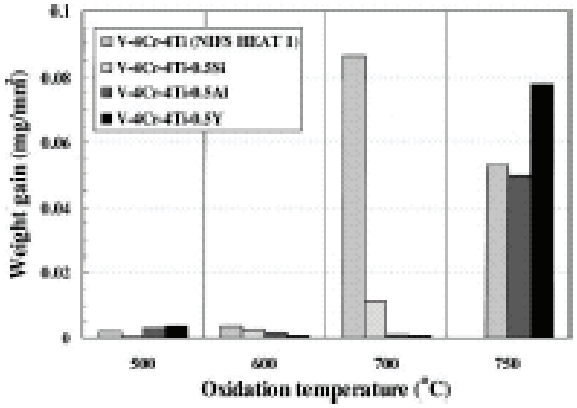

Fig. 1. Weight gain for V–4Cr–4Ti type alloys after oxidation in air for 1 h.

denseness of the scale in this alloy. Yttrium plays two roles to impart a slower growth rate in this alloy. The presence of Y in the alloy seems to lower the oxygen partial pressure in the near-surface region of the scale thereby stabilizing the VO_2 phase in the scale, and the Y segregation near the surface suppresses inward diffusion of oxygen into the alloy.

Fig. 5 shows the relationship between tensile behavior and oxidation morphology of the V–4Cr–4Ti alloy. The morphological structure of the fracture surface obtained after oxidation can be related to the concentration of oxygen that diffused into the alloy during oxidation. The fracture surface was composed of an oxide scale, a cleavage fracture zone, and a ductile rupture zone, the thickness of each of which depended on the oxygen concentration. The tensile behavior of the oxidized-

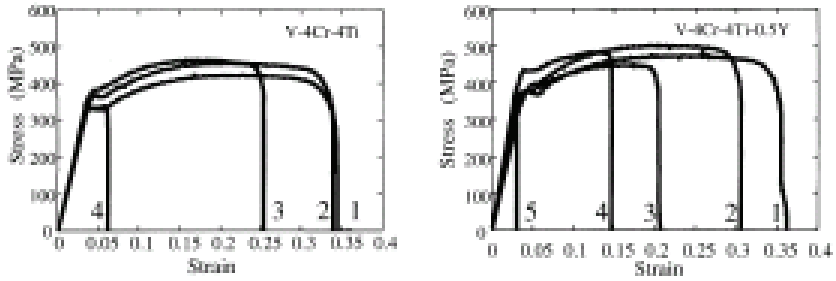

Fig. 2. Stress–strain curve for V–4Cr–4Ti and V–4Cr–4Ti–0.5Y alloys tested at room temperature: (1) as annealed, (2) 500°C oxidation, (3) 600°C oxidation, (4) 700°C oxidation, (5) 750°C oxidation.

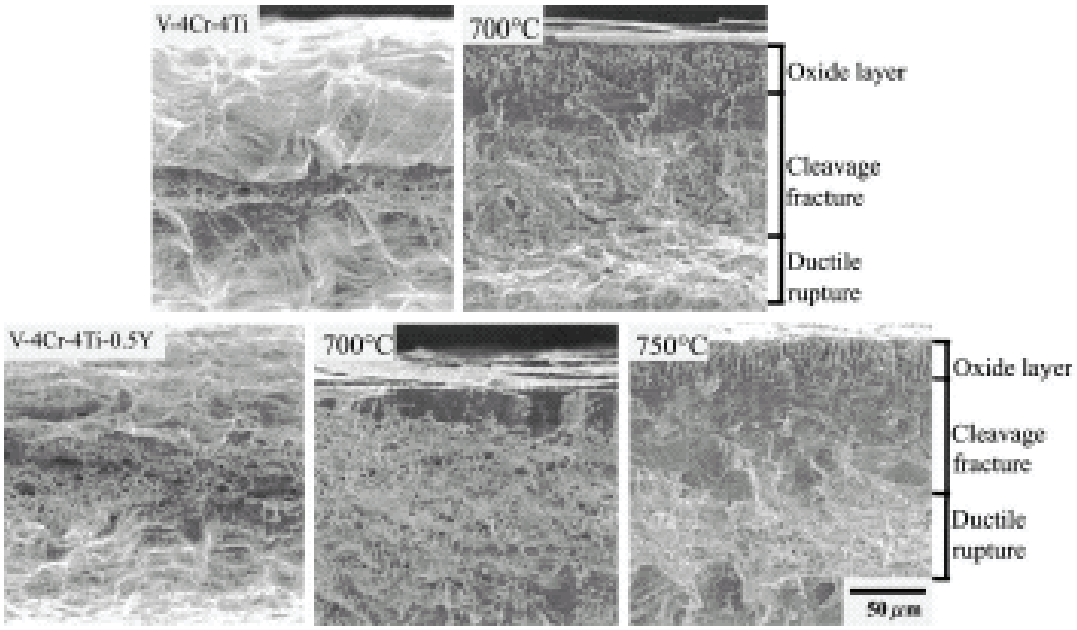

Fig. 3. Scanning electron micrographs of fracture surfaces after tensile test, V–4Cr–4Ti alloy and V–4Cr–4Ti–0.5Y alloy after oxidation at 700 and 750°C for 1 h, and as annealed.

material seemed to show the material tensile behavior that stretched the three materials of which characteristics differ, because it has the strength in which this organization respectively differs. The thickness of the brittle zone (comprising of the scale and the cleavage fracture areas) relative to the ductile zone increased with temperature, primarily because of increased diffusion of oxygen and increased oxygen ingress into the alloy. A quantitative assessment of the beneficial effects of dopant elements on oxidation resistance of the alloys and on ductility loss needs further experimental work that involve a range of oxygen partial partial pressures in the exposure environment and may be longer exposure time.

8. Conclusion

The compatibility of V–4Cr–4Ti, V–4Cr–4Ti–0.5Si, V–4Cr–4Ti–0.5Al, and V–4Cr–4Ti–0.5Y alloys with oxygen was examined in dry air. The results showed improved oxidation resistance for the Y-containing alloy at temperatures up to 700°C. The implication of this improved resistance is that under accident conditions that involve air ingress at elevated temperatures, the Y-containing alloy may offer adequate resistance when compared with that of the alloy without Y addition. For example, if the alloys were exposed to air at 700°C for 1 h during an accidental air ingress situation, the depth of the brittle layer in the alloys with and without Y would be 20 and 100μm, respectively

Acknowledgments

This work was partly supported by the JUPITER program (Japan–USA Program of Irradiation Test for Fusion Research) and a Grant-in-Air for Scientific

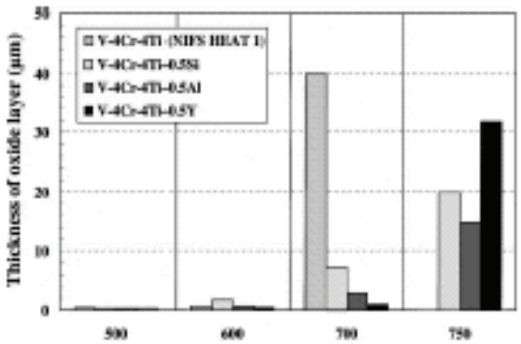

Fig. 4. Thickness of the oxide layer for each alloy oxidized in air for 1 h.

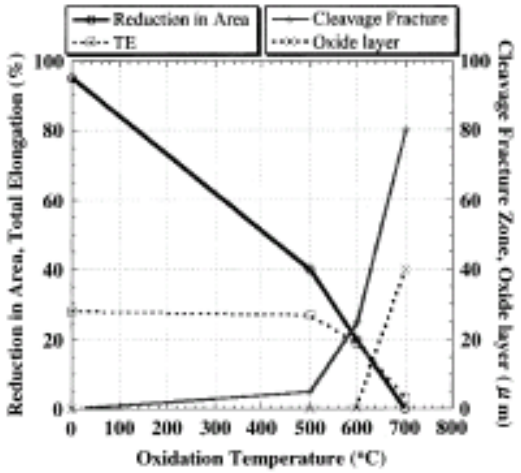

Fig. 5. Tensile properties and oxidation morphology of the V–4Cr–4Ti alloy oxidized in air for 1 h.

Research from the Ministry of Education, Culture, Sports, Science and Technology, Japan.

References

[1] S.J. Zinkle et al., J. Nucl. Mater. 258–263 (1998) 205.
[2] M. Satou et al., J. Nucl. Mater. 191–194 (1992) 956.
[3] M. Satou et al., J. Nucl. Mater. 212–215 (1994) 794.
[4] M. Satou et al., J. Nucl. Mater. 233–237 (1996) 447.
[5] H.M. Chung et al., J. Nucl. Mater. 212–215 (1994) 804.
[6] B.A. Loomis et al., J. Nucl. Mater. 212–215 (1994) 799.
[7] M. Satou et al., J. Nucl. Mater. 179–181 (1991) 757.
[8] H. Kayano, Sci. Rep. RITU A40 (1) (1994) 105.
[9] M. Uz, K. Natesan, V.B. Hang, J. Nucl. Mater. 245 (1997)191.
[10] K. Natesan, W.K. Soppet, J. Nucl. Mater. 233–237 (1996)482.
[11] K. Natesan et al., J. Nucl. Mater. 258–263 (1998) 1476.
[12] Conference of Large Helical Device Project, National Institute for Fusion Science, Japan, 1998.
[13] F. Najmabadi et al., The ARIES-I Tokomak Reactor Study Report UCLA-PPG-1323, UCLA, CA, 1991.
[14] F. Najmabadi and the ARIES team, Fus. Eng. Des. 38 (1997) 3.
[15] A. Sagara et al., Fus. Eng. Des. 29 (1995) 51.
[16] D.R. Diercks, D.L. Smith, J. Nucl. Mater. 141–143 (1986) 617.
[17] M. Fujiwara et al., J. Nucl. Mater. 258–263 (1998) 1570.
[18] M. Fujiwara et al., J. Nucl. Mater. 283–287 (2000) 1311.
[19] M. Fujiwara et al., Mater. Trans. 42 (6) (2001) 1048.

Microstructural examination of V- (Fe or Cr)-Ti alloys after thermal-creep or irradiation-creep tests

K.Fukumoto [a], S.Takahashi [a], R.J.Kurtz [b], D.L.Smith [c] and H.Matsui [a]

[a] Institute for Materials Research, Tohoku University, Sendai 980-8577, Japan
[b] Pacific Northwest National Laboratory, Richland, WA 99352, USA
[c] Argonne National Laboratory, IL 60439, USA

Abstract

Microstructural examinations have been performed on irradiation-creep and thermal-creep pressurized tube specimens of V-3Fe-4Ti-0.1Si in order to understand failure and creep mechanisms. There are no typical microstructural differences between unstressed and pressurized creep tube specimens irradiated in ATR-A1 in the irradiation temperature regime from 212 to 300°C. Failed thermal creep specimens show dislocation structures dependent on the tube specimen geometry. This can be interpreted in terms of a large number of slip dislocations oriented for optimum slip.

1. Introduction

Since vanadium alloys are candidate materials for fusion reactor structural materials, particularly because of their potentially high service temperatures, it is necessary to assess the performance of vanadium alloys at high temperature regime from 700 to 800°C [1]. However information on the creep properties of vanadium and vanadium alloys is limited since only a few studies have been performed.

On the other hand, irradiation creep is one of important research and development issues for first wall and blanket structures of fusion reactor materials. The effect of irradiation on creep properties has been investigated and a pressurized creep tube technique has been mostly employed for in-pile creep tests [2]. A study of biaxial thermal creep properties of V-Cr-Ti alloys has been performed successfully using pressurized creep tube techniques [3]. In the ATR-A1 irradiation in the JUPITER program [4], a study of biaxial irradiation creep properties of V-Cr-Ti alloys has been performed and data of a significant irradiation creep rate were obtained [5,6]. However information on the microstructure of thermal and irradiation creep in vanadium alloys have not been reported so far. It is necessary to obtain reliable microstructures in creep deformation in order to clarify the mechanism of thermal creep and irradiation creep behavior. In this study, a vanadium alloy of V-3Fe-4Ti-0.1Si (Heat number VM9502) was used, subjected to both thermal and irradiation creep tests as in V-Cr-Ti alloy [2] and creep data were also obtained. It has been pointed out that Fe included in vanadium alloy combines with helium strongly during neutron irradiation and suggested that V-Fe-Ti alloy will show high resistance to void swelling and intergranular degradation by helium implantation at high temperatures [7]. The V-Fe-Ti alloy is considered to be superior creep strength at high temperature to the V-Cr-Ti alloy, because it has larger binding energy with He/vacancy complex cluster than the V-Cr-Ti alloy. It has been reported that the mechanical properties of the V-Fe-Ti alloys are not so much different from that of the V-Cr-Ti alloys in out-pile and in-pile irradiation conditions [6, 8, 9]. The purpose of this study is to clarify the relationship between microstructures and creep behavior through transmission electron microscope (TEM) observations on thermal and irradiation creep specimens.

2. Experimental procedure

2.1. Biaxial thermal creep tests

The chemical composition of the V-3Fe-4Ti-0.1Si alloy has been already reported [6]. Detailed descriptions of the creep pressurized tube specimen preparation and the experimental environment are reported in refs [5,6,9,10]. The creep specimens in the ATR-A1 experiments and thermal creep test in Pacific Northwest National Laboratory (PNNL) were pressurized tubes with welded end plugs. The tubes were prepared from the V-3Fe-4Ti-0.1Si laboratory heat produced at Tohoku University in Japan. The tubes of V-3Fe-4Ti-0.1Si alloys were produced by machining in Argonne National Laboratory (ANL). All specimens had a nominal 4.57 mm outer diameter (OD), 0.25 mm wall thickness, and 25.4 mm length. The machining tubing was inspected with available ultrasonic or eddy current methods and radiography. Tube sections with questionable mass densities were excluded.

In order to fabricate creep tubes, the circumferential plug-to-tube welds were made with an electron-beam welder in vacuum. After the end plugs were attached, the assemblies were annealed at 1000°C for 1.0 h in vacuum while wrapped in a Ti getter foil. They were then pressurized to the desired level, through a 0.25-mm diameter hole in the top end plug, with high-purity helium in a pressure chamber. Two of the unpressurized #832665 specimens were designated as stress-free swelling controls. The final closure weld of the 0.25mm diameter of hole was made with a helium gas enclosure machine in ANL. The specified pressure loading was determined with a code that

accounted for thermal expansion of the vanadium alloy tubing, compressibility of the helium gas, and anticipated specimen temperature. Following the leak check and visual inspection, the dimensions of the assembled creep specimens were measured with a laser profilometer. The measurements were made at 5 axial locations (x/l of 0.1, 0.3, 0.5, 0.7 and 0.9) at every 9° azimuthal interval, and the 19 azimuthal readings were averaged to yield the mean diameter for each axial location of the specimens.

Thermal creep experiments were performed in PNNL [3]. Prior to insertion into the vacuum furnace, each specimen was loosely wrapped with titanium foil to provide additional protection against oxygen pickup during the experiment. The specimen OD was again measured using a laser profilometer to determine the elastic diametral displacements for each tube. For creep tests of the V-3Fe-4Ti-0.1Si alloys, two test temperatures were selected, 700 and 800°C.

Conventional analyses of grain boundary microstructure of an unstressed tube and a sample after creep test were performed by using a scanning electron microscope equipped with electron back scattering diffraction and orientation imaging microscope system (SEM–EBSP/OIM).

2.2. Biaxial irradiation creep tests

Detailed irradiation conditions have been reported in refs [5,6]. The ATR-A1 experiment consisted of 15 stacked, lithium-bonded subcapsules. The 10 creep specimens were each contained in a subcapsule to preclude interactions should any one rupture unexpectedly. To reduce the atypical transmutation of V into Cr due to the reactor's thermal flux, a neutron filter made of Gadolinium was installed in each subcapsule. The duration of the irradiation was 132.9 effective-full-power days. The experiment had two target temperatures: 200 and 300°C. However, because of the space limitation and axial flux gradient, the achieved displacement damage and specimen temperatures were not uniform, particularly for the nominally 200°C specimens. In calculating the effective strains for V-3Fe-4Ti-0.1Si alloy specimens the averaged diameters were determined with the laser profilometer in the same manner as before irradiation. For the unstressed specimens for the 200 and 300°C groups, the diametral strains of V-4Cr-4Ti alloys (the #832665-heat specimens) were used as that of the unstressed specimens for V-3Fe-4Ti-0.1Si alloys [5].

2.3. Preparation of TEM specimens and TEM observation

Ring sections of creep tubes were sectioned and cut into 2mm square plates by a multi wire-saw for thermal creep tubes and by an electrical discharge machining (EDM) apparatus installed in a radiation controlled area at Oarai branch in Institute for Materials Research /Tohoku University for irradiation creep tubes. The plate was thinned by grinding and then electro polished. No evidence of damage due to grinding could be seen in the cold-run test using an annealed and untested creep tube, therefore there were no artificial dislocations and no feature of anisotropic microstructures induced by sample preparation. TEM observations were carried out. In the TEM observation for thermal creep pressurized tube specimens, a $\boldsymbol{g}\cdot\boldsymbol{b}=0$ technique was performed in order to determine the Burgers vectors of dislocations. Based on the <001> orientation, at least four beam injection of <012> and <112> directions and ten types of reflection, {011}, {002} and {112}, were selected and used for each specimen. As a result, all types of <001>, <011> and <111> Burgers vector were completely distinguished.

3. Results & discussions

3.1. Microstructural examination for thermal creep pressurized tube specimens

Table 1 gives the information of thermal creep test conditions. The chemical analyses before and after thermal creep tests were carried out. An untested pressurized tube creep specimen contains 890wppm oxygen and 80wppm of nitrogen. On the other hand, a specimen tested at 700°C with rupture time of 3887hrs showed contents of 680wppm oxygen and 30wppm nitrogen. The reduction of nitrogen from V alloys during creep test could not be understood well in this study. However, it is considered that the amounts of nitrogen contents before and after creep test do not change significantly and are within the experimental errors. From the chemical analysis, any impurity incursion during the creep tests could not be recognized. Conventional analyses of grain boundary microstructure of an unstressed tube and a sample after creep test at 700°C and 129MPa were performed by using the SEM–EBSP/OIM system.

Table 1 : Test conditions for thermal creep pressurized tube specimens of V-Fe-Ti alloys

Temp (°C)	Effective stress (MPa)	Time to rupture (hr)	Effective mid-wall strain (%)	Minimum creep rate (%/h)
700	92	3418	15.8	6.4×10^{-4} at 101hr
	129	3887	17.3	5.7×10^{-4} at 101hr
	160	585	12.2	3.3×10^{-3} at 101hr
800	55	No rupture (till 5242)	0 at 5242hrs	4.3×10^{-5}
	74	427	6.9	2.5×10^{-2}
	92	101	20.0	2.0×10^{-1} at 101hr

From the analyses of grain boundary microstructures, there were no typical differences of the grain size distribution, misorientation angle distribution and CSL (coincidence site lattice) boundaries distribution between an unstressed tube and a pressurized tube after creep test. This suggests that the grain growth, polygonization and anisotropic flow of mass transfer did not occur during the creep test at 700°C and 129MPa.

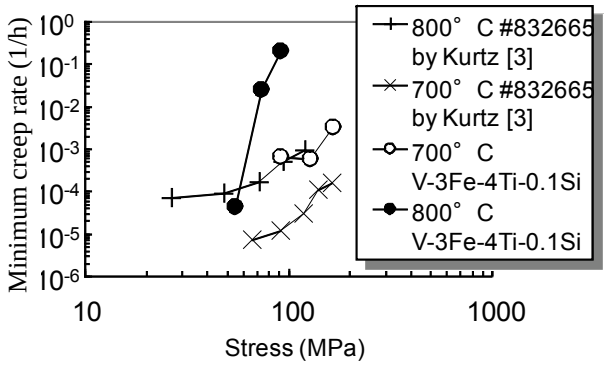

Fig. 1: Stress dependence of minimum creep rate of the US heat #832665 of V-4Cr-4Ti and the V-3Fe-4Ti-0.1Si

Fig. 1 shows a comparison of stress dependence of the minimum creep rate between the US heat 832665 of V-4Cr-4Ti alloys [3] and the V-3Fe-4Ti-0.1Si alloys. The steady-state creep regimes of strain-time curves for the V-3Fe-4Ti-0.1Si alloys were very short or not observed. In the case of no steady-state creep regimes, the first creep rates on strain-time curves were adopted as minimum creep rates. The creep rates of the V-3Fe-4Ti-0.1Si alloys were faster than V-4Cr-4Ti, #832665 alloys [3] as shown in Fig. 1. The stress exponent, n derived from a relationship between the creep rate and effective stress was 2.3 at 700°C, which suggests that the creep mechanism is typical of solid-solution alloy. However since the steady state creep was not observed in 700°C creep tests, the value of stress exponent is unreliable. In 800°C creep tests, a large stress exponent of n=11 was obtained, likely due to the presence of a threshold stress. Fig. 2 (A) shows an example of dislocation structures in a V-3Fe-4Ti-0.1Si tested at 800°C and 74MPa. A lot of dislocations were formed and many precipitates were seen in grains. The dislocation structure was distributed homogeneously in grains and some dislocations were pinned at precipitates here and there. The cell walls of dislocations were seldom identified in any specimens.

On the other hand, the sub grain boundary structures, like cell walls, could be seen in a V-4Cr-4Ti alloy. A large ingot of highly purified V-4Cr-4Ti alloy, NIFS-Heat1 [11] has been examined in creep deformation test using uniaxial tensile specimens. Fig. 2 (B) shows the BF images of a NIFS-Heat1 in a steady state creep regime during a creep test at 800°C and 200MPa using uniaxial tensile specimens [12]. Sub grains with widths of about 1□m were distributed through grains in the NIFS-Heat1 alloy.

The difference between these alloys may be caused by the creep deformation mechanism. The type for V-3Fe-4Ti-0.1Si alloys is of the dislocation creep of solid solution alloy, and for NIFS-Heat1 alloys is of the dislocation creep of pure metal. It indicates that the dislocation glide controls the creep rate in the NIFS-Heat1 alloys, whereas solute atoms in the V-3Fe-4Ti-0.1Si alloys act as lattice resistance to dislocation motion and the glide velocity is less than the climb velocity of a dislocation.

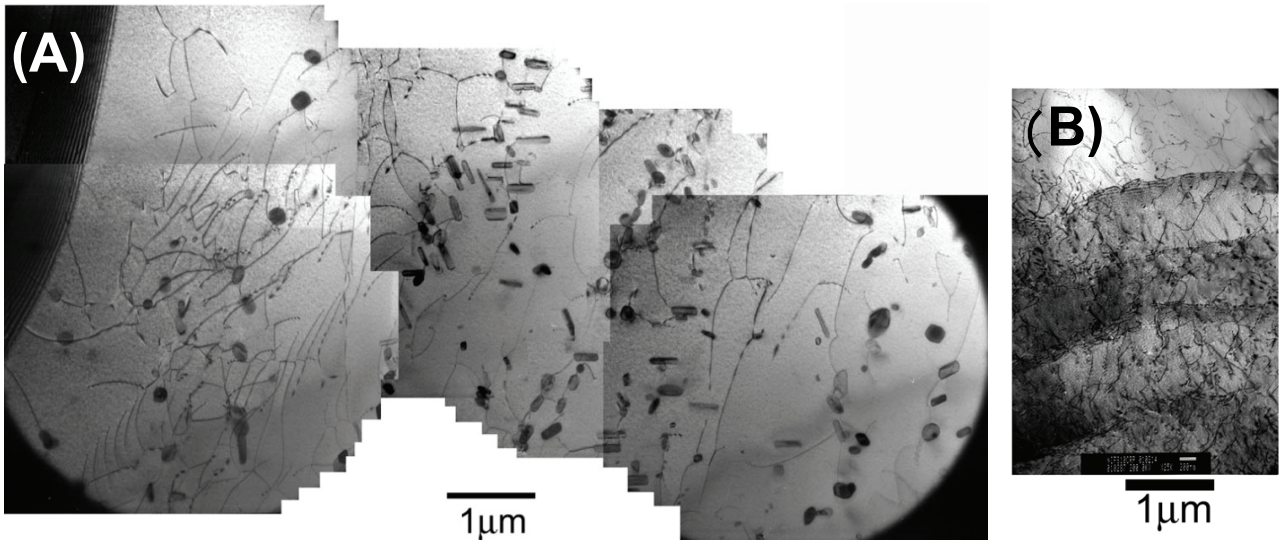

Fig. 2: Microstructures in V-3Fe-4Ti-0.1Si alloys tested at 800°C with a stress of 74MPa (A), and a NIFS-Heat1 tested at 800°C with a stress of 200MPa (B). The image (A) was taken from a failed specimen and (B) taken from a specimen ceased a creep test at the beginning of steady state creep.

Detailed investigation of dislocation characteristics and configuration was performed in all failed specimens. Fig. 3 shows an example of the microstructure of the V-3Fe-4Ti-0.1Si alloys tested at 800°C and 92MPa. Most of the dislocations had parallel alignment with the longitudinal direction of the creep tube specimens. The Burgers vector for the dislocations was 1/2<111>. Since the direction of <111> vector was perpendicular direction to dislocation line, the dislocations should be edge dislocations. The short dislocations intersecting long <111> dislocations had the <100> Burgers vector, which are the reaction dislocations among the different slip of <111> dislocations. Since the determination of dislocation character for many grains is difficult, the configuration of dislocations was obtained by the measurement of a direction along a dislocation line. Fig. 4 shows the plot of dislocation length distribution as a function of the angle between a longitudinal direction of creep tube and a direction along a dislocation line. A lot of long dislocations may be aligned with a longitudinal direction of creep tube at 700°C as shown in the Fig. 4 (A). On the other hand, the dislocation alignment at 800°C is deviated from the longitudinal direction of the tubes, however most of alignment angle is concentrated within a 45º angle from the longitudinal direction of the tubes. The deviation of angle is caused by the crystallographic geometry of each grain because the distribution of concentrated regime of dislocations is unimodal or bimodal like grain A, B and D in Fig. 4(B).

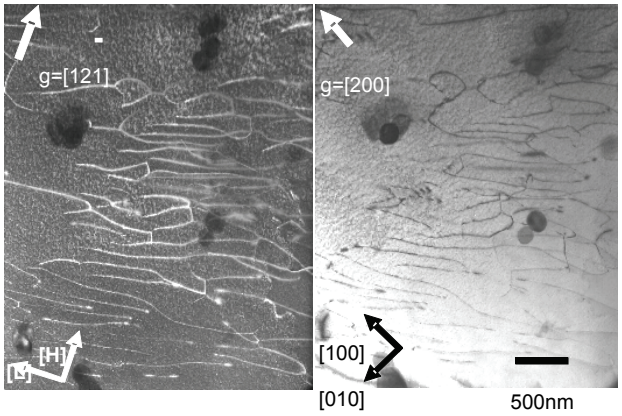

Fig. 3: Example of TEM images of a dislocation structure of the V-3Fe-4Ti-0.1Si alloy tested at 800°C with a stress of 92MPa. Arrows on upper part in images show the g-reflection vectors, $(12\bar{1})$ for left and (002) in right. A set of arrows in the bottom of left shows the direction in pressurized creep tube geometry; [L] indicates a longitudinal direction in the tube and [H] a hoop direction. A set of arrows in the bottom of middle part shows the crystallographic directions; the projection axes is [001] direction and close to the perpendicular direction for the creep tube surface within 5°.

From the general stress analysis of pressurized creep tubes [5,13], a hoop stress and a longitudinal stress is described as $\sigma_\theta=(r_m/t)\Delta P$ and $\sigma_z=(0.5r_m/t)\Delta P$, respectively. The r_m is the midwall radii of tubes, t is the wall thickness and ΔP is the difference in internal and external gas pressure at the temperature. The direction of the main stress is the hoop direction on the pressurized creep tubes. In order to determine which slip system is dominant in creep tube deformation, trace analyses were done for the Burgers vectors of dislocations, the foil normal and the direction of the critical resolved shear stress. It is assumed that the preferential slip planes in vanadium alloys [14] are {110} or {112} and the "easiest" slip plane was determined for each examination. Fig. 5 shows the fractional distribution for the Burgers vector of dislocations in the creep-tested V-3Fe-4Ti-0.1Si alloys.

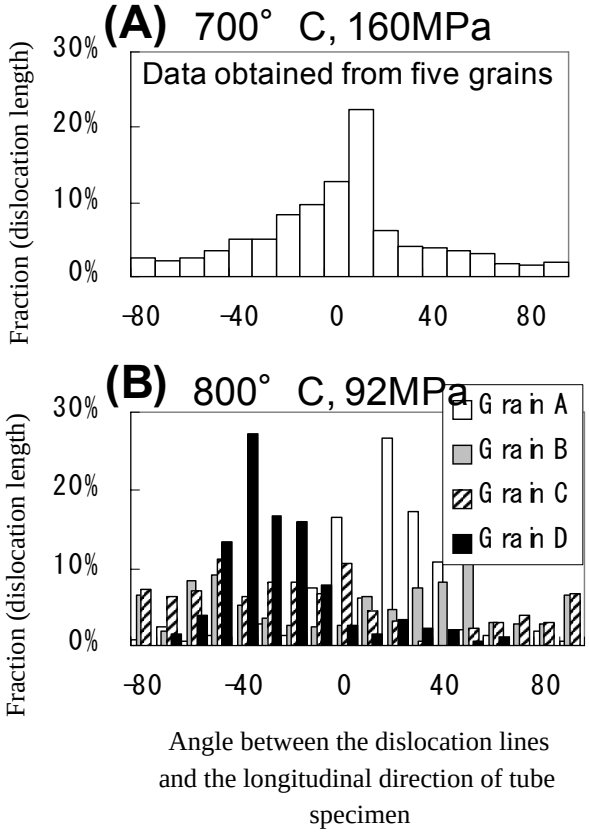

Fig. 4: The plots of dislocation length distribution as a function of an angle between a longitudinal direction of creep tube and a direction along a dislocation line. (A) 700°C and (B) 800°C.

The dislocation densities of <111> Burgers vector were divided into two portion; the one that takes the easiest slip system and the others. Since the specimens were taken from

the ruptured area in failed specimens, the dislocation densities for all specimens were almost the same, independent of the stress levels. The fraction of the <111> Burgers vector for the main slip is about 60-70%. It can be interpreted to contain a large number of slip dislocations oriented for optimum slip during creep tests. Multiple slip should be facilitated by geometrical effects arising from experimental constraints, but the pressurized tube is so thin that the constraint effect may not be stronger than tensile and compression tests.

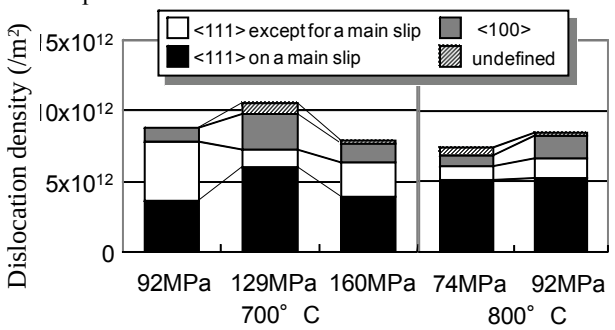

Fig. 5: Dislocation density distribution for the various types of dislocations in the creep-tested V-3Fe-4Ti-0.1Si alloy. The dislocation types were classified into four groups; (1) the <111> main slip; the slip dislocation oriented for optimum slip system during tests, (2) the <111> except for main slip; the slip dislocation oriented for different slip system from the optimum one, (3) <001> dislocation; the reaction dislocation produced by the intersection of dislocation movements, and (4) undefined dislocations.

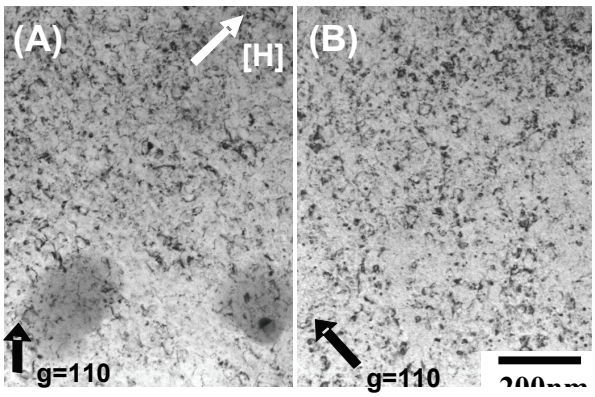

Fig. 6: Comparison of microstructures between unstressed and creep specimens of the V-3Fe-4Ti-0.1Si alloys irradiated at 300°C in ATR-A1. (A) a pressurized creep tube specimens and (B) an unstressed TEM specimen. The arrow [H] in top in (A) indicates a hoop direction of the creep tube specimen.

In general, the mechanical properties of bcc metals and alloys are strongly dependent on temperature, strain rate, sign of stress and impurity contents. In particular, characteristic of bcc metals is the existence of two different deformation behaviors below and above a so-called transition temperature T_0, which lies somewhere between 0.1 T_m and 0.2 T_m. The marked low temperature rise of the critical shear stress is today generally ascribed to the specific mobility of the screw dislocations with Burgers vectors of the type a/2<111> below T_0. Conversely non-screw dislocations possess a planar core and are therefore considerably more mobile than screw dislocations. Because of their complicated core structure the screw dislocations exhibit a high Peierls stress. After low temperature strain bcc metals and alloys principally contain long screw dislocations of different a/2<111> Burgers vectors in homogeneous distributions without any excess of dislocations of one sign. However, with increasing temperature the difference between the mobilities of the screw and non-screw dislocations becomes progressively smaller as a result of thermal activation, so that the conditions become increasingly similar to those in fcc metals. Above the transition temperature, T_0, when the mobilities of screw and edge dislocations are comparable, there exist marked analogies in the deformation behavior of bcc and fcc metals [15]. The Peierls barrier in bcc metals for edge dislocation motion is comparable to that for screw dislocation motion above 700ºC (>0.4T_m). Hence a lot of dislocations can possess edge character after creep deformation. The plastic anisotropy during creep deformation is essential in vanadium alloys as well as other bcc metals and alloys at high temperatures around 0.5 T_m. The types of active slip system for edge dislocations in this alloy are considered to be <111>{110} and <111>{112} at high temperatures. Most of dislocation structures after thermal creep tests consist of <111> edge dislocation in this study. Therefore these results conform well with the general dislocation theory at high temperatures mentioned above.

The preferential glide movement of dislocations in the V-3Fe-4Ti-0.1Si alloys causes the faster creep rate compared to V-4Cr-4Ti, and the recovery of dislocations is greater than in V-Cr-Ti alloys. The reason why the creep strength of the V-3Fe-4Ti-0.1Si alloy is lower than V-4Cr-4Ti is considered to be due to the difference of creep deformation mechanism, since the a V-4Cr-4Ti alloy forms the cell wall structure in spite of little difference in climb velocity and vacancy diffusion.

3.2. Microstructural examination for irradiation creep pressurized tube specimens

For the V-3Fe-4Ti-0.1Si alloys in this study, the effective strain and stress were 0.75%, 163MPa and 0.91%, 165MPa for specimens irradiated at 300°C and 212°C, respectively. After the irradiation, the surface of the creep tubes appeared to be darkened.

The microstructures of both an unstressed TEM specimen and a pressurized creep tube specimen irradiated at 300°C are shown in Fig. 6. An arrow [H] inside the

figure shows the hoop direction of the creep tube specimen. There are high densities of dislocations and defect clusters in both specimens. No precipitates can be seen in pressurized creep tube specimens irradiated at 212°C and 300°C. Fine contrasts are seen in unstressed TEM specimens but it was difficult to identify them as precipitates by diffraction and image techniques. In order to determine the Burgers vectors of the defect clusters, images with several reflections were taken in the same area. However the character of the defect clusters could not be determined because of the high densities of defect clusters.

In order to investigate the anisotropic formation of defect clusters in pressurized creep tube specimens, microstructures on several grains were taken, but no features typical of anisotropic microstructures of dislocation and defect clusters were observed. Fig. 7 shows the densities of defect clusters as a function of irradiation temperature. No significant difference of microstructures between unstressed and creep tube specimens was obtained. The densities of defect clusters in both specimens were the almost same and about $2x10^{22}$ clusters/m^3 at temperatures from 212°C to 300°C. There is no anisotropic feature of the defect cluster formation in pressurized creep tube specimens during irradiation.

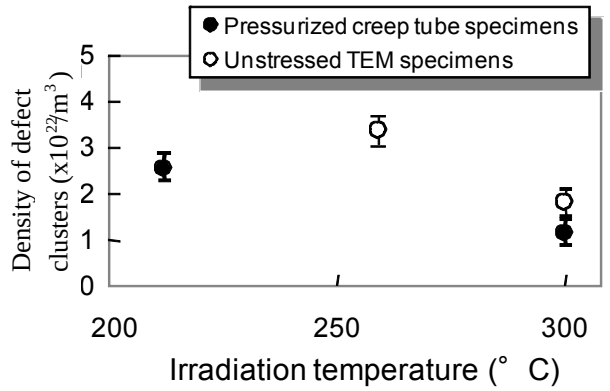

Fig. 7: Density of defect clusters in pressurized creep tubes and unstressed specimens.

Since the high density of fine defect clusters and low temperature irradiation make the long-range diffusion of defects difficult, the difference in microstructural evolution between the stressed and unstressed specimens under irradiation was not apparent. Even though the diametric strains of unstressed specimens were for V-4Cr-4Ti alloys, the swelling of the unstressed V-4Cr-4Ti alloy is not considered to be much different from that of unstressed V-3Fe-4Ti-0.1Si alloys in the same irradiation condition in this study. The amount of swelling for the unstressed V-4Cr-4Ti alloys was 0.05 and 0.11% for the specimens irradiated at 212°C and 300°C, respectively. However, the effective strains in the creep specimens at 212°C and 300°C were about 0.75% and 0.91%, respectively. The amount of creep strain was much larger than that of volume expansion in unstressed specimens and quite large compared with ferritic steel and other alloys [2]. The origin for the enormous creep deformation in the creep specimens is still not identified from the microstructural observation using TEM. The dense defect clusters with a nano-scale size, such as microvoids, invisible interstitial clusters or impurity-titanium complexes may cause the creep strain rate and volume expansion during irradiation. However it is not clear why the fine defect structures are induced in stressed environment at low temperature. This is the future problem that must be studied more in detail.

4. Conclusions

Microstructural examinations for thermal creep and irradiation creep specimens of the V-3Fe-4Ti-0.1Si alloys were performed.

No anisotropic defect cluster formation was observed in pressurized creep tubes irradiated in ATR-A1 at temperatures from 212 to 300°C. The cause for the large creep strain rate in creep specimens was not clear, as there was little difference in microstructural evolution between unstressed TEM specimens and pressurized creep tube irradiated in ATR-A1.

The type of creep deformation mechanism for V-3Fe-4Ti-0.1Si alloys was a dislocation glide creep controlled by solid solution strengthening. The formation of dislocation structures was caused by a large number of slip dislocations oriented for optimum slip.

Acknowledgement

The authors would like to express their thanks to Prof. S. Tsurekawa of Tohoku Univ. for using the SEM–EBSP/OIM system and Mr. T. Matsuzaki for his help in the SEM–EBSP/OIM experiment. This work was partly supported by JUPITER program (Japan-USA Program of Irradiation Test for Fusion Research).

References

[1] R. J. Kurtz, K. Abe, V. M. Chernov, V. A. Kazakov, G. E. Lucas, H. Matsui, T. Muroga, G. R. Odette, D. L. Smith and S. J. Zinkle, J. Nucl. Mater. 283-287 (2000) 70.

[2] A. Kohyama, Y. Kohno, K. Asakura and M. Yoshino, Mat. Trans. JIM 34 (1993) 1061.

[3] R. J. Kurtz and M. L. Hamilton, J. Nucl. Mater. 283-287 (2000) 628.

[4] K. Abe, A. Kohyama, C. Namba, F. W. Wiffen and R. H. Jones, J. Nucl. Mater. 258-263 (1998) 2075.

[5] H. Tsai, H. Matsui, M. C. Billone, R. V. Strain and D. L. Smith, J. Nucl. Mater. 258-263 (1998) 1471.

[6] K. Fukumoto, H. Matsui, H. Tsai and D. L. Smith, J. Nucl. Mater. 283-287 (2000) 492.

[7] H.Matsui and H.Nakajima, Sci. Rep. RITU, A-vol.35, No.2 (1991) 196

[8] K. Fukumoto, T. Morimura, T. Tanaka, A. Kimura, K. Abe, H. Takahashi and H. Matsui, J. Nucl. Mater., 239 (1996) 170

[9] K. Fukumoto. Y. Yan. H. Tsai. D. L. Smith and H. Matsui, Proc. 4th Pacific Rim Int Conf. on Advanced Materials and Processing, ed. By S.Hanada, et al., (2001) 1319
[10] H. Tsai, T. S. Bray, H. Matsui, M. L. Grossbeck, K. Fukumoto, J. Gazda, M. C. Billone and D. L. Smith, J. Nucl. Mater. 283-287 (2000) 362.
[11] T. Muroga, T. Nagasaka, A. Iiyoshi, A. Kawabata, S. Sakurai and M. Sakata, J. Nucl. Mater. 283-287 (2000) 711
[12] K. Fukumoto, T. Yamamoto, N. Nakao, S. Takahashi and H. Matsui, J. Nucl. Mater. 307-311 (2002) , 610.
[13] E. R. Gilbert, L. D. Blackburnm, J. Eng. Mater. Tech. ASME. Trans (1977) 168.
[14] J. W. Edington and R. E. Smallman, Acta Met. 12 (1964) 1313.
[15] A. Luft, Prog. Mater. Sci. 35 (1991) 97.

Manufacturing pressurized creep tubes from highly purified V-4Cr-4Ti alloys, NIFS-Heat2

K. Fukumoto [1], H. Matsui [1], M. Narui [2], T. Nagasaka [3] and T. Muroga [3]

1 IMR/Tohoku Univ., 2-1-1 Katahira, Aoba-ku, Sendai 980-8577, Japan
2 Oarai branch, IMR/Tohoku Univ., Oarai, Ibaraki 311-1313, Japan
3 National Institute for Fusion Science, 322-6 Oroshi, Toki, Gifu 509-5292, Japan

Abstract
A fabrication process for pressurized creep tubes (PCTs) for a highly purified V-4Cr-4Ti alloy, NIFS-heat2 was established. No increase in impurity contents in PCTs was detected during the tube manufacturing process. In a preliminary thermal creep test, homogeneous deformation was observed over entire tube length, which verifies reliability of creep measurement by using the present PCTs.

1. Introduction

Creep deformation is one of the important issues that affect the lifetime of materials in a fusion reactor. At fusion relevant high temperature, creep strain rate of the materials at high temperature can be larger when excess point defects were generated by irradiation. In order to measure irradiation creep in pile of a reactor, several irradiation creep tests have been done using pressurized creep tubes (PCTs) [1-3]. Recently, high-purity V-4Cr-4Ti ingots (NIFS-HEAT-1 and 2) were provided by National Institute for Fusion Science (NIFS), Japan [4-6]. The oxygen content of NIFS-HEAT-2 is almost half that of a large heat of V–4Cr-4Ti produced by a US-DOE (Department of Energy) program [7]. In order to examine irradiation creep test for the highly purified V-4Cr-4Ti alloy, a manufacturing process of pressurized creep tube should be established at first with avoiding contamination of interstitial impurities during the process. We briefly report the manufacturing process of PCTs of highly purified V-4Cr-4Ti, NIFS-Heat2 that is planned to be used for high fluence neutron irradiation experiments in the future.

Table 1 : Interstitial impurity contents in the materials on the fabrication process.

	C	N	O
Ingot	80	108	124
As-rolled tube	140	100	305
Heat-treated tube	120	120	330
Final status of creep tube	40	80	375

2. Materials and manufacturing process of PCTs

Fig. 1 shows a flow chart of manufacturing process for pressurized creep tubes of NIFS-heat2 alloys. Tube processing of NIFS-Heat2 alloys was successfully done by NIFS and Daido Co. The detailed tubing process has been reported in the ref [6]. The tubes were cut into pieces of pipes with one-inch (25.4mm) length. Table1 shows the contents of interstitial impurities in NIFS-Heat2 alloys used in this study. The results, shown in Table l, indicate discernible uptake of oxygen during the tube fabrication. However the extent of oxygen content in the creep tubes is smaller than those in the previous creep tubes. The significant reduction of contamination of interstitial impurities during tube fabrication process was achieved by using the newly developed rolling process reported in Ref. [6] and the suitable intermediate annealing. Fig. 2 shows a blueprint of creep tube in this study. The design of the creep tube specimens was made in accordance with the previous work of creep tube specimens of vanadium alloys and ODS-ferritic steel [8]. A 8mm ϕ rod of the NIFS-heat2 alloy was cold-rolled to the 6mm ϕ rod. The end plugs were fabricated from a rod by using a lathe, and a 0.6mmϕ / 0.25mmϕ hole was bored in the top end plug with electro-discharge machining. The profile and dimension of the hole in the end plug was restricted by the request from helium gas enclosure technique. The circumferential plug-to-tube welds were made with an electron-beam (EB) welder in vacuum in a machine shop in Japan Atomic Energy Research Institute (JAERI), Tokai, Japan. A rotating revolver holder for six specimens was installed in the EB welder to reduce the frequency of opening the chamber of the EB welder. A condition of EB weld for PCTs of NIFS-Heat2 alloys was as follows; 150kV for accelerating voltage of electron beams, 0.2mA for beam current, two turn of 20 rpm for rotation frequency of specimen holder and $<1x10^{-2}$ Pa for the degree of vacuum. A quality inspection of defective welding and welding distortion was done for each PCTs after EB welding in JAERI by using radiography. The final heat treatment of PCTs was done at 1000°C for 2 hrs in vacuum of $<1x10^{-4}$ Pa. A helium gas sealing was done in a helium gas enclosure at the Oarai branch of Japan Nuclear Cycle Development Institute (JNC), Oarai, Japan. In this helium gas enclosure case, a plug pin was not used for enclosing. A top part of end plug was melted at a laser shot and solidified around 0.6mm-hole-diam in the top end plug. The gas enclosure was done by the solidification of molten pool around an upper hole in the end plug. According to the request from gas enclosure system, the diameter of hole must be limited below 0.6mm for upper part and below 0.3mm for bottom part in the top end plug. In order to confirm that the laser weld does not make any pores or defects in the top end plug of NIFS-Heat2 alloy, several designs of top end plugs have

been used for demonstration tests. Finally, we determined the design of top end plug as shown in Fig.2. The final closure welding of the 0.25-mm-diam holes were made with a laser of 50J power (420V) through the quartz window at RT. The degree of vacuum was <1Pa after 3 times of helium gas exchanges. The high purity helium gas (6N grade, <1wppm moisture and <1wppm oxygen) was used. A maximum limit of inner pressure for inert gas enclosure is 29MPa in this device. As a result, a helium gas enclosure with 12MPa at RT was sufficiently achieved with the PCTs of NIFS-Heat alloy. For an example, a helium gas pressure of 11.2MPa at RT is required in a helium gas enclosure in order to obtain an effective applied stress of 200MPa in a PCT at 450°C. Following a leak check, the dimensions of the assembled creep specimens were measured with a precision laser profilometer at five axial and 18 azimuthal locations to an accuracy of 1μm. The details of creep strain measurement were referred to the previous works [1,2,9]

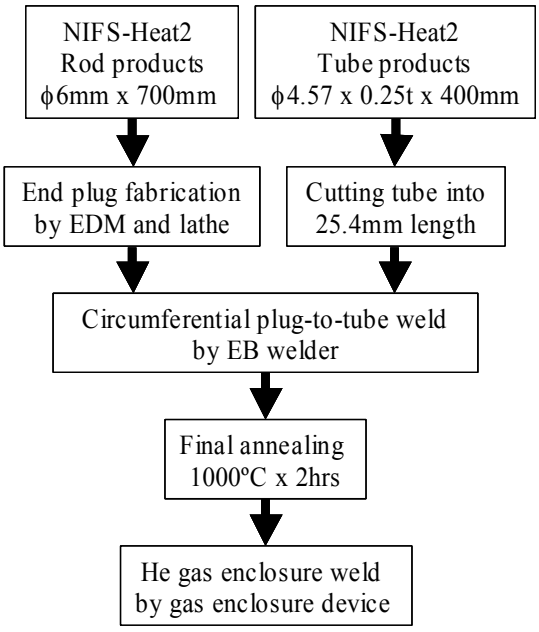

Fig. 1: Manufacturing process of a pressurized creep tube for NIFS-Heat2 alloy.

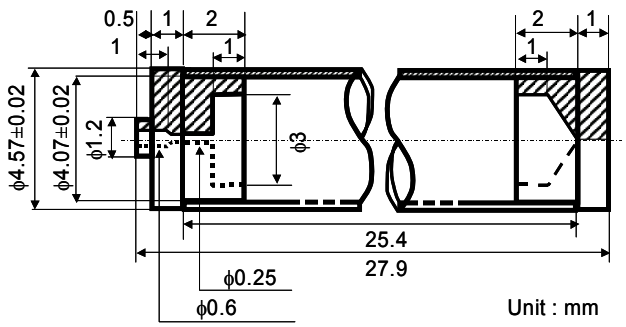

Fig. 2 : A blue print of a pressurized creep tube for NIFS-Heat2 alloy.

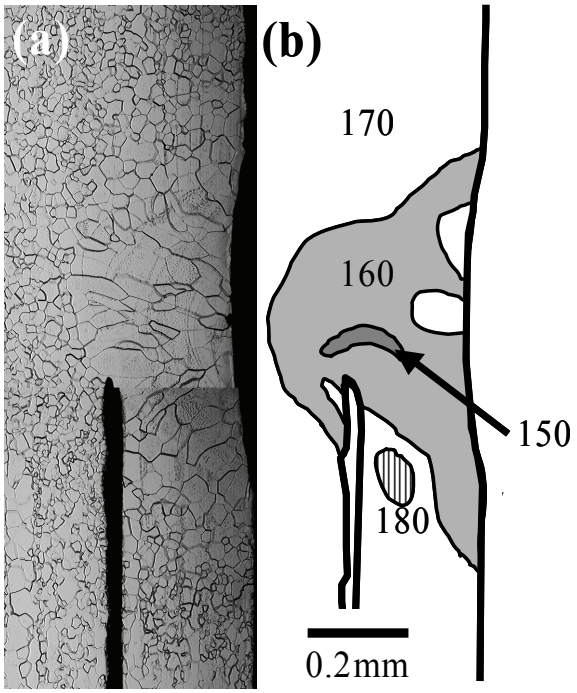

Fig. 3 : An optical micrograph and a hardness contour map of the cross section of plug-to-tube weld.

3. Quality inspection of fabrication process for PCT specimens

Total numbers of finished creep tube specimens prepared for experiments were 52 so far. Eleven creep tube specimens were for thermal creep tests in liquid lithium environment, fourteen specimens for thermal creep tests in vacuum, six specimens for thermal creep in liquid sodium environment, and twenty-one specimens for irradiation creep tests in the experimental fast reactor, JOYO. The final yield rate of successful creep tube fabrication, as defined by the ratio of the number of finished creep tubes to the total numbers of creep tubes, was about 80%, 52 successful cases out of 65 trials. However, most of failures were detected at the process of EB welding in early days. It is anticipated that the yield rate will be improved with experiencing manufacturing many times.

A macroscopic examination of the welds indicated relatively smooth weld zones without any cracks, porosity, or other significant weld flaws. Weld cross-sections of the specimens with inner charged pressure of 12MPa at room temperature were examined by confocal laser microscope. In addition, Vickers microhardness measurements with loads of 25g and 200g were made at the weld zone in the plug-to-tube welds and the helium-gas closure welds of top-end plug. The load of 25g in Vickers microhardness was employed in order to investigate a hardness profile in a selected area and the load of 200g was employed in order to measure the accurate hardness value. Fig. 3(a) shows an optical photomicrograph of the cross section of plug-to-tube weld made by the EB welder. Specimens were chemically etched in a solution of 10%HF-40%HNO_3-50%water for metallographic

examination. The grains in the weld zone were of the order of 3 ~ 8 times larger than those of the base metal away from the weld. The center of weld zones did not contain any fine structures of precipitates in a grain, but the weld cross section shows the definite contours around the root region of welded zone, along which preferential segregation of impurities can occur. Fig. 3(b) shows a Vickers microhardness distribution of weld zones made with EB welder. The mean hardness of tube and plug were 160±2 and 160±3, respectively. The hardness profiles indicated a small drop in the weld centerline region from 160 to 150. The significant increase of hardness due to the preferential segregation of impurities could not be seen in the root of weld zone. From these results, it is deduced that the contamination by interstitial impurities during the EB weld did not occur in the circumferential plug-to-tube welds.

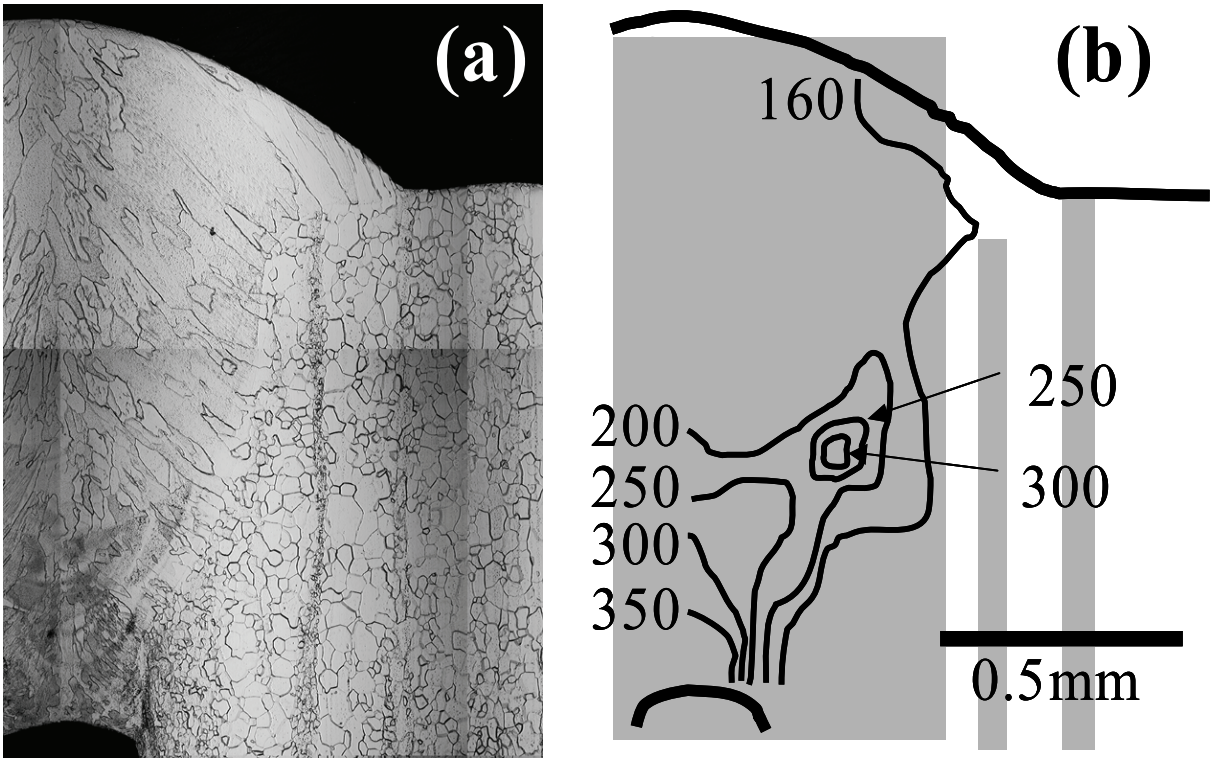

Fig. 4 : An optical micrograph and a hardness contour map of the cross section of helium-gas closure weld.

Fig. 4(a) shows an optical photomicrograph of the cross section of helium-gas closure weld made with the laser welder. The grains near the top of the weld zone in the end plug were columnar, which is dictated by heat flow and solidification. Even in the root of the weld, the grains were of the order of two to eight times larger than those of the base metal. In addition, the fine structures in the grain indicating the precipitates were observed in the fusion zone. Fig. 4(b) shows a hardness distribution of weld zones made with gas enclosure welder on the top end plug. The hardness on heat-affected zone near outside surface did not change significantly from the base metal. In Fig. 4(b), gray zones indicate the areas where fine structures in the welded zone and precipitate bands in the tube part can be seen. There were no fine structures in grains of heat-affected zone near the outside free surface. Around the center of welded zone near the top surface, the hardness increased up to 180 and fine structures in columnar grains were observed. The hardness increased along the line from the top surface to the root of welded zones in the end plug. Though not shown in Fig. 4(b), the hardness profile shows a peak value of 410 at the bottom of weld zone in the end plug. Nagasaka has reported that the change in the hardness due to gas tungsten arc (GTA) welds depended on the oxygen level of the base metals, and the precipitation hardening due to post weld heat treatment increased with increasing the oxygen level [10]. The fine structures in grains in the welded zones in this study appear to be Ti(O,N,C) precipitates, though the microstructural analysis of them has not been done. It is considered that increases of the densities of precipitates cause the significant increases of hardness in the welded zones. Especially, it is considered that contaminant oxygen and other interstitial impurities entered into welded pool at the root of the top end plug from helium gas during the gas enclosure welds, since the significant changes of hardness up to 400 were observed. However, the hardening is not expected to have deleterious effect on the performance on creep tests, because the solid solute hardening due to interstitial impurities will increase the creep strength.

4. Preliminary creep examinations

Preliminary creep tests for checking the deformation behavior of PCTs were done. Fig. 5 shows examples of PCTs after creep test at 850°C and a sample with 4.57mm of outer diameter for comparison. The specimens showed the uniform dilatation at the tube part and values of effective creep strain of specimens were estimated to be 20% for the specimens. It is suggested that there is no fabrication defect in the tube leading to unexpected rupture during the creep test, and it is possible to measure the effective creep strain up to 20%. Further thermal creep tests for NIFS-Heat2 from 600 to 800°C by using these PCTs are in progress. Consequently, the procedure for the PCT fabrication of highly purified V-4Cr-4Ti alloys has been established.

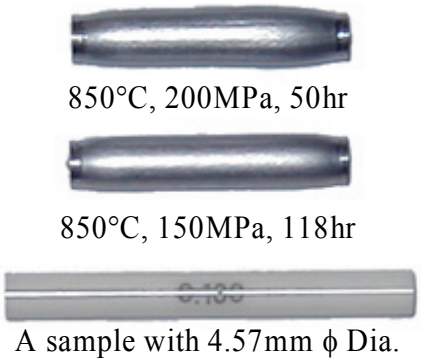

Fig. 5 : Examples of PCTs after creep test. A standard rod of 4.57mm in diameter was shown as well as creep samples.

5. Conclusion

Thin-wall tubing was produced from the NIFS-Heats of highly purified V-4Cr-4Ti to study the thermal and irradiation creep behavior. In order to fabricate PCTs for NIFS-Heat alloys, a fabrication process for PCTs was established with taking care of avoiding contamination of interstitial impurities during fabrication process. In the EB weld, there was no defective weld and significant hardening in the welded zone. In the helium gas enclosure, no defective weld like pore could be seen. No increase in impurity contents in PCTs was detected during the tube manufacturing process. In a preliminary thermal creep test at 850°C, homogeneous deformation was observed over entire tube length up to 20% of effective creep strain after creep test. It is suggested that there is no fabrication defect in the tube part to make unexpected rupture during the creep test and the procedure for the PCT fabrication of highly purified V-4Cr-4Ti alloys has been established here.

Acknowledgements

This work has been performed in collaboration with the NIFS, JAERI-Tokai and JNC-Oarai. Especially, the authors wish to thank S. Onose, Y. Abe and S. Ichikawa of JNC-Oarai and T. Kikuchi and F. Isozaki of JAERI-Tokai for their technical skill for creep tube fabrication.

References

[1] H. Tsai, H. Matsui, M. C. Billone, R. V. Strain and D. L. Smith, J.Nucl.Mater. 258-263 (1998) 1471.
[2] K. Fukumoto, H. Matsui, H. Tsai and D. L. Smith, J.Nucl.Mater. 283-287 (2000) 492.
[3] J. M. Vitek, D. N. Brrraski and J. A. Horak, J.Nucl.Mater. 141-143 (1986) 982.
[4] T. Muroga, T. Nagasaka, A. Iiyoshi, A. Kawabata, S. Sakurai and M. Sakata, J.Nucl.Mater. 283-287 (2000) 711.
[5] T. Muroga, T. Nagasaka, K. Abe, V. M. Chernov, H. Matsui, D. L. Smith, Z. -Y. Xu and S. J. Zinkle, J.Nucl.Mater. 307-311 (2002) 547.
[6] T. Nagasaka, T. Muroga and T. Iikubo, Fusion Sci.Tech. 44(2003) 465.
[7] H. M. Chung, B. A. Loomis and D. L. Smith, J.Nucl.Mater. 239 (1996) 139.
[8] S. Ukai, M. Harada, H. Okada, M. Inoue, S. Nomura, S. Shikakura, T. Nishida, M. Fujiwara and K. Asobe, J.Nucl.Mater. 204 (1993) 74.
[9] R. J. Kurtz and M. L. Hamilton, J.Nucl.Mater. 283-287 (2000) 628.
[10] T. Nagasaka, T. Muroga, M. L. Grossbeck and T. Yamamoto, J.Nucl.Mater. 307-311 (2002) 1595.

Creep mechanism of highly purified V-4Cr-4Ti alloys during thermal creep in a vacuum

Ken-ichi Fukumoto[1], Takuya Nagasaka[2], Takeo Muroga[2], Nobuyasu Nita[3], Hideki Matsui[3]

[1]*Graduate School of Nuclear Power and Energy Safety Engineering: University of Fukui, Fukui 910-8507, Japan*
[2]*National Institute for Fusion Science, Toki, Gifu 509-5292, Japan*
[3]*Institute for Materials Research : Tohoku University, Sendai 980-8577,Japan*

Abstract

Pressurized thermal creep tubes of highly purified V-4Cr-4Ti, the NIFS-Heat2 alloy have been examined following testing in the range 700 to 850°C. It was found that the creep stress exponent of the NIFS-Heat2 alloy is about 5 and that the characteristic creep mechanism was the dislocation creep usually observed in pure metals. The apparent activation energy of creep deformation is about 210kJ/mol in the temperature range 700 to 850°C. Creep deformation was considered to be controlled by climb-controlled dislocation glide at 850°C, where sub-grain boundary structure predominates and consists of dislocation dipole structures and pile-ups of dislocations.

Introduction

Vanadium alloys are candidate materials for fusion reactor blanket structural applications because of their potentially high operation temperatures. However the knowledge about the creep properties of vanadium alloys at fusion-relevant temperatures is limited and there are uncertainties that may have influenced the results such as the interstitial impurity content of specimens. In order to measure irradiation creep, several tests have been done using pressurized creep tubes (PCTs) [1-3]. Recently, high-purity V-4Cr-4Ti ingots (NIFS-HEAT-1 and 2) were provided by the National Institute for Fusion Science (NIFS), Japan [4-6]. In order to perform creep tests on highly purified V-4Cr-4Ti alloys, a manufacturing process for pressurized creep tubes has been established with the aim of avoiding contamination by interstitial impurities during the process [6,7].

The objective of this study is to investigate the thermal creep properties and microstructural changes of a highly purified V-4Cr-4Ti alloy, the NIFS-HEAT2, by using PCTs, as a preliminary study to enable future in-pile creep tests.

Experimental Procedures

The V-4Cr-4Ti alloy used in this study was produced by NIFS and Taiyo Koko Co. and is designated NIFS-HEAT2 [5]. The detailed fabrication processes for tubing and for PCTs have been reported [6,7]. Table 1 shows the creep test conditions for PCTs. The PCTs wrapped with Ta and Zr foils were encapsulated in a quartz tube in a vacuum of <~$5x10^{-3}$Pa. In order to remove gas impurities from the quartz tube, about 100cm^2 of Zr foil were included as a getter. Thermal creep tests were performed by placing the sealed quartz tubes in a muffle furnace. Dimensional changes of PCTs were measured with a precision laser profilometer manufactured by KEYENCE, LM-7030MT. Diameters were determined to an accuracy of ±1μm. When the creep strain exceeded 20%, the creep test was terminated. Transmission electron microscopy (TEM) observations were performed on pieces cut from selected PCTs. The detailed fabrication procedure for TEM specimens from PCTs has been reported [2]. TEM observations were performed using a JEOL-2000FX at the Univ. of Fukui. Chemical analyses for oxygen and nitrogen were performed on two of the 850°C PCT specimens using the rest of the specimens.

Table 1. : Creep test conditions for NIFS-Heat2 PCTs. The label (*) indicates that TEM observations have been performed on that specimen.

Test Temperature (C)	700	750	800	850
Tubing annealed 2h at 1000C				
Effective stress (MPa)	200 150 110	200 150 100	200 150 90 70 50	 150 100
As-drawn tubing				
Effective stress (MPa)			137	

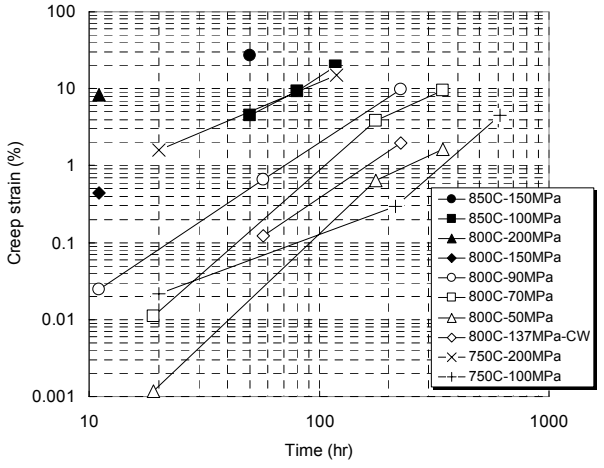

Fig.1. : Time dependence of the effective mid-wall creep strain of a highly purified V-4Cr-4Ti, the NIFS-Heat2 alloy for the 700, 750, 800 and 850°C test temperatures.

Results

Creep strain measurement

Fig. 1 shows the time dependence of the effective mid-wall creep strain for 700°C, 750°C, 800°C and 850°C test temperatures. In fig.1, primary creep can not be observed as the duration of primary creep is expected to be short [8, 9].

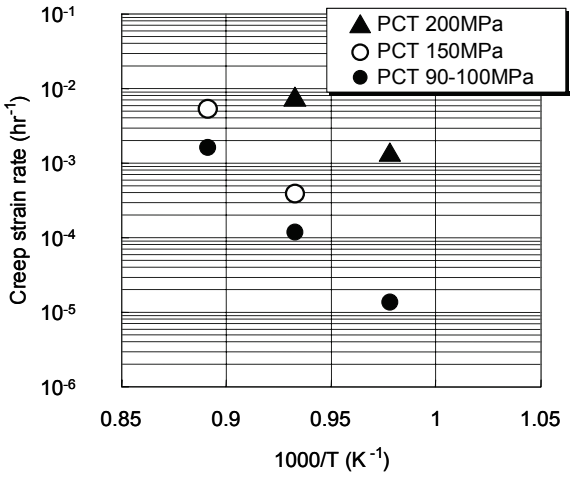

Fig.2. : Arrhenius plot of creep strain rate of a highly purified V-4Cr-4Ti, the NIFS-Heat2 alloy. Stress levels are 200, 150 and 90-110MPa.

Fig.2 shows an Arrhenius plot of creep strain rate obtained from data in Fig.1. Creep strain rates were determined by using data for effective strains less than about 1% to exclude any ternary creep data, even though the remaining number of data are few. From Fig.2, the activation energy for creep of V-4Cr-4Ti was estimated for effective stress levels of approximately 100 and 150MPa. Activation energies ranging from 197 to 227kJ/mol were obtained, with an average value of 210kJ/mol. The activation energies do not vary inversely with stress as has been observed for pure vanadium [8, 10]. These values are similar to those obtained for the NIFS-Heat in uniaxial creep tests about 180 to 210kJ/mol in the 750 - 800°C temperature range [9]. However, these values are somewhat smaller than the activation energy for self diffusion in pure vanadium, which is about 270kJ/mol in the 700-800°C temperature range [8, 11].

The stress dependence of creep strain rate was also deduced from Fig.1. The data in Fig.1 were fitted with the equation $d\varepsilon/dt=A\sigma^n$, where A is a constant, n the creep stress exponent, ε the effective creep strain rate and σ is the effective stress. The stress exponent was found to be 4.9 for 800°C creep data. It has been reported that the strain exponents, n, for pure V and V-Ti alloys [10,12,13] are greater than 5 for creep test conditions similar to those used in this work, indicating that the creep mechanism is climb-assisted glide of dislocations.

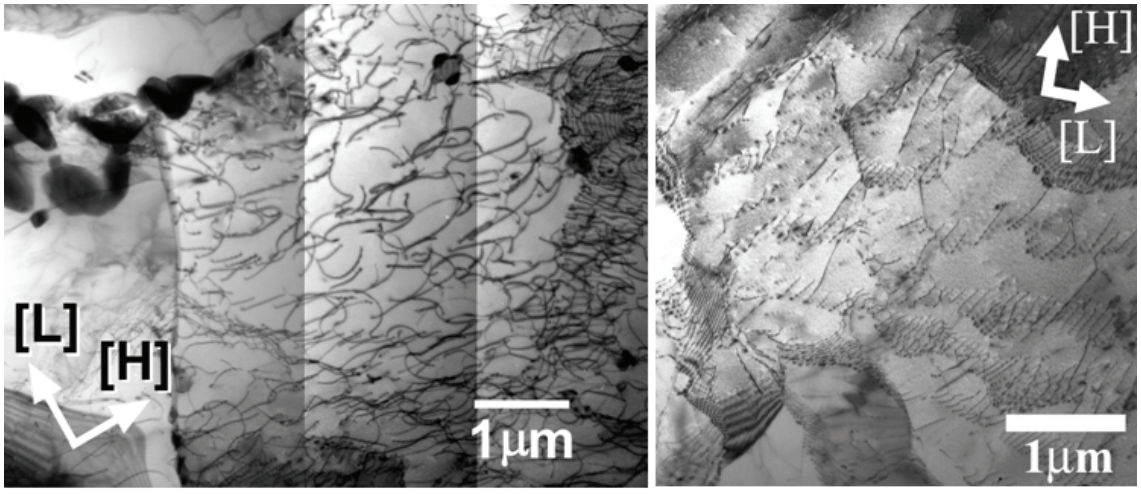

Fig.3. : Examples of TEM images of a highly purified V-4Cr-4Ti, the NIFS-Heat2 alloy, tested at 850°C under creep stresses of 100MPa and 150MPa. Arrows indicate the directions related to the pressurized creep tube geometry; [L] indicates a longitudinal direction along the tube and [H] a hoop direction.

The average oxygen and nitrogen levels have been measured to be 330 and 110wppm after 51h, and 520 and 140wppm after 118h for the 850°C PCT specimens. On the other hand, the oxygen content and the nitrogen content were 270wppm and 110wppm after 660h for the 750°C PCT specimens, respectively. These levels may be compared to the as-received values of 370wppmO and 100wppmN. It is indicated that impurity pick up does not occur in creep tests with a quartz tube due to careful sealing treatment. However, there is a possibility that residual gas impurity unexpectedly remained in the quartz tube and was absorbed by some specimens during vacuum encapsulation

Microstructural analysis

The two specimens tested at 850°C were selected for

TEM observation and for chemical analyses in order to identify the operating creep mechanism. TEM micrographs of the NIFS-Heat2 alloy tested at 850°C are presented in Fig. 3. Moderately high dislocation densities can be seen in the 100MPa specimen, where the dislocations tend to be confined to sub-grain boundaries like cell structures and to lie in randomly arrays inside the sub-grains. On the other hand, dislocation cell structures are fully developed in a uniform array at regular intervals of about 0.8□m in the 150MPa specimen. Precipitates of Ti(OCN) are located in non-uniform distributions in grains and/or at grain boundaries. The precipitate particles were present prior to testing and did not change significantly as a result of creep testing; they are similar in size to those reported by Heo [14].

In order to identify the dislocation Burgers vectors, the $\boldsymbol{g}\cdot\boldsymbol{b}$=0 technique was applied. Such an analysis revealed that most of the free dislocations not associated with sub-grain boundaries in the 100MPa specimen are of the a/2<111> type. Fig.4 shows TEM images of a dislocation array in the specimen tested at 850°C at a stress of 150MPa. The straight dislocations running from upper left to lower right consist of dislocations with two types of Burgers vector, [111] and [-111]. Orientation trace analysis show they are edge dislocations. Therefore, this dislocation array consists of edge dipoles made of different types of dislocations. Other examples were found showing that the sub-grain boundaries were comprised mainly of edge dislocations

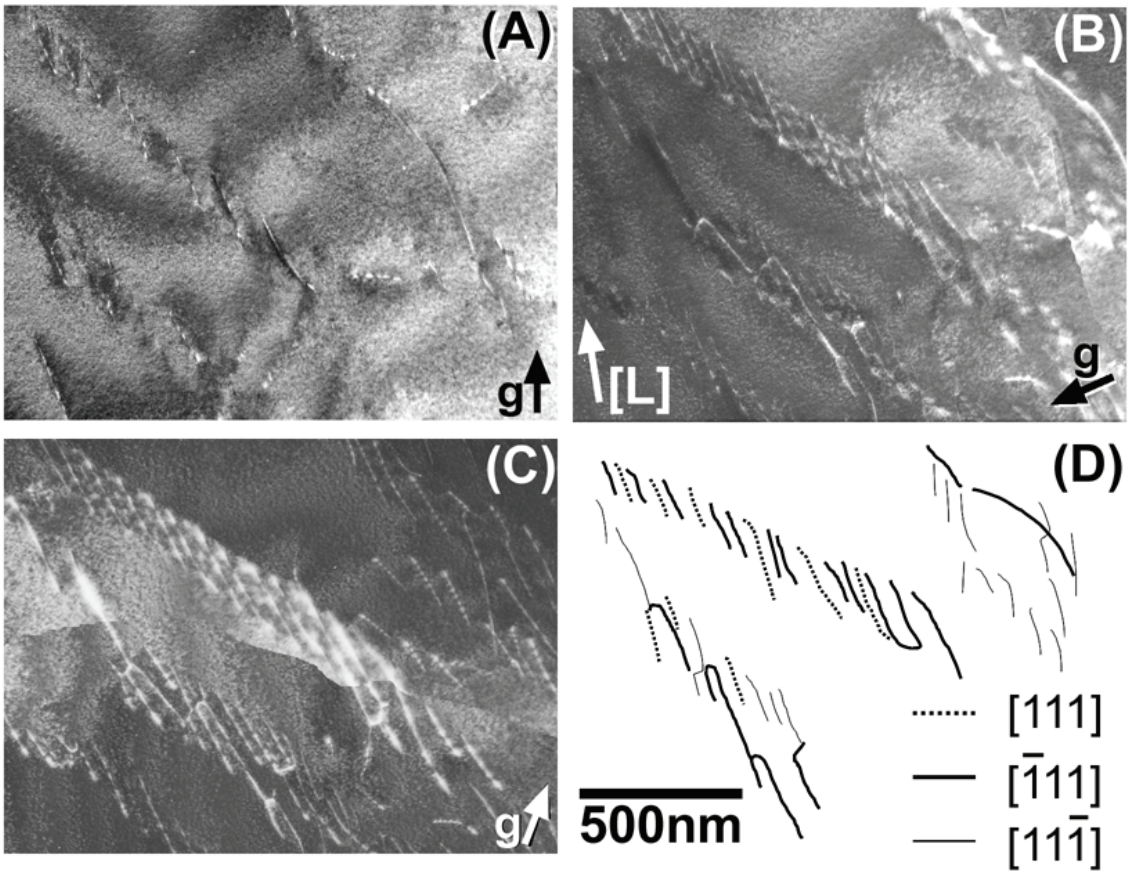

Fig.4. : Examples of TEM images of dislocation structures in the V-4Cr-4Ti alloy tested at 850°C with a stress of 150MPa. (A) (1 $\bar{1}$ 0) diffraction vector, (B) ($\bar{1}$ 21) diffraction vector, (C) (121) diffraction vector, and (D) a characterization map for Burgers vector of dislocations. The arrow inserted in each photo shows the direction of the g-reflection.

Discussion

Both uniaxial [9, 15] and biaxial [8, 16] creep tests were performed in vacuum with different starting concentrations of interstitial O in recent studies. A review of thermal creep of V-Cr-Ti alloys by Kurtz [16], found the activation energy for creep between 700 and 800°C to be about 300kJ/mol, which is similar to the activation energy for self-diffusion in pure V. This suggests that in this regime of temperature and stress the predominant creep mechanism is climb-assisted dislocation motion. The apparent activation energy in the present study is 210kJ/mol for stresses between 100 and 150MPa. These values are lower than the activation energy found for the US-Heat #832665 of V-4Cr-4Ti, 299kJ/mol [8], and higher than the values found for V-2.8Ti, 125kJ/mol [12,17]. It has been reported that the strong scavenging effect of titanium and low oxygen solubility in V-3Ti correspond to the lowest activation energy for creep in V-Ti alloys [11]. This result indicated that the oxygen content may be significantly lower in V-3Ti than in any

other V-Ti alloy and that the reduction of matrix impurity contents may lead to a lower amount of activation energy. The reduction in oxygen and interstitial impurity content, may explain why the activation energies for NIFS-Heat alloys are lower than the energy for other V-4Cr-4Ti alloys containing above 1000wppm of O, C, N. It suggests that the reduction of impurity content lowers the potential barrier for vacancy diffusion and impurities in V-Cr-Ti alloys act as trapping site for vacancies, leading to the formation of Ti solute – impurity – vacancy complexes. It is also possible these complexes are obstacles to climb-assisted vacancy diffusion to dislocation cores in these creep conditions.

The power law dependence of the secondary creep rate on stress with n=4.9, in this study is in good agreement with the value of stress exponent of n=~4 reported in a review of thermal creep for V-4Cr-4Ti by Kurtz [16]. This result also suggests that the operating creep mechanism is climb-assisted dislocation motion and this idea is supported by the microstructural analysis. The cell structure formation occurring during thermal creep also indicates that the creep mechanism is of pure metal type and that dislocation core diffusion plays an important role as the rate controlling process for creep deformation. The cell structure is made of arrays of edge dislocation dipoles formed during thermal creep and did not result from post-creep deformation. The other dislocation arrays made of dislocations with one type of Burgers vector also appears to be formed during thermal creep. Both types of dislocation arrays formed in the same grain without free dislocations between cell walls indicating no post-creep deformation. The dependence of the microstructure on stress also suggests that at high stresses glide-controlled creep behavior predominates over the climb-controlled creep such that free dislocations in a sub-grain are absorbed in the sub-grain walls. The increase in density of free dislocations between sub-grain boundaries at lower stress levels indicates that climb controlled creep dominates and dislocations then distribute randomly. With increasing density of free dislocations, the creep stress exponent gradually decreases to a value of about 3, indicating a solid-solute creep behavior [18]. Since the target of this study was to explore creep deformation under moderately high stress level, the data are not sufficient to establish the creep mechanism diagram for V-4Cr-4Ti. Further work at lower stresses and elevated temperatures are needed to determine the thermal creep mechanisms as a baseline for future irradiation creep measurements.

Summary

In order to investigate the thermal creep properties and microstructural changes of the highly purified NIFS-HEAT2 V-4Cr-4Ti, thermal creep tests were performed in the range 700 to 850°C using PCTs. The creep stress exponent for the NIFS-Heat2 alloy was about 5 which is characteristic of dislocation-glide creep observed in pure metals. The apparent creep activation energy of creep deformation was about 210kJ/mol in the temperature range 750 to 800°C. Microstructural analysis showed dislocation cell structures developed at 850°C under with the highest applied stress. This also suggests that climb-assisted glide of dislocations is the rate-limiting creep process at 850°C.

Acknowledgements

This work was supported by NIFS Budget Code, NIFS04KFRF01

Reference

[1] : H. Tsai, H. Matsui, M. C. Billone, R. V. Strain and D. L. Smith, J. Nucl. Mater. 258-263 (1998) 1471.
[2] : K. Fukumoto, S. Takahashi, R. J. Kurtz, D. L. Smith and H. Matsui, J. Nucl. Mater. 341 (2005) 83.
[3] : J.M. Vitek, D.N. Bras ki, J.A. Horak, J. Nucl. Mater. 141–143 (1986) 982.
[4] : T. Muroga, T. Nagasaka, A. Iiyoshi, A. Kawabata, S. Sakurai, M. Sakata, J. Nucl. Mater. 283–287 (2000) 711.
[5] : T. Muroga, T. Nagasaka, K. Abe, V.M. Chernov, H. Matsui, D.L. Smith, Z.-Y. Xu, S.J. Zinkle, J. Nucl. Mater. 307–311 (2002) 547.
[6] : T. Nagasaka, T. Muroga, T. Iikubo, Fusion Sci. Tech. 44 (2003) 465.
[7] : K. Fukumoto, H. Matsui, M. Narui, T. Nagasaka, T. Muroga, J. Nucl. Mater. 335 (2004) 103
[8] : R. J. Kurtz and M. L. Hamilton, J. Nucl. Mater. 283-287 (2000) 628
[9] : K. Fukumoto, T. Yamamoto, S. Nakao, S. Takahashi and H. Matsui., J. Nucl. Mater. 307-311 (2002) 610
[10] : K.R. Wheeler, E.R. Gilbert, F.L. Yaggee, S.A. Duran, Acta Metall. 19 (1971) 21.
[11] : D.L. Harrod, R.E. Gold, Int. Met. Rev. 4 (1980) 163.
[12] : H. Boehm, et al., J.Less-Common Met. 12(1967) 280
[13] : T. Kainuma, N. Iwao, T. Suzuki and R. Watanabe, J.Less-Common Met. 86 (1982) 263
[14] : N. J. Heo, T. Nagasaka and T. Muroga, J. Nucl. Mater. 325 (2004) 53
[15] : K. Natesan, W.K. Soppet, A. Purohit, J. Nucl. Mater. 307–311 (2002) 585.
[16] : R.J. Kurtz, K. Abe, V.M. Chernov, D.T. Hoelzer, H. Matsui, T. Muroga, G. R. Odette, J. Nucl. Mater. 329–333 (2004) 47
[17] : H. Boehm et al., Z.Metallkdet. 59 (1968) 715
[18] : J. Cadek, “Creep in metallic materials” (Elsevier, 1988) p.115

TUNGSTEN COATING ON LOW ACTIVATION VANADIUM ALLOY BY PLASMA SPLAY PROCESS

TAKUYA NAGASAKA *National Institute for Fusion Science, Oroshi 322-6, Toki, Gifu 509-5292, Japan*
+81-572-58-2252, nagasaka@nifs.ac.jp
TAKEO MUROGA *National Institute for Fusion Science, Oroshi 322-6, Toki, Gifu 509-5292, Japan*
+81-572-58-2119, muroga@nifs.ac.jp
NOBUAKI NODA *National Institute for Fusion Science, Oroshi 322-6, Toki, Gifu 509-5292, Japan*
+81-572-58-2124, noda@nifs.ac.jp
MASASHI KAWAMURA *Kawasaki Heavy Industries, LTD., Akashi 673-8666, Japan*
+81-78-921-1301, kawamura@ati.khi.co.jp
HIDEO ISE *Kawasaki Heavy Industries, LTD., Koto-ku, Tokyo 136-8588, Japan*
+81-3-3615-5147, ise_h@khi.co.jp
HIROAKI KURISHITA *Institute for Materials Research, Tohoku University, Oarai, Ibaraki 311-1313, Japan*
+81-29-267-3181, kurishi@imr.tohoku.ac.jp

Tungsten (W) coating on fusion candidate V-4Cr-4Ti (NIFS-HEAT-2) substrate was demonstrated with plasma spray process for the purpose of applying to protection of the plasma facing surface of a fusion blanket. Increase in plasma input power and temperature of the substrate was effective to reduce porosity of the coating, but resulted in hardening of the substrate and degradation of impact property at 77 K. The hardening seemed to be due to contamination with gaseous impurities and deformation by thermal stress during the coating process. Since all the samples showed good ductility at room temperature, further heating seems to be acceptable for the vanadium substrate. The fracture stress of the W coating was estimated from bending tests as at least 313 MPa, which well exceeds the design stress for the vanadium structure in fusion blanket.

I. INTRODUCTION

Tungsten (W) is the promising candidate for the plasma facing material of fusion reactors, because of the high melting point (3683 K)[1], and low sputtering rate in fusion plasma environment[2]. Low activation and low impurity vanadium alloys have been recognized as attractive candidate structural materials in fusion blanket system operated at 720-1000 K, and they have demonstrated high mechanical performance and manufacturing feasibility[3, 4]. In the present study, W coatings on the low activation vanadium alloy were fabricated by plasma spray process, which is practical for large area coating because of its high coating rate. In the process, heating of the substrate is requisite for sound coating by keeping liquidity and flow of the melted metal particles on the surface. In the case of vanadium alloys, the heating can cause contamination with impurities, such as C, N and O, which are known to induce large hardening and degradation of mechanical properties of the vanadium alloys. The coating layer, the interface and the vanadium alloy substrate after coating were characterized in this study for the W-coated vanadium alloys produced. Engineering issues, bonding property and behavior of the constituent element of the coating and pick-up impurities were discussed.

II. EXPERIMENTAL PROCEDURE

The substrate used was a 1.9 mm-thick plate of NIFS-HEAT-2 (NH2), which is a reference high purity V-4Cr-4Ti alloy[5, 6]. The substrate of SUS 420J2 was also used for trial and comparison purposes. Tungsten powders of 99.9 % grade and in 325 mesh size were used as coating materials for plasma spray process. Before the spray, the substrate surface was blustered with alumina and cleaned by argon arc sputtering. The tungsten powders were carried by argon (>99.99 % grade) gas to the plasma jet of argon (>99.998 % grade) and hydrogen (99.9 % grade) mixture. The jet sprayed the substrate with the melted tungsten particles. Table 1 shows the process parameters examined in the plasma spray process. Underlines show the difference between W5 and W6, or W7.

The coated samples were characterized by (1) microstructural observation with optical microscope (OM), elec-

Table 1 Process parameters examined in the plasma spray process.

		W5	W6	W7
Cleaning	Number of sputtering	5	5	5
	Number of heating	2	2	2
	Number of re-sputtering	5	2	2
Coating	Plasma input power, kW	45	45	46
	Plasma gun / substrate distance, mm	200	200	240
	Traveling speed, mm/sec	75	75	75
	Pressure in plasma chamber, X 10^5 Pa	0.12	0.095	0.12
	Number of coating layers	8	10	10

tron scanning microscope (SEM), electron probe X-ray micro analyzer (EPMA), (2) Vickers microhardness tests with the load of 500 g, (3) 3 point bending tests and (4) impact tests. The size of the specimen for the bending tests and impact tests was 2.4 mm in thickness including 1.9 mm of NH2 substrate and 0.5 mm of W coating, 3.3 mm in width and 25.4 mm in length. The loading point was on the substrate surface, so that tension stress was loaded on the W coating. The span at the bending tests and the impact tests was 20.3 mm and 15 mm, respectively. The crosshead speed for the bending tests and the impact tests was 0.01 mm / s and 4.5 m / s, respectively.

III. RESULTS

Figure 1 (a)-(d) shows cross sections of the coated samples. Many pores were observed in the coating of W5-2 (NH2 substrate + W coating) compared with W5-1 (SUS + W), W6 and W7. Fig. 2 shows the substrate temperature during the coating process. In W6, the temperature at the end of coating was 1080 K, which was above 100 K higher than that in W5 and W7. As shown in W6 and W7 in Table 1, the number of re-sputtering was decreased to keep substrate temperature high after heating during the cleaning process. In W6, pressure in the plasma chamber was decreased to keep substrate temperature by suppress of heat transfer to the atmosphere. In W7, plasma input power was increased to melt W particle further in the plasma jet. In W7, the distance between plasma gun and the substrate was, however, increased to avoid excess substrate heating. By these improvements, the melted W particles were considered to keep liquidity and flow on the surface. As a result, porosities in the W coating were much reduced in W6-4 (NH2 + W) and W7-4 (NH2 + W). The thickness of the coating was proportional to the number of coatings. 8 pass coatings in W5 made about 0.4 mm in coating thickness, while 10 pass in W6 and W7 resulted in about 0.5 mm in thickness. On the other hand, in high magnification images after electropolishing, crack type defects were observed in the W coating at all the conditions as shown in Fig. 1 (e). The defects lay vertical to the plasma spray direction and parallel to the coating surface. The spacing between the defect lines was about 20 μm as indicated in the arrows.

Figure 3 shows hardness distribution through the W coating and NH2 substrate. Hardness around the center of the substrate in W6-4 and W7-4 was 174 Hv and 157 Hv, respectively, which showed hardening compared with 139 Hv before the coating. Further hardening was observed within 300 μm in W6-4 and 100 μm in W7-4 from the interface between the W coating and the NH2 substrate. Maximum hardness in W6-4 and W7-4 was 216 Hv and 179

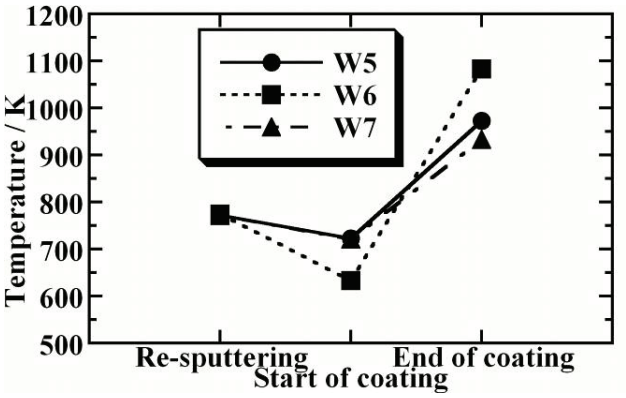

Fig. 2 Temperature of NH2 substrate during the plasma spray process.

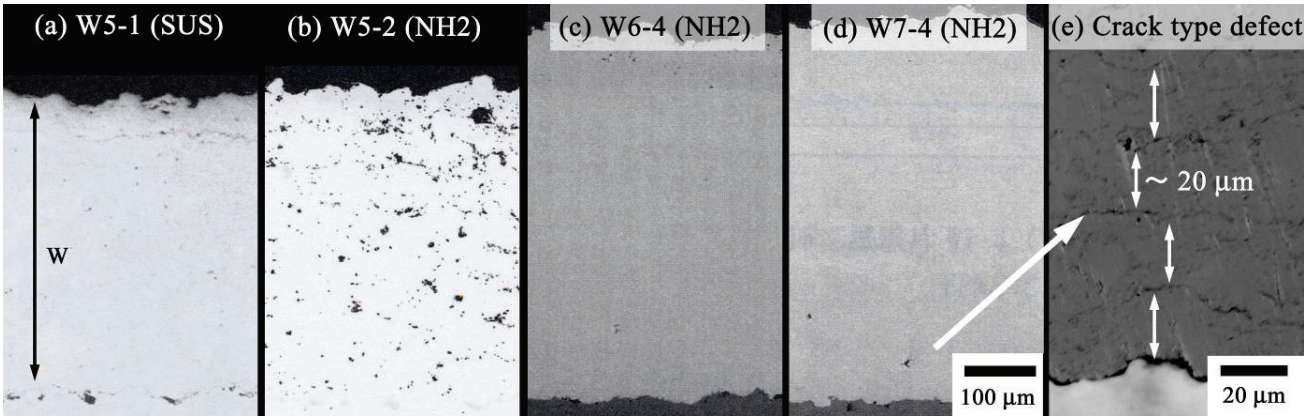

Fig. 1 (a) – (d) Cross section of W coatings as mechanically ground. (e) Crack type defects parallel to the coating surface appeared after electropolishing in W7-4.

Hv, respectively.

Figure 4 shows the distribution of the constituent elements, such as W, V, Cr and Ti, and impurities, such as Al and O, around the interface of W7-4. In the line analysis on both the W6-4 and W7-4, diffusion of W, V, Cr and Ti to each other was limited within 10 μm from the interface. From the mapping, images of Al and O overlapped and distributed in the NH2 substrate within 20 μm from the interface.

Load-deflection curves in bending tests at room temperature (297 K) are shown in Fig. 5. In W6-4 and W7-4 large load drop after elastic deformation was observed. W coating fracture observed after the bending test is shown in Fig. 6. The fracture mode of the W coating at the primary crack vertical to the W coating surface was intergranullar. The secondary crack parallel to the interface occurred in the W coating, and propagated along 50 μm from the interface. Some cracks propagated across the interface from the W coating into the NH2 substrate. After the fracture of the coating, the load in W6-4 and W7-4 in Fig. 5 was still higher than that in NH2 before coating.

Figure 7 shows Load- deflection curves in impact tests at 77 K and room temperature (295 K). Load level was increased in the same order as the bending test, such as NH2 before coating, W7-4 to W6-4. In the impact tests, large load drop at the end of elastic deformation could not be recognized because of large noise in load signal. In W6-4 at 77 K, rapid load decrease during plastic deformation was observed. Only in this case, the sample was fractured, and absorbed energy was much smaller than that of the other samples. Fig. 8 shows the fracture surface of W6-4. Ratio of the ductile fracture area with dimple pattern and the brittle area with river pattern was 23 % and 77 %, respectively.

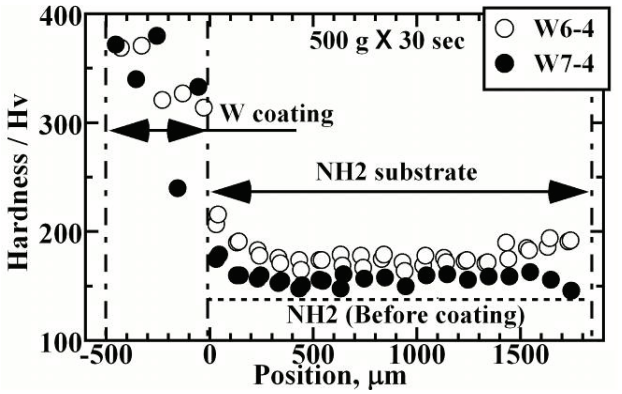

Fig. 3 Hardness distribution through W coating and NH2 substrate. The dashed line indicates the hardness level before coating.

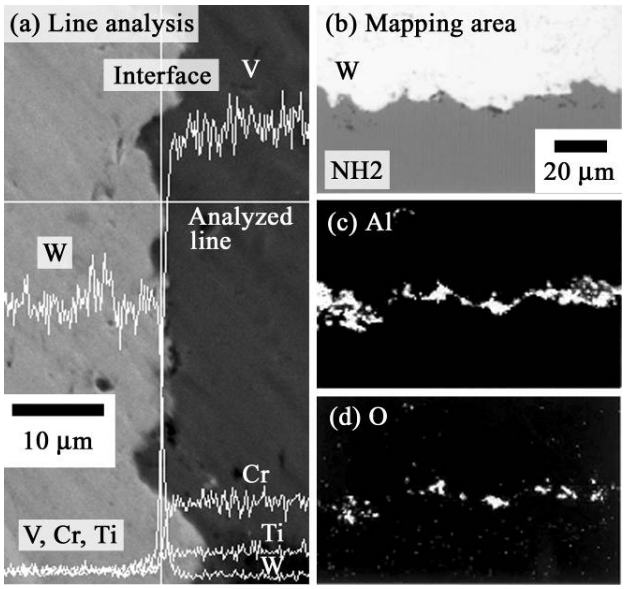

Fig. 4 Distribution of (a) the constituents, W, V, Cr and Ti, and (b) (c) (d) impurities, Al and O, around the interface in W7-4. (a) shows intensity at line analysis. (c) and (d) are mapping images at the area indicated by (b).

IV. DISCUSSION

As shown in Fig. 1, direct deposition of W on vanadium alloy by plasma spray process was successfully demonstrated. The more porosities in Fig. 1 (b) compared with

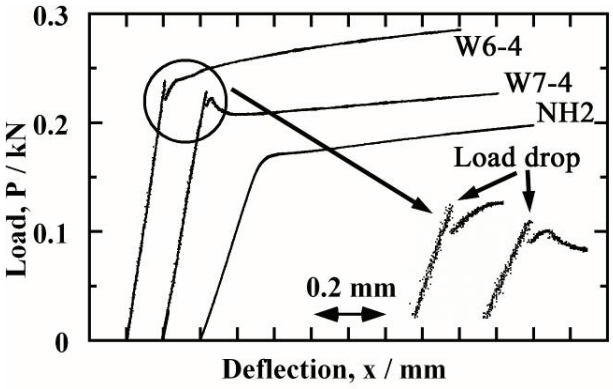

Fig. 5 Load-deflection curve for the bending tests at room temperature (297 K). NH2 is the un-coated substrate.

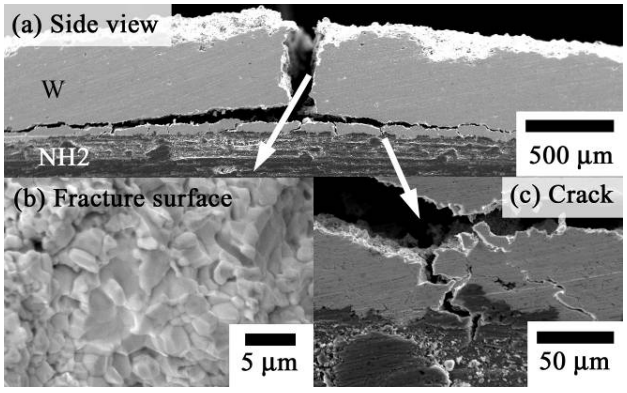

Fig. 6 Fractured W coating of W7-4 after bending test. Stress during the test in the W coating was tension.

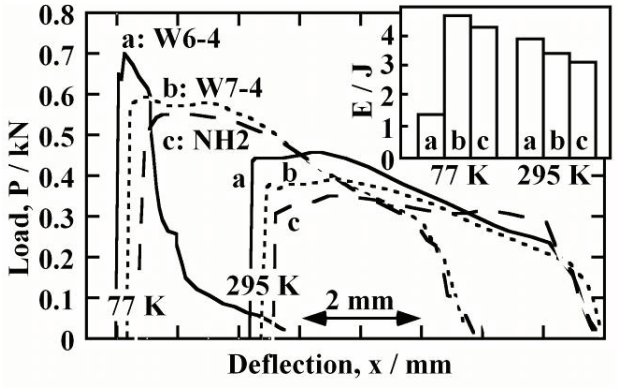

Fig. 7 Load-deflection curve for the impact tests at 77 K and room temperature (295 K). Absorbed energy is also plotted.

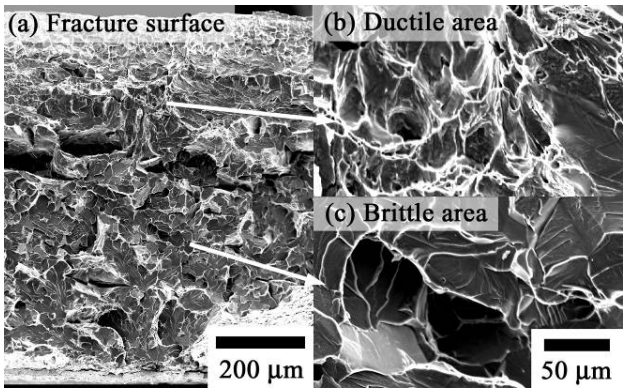

Fig. 8 Fracture surface of W6-4 after the impact test. High magnification images for ductile area and brittle area are also shown.

Fig. 1 (a) indicate less liquidity and flow of W particles on the NH2 substrate by rapid cooling, which is consistent with higher thermal conductivity of NH2, such as 43 W / m K at 1073 K, than that of SUS, typically 25 W / m K at 1073 K. In order to obtain less porosity coating, the change in plasma process parameter shown in Table 1 was effective. However increase in plasma chamber pressure and higher temperature of the NH2 substrate enhance contamination with gaseous impurities, such as C, N and O from C_xH_y, N_2, O_2 and H_2O in the atmosphere.

From Fig. 6, some cracks propagated across the interface, and they are thought to induce brittle fracture shown in Fig. 8. The NH2 substrate in W6-4 was significantly hardened at 77 K as Fig. 7, where deformation stress was considered higher than cleavage fracture stress. As shown in Fig. 3, hardening was observed through the NH2 substrate, and was significant within 100-300 μm from the interface. Fig. 4 shows diffusion of W and segregation of Al and O in the NH2 substrate. The Al and O are thought as remaining alumina particles used in blustering before coating. However, the diffusion and segregation was limited within 10-20 μm from the interface, and cannot explain the farther hardening. Uz et al. has reported hardening by oxygen diffusion in V-4Cr-4Ti alloy, and determined diffusion coefficient, D, and activation energy, Q, at 773 K, such as 4.0×10^{-6} m^2 s^{-1} and 130 kJ mol^{-1}, respectively[7]. Extrapolating them to higher temperature by followings,

$$D = D_0 \exp\left(-\frac{Q}{R\,T}\right) \quad (1)$$

$$L = \sqrt{D\,t} \quad (2)$$

where D_0: constant, R: gas constant = 8.3144 J mol^{-1} K^{-1}, T: temperature, L: diffusion range, t: diffusion time

diffusion range can be estimated as 80 μm at 1073 K, 260 μm at 1273 K and 600 μm at 1473 K for 3.6 ks. The ranges seem to be consistent with the extra-hardening area depth from the interface, 100-300 μm, assuming that the substrate surface was locally heated up to higher temperature, such as above 1273 K, than that measured in Fig. 2. On the other hand, hardening at the center of the NH2 substrate has not been understood yet. Possible hardening criteria are contamination with hydrogen from the plasma jet, and deformation hardening by thermal stress during the coating process. Diffusion parameters for hydrogen have been reported as 3.5×10^{-8} m^2 s^{-1} in D_0 and 6.1 kJ mol^{-1} in Q[8], which are equivalent to 1000 μm in diffusion range even at 773 K for 80 s. The thermal stress is due to the difference in thermal expansion coefficient between W; 4.6×10^{-6} K^{-1} (RT-773 K), and NH2; 1.0×10^{-5} K^{-1} (RT-673 K). High temperature during coating for W-6-4 in Fig. 3 can be responsible for the heavier contamination with the gaseous impurities and larger deformation by thermal stress, resulting in larger hardening than that of W7-4 observed in Fig. 3, and also in Fig. 5 and Fig. 7. Degassing with hydrogen and reduction in hardness has been reported to be possible at 673 K[9]. It has been also reported that deformation hardening started to recover at 873 K[10]. From the above discussion, effective process management to avoid hardening of the NH2 substrate is likely to be appropriate annealing after coating as well as temperature control suppressing diffusion of gaseous impurities.

Bending strain, ε, and stress, σ, for homogeneous materials, such as NH2 before coating, are generally defined as the followings in elastic region[11],

$$\varepsilon = \frac{6\,T\,x}{S^2} \quad (3)$$

$$\sigma = \frac{3\,P\,S}{2\,B\,T^2} \quad (4)$$

where T: specimen thickness, x: deflection, S: span, P: load, B: specimen width.

For the cladding materials, such as W6-4 and W7-4, Eq. (4) is not applicable, so that elastic modulus for W coating, E_W, and bending stress for the W coating, σ_W, are estimated by the following equation[12].

$$\frac{1}{E_{NH2+W}} = \frac{\alpha_W}{E_W} + \frac{\alpha_{NH2}}{E_{NH2}} \quad (5)$$

$$\sigma_W = E_W \varepsilon_W \quad (6)$$

where E_{NH2+W}: apparent elastic modulus for the cladding materials, $\alpha_W = 0.24$, $\alpha_{NH2} = 0.76$: volume ratio of each materials to the specimen volume, E_{NH2}: Elastic modulus for the NH2 substrate, ε_W: bending strain for the W coating = ε from Eq. (4) with specimen thickness of the cladding materials.

Propagation of the primary crack of the W coating was considered to induce the load drop in Fig. 5. From the load and the deflection data for the elastic limit at the load drop, elastic modulus and fracture stress for the W coating were estimated as shown in Table 2. Elastic modulus and fracture stress estimated in the present study, such as 469 MPa and 313 MPa, are much smaller than 1000 MPa of the previous data for bulk W[1]. W coating itself is probably weaker than W bulk, because the coating contained many defects shown in Fig. 1 and indicated intergranullar fracture shown in Fig. 6. For structural materials, design stress is defined typically as 1/3 level of the yield stress, such as 100 MPa for vanadium alloys. This stress produces 0.1 % of strain in NH2 from Eq. (6) and the elastic modulus obtained in Table 2. From again Eq. (6), the 0.1 % strain induces stress of 129 MPa and 77 MPa in W6-4 and W7-4, respectively. The fracture stress of 469 MPa and 313 MPa well exceeds the induced stress. This means that the W coating require no change in design stress.

Figure 6 shows the secondary crack propagated along 50 μm far from the interface, and this indicates that the interface is stronger than W coating. The crack path is thought to be along the crack type defects shown in Fig. 1. The defects seem to degrade heat transfer toward vertical direction to coating surface. The defects are considered to be the interface between sprayed particles, because the defect spacing, 20 μm, is comparable to the W particle size, several 10 μm. From Fig. 7, W6-4 exhibited the comparable absorbed energy to NH2 before coating at room temperature, thus more extent of heat is acceptable for the NH2 substrate. Increasing in plasma input power and substrate temperature are expected to reduce the crack type defects and to improve thermal conductivity.

Table 2 Mechanical property parameters estimated from the bending tests.

	Present study	Previous data
NH2 before coating		Ref. [13]
Elastic modulus, E_{NH2} / GPa	101	129
0.2 % proof stress, $\sigma_{0.2\,\%}$ / MPa	469	318
W coating	W6-4	Ref. [1]
Elastic modulus, E_W / GPa	129	410
Fracture strain, ε_f / %	0.36	< 0.4
Fracture stress, σ_f / MPa	469	1000
	W7-4	
Elastic modulus, E_W / GPa	77.0	
Fracture strain, ε_f / %	0.41	
Fracture stress, σ_f / MPa	313	

V. CONCLUSION

W coating on vanadium alloy by direct deposition with plasma spray process has been successfully demonstrated. It was suggested that the fracture stress of the W coating was at least 313 MPa, and that no change in design stress was required by the coating. The vanadium substrate was hardened during the process seemingly by gaseous impurity contamination and by thermal stress deformation. Cracks initiated in the W coating could propagate across the interface between the coating and the vanadium alloy substrate. They also could induce brittle fracture at 77 K, if the substrate is significantly hardened. Since the hardest substrate still showed good ductility at room temperature, more heat is acceptable during the coating to obtain defect-less coating and good thermal conductivity.

ACKNOWLEDGMENT

Authors are grateful to the staff of International Research Center for Nuclear Materials Science, Institute for Materials Research, Tohoku University for bending tests and impact tests.

REFERENCES

[1] I. Smid et al., "Development of tungsten armor and bonding to copper for plasma-interactive components", *J. Nucl. Mater.*, **258-263**, 160-172 (1998).

[2] R. Neu et al., "The tungsten experiment in ASDEX Upgrade", *J. Nucl. Mater.*, **241**, 678-638 (1997).

[3] R. J. Kurtz et al., "Critical issues and current status of vanadium alloys for fusion anergy applications", *J. Nucl. Mater.*, **283-287**, 70-78 (2000).

[4] T. Muroga et al., "Vanadium alloys – overview and recent results" *J. Nucl. Mater.*, **307-31**1, 547-554 (2002).

[5] T. Nagasaka et al., "Examination of fabrication process parameters for improvement of low-activation vanadium alloys", *Fusion Eng. Des*., **61-62**, 757-762 (2002).

[6] T. Nagasaka et al., "Low Activation Characteristics of Several Heats of V-4Cr-4Ti Ingot", *J. Plasma and Fusion Res.*, **5**, 545-550 (2002).

[7] M. Uz et al., "Oxidation kinetics and microstructure of V-(4-5) wt% Cr-(4-5) wt% Ti alloys exposed to air at 300-650°C", *J. Nucl. Mater.* **245**, 191-200 (1997).

[8] D. L. Harrod et al., "Mechanical properties of vanadium and vanadium-base alloys", *Intl. Metals Reviews*, **25** 163-221 (1980).

[9] T. Nagasaka et al., "Effects of post-weld heat treatment conditions on hardness, microstructures and impact properties of vanadium alloys", *J. Nucl. Mater.*, **307-311**, 1595-1599 (2002).

[10] N. J. Heo et al., "Recrystallization and precipitation behavior of low activation V-Cr-Ti alloys after cold rolling", *J. Nucl. Mater.*, **325**, 53-60 (2004).

[11] Example: Y. Ikuhara et al., "Grain boundary and high-temperature strength of sintered SiC", Yogyo-Kyokai-Shi, **95**, 638-645 (1987).

[12] Example: "Kinzoku Binran (Metal Handbook) 4th Ed.", Maruzen Co., Ltd., Tokyo, Japan, p. 984, (1982).

[13] A. Nishimura et al., "Effect of Precipitation and Solution Behavior of Impurities on Mechanical Properties of Low Activation Vanadium Alloy", *J. Nucl. Mater.*, In press.

THE MICROSTRUCTURE OF LASER WELDED V-4Cr-4TI ALLOY AFTER NEUTRON IRRADIATION

H. Watanabe[a], K. Yamasaki[b], A. Higashizima[b], N. Yoshida[a], T. Nagasaka[c] and T. Muroga[c]

[a] Research Institute for Applied Mechanics, Kyushu University, 6-1, Kasuga-kouenn, Kasugashi, Fukuoka, 816-8580, Japan
[b] Interdisciplinary Graduate School of Engineering Sciences, Kyushu University, 6-1, Kasuga-kouenn, Kasugashi, Fukuoka, 816-8580, Japan
[c]National Institute for Fusion Science, 322-6, Oroshi, Tokai, Gifu, 509-5292, Japan

Effects of neutron irradiation on YAG laser welded V-4Cr-4Ti alloy were studied in JMTR (Japanese Materials Testing Reactor). The samples with and without post-weld heat treatment (PWHT) at 1073K were irradiated in the temperature range of 673 – 873K up to the dose of 0.45 dpa. After the irradiation, the microstructure and Vickers hardness of the welded samples were compared of the base metal, which were simultaneously irradiated at the same irradiation cycle.

I. INTRODUCTION

It is recognized that welding procedure is one of the key technologies for use of V-4Cr-4Ti alloys in a large component [1]. However the susceptibility of these alloys to the embrittlement caused by interstitial impurities during welding is highly pronounced. To avoid the pick-up of impurities (e.g. oxygen and nitrogen) from the welding environment, electron beam (EB) and gas tungsten arc (GTA) welding [2,3] were conducted using a vacuum chamber or a glove box. Recently, laser welding technology for the alloys was developed by NIFS (National Institute for Fusion Science) by controlling the flow rate of high purity argon gas [4]. Because of the flexible, in-field, automated and remote operation, and small weldment and heat affected zone (HAZ), laser welding is an attractive welding technology.

Our recent ion irradiation on these materials [5] revealed that the defect cluster density (mainly interstitial type dislocation loops) of weld metal is almost comparable to that of base metal after ion irradiation at 573K. On the other hand, after irradiation at 873K, fine titanium oxides with {100} habit planes were detected even at the dose of 0.75 dpa. This means that the behavior of oxygen atoms, which dissolve from the large precipitates during laser welding, strongly affects microstructural evolution of welded V-4Cr-4Ti alloys during irradiation at 873K.

However, little is known regarding the effects of neutron irradiation on the weldment. Nagasaka et al. [6] revealed that weld metal showed larger irradiation hardening than that of the base metal after neutron irradiation at 563K. The hardening of the weld metal was effectively reduced by post-weld heat treatments (PWHT) at 873K and 1223K. The irradiation hardening at 563K was mainly controlled by a very high density of dislocation loops, but higher in irradiation temperature regimes, formation of radiation-induced Ti(CON) precipitates becomes dominant. The present paper summarizes the recent progress on the microstructural evolution of laser welded V-4Cr-4Ti alloy during neutron irradiation at higher irradiation temperature regimes.

II. EXPERMENTAL

Welded joints used in this study were prepared from a high purity V-4Cr-4Ti alloy, which was designated as NIFS-HEAT-2 [1,7]. Before the YAG laser welding (bead-on-plate welding) in a high purity argon atmosphere, the samples were annealed in vacuum at 1273K for 2hr. The detailed welding procedure was described elsewhere[3]. Oxygen concentrations of the sample before and after welding were 139 and 158 wt ppm, respectively. The PWHT was carried out in a vacuum of about 1×10^{-5} Pa at 1023K for 1 or 100hr. Before the annealing, the samples were sandwiched between tantalum sheets and they were wrapped in zirconium foil. The samples were encapsulated in quartz glass to prevent the contamination of impurities. Fission neutron irradiation was carried out in JMTR under improved temperature control condition at 673, 723 and 873K in the same irradiation cycle (namely, JMTR 03M-69U). The total neutron dose of irradiation was $5.18 \times 10^{24}/m^2$ (>1.0 MeV), which corresponds to 0.45 dpa.

III. RESULTS

III.A. Temperature dependence of microstructure

The microstructure of laser welded NIFS-HEAT-2 was strongly dependent on irradiation temperature. The upper part of fig. 1 shows the TEM images of base metal (a), and weld metal (b), after irradiation at 673K. The corresponding images of base metal and weld metal which were post-weld heat treated at 1073K for 100 hour are also shown. The figure shows the radiation enhanced formation of Ti(CON) precipitates with {100} habit

planes and dislocations. Ti(CON) precipitates were homogenously formed in the weld metal. The measured number density of precipitates in the base metal and weld metal were 1.4 x 10^{21} and 4.3 x 10^{21}(m^{-3}), respectively. The average precipitate size in the base metal and weld metal was 44 and 18 (nm), respectively. From our previous results [8], a highly segregated distribution of Ti(CON) precipitates were formed during the PWHT at 1073K. Namely, after the annealing, the microstructure of the weld metal was divided into two regions, precipitate-segregation (PS) and precipitate-free (PF) areas. As shown in fig.1 (d), after the irradiation at 673K, relatively larger Ti(CON) precipitates were observed in PS areas and small precipitates of about 40 (nm) (shown by arrows in the figure) were observed in PF areas of the weld metal.

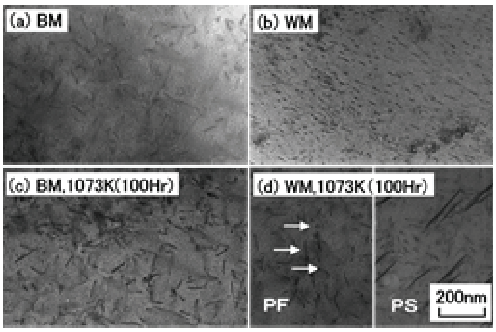

Fig. 1 Microstructure of the samples irradiated at 673K. (a) base metal, (b) weld metal, (c) base metal with PWHT (1073K,100hr), (d) weld metal with PWHT (1073K,100hr)

Fig. 2 shows the microstructure of weld metal irradiated at 873K. At this temperature, PS and PF areas were also observed in weld metal without the PWHT at 1073K. Fig 3 shows the microstructure of base metal (a), weld metal (b); base metal and weld metal which were given the PWHT of 1073K(100hr) are shown in (c) and (d). Relatively large Ti(CON) precipitates of about 200 (nm) and tiny Ti(CON) precipitates of about 10 (nm) were observed together in all samples.

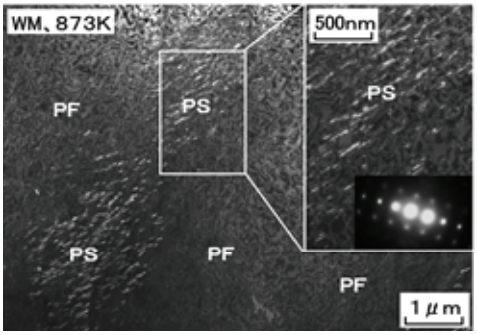

Fig.2 Dark field images of weld metal irradiated at 873K. At this temperature, PS and PF areas were also observed in weld metal without the PWHT.

Size distributions of precipitates for the sample of base metal and weld metal are shown in fig. 4 (a) and (b), respectively. In the figure, measured values of the samples irradiated at 673K are also shown.

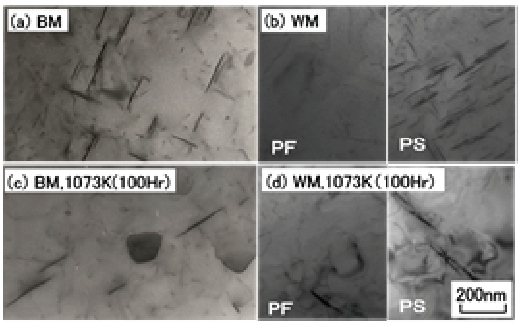

Fig.3 Microstructure of the samples irradiated at 873K. (a) base metal, (b) weld metal, (c) base metal with PWHT(1073K,100hr), (d) weld metal with PWHT(1073K,100hr)

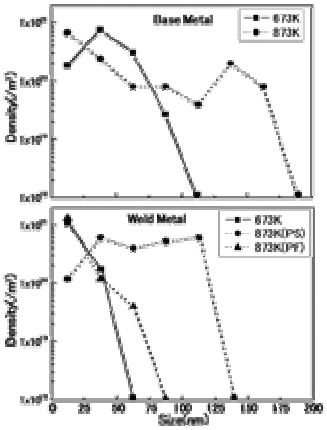

Fig. 4 Measured precipitate size distributions of the samples irradiated at 673K and 873K. (a) base metal, (b) weld metal

III.B. Hardness changes and microstructure after the irradiation at 723K

Fig. 5 shows the microstructure after irradiation at 723K. In the left corner of each photo, void contrast images (s >> 0) taken by higher magnification are inserted. After the irradiation at 723K, PS and PF areas were also formed in weld metal without PWHT. But higher magnification of void contrast images revealed that precipitates were also existed in PF area in weld metal with and without PWHT (shown by arrows in fig. 5(b) and (c)).

Fig. 6 shows the hardness distribution around the bead centre before and after the irradiation at 723K. From the microstructural observations, the width of the weld metal

was 1mm as indicated in the figure. At 723K, Vickers hardness of base metal was almost comparable to that of weld metal. In the figure, hardness changes due to the irradiation at 563K, are also shown for comparison [8]. At 563K, irradiation hardening of the weld metal was relatively larger than that of the base metal, but at high irradiation temperatures, irradiation hardening of the base metal became prominent. The PWHT at 1073K was very effective before and even after the irradiation at 563K [8]. These results mean that the PWHT improved the CVN properties for both the unirradiated material and for the materials irradiated at 563K.

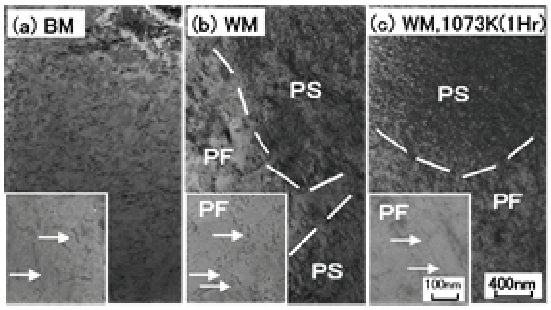

Fig.5 Dislocation contrast images of the samples irradiated at 723K. (a) base metal, (b) weld metal, (c) weld metal with PWHT(1073K,1hr).

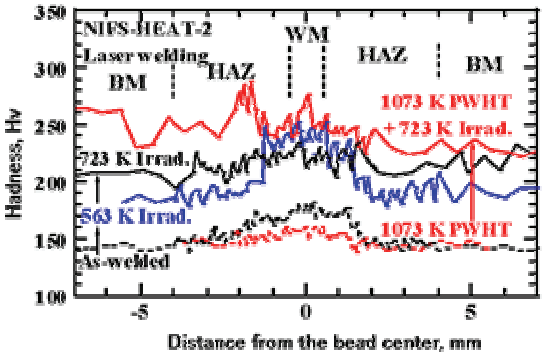

Fig.6 Hardness distribution around the bead. The vertical dashed lines indicate regions of weld metal (WM) , heat affected zone (HAS) and base metal (BM).

IV. DISCUSSION

In NIFS-HEAT-2, it is known that blocky (larger) Ti-rich and small Ti-C-O precipitates existed in the base metal before laser welding. Theses precipitates were dissolved in the weld metal during the welding procedure, resulting in an increase in the concentration of interstitial impurity (mainly oxygen) and/or titanium. The increase in hardness in the as-welded condition could be explained by the interstitial impurity in solid solution in the matrix. The PWHT at 1073K results in an increase in the absorbed energy during impact testing of welded samples by forming PS and PF areas in the weld metal [8]. From our previous studies using the identical samples [5,6], at lower irradiation temperatures, radiation induced-hardening of welded samples can be quantitatively explained by the number density and size of radiation induced defects (dislocation loops and/or precipitate) using Orowan's equations. For the case of ion irradiation at 573K, for example, the number density of defects in weld metal and base metal were almost the same from 0.75 to 7.5 dpa, but the measured hardness in the weld metal was about 10% higher than that of base metal. Besides dislocation loops, very small Ti(CON) precipitates of about 1-2 nm were detected in the weld metal by high resolution electron microscopy (HRTEM) [5]. This suggests that the additional radiation hardening in the weld metal is presumably due to the enhanced formation of small Ti(CON) precipitates.

With increasing irradiation temperature, growth of Ti(CON) precipitates became prominent and the precipitate was easily identified by their habit planes. As shown in fig.1, for the 673K irradiation, Ti(CON) precipitates were homogenously formed in the weld metal and the number density of Ti(CON) precipitates was about three times higher than that of the base metal. At temperature above 723K, Ti(CON) precipitates were not formed uniformly. Namely, precipitate – segregation (PS) and precipitate-free (PF) areas, which were commonly observed after the PWHT at 1073K, also appeared in the weld metal. At 873K, large Ti(CON) precipitates were commonly observed in the PF areas in the weld metal. It is important to note that the absorbed energy of the welded sample increases significantly, when the microstructure is divided into PS and PF areas. But once the the plate-like precipitates with typical {100} orientation are formed, the absorbed energy of welded sample drops drastically. Therefore, the effects of PHWT on weld metal, which are useful for unirradiated and lower temperature irradiations, are not effective or very limited at higher irradiation temperatures where plate like Ti(CON) precipitates are formed.

V. CONCLUSIONS

The microstructral developments and changes in Vickers hardness due to the neutron irradiation at 673-873K were investigated with and without a PHWT at 1073K. The main results are summarized as follows.

(1) At 673K, tiny Ti(CON) precipitates were homogeously formed in the weld metal and the formation was prominent in comparison with base metal. Above 723K, the microstructure of the weld metal was divided into two regions precipitate – segregation (PS) and precipitate-free (PF) area.

(2) After the irradiation at 723K, in the base metal, radiation hardening due to the formation of dislocations and Ti(CON) precipitates became

prominent. The hardness of the base metal was almost the same level as the weld metal.

(3) The effects of PHWT on weld metal, effectively improve the CVN impact properties for unirradiated material and for material irradiated at lower temperatures are not effective or have a very limited effect at higher irradiation temperatures where plate like Ti(CON) precipitates were formed.

ACKNOWLEDGMENTS

This study was supported by JUPITER-II program (Japan-USA Program of Irradiation Test for Fusion Research). This work was also supported by NIFS Budget Code NIFS05KFRF021.

REFERENCES

[1] T. Muroga, T. Nagasaka, K. Abe, V. M. Chernov, H. Matsui D. L. Smith, Z. -Y. Xu and S. J. Zinklel, J. Nucl. Mater. 307-311(2002)547.

[2] M.L. Grossbeck, J.F. King, T. Nagasaka, S.A. David, J. Nucl. Mater. 307-311(2002)1590

[3] T. Nagasaka, T. Muroga, M. L. Grossbeck, T.Yamamoto, J. Nucl. Mater. 307-311 (2002)1595.

[4] Nam-Jin Heo, T. Nagasaka, T. Muroga, A. Nishimura, K. Sinozaki and H. Watanabe, Fusion Science and Technology, 44(2003)470.

[5] H. Watanabe, M. Nagamine, K. Yamakaki, N. Yoshida, Nam-Jin Heo, T. Nagasaka and T. Muroga, Materials Science Forum Vols. 475-479(2005)1491

[6] T. Nagasaka, Nam-Jin Heo, T. Muroga, A. Nishimura, H. Watanabe and K. Sinozaki, J. Nucl. Mater. 329-333 (2004)1539.

[7] T. Muroga, T. Nagasaka, A. Iyoshi, A. Kawabata, S. Sakurai and M. Sakata, J. Nucl. Mater. 283-287(2000)711.

[8] Nam-Jin Heo, T. Nagasaka, T. Muroga, A. Nishimura, K. Sinozaki and H. Watanabe, to be published in J. Nucl. Mater.

[9] H. Watanabe, M. Nagamine, K. Yamasaki and N. Yoshida, to be published

Modeling the Multiscale Mechanics of Flow Localization-Ductility Loss in Irradiation Damaged BCC Alloys

G. R. Odette[1], Ming Y. He[1], E. G. Donahue[1], P. Spatig[2] and T. Yamamoto[3]

[1]University of California Santa Barbara-USA, [2]CRRP EPFL-Switzerland and [3]Tohoku University-Japan

Abstract

Multiscale processes control the true [$\sigma(\varepsilon)$] and engineering [s(e)] stress-strain behavior of alloys. Strain hardening in unirradiated bcc alloys is modeled as a competition between production and annihilation of stored dislocations. Large increases in yield stress, σ_y following irradiation are accompanied by loss of uniform engineering strain (e_u). All major features of the tensile test, including the effect of irradiation, can be modeled using finite element (FE) methods and a self-consistent $\sigma(\varepsilon)$ that differs markedly from s(e) at higher strains. The irradiated $\sigma(\varepsilon)$ reflect large increases in σ_y and reductions in strain hardening. The very low tensile e_u following irradiation is due to enhanced continuum necking instabilities as a consequence of the intrinsic property changes. However, large elevations of $\sigma(\varepsilon)$ persist up to very high strains. Homogeneous deformation constitutive and plasticity theory can be used in continuum FE modeling of irradiated alloys. On a mesoscopic scale, FE simulations indicate that the irradiated $\sigma(\varepsilon)$ may be linked to an array of severely strain softening shear bands embedded in an irradiation and strain hardening matrix.

I. Introduction

The ultimate objective of this work is to develop unified, physically-based models of deformation of bcc alloys for use in fusion reactor first wall and blanket structures. We focus here on the true stress-strain $\sigma(\varepsilon)$ constitutive behavior, typically characterized in tensile tests, outside both the creep and dynamic strain aging regimes. First we apply a simple phenomenological model of strain hardening in unirradiated alloys based on dislocation theory concepts. The mechanism based form proposed for the $\sigma(\varepsilon)$ law facilitates modeling its relation to the underlying material microstructure, as well as its use in finite element (FE) studies. Modeling the effects of irradiation initially focuses on the relation of the $\sigma(\varepsilon)$ to the engineering stress-strain s(e) curve obtained from tensile tests. In particular, we seek to develop a framework for developing a multi-scale understanding of post-yield strain hardening and the associated measures of tensile ductility. To this end, we also carry out FE simulations heterogeneous deformation in materials with locally strain softening shear band regions embedded in a strain-hardening matrix.

The phenomenological true stress-true strain model for unirradiated bcc alloys extends previous work on the strain rate (ε') and temperature (T) dependence of the yield stress, $\sigma^y(\varepsilon, \varepsilon', T)$ and more empirical descriptions of the substantial post-yield strain hardening in both ferritic-martensitic steels and vanadium alloys. Details of the work are summarized elsewhere and only the most salient results are summarized below [1-3].

Intermediate temperature irradiation to a few dpa results in significant radiation hardening and severe loss of uniform *engineering* strain (e_u) capacity [e.g., see references 5-7]. Note, we use e_u to emphasize that it is a measure specific to the tensile test; however, e_u can be readily related to the true uniform stain through the standard relation, $\varepsilon_u = \ln(1+ e_u)$. As discussed in Section III, beyond the point of necking, the relationship between ε and e is much more complex. Figure 1 shows a typical set of s(e) curves in the unirradiated condition and following irradiation for the program heat of the V-4Cr-4Ti alloy irradiated to $\approx$ 0.4 dpa over a range of temperature [5]. The unirradiated s(e) curve shows a typical Luder's-type behavior followed by significant strain hardening. The irradiated curves at 420 and 325 C show the progressive effects increasing in σ_y and decreasing e_u which approaches 1% or less as temperature diminishes and is negligible at 270 and 110 C. At low irradiation temperatures the s(e) curves also show an apparent yield drop, followed by a more gradual decrease in load. Note these apparent yield drops are neither sudden nor followed by a lower yield stress plateau as is observed typically in alloys with so-called source hardening by dislocation atmospheres of interstitial solutes.

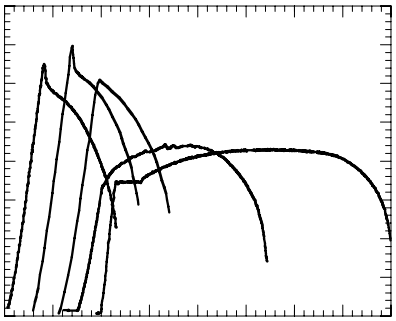

Figure 1. Experimental load-displacement engineering stress-strain curves for a V-4Cr-4Ti alloy in the unirradiated and irradiated conditions (the curves are off-set for clarity and include the effects of load train compliance).

Ductility loss is accompanied by increasingly heterogeneous internal deformation patterns ranging from some coarsening of slip to formation of very localized and highly strained flow channels which have been predominantly studied in fcc metals and alloys [6-8]. It is assumed that these phenomena are due to one or more of the following processes: a) source hardening and unlocking of dislocations from atmospheres of cluster defects [6,7]; b) destruction of pinning defects in strain softening in flow channels [7-11]; twinning [12]; and retardation of cross slip [13].

However, the role of flow localization in macroscopic ductility loss has not been established. Indeed, some degree of heterogeneous deformation is common even in materials with substantial e_u; and even the occurrence of channeling does not always result in low uniform strains. Indeed, we recently showed that the loss of uniform strain in a tensile test is dominated by the macroscopic onset of necking and can be rationalized without recourse to the occurrence of heterogeneous flow [14]. Thus to understand low e_u, it is necessary to make a clear and quantitative distinction between engineering s(e) curves and the underlying *effective* true stress (σ)-*effective* plastic strain (ε) constitutive law, $\sigma(\varepsilon)$. In a tensile test, the relation between s(e) and $\sigma(\varepsilon)$ can be established simply only up to the point of necking. Since the corresponding strain range is small to negligible in the irradiated materials of interest, great caution must be used in interpreting the macroscopic observables from a tensile test in terms of the basic microscopic material behavior.

We have previously derived a simple analytical model demonstrating that e_u is controlled by both the yield stress (σ_y) and strain hardening, using a power law model as $\sigma(\varepsilon) = \sigma_y + \kappa_{sh}(\varepsilon/\varepsilon_y)^n$ [14]. The model shows that large increases in σ_y, coupled with reduced, but finite, $\kappa_{sh}(\varepsilon/\varepsilon_y)^n$ result in very low ε_u and e_u. Further, we have shown that *all the key features* of s(e) curves, including the high ε region in the neck, can be reproduced by FE simulations of the tensile test based on standard continuum, homogeneous plasticity models. As summarized below, even in the most severe cases with $e_u \approx 0$ and an apparent yield drop, the engineering s(e) are consistent with a $\sigma(\varepsilon)$ constitutive law characterized by a region of modest softening over a increment of a few percent of ε, followed by a strain hardening regime up to high ε. Notably, a large fraction of the of irradiation hardening at yield ($\Delta\sigma_y$) also persists in the irradiated $\sigma(\varepsilon)$ up to high strains.

The key physical link between the macro and micro phenomena is the compatibility and equilibrium requirements of the *laws* of solid mechanics. Specifically, redistribution of stress and stress-state occur in any heterogeneously deforming material. These re-distributions are also influenced by the overall deformation pattern. For example, in a very thin specimen or single crystal test, particularly when displacements normal to the tensile axis are relatively unconstrained, deformation may occur in only a single, or a few, dominant shear bands. In contrast, deformation in the interior grains of a polycrystalline alloy in a specimen with axial displacement constraint, requires multiple slip orientations. In this case, the compatibility requirement tends to homogenize deformation even in constitutively heterogeneous materials. Specifically, the effective deviatoric stresses in soft regions are reduced by local redistribution of loads to the adjoining harder regions as well as increases of the multi-axial mean stress. We address this issue in Section IV using a composite cell model composed of strain softening shear bands embedded in a strain hardening matrix.

A key practical question is as follows: can continuum level descriptions of the macroscopic behavior that are relatively independent of the

microscopic detail adequately describe macroscopic stress-strain (load-displacement) behavior in test specimens and structures (and if so when)? From a more fundamental perspective, deformation is an inherently multiscale phenomena. Thus proper modeling the effects of the meso-scale and macro-scale processes is necessary for achieving real understanding of both the causes and consequences of the microscale phenomena, such as localization and channeling.

II. A Dislocation Theory Based Unified Constitutive Model for BCC Alloys

We begin with some background by describing the constitutive law as:

$$\sigma(\varepsilon, \varepsilon', T) = \sigma_{yt}(\varepsilon', T) + \sigma_{ya} + \sigma_{sh}(\varepsilon, T) \qquad (1)$$

Here, the thermally activated component of the yield stress, $\sigma_{yt}(\varepsilon',T)$, depends on both temperature and strain rate. This term is primarily controlled by the lattice Peierls stress and, to a lesser extent, by other processes such as short-ranged dislocation pinning sites including interstitial carbon and nitrogen. The second σ_{ya} term represents the athermal component of the yield stress that depends weakly on temperature, scaling with the elastic modulus. Dispersed obstacles to dislocation slip, as well as the grain and dislocation network-cell substructures control the magnitude of this term. Interstitial solute and possibly irradiation defect atmospheres segregated to the dislocation strain fields may also add to σ_{ya}. Both the $\sigma_{yt}(\varepsilon',T)$ and σ_{ya} terms where characterized in previous studies of both unirradiated martensitic steels and V-4Cr-4Ti alloys [1-3] and are more generally the subject of a very large historical literature; hence, they will not be discussed further in this paper. The third term $\sigma_{sh}(\varepsilon)$ represents the alloy strain-hardening behavior. In contrast to the typical power law representation of strain hardening ($\sigma \alpha \varepsilon^n$), the Zerelli-Armstrong representation [15] provides a proper basis to decompose the physics that control initial yielding from the processes mediating subsequent strain hardening. For example, strain hardening is typically much less sensitive to temperature than σ_y, and primarily depends on the combination of coarse phase, grain and subgrain structures that control dislocation evolution as a function of plastic strain. Note the present study does not attempt to deal with strain rate or temperature dependent dynamic strain aging, leading to additional hardening and serrated flow curves at finite plastic strains [5].

The strain-hardening model is based on competing dislocation storage and annihilation processes [16, 17]. Plastic strain (ε) creates new dislocations with a total density, ρ, in the form of network and sub-cell structures, at a rate $d\rho_+/d\varepsilon$ as primarily controlled by a characteristic slip length. The slip length is on the order of a characteristic 'grain' dimension, D_c, believed to be approximately the lath size in martensitic steels. Dislocations are annihilated at a rate $d\rho_-/d\varepsilon$ proportional to the net stored dislocation density, ρ. Strain hardening increases with $\sqrt{\rho}$ up to saturation where $d\rho_+/d\varepsilon = d\rho_-/d\varepsilon$.

The simple model was used to fit the strain hardening data in three martensitic steels. The characteristic $D_c \approx$ 3-10 μm is on the order of the lath size, but may be slightly temperature dependent. The values of D_c are roughly similar in the three steels, but is largest in a F82H and smallest in a JFL-1. The annihilation rate parameter is also similar in all three cases, but again is slightly larger in F82H and slightly smaller in JFL-1. The $d\rho_-/d\varepsilon$ increases approximately linearly with temperature, reflecting reduced dislocation mobility, from ≈ 0 at 100 K to a very high of level $\approx 90\rho$ at 700 K.

Figure 2a shows the $\sigma_{sh}(\varepsilon)$ for Eurofer 97 over a wide range of temperature. Figure 2b shows the corresponding curves at 298 K for the three FM steels that exhibit generally similar behavior. Note the nominal maximum saturation level for σ_{sh} increases with decreasing temperature, but is reached only at higher strains. However, over the strain range which is experimentally limited by the onset of necking, the curves in Figure 2a tend to overlap. As shown in Figure 2b, strain hardening in the V-4Cr-4Ti alloy (this example is at 25 C) is qualitatively similar to that observed in the martensitic steels. However, in this case the hardening rate lower by a factor of ≈ 10 to 15, very consistent with the large grain size in the recrystallized vanadium alloy.

These results indicate the critical microstructural feature controlling strain hardening in the unirradiated alloys examined in this study is the grain or subgrain dimension.

Finer scale precipitate features play a role in σ^y but not $\sigma_{sh}(\varepsilon)$. Verification of the $\sigma_{sh}(\varepsilon)$ at higher strains is underway.

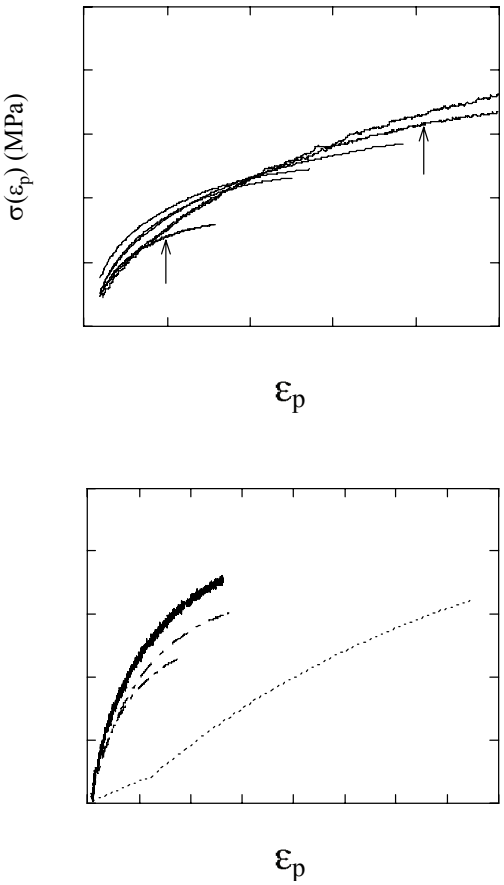

Figure 2 a) $\sigma_{sh}(\varepsilon,T)$ for Eurofer 97 over a wide range of temperatures. b) $\sigma_{sh}(\varepsilon,T)$ at 298 K for the three FM steels.

III. Effects of Irradiation on e^u and the Relation Between s(e) and σ(ε)

If strain hardening is represented by a simple power law term as $\sigma(\varepsilon) = \sigma_y + \kappa_{sh}(\varepsilon/\varepsilon_y)^n$, the necking instability at $\varepsilon_u = \ln(1+e_u)$ occurs at the point where the load (P) for continued deformation peaks is given by the implicit expression [14]:

$$\varepsilon_u^{n-1} = [\varepsilon_y^n \sigma_y/\kappa_{sh} + \varepsilon_u^n]/n \qquad (2)$$

Thus ε_u is controlled not only by κ_{sh} and n, but also by σ_y. Thus increases in σ_y lead to a decrease in ε_u, even when κ_{sh} and N are constant.

Equation 2 is a completely general result, that differs from the normal simple power law stability criteria $e_u \approx n$. Thus the low values of e_u observed in irradiated alloys are consistent with a *combination* of a reduced, but finite, strain hardening *and* large increases in σ_y, *without* flow localization as a necessary controlling mechanism. This is illustrated in Figure 3, which shows values of ε_u for κ_{sh} =17.6 MPa, ε_y = 0.002, and varying n and σ_y. The filled circles illustrate a possible trajectory of irradiation induced decreases in n and increases in σ^y that produce a very large reduction in ε^u.

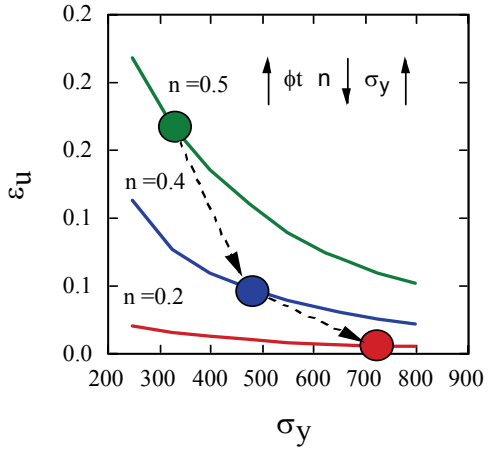

Figure 3. Variation of ε_u with σ_y and n for a constitutive equation with κ_{sh} =17.6 MPa and ε_y = 0.002.

The simple necking instability analysis cannot model the post-necking s(e) needed provide information on σ(ε) at high ε. Thus the ABAQUS finite element (FE) code [18] was used to simulate tensile tests of flat dogbone-shaped tensile specimens with an initial length (L_0), width (W_0), and thickness (t_0) with ratios of 4:1:0.2 to relate the *extrinsic* <u>*observable*</u> s(e) to a corresponding specified *intrinsic material* σ(ε) *that cannot be directly observed in a tensile test*. Note it is important to emphasize that the σ(ε) is an *effective* stress-strain relation, defined within the framework of J_2 incremental flow theory. Details of a large set of parametric simulations was used to gain a general insight on the effect of systematic variations σ(ε) on the corresponding s(e) are given elsewhere [14].

One example is shown Figure 4 for linear strain softening with σ^y = 800 and $\sigma(\varepsilon) = \sigma_y - C\varepsilon$ for C from 0 to 4000 MPa (Figure 4a). As a consequence of immediate necking, e^u is ≈ 0 in

all cases. True-strain softening effects are greatly amplified in the corresponding rate of drop-off in the s(e) curve. Even a modest reduction in the magnitude of strain softening of 40 MPa at $\varepsilon = 0.01$ (only 5% of σ_y) leads to a large reduction of the engineering strain at $s_y/2$ to $e = 0.01$ compared to $e = 0.08$ for the perfectly plastic, $C = 0$ case (Figure 4b). When compared with experimental s(e) curves, these results place distinct limits on the rate and persistence of strain softening.

A $\sigma(\varepsilon)$ that provides a good approximation of a particular experimental s(e) curve can be found based on the FE simulations by iteration. Figure 4 shows $\sigma(\varepsilon)$ (Figure 4c) fits to experimental s(e) (dashed lines in Figure 4d) for V-4Cr-4Ti alloy shown in Figure 1 for both the 100°C unirradiated (u) and 270°C irradiated (i) conditions. The unirradiated $s_u(e)$ curve requires a $\sigma^u(\varepsilon)$ with a small low hardening Luders-type strain region, followed by significant strain hardening. In contrast, the $\sigma_i(\varepsilon)$ *that is required to be to be consistent with the experimental irradiated* $s_i(e)$, is characterized by a small initial increment of strain softening, followed by a modest strain hardening regime. A very notable result is that the irradiated $\sigma_i(\varepsilon)$ remains substantially higher than the corresponding $\sigma_u(\varepsilon)$ at all strains. That is, *irradiation hardening is persistent* and is only modestly decreased by high plastic strain. The dashed-dotted line in Figure 4c shows a lower bound estimate of irradiation hardening $\Delta\sigma(\varepsilon) \approx \sigma_i(\varepsilon) - \sigma_u(\varepsilon)$, ignoring the difference in test temperature and assuming that the 'normal' strain hardening is not effected by irradiation. Even for these bounding assumptions, approximately 70% of the initial irradiation hardening persists up to $\varepsilon = 0.4$.

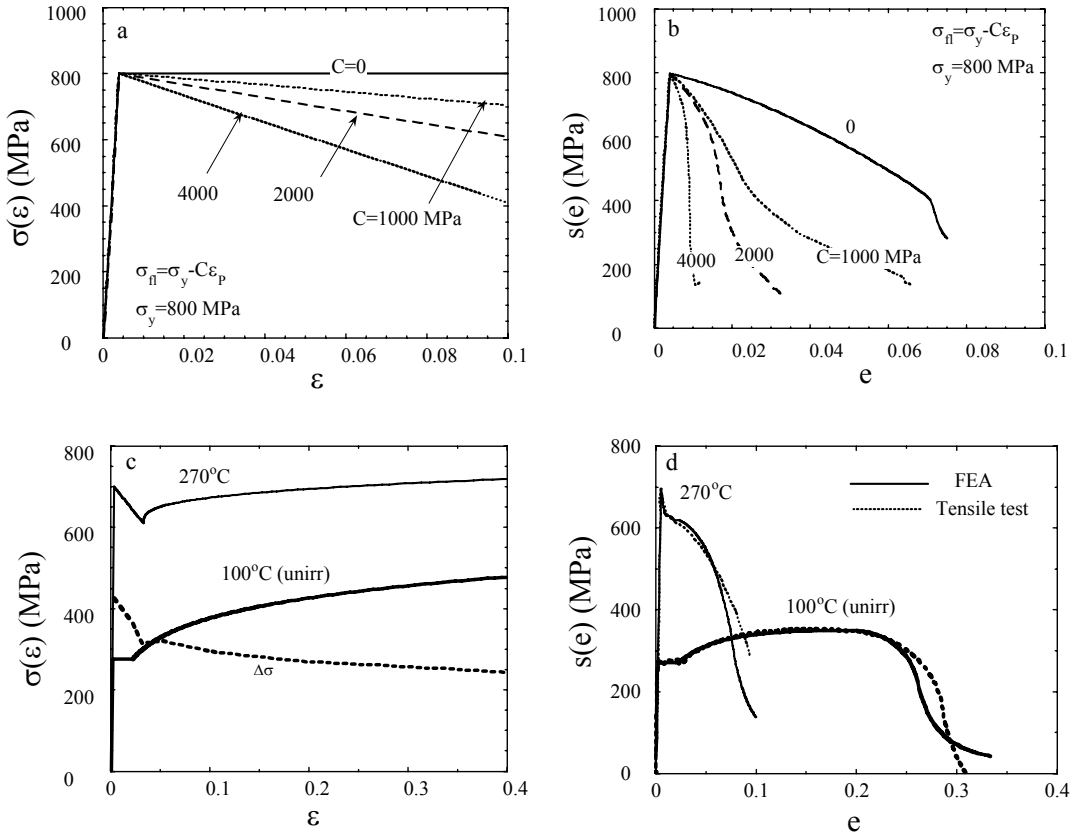

Figure 4 - a) The $\sigma(\varepsilon)$ with systematic variation in the strain softening coefficient C; b) the variation of calculated engineering stress strain curves with increasing C. c) The $\sigma(\varepsilon)$ that provide reasonable fits to the unirradiated (100 C) and irradiated (270 C) s(e) curves, and the difference representing a lower bound

estimate of the hardening due to irradiation as a function of ε; d) the unirradiated and irradiated s(e) curves corresponding to the σ(ε) in Figure 4c.

IV. Modeling of Strain Softening Due to Shear Bands

As noted in the introduction, materials that undergo heterogeneous deformation, such as channeling, still must obey the basic continuum laws of solid mechanics. Thus we also investigated the interplay between the effects of spatially varying constitutive behavior. Specifically effective mesoscale continuum mechanics σ(ε) were derived from FE simulations of strain softening shear bands $\sigma_{sb}(\varepsilon)$ that are embedded in a strain hardening matrix $\sigma_m(\varepsilon)$. The basic objective is to determine the overall *composite material* σ(ε) as a function of the combined characteristics of the shear bands and matrix. Note this σ(ε) differs from a true stress-strain constitutive law for a homogeneously deforming material, but provides a physically weighted average of the effects of the parameters describing the individual regions. While the computations themselves do not contain an absolute length, these results apply on a mesoscopic scale of the actual shear band dimensions. The overall composite σ(ε) is controlled by the combination of parameters describing $\sigma_{sb}(\varepsilon)$ and $\sigma_m(\varepsilon)$, the geometry of the shear bands, the boundary conditions imposed on the computational cell and the general deformation stress-state. Baseline unit cell ABAQUS simulations were carried out for as follows:

1. The shear band zones were modeled as an elliptic zone in plane-strain in the larger transverse, width direction with free mirror boundary in the smaller transverse, thickness direction. The mirror condition ensures planar boundaries are maintained as the cell deforms. In contrast, use of periodic boundary conditions leads to shape changes in the cell. However, a direct comparisons showed that the σ(ε) are generally similar for mirror and periodic boundaries. The plane-strain condition is one computable limit on the degree of constraint on the deformation. Another is plane-stress. While reality probably falls in between, the plane-strain condition is believed to be somewhat more applicable to shear bands in polycrystalline grains in the necking region of the specimen. Direct comparisons showed that at low ε the σ(ε) for plane -tress is qualitatively similar to that for plane strain. However compared to plane-strain where initial softening is followed by re-hardening (see the plane strain results below), plain-stress conditions result in continual gradual strain softening beyond the initial drop. More detailed evaluations of cell boundary stress-state effects are underway and the results will be reported in future publications.

2. The shear band geometry is characterized by orientation with respect to the tensile axis (θ = 0 to 45°) and volume fraction (f_{sb}). The θ and f_{sb} also represent the mirror symmetry planes occupied by the shear bands and the extent which they approach a fully interconnected network.

3. Separate local constitutive models are applied to the shear bands matrix: matrix -- $\sigma_m(\varepsilon) = \sigma_y + C_m[(\varepsilon/0.0025)^n - 1]$ and shear band -- $\sigma_{sb}(\varepsilon) = \sigma_y - C_{sb1}\varepsilon$ down to a minimum flow stress, σ_{sbm}; alternately we used $\sigma_{sb}(\varepsilon) = \sigma_y - C_{sb2} + C_{sb2}[\exp(-\varepsilon/\lambda)]^{1/2}$, where the σ_y, C_m, C_{sb1} and C_{sb2} characterize a specified combination of stress-strain laws for the two regions. Figure 5 illustrates the cell model and structure of the ABAQUS FE mesh. A typical mesh has 384 eight-node biquadratic elements and 1243 nodes.

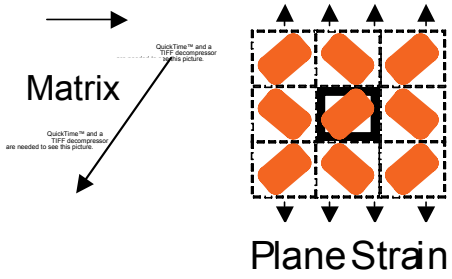

Figure 5. Finite element mesh for the cell model of heterogeneous deformation.

Figure 6a and b show σ(ε) for two f_{sb} of 0.025 and 0.05 along with θ = 45°, $\sigma_y = C_m$ = 500 MPa, C_{sb1}= 1000 MPa and σ_{sbm} = 100 MPa. There is a decrease in σ(ε) after a small increment of hardening in both cases. The drop-off is larger and occurs at lower strains for f_{sb} = 0.05. The effect of a perfectly plastic shear band (n = 0) and shear band with σ = 0, or a hole, are also shown. Perfectly plastic shear bands have only a small effect of σ(ε), while the hole reduces σ(ε) by factors of ≈ 0.5 (f_{sb} = 0.05) to

0.75 (f_{sb} = 0.025). The minimum strength of a strain-softening shear band, σ_{sbm} = 100 MPa, keeps the $\sigma(\varepsilon)$ slightly above that for a hole. Figure 6c shows the effect of increasing the shear band softening rate from 500 to 2000 MPa for f_{sb} of 0.025 with all other parameters fixed at the values in Figure 6a and b. Increasing C_{sb1} decreases the regime of hardening and increases the rate of drop-off in $\sigma(\varepsilon)$; however it does not influence the hardening region at high strain. Figure 6d shows the effect of variations in θ of 0, 22.5 and 45° for C_{sb1} = 1000 and all other parameters fixed as in Figures 6c. Compared to the 45° case, the effects of the shear bands are very small for θ = 0 and much less for θ = 22.5°.

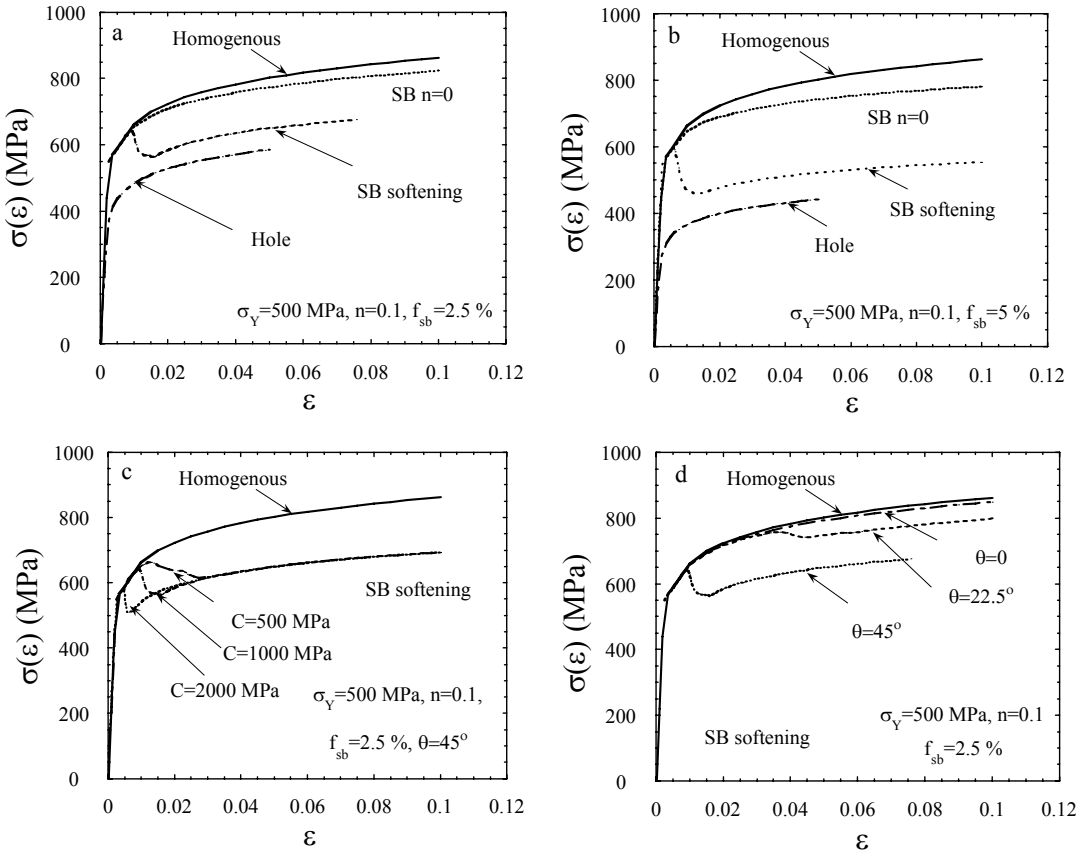

Figure 6 - a) and b) Stress-strain curves $\sigma(\varepsilon)$ obtained by the cell model for two f_{sb} of 0.025 and 0.05 for θ = 45°, $\sigma_y = C_m$ = 500 MPa, C_{sb1}= 1000 MPa and σ_{sbm} = 100 MPa; c) the effect of increasing the shear band softening rate from 500 to 2000 MPa for f_{sb} of 0.025 with all other parameters fixed as in Figure 6a; d) the effect of variations in θ of 0, 22.5 and 45° for C_{sb1} = 1000 MPa and all other parameters fixed as in Figure 6a.

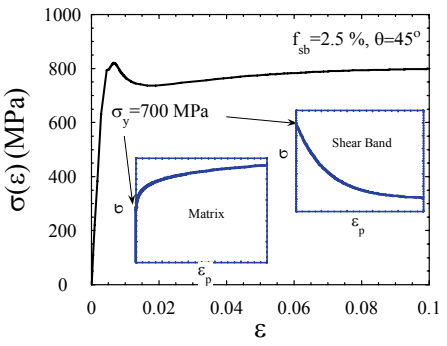

Figure 7. Stress-strain curves $\sigma(\varepsilon)$ obtained for the cell model for f_{sb}= 0.025, σ_y = 700 MPa, n = 0.1, θ = 45°, C_{sb2} = 600 MPa and λ = 0.12.

Figure 7 shows the result for a f_{sb} = 0.025, σ_y = 700 MPa, n = 0.1, θ = 45°, C_{sb2} = 600 MPa and λ = 0.12. This $\sigma_{sb}(\varepsilon)$ model approximates the local strain dependent destruction of dislocation pinning features in a shear band. The resulting curve qualitatively resembles the $\sigma(\varepsilon)$ shown in Figure 4c that is consistent with irradiated engineering s(e) curve with $e^u \approx 0$ and an apparent yield drop shown in Figure 4d.

It is emphasized that these simulations primarily provide qualitative insight rather than a unique quantitative description of the underlying parameters that result in $\sigma(\varepsilon)$ characteristic of irradiated materials. Implications of this insight are discussed briefly below.

V. Discussion

The analysis presented in sections III and IV provide the first linkages between the micro and meso scale phenomena of flow localization in irradiated alloys and the key macroscopic observable in a tensile test. Perhaps the most important result is given in Section III, linking the intrinsic material $\sigma(\varepsilon)$ curve to extrinsic engineering s(e) data. These FE simulations lead to several important conclusions: 1) the actual regime of strain softening is limited and gradual and is followed by strain hardening; and 2) standard plasticity models based on J^2 flow theory can be used, at least in some cases like for the tensile test, in FE simulations of deformation for finite geometry conditions; 3) radiation hardening persists up to high strains. Further, it is noted that that the *apparent* yield drops of the type seen in Figure 1 previously have been *qualitatively* interpreted to demonstrate a dislocation source hardening mechanism associated with unlocking dislocations from defect atmospheres. Further, the low uniform engineering strains have been *qualitatively* causally linked to localization of flow in narrow channels associated with strain induced destruction of hardening defects. However, both of these conceptual interpretations lack physical rigor and the more quantitative results presented in this work clearly demonstrate that neither hypothesis is necessary nor sufficient to explain the observables in a tensile test.

The analysis of the consequences of heterogeneous deformation in materials with strain softening shear bands presented in section IV represents an attempt to add some rigor to the analysis of deformation in irradiated metals and alloys. Note more detailed analysis of the FE results, including assessment of stress, strain and stress-state distributions as a function of the composite strain has been carried out, but cannot be described due to length limitations in this paper. Space also does not permit a full discussion of the implications of the models to ongoing and future experiments. Indeed, while these results do not represent a final and comprehensive model, they provide considerable insight, particularly for guiding basic experimental observations. In summary, the empirical $\sigma(\varepsilon)$ for irradiated alloys are consistent with heterogeneous deformation in cases where the shear bands that become very soft with respect to the surrounding matrix, but only under limited and experimentally verifiable conditions. For example, in addition to clearing the bands of irradiation hardening defects it appears that processes like retardation of cross slip are important. Further, the shear bands are effective only if they form an array of roughly 45_ segments that occupy roughly 50% of the set of interconnected shear band planes. Other tests against observation include mesoscopic strain distribution mapping, the types and variations in dislocation structures in the shear bands and matrix and the residual hardness in shear band and matrix regions at high strains. It is necessary to obtain such information at high strains that are not accessible in simple tensile tests. However, we have compared the FE simulations to measured three-dimensional geometry changes in the evolving neck region of a tensile specimen. The good excellent between the simulated and experimentally observed neck evolution demonstrate the reliability and uniqueness of the $\sigma(\varepsilon)$ results derived by fitting the s(e) data. Such comparisons are being extended to a variety of other test configurations, like indentations, compression and beam bending, that can more readily access high strains. Again, the key to the interpretation of such tests will be a direct comparison with FE simulations (analogous to that done for the tensile test in this paper) and well focussed links to observation.

Finally, we can only briefly note that the results in this study have very important practical implications with regard to the deformation limits in actual irradiated structures. Specifically deformation is controlled by a interacting combination of intrinsic and extrinsic factors. For example, deformation in compression would be expected to be more stable than in tension or shear dominated conditions.

Summary and Conclusions

As noted in the introduction, a hierarchy of multiscale processes controls the unusual engineering tensile stress strain behavior, s(e), of metals and alloys. Both the yield stress and strain hardening behavior can be modeled in

terms of the underlying microstructure and microstructural evolution process associated with processing, irradiation service and deformation. Specifically, it is shown that strain hardening in unirradiated alloys can be treated on the basis of a competition between dislocation production and annihilation processes. Further, the key features of tensile test engineering s(e) curves can be understood and modeled in terms of the corresponding continuum true stress-strain constitutive laws. The low e^u in tensile tests of irradiated alloys, reflects large increases in σ^y and reductions in strain hardening due to macroscopic necking that greatly amplifyies the effects of more subtle changes in the high strain constitutive law.

We have specifically examined an extreme case of irradiated s(e) curves, with negligible uniform strains, a pseudo yield drop, and continuous softening to failure at reduced total strains. The low uniform strains are due to continuum necking instabilities caused by *both* higher σ^y and reductions in the post-yield strain hardening. In this case the post yield $\sigma(\varepsilon)$ shows an initial regime of modest strain softening over the first few percent of plastic strain, followed by a slight, but positive strain hardening. Lower bound estimates show substantial irradiation hardening persists up to high strains. Significantly, homogeneous constitutive models and J^2 incremental flow plasticity theory, used in large- scale deformation FE simulations, provide a useful engineering description of irradiated alloys. Further, macroscopic manifestations of irradiation effects on deformation can be represented by a continuum $\sigma(\varepsilon)$ in a way that is, at least in some cases, insensitive to details of the processes taking place on a finer scale, like flow localization.

A qualitative link between $\sigma(\varepsilon)$ and heterogeneous deformation is provided by a severely strain softening array of shear bands embedded in an irradiation and strain hardened matrix. Additional FE studies and analysis of the results will be combined with a wide array of experiments and observations to develop robust and fully quantitative deformation models.

Acknowledgements

This work was supported by the US Department of Energy Grant DE FG03-87-ER-52143. We also thank Steve Zinkle of ORNL for supplying the tensile data on irradiated and unirradiated V-4Ti-4Cr.

References

1. P. Spatig, G. R. Odette and G. E. Lucas, *J. Nuc. Mat 275* (1999) 324.
2. E. G.Donahue, G. R. Odette and G. E. Lucas, *J. Nuc. Mat*., 283-287 (2000) 637.
3. P. Spatig, G. R. Odette, E. Donahue, G. E. Lucas, *J. Nuc. Mat*., 283-287 (2000) 721.
4. A.F. Rowcliffe, J. P. Robertson, R. L. Klueh, K. Shiba, D. J. Alexander, M. L. Grossbeck and S. Jitsukawa, *J. Nuc. Mat*., 258-263 (1998) 1275
5. A. F. Rowcliffe, S. J. Zinkle and D. T. Hoelzer, *J. Nuc. Mat*., 283-287 (1998) 508
6. B.N. Singh, A.J.E. Foreman, H. Trinkaus, *J. Nucl. Mat.* 249 (1997) 103.
7. N.M. Ghoniem, S.H. Tong, B.N. Singh, and L.Z. Sun, "On Dislocation Interaction with Radiation-induced Defect Clusters and Plastic Flow Localization in FCC Metals", *Phil. Mag.*, in press (2001).
8. M. Victoria, N. Baluc, C. Bailat, Y. Dai, M. I. Luppo, R. Schaublin and B. N. Singh, *J. Nuc. Mat*. 276 (2000) 114.
9. J.L. Brimhall, J.I. Cole, J.S. Vetrano and S.M. Bruemmer, *Microstructure of Irradiated Materials*, MRS Symposium Proceedings 373, I.M. Robertson et al. eds., Materials Research Society, Pittsburgh, PA (1995) 177.
10. H.M. Zbib, T. Diaz de la Rubia, M. Rhee and J.P. Hirth, *J. Nucl. Mat.* 276 (2000) 154.
11. P. M. Rice and S. J. Zinkle, *J. Nuc. Mat*., 258-263 (1998) 1414.
12. E. H. Lee, T.S. Byun, J. D. Hunn, N. Hashimoto, K. Farrell, *J. Nucl. Mat.* 281 (2000)
13. Z.S. Basinski, M.S. Szczerba and J.D. Embury, *Philos. Mag.* A 76 (1997) 743.
14. G. R. Odette, M. Y. He, E. G. Donahue and G. E. Lucas, ìOn the Relation Between Engineering Load-Displacement and True Stress-strain Behavior in Tests of Flat Tensile Specimens, *Small Specimen Test Techniques-IV*, ASTM SPT 1418, M. Sokolov et. al. eds., American Society for Testing and Materals, West Conshohocken , PA (2001) in press
15. F. J. Zerilli and R. W. Armstrong, J. Appl. Phys. 61 (1987) 637
16. P. Sp‰tig, R. Sch‰ublin, M. Victoria, *Material Instabilities and Patterning in Metals*, MRS Symp. Proc. 683, H. M. Zbib et. al. eds (2001) BB1.10.1-BB1.10.6.
17. P. Sp‰tig, G. R. Odette,G. E. Lucas and M. Victoria, On the Mechanical Properties of the Advanced Martensitic Steel EUROFER97, under review this conference

18. ABAQUS V5.8, *ABAQUS Standard Users Manual*, Hibbitt, Karlsson and Sorenson, Inc, Providence Rhode Island, 1998.

OPTIMIZATION AND CHARACTERIZATION OF CHEMICAL VAPOR INFILTRATED SiC/SiC COMPOSITES

T. Hinoki[1], L.L. Snead[1], T. Taguchi[2], N. Igawa[2], W. Yang[3], T. Nozawa[3], Y. Katoh[3] and A. Kohyama[3]

[1] *Oak Ridge National Laboratory, Oak Ridge, TN 37831, USA*
[2] *Japan Atomic Research Institute, Tokai, Ibaraki 319-1195, Japan*
[3] *Institute of Advanced Energy, Kyoto University, Gokasho, Uji, Kyoto 611-0011, Japan*

SiC/SiC composites were fabricated by the forced-flow, thermal gradient chemical vapor infiltration (FCVI) method at the Oak Ridge National Laboratory (ORNL) and by the iso-thermal chemical vapor infiltration (ICVI) method at the Japanese National Institute for Materials Science (NIMS). The FCVI approach can fabricate relatively large composites in relatively short time, while the ICVI has significant controllability of fiber/matrix interphase formation. Fiber types included the near stoichiometric Tyranno SA and Hi-Nicalon Type-S. SiC/SiC composites 12.5 mm in thickness with either75 or 300 mm in diameter were fabricated at ORNL. SiC/SiC composites with 40 mm in diameter and 1.5~3.0 mm in thickness were fabricated at NIMS. The microstructure of these materials was studied using SEM with EDS and TEM while their mechanical properties were evaluated by tensile, flexural and single fiber push-out testing.

Density, the uniformity of fiber/matrix interphase and mechanical properties improved by increasing fiber volume fraction, optimizing processing conditions for both the FCVI and the ICVI processes. Porosity was decreased to approximately 15%. The effect of the interphase on mechanical properties and fracture behavior were studied. Tensile strength of 2D composites reinforced with Tyranno SA fibers and with optimized multilayer SiC/C interphase was approximately 300 MPa.

I. INTRODUCTION

CVI produces a stoichiometric, crystalline β-SiC. The major advantage of CVI over other processing routes is the low thermal and mechanical stress of the densification process owing in large part to the lower deposition temperature. In addition, the process imparts little mechanical stress to the preform. The excellent controllability of formation of fiber/matrix interphase, which affects mechanical properties significantly, is also advantage of the method. However it takes long time for CVI processing and the size was limited to relatively small fabric.

The forced-flow thermal-gradient chemical vapor infiltration (FCVI) developed at ORNL overcomes the problems of slow diffusion and restricted permeability [1,2] even in the large component with 300 mm in diameter and 15 mm in thickness. Composites have been fabricated using Nicalon™ fibers. However the optimum conditions using recent near stoichiometric high purity fibers such as Tyranno™ SA and Hi-Nicalon™ Type-S has not been established. The isothermal chemical vapor infiltration (ICVI) method at NIMS [3] can form precise uniform fiber/matrix interphase within a composite. The interphase is one of keys to improve mechanical properties of composites [4,5]. The optimization of the interphase for composites reinforced with high-purity fibers is required.

SiC-sintered fibers, which are near stoichiometric, highly crystalline and high elastic modulus, such as Sylramic™ [6] of Dow Corning, Hi-Nicalon™ Type-S [7] of Nippon Carbon and Tyranno™ SA [8,9] of UBE industries are now available. These SiC fibers have been reported to show superior thermal stability compared to low-oxygen fibers, since the oxidation of excess C in air into CO at high temperatures resulted in the formation of pores in the latter [9]. These fibers are also expected to be stable under neutron irradiation. Therefore development and evaluation of the SiC/SiC composites reinforced with the highly crystalline fibers is desired.

One of the objectives of this study is to optimize processing conditions of both ICVI and FCVI using high purity SiC fibers focusing to increase density and to obtain a uniform fiber/matrix interphase through the plate thickness. Another objective is to characterize the fiber/matrix interphase and improve mechanical properties of the composites. The effect of the interphase on mechanical properties was evaluated. Commonly advantages of ceramic matrix composite compared with monolithic ceramic are larger fracture toughness and a narrow distribution in failure strength. The trend of development of SiC/SiC composites using high elastic modulus fibers in this work is toward high modulus, high proportional limit stress and high strength with a narrow distribution rather than low strength with large fracture toughness.

II. EXPERIMENTAL

SiC/SiC composite disks with 40 mm in diameter and 1.5~3.0 mm thick were fabricated using plain woven Hi-Nicalon and Tyranno SA fibers by ICVI at NIMS. The fibers were stacked in [0°/90°] direction. 7 sheets of Hi-

Nicalon fibers or 9 sheets of Tyranno SA fibers were used to fabricate composites with 1.7 mm thick. C and multilayers of C and SiC were applied as the interphase between fiber and matrix. The precursors were methane (CH4) for C deposition and methyltrichlorosilane (MTS, CH3SiCl3) or ethyltrichlorosilane (ETS, C2H5SiCl3) for SiC deposition. Hydrogen was used as carrier gas for MTS and ETS. The temperature (900~1100 °C) of the furnace and flow rate of gas were controlled. Each gas flows into the bottom of the furnace. Thickness control of interphase in this system is difficult due to changing conditions through the thickness of the preform. Temperature should preferably be constant within the fabric. Slower deposition rate is better to control the thickness of interphase. In order to obtain uniform thickness of interphase within a composite, effects of temperature, gas flow rate and position of a preform on microstructure were evaluated and those experimental conditions were optimized.

At ORNL, SiC/SiC composites were fabricated by FCVI using plain-woven high-purity SiC fibers, Tyranno SA and Hi-Nicalon Type-S. The fibers were stacked in [-30°/0°/30°] or [0°/90°] directions in a graphite holder. 45~55 sheets of Hi-Nicalon Type-S fibers or 55~60 sheets of Tyranno SA fibers were used. The fabric size for small furnace is 75 mm diameter and 12.5 mm thick and that for large furnace is 300 mm diameter and 12.5 mm thick. C, SiC/C or multilayer (SiC/C)6 was applied to fiber/matrix interphase followed by matrix SiC deposition. C was deposited by decomposition of propylene (C3H6) at 1100 °C. SiC was deposited by decomposition of MTS at 1000~1200 °C. A graphite coating chamber radiatively heats the fibrous preform exterior and its interior is cooled with a water-cooled line following deposition of the fiber/matrix interphase. The MTS carried in hydrogen is injected inside the preform. The gas infiltrates through the preform thickness and exhausts at atmospheric pressure. The properties of the composites fabricated in this study are summarized in table I. The ID number is the chronological order in which composites were fabricated. The fiber volume fraction (Vf) was estimated from the size and mass of the preform while the porosity values listed in the table I were estimated from cross-sectional scanning electron microscopy (SEM) images. The values

Table I. Properties of SiC/SiC composites with 75 mm in diameter fabricated by FCVI

ID	Fiber	Orientation	F/M Interphase	Nominal thickness of Interphase [nm]	V_f [%]	Density [Mg/m^3]	Porosity [%]
1256	Tyranno SA	[-30/0/30]	PyC	150	37	2.76	15.1
1257	Hi-Nicalon Type-S	[-30/0/30]	PyC	150	33	2.39	23.5
1258	Hi-Nicalon Type-S	[-30/0/30]	PyC	75	36.1	2.7	-
1259	Hi-Nicalon Type-S	[-30/0/30]	PyC	300	35	2.58	13.9
1260	Tyranno SA	[-30/0/30]	PyC	300	30.2	2.28	24.2
1261	Tyranno SA	[-30/0/30]	PyC	75	33.3	2.54	20.4
1264	Tyranno SA	[0/90]	PyC	150	35.4	2.61	23.3
1265	Tyranno SA	[0/90]	PyC	300	35.3	2.72	18
1266	Tyranno SA	[0/90]	PyC	75	35.2	2.62	18.1
1267	Tyranno SA	[0/90]	SiC/C	100/150	38.8	2.74	15.7
1268	Tyranno SA	[0/90]	SiC/C	100/150	38.8	2.69	18
1269	Tyranno SA	[0/90]	SiC/C	100/300	38.8	2.71	17.2
1270	Tyranno SA	[0/90]	$(SiC/C)^6$	$50/50/(200/50)^3/(500/50)^3$	39.8	2.52	26.88
1271	Hi-Nicalon Type-S	[0/90]	PyC	150	Not evaluated		
1272	Tyranno SA	[0/90]	$(SiC/C)^6$	$50/20/(200/20)^3/(500/20)^3$			

of the thickness of interphase listed in Table I correspond to nominal values.

Mechanical properties of composites were evaluated by three-point flexural tests and tensile tests. Specimens with dimensions 30 mm (long) × 4 mm (wide) × 1.5 mm (thick) were used for flexural testing. More than three specimens were tested for each composite. The test span of the flexural tests was 18 mm. The flexural tests were conducted at a cross-head speed of 1.8 mm/min at ambient temperature. Tensile tests were conducted on the basis of ASTM C1275. The test specimens were edge-loaded with dimensions 41.3 mm (long) × 6.0 mm (wide) × 2.3 mm (thick). The dimensions of the gauge section were 15.0 mm (long) × 3.0 mm (wide) × 2.3 mm (thick). Details of the specimen and the tensile test are described elsewhere [10]. More than four valid test results were obtained for each composite. All tests were conducted at a cross-head speed of 0.5 mm/min at ambient temperature. The step-loading tests were performed for the precise evaluation of damage accumulation near proportional limit [11]. The mechanical properties of fiber/matrix interphase were evaluated by single-fiber push-out tests [12]. Specimens were sliced from composites normal to the fiber direction, which were mechanically polished to a final thickness of approximately 50 μm. For the tests the specimens were mounted on top of a holder containing a groove 50 μm wide. Isolated fibers with the fiber direction perpendicular to the holder surface on the groove were selected with a video microscope and were pushed out using a Berkovich-type pyramidal diamond indenter tip with maximum load capability of 1 N. Microstructure was observed by optical microscopy and field emission SEM (FE-SEM). The thickness of interphase was measured by FE-SEM at several regions in a specimen. Fracture surface after tensile tests was examined by SEM with EDS.

III. RESULTS

III.A. Optimization of ICVI

In previously fabricated composites, the deposition rate of C was so high that most of the C precursor was deposited at the upstream side. The thickness of C interphase was quite different between upstream side and downstream side. For example, the thickness of C interphase at upstream was more than 1 μm, whereas no C interphase was identified on the downstream side. However the uniformity of interphase thickness was significantly improved by optimizing the experimental conditions, temperature, gas flow rate and position of the sample in the furnace. The optimized deposition rates of C and SiC are approximately 2 μm/min and 20 μm/min respectively. The scatter of temperature within composites improved to less than 1 % of controlled temperature. Apparent difference of interfacial thickness between upstream side and downstream side was not identified in the optimized composites.

Density of SiC/SiC composites was also increased with optimization of CVI conditions, while CVI processing time was significantly shortened from 40~50 hour to 15~20 hour. In the case of previous composites, upstream side was deposited easily and sealed prior to infiltration within the sample. Then the composites were removed and reversed to infiltrate the opposite side. In contrast to previous composites, the deposition began inside of composites without sealing of SiC at upstream side in the optimized deposition conditions. Another key to increase the density was increasing fiber volume fraction. Fiber fabrics were well-aligned stacked and thickness of the preform was reduced from 2.0 mm to 1.7 mm in the case of Hi-Nicalon preform with 7 sheets. The density of the optimized composites reinforced with Hi-Nicalon was approximately 2.5~2.6 Mg/m3, which corresponds to approximately 85% of the theoretical density. The density was 2.0~2.2 Mg/m3 in the previous composites, which corresponds to approximately 70 % of the theoretical density.

III.B. Characterization of fiber/matrix interphase

To understand interfacial mechanical properties, single fiber push-out tests were carried out. The interfacial shear strength (ISS) (τis) was obtained from the 'push-out' load (P) in single fiber push-out testing and calculated from Eq. 1.

$$\tau_{is} = \frac{P}{\pi D t} \quad (1)$$

where D is fiber diameter and t is specimen thickness. The resultant effect of thickness of C interphase on the interfacial shear strength of composites reinforced with Hi-Nicalon and composites reinforced with Tyranno SA is shown in Fig. 1. The interfacial shear strength

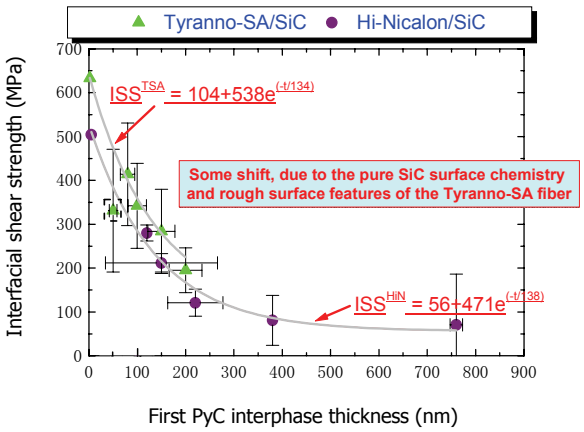

Fig. 1. Effects of thickness of PyC interphase on interfacial shear strength

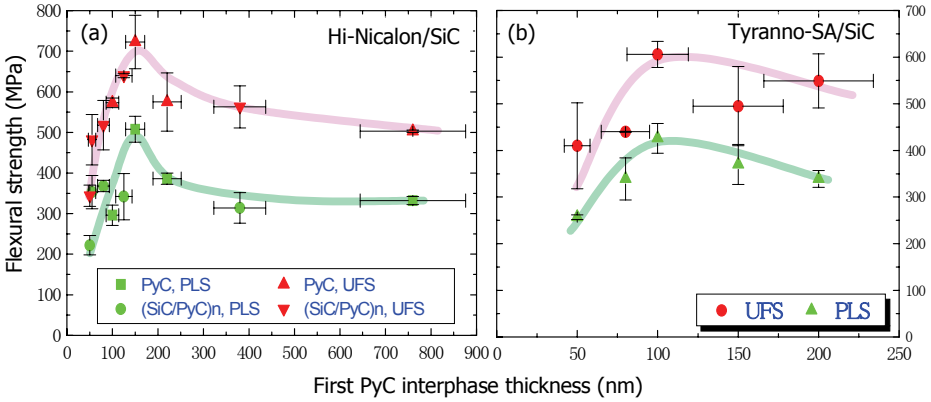

Fig. 2. Effect of C interphase thickness on the Flexural Strength

drastically decreased with increasing C interphase thickness. Similar results using Nicalon CVI composites have been reported [13]. It was found that the interfacial shear strength of composites reinforced with Tyranno SA fibers was slightly larger than that of composites reinforced with Hi-Nicalon if the thickness of C interphase is same.

The effect of thickness of C interphase on the proportional limit stress (PLS) of flexural test and flexural strength of composites reinforced with Hi-Nicalon (a) and composites reinforced with Tyranno SA (b) is shown in Fig. 2. The composites reinforced with Hi-Nicalon fibers showed the peak PLS and the flexural strength at about 150 nm thick of C interphase, while the composites reinforced with Tyranno SA showed the peak at about 100 nm. It was found that the mechanical properties of composites reinforced with Tyranno SA fibers are more insensitive to C interphase thickness than those of composites reinforced with Hi-Nicalon fibers.

SEM and TEM observation showed that the interfacial crack almost always propagated along the interface between fiber and interphase [12]. This behavior was not limited only to C interphase. Multilayer C/SiC and "porous" SiC interphase showed the same behavior. Fracture surface of fibers was smooth. This led to low frictional stress of the debonded interface allowing easy crack propagation. This fracture behavior is attributed to a smooth fiber surface and weaker bond between the interphase and fiber than between the interphase and matrix SiC. In particular, the bond between fiber and C layer is weaker than the bond between C layer and SiC matrix. In order to improve interfacial fracture behavior and mechanical properties, PLS and maximum strength in particular, a SiC layer was formed on the fibers. Fiber and fiber bundle pull-out of composites with the SiC/C interphase reinforced with Hi-Nicalon fibers were shorter than those of composites without the first SiC layer. Both C and Si were detected from pull-out fiber surfaces of the composites without the SiC layer by EDS, and the atomic ratio of C to Si corresponded to that of Hi-Nicalon fiber [6]. In the case of composites with the first SiC layer, almost all species detected on pull-out fiber surface were C. The first SiC layer on Hi-Nicalon fiber induced strong bond between fiber and interphase and turned the crack path from between the fiber and the interphase to the inside of C interphase. Rough fracture fiber surface was seen, interfacial frictional stress was increased and mechanical properties of tensile tests were improved [14].

III.C. Optimization of FCVI

To understand the distribution of thickness of interphase and porosity within a composite, thickness of interphase and porosity were measured at nine regions in a composite. The porosity of composites fabricated earlier was high and mostly more than 20% as shown in Table I. The bottom region, which is the upstream side of precursor gas, and the outer region tended to have higher porosity in the composites. It was found that porosity was significantly affected by fiber volume fraction. As the fiber volume fraction increased, the porosity decreased as shown in Table I. Fig. 3 compares the distribution of porosity of improved composites (1267) with that of previous composite (1260). In the improved composites porosity is independent of position, and the porosity trends seen in the previous composites was not observed.

The thickness of interphase varied thorough the plate thickness. The interphase of bottom region was thicker than that of top region as shown in Fig. 4 (1256). One of the solutions to decrease the scatter of the thickness was to change the upstream side and the downstream side of the preform in the middle of interphase deposition process. Fig. 4 shows the distribution of the thickness of interphase. The scatter of the thickness was significantly improved by changing the upstream side and the downstream side.

The thickness range of C interphase applied was about 20~300 nm. The average thickness of SiC layer of the SiC/C interphase was approximately 60 nm. Apparent effects of C interphase thickness and the first SiC layer on tensile properties were not seen. The multilayer interphase

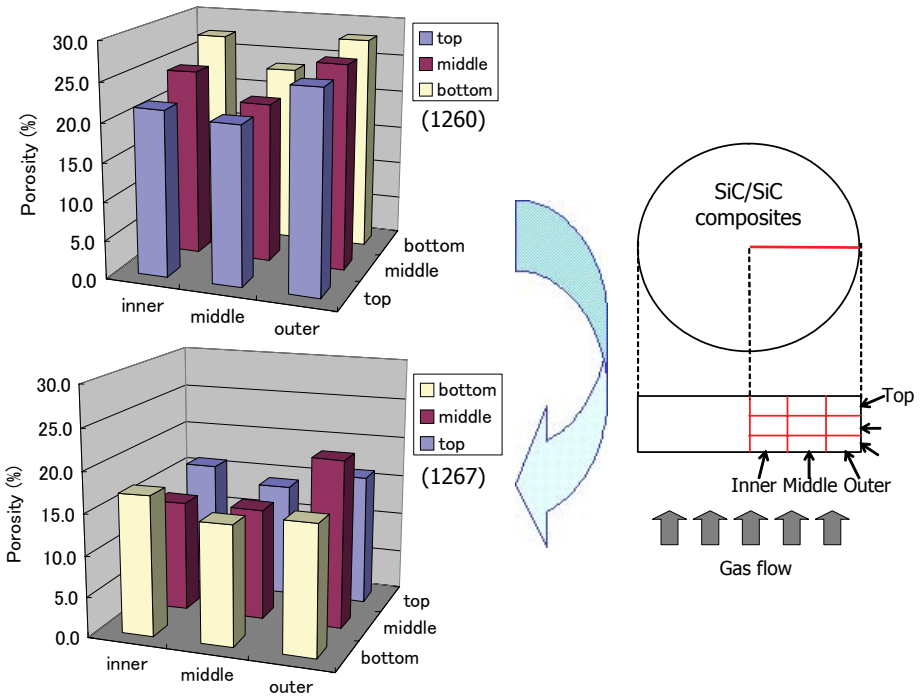

Fig. 3. Distribution of Porosity in Composites

with new concept was developed in this study. Fig. 5 shows SiC/C multilayer interphase. The first thin SiC layer (50 nm) is to strengthen bond between fiber and interphase. The next three SiC layers (200 nm) are for multiple interfacial fractures of fibers. The next two thick SiC layers (500 nm) are for multiple fractures of bundles. Thin C layers (50 nm) are used just to separate SiC layers. The composites with the multilayer SiC/C interphase showed the multiple fracture of interphase. The tensile strength of the composites with the multilayer was nearly 30 % larger than the composites with C interphase and with SiC/C interphase as shown in Fig. 6. Elastic modulus and PLS was normalized by porosity as shown in Eq. 2.

$$\text{Normalized Value} = \frac{\text{Original Value}}{1 - \text{Porosity}} \tag{2}$$

The elastic modulus of composites fabricated in this work is almost twice as large as the reported elastic modulus of the composites reinforced with Nicalon fibers fabricated by CVI [15]. The fracture strain of composites fabricated in this work is less than half of that of the

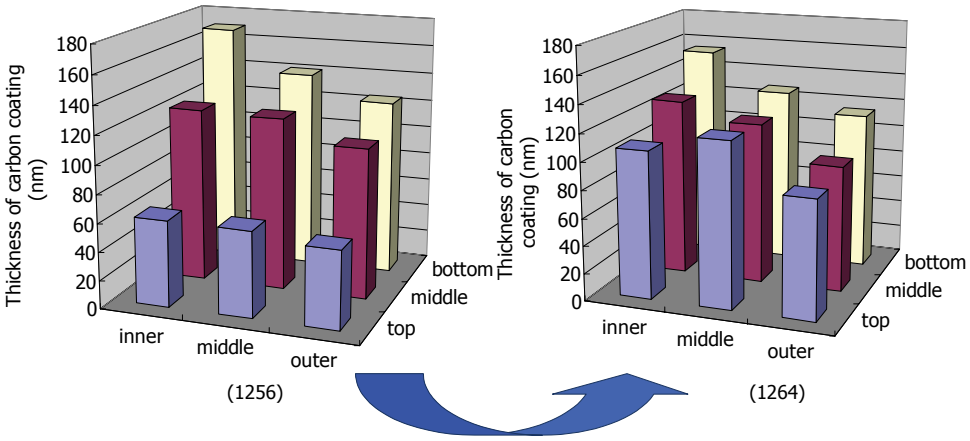

Reverse upstream side and downstream side in middle of deposition

Fig. 4. Improvement of Scatter of F/M Interphase Thickness

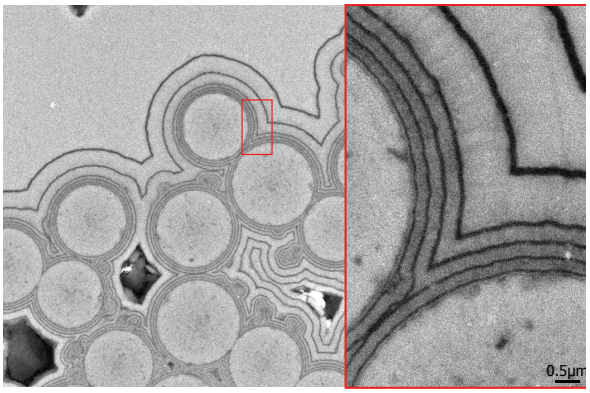

Fig. 5. SEM Images of Composites with SiC/C Multilayer Interphase

composites reinforced with Nicalon fibers. These properties are attributed to the intrinsic fiber properties. Both tensile strength and proportional limit stress of composites fabricated in this work are superior to those of composites reinforced with Nicalon fibers.

The large composite plates (300 mm diameter) are supposed to be fabricated using Tyranno SA fibers for irradiation experiments and round robin tests. Prior to using Tyranno SA fibers, the large composites were fabricated using Nicalon fibers to understand distribution of porosity and uniformity of interphase. Dense composites were fabricated in the first trial. Although the porosity of outermost regions was higher than that of the other, the average porosity was 14.4 %. The interphase was not formed uniformly. There was a gradient of the thickness, i.e. the interphase at the top side and the center was thicker.

IV. DISCUSSION

Pores existing within fiber bundle are limited and they don't affect porosity significantly in case of CVI composites. It is difficult to fill large space at inter-bundle of fibers by CVI processing. The large pores existing at inter-bundle of fibers significantly affect the porosity. In this study, increasing fiber volume fraction decreased porosity. Increasing the fiber volume fraction decreased the porosity at inter-bundle of fibers and the total amount of large pores existing inter-bundle of fibers decreased.

The composites reinforced with Hi-Nicalon fibers showed the peak PLS and the flexural strength at about 150 nm in thickness of C interphase. The ISS of composites reinforced with Hi-Nicalon fibers was about 200 MPa for a 150 nm thick C interphase. The composites reinforced with Tyranno SA showed the peak at C interphase thickness of about 100 nm. The ISS of composites reinforced with Tyranno SA fibers was about 350 MPa for the 100 nm C interphase case. The optimum ISS to obtain the largest flexural strength for the composites reinforced with Hi-Nicalon fibers is less than that for composites reinforced with Tyranno SA. The elastic modulus of Hi-Nicalon (270 GPa) is much smaller than elastic modulus of CVD SiC (461 GPa), while the elastic modulus of Tyranno SA (381 GPa) is similar to CVD SiC. It means that the tensile stresses in the matrix are larger than those in the Hi-Nicalon fiber before crack initiation, whereas it is similar in composites reinforced with Tyranno SA fibers. Matrix cracking stress (σm) depends on fiber modulus (Ef) as shown in Eq. 3 [16].

$$\sigma_m = \left(\frac{6\tau G_m V_f^{\,2} E_f E_{cl}^{\,2}}{(1-V_f) E_m^{\,2} r} \right)^{1/3} - \sigma_r \qquad (3)$$

where σr is the residual stress, τ is the interfacial frictional stress, Gm is the critical mode I energy release rate, Vf is the volume fraction of fibers, E is the elastic modulus of the matrix (m) or composite (cl) and r is fiber radius. One of the roles of the interphase is to deflect matrix cracks by interfacial debonding. It is assumed that the optimum ISS of the composites reinforced with Tyranno SA fibers is larger than that of composites reinforced with Hi-Nicalon fibers since the matrix

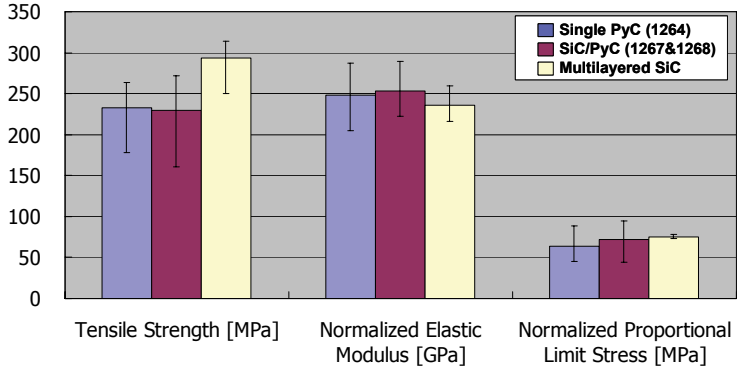

Fig. 6. The effect of fiber/matrix interphase on tensile properties

cracking stress of the composites reinforced with Tyranno SA fibers is larger than that of the composites reinforced with Hi-Nicalon fibers. The gap between matrix cracking stress and maximum strength is relatively small in composites reinforced with Tyranno SA fibers. The effect of interphase on mechanical properties of composites reinforced with Tyranno SA fibers is smaller than that of composites reinforced with Hi-Nicalon.

The first SiC layer in the fiber/matrix interphase was very effective for composites reinforced with Hi-Nicalon fibers. The crack path in the interphase was turned from fiber/interphase interface to within the interphase. The interfacial frictional strength increased. The interfacial fracture behavior and mechanical properties were improved. However the apparent effect of the first SiC layer was not evident in the composites reinforced with Tyranno SA fibers. One of the reasons is due to fiber modulus as discussed in the previous paragraph. The matrix cracking stress of composites reinforced with Tyranno SA fibers should be larger than that of composites reinforced with Hi-Nicalon fibers. The effect of interfacial shear strength on mechanical properties of composites reinforced with Tyranno SA fibers is smaller than that of composites reinforced with Hi-Nicalon fibers. Another reason is the rougher surface of Tyranno SA fiber compared with that of Hi-Nicalon fiber. It is considered the interfacial frictional stress is sufficiently large without the first SiC layer. The first SiC layer is expected to be effective under severe environment in which the interfacial shear strength is reduced by oxidation or neutron irradiation. Further experiments under such severe environments are required to understand the necessity of the SiC layer.

The multilayer interphase with this new concept was developed in this study. It is considered that not only fiber pull-out but also fiber bundle pull-out plays an important role, so the concept of the bundle interphase was applied to the multilayer. Most composites with C/SiC multilayer interphase without the first SiC layer on fibers did not have multiple fracture of the interphase and the interfacial fracture behavior depended on the first C layer thickness. However both the multiple fracture of fibers and fiber bundles were attained in the composites with the multilayer SiC/C interphase. It is considered that the first SiC layer is the key for multiple fracture.

V. CONCLUSIONS

1. The SiC/SiC composites fabricated by the ICVI system at NIMS were significantly improved by optimization of gas flow rate, temperature, the position of the preform inside the furnace, increasing fiber volume fraction and the precursor gas. The uniformity of the fiber/matrix interphase, the density and mechanical properties were significantly improved while the time for fabrication became less than half of that for previous runs.
2. The interfacial shear strength drastically decreased with increasing C interphase thickness. It was found that the interfacial shear strength of composites reinforced with Tyranno SA fibers was slightly larger than that of composites reinforced with Hi-Nicalon if the thickness of C interphase is same.
3. The composites reinforced with Hi-Nicalon fibers showed the peak PLS and the flexural strength at about 150 nm C interphase thickness, while the composites reinforced with Tyranno SA fibers showed the peak at about 100 nm thickness. It was found that the mechanical properties of composites reinforced with Tyranno SA fibers are more insensitive to C interphase thickness than those of composites reinforced with Hi-Nicalon fibers.
4. The first SiC layer in the fiber/matrix interphase improved interfacial fracture behavior and mechanical properties significantly in composites reinforced with Hi-Nicalon fibers, while the apparent effect of the first SiC layer was not seen in composites reinforced with Tyranno SA fibers due to large modulus and rough feature of fiber surface.
5. The density and the scattering on interphase of composites fabricated by FCVI was significantly improved by optimization of temperature and gas flow, increasing fiber volume fraction and reversing the up-stream side and down-stream side of the gas in the middle of deposition.
6. Although thickness of C interphase and the first SiC layer didn't affect tensile properties of composites reinforced with Tyranno SA significantly, the tensile strength of the composites with the multilayer SiC/C interphase was improved.
7. Large composites with 300 mm in diameter were successfully fabricated by FCVI with the porosity of 14.4 %, although the interphase was not formed uniformly.

ACKNOWLEDGMENTS

Authors would like to thank T. Noda and H. Araki of NIMS and J.C. McLaughlin of ORNL for the assistance of the fabrication of SiC/SiC composites. This work was supported by Core Research for Evolutional Science and Technology operated by the Japan Science and Technology Corporation, by Japan/USA Program of Integration of Technology and Engineering for Fusion Research (JUPITER II) and by the office of Fusion Energy Science, US DOE under contract DE-AC-05-00OR22725 with UT-Battelle, LLC.

REFERENCES

1. T.M. Besmann, D.P. Stinton and R.A. Lowden, MRS Bull. XIII [11] (1988) 45.
2. T.M. Besmann, J.C. McLaughlin, Hua-Tay Lin, J. Nucl. Mater., 219 (1995) 31-35.
3. H. Araki, H Suzuki, W. Yang, S. Sato and T. Noda, J. Nucl. Mater., 258-263 (1998) 1540-1545.
4. E. Lara-Curzio, Comprehensive Composites Encyclopedia, Elsevier, (2000) 533-577.
5. E. Lara-Curzio and M. K. Ferber, Numerical Analysis and Modeling of Composite Materials, Ed. J. W. Bull, Blackie Academic & Professional (1995) 357-399.
6. R.E. Jones, D. Petrak, J. Rabe and A. Szweda, J. Nucl. Mater., 283-287 (2000) 556-559.
7. M. Takeda, A. Urano, J. Sakamoto and Y. Imai, J. Nucl. Mater., 258-263 (1998) 1594-1599.
8. T. Ishikawa, Y. Kohtoku, K. Kumagawa, T. Yamamura and T. Nagasawa, Nature, 391 (1998) 773-775.
9. T. Ishikawa, S. Kajii, T. Hisayuki, K. Matsunaga, T. Hogami and Y. Kohtoku, Key Eng. Mater., 164-165 (1999) 15-18.
10. T. Nozawa, E. Lara-Curzio, Y. Katoh, L.L. Snead and A. Kohyama, Fusion Materials Semi-Annual Progress Reports, DOE/ER-0313/31 (2001) 40-46.
11. M. Steen and J.L Valles, ASTM STP 1309, (1997) 49.
12. T. Hinoki, W. Zhang, A. Kohyama, S. Sato and T. Noda, J. Nucl. Mater., 258-263 (1998) 1567-1571.
13. E. Lara-Curzio, M. K. Ferber and R.A. Lowden, Ceram. Eng. and Sci., 15 [5] (1994) 989-1000.
14. T. Hinoki, W. Yang, T. Nozawa, T. Shibayama, Y. Katoh and A. Kohyama, J. Nucl. Mater., 289 (2001) 23-29.
15. P. Lipetzky, G.J. Dvorak and N.S. Stoloff, Mater. Sci. Eng., A216 (1996) 11-19.
16. W.A. Curtin, J. Am. Ceram. Soc., 74 [11] (1991) 2837-2845.

TENSILE STRENGTH OF CHEMICAL VAPOR INFILTRATED ADVANCED SiC FIBER COMPOSITES AT ELEVATED TEMPERATURES

T. Nozawa[1], K. Hironaka[1], Y. Katoh[1], A. Kohyama[1], T. Taguchi[2], S. Jitsukawa[2] and L.L. Snead[3]

[1]*Institute of Advanced Energy, Kyoto University, Gokasho, Uji, Kyoto 611-0011 Japan, nozawa@iae.kyoto-u.ac.jp, hironaka@iae.kyoto-u.ac.jp, katoh@iae.kyoto-u.ac.jp, kohyama@iae.kyoto-u.ac.jp*
[2]*Japan Atomic Energy Research Institute, Tokai, Ibaraki 319-1195 Japan, taguchi.tomitsugu@jaeri.go.jp, jitsukawa.shiro@jaeri.go.jp*
[3]*Oak Ridge National Laboratory, Oak Ridge, TN 37831 USA, sneadll@jornl.gov*

SiC/SiC composites composed of high-crystalline, near-stoichiometric SiC fiber, like Hi-Nicalon™ Type-S and Tyranno™-SA, are promising structural materials for fusion and other high-temperature applications, because of their excellent chemical, physical and mechanical stabilities at high-temperature. In order to explore show the excellent performance of recently developed advanced SiC/SiC composites under severe environment and to identify the key issues for the further material development, room- and high-temperature tensile tests were conducted under the mild oxidizing environment at 1300°C for Tyranno™-SA fiber reinforced SiC matrix composites with two kinds of the fiber and matrix (F/M) interphase: pyrolytic carbon (PyC) and SiC/PyC, fabricated by the forced-flow/thermal-gradient chemical vapor infiltration (F-CVI) method. Tensile strength of both composites was significantly stable to high-temperature exposure up to 1300°C in mild oxidizing environment, with no clear difference for two interfacial structures. Also, there was no dependence of PyC thickness on tensile strength for both interphase systems. In other words, the rough surface of Tyranno™-SA fiber had the same role with the SiC pre-coating.

I. INTRODUCTION

SiC/SiC composites are considered one of the promising materials for fusion and other applications in advanced energy industries, because silicon carbide (SiC) has inherent mechanical property stability at high-temperature, low-induced activation, after heat, and excellent corrosion resistance[1]. High-crystalline and near-stoichiometric SiC fibers like Hi-Nicalon™ Type-S and Tyranno™-SA are, in particular, stable to oxidation at high-temperature and to severe neutron exposure, because of less impurities such as oxygen and good structural order[2]. Similarly, β-SiC matrix derived by forced-flow/thermal-gradient chemical vapor infiltration (F-CVI) process, which has a highly-crystalline structure, would show good stability of strength against neutron exposure[3-5]. From these reasons, SiC/SiC composites with high-crystalline and near-stoichiometric SiC fiber and matrix are considered to have excellent physical and mechanical properties under these severe conditions. Therefore, many investigations on F-CVI process have been enthusiastically carried out at Oak Ridge National Laboratory (ORNL), as a part of Japan-US collaborations. This study focused on tensile properties of SiC/SiC composites with recently developed new SiC fibers, for the optimization of F-CVI process.

In case of the design of ceramic matrix composites, interfacial materials such as pyrolytic carbon (PyC) are, in general, formed between fiber and matrix in order for the improvement of toughness. The role of the interphase is to deflect the main cracks at the weak fiber and matrix (F/M) interface and to cause many fiber pullouts. Interfacial shear strength and friction cause the ductile fracture behavior and produces high fracture toughness. However, there has been a concern that cracks propagated along the smooth surface of the fibers such as Hi-Nicalon™ would have insufficient interfacial friction for load transfer. A rough SiC layer was designed to deposit on the fiber surface to promote the crack deflection within the interphase[6]. In addition, multi-layered SiC interphase has been developed in order to make the crack path more complex and to prevent the outer reaction gases from flowing into the crack paths.

The objective of this study is to investigate mechanical performance of recently developed stoichiometric SiC fiber reinforced F-CVI SiC matrix composites and also to identify the key implementation for the improvement of F-CVI technique. In particular, high-temperature tensile properties and the effect of several interfacial structures were discussed.

II. EXPERIMENTAL

II.A. Materials

All the composite disks with a 3-inch diameter and a half-inch thickness were fabricated by F-CVI method at ORNL (Table 1). Plane-woven (P/W) sheets of Si-Al-C fiber: Tyranno™-SA (Ube Industries), which were stacked in the [0°/90°] direction, were used as reinforcements. Then, β-SiC matrix was deposited by using methyltrichlorosilane (MTS) carried with hydrogen.

Table 1 Test Materials

ID	Composite Structure	Aimed Interlayer Thickness [nm]	Fiber Volume Fraction [%]	Density [Mg/m^3]	Porosity [%]
1264	Tyranno-SA/PyC/FCVI-SiC	150	35.4	2.61	23.3
1265	Tyranno-SA/PyC/FCVI-SiC	300	35.3	2.72	18.0
1266	Tyranno-SA/PyC/FCVI-SiC	75	35.2	2.62	18.1
1267	Tyranno-SA/(SiC/PyC)/FCVI-SiC	100/150	38.8	2.74	15.7
1268	Tyranno-SA/(SiC/PyC)/FCVI-SiC	100/150	38.8	2.69	18.0
1269	Tyranno-SA/(SiC/PyC)/FCVI-SiC	100/300	38.8	2.71	17.2

Pyrolytic carbon (PyC) interphase and SiC/PyC interphase were deposited on the surface of each fiber before the F-CVI densification. Three kinds of thickness of PyC interphase; 75, 150 and 300 nm, were chosen for the evaluation of influences of their thickness on tensile properties. In order to fabricate a uniform interphase in the F/M interface, deposition of PyC was carried out in two steps: initial infiltration followed by turning the specimens upside down and infiltrating again. All the composites had a small gradient of the interfacial thickness with a maximum at the center of the upstream side. More details were discussed elsewhere[7].

II.B. Tensile Test

Tensile tests were conducted by an electromechanical testing machine (Instron Japan Co. Ltd.) on the basis of ASTM C1275 and C1359. Miniature edge-loaded tensile specimen was used (Fig. 1). All the tests were conducted at the crosshead speed of 0.5 mm/min. The step-loading tests were performed for the room-temperature tension in air for the precise evaluation of the damage accumulation around proportional limit. Simple monotonic tests were performed for high-temperature tension at 1300°C in a flow of commercial argon with about 0.1 Pa of oxygen in partial pressure. High-temperature tests were carried out following a 20 min ramp to the test temperature and a subsequent equilibration time of about 10 min. More details were described elsewhere[8].

After the tensile tests, fracture surfaces of all the specimens were examined by using scanning electron microscopy (SEM). Besides, porosity, fiber volume fraction and thickness of the PyC interphase were also measured.

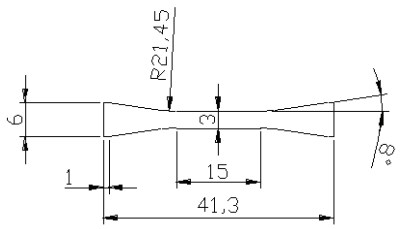

Fig. 1 Schematic illustration of the miniature edge-loaded tensile specimen

II.C. Analysis

Tensile properties were analyzed by using the normalized value as shown in equation (1), which takes into consideration the large scatter of porosity among as-received materials. It was revealed that elastic modulus and proportional limit stress were in roughly inverse proportion to the porosity[9]. In this equation, stress was calculated as applied force divided by the true cross-sectional area excluding the area occupied by pores.

$$\text{Normalized Value} = \frac{\text{Original Value}}{1 - \text{Porosity}} \qquad (1)$$

It is noted that, in this analysis, it was assumed that porosity was distributed equally in any cross-section.

III. RESULTS AND DISCUSSION

III.A. High-Temperature Tensile Fracture Behaviors of Advanced SiC/SiC Composites

Tyranno™-SA/ FCVI-SiC had good stability in tensile properties under the high-temperature exposure regardless of the interfacial structures (Fig. 2). There was only a minor degradation of tensile strength at 1300°C in mild oxidizing environment.

SiC easily formed into SiO_2 in air by the oxidation and, even if in inert environment, SiC is oxidized due to the reaction with oxygen included as the impurity[10, 11].

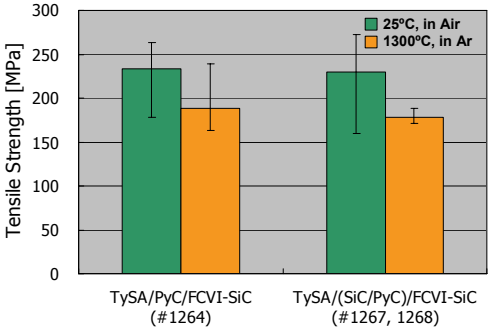

Fig. 2 High-temperature tensile strength of advanced SiC/SiC composites

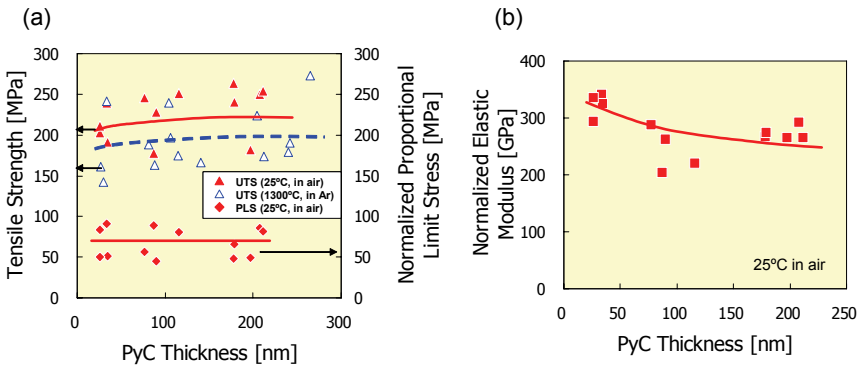

Fig. 3 PyC thickness dependencies on (a) tensile strength, normalized PLS and (b) normalized elastic modulus (single PyC interphase)

The former is well known as passive oxidation and the latter is referred to as active oxidation. SiC fiber and matrix used in this study were high-crystalline and near-stoichiometric composition, and hence there were few impurities. Also, it is reported that there was no significant degradation of tensile strength in Tyranno™-SA fiber itself after the heat treatment below 1300°C in inert environment[12]. These good stabilities of each component made tensile strength of composites stable to the oxidizing attack. However, slight degradation of tensile strength should not be ignored. In air, PyC might be easily burned out by oxidation. However, under the mild-oxidizing environment, PyC oxidation seemed quite small. It might be due to the severe degradation of the in-situ fiber strength or interfacial shear properties at 1300°C.

III.B. Effect of the PyC Thickness on RT/HT Tensile Properties – Single PyC Interphase

It is reported that Tyranno™-SA/SiC composite had maximum flexural strength for a 200 nm PyC thickness. For thinner PyC thickness, there existed significant large stress drops[13]. However, in tension, there was no clear dependence on the PyC thickness. Tensile strength and proportional limit stress (PLS) were nearly constant over the wide range of the PyC thickness (Fig. 3). On the contrary, tensile modulus tended to decrease with the PyC thickness.

Similar to the results at room temperature, there was no effect of the PyC thickness on the tensile strength at 1300ºC in Ar, although the magnitude of tensile strength decreased about 20 %. Tensile strength at high-temperature in inert environment was nearly constant in the broad range of the PyC thickness. According to the microscopic observation of the fracture surface (Fig. 4), PyC was burned out only near the surface of the composite, and, macroscopically, PyC degradation was never critical to the reduction of tensile strength. The reason for the degradation of the tensile strength at 1300ºC in Ar might be the in-situ degradation of tensile strength of fiber itself.

On considering the application to neutron irradiation, thin PyC interphase also becomes an advantage because of less degradation by neutron damage. Also excellent mechanical performance in the thinner PyC is very important fact for the design of the multi-layered interphase, which is structured of the sequence of thin SiC and PyC layers.

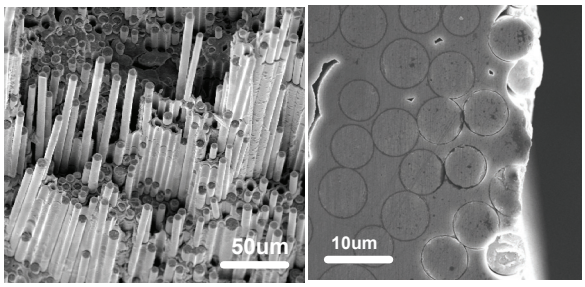

Fig. 4 Typical fracture surface appearances of advanced SiC/SiC with single PyC interphase after tension at 1300ºC in mild oxidizing environment

III.C. High-Temperature Tensile Fracture Behaviors of Advanced SiC/SiC Composites

Fig. 5 shows the PyC thickness dependency on the room-temperature tensile properties of SiC/SiC with SiC/PyC interphase. It was the same behavior as that in the case of using the single PyC interphase. In addition, the fracture behavior at high-temperature in inert environment was also very similar. There was about 20 % degradation of tensile strength and PyC burned out partially (Fig. 6). This is because the rough surface of Tyranno™-SA fiber played the same function of the rough SiC pre-coating, which was formed for the

promotion of the crack path within the first PyC interlayer. Possibly, rough surface of Tyranno™-SA fiber promoted the crack deflection within the first PyC interlayer.

IV. CONCLUSIONS

In order to investigate the performance of recently developed high-crystalline, near-stoichiometric F-CVI SiC/SiC composites, room- and elevated-temperature tensile tests were conducted by using small specimen test technique. In particular, roles of the various PyC based interphase; single PyC and SiC/PyC were identified. Key conclusions are summarized as follows.

1. High-crystalline, near-stoichiometric F-CVI SiC/SiC composites showed the excellent mechanical performance and they were characteristic in high strength, high modulus in tension.
2. Tensile strength and PLS were independent of the PyC thickness in the broad range. However, elastic modulus depended on it. It tended to decrease as the PyC thickness increasing.
3. There was no clear difference in tensile behavior between single PyC and (SiC/PyC) inter-layered composites. The PyC thickness effect on Tyranno™-SA/(SiC/PyC)/SiC composites was quite similar to that on Tyranno™-SA/PyC/SiC composites. Rough surface of Tyranno™-SA fiber had the same function with the SiC pre-coating.
4. Advanced F-CVI SiC/SiC composites with single PyC and SiC/PyC interphase showed the excellent high-temperature performance, respectively. Both types of SiC/SiC composites could maintain over 80% of their tensile strength at 1300ºC in Ar. In-situ fiber strength and interfacial shear properties might

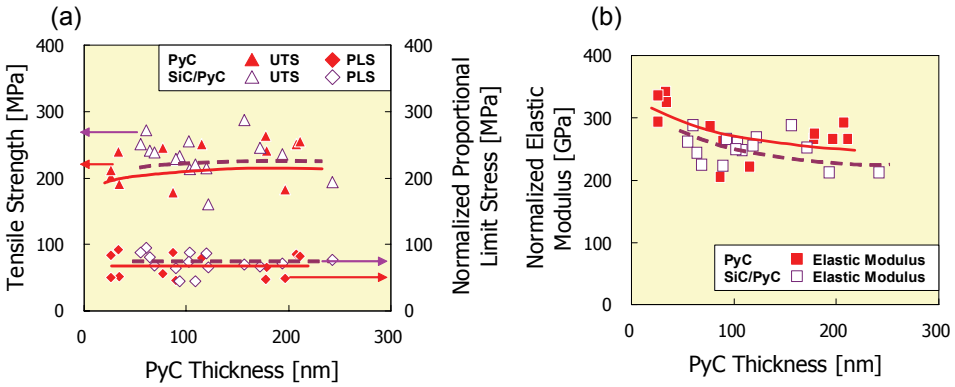

Fig. 5 PyC thickness dependencies on (a) tensile strength, normalized PLS and (b) normalized elastic modulus (at room temperature in air)

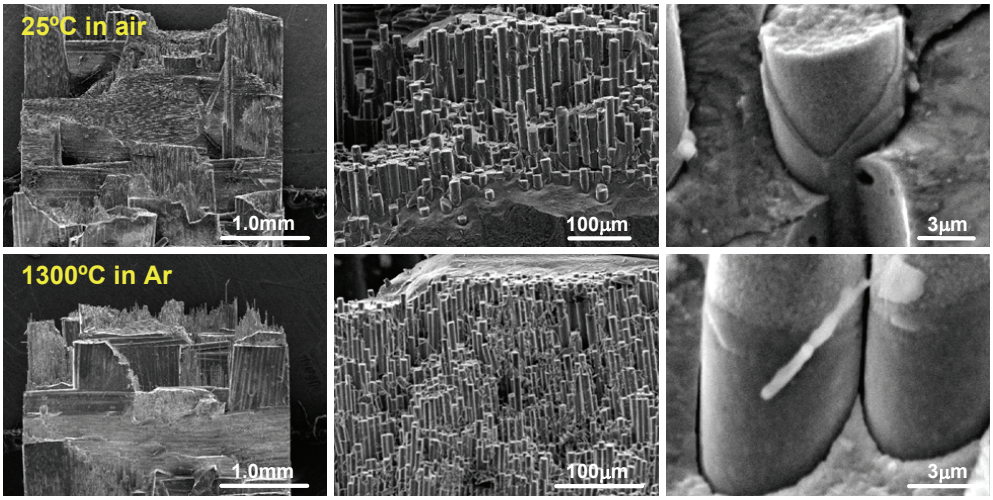

Fig. 6 Typical fracture surface appearances of SiC/PyC inter-layered SiC/SiC composites. There existed special gaps at the F/M interface after HT-tension

be degraded, because of no significant difference between the two different interphase types at elevated temperature.

ACKNOWLEDGMENTS

The authors would like to express their sincere appreciation to Mr. J.C. McLaughlin and Dr. T.M. Besmann, Oak Ridge National Laboratory for the fabrication of materials. This work was performed as a part of collaborations at Japan-US Program for Irradiation Test of Fusion Materials (JUPITER-II) and US-DOE/JAERI Collaborative Program on FWB Structural Materials in Mixed-Spectrum Fission Reactors, Phase IV. This study was also supported by Core Research for Evolutional Science and Technology (CREST).

REFERENCES

1. R.H. JONES, L.L. SNEAD, A. KOHYAMA and P. FENICI, "Recent Advances in the Development of SiC/SiC as a Fusion Structural Material," Fusion Engineering and Design," *Fusion Engineering and Design*, **41**, 15 (1998).
2. L.L. SNEAD, Y. KATOH, A. KOHYAMA, J.L. BAILEY, N.L. VAUGHM and R.A. LOWDEN, "Evaluation of Neutron Irradiated Near-Stoichiometric Silicon Carbide Fiber Composites," *Journal of Nuclear Materials*, **283-287**, 551 (2000).
3. R.J. PRICE, "Effects of Fast-Neutron on Pyrolytic Silicon Carbide," *Journal of Nuclear Materials*, **33**, 17 (1969).
4. R.J. PRICE and G.R. HOPKINS, "Flexural Strength of Proof-Tested and Neutron-Irradiated Silicon Carbide," *Journal of Nuclear Materials*, **108-109**, 732 (1982).
5. M.C. OSBORNE, J.C. HAY, L.L. SNEAD and D. STEINER, "Mechanical- and Physical-Property Changes of Neutron-Irradiated Chemical-Vapor-Depposited Silicon Carbide," *Journal of the American Ceramics Society*, **82**, 2490 (1999).
6. T. HINOKI, W. YANG, T. NOZAWA, T. SHIBAYAMA, Y. KATOH and A. KOHYAMA, "Improvement of Mechanical Properties of SiC/SiC Composites by Various Surface Treatments of Fibers," *Journal of Nuclear Materials*, **289**, 23 (2001).
7. T. TAGUCHI, N. IGAWA, T. NOZAWA, K. HIRONAKA, L. L. SNEAD, T. HINOKI, Y. KATOH, S. JITSUKAWA, A. KOHYAMA and J. C. McLAUGHLIN, "Optimizing the Fabrication Process for Superior Mechanical Properties in the Stoichiometric SiC Fiber Reinforced FCVI SiC Matrix Composite System," *Fusion Materials*, **DOE/ER-0313/31**, 47 (2001).
8. T. NOZAWA, K. HIRONAKA, T. TAGUCHI, N. IGAWA, L.L. SNEAD, Y. KATOH, S. JITSUKAWA and A. KOHYAMA, "Tensile Properties of Stoichiometric Silicon Carbide Fiber Reinforced F-CVI Derived Silicon Carbide Matrix Composites," *Fusion Materials*, **DOE/ER-0313/31**, 40 (2001).
9. T. NOZAWA, T. HINOKI, Y. KATOH, A. KOHYAMA, E. LARA-CURZIO, "Specimen Size Effects on Tensile Properties of 2-D/3-D SiC/SiC Composites," *ASTM STP*, **1418** (2002), to be published.
10. C. LABRUGERE, A. GUETTE and R. NASLAIN, "Effect of Ageing Treatment at High Temperatures on the Microstructure and Mechanical Behavior of 2D Nicalon/C/SiC Composites.1: Ageing under Vacuum or Argon," *Journal of the European Ceramics Society*, **17**, 623 (1997).
11. C. LABRUGERE, L. GUILLAUMAT, A. GUETTE and R. NASLAIN, "Effect of Ageing Treatment at High Temperatures on the Microstructure and Mechanical Behavior of 2D Nicalon/C/SiC Composites.2: Ageing under CO and Influence of a SiC Seal-Coating," *Journal of the European Ceramics Society*, **17**, 641 (1997).
12. R.E. TRESSLER, "Recent Developments in Fibers and Interphases for High Temperature Ceramic Matrix Composites," *Composites A*, **30**, 429 (1999).
13. W. YANG, H. ARAKI, T. NODA, Y. KATOH, J. YU and A. KOHYAMA, "CVI Tyranno-SA/SiC Composites with PyC and SiC Multi-interlayers," *Ceramics Engineering & Science Proceedings*, **22**, 481 (2001).

TENSILE AND THERMAL PROPERTIES OF CHEMICALLY VAPOR-INFILTRATED SILICON CARBIDE COMPOSITES OF VARIOUS HIGH-MODULUS FIBER REINFORCEMENTS

T. Nozawa[1], Y. Katoh[1], L.L. Snead[1], T. Hinoki[2] and A. Kohyama[2]

[1]*Oak Ridge National Laboratory, Oak Ridge, TN 37831 USA, nozawat@ornl.gov, katohy@ornl.gov, sneadll@ornl.gov*
[2]*Institute of Advanced Energy, Kyoto University, Gokasho, Uji, Kyoto 611-0011 Japan, hinoki@iae.kyoto-u.ac.jp, kohyama@iae.kyoto-u.ac.jp*

Chemically vapor-infiltrated (CVI) silicon carbide (SiC) matrix composites are candidate structural materials for proposed nuclear fusion and advanced fission applications due to their high temperature stability under neutron irradiation. To optimize the thermal stress properties for nuclear applications, CVI-SiC matrix composites were produced with three-dimensional (3D) fiber architectures with varied Z-fiber content, using the highly-crystalline and near-stoichiometric SiC fiber Tyranno™-SA. In addition, hybrid SiC/SiC composites incorporating carbon fibers were fabricated to improve thermal conductivity. The purpose of this work is to obtain thermal and mechanical properties data on these developmental composites. Results show that the addition of small amount (>10 %) of Tyranno™-SA fiber remarkably increases the composite thermal conductivity parallel to the fiber longitudinal direction, in particular the through-thickness thermal conductivity in the orthogonal three-dimensional composite system due to the excellent thermal conductivity of Tyranno™-SA fiber itself. On the other hand, tensile properties were significantly dependent on the axial fiber volume fraction; 3D SiC/SiC composites with in-plane fiber content <15 % exhibited lower tensile strength and proportional limit failure stress. Results show that the composites with axial fiber volume >20 % exhibit improved axial strength. The carbon fiber was, in general, beneficial to obtain high thermal conductivity. However matrix cracks induced due to the mismatch of coefficients of thermal expansion (CTE) restricted heat transfer via matrix, limiting the improvement of thermal conductivity and reducing tensile proportional limit stress.

I. INTRODUCTION

Silicon carbide fiber reinforced silicon carbide (SiC/SiC) composites are candidate materials for nuclear fusion and advanced fission reactors because of elevated-temperature mechanical capability, low induced-radioactivity, and after-heat[1]. The latest composites fabricated from high modulus SiC fibers, i.e., highly-crystalline and near-stoichiometric SiC fibers such as Tyranno™-SA and Hi-Nicalon™ Type-S, and β-SiC matrix provide good geometrical stability and strength retention after neutron irradiation[2-4]. Also, enhanced thermal and thermo-mechanical properties of the highly crystalline SiC composites have the added advantage to providing higher system efficiency. In addition, composites with higher thermal conductivity and strength exhibit much better resistance to thermal shock.

Constituent materials are one important factor to maximize the thermal properties of composites. Among various processing techniques, chemical vapor infiltration is regarded as the technique that produces the highest crystallinity of SiC with inherently high thermal conductivity[5]. Tyranno™-SA and Hi-Nicalon™ Type-S are also beneficial to use due to their crystalline structure. Tyranno™-SA fiber exhibits the thermal conductivity of 65 W/m-K, while 18 W/m-K for Hi-Nicalon™ Type-S. Further thermal conductivity improvements have been proposed whereby hybrid composite concepts using carbon fibers as reinforcements mixed with SiC fibers (SiC-C/SiC composites) are utilized[6]. Specifically, pitch-based carbon fibers possess much higher thermal conductivity (22~1000 W/m-K), as compared to SiC or other graphite fibers. For many nuclear applications, heat transport in the direction orthogonal to the plane of the primary stress is required. For this reason, a Z-stitch of high conductivity graphite fiber into an X-Y weave of SiC fibers has been considered. Matrix densification is also important to keep good heat transfer via matrix. The through-thickness thermal conductivity of ~70 W/m-K, which is higher than that of conventional composites (~20 W/m-K), has been reported for two dimensional (2D) SiC/SiC composite with the density of ~3.1 g/cm^3, fabricated by nano-infiltration transient eutectic phase sintering (NITE) process[7].

The objective in this study is to evaluate the thermal and mechanical properties of various architecture types of SiC/SiC and hybrid SiC-C/SiC composites reinforced by the high-modulus SiC and carbon fibers, designed to provide high thermal conductivity.

II. EXPERIMENTAL

The materials were CVI-SiC matrix composites with the highly crystalline and near-stoichiometric SiC fibers: Tyranno™-SA Grade-3 and Hi-Nicalon™ Type-S. Also

Table 1. SiC/SiC and hybrid SiC-C/SiC composites under investigation.

Composite ID	Fiber	Architecture	X- (and Y-) fiber volume fraction [%]	Z-fiber volume fraction [%]	Density [Mg/m^3]	Porosity [%]
P/W SA	SA[*1]	P/W	20	-	2.51	20
S/W HNLS	HNLS[*2]	5-harness S/W	22	-	2.52	19
3D(1:1:4) SA	SA[*1]	3D(X:Y:Z=1:1:4)	10	40	2.76	10
3D(1:1:1) SA	SA[*1]	3D(X:Y:Z=1:1:1)	15	15	2.78	11
Hybrid 2D	SA[*1]+C[*3]	P/W	SA[*1]:8, C[*3]:18	-	2.25	19
Hybrid 3D	SA[*1], C[*3]	3D(X,Y:SA[*1], Z:C[*3])	SA[*1]:12	C[*3]:21	2.19	25

[*1]SA: Tyranno^{TM}-SA Grade 3 fiber, [*2]HNLS: Hi-Nicalon^{TM} Type-S fiber, [*3]C: P120S fiber

hybrid CVI-SiC matrix composites with Tyranno™-SA Grade-3 and pitch-based carbon (P120S: ~640 W/m-K in longitudinal, ~2.4 W/m-K in radial) fibers were prepared. All materials were produced by isothermal/isobaric CVI process. Two types of 2D SiC/SiC composites with plain-weave (P/W) Tyranno™-SA and 5-harness satin-weave (S/W) Hi-Nicalon™ Type-S, two types of orthogonal 3D SiC/SiC composites with differed through-thickness (Z-direction) fiber content: X: Y: Z = 1: 1: 1 and 1: 1: 4, and two types of hybrid composites with a P/W and an orthogonal 3D architecture composed of Tyranno™-SA and P120S fibers were fabricated, respectively (Table 1). It is noted that the Z-direction fibers of both 3D SiC/SiC composites were made into SA grade (Si-Al-C) from AM grade (Si-Al-C-O) Tyranno™ fiber at the temperature of ~2073 K in inert environment after weaving. All composites had 150 nm thick pyrolytic carbon (PyC) as fiber/matrix (F/M) interphase.

Tensile specimens were machined from the composite plates so that the longitudinal direction was parallel to either of X or Y fiber directions. Miniature tensile geometry that had been developed for neutron irradiation studies on ceramic composites[8] was employed. The rectangular geometries (length × width × thickness) of 15.0 mm × 4.0 mm × 2.3 mm for the 2D SiC/SiC and/or the 2D and 3D hybrid SiC-C/SiC composites, and 20.0 mm × 6.0 mm × 2.5 mm for the 3D SiC/SiC composites are used. Tensile tests were conducted following the general guidelines of ASTM standard C1275. The tensile test incorporated several unloading/reloading sequences in order to allow hysteresis analysis. For the testing at room temperature, specimens were clamped by wedge grips with aluminum end tabs on both faces of the gripping sections. The strain was determined by averaging the readings of strain gauges bonded to both faces of the center gauge section. The crosshead displacement rate was 0.5 mm/min for all tests.

Room temperature thermal diffusivity was measured using a xenon flash technique and thermal conductivity was calculated using the measured composite density and specific heat. Specific heat of composites was calculated assuming the rule of mixtures. Microstructures and tensile fracture surfaces to selected samples were examined with an optical microscopy and a field emission scanning electron microscopy (FE-SEM).

III. RESULTS AND DISCUSSION

III.A. Microstructure

Fig. 1 shows the typical cross-sectional images of as-received composites. Two dimensional SiC/SiC composites had large pores in most cases in weaving cross-sectional pockets, resulting in a density of ~2.5 g/cm^3. By contrast, both 3D SiC/SiC composites were well-densified even in the pocket regions, yielding a density of ~2.7 g/cm3. Both 2D and 3D hybrid composites had large pores in pocket regions. Therefore less densification of the matrix yielded a lower density (~2.2 g/cm^3) than that of ideally densified composites (~2.8 g/cm^3). In addition, the hybrid composites contained transverse matrix cracks around every carbon fiber bundle. Specifically major cracks propagated within laminated plies for some 2D hybrid composites. This is attributed to the large CTE mismatch between the SiC matrix and the carbon fiber.

III.B. Thermal Conductivity

Table 2 lists a relationship between the axial fiber content and the thermal conductivity. The 3D SiC/SiC composites with the Tyranno™-SA fiber exhibited the highest improvement of the thermal conductivity in Z-direction. The in-plane thermal conductivity was also high (~50 W/m-K) similar to the through-thickness thermal conductivity due to the presence of continuous X- or Y-direction fibers. In contrast, the SiC/SiC composite of Hi-Nicalon™ Type-S with relatively lower thermal conductivity exhibited less improvement of the in-plane thermal conductivity, though high axial (in-plane) fiber volume fraction. Similarly, the carbon fiber with higher thermal conductivity of 640 W/m-K is, in general,

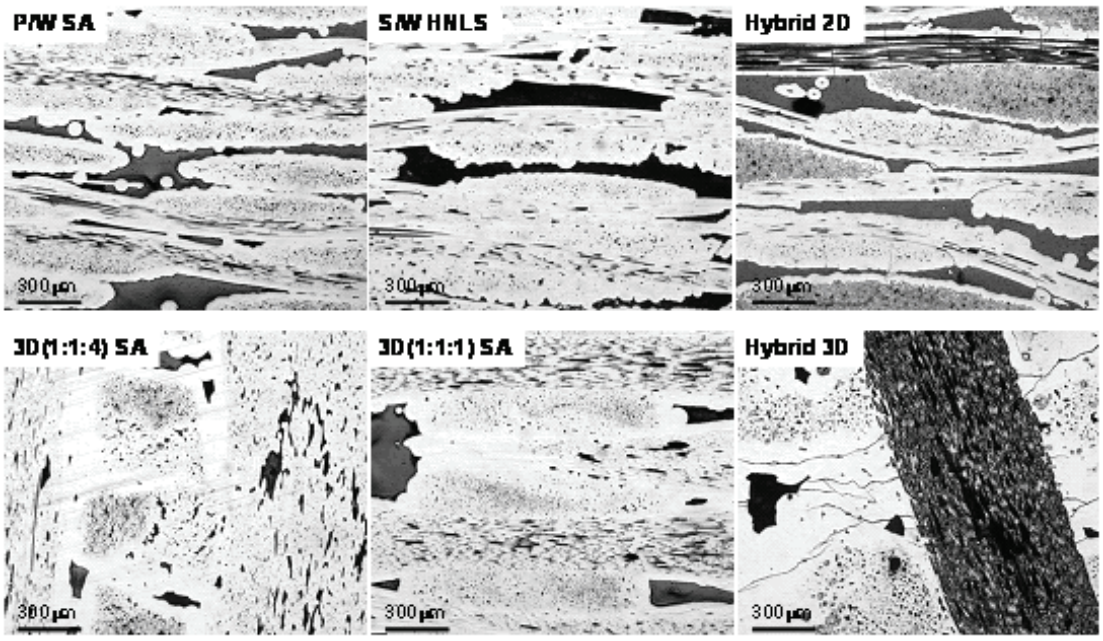

Fig. 1. Cross-sectional images of as-received SiC/SiC and hybrid SiC-C/SiC composites. Both hybrid SiC-C/SiC composites underwent matrix cracking due to CTE-mismatch.

Table II. In-plane and through-thickness thermal conductivity.

Composite ID	In-plane		Through-thickness	
	Fiber volume fraction [%]	Thermal conductivity [W/m-K]	Fiber volume fraction [%]	Thermal conductivity [W/m-K]
P/W SA	20	47.8 (1.3)	0	18.9 (0.3)
S/W HNLS	22	34.7 (1.3)	0	18.1 (0.3)
3D(1:1:4) SA	10	46.2 (1.4)	40	58.2 (1.8)
3D(1:1:1) SA	15	47.4 (1.0)	15	46.1 (0.9)
Hybrid 3D	12	32.6 (0.5)	21	53.0 (13.5)

*The numbers in parenthesis indicate standard deviation.

considered effective to provide the high through-thickness thermal conductivity. Less improvement of the thermal conductivity of the 3D hybrid composite was primarily due to large porosity. However, many CTE mismatch induced cracks might prevent thermal diffusion via matrix of carbon fiber containing composites. In addition, inherently lower radial thermal conductivity of the carbon fiber is also disadvantage to obtain the good in-plane thermal conductivity.

III.C. Tensile Properties

Fig. 2 exhibits the typical tensile stress-strain curves and tensile data are shown in Table III. Each of the curves for 2D SiC/SiC composites comprises an initial proportional segment that corresponds to the elastic deformation, followed by a non-linear portion due to domination of the matrix cracks and the fiber failures. The highest tensile strength of about 200 MPa for 2D SiC/SiC composites is similar to that obtained from conventional 2D CVI-SiC/SiC composites[5]. The higher tensile Young's modulus of ~270 GPa of the 2D SiC/SiC composites is attributed to the use of highly-crystalline SiC fibers and matrix. The large scatters were due to varied pore content. In contrast, the dense 3D SiC/SiC composites exhibited high Young's modulus, though significantly lower tensile strength than the 2D CVI SiC/SiC composites. They are roughly distinguished into two types of fracture patterns: brittle and quasi-ductile with non-linear portion, although both fracture behaviors exhibited limited short fiber pullout (Fig. 3). Most of the brittle specimens failed just after the proportional limit stress (PLS). The brittle

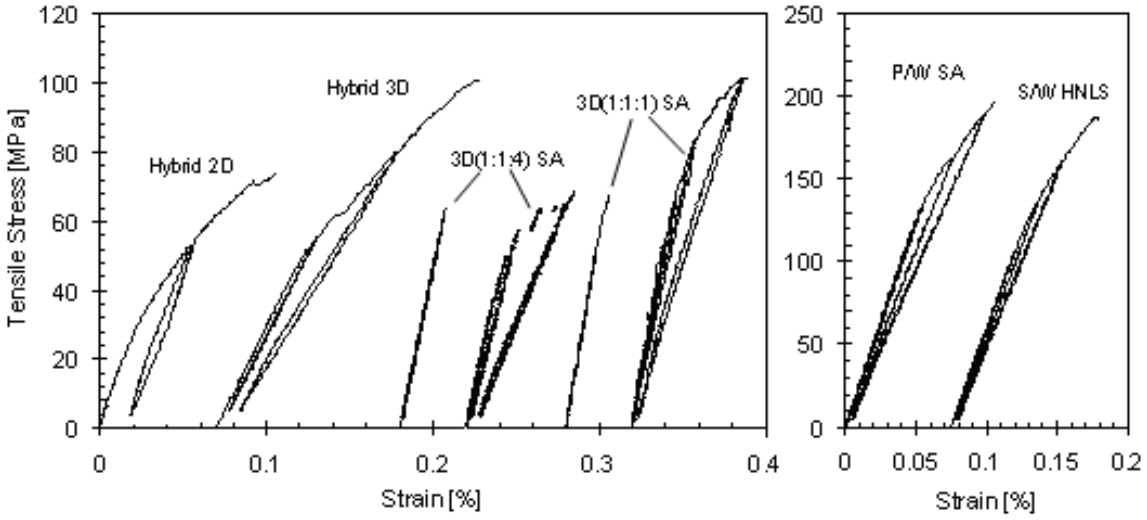

Fig. 2. Typical tensile stress-strain curves of SiC/SiC and hybrid SiC-C/SiC composites.

Table 3. Tensile data of various SiC/SiC and hybrid SiC-C/SiC composites.

Composite ID	Young's modulus [GPa]	Proportional limit stress [MPa]	Tensile strength [MPa]	Misfit stress [MPa]
P/W SA	273(23)	103(21)	199(2)	11(11)
S/W HNLS	244(6)	101(9)	226(50)	9(7)
3D(1:1:4) SA - brittle	213(26)	64	64	-
3D(1:1:4) SA	224(5)	35(2)	59(13)	7(2)
3D(1:1:1) SA - brittle	264(18)	60(4)	65(4)	-
3D(1:1:1) SA	277	53	102	-7(8)
Hybrid 2D	138(28)	8(1)	94(28)	32
Hybrid 3D	95(10)	47(1)	98(3)	18(4)

*The numbers in parenthesis indicate standard deviation.

specimens of 3D(1:1:1) therefore exhibited very lower tensile strength (~65 MPa). However, there is no significant difference between the brittle and the non-brittle composites for 3D(1:1:4). Young's moduli for both the brittle and the non-brittle composites were still in same range.

A feature of the hybrid composites is significantly lower Young's moduli, ~140 GPa for 2D and ~100 GPa for 3D, respectively. In contrast, the estimated Young's moduli by parallel-serial approach based on the rule of mixtures[9] yielded ~270 GPa for 2D and ~100 GPa for 3D. It is noted that the Young's modulus of the P/W hybrid composites was roughly estimated by replacing with the orthogonal 2D architecture. Therefore, the estimated Young's modulus should be significantly influenced by pore distribution and waviness. Processing-induced matrix cracks perpendicular to the loading axis of the 2D hybrid composites could reduce the initial Young's modulus. Damaged matrices also caused less proportional segment, followed by progressive damage accumulations in lower stress level. However, severe degradation of the Young's modulus might also be explained by additional factors such as fiber damage induced by preparing a hybrid weaves, although it is still unclear. Contrarily, the 3D hybrid composites with transverse matrix cracks around Z-stitch carbon fibers, which existed parallel to the axial fibers, exhibited less degradation of the Young's modulus.

The significant difference of tensile strength in the composite types is attributed primarily to the effective fiber volume content in the loading axis. According to Curtin[10], the intact fibers transfer the applied load beyond

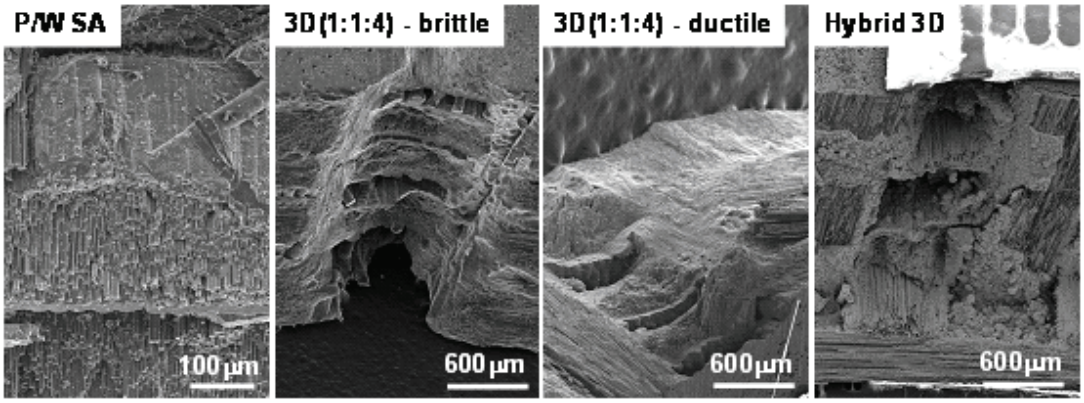

Fig. 3. Typical tensile fracture surfaces of SiC/SiC and hybrid SiC-C/SiC composites.

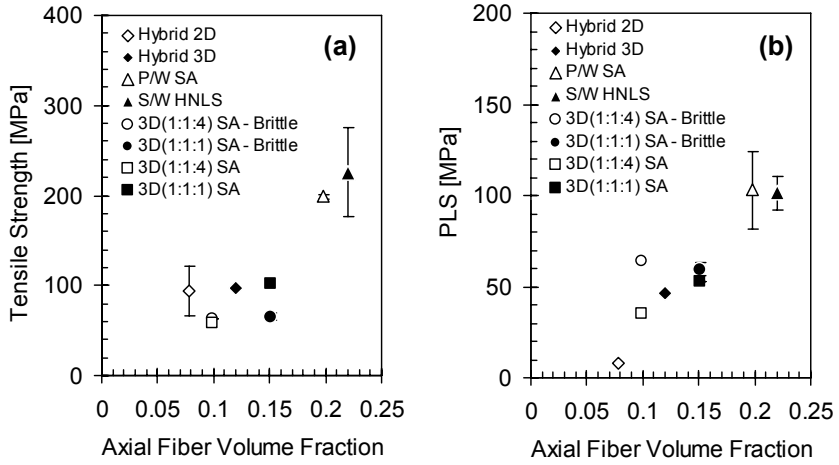

Fig. 4. Relationships among tensile properties and the axial fiber volume fraction.
(a) Tensile strength and (b) proportional limit stress

the fiber failure. In particular, it is simply assumed that intact fibers equally convey the applied load, well known as the global load sharing (GLS) theory. This indicates that the ultimate tensile strength is proportional to the axial fiber volume fraction. Composites tested in this study were designed with varied fiber volume content. As plotted in Fig. 4(a), the large differences in axial fiber content provided the differed tensile strength in each composite. Both 3D SiC/SiC composites with large structural unit, ~3.0 mm, are subjected to change in fiber volume fraction in cutting position. The bare fibers located at the edges of the specimen are mostly damaged, i.e. discontinuous along the gauge length, and those are ineffective in load transfer. In this case, less ability to transfer the applied load resulted in the quasi-brittle failure at the PLS. Even in the non-brittle case, very low axial fiber content leaded to low composite tensile strength. Additionally, the possible slight processing damage on reinforcing fibers of 3D SiC/SiC composites during heating up to 2073 K may have degraded the composite tensile strength.

As with the tensile strength, the difference of the PLS in composite types may be attributed primarily to the axial fiber volume content (Fig. 4(b)). In particular, the 2D hybrid composites with severe processing-induced matrix damages had much lower PLS.

The residual thermal stress is inevitable when the coefficients of thermal expansion are different between the fibers and the matrix. In the Tyranno™-SA or Hi-Nicalon™ Type-S/PyC/CVI-SiC system, the residual stress should be minimal, because the fibers consist primarily of cubic (beta-phase) SiC, i.e. equivalent to the matrix constituent. The thermal residual stress estimated by the method proposed by Vagaggini, et al.[11] exhibits

nearly zero for 3D SiC/SiC composites and residual tension of ~10 MPa for 2D SiC/SiC composites (Table 3), while ~100 MPa in a ceramic grade Nicalon™/ PyC/CVI-SiC composite[12]. The slightly larger residual stress of 2D SiC/SiC composites might be due to restriction by weaving structure. The hybrid SiC-C/SiC composites exhibited relatively higher tensile residual stress due to large CTE mismatch of the SiC and the carbon.

IV. CONCLUSIONS

This work aims to obtain thermal and mechanical property data for advanced CVI silicon carbide matrix composites using high-modulus SiC and carbon fibers. The major conclusions drawn from this study are summarized as follows.

1. The 3D SiC/SiC composites with Tyranno™-SA fibers exhibited the highest thermal conductivity, due to excellent thermal conductivity of Tyranno™-SA fiber itself
2. Tensile properties of SiC/SiC composites were significantly dependent on the axial fiber volume fraction; 3D SiC/SiC composites with less in-plane fiber content exhibited lower tensile strength and proportional limit stress. The high volume fraction of the axial fibers, >20%, is required to obtain good tensile properties.
3. The carbon fiber was, in general, beneficial to obtain high thermal conductivity. However matrix cracks due to the mismatch of coefficients of thermal expansion restricted heat transport via matrix, limiting the improvement of thermal conductivity, and significantly reducing tensile properties.

ACKNOWLEDGMENTS

The authors would like to thank Dr. Edgar Lara-Curzio and Dr. Hsin Wang at Oak Ridge National Laboratory for mechanical testing and thermal conductivity measurement, respectively. This research was sponsored by the Office of Fusion Energy Sciences, US Department of Energy under contract DE-AC05-00OR22725 with UT-Battelle, LLC and 'JUPITER-II' US-Department of Energy/ Japanese Ministry of Education, Culture, Sports, Science and Technology (MEXT) collaboration for fusion material system research.

REFERENCES

1. A.R. RAFFRAY, R. JONES, G. AIELLO, M. BILLONE, L. GIANCARLI, H. GOLFIER, A. HASEGAWA, Y. KATOH, A. KOHYAMA, S. NISHIO, B. RICCARDI and M.S. TILLACK, "Design and Material Issues for High Performance SiCf /SiC-Based Fusion Power Cores," *Fus. Eng. Des.*, **55**, 55 (2001).
2. L.L. SNEAD, Y. KATOH, A. KOHYAMA, J.L. BAILEY, N.L. VAUGHN and R.A. LOWDEN, "Evaluation of Neutron Irradiated Near-Stoichiometric Silicon Carbide Fiber Composites," *J. Nucl. Mater.*, **283-287**, 551 (2000).
3. T. HINOKI, L.L. SNEAD, Y. KATOH, A. HASEGAWA, T. NOZAWA and A. KOHYAMA, "The Effect of High Dose/High Temperature Irradiation on High Purity Fibers and Their Silicon Carbide Composites," *J. Nucl. Mater.*, **307-311**, 1157 (2002).
4. T. NOZAWA, L.L. SNEAD, Y. KATOH and A. KOHYAMA, "Neutron Irradiation Effects on High-Crystallinity and Near-Stoichiometry SiC Fibers and Their Composites," *J. Nucl. Mater.*, **329-333**, 544 (2004).
5. Y. KATOH, A. KOHYAMA, T. HINOKI and L.L. SNEAD, "Progress in SiC-Based Ceramic Composites for Fusion Applications," *Fus. Sci. Technol.*, **44**, 155 (2003).
6. L.L. SNEAD, M. BALDEN, R.A. CAUSEY and H. ATSUMI, "High Thermal Conductivity of Graphite Fiber Silicon Carbide Composites for Fusion Reactor Application," *J. Nucl. Mater.*, **307-311**, 1200 (2002).
7. Y. LEE, T. NOZAWA, T. HINOKI and A. KOHYAMA, "Thermal and Thermo-Mechanical Properties of SiC/SiC," submitted to Proceedings of the Sixth IEA Workshop on SiC/SiC Composites for Fusion Energy Application, International Energy Agency.
8. T. NOZAWA, Y. KATOH, A. KOHYAMA and E. LARA-CURZIO, "Specimen Size Effects in Tensile Properties of SiC/SiC and Recommendation for Irradiation Studies," *Proceedings of the Fifth IEA Workshop on SiC/SiC Composites for Fusion Energy Application, International Energy Agency*, 74 (2002).
9. T. ISHIKAWA, K. BANSAKU, N. WATANABE, Y. NOMURA, M. SHIBUYA and T. HIROKAWA, "Experimental Stress/Strain Behavior of SiC-Matrix Composites Reinforced with Si-Ti-C-O Fibers and Estimation of Matrix Elastic Modulus," *Compos. Sci. Technol.*, **58**, 51 (1998).
10. W.A. CURTIN, "Theory of Mechanical Properties of Ceramic-Matrix Composites," *J. Am. Ceram. Soc.*, **74**, 2837 (1991).
11. E. VAGAGGINI, J-M. DOMERGUE and A.G. EVANS, "Relationship between Hysteresis Measurements and the Constituent Properties of Ceramic Matrix Composites: I, Theory," *J. Am. Ceram. Soc.*, **78**, 2709 (1995).
12. J-M. DOMERGUE, E. VAGAGGINI and A.G. EVANS, "Relationship between Hysteresis Measurements and the Constituent Properties of Ceramic Matrix Composites: II, Experimental Studies on Unidirectional Materials," *J. Am. Ceram. Soc.*, **78**, 2721 (1995).

Impact of material system thermomechanics and thermofluid performance on He-cooled ceramic breeder blanket designs with SiC_f/SiC

A. Y. Ying[1], T. Yokomine[2], A. Shimizu[2], M. Abdou[1] and A. Kohyama[3]

[1]*Mechanical and Aerospace Engineering Department, University of California, Los Angeles, CA 90095-1597, USA*
ying@fusion.ucla.edu, abdou@fusion.ucla.edu
[2]*Kyushu University, Fukuoka 816-8580, Japan, shimizu@ence.kyushu-u.ac.jp, yokomine@ence.kyushu-u.ac.jp*
[3]*Kyoto University, Kyoto 611-0011, Japan, kohyama@mail.iae.kyoto-u.ac.jp*

This paper presents results from a recent effort initiated under the JUPITER-II collaborative program for high temperature gas-cooled blanket systems using SiC_f/SiC as a structural material. Current emphasis is to address issues associated with the function of the helium gas considered in the DREAM and ARIES-I concepts by performing thermomechanical and thermofluid analysis. The objective of the analysis is to guide future research focus for a task in the project. It is found that the DREAM concept has the advantage of achieving uniform temperature without threatening blanket pebble bed integrity by differential thermal stress. However, its superiority needs to be further justified by investigating the feasibility and economic issues involved in the tritium extraction technology.

1. Introduction

As a candidate for fusion blanket structural materials, SiCf/SiC shows significant advantages for use in high temperature operations. Its use has been suggested with LiPb blanket systems as well as with helium-cooled ceramic breeder blanket systems. Thus, both the design and issue relevant R&D emphasis for SiC_f/SiC can be different depending on the breeder/SiC/coolant combination. This paper focuses on the issues derived from a recent effort initiated under the JUPITER II collaborative program and centers around the SiC_f/SiC based helium gas-cooled ceramic breeder blanket systems of DREAM Nishio et al. [1,2] and ARIES-I Najmabadi et al. [3] design concepts. One of the major differences between the DREAM and ARIES-I concepts is the function and the associated operating conditions of the helium gas. This generates an immediate impact on the SiC/breeder/helium material system R&D, and thus warrants a careful evaluation of the merits and feasibility of each concept.

Both design concepts utilize millimeter-size pebble materials for neutron multiplying and tritium breeding regions, with helium gas flowing through it. The helium gas in the DREAM concept serves as the coolant for heat removal as well as the purge gas for tritium removal and flows directly through the pebble bed regions. In contrast, there are two helium streams adopted in the ARIES-I concept: a high pressure, high velocity one which serves as the coolant, and a low pressure stream with a much lower velocity for tritium purge. In this system, only the low-pressure purge gas flows through the packed bed regions. A single gas stream system, as in the DREAM concept, has the advantage of a simpler blanket design with a more uniform temperature distribution to maximize SiC's potential for high thermal efficiency. However, its thermofluid characteristics, such as flow distribution and stability, are questionable and become the focus of the present study. On the other hand, the consequence of the thermomechanical interaction between the pebble materials and SiC_f/SiC structural clad poses a threat to the thermomechanical integrity of breeder and beryllium pebble beds. Recent results in this area of JUPITER-II efforts are presented and discussed in Section 3.

2. Thermofluid analysis of helium gas in the DREAM concept

In the DREAM concept, helium gas first flows through the cooling paths in the side wall to the first wall. It then flows into the module through the porous partition wall, cools the internal pebble bed breeding materials and is collected at the outlet pipe. The 10 MPa helium gas enters the module at an inlet temperature of 873 K (in the calculation,the inlet temperature to the blanket zone is set at 938 K). The estimated module flow rate is about 0.48 kg/s for a coolant temperature rise of 250 K in the blanket zone. A typical size of the module is about 0.5 m in the toroidal direction with internal zone sizes of 0.18 and 0.115 m for breeding and multiplier zones, respectively. In addition, a single size pebble bed in the proposed geometrical dimension has a typical packing density of 62% in the bulk region. The analysis of helium gas flow through a packed bed is based on Darcy-Brinkman-Forchheimer's equation for an incompressible steady flow [4]. It states that:

$$\rho\frac{\partial}{\partial x_\beta}(\phi\langle u_\alpha\rangle^i\langle u_\beta\rangle^i) = -\frac{\partial}{\partial x_\alpha}(\phi\langle p\rangle^i) + \mu\frac{\partial^2}{\partial x_\beta^2}(\phi\langle u_\alpha\rangle^i) - \frac{\mu_{\text{eff}}}{K}\phi^2\langle u_\alpha\rangle^i - \frac{F\rho}{\sqrt{K}}\phi^3|\langle u_\beta\rangle^i\cdot\langle u_\beta\rangle^i|\langle u_\alpha\rangle^i, \quad (1)$$

where u_α and u_β are the velocities in the toroidal and radial directions, ρ is gas density, x the coordinate, p the pressure, ϕ the porosity, μ and μ_{eff} are the dynamic and effective dynamic viscosity. The subscript α and β are for coordinates. The superscript i implies that the quantity is defined as the fluid-based average value. Definitions of the permeability (K) and the inertia coefficient (F) can be found in Ref. [4].

A two-fluid, non-thermal equilibrium model is considered to solve the heat transfer characteristics and temperature distribution inside the blanket zone. The energy equations based on Amiri and Vafai [5] are applied to solve the temperature distribution. Additional details in the model include adopting a detailed porosity distribution for the pebble bed Muller [6] and Wakao and Kaguei's [7] model to account for lateral heat dispersion. The numerical model for thermofluid analysis of such a blanket module includes 114×57×40 grid points for a half-blanket region considering symmetry at the center plane. Moreover, the model includes a 3-mm thick membrane partition plate with a 10% porosity to separate the beryllium pebble bed region from the breeder bed region. The SIMPLE method is adopted to solve the aforementioned differential transport equations.

A distinct feature associated with the velocity distribution is a wall channeling effect, as shown in Fig. 1, where the velocity overshoot can be seen near the sidewalls. This is attributed to the fact that the porosity near the wall is higher and thus the permeability is also higher. The helium flow becomes slightly stagnant behind the partition membrane plate as shown in the same figure. However, this reduction in velocity does not cause a significant increase in the temperature. As shown in Fig. 2, the calculated maximum temperature of 1191 K at the outlet is similar to the estimated temperature according to the simple energy balance analysis of 1188 K. The temperature near the wall is slightly higher than that of the core region because the low conductivity gas is concentrated near the region, as well as the fact that an insulated boundary is assumed. Interestingly, the helium velocity increases as it moves toward the manifold because its temperature magnitude increases. The overall helium pressure drop (~0.2 MPa) is small due to a relatively short flow path.

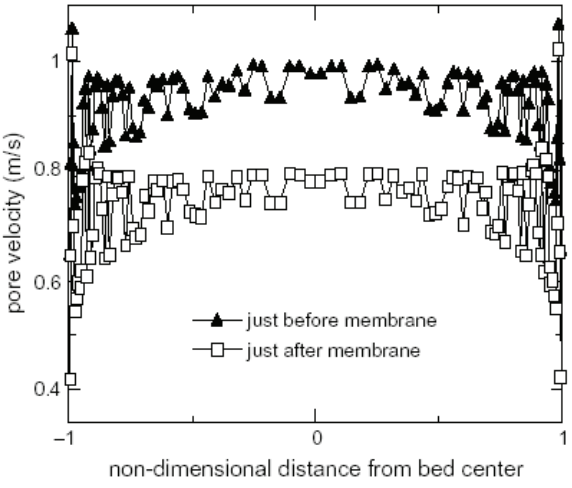

Fig. 1. Spanwise helium velocity profile before and after the partition membrane plate (the total width of the blanket zone is 50 cm).

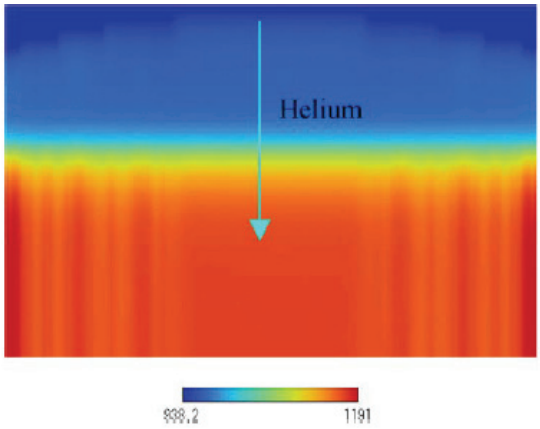

Fig. 2. Helium coolant temperature (°K) profile across the blanket zone.

3. Thermomechanic interaction of breeding pebble beds and SiC/SiC$_f$

In the ARIES-I design, pebble beds of lithium ceramics and of beryllium are clad between two SiC composite coolant panels, which are cooled by high pressure helium gas. A disadvantage of such a design arrangement is the narrow operating temperature window for the solid breeder, which undermines the benefit of the high temperature capacity of SiC/SiC$_f$. A typical operating temperature window for solid breeders such as Li_2TiO_3 falls between 673 and 1193 K. To take full advantage of the SiC operation for high thermal efficiency (such as temperature above 1073 K), this can leave an extremely small temperature window (of ~100 K) for solid breeder operation. The thermal efficiency for ARIES-I is about 46% as compared to the thermal efficiency of 50% as indicated in the DREAM concept. A design goal is to improve the thermal conductance of a

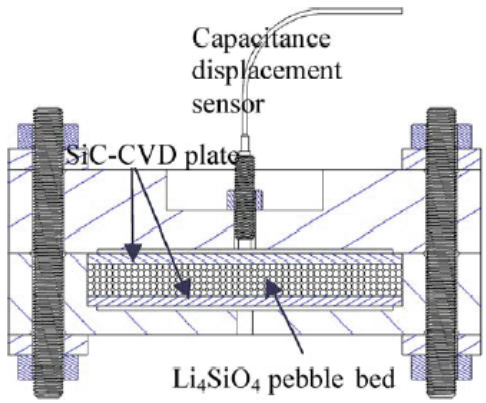

Fig. 3. Schematic view of experimental set-up for thermomechanical interaction study.

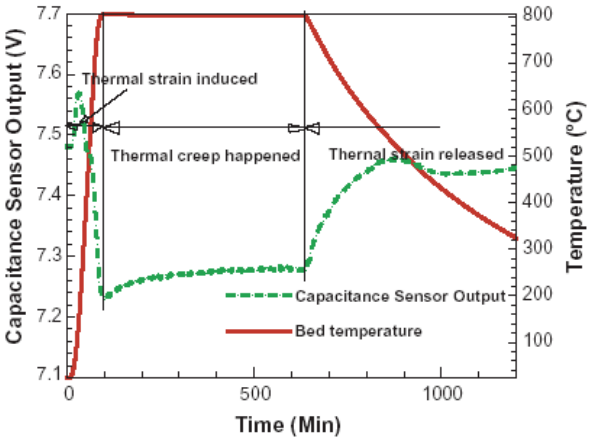

Fig. 4. Deformation traces with respect to temperature history.

relevant SiC/breeder bed unit-cell such that a uniform temperature distribution can be achieved with an engineering practical spacing between SiC/SiC_f coolant panels.

However, a more important issue for such an arrangement is the consequence of the thermomechanic interaction between different blanket elements. During reactor operation, the stresses generated from differential thermal expansion between breeder pebble bed and SiC/SiC_f containment structure, and/or the irradiation swelling of particles may break the particles and endanger safe blanket operation, particularly if heat and tritium removal significantly deteriorate due to ceramic particle breakage. Thus, the determination of the resultant stress magnitude and its evolution is important in the design of a solid breeder blanket. In viewing this, a cylindrical pebble bed thermomechanical test assembly (as shown in Fig. 3) was constructed to evaluate this effect. Specifically, the ceramic lithium orthosilicate pebbles were enclosed between two CVD SiC plates that were fixed at their circumference. In the experiment, the deformations of the

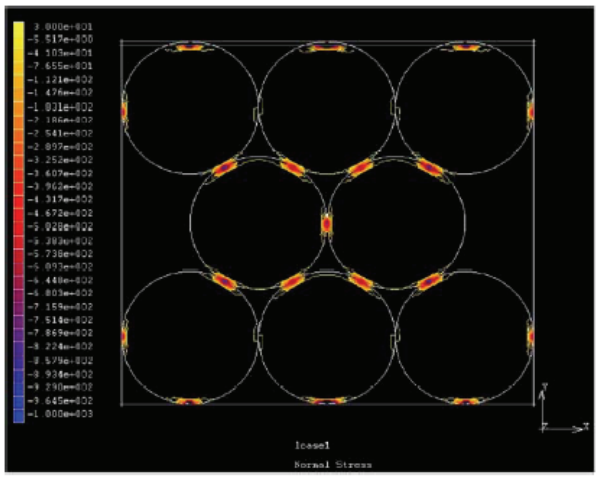

Fig. 5. Calculated contour plot of normal contact stress at particle contacts. The global stress exerted on the plate is 2 MPa, yet the stress at the contact is hundreds of MPas.

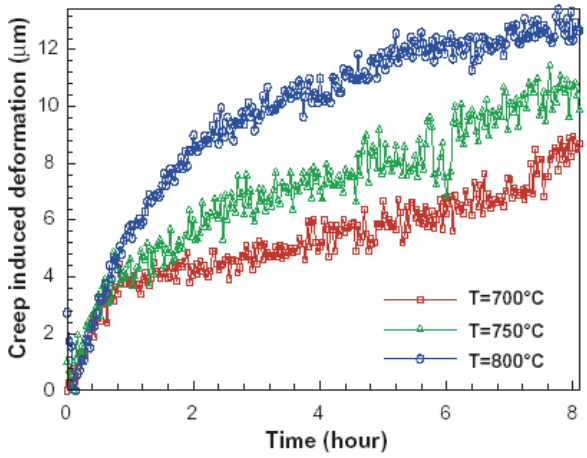

Fig. 6. Effect of temperature on pebble bed system creep evolutions.

top SiC plate, with respect to temperature rise, were measured and shown in Fig. 4. The deformation reflected the amount of bending of the SiC plate under the effect of the differential thermal stress and the applied constrained mechanical boundary. The maximum thermal stress magnitude was estimated to be 2.0 MPa using a bed modulus calculated from a discrete element micro-thermomechanic code Lu [8], which was then inputted to a finite element code MARC [9] for the pebble bed thermomechanical analysis. This small stress magnitude has been significantly magnified at the particle/wall and particle/particle contacts as a result of small contact areas, as shown in Fig. 5. This also caused a thermal creep to occur as revealed in Fig. 4,as the deformation decreased as the bed temperature was kept at a constant value. The effect of temperature on bed thermal creep behavior was studied and presented in Fig. 6. As shown, as creep was

initiated, both the stress magnitude and the creep rate were reduced. However, at a bed temperature of 1000 K, the creep evolution followed a parabolic behavior for a longer time, as opposed to the linear function of time observed at lower bed temperatures. The creep as a function of time was studied numerically and compared with the experimental data using a modified effective macro-creep model Buehler [10]:

$$\dot{\varepsilon} = A(T)\sigma^{1.86}t^{-0.2}, \tag{2}$$

where $A(T)$ has been obtained experimentally Reimann and Woermer [11], and the macro scale stress σ was estimated through the stress at the contact σ_c using the contact (r_c) and the particle (r_p) radii:

$$\sigma = \sigma_c \frac{r_c^2}{r_p^2}. \tag{3}$$

The comparison shown in Fig. 7 indicated that the numerical simulation by DEM Ying et al. [12] using the Buhler effective macro-model was able to capture the trend of the experimental data concerning thermal creep characteristics; however, the absolute values would still need to be resolved by finding the correct material properties.

4. Summary

In this paper, two SiC composite structure based helium-cooled ceramic breeder blanket design concepts were assessed and focused on the issues associated with the scheme and function of the helium considered in the designs. The results indicate that flowing helium coolant directly through the pebble beds as in the DREAM concept appears to give a simpler configuration and shows a much more uniform temperature profile in the blanket zone. The wall channeling effect produces a slight disturbance to the helium velocity profile, but does not spoil the temperature distribution. On the other hand, thermomechanical interaction as a result of the operating temperature difference between the breeder pebble bed and SiC/SiC_f coolant plate remains as a key issue for ARIES-I type concept. Design solutions such as spring loading and/or a floating boundary could be implemented to minimize the interaction as well as to accommodate any consequences that result from differential thermal stress and irradiation swelling.

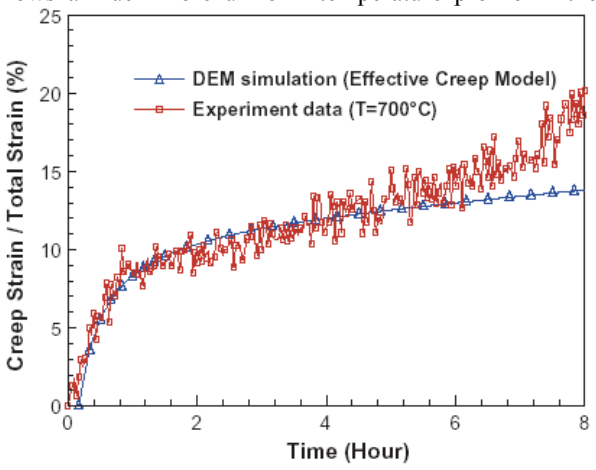

Fig. 7. Numerical versus experimental data on normalized creep deformation as a function of time.

However, the superiority of directly flowing helium coolant through the pebble bed depends on the feasibility and economic considerations involved in tritium extraction. A typical solid breeder blanket design utilizes a low-pressure helium gas for tritium removal. Extracting tritium from the high pressure, high temperature helium coolant could be costly due to a much lower tritium concentration existing in the coolant. This possibility should be assessed.

Acknowledgments

This work was performed under US Department of Energy Contract DE-FG03-ER52123 and under the US-JA JUPITER-II collaborative effort.

References

[1] S. Nishio et al.,Fus. Eng. Des. 48 (2000) 271.

[2] S. Nishio,S. Ueda,I. Aoki,R. Kurihara,T. Kuroda, H. Mirura,T. Kunugi,Y. Seki,T. Nagashima, M. Ohta, J. Adachi,S. Yamazak, I. Kawaguchi, T. Hashimoto, K. Shinya,Y. Myrakami, H. Takase,T. Nakamura,Fus. Eng. Des. 41 (1998) 357.

[3] F. Najmabadi et al.,The ARIES-I Tokamak Reactor Study: Final Report,UCLA-PPG -1323, 1991.

[4] D.B. Ingham,I. Pop,Transport Phenomena in Porous Media II,Pergamon, 2002,p. 1.

[5] A. Amiri,K. Vafai,Int. J. Heat Mass Trans. 37 (6) (1994), 939.

[6] G.E. Muller,Powder Technol. 72 (1992) 269.

[7] N. Waka,S. Kaguei, Heat and Mass Transfer in Packed Beds,Gordon and Breach Science, 1982.

[8] Z. Lu,Numerical Modeling and Experimental Measurement of the Thermal and Mechanical Properties of Packed Beds,PhD thesis,2000.

[9] MSC MARC,MSC Software Corporation,Los Angeles, March,2000.

[10] L. B.uhler,Continuu m models for pebble beds in fusion blankets,FZKA 6561,2002.

[11] J. Reimann,G. W.ormer,Fus. Eng. Des. 58&59 (2001), 647.

[12] A. Ying,H. Huang, M. Abdou,J. Nucl. Mater. 307-311(2002)827.

Experimental study of the interaction of ceramic breeder pebble beds with structural materials under thermo-mechanical loads

P. Calderoni *, A. Ying, T. Sketchley, M.A. Abdou
MAE Department, UCLA, 44-114 Engineering IV, Los Angeles, CA 90095, USA

This paper presents the first results obtained in a facility constructed at the University of California, Los Angeles to study the interaction of ceramic breeder pebble beds with structural materials in conditions relevant to fusion energy power plant blanket operations. The experiments study the thermo-mechanical performance of lithium meta-titanate oxide (Li_2TiO_3) pebbles and silicon carbide clad constrained by a low thermal expansion alloy in vacuum and He atmosphere. The results show that large deformations due to induced thermal stresses are present during the first heat cycle but afterward are accommodated by a combination of pebble re-arrangement within the bed and thermally induced creep deformation. Initial results of a numerical simulation of the experiments using a finite element code that includes creep deformation is also presented. Planned operation of the UCLA thermo-mechanics test facility is summarized to conclude the paper.

I. Introduction

The thermo-mechanical performance of lithiumbased ceramic materials is a critical issue for assessing the reliability of solid breeder blanket concepts over the lifetime of the component. The investigation of the effect of the thermal cycling typical of a fusion energy power plant on the blanket components is complicated by the coupling of the thermal and structural behavior intrinsically related to the use of pebble beds as breeding material. The pebble bed as a whole can be described as an intermediate phase between solid and liquid, with properties depending on the fraction of voids present in the bed volume. The void fraction initially depends on the porosity and the initial packing of the pebbles, but can vary locally through the component lifetime due to the cycling variation of the applied stresses and to irradiation. For example, the formation of a void between the pebble bed and the structure due to creep relaxation would lead to a local deterioration of the interface heat transfer and the creation of a hot spot. The effect of thermal cycling is further aggravated by the degradation of materials mechanical properties due to neutron irradiation, and final assessment of blanket component reliability will only come from an integrated experiment such as ITER.

The focus of the experimental work initiated at the University of California, Los Angeles is the investigation of the combined thermal and structural response of blanket candidate materials exposed to thermal cycles that are representative of fusion energy power plant conditions. In particular, the study is aimed at the characterization of the cumulative effect of the plastic behavior of the pebbles resulting from thermal cycling on various assemblies that integrate all the components of different blanket concepts: breeding material, structure and coolant. The integrated tests will generate comparative data on various candidate materials and guide the design of more complex experimental facilities such as the ITER Test Blanket Module. This paper specifically reports on the results obtained with a test article that integrates lithium *meta*titanate oxide (Li_2TiO_3) as breeder, silicon carbide as cladding and a low thermal expansion alloy (Kovar) as the structure. The choice is motivated in part by the ongoing research effort under the JUPITER II collaborative program that is aimed at the development of high temperature gas-cooled blanket systems with coolant output temperature as high as 900 ^{o}C [1,2]. The experimental data available on the thermo-mechanical properties of Li2TiO3 are not as extensive as for other ceramic breeder candidate materials and even fewer data are available on compatibility with silicon carbide.

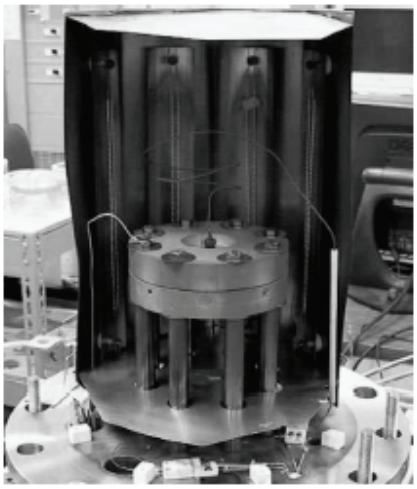

Fig. 1. Test article inside high temperature furnace.

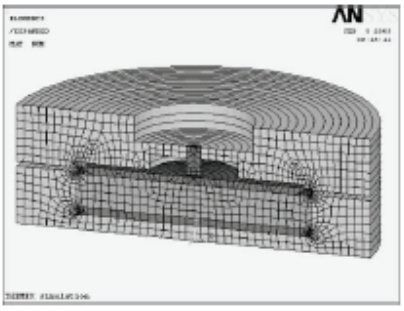

Fig. 2. Test article schematic and finite element meshing.

II. Thermo-mechanic response of Li_2TiO_3 pebble beds and silicon carbide

The thermo-mechanic tests described in this paper have been performed in a cylindrical vacuum vessel 0.4m in diameter and 0.46m high. The vessel houses a second stainless steel enclosure that is designed as a radiative shield as well as a support for the heating filaments. The enclosure is formed by two hemispherical halves plus a top and bottom plate. Fig. 1 shows one of the hemispherical halves mounted on the vessel base while the other is removed to access the test article. Eight pairs of tungsten filaments mounted around the test article are used as radiative heating elements with a peak power of 3.6kW. The filaments are mounted over a molybdenum shield insulated by ceramic posts that serves as primary radiative and thermal shield. The test article is shown in Fig. 2 as a map of the finite element mesh used in the simulation that is described in more details at the end of this paper. It is formed by two 0.15m Kovar flanges and a sandwiched assembly of two commercial graded CVD silicon carbide discs and Li_2TiO_3 pebbles supplied by C.E.A. Saclay and fabricated with the extrusion–spheronisation–sintering process [3]. The discs are 0.10m in diameter and 3.2×10^{-3} m thick, while the average diameter of the pebbles is 7×10^{-4} m. The initial bed height is 15.3×10^{-3} m. The temperature is measured at the center of the bottom SiC disc and on two diametrically opposite locations of the upper disc side. The properties of the materials are summarized in Table 1.

The listed properties of Li_2TiO_3 are the "effective" properties of the pebble bed used for the finite element analysis [4]. The temperature dependence of the thermal expansion coefficient of the materials is separately plotted in Fig. 3. Measured densities of the bed obtained on a vibration table range from 1997 to 2023 kg/m^3, which corresponds to packing fractions ranging between 58 and 59% of the theoretical density of Li_2TiO_3 (3440 kg/m^3) or 67.5 and 68.4% of the effective density of the pebbles (86% of TD due to material porosity). The pebbles color changes slightly after each cycle, turning from white to a light color between blue and gray. The change has been previously observed and explained as a phase transformation during annealing in an oxygen-free atmosphere that leads to the formation of different Ti oxides on the pebbles surface [5,6]. The function of the flanges is to establish an initial known compression on the silicon carbide and pebble bed assembly and to ensure an adequate mechanical constrain through the thermal cycle. Eight equally spaced bolts initially compress the flanges with a measured force of about 1300N each. They are machined from the same low thermal expansion material of the flanges to ensure the same response to the thermal cycle. The force is transferred from the upper flange to a small section at the edge of the silicon carbide disc, constraining the edge of the disc but allowing the center to expand during the heat cycle. If the compressive load is assumed to be uniform on the whole pebble bed contact area the resulting precompression is 1.32×10^6 Pa. The large dimension of the flanges ensures that the load is distributed relatively uniformly across the pebbles, allowing high compressive stresses but local contact forces below the failing threshold of the ceramic material. The drawback is that the current test article has a large thermal inertia with typical thermal cycles are of a few hours. As the temperature increases the pebbles act on the SiC disc because of the higher thermal expansion. As a result the disc bends, and the capacitive sensor embedded in the upper flange reads the maximum displacement at the plate center. The analysis of the experimental results is complicated by the fact that the sensor is not an absolute reference, since it is mounted on a structure also subject to deformation. The effect of the expansion of the sensor (which has a stainless steel enclosure) and the alloy structure in which is embedded was evaluated by testing the assembly without a compressive force, and the resulting deformation was measured to be less then 40μm and constant after 600 ^{o}C. This effect is responsible for the initial increase of the measured gap observed in the data. Fig. 4 shows a representative set of data from the first (# 0) and second (# 1) thermal cycle of a thermo-mechanics experiment with the described test article. At low temperatures the expansion of the pebbles is countered by that of the flange on which the measuring sensor is embedded. During the first cycle at temperatures above 700 ^{o}C, the gap is gradually reduced by about 580μm due to a combined effect of thermal expansion and pebble re-arrangement in the bed. After about 3 h from the start of the heating cycle and 30 min at a constant temperature of 800 ^{o}C the effect of the stress relaxation due to the thermally induced creep in the ceramic material becomes visible and the gap increases logarithmically at constant temperature to an asymptotic value 120μm smaller than the initial value, which is completely recovered after cooling indicating that the disc is again straight. It is to be noted here that the uniform plastic deformation of the pebbles induced by the creep as well as the compacting of the bed due to re-arrangement during the thermal cycle cannot be recorded by the sensor, which measure only the displacement of the SiC disc center. However, the bed height after the second cycle

Table 1
Properties of test article materials

	Density (kg/m^3)	Specific heat capacity (J/kg K)	Thermal conductivity (W/m K)	Young modulus (Pa)	Poisson ratio
Kovar[a]	8360	502.4	16.8	137.9×10^9	0.3
Li_2TiO_3[a]	2000	1080.3	0.93	0.262×10^9	0.3
CVD SiC[b]	3210	574	333	460×10^9	0.21
SS 316L[b]	8040	456.28	13.28	200.4×10^9	0.29

[a] At 20 C.
[b] At 0 C.

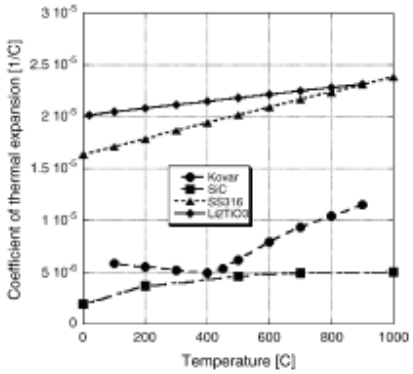

Fig. 3. Temperature dependence of test article materials coefficient of thermal expansion.

was measured to be about 200μm smaller than its initial value, accounting for an effective residual volumetric deformation of about 1.3%. Future experiments will include absolutely referenced LVDT sensors to accurately measure the accumulated plastic strain. During the second cycle showed the pebbles have already been compacted and the gap reaches the same asymptotic value without the initial swelling. Further consecutive thermal cycles of the same materials have been performed after re-arranging the pebble bed to recover the initial compressive load. The results are similar to the second cycle showed in Fig. 4, with the exception that the asymptotic value is lower due to the higher initial stress, ranging between 250 and 150μm lower than the initial value.

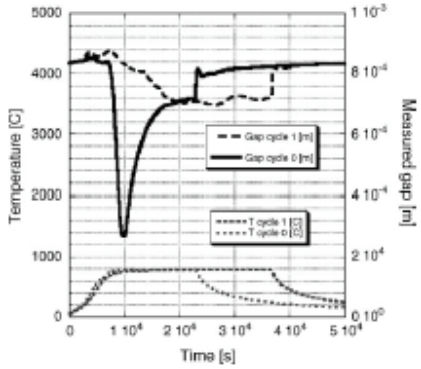

Fig. 4. Displacement and temperature data from two heat cycles of test # 4.

III. Finite element method numerical simulation

There has been a wide research effort recently aimed at quantifying the properties of lithium-based ceramic pebble beds [7,8]. The simplest models rely on the continuum material assumption and are derived by fitting a generalized expression with data collected from simplified experiments with a limited number of variables, such as the uni-axial compressive tests at FZK [9,10]. As mentioned in Section 1, the thermo-mechanic tests described in this paper offer an opportunity to compare different models against experimental data obtained in an integrated experiment. The modeling effort here presented was carried on using the finite element code ANSYS [11]. The code was chosen because UCLA already has the capability of running it on parallel processors, which could allow for future modeling of large three-dimensional blanket structures. ANSYS contains a graphical user interface which allows the generation of complex, adaptable meshes once a geometrical model and a set of loads are defined (Fig. 2). The model assumes axi-symmetrical geometry and loads, as well as simplified interface conditions between the various materials (all the degrees of freedom are coupled for adjacent elements) and uniform material properties in all directions (Table 1). The ANSYS thermal analysis tool is first used to derive the nodal temperatures as a function of time. The experimental heat cycle was simulated by imposing a uniform, time-dependent temperature at all nodes corresponding to the locations in the experiment that are exposed to the radiative heat flux. The ANSYS mechanical analysis tool was then used to calculate the stresses and deformations due to the thermal cycle with the additional boundary condition of zero displacement in the vertical directions at the nodes corresponding to the locations in the experiments covered by the bolts washers. The thermally activated creep model derived by Buhler and Reimann [7] was introduced by using the time hardening option of ANSYS where the equivalent creep strain rate is:

$$\dot{\varepsilon}_{cr} = 0.12C\, e^{-7576/T}\, \sigma^{0.65} t^{-0.82}$$

where T is the absolute temperature, σ the equivalent stress, t is time and C a correction factor that accounts for the fact that the measured data from which the constants are derived refer to the volumetric strain rate [4]. The model predicts a swelling of the center of the upper disc of 640μm after 3 h, which is consistent with the experimental results. However, the few elements in contact with the edge of the disc

howunrealistic values of stress and deformation. Furthermore, because of the large local deformation convergence of the non-linear, time-dependent structural solution is obtained only for small time steps, which is incompatible with the simulation of the cumulative effect of multiple heating cycles over extended period of time. Further refinement of the model is needed in the contact regions where the element sizes becomes comparable or smaller than the single pebbles diameter, possibly by using tailored contact elements to better simulate effective interface and experimental load conditions.

IV. Conclusions and future plans

The first of a series of integrated experiments aimed at characterizing the thermo-mechanic performance of various structural, cladding and breeding materials for fusion energy blankets has been presented. Lithium *meta*-titanate oxide and silicon carbide were chosen among the material candidates to investigate the feasibility of high temperature gas-cooled blanket concept. The experimental results indicate that high thermal stresses and deformations are present during the initial thermal cycle of the assembled test article, but are successively accommodated due to a combination of pebble re-arrangement within the bed and creep induced deformation. This suggests that a few thermal cycles under controlled atmosphere and a compressive load before final assembling of blanket sections would allow a beneficial reduction of the swelling and related thermal stresses during start-up. Future plans include further experiments with low mass test articles with local active cooling that will allow to reproduce thermal cycles that are more representative of fusion energy power plant operation, as well as controlled thermal gradients across the pebble bed. Different combinations of structural, cladding and breeding materials as well as test article geometries will be tested. The cumulative effect of the plastic deformation of the bed will be studied to investigate the possible formation of gaps between the pebbles and the surrounding structural material. The finite element model will be refined and the results of time hardening due to creep deformation compared to those of the experiments over shorter, multiple heat cycles.

Acknowledgement

TThisworkwas performed under U.S. Department of Energy contract DE-FG03-ER52123 and under US-JA JUPITER-II collaborative effort.

References

[1] S. Nishio, S. Ueda, R. Kurihara, T. Kuroda, H. Miura, K. Sako,et al., Prototype tokamak fusion reactor based on SiC/SiC composite material focusing on easy maintenance, Fus. Eng. Des.48 (2000) 271–279.

[2] The ARIES Team, High performance blanket for ARIES-AT power plant, Fus. Eng. Des. 58–59 (2001) 549–553.

[3] J.D. Lulewicz, N. Roux, Fabrication of Li2TiO3 pebbles by the extrusion–spheronisation–sintering process, J. Nucl. Mater. 307–311 (2002) 803–806.

[4] J.H. Fokkens, Thermo-mechanics finite element analysis for the HCPB in-pile test element, NRG report #21477/02.50560/P, 2003.

[5] G. Piazza, J. Reimann, E. Gunther, R. Knitter, N. Roux, J.D. Lulewicz, Behavior of ceramic breeder materials in long time annealing experiment, Fus. Eng. Des. 58–59 (2001) 653–659.

[6] L.C. Alves, E. Alves, M.R. da Silva, A. Paul, A. La Barbera, Li ceramic pebbles chemical compatibility with Eurofer samples in fusion relevant conditions, J. Nucl. Mater. 329–333 (2004) 1295–1299.

[7] L. Buhler, J. Reimann, Thermal creep of granular breeder materials in fusion blankets, J. Nucl. Mater. 307–311 (2002) 807–810.

Numerical characterization of thermo-mechanical performance of breeder pebble beds

Zhiyong An *, Alice Ying, Mohamed Abdou
a Mechanical and Aerospace Engineering Department, UCLA, Los Angeles, CA 90095-1597, USA

A numerical approach using the discrete element method (DEM) has been applied to study the thermo-mechanical properties of ceramic breeder pebble beds. This numerical scheme is able to predict the inelastic behavior observed in a loading and unloading operation. In addition, it demonstrates that the average value of contact force increases linearly with overall pressure, but at a much faster rate, about 3.4 times the overall pressure increase rate. In this paper, the thermal creep properties of two different ceramic breeder pebble materials, Li_4SiO_4 and Li_2O, are also examined by the current numerical code. The difference found in the properties of candidate materials is reflected numerically in the overall strain in the pebble bed when the stress magnitude becomes smaller.

I. Introduction

Ceramic breeder pebble bed is an important component in the solid breeder blankets. Practical use of the breeder pebble beds in fusion power reactors requires good characterization of the thermomechanical behavior and irradiation effects of the pebble beds. Different from solid materials, mechanical behavior of the pebble beds is not only dependent on the pebble materials, but also related to other parameters (e.g., pebble size, packing density of the pebble bed and bed structure, etc.). Experimental and numerical approaches [1−3] have been tried to quantify the thermo-mechanical characteristics of ceramic breeder pebble beds. According to previous works, ceramic pebble beds show inelastic mechanical behavior, and at elevated temperatures, the pebble bed behavior is affected by thermal creep deformation, especially in the first 10 h of operation. However, due to the lack of a detailed and insightful description of pebble bed properties, the existing predictive capability mainly based on experimental approaches may not fully quantify their thermomechanical state. A numerical algorithm based on the discrete element method is currently being developed by the UCLA Fusion Science and Technology Center to predict the thermo-mechanical behavior of ceramic breeder pebble beds, particularly in the timedependent creep deformation regime. In the discrete element method (DEM), each individual particle is separately considered; particles are connected only through contacts by appropriate physics-based interaction laws. As mentioned in a previous paper [4], compared to experimental work, this numerical algorithm can provide more comprehensive information, such as the magnitude of the force at inter-particle contacts, as well as the stress−strain relationships of a pebble bed. With that information, we can obtain information on the likelihood of particle breakage and the thermal conductance at the bed/clad interface. In this paper, we will exploit the thermo-mechanical properties of ceramic breeder pebble beds with respect to compressive loading at high temperature. For our program, a new inter-particle model, which is based on Hertz－Mindlin's formulation [5], has been updated to include thermal creep deformation. In general, for contacted particles, thermal creep deformation increases contact area and decreases contact stresses. The new microstructural plasticity model describes the creep behavior of contacted particles, which can be easily incorporated into our discrete element program.

II. Algorithm of numerical simulation

In the DEM program, the thermo-mechanical behavior of the ceramic breeder pebble bed can be modeled as a collection of particles interacting via Hertz−Mindlin contact interactions. When the stresses and temperature are high enough, creep deformation needs to be considered. Fig. 1 shows two typical particles in contact in a packed pebble bed. The inset figure on the right shows the von Mises

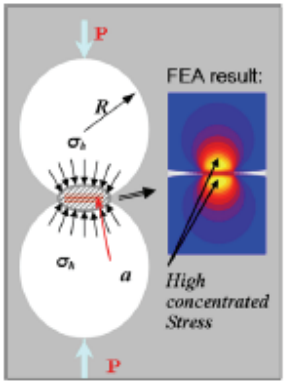

Fig. 1. Sketch of two contacting particles. (The right-inset figure shows a FEA simulation and light color areas stand for the highest stress.)

stress distribution calculated by finite element analysis (FEA). We can see that stresses are non-uniform and are highly concentrated near the contact. During the simulation, the contact radius, a, is an important parameter for determining the displacement of two particles. At each contact, a virtual spring is applied to simulate the particle−environment relationship. A contact force can be calculated by the deformation and the stiffness of the virtual spring. The stiffness of the virtual spring, including contact normal and shear stiffness, is determined by the properties of the contacting particles and their deformation. In this code, all

ceramic breeder pebbles are assumed to have a spherical shape. The contact force and the stiffness of the contacting pebbles are estimated from Hertz−Mindlin's formulation. The contact force and stiffness will be updated when creep deformation needs to be considered. For each particle, the resultant force and stiffness are directly obtained by summing these properties over all its contacts. During our simulations, the contacts inside a pebble bed will be determined by particle position and geometry. Between each cycle, the pebble bed is unsteady and the movement of each particle will be calculated by its summed contact force and stiffness. For example, if the resultant force of a particle in the x-direction is not equal to zero, there is an incremental displacement in the x-direction, which is obtained by dividing the resultant force by the stiffness. In our program, the friction at the contacts is also considered. The following equations are used to determine the movement of particles:

$$\Delta D_x = 0 \quad \text{for} \quad \left|\sum_i F_{ix}\right| \le k_f \sum_i |F_{iy}|. \qquad (1)$$

Otherwise,

$$\Delta D_x = \frac{\sum_i F_{ix} - k_f \sum_i |F_{iy}|}{k_x}, \qquad (2)$$

where $k_f = \tan\varphi \cdot \mu$ is the friction coefficient at contacts and k_x is the resultant stiffness in x-direction. At high stresses and elevated temperatures, creep deformation will affect the normal and friction forces at the contact. In particular, contact stresses will be relaxed due to contact neck increase. In general, creep deformation for materials can be evaluated by power-law creep:

$$\dot{\varepsilon}_c = c\sigma^n, \qquad (3)$$

where the coefficient c is dependent on material properties and temperature, r is the von Mises stress in MPa, n is the stress exponent and ε̇ is the creep rate in s^{-1}. In the literature [6,7], a stress exponent of around 3.6 ± 0.5 was found for Li_2O in the temperature range of 700−800 °C and stress range of 15−45 MPa. For 90% dense Li_4SiO_4, the stress exponent is about 3.6 ± 0.2 with a temperature around 850 °C and the stress range is about 50 − 200 MPa. In our numerical program, it is assumed that the rate of increase in contact radius due to creep deformation is on the same order as the shrinkage rate of the two contacting particles. As shown in Fig. 1, for two contacting particles, high stresses are concentrated at the contact area. Under Hertz−Mindlin's contact theory, the maximum stress is located at about 0.57a from the contact interface, where a is the radius of the contact circle. According to the geometry of two contacting spheres, the power-law creep deformation will affect the contact area as shown in the following equation:

$$\dot{a}_{oc} = \alpha \dot{\varepsilon}_a, \qquad (4)$$

where α = 0.57a. And in the above equation, $\dot{\varepsilon}_a$ can be obtained by solving:

$$\alpha(\dot{\varepsilon}_a t)(1 + \dot{\varepsilon}_a t)^{2n} = ct\left(\frac{P}{\pi a_0^2}\right)^n, \qquad (5)$$

where t is creep time and a_0 is the initial value of the contact radius. Fig. 2 shows the local contact creep deformation model for particle material with $c = 10^{-17}$ and n = 4.0. The above equation is in good agreement with the finite element analysis result, where creep deformation is calculated for two particles. The above creep model is derived from two perfect contacting spherical particles, without any breaking during deformation. For non-spherical particles, the mass involved with creep deformation is difficult to calculate, however, a contact circle with the same area size can be equivalent to an irregular contact area. Further study needs to specify the coefficient in Eq. (4).

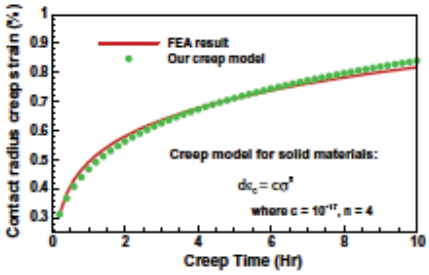

Fig. 2. Verification of DEM creep model compared with FEA simulation of two particles.

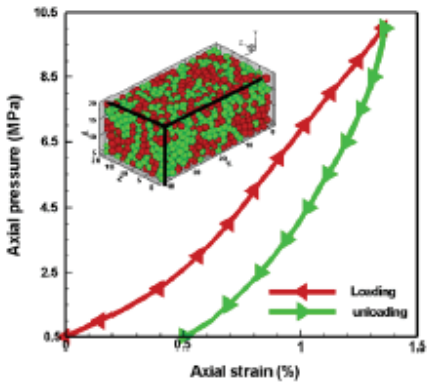

Fig. 3. Stress−strain behavior of a rectangular pebble bed under uniaxial pressure (along y-direction).

III. Mechanical properties of pebble beds

Fundamental mechanical properties of lithium ceramics have been obtained from previous experiments. However, after a lithium ceramic is packed in the form of a pebble bed, its mechanical properties are much different from its properties as a bulk material. Based on experimental results, Reimann et al. [1] provided the effective mechanical properties of ceramic breeder pebble beds. The effective constitutive equations derived from these experiments show

a nonlinear behavior of the macroscopic stress－strain relation. As they are based on a continuous model, no detail can be derived on 'particle' quantity like the deterministic way whether or not the particle is under stress high enough for creep deformation.

Fig. 3 shows the stress－strain response of a ceramic pebble bed with Li_4SiO_4 breeder materials. The small figure shows the geometry of the tested pebble bed. First, numerical results show that the mechanical behavior of a pebble bed system is inelastic, and the stiffness of a pebble bed is dependent on applied loading. Second, the results show that irreversible pebble displacement is generated after one loading－unloading cycle. This is a plastic-like behavior of particular materials. In other tests, it has been found that this property is related to bed packing properties such as packing density, particle size distribution, geometry of the pebble bed container, etc. For fusion blanket design, vibration packing is an important process to achieve consistent experimental results in order to eliminate or minimize this effect. One advantage of discrete element analysis is that information about pebble-to-pebble contacts inside the pebble beds can be obtained through calculation.

Fig. 4 shows the distribution of contact force under different loads. The contact forces inside the pebble bed increase significantly with loading. The inset figure shows that the rate of increase in the average contact force value is about 3.4 times the rate of increase of the applied pressure. Based on this information, breeder structure loads can be designed to prevent exceeding the crush force of breeder pebbles.

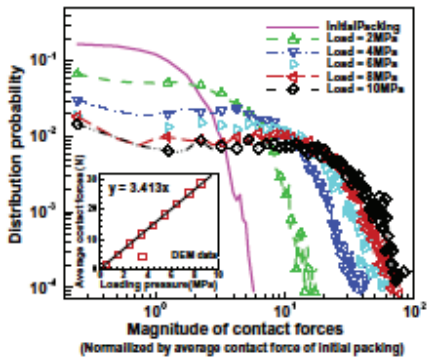

Fig. 4. Distribution of particle contact force as a function of applied load. (The inset figure shows the magnitude relationship between average contact force and overall pressure.).

IV. Analysis of creep deformation

Creep deformation under constant thermal deformation is more typical for fusion blanket design. Under compression, deformation will increase the contact area between particles and reduce the thermal stresses generated inside the pebble beds. On the other hand, when the breeding blanket is exposed to a pulsed irradiation environment, the creep deformation will cause a total volume loss in the pebble beds and may generate some gaps between the pebble beds and the structure container, which potentially can cause the breeder material to exceed its operating temperature limit and endanger the operation of the fusion reactor.

In previous experiments and numerical simulations [1,3], the creep deformation has been observed to exist in a pebble bed when the temperature is sufficiently high. In this paper, the relation between the creep strain rate of materials in bulk and pebble bed form will be explored. Our DEM simulation code was applied to two different breeder materials, Li_4SiO_4 and Li_2O. The mechanical properties are listed in Table 1.

Fig. 5 shows the code prevision for the axial creep strain and strain rate of Li_4SiO_4 and Li_2O pebble beds under uniaxial pressure, when the temperature is about 850 ^oC. The pressure applied in this calculation is about 10 MPa on the top and bottom surfaces. The two of the lines show that the creep strains of pebble beds with different breeder materials are similar during the first three hours, but the Li_2O pebble bed shows a larger creep strain after three hours. Two data points in Fig. 5 show the creep strain rates of the same two pebble beds; there is not much difference between them. Similar to experimental results, numerical data of both ceramic breeder pebble beds show that the creep strain rate decreases over time, even though the load remains constant. When considering the load on a pebble bed as equivalent to the pressure on a bulk material, the strain rate of a pebble bed is much higher than that of solid material. This means that contact stresses concentrated near the contact areas can enhance the creep deformation of materials.

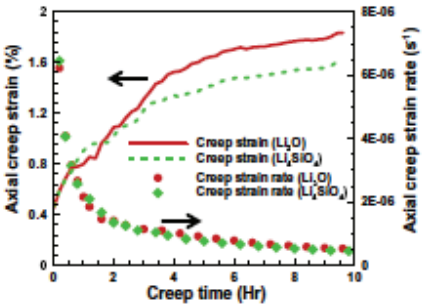

Fig. 5. Axial creep strain and strain rate of Li_4SiO_4 and Li_2O pebble beds under uniaxial pressure (P = 10 MPa).

Table 1
Summary of material properties of lithium ceramic breeder materials

	E (GPa)	μ (GPa)	K (GPa)	Poisson ratio (ν)	Constant coefficient (c in Eq. (3))	Stress component (n in Eq. (3))
Li_4SiO_4	138	55.4	68.8	0.25	5.2×10^{-13}	3.6
Li_2O	141	60.3	75.8	0.19	9.277×10^{-11}	3.6

V. Conclusion

The current numerical approach will help us to better understand the thermo-mechanical properties and characteristics of ceramic breeder pebble beds. As revealed in the analysis, it is particularly exciting that the contact force at particle/particle contacts can be correlated with the external applied pressure. Our approach provides a flexible method to predict the mechanical performance of breeder pebble beds under different temperature or boundary conditions, as well as thermal creep deformation. Numerical results of two different ceramic breeder pebble materials, Li_4SiO_4 and Li_2O, show that the creep strain rate of pebble beds are higher than bulk materials at steady state, while the difference between different pebble beds thermal creep magnitude is less significant than the difference between pebble beds and the bulk material. In the future, more complex cases, including thermal expansion and tri-axial loading, will be developed to examine the coupled thermo-mechanical behavior of ceramic breeder pebble beds.

Acknowledgement

This work was performed under US Department of Energy Contract DE-FG03-ER52123.

References

[1] J. Reimann, J. Boccaccini, M. Enoeda, A.Y. Ying, Fus. Eng. Des. 61&62 (2002) 319.
[2] L. Bu¨ hler, Continuum models for pebble beds in fusion blankets, FZKA 6561, 2002.
[3] Z. An, A. Ying, M. Abdou, Fus. Sci. Technol. 47 (4) (2005)1101.
[4] Z. An, A. Ying, M. Abdou, in: Seventh International Symposium on Fusion Nuclear Technology, Tokyo, Japan, 22−27 May, 2005.
[5] R.D. Mindlin, Arch. Ration. Mech. Anal. 16 (1969) 51.
[6] M.C. Billone, Y.Y. Liu, R.B. Poeppel, J.L. Routbort, K.C. Goretta, D.S. Kupperman, J. Nucl. Mater. 141−143 (1986) 282.
[7] C.-Y. Chu, K. Bar, J.P. Singh, K.C. Goretta, M.C. Billone, R.B. Poeppel, J.L. Routbort, J. Am. Ceram. Soc. 72(9) (1989) 1643.

The effect of high dose/high temperature irradiation on high purity fibers and their silicon carbide composites

T. Hinoki [a*], L.L. Snead [b], Y. Katoh [a,c], A. Hasegawa [d], T. Nozawa [a], A. Kohyama [a,c]

[a] Institute of Advanced Energy, Kyoto University, Gokasho, Uji, Kyoto 611-0011, Japan
[b] Metals and Ceramics Division, Oak Ridge National Laboratory, P.O. Box 2008, Oak Ridge, TN 37831-6140, USA
[c] CREST-ACE, Japan Science and Technology Corporation, 4-1-8 Honmachi, Kawaguchi, Saitama 332-0012, Japan
[d] Department of Quantum Science and Energy Engineering, Tohoku University, Aoba, Sendai 980-8579, Japan

Silicon carbide composites were fabricated by chemical vapor infiltration method using high purity fiber, Hi-Nicalon Type-S and Tyranno SA, and non-high purity fiber Hi-Nicalon. Bare fibers, SiC/SiC composites and CVD SiC were irradiated at 7.7 dpa and 800 ^{o}C or 6.0 dpa and 300 ^{o}C. The density of fiber and CVD SiC was measured by gradient column technique. Mechanical properties of the composites were evaluated by four-point flexural tests. Fracture surfaces were observed by SEM. Tyranno SA fiber and CVD SiC showed similar swelling behavior following irradiation at 7.7 dpa and 800^{o}C. Mechanical properties of composites reinforced with Hi-Nicalon Type-S and Tyranno SA fibers were stable even following neutron irradiation at 7.7 dpa and 800 ^{o}C. Fracture surfaces of these composites following irradiation were similar to those of non-irradiated composites with relatively short fiber pull-out.

I. Introduction

The superior high temperature mechanical properties and low activation make SiC/SiC composites very attractive as fission and fusion reactor materials [1,2]. The higher thermal efficiency associated with self-cooled solid blanket [3,4] or gas-cooled solid blanket [5], where potential plant efficiency is 50%, can be available in the fusion blanket using SiC/SiC composites. In fusion reactor environment, nuclear collisions and reactions with high-energy neutrons and particles from fusion plasma have strong impacts on materials through the production of displacement damage and transmutation effects [6]. Degradation of material performance such as mechanical properties, thermal properties and so on has been recognized as the key issues and extensive efforts have been conducted [7]. Up to this point, interfacial properties between the fiber and matrix of neutron-irradiated SiC/SiC composites limited mechanical performance [8]. This limitation has been attributed primarily to shrinkage in the SiC-based fibers due to irradiation-induced grain growth of microcrystalline fibers [9,10], irradiation-assisted oxidation [11], and potentially large dimensional changes of the graphite [10,12] interphase applied to the fibers, while matrix swells a little by irradiation-induced point defect. Fiber shrinkage leads to fiber/matrix debonding as reported by Snead et al. [13] and a decrease in elastic modulus and fracture strength. Therefore, there is a critical need to optimize the microstructure of SiC/SiC composites (i.e. fiber, fiber/matrix interphase and matrix) to retain the interfacial shear strength between the fiber and matrix. To mitigate radiation effects, the recent trend in SiC fiber development is toward lower oxygen content, reduced free carbon and enhanced crystallinity. The development of more radiation-resistant SiC composites is based on the use of near stoichiometric SiC fibers with lower oxygen and SiC-based interphases. Recently, near stoichiometric SiC fibers have been developed including Hi-Nicalone Type-S [14], Sylramice [15] and Tyrannoe SA [16]. However the effect of high dose and high temperature irradiation on the SiC/SiC composites reinforced with highly crystalline fibers has not been revealed yet. The objective of this work is characterization of neutron irradiation effects on high purity fibers and their silicon carbide composites for fusion application. For this purpose, the effects of high dose and high temperature neutron irradiation on mechanical properties of SiC/SiC composites reinforced with high purity fiber were evaluated.

II. Experimental procedure

The fibers used in this work were Tyranno^{TM} SA (Ube Industries Ltd., Ube, Japan), Hi-Nicalon Type-S and Hi-Nicalone SiC fibers (Nippon Carbon Co., Tokyo, Japan). Both satin woven and plain woven fibers were used to fabricate composites with orientation of 0/90^{o} ± 30^{o}. Tyranno SA and Hi-Nicalon Type-S fibers contain a reduced amount of oxygen and a near-stoichiometric chemical composition and consist of b-SiC polycrystalline structures while another low oxygen fiber, Hi-Nicalon, has excess carbon and does not have highly crystalline structure compared with Tyranno SA and Type-S. Representative properties and chemical compositions of the fibers [14,17] reported by the manufactures are compiled in Table 1. Note Tyranno SA fiber used in this work was the first trial piece. Tyranno SA fiber has been improved and the mechanical properties of a current fiber are slightly different from those of the Tyranno SA fiber used in this work. The matrix of composite was formed by forced-flow thermal-gradient chemical vapor infiltration (FCVI) method [18] at Oak

Table 1
The properties of fibers used in this work

SiC fiber	C/Si atomic ratio	Oxygen content (wt%)	Tensile strength (GPa)	Tensile modulus (GPa)	Elongation (%)	Density (Mg/m^3)	Diameter (μm)
Tyranno SA	1.07	<0.5	1.8	320	0.7	3.02	10
Hi-Nicalon Type-S	1.05	0.2	2.6	420	0.6	3.1	12
Hi-Nicalon	1.39	0.5	2.8	270	1.0	2.74	14

Ridge National Laboratory. A pyrolitic carbon interphase was applied to the fibers by CVI prior to the matrix processing. The nominal thickness of the interphase was 150 and 500 nm. The properties of material used in this work are summarized in Table 2. Neutron irradiation was carried out in the HFIR 14J capsule at Oak Ridge National Laboratory, USA. The fluence and temperature of the irradiation were 7.7×10^{25} nm-2 (E > 0.1MeV) at 800 °C and 6.0×10^{25} nm^{-2} (E > 0.1 MeV) at 300 °C. The sample temperature was controlled by electric heaters.

Density was measured using density gradient column and chemicals were mixed to generate a column. The Density was measured using density gradient column and chemicals were mixed to generate a column. The column with a density range between 2.90 and 3.10 g/cm^3 was mixed with bromoform and diiodomethane. Following a HF bath at room temperature to remove any surface silica, samples were dropped into the column. When the sample position was stable, accurate density was measured.

The composites were square-cut into 30 (long) × 6.0 (wide) × 2.2 (thick) mm^3 bar for the flexural tests. Four-point flexural tests were carried out at ambient temperature prior to and after the irradiations. The support span and the loading span were 20 and 5 mm, respectively. The crosshead speed was 0.51 mm/min. Fracture surfaces were observed by SEM following the flexural tests.

Table 2 The properties of samples used in this work

Fiber	Woven type	C thickness (nm)	Irradiation temperature (°C)
Tyranno SA	Plain woven	150	800
Tyranno SA	Satin woven	150	300, 800
Hi-Nicalon Type-S	Plain woven	150	300, 800
Hi-Nicalon Type-S	Satin woven	150	300, 800
Hi-Nicalon Type-S	Satin woven	500	300
Hi-Nicalon	Plain woven	150	800

III. Results

Figs. 1−3 show the effect of neutron irradiation on strain−stress behavior of the four point flexural tests of SiC/SiC composites reinforced with plain woven fibers. Both composites reinforced with Hi-Nicalon Type-S fibers and Tyranno SA fibers were stable to neutron irradiations Figs. 4 and 5 show the fracture surface of composites reinforced with Hi-Nicalon Type-S and Tyranno SA fibers following irradiation at 800 °C. In the previous composites containing off-stoichiometric SiC fibers such as Nicalon, Tyranno Lox M and Hi-Nicalon, significantly long fiber pull-out with more than several hundred lm length was seen following irradiation [8,19]. However in the composites reinforced with Hi-Nicalon Type-S fibers, fiber pull-out was relatively short and seemed almost same with non-irradiated composites even following 7.7 dpa irradiation. Composites reinforced with Tyranno SA fibers showed brittle fracture surface and seemed almost same with the non-irradiated composites, too. Mechanical properties of SiC/SiC composites following irradiation at 800 and at 300 °C are compared with those prior to the irradiation in Figs. 6 and 7. The Figs. show the relative values, i.e. the value after irradiation/ the value prior to irradiation, of modulus, PLS obtained from 0.01% strain offset and flexural strength. Error bars show maximum and minimum values. The composites reinforced with Type-S fibers and Tyranno SA fibers with plain weave fabric kept their flexuralstrength following irradiation, while the composites reinforced with Hi-Nicalon fibers decreased. Most of PLS decreased following the irradiation at 800°C, while they increased following the irradiation at 300 °C. In all composites, the elastic modulus decreased following the irradiation with the exception of the composites reinforced with Hi-Nicalon Type-S plain weave fabric. Normalized density change of Tyranno SA fiber and CVD SiC irradiated at 7.7 dpa and 800 °C are shown in Fig. 8 with those of previous fibers, Nicalon and Hi- Nicalon and CVD SiC irradiated at 150°C. Tyranno SA fiber swelled slightly following irradiation, while the other fibers underwent radiation-induced densification.

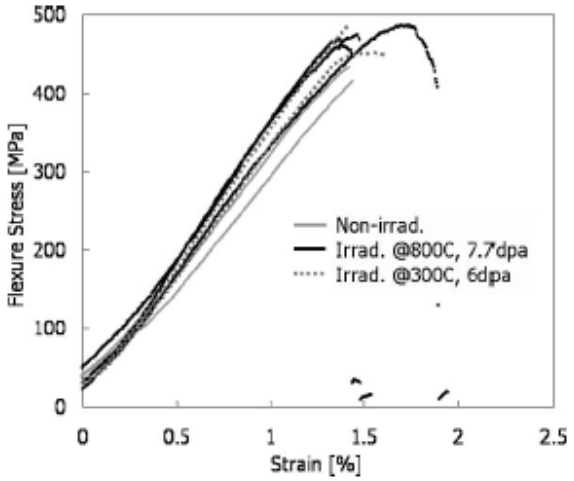

Fig. 1. Effect of irradiation on flexural behavior of Hi-Nicalon Type-S (P/W) samples.

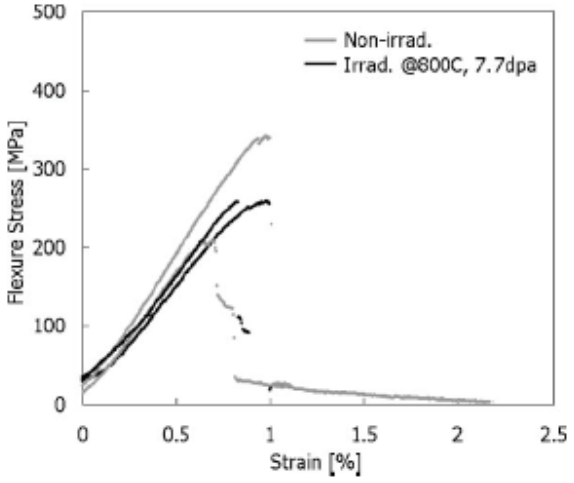

Fig. 2. Effect of irradiation on flexural behavior of Tyranno SA (P/W) samples.

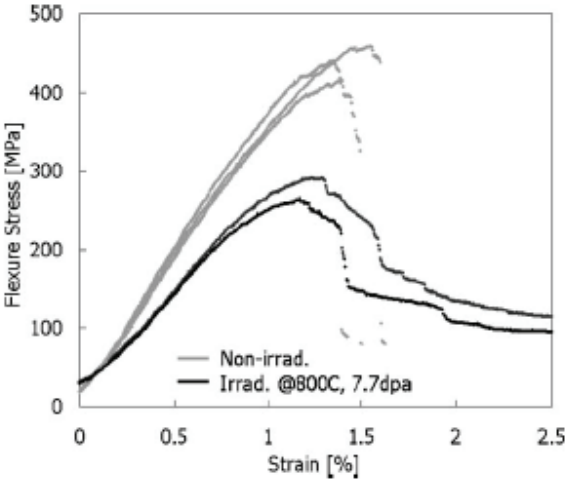

Fig. 3. Effect of irradiation on flexural behavior of Hi-Nicalon (P/W) samples.

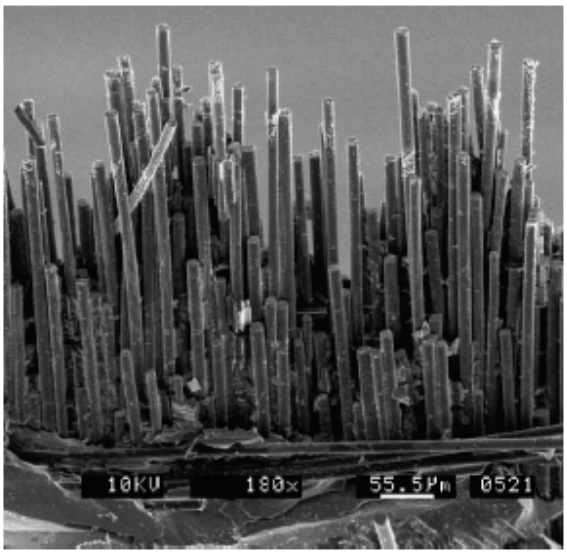

Fig. 4. Fracture surface of Hi-Nicalon Type-S sample following the irradiation at 800 ^{o}C.

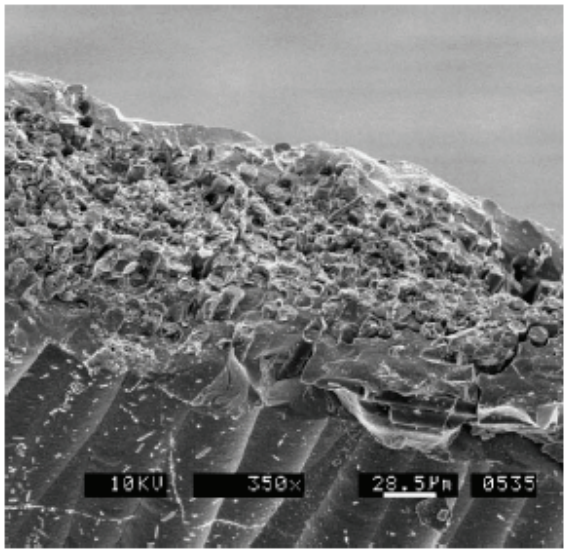

Fig. 5. Fracture surface of Tyranno SA sample following the irradiation at 800 °C.

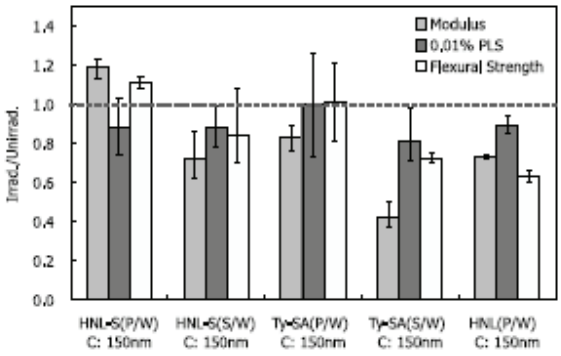

Fig. 6. Effect of irradiation at 7.7 dpa and 800 °C on mechanical properties.

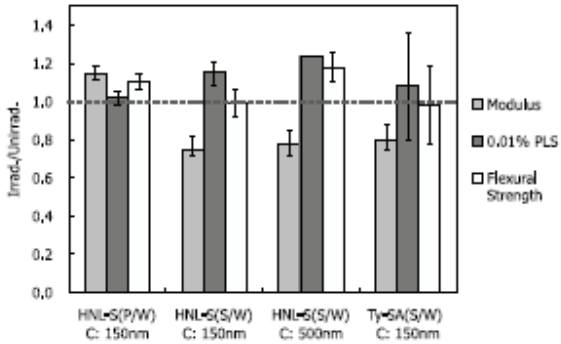

Fig. 7. Effect of irradiation at 6.0 dpa and 300 °C on mechanical properties.

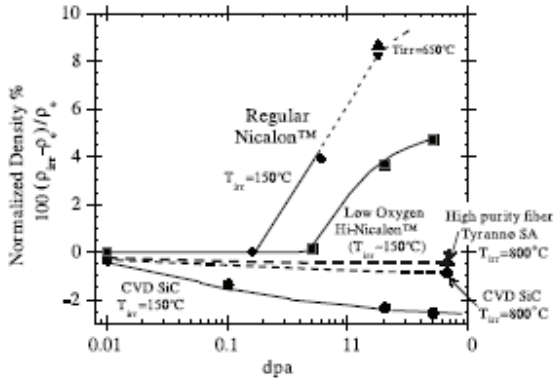

Fig. 8. Relative density change of SiC fibers and CVD SiC by neutron irradiation.

IV. Discussions

Both composites reinforced with Hi-Nicalon Type-S and Tyranno SA fibers showed stable mechanical properties to even high dose and high temperature irradiation. Of particular note, the fracture behavior was completely different from previous composites reinforced with nonhigh purity fibers. In composites reinforced with nonhigh purity fibers, the composites fractured with long fiber pull-out following irradiation due to debonding of fiber/matrix interface. However, composites reinforced with Hi-Nicalon Type-S and Tyranno SA fibers fractured with relatively short fiber pull-out even with C interphase, and the fracture behavior of the composites following irradiation was similar with that of non-irradiated composites. C interphase was considered one of the critical issues for the degradation of interfacial shear strength. However the apparent effect of C interphase degradation on mechanical properties were not seen in this results. Composites reinforced with Tyranno SA fibers showed brittle fracture behavior even following irradiation due to weaker fiber strength and rough fiber surface attributed to larger grain size than Hi-Nicalon Type-S even with same fiber/matrix interphase. This fracture behavior is not ideal for composite materials. However, it was completely different from previous composites after irradiation. Tyranno SA fiber have been improved. The grain size decreased and the fiber strength increased. Composites reinforced with the current Tyranno SA fibers are expected to show superior mechanical properties. Similar fracture behavior between irradiated composites and unirradiated composites with relatively short fiber pull-out is attributed to similar swelling behavior between the fiber and matrix. As shown in Fig. 8, there was a large mismatch of swelling between previous fiber, such as Nicalon and Hi-Nicalon, and CVD SiC. This mismatch caused fiber/matrix interfacial debonding and reduced mechanical properties with long

fiber pull-out. Normalized density of Tyranno SA is quite similar to CVD SiC irradiated at same condition. That is the reason that both composites reinforced with Hi-Nicalon Type-S and Tyranno SA fibers retain their fiber/matrix integrity and mechanical properties. In most of composites, degradation of modulus was seen. The degradation of elastic modulus of CVD SiC following irradiation has been reported [20,21] and considered that the degradation is inversely proportional to the amount of swelling. Fig. 8 shows slight swelling of both fiber and CVD SiC, and it is considered that the modulus of both fiber and matrix decreased. However effect of irradiation temperature on elastic modulus was not clear, while the amount of swelling of CVD SiC depends on irradiation temperature. Typically, swelling and mechanical properties of ceramics saturate by a few dpa [21,22]. Perhaps this indicates that composite will be stable to much higher dpa, although further experiment of much higher dpa is required to confirm it.

V. Conclusions

1. Stoichiometric fibers are dimensionally stable to doses and temperatures of this study like CVD SiC.
2. The SiC/SiC composites with reinforced with high purity fibers showed stable mechanical properties to high dose (7.7 dpa)/high temperature (800^{o}C) irradiation. Acknowledgements The authors would like to thank Lou Qualls and Jeff Bailey for assistance with the irradiation. This work was supported by Japan/USA Program of Integration of Technology and Engineering for Fusion Research (JUPITER- II) and by the office of Fusion Energy Science, US DOE under contract DE-AC-05-00OR22725 with UT-Battelle, LLC.

References

[1] P. Fenici, A.J. Frias Rebelo, R.H. Jones, A. Kohyama, L.L. Snead, J. Nucl. Mater. 258−263 (1998) 215.
[2] A. Hasegawa, A. Kohyama, R.H. Jones, L.L. Snead, B. Riccardi, P. Fenici, J. Nucl. Mater. 283−287 (2000) 128.
[3] A.R. Raffray et al., Fus. Eng. Des. 58&59 (2001) 549.
[4] L. Giancarli, M. Ferrari, M.A. F€utterer, S. Malang, Fus. Eng. Des. 49&50 (2000) 445.
[5] S. Nishio et al., Fus. Eng. Des. 41 (1998) 357.
[6] L. Giancarli, J.P. Bonal, A. Caso, G. Le Marois, N.B. Morley, J.F. Salavy, Fus. Eng. Des. 41 (1998) 165.
[7] L.L. Snead, R.H. Jones, A. Kohyama, P. Fenici, J. Nucl. Mater. 233−237 (1996) 26.
[8] L.L. Snead et al., J. Nucl. Mater. 253 (1998) 20.
[9] A. Hasegawa, G.E. Youngblood, R.H. Jones, J. Nucl. Mater. 231 (1996) 245.
[10] Y. Katoh, T. Hinoki, A. Kohyama, T. Shibayama, H. Takahashi, Ceram. Eng. Sci. Proc. 20 (4) (1999) 325.
[11] L.L.Snead, M.C.Osborne, K.L.More, J.Mater.Res.10(3)(1995) 736.
[12] J.H.W. Simmons, Radiation Damage in Graphite, Pergamon Press, NY, 1965.
[13] L.L.Snead, D.Steiner, S.J.Zinkle, J.Nucl.Mater.191−194(1992) 566.
[14] M. Takeda, A. Urano, J. Sakamoto, Y. Imai, J. Nucl. Mater. 258−263 (1998) 1594.
[15] R.E. Jones, D. Petrak, J. Rabe, A. Szweda, J. Nucl. Mater. 283−287 (2000) 556.
[16] T. Ishikawa, Y. Kohtoku, K. Kumagawa, T. Yamamura, T. Nagasawa, Nature 391 (1998) 773.
[17] K. Kumagawa, H. Yamaoka, M. Shibuya, T. Yamamura, Ceram. Eng. Sci. Proc. 18 (3) (1997) 113.
[18] T.M. Besmann, E.R. Kupp, E. Lara-Curzio, K.L. More, J. Am. Ceram. Soc. 83 (12) (2000) 3014.
[19] T. Hinoki, Y. Katoh, A.Kohyama, Mater.Trans.JIM43(4)(2002) 617.
[20] L.L.Snead, S.J.Zinkle, D.Steiner, J.Nucl.Mater.191−194(1992) 560.
[21] M.C. Osborne, J.C. Hay, L.L. Snead, D. Steiner, J. Am. Ceram. Soc. 82 (9) (1999) 2490.
[22] H. Kishimoto, Y. Katoh, A. Kohyama, M. Ando, ASTM STP 1405 (2001) 786.

Nuteron irradiation effects on high-crystallinity and near-stoichiometry SiC fibers and their composites

T. Nozawa [a*], T. Hinoki [b], L.L. Snead [b], Y. Katoh [a,b], A. Kohyama [a]

a Department of Quantum Science and Energy Engineering, Tohoku University, 01 Aramaki-aza-Aoba, Aoba-ku, Sendai 980-8579, Japan
a Institute of Advanced Energy, Kyoto University, Gokasho, Uji, Kyoto 611-0011, Japan
b Metals and Ceramics Division, Oak Ridge National Laboratory, Oak Ridge, TN 37830, USA

Key characteristics required for the development of fusion-grade SiC/SiC composites are high-crystallinity and nearstoichiometry. To identify the primary mechanisms of degradation caused by neutron irradiation, the radiation behavior of the constituent SiC fibers needs to be examined. In this study, single filament tensile tests were conducted after neutron irradiation on a recently developed highly-crystalline and near-stoichiometric SiC fiber; Hi-Nicalon^{TM} Type-S. Hi-NicalonTM Type-S fiber exhibited excellent strength retention up to 7.7 dpa independent of irradiation temperature up to 800 ^{o}C. The radiation stability of the Hi-Nicalon^{TM} Type-S fiber directly contributed to the excellent radiation performance in composites made with this fiber. The observed 14-20% decrease of elastic modulus due to neutron irradiation of Hi-Nicalon^{TM} Type-S fiber had a minor effect on composite strength.

I. Introduction

Silicon carbide based composites (SiC/SiC), considered to be a candidate as a structural fusion-grademateriał, require excellent radiation stability of all constituents:reinforcing fiber, matrix and interphase. Siliconcarbide, in nature, exhibits excellent radiological properties such as low induced radio-activation and low after-heat [1]. Moreover, it was revealed that high-crystallinityand near-stoichiometry b-SiC matrix, formed by chemical vapor infiltration (CVI), exhibited superior dimensional and mechanical stabilities under neutron irradiation up to 10 dpa [2,3]. In contrast, SiC-based fibers containing glassy siliconoxycarbide phases (SiCxOy) such as Nicalon^{TM} and Hi-Nicalon^{TM} (Nippon Carbon Co. Ltd.) exhibited severe dimensional and mechanical property changes due to extensive shrinkage caused by crystallization of the amorphous SiC phase and the presence of radiationinstable impurities such as excess carbon [4]. As a result, fiber shrinkage and swelling of high-crystallinity SiC matrix caused stress-induced debonding of the fiber/ matrix (F/M) interphase [5]. Recently developed Hi-Nicalon^{TM} Type-S (Nippon Carbon Co. Ltd.) and Tyranno^{TM}-SA (Ube Industries, Ltd.) fibers have offered the possibility of improved radiation stability due to the similar microstructures with radiation-stable b-SiC; high-crystallinity and nearstoichiometry. In fact, SiC/SiC composites with these fibers did exhibit excellent tolerances in shape and mechanical properties under neutron irradiation [6,7]. To further understand why these composites exhibited improved radiation performance, the effect of neutron irradiation on fiber constituent alone needs to be assessed. The objective in this study is to identify the effect of neutron irradiation on mechanical properties of highly-crystalline and near-stoichiometric SiC fiber by single filament tensile testing. Specifically, the effect of high-temperature irradiation on composite strength up to 800 ^{o}C is evaluated. The effects of neutron irradiation on chemical vapor deposited (CVD) SiC and advanced SiC/SiC composites are also assessed to explore the confirmed development of fusion-grade SiC/SiC composites.

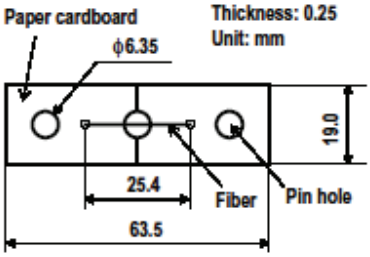

Fig. 1. Schematic illustration of cardboard specimen holder for single filament tensile test.

II. Experimental

Highly-crystalline and near-stoichiometric SiC fiber; Hi-Nicalon^{TM} Type-S, was used. Key characteristics of Hi-Nicalon^{TM} Type-S fiber are listed in Table 1. Neutron irradiation was carried out in the High Flux Isotope Reactor (HFIR) at Oak Ridge National Laboratory as a part of the HFIR-14J experiment. Irradiation temperatures were 300, 500 and 800 ^{o}C, and the irradiation fluence was 6.0, 6.0 and 7.7 dpa, respectively. It was assumed that 1 dpa corresponds to 1.0×10^{25} n/m^2 (E > 0:1 MeV). Experimental details are described elsewhere [8].
Fig. 1 shows a design of the cardboard specimen holder. Gauge length of tested fibers was 25.4 mm. Both ends of a single filament were adhered on the cardboard by epoxy. Viscous grease was spread on the fiber surface to capture broken fiber segments. Tensile strain was calculated from

the distance between two stripes on the flags measured by a laser extensometer. The stiffness of test fixture is high compared with fiber and its effect on fiber strain was considered quite a small. For stress calculation, the fiber diameter was estimated by taking the average of three measurements on each individual fiber by video microscopy. Prepared cardboard specimen was mounted by the connecting pins to main fixture and the center of the cardboard was cut by scissors taking care not to damage the tested fiber just before the testing. Crosshead displacement rate was 0.5 mm/min (strain rate: 2.0×10^{4} s^{-1}). Fibers broken within the gauge length were recognized as valid. All of the valid data were analyzed by Weibull statistics. A detailed description of the test methodology was referred in the modified standard by Lara-Curzio [9].

	Hi-Nicalon™ Type-S (HNL-S)	Hi-Nicalon™ (HNL)	Nicalon™ (CG-NL)
C/Si atomic ratio	1.05	1.39	1.34
Oxygen content (wt%)	0.2	0.5	11.7
Tensile strength (GPa)	2.6	2.8	3.0
Tensile modulus (GPa)	420	270	220
Elongation (%)	0.6	1.0	1.4
Density (Mg/m^3)	3.10	2.74	2.55
Diameter (μm)	11	14	14

Table 1
Key characteristics of silicon carbide fibers

Irradiation (T_{irr}, dose)	Weibull modulus	Weibull characteristic strength, σ_0 (GPa)	Weibull mean strength, $\bar{\sigma}$ (GPa)	Weibull standard deviation, s (GPa)	Tensile modulus (GPa)	Number of specimens
None	6.0	3.4	3.2	0.6	400 ± 51	22
300 °C, 6.0 dpa	4.6	3.6	3.3	0.8	316 ± 76	38
500 °C, 6.0 dpa	4.3	3.5	3.2	0.8	338 ± 66	36
800 °C, 7.7 dpa	4.8	3.5	3.2	0.7	344 ± 51	27

Table 2
Tensile properties of Hi-Nicalon Type-S fibers irradiated at 300, 500 and 800 ^{o}C

III. Results and discussion

III.A. Effect of neutron irradiation on Hi-Nicalon™ Type-S SiC fiber

Table 2 and Fig. 2 show tensile strength test results for Hi-Nicalon™ Type-S fiber. It is noted that 5-10% of measurement errors of the fiber diameter affected the large scatters of tensile strength and tensile modulus. A slight decrease in Weibull modulus is observed but there was no overall degradation in tensile strength after neutron irradiation. Little effect of the irradiation temperature on Weibull mean strength was observed (approximately +5%, after irradiation). Fig. 3 shows normalized Weibull mean strength represented as the retention ratio after neutron irradiation. According to Osborne et al. [4], strength increase by neutron irradiation was typical for amorphous based SiC fibers; Nicalon™ and Hi-Nicalon™, due to crystallization of the amorphous SiCxOy phase or excess carbon. In contrast, Hi-Nicalon™ Type-S fiber maintained its tensile strength at the original level under neutron irradiation. The dose dependency of tensile strength for Hi-Nicalon™ Type-S fiber was very similar to that of flexural strength for crystalline and pure SiC, i.e. CVD-SiC [2,3,10]. Both CVD-SiC and Hi-Nicalon™ Type-S fiber, in principle, kept its strength under heavy neutron irradiation under the same surface finish in materials preparation for CVD-SiC. A slight increase of flexural strength by Snead et al. might be explained by the increase of fracture toughness [10]. However, the primary mechanism is still uncertain. Fig. 4 shows the effect of neutron irradiation on the tensile modulus of Hi-Nicalon™ Type-S fiber. Specifi-cally, the tensile modulus tended to decrease attaining a maximum change of 20% for the 300 °C irradiation, 16% at 500 °C and 14% at 800 °C. Conversely, crystallization of Nicalon™ with its amorphous SiCxOy phase and Hi-Nicalon™ with excess carbon had significant effects on the change of their lattice parameters resulting in increase of the elastic modulus. However, it is noted that the Hi-Nicalon™ fiber swells slightly in the low fluence neutron irradiation range due to its well-organized crystal structure [4]. In this range, no significant change of the tensile modulus was identified. The degradation of the elastic modulus for Hi-Nicalon™ Type-S fiber was also very similar to that for CVD-SiC [2,11,12]. The tendency toward greater reduction in elastic modulus for lower

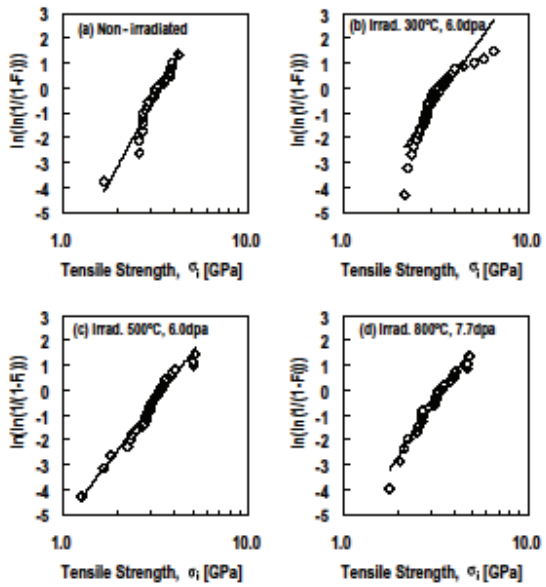

Fig. 2. Weibull statistical plots for tensile strength of Hi-Nicalon™ Type-S fibers; (a) non-irradiated and irradiated at (b) 300 °C, (c) 500 °C and (d) 800 °C.

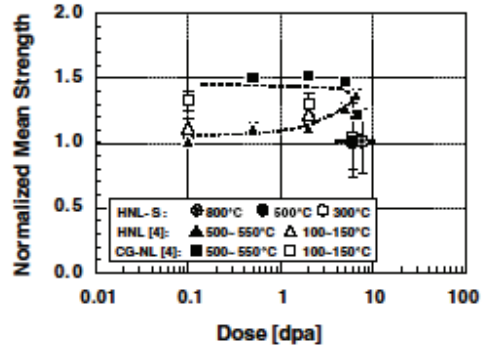

Fig. 3. Effect of neutron irradiation on Weibull mean strength of Nicalon™ (CG-NL), Hi-Nicalon™ (HNL) and Hi-Nicalon™ Type-S (HNLS).

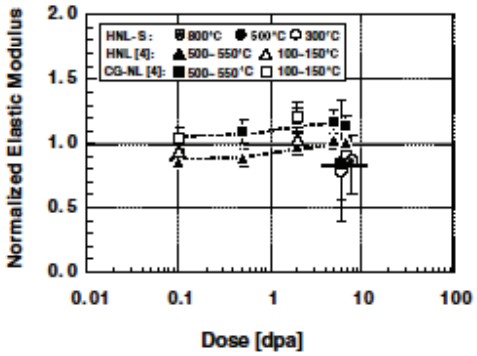

Fig. 4. Effect of neutron irradiation on elastic modulus of Nicalon™ (CG-NL), Hi-Nicalon™ (HNL) and Hi-Nicalon™ Type-S (HNLS).

temperature irradiation is attributed to the higher amount of surviving defects consistent with the higher level of saturation swelling at low temperature. Moreover, wellcrystallized, higher initial modulus structures such as CVD-SiC are more sensitive. However, at higher temperatures, surviving defects following neutron cascades are reduced, leading to smaller elastic modulus change.

III.B. Effect of neutron irradiation on highly-crystalline and near-stoichiometric SiC/SiC composites

Several mechanical test results after neutron irradiation have been reported for advanced SiC/SiC composites [6,7,13]. SiC/SiC composites with high purity SiC fiber and matrix exhibited stable flexural strength under high dose (7.7 dpa) and high-temperature (800 °C) irradiation. The radiation stability in tensile strength for Hi-Nicalon™ Type-S fiber contributed the excellent radiation performance in composite strength. However, the 10-20% of degradation in flexural modulus of composites was identified, even at low-fluence neutron irradiation up to 1 dpa [13].

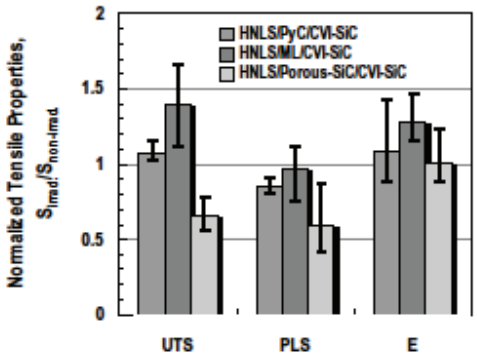

Fig. 5. Effect of neutron irradiation on ultimate tensile strength (UTS), proportional limit stress (PLS) and elastic modulus (E) of Hi-Nicalon™ Type-S fiber reinforced CVI-SiC matrix composites with single PyC, multilayered SiC/PyC and porous SiC interphase.

Conversely, recent our work offers no degradation of the tensile modulus of composites after neutron irradiation. Fig. 5 shows the preliminary test result about the effect of neutron irradiation on tensile properties of Hi- NicalonTM Type-S fiber reinforced CVI-SiC matrix composites with single PyC, multilayered (ML) SiC/PyC and pseudo porous SiC interphase after neutron irradiation at 800 °C up to 1 dpa performed in the Japan Materials Testing Reactor (JMTR) at Oarai. Materials tested are summarized in elsewhere [14]. This indicates

that the radiation-induced change in tensile modulus of fiber is not the primary mechanism for the degradation of the composite modulus. Moreover, Fig. 5 shows that the significant reductions of the tensile strength and proportional limit stress were identified in only a porous SiC interlayer composite. This also implies the importance of the F/M interphase to maintain good radiation performance in composite strength. Further investigations are addressed to confirm this issue.

IV.Conclusions

In order to identify the effect of neutron irradiation on recently developed highly-crystalline and near-stoichiometric SiC fiber; Hi-Nicalon^{TM} Type-S, single filament tensile tests were carried out after neutron irradiation. Hi-Nicalon^{TM} Type-S fiber exhibited no statistically significant degradation in tensile strength up to 7.7 dpa at 300-800 ^{o}C, leading to the excellent radiation performance in composite strength. The observed 14▪0% decrease of elastic modulus due to neutron irradiation of Hi-Nicalon^{TM} Type-S fiber had a minor effect on composite strength. However, this needs to be verified in the following microstructural observation.

Acknowledgements

This work was performed as a part of DOE/MEXT JUPITER-II Collaboration for Development of Advanced Blanket Performance under Irradiation and System Integration. This work was also performed as a part of corroboration works at Irradiation Experimental Facility, Institute for Materials Research, Tohoku University, Japan.

References

[1] R.H. Jones, L. Giancarli, A. Hasegawa, Y. Katoh, A. Kohyama, B. Riccardi, L.L. Snead, W.J. Weber, J. Nucl. Mater. 307▪11 (2002) 1057.
[2] R.J. Price, Nuclear Technology 35 (1977) 320.
[3] R.J. Price, G.R. Hopkins, J. Nucl. Mater. 108&109 (1982) 732.
[4] M.C. Osborne, C.R. Hubbard, L.L. Snead, D. Steiner, J. Nucl. Mater. 253 (1998) 67.
[5] L.L. Snead, D. Steiner, S.J. Zinkle, J. Nucl. Mater. 191▪194 (1992) 566.
[6] T. Hinoki, L.L. Snead, Y. Katoh, A. Hasegawa, T.Nozawa, A. Kohyama, J. Nucl. Mater. 283▪87 (2002) 1157.
[7] L.L. Snead, Y. Katoh, A. Kohyama, J.L. Bailey, N.L.Vaughn, R.A. Lowden, J. Nucl. Mater. 283▪87 (2000)551.
[8] A.L. Qualls, Fusion Materials, DOE/ER0313/28 (2000)241.
[9] E. Lara-Curzio, Ceram. Trans. 144 (2002) 233.
[10] L.L. Snead, T. Hinoki, Y. Katoh, Fusion Materials, DOE/ER-0313/33 (2003) 49.
[11] M.C. Osborne, J.C. Hay, L.L. Snead, D. Steiner, J. Am.Ceram. Soc. 82 (1999) 2490.
[12] S. Nogami, A. Hasegawa, L.L. Snead, J. Nucl. Mater. 307▪311 (2002) 1163.
[13] T. Nozawa, T. Hinoki, Y. Katoh, A. Kohyama, J. Nucl.Mater. 307,11 (2002) 1173.
[14] T. Hinoki, L.L. Snead, E. Lara-Curzio, J. Park, Y. Katoh.A. Kohyama, Fusion Materials, DOE/ER-0313/32 (2002) 13.

EFFECT OF HE PRE-IMPLANTATION AND NEUTRON IRRADIATION ON MECHANICAL PROPERTIES OF SiC/SiC COMPOSITE

Shuhei Nogami [a*], Akira Hasegawa [a], Lance L. Snead [b], Russell H. Jones [c], Katsunori Abe [a]

a Department of Quantum Science and Energy Engineering, Tohoku University, 01 Aramaki-aza-Aoba, Aoba-ku, Sendai 980-8579, Japan
b Oak Ridge National Laboratory, Oak Ridge, TN 37831 6138, USA
c Pacific Northwest National Laboratory, Richland, WA 99352, USA

Mechanical property changes of SiC/SiC (Hi-Nicalon/C/SiC) composite caused by uniform He pre-implantation up to about 170 at.ppm at 400–800 °C followed by neutron irradiation up to about 7.7×10^{25} n/m2 (En > 0:1 MeV) at 800 _C in HFIR were investigated by the three-point bend tests and nano-indentation tests. Degradation of the composite bend properties due to neutron irradiation was observed. The hardness increased after neutron irradiation for both the SiC-matrix and the Hi-Nicalon fiber. There was almost no change in the elastic modulus of the SiC-matrix, but there was an increase in the modulus of the Hi-Nicalon fiber after neutron irradiation. He pre-implantation had almost a negligible effect on the mechanical properties of the composite specimen.

I. Introduction

Silicon carbide (SiC) fiber-reinforced SiC-matrix composites (SiC/SiC composites) are being considered as a structural material for components in future fusion reactor blankets [1,2]. Displacement damage and transmutation products such as helium (He) will be produced in these materials during high energy (about 14 MeV) neutron irradiation. In a full power year, the displacement damage and He concentration in a SiC component of the blanket of the ARIES-IV concept reactor were calculated to be approximately 57 dpa and 15 380 at.ppm, respectively [2]. The He concentration per dpa in SiC will be about 10 times larger than that in other candidate materials (ferritic steels and vanadium alloys). A relatively large number of studies of the displacement damage effect on the mechanical properties of SiC/SiC composites have been carried out. Advanced SiC/SiC composites, developed in recent years using stoichiometric and high crystalline SiC-fibers such as Hi-Nicalon Type-S [3] and Tyranno SA [4], have exhibited improved radiation resistance up to about 7.7×10^{25} n/ m2 [5]. There have also been some studies of the effect of transmutant He on the mechanical properties of SiC/SiC composites [6–8]. Using bend tests, the ultimate fracture strength of a Nicalon CG/C/SiC composite (C: carbon) [6] and a Hi-Nicalon/C/SiC composite [7] decreased after He-implantation up to 2500 at.ppm at 900 °C and up to 150–170 at.ppm at 400–800 °C, respectively. For composite studies utilizing the nano-indentation test, both hardness and elastic modulus of the SiC-matrix and SiC fibers (Hi-Nicalon and Hi-Nicalon Type-S) decreased after He-implantation up to 20 000 at.ppm below 100 °C [8]. However, the effects of He, and of displacement damage, and their synergistic effect on the mechanical property changes of SiC/SiC composites were not clearly distinguished in all cases. The purpose of this study is to investigate the effect of He pre-implantation followed by neutron irradiation on the mechanical properties of a SiC/SiC composite.

II. Experimental Procedure

A SiC/SiC composite with Hi-Nicalon fibers ($0^o/90^o$ plain-weave) manufactured by DuPont Lanxide [9] was examined in this study. The SiC-matrix(crystalline b-SiC) was fabricated by an isothermal chemical vapor infiltration (ICVI) process. The interface material between SiC-fibers and SiC-matrix was a pyrolytic carbon (_150 nm thickness), which was fabricated by a chemical vapor deposition (CVD) process. Hi-Nicalon is composed of b-SiC grains whose size is about 5–10 nm and have some of residual oxygen (<0.5 wt%), but substantial amounts of carbon (C/Si atomic ratio_1.39) [3]. The geometry of the specimens for irradiation and bend tests was approximately 4w × 1t × 20l mm3 (machined from specimens with an original geometry of 6w × 2t × 20l mm^3). The compression side of the bend specimens was machined to 1 mm thickness, while tension side was not machined. As a result, a CVI b-SiC overlayer remained on the tension side. Fig. 1 shows the schematic illustration of the specimen dimensions and test configurations in this study.

Helium pre-implantation was performed using the cyclotron accelerator at Tohoku University. The acceleration energy of He-ions was 36 MeV. The projected range of 36 MeV He-ions in SiC was calculated to be about 470 lm by the TRIM code [10]. Tandem type energy degrader wheels were used to obtain uniform depth distribution of He-atoms. The nominal He concentration was about 170 at.ppm. The displacement damage in the He implanted region was calculated to be about 0.009 dpa using a threshold displacement energy of

40 eV. The implantation temperature was 400–800°C. He-ions were implanted to the tension side of the bend specimens within an area of about 4w × 4l mm^2 located at the center of the specimens as shown in Fig. 1. Neutron irradiation was performed in the High Flux Isotope Reactor (HFIR) at Oak Ridge National Laboratory.

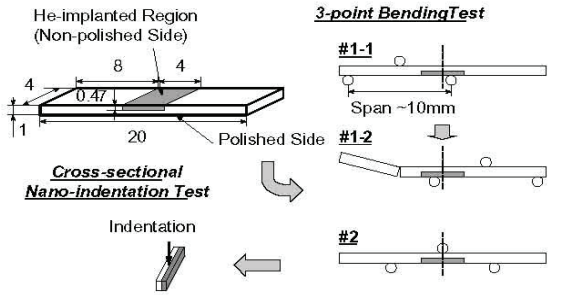

Fig. 1. The schematic illustration of the specimen dimensions and test configurations in this study.

Specimens were irradiated at 800 °C up to about 7.7 × 1025 n/m^2 (En > 0:1 MeV), which corresponds to about 7.7 dpa using an assumption that the displacement energy of 40 eV for both the Si and C sublattices. Three point bend tests were performed at room temperature in air. The support span length and crosshead speed were 10 mm and 0.5 mm/min, respectively. Configurations #1–1 and #1–2 in Fig. 1 were used for the bend test measurements of the non-He-implanted, but neutron-irradiated region. Configuration #2 was for the measurements of the He-implanted and neutron irradiated region. Fractography observations were performed using a scanning electron microscope (SEM). Cross-sectional nano-indentation tests were performed at room temperature using a NANO INDENTER®II (Nano-instruments) equipped with a Berkovich diamond tip. The indentation depth and loading (unloading) rate were constant, 50 nm and 50 mN/s, respectively. Specimens were mechanically sliced perpendicular to the He-implanted surface as shown in Fig. 1. The cross-section of the cut specimens for indentation was mechanically polished with a 0.5 lm diamond slurry. Hardness H and elastic modulus E were evaluated using an unloading curve and the method proposed by Oliver and Pharr [11]. H is calculated from the following formula:

$$H = P_{\max}/A(h_c), \quad (1)$$

where P_{max} is the maximum indentation load and A, which is a function of constant indentation depth h_c, is the contact area of the indenter with the specimen surface. E is defined as follows:

$$E = \left(1 - \nu_s^2\right)/\left(1/E_r + \left(1 - \nu_i^2\right)/E_i\right), \quad (2)$$

where ms; mi; Er and Ei are the Poisson's ratio of specimen, the indenter (0.07 for diamond), the reduced modulus and the elastic modulus of the indenter (1141 GPa for diamond), respectively. Further details of this method are given in Ref. [11].

III. Results

Fig. 2 shows the summary of the bend test results (ultimate fracture strength, elastic modulus and proportional limit stress – PLS) for the as-received, the non-He-implanted and neutron-irradiated (Non-He/ Neutron), and the He-implanted and neutron-irradiated

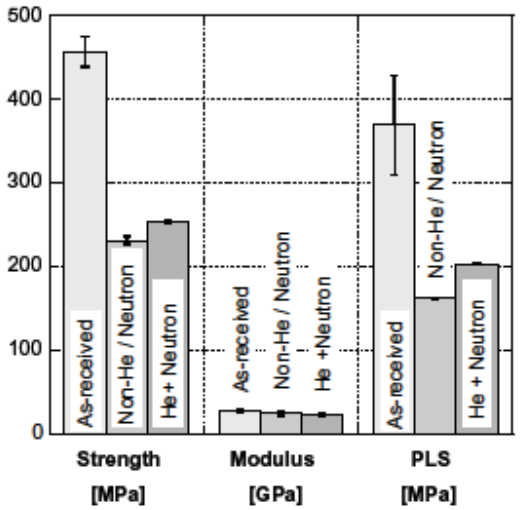

Fig. 2. The summary of the bend test results (ultimate fracture strength, elastic modulus and proportional limit stress (PLS, offset strain_0.0005)) for the as-received, the non-He-implanted and neutron-irradiated (Non-He/Neutron), and the He implanted and neutron-irradiated (He+Neutron) composites.

(He+Neutron) composites. The elastic modulus was calculated using the slope of the linear range of the stress–strain curves. The PLS was the stress value when offset strain was about 0.0005. The ultimate fracture strength, elastic modulus and proportional limit stress decreased due to neutron irradiation by about 50%, 10% and 55%, respectively. The 'He +Neutron' specimens had similar bend properties to the 'Non-He/Neutron' specimens.

Fig. 3 shows a typical observation of the fracture surface by SEM for the 'as-received', the 'Non-He/ neutron', and the 'He + Neutron' composites. He-ions were implanted from the bottom side of the pictures. The pull-out lengths of the Hi-Nicalon fibers for the 'Non-He/Neutron' composite were longer than that for the 'as-received' composite. Almost no differences of the pull-

out lengths for the Hi-Nicalon fibers were observed between 'Non-He/Neutron' and 'He + Neutron' composites. Figs. 4 and 5 show the hardness and elastic modulus of the SiC-matrix and Hi-Nicalon fiber of the 'asreceived', 'Non-He/Neutron', and 'He + Neutron' composites. The data for non-He-implanted, but neutron-irradiated region and data for He-implanted and neutron-irradiated region were the average of the data points at the depth of 0–470 and 470–1000 lm from the He-implanted surface, respectively. The hardness increased by about 30% after neutron irradiation (no helium) for both the SiC-matrix and the Hi-Nicalon fibers. Almost no change in the elastic modulus for the irradiated SiC-matrix was observed, but about a 30% increase for the irradiated Hi-Nicalon fibers was observed. The 'He+ Neutron' specimens exhibited almost the same hardness and elastic modulus as the 'Non-He/ Neutron' specimens.

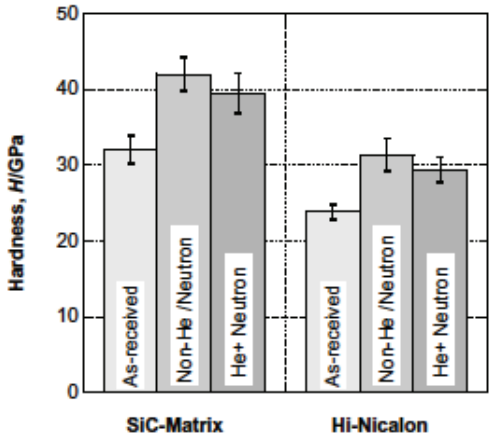

Fig. 4. The hardness of the SiC-matrix and Hi-Nicalon fiber for as-received, non-He-implanted and neutron-irradiated (Non- He/Neutron) and He-implanted and neutron-irradiated (He+Neutron) composite.

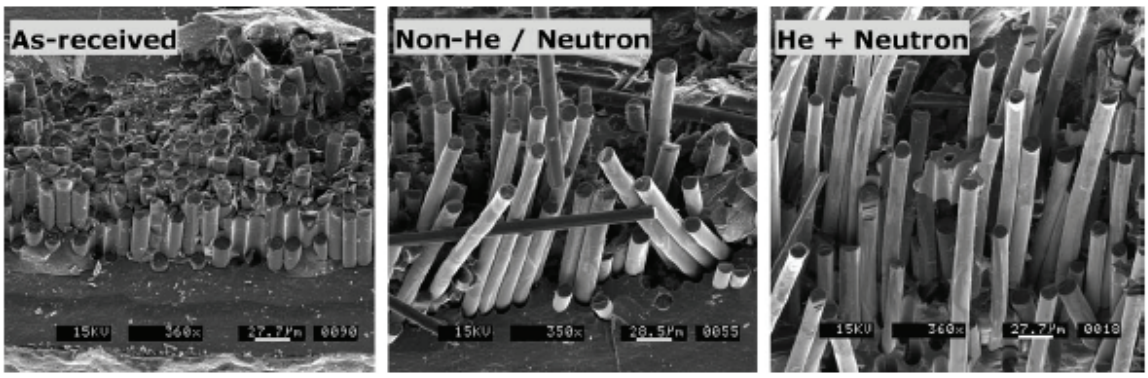

Fig. 3. Typical fracture surface observations by SEM for as-received, non-He-implanted and neutron-irradiated (Non-He/Neutron) and He-implanted and neutron-irradiated (He+Neutron) composites. He-ions were implanted from the bottom side of the pictures.

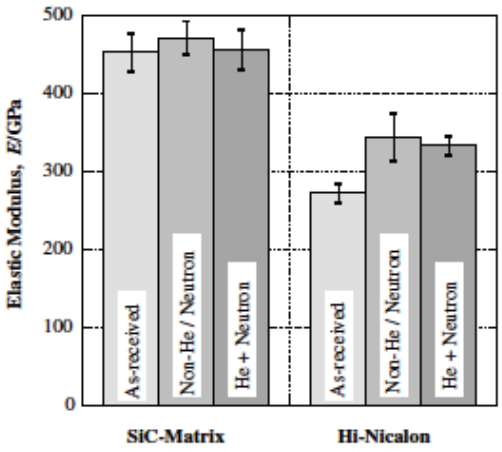

Fig. 5. The elastic modulus of the SiC-matrix and Hi-Nicalon fiber for as-received, non-He-implanted and neutron-irradiated (Non-He/Neutron) and He-implanted and neutron-irradiated (He+Neutron) composites.

IV. Discussion

A 10% reduction in the elastic modulus for the composite was observed. In contrast, almost no change in the elastic modulus for the SiC-matrix and about 30% increase for the Hi-Nicalon fiber were observed. Thus, so called the sum rule defined as follows is not applicable for the neutron-irradiated composite in this study:

$$E_c = E_f \times f_f + E_m \times f_m, \quad (3)$$

where Ec; Ef and Em are the elastic modulus of the composite, fiber and matrix, ff and fm are the volume fraction of the fiber and matrix in composite, respectively. Therefore, it can be predicted that the degradation (e.g. crack and debonding) of the interface between the SiC-matrix and Hi-Nicalon fiber was occurred due to neutron irradiation. Shrinkage of Hi-Nicalon fibers during neutron irradiation was observed in previous studies [12–15]. A previous study [16] also showed the presence of microcracks and debonding of the C-interface of Hi-Nicalon/C/SiC composite due to C-ions irradiation up to

about 10 dpa at 800 °C. Moreover, tensile strength of Hi-Nicalon fiber increased with neutron dose [17]. Thus, bend property degradations of Hi-Nicalon/C/SiC composite due to neutron irradiation might be related to the formation of microcracks and debonding of the C-inter interface induced by the shrinkage of the Hi-Nicalon fibers.

The effect of He pre-implantation treatment prior to neutron irradiation on mechanical properties was almost negligible (relative to the mechanical properties of the neutron irradiated specimens) up to a concentration of 170 at.ppm for the composite and the individual components of the composite. In previous work [8], the total number of released He atoms from the room temperature He-implanted Hi-Nicalon/C/SiC composite and carbon material during the annealing to 1500 °C werecalculated to be about 30% and 80% of the original number of the implanted-He atoms, respectively. Moreover, a previous work [16] showed no cavity formation in the Hi-Nicalon/C/SiC composite due to simultaneous C- and He-ion irradiation up to about 10 dpa and 1000 at.ppm-He at 800 °C. Therefore, it can be assumed that the pre-implanted-He in the Hi-Nicalon/C/SiC composite in this study remained in the specimens (especially in the SiC-matrix and Hi-Nicalon fibers) as small clusters and single atoms after the neutron irradiation at 800 °C. However, it may be indicated that the effect of the pre-implanted He (~170 at.ppm) on the mechanical properties of Hi-Nicalon/C/SiC composite in this study was relatively smaller than that of displacement damage caused by the He pre-implantation and neutron irradiation.

V. Summary

Mechanical property changes of SiC/SiC composite, its matrix and fibers (Hi-Nicalon) were studied for He pre-implantation up to about 170 at.ppm at 400–800 °C followed by neutron irradiation up to about 7.7×10^{25} n/m^2 (En > 0:1 MeV) at 800 °C in HFIR using bend tests and nano-indentation. The following results were obtained:

(1) The composite ultimate fracture strength, elastic modulus and proportional limit stress decreased due to neutron irradiation by about 50%, 10% and 55%, respectively. Specimens that were He pre-implanted and then neutron irradiated had similar bend properties to specimens irradiated with neutron only.

(2) The pull-out lengths of Hi-Nicalon fibers for non-He-implanted, but neutron-irradiated composites were longer than that for as-received composites. Almost no differences in pull-out lengths of Hi-Nicalon fibers were observed between non-He-implanted and neutron-irradiated composites and He-implanted and neutron-irradiated composites.

(3) The hardness increased by about 30% due to neutron irradiation for both SiC-matrix and Hi-Nicalon fiber. The specimens that were He pre-implanted and neutron irradiated had almost the same hardness properties as the specimens that were only exposed to neutrons.

(4) Almost no change in the elastic modulus of the SiC matrix, but about a 30% increase in elastic modulus of the Hi-Nicalon fibers was observed after neutron irradiation. The specimens that were He pre-implanted and neutron irradiated had almost the same elastic modulus values as the specimens that were only neutron irradiated.

ACKNOWLEDGMENTS

The authors are grateful to the staff at Tohoku University relating to the implantation test and to the staff at Oak Ridge National Laboratory relating to the irradiation program and the post-irradiation experiments. This work was supported by the JUPITER (Japan–USA Program of Irradiation Testing for Fusion Research) and JUPITER-II programs.

REFERENCES

[1] S. Ueda, S. Nishio, Y. Seki, R. Kurihara, J. Adachi, S. Yamazaki, J. Nucl. Mater. 258–263 (1998) 1589.
[2] L.A. El-Guebaly, Fus. Eng. Des. 28 (1995) 658.
[3] M. Takeda, A. Urano, J. Sakamoto, Y. Imai, J. Nucl. Mater. 258–263 (1998) 1594.
[4] T. Ishikawa, Y. Kohtoku, K. Kumagawa, T. Yamaura, T. Nagasawa, Nature 391 (1998) 773.
[5] T. Hinoki, L.L. Snead, Y. Katoh, A. Hasegawa, T.Nozawa, A. Kohyama, J. Nucl. Mater. 307–311 (2002) 1157.
[6] A.J. Frias Rebelo, H.W. Scholz, H. Kolbe, G.P. Tartaglia, P. Fenici, J. Nucl. Mater. 258 (1998) 1582.
[7] A. Hasegawa, M. Saito, K. Abe, R.H. Jones, J. Nucl. Mater. 253 (1998) 31.
[8] S. Nogami, S. Miwa, A. Hasegawa, K. Abe, Effects of Radiation on Materials, ASTM STP 1447, in press.
[9] G.E. Youngblood, C.H. Henager Jr., R.H. Jones, DOE/ ER-0313/20 (1996) 140.
[10] J.F. Ziegler, J.P. Biersack, U. Littmark, in: The Stopping and Ranges of Ions in Materials, vol. 1, Pergamon, New York, 1985.
[11] W.C. Oliver, G.M. Pharr, J. Mater. Res. 7 (6) (1992) 1564.
[12] G.E. Youngblood, R.H. Jones, A. Kohyama, L.L. Snead, J. Nucl. Mater. 258–263 (1998) 1551.
[13] M.C. Osborne, C.R. Hubbard, L.L. Snead, D. Steiner, J. Nucl. Mater. 253 (1998) 67.
[14] L.L. Snead, M.C. Osborne, K.L. More, J. Mater. Res. 10 (3) (1995) 736.
[15] L.L. Snead, R.H. Jones, A. Kohyama, P. Fenici, J. Nucl. Mater. 233–237 (1996) 26.
[16] S. Nogami, A. Hasegawa, K. Abe, T. Taguchi, R. Yamada, J. Nucl. Mater. 283–287 (2000) 268.
[17] M.C. Osborne, C.R. Hubbard, L.L. Snead, D. Steiner, J. Nucl. Mater. 253 (1998) 67.

Mechanical properties of advanced SiC/SiC composites after neutron irradiation

K. Ozawa [a,*], T. Nozawa [b], Y. Katoh [b], T. Hinoki [c], A. Kohyama [c]

a Graduate School of Energy Science, Kyoto University, Gokasho, Uji, Kyoto 611-0011, Japan
b Materials Science and Technology Division, Oak Ridge National Laboratory, P.O. Box 2008, Oak Ridge, TN 37831-6138, USA
c Institute of Advanced Energy, Kyoto University, Gokasho, Uji, Kyoto 611-0011, Japan

The effect of neutron irradiation on tensile properties in advanced 2D-SiC/SiC composites was evaluated. The composites used were composed of a SiC matrix obtained by the forced-flow chemical vapor infiltration (FCVI) process and either TyrannoTM-SA Grade-3 or Hi-NicalonTM Type-S fibers with single-layered PyC coating as the interphase. Neutron irradiation fluence and temperature were 3.1 × 10^{25} n/m^2 (E > 0.1 MeV) and 1.2 × 10^{26} n/m^2 at 740−750 °C. Tensile properties were evaluated by cyclic tensile test, and hysteresis loop analysis was applied in order to evaluate interfacial properties. Both composites exhibited excellent irradiation resistance in ultimate and proportional limit tensile stresses. From the hysteresis loop analysis, the level of interfacial sliding stress decreased significantly after irradiation to 1.5× 10^{26} n/m^2 at 750 °C.

Ⅰ. Introduction

Silicon carbide (SiC) continuous fiber-reinforced SiC matrix composites (SiC/SiC composites) are attractive structural materials for fusion reactors and advanced fission reactors because of their superior mechanical properties and good irradiation resistance at high temperatures [1]. The mechanical properties of SiC/SiC composites after irradiation is determined by the properties of their constituents, especially the fiber/matrix (F/M) interphase in case of composites with high modulus matrix. In earlier studies, SiC/SiC composites reinforced with nanocrystalline and non-stoichiometric SiC fibers have shown interfacial debonding due primarily to fiber contraction, which caused severe degradation in flexural strength [2 − 5]. In recent studies, however, advanced SiC/SiC composites appeared to retain ultimate flexural strength due to improved irradiation stability of the high crystallinity and near-stoichiometric SiC fibers [5,6].

For composites with highly irradiation-resistant matrices and fibers, irradiation effects on F/M interfacial properties has become one of the most important issues to be investigated. However, it is difficult to use the simple flexural testing to develop an understanding of irradiation effects on interfacial properties, because it is hard to analyze the data due to mixed failure modes. Simple failure modes, such as are obtained in tensile tests enable the fracture behavior of SiC/SiC composites after irradiation to be understood more precisely. Recent studies have employed tests yielding simple failure modes to evaluate interfacial properties [7−9]. The main purpose of this work is to identify neutron irradiation effects on tensile and interfacial properties of advanced SiC/SiC composites reinforced with two commercially available, high crystallinity, near-stoichiometric SiC fibers. For this purpose, tensile properties were evaluated in an unloading/reloading cyclic tensile test and the hysteresis loop analysis method was applied to predict interfacial properties.

Ⅱ. Experimental procedure

The composites used in this study were produced thorough a forced-flow thermal gradient chemical vapor infiltration (FCVI) process developed at Oak Ridge National Laboratory. Either TyrannoTM- SA 3rd grade (hereafter TySA) or Hi-NicalonTM Type-S (hereafter HNLS) fibers were used as reinforcements. These were stacked in a [0_/90_] orientation and held tightly in a graphite fixture for interphase deposition and subsequent matrix dentification. The F/M interphase was singly-layered pyrolytic carbon (PyC) and the thickness was 20−60 nm. The density of the composites was 2.3−2.7 g/cm3, and the fiber volume fraction and porosity were _38% and 17−25%, respectively. More detailed information about the materials fabrication is given elsewhere [10,11].

Neutron irradiation was performed in JOYO fast spectrum reactor at Oarai, Japan, in JNC-54 and -61 capsules as part of the CMIR-6 irradiation campaign. Neutron fluence and irradiation temperature were 3.1 × 10^{25} n/m^2 (E > 0.1 MeV) at 740 °C and 1.2 × 10^{26} n/m^2 at 750 °C. An equivalence of one displacement per atom (dpa) = 1 × 10^{25} n/m^2 (E > 0.1 MeV) is assumed in the following sections. The irradiation temperature was passively controlled by a fixed composition gas gap technique. Tensile tests were conducted in accordance with ASTM C1275 at room temperature under crosshead displacement control at 0.5 mm/min by using a faceloaded miniature specimen developed previously [12,13]. The gauge dimensions were 3 × 1.5 × 15 mm and the specimen machining involved surface grinding into fabric layers [10]. A 1.0 mm-thick aluminum tab was attached to each end of the rectangular specimens, and a

pair of 6.0 mm-length strain gauges were adhered in the center of gauge sections on both sides. Specimens were mounted in the test frame by connection of a wedge-type gripping system that was kept in the plastic bags during the test. Successful tests typically retained intact tab adhesion to the samples. In order to avoid fractional bending during the tests, both sides of the wedge fixture were fixed at 60 kN m equally using a torque driver. The detailed tensile setup is given elsewhere [7].

After the tensile tests, the fractured surfaces of the specimens were observed using an optical microscope and scanning electron microscope (SEM).

Ⅲ. Results

Fig. 1 exhibits typical tensile stress−strain curves of TySA and HNLS composites after neutron irradiation. The composites in all conditions exhibited quasi-ductile behaviors. There was an initial steeper linear region in the stress−strain curve, with a second, nearly linear region at higher strains during tensile loading with multiple unloading/reloading sequences. The initial linear portion corresponds to the linear elastic deformation of the composite, whereas the second linear portion corresponds to a process of progressive development and opening of the multiple matrix micro-cracks. Table 1 lists a summary of unirradiated and irradiated tensile properties: proportional limit stress (PLS), ultimate tensile stress (UTS) and elastic modulus (E) obtained from the tensile tests, and Fig. 2 shows the tensile properties after neutron irradiation. Both composites exhibited excellent irradiation resistance. Almost no degradation in PLS and UTS occurred under both irradiation conditions, and an increase of about 50% was measured in PLS of TySA composites irradiated to 12 dpa at 750 _C. In elastic modulus, a 15−20% decrease was obtained for both composites. Fig. 3 exhibits the maximum hysteresis loop width at each peak stress where rp is the transition stress from reloading to unloading. For both composites, the hysteresis loop width after irradiation up to 3.1 dpa became narrower than that of the unirradiated one. After neutron irradiation to 12 dpa, the hysteresis loop width of TySA composites remained narrower, while that of HNLS exhibited almost the same behavior as the unirradiated material. Fig. 4 exhibits typical fracture surfaces of composites observed by SEM. No significant change of fiber pull-out was observed for both composites after irradiation. Fiber pull-out in TySA composites were shorter than that in HNLS composites under all conditions.

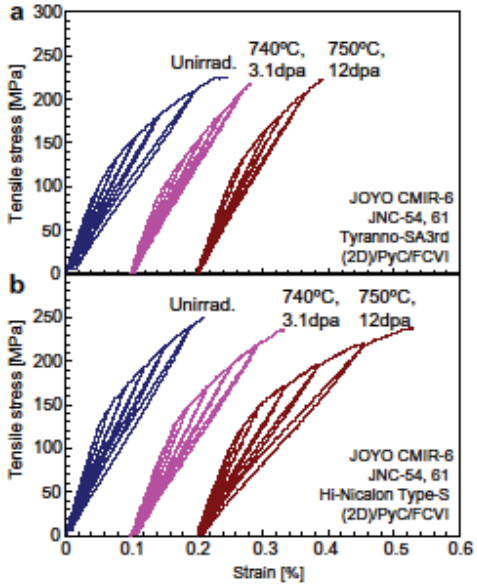

Fig. 1. Representative tensile stress−strain curves and hysteresis loops for (a) TySA (2D)/PyC/FCVI, (b) HNLS (2D)/PyC/FCVI composites after neutron irradiation.

Table 1
Summary of unirradiated and irradiated tensile properties

ID	Irradiation condition	*E* (GPa)	PLS (MPa)	UTS (MPa)	Number of test
#1266	Unirrad.	257 (32)	76 (31)	218 (18)	6
	740 °C, 3.1 dpa	216 (11)	80 (9)	241 (30)	3
	750 °C, 12 dpa	198 (19)	112 (12)	209 (11)	3
#1272	Unirrad.	253 (25)	98 (17)	227 (27)	10
	740 °C, 3.1 dpa	222 (33)	107 (9)	210 (18)	3
	750 °C, 12 dpa	200 (5)	100 (18)	220 (16)	4

Numbers in parenthesis show standard deviations. #1266, TySA (2D)/PyC/FCVI; #1272, HNLS (2D)/PyC/FCVI; *E*, tensile elastic modulus; PLS, proportional limit stress; UTS, ultimate tensile strength.

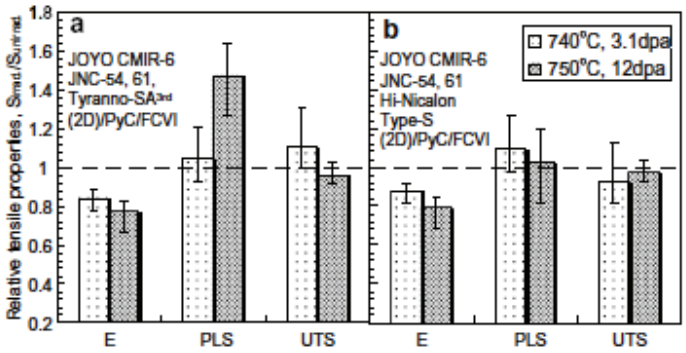

Fig. 2. Ratio of irradiated to unirradiated tensile properties of (a) TySA (2D)/PyC/FCVI, (b) HNLS (2D)/PyC/FCVI composites after neutron irradiation. Error bars show maximum and minimum.

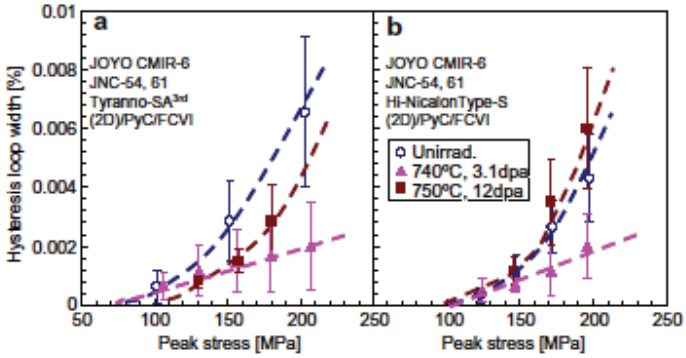

Fig. 3. Hysteresis loop width plotted against peak stress; (a) TySA (2D)/PyC/FCVI, (b) HNLS (2D)/PyC/FCVI composites. Error bars show standard deviation.

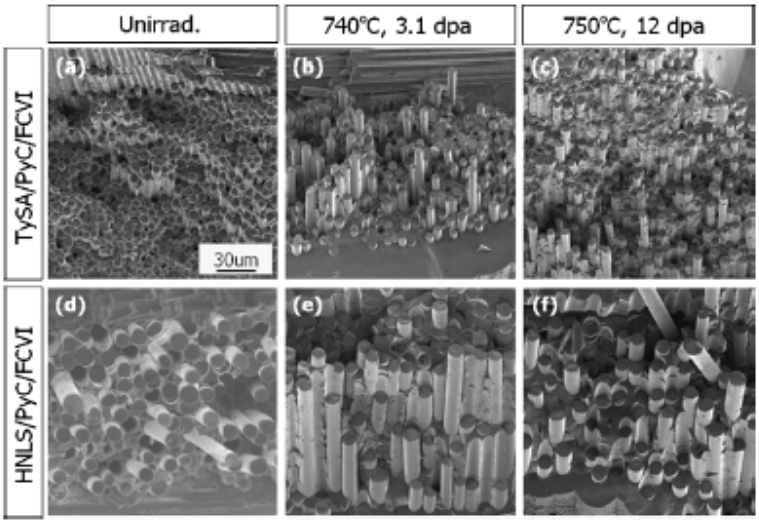

Fig. 4. Typical fracture surfaces of unirradiated and neutron-irradiated tensile specimens; (a) unirradiated, (b) 740 °C, 3.1 dpa and (c) 750 °C, 12 dpa for TySA (2D)/PyC/FCVI, and (d) unirradiated, (e) 740 °C, 3.1 dpa and (f) 750 °C, 12 dpa for HNLS (2D)/PyC/FCVI.

Ⅳ. Discussion

Both composites irradiated to 3.1 dpa at 740 °C exhibited narrower hysteresis loop widths, a slightly steeper slope in the second linear portion of the curve and nearly unchanged fiber pull-out length, all of which imply retaining or increasing of interfacial sliding stress.

For further investigation of interfacial properties, the method of unloading/reloading hysteresis loop analysis methodology proposed by Vagaggini, Domergue and Evance was applied [14–17]. In this analysis, the inelastic strain index, which is the most important parameter for estimating interfacial properties, and Young's modulus of the material with matrix cracks were obtained from values of the inverse tangent moduli of reloading tensile stress–strain curves at different peak stress. A detailed description of this analysis method for 2D composites is found elsewhere [17].

The maximum hysteresis loop width (dmax) before and after irradiation is dependent on both interfacial sliding stress (s) and mean matrix crack spacing (_dT. The composites in all conditions met the large debond energy condition. For this condition, the maximum hysteresis loop width (dmax) is given by [14,17],

$$\delta_{\max} = 4\lambda\sigma_p^2\left(1-\frac{\sigma_i}{\sigma_p}\right)^2 = \frac{b_2(1-a_1 f)^2}{f^2\tau E_m}\frac{R}{d}\sigma_p^2\left(1-\frac{\sigma_i}{\sigma_p}\right)^2, \quad \text{for } \sigma_i/\sigma_p \cong 0.85, \qquad (1)$$

for ri=rp ffi 0:85; d1T where k is inelastic strain index, ri is 'debond' stress [14], Em is Young's modulus of matrix, R is fiber radius, f is fiber volume fraction, and a1 and b1 are the Hutchinson–Jensen parameters [18]. All the parameters except interfacial sliding stress and mean matrix crack spacing remain almost unchanged during irradiation. Unfortunately, the mean matrix crack spacing was not measured, so the interfacial sliding stress parameter t=t×d/R obtained from the inelastic strain index was used for this analysis. Thus, the evaluation of interfacial sliding stress parameter at the same matrix crack spacing (i.e. same matrix damage level) is required. The matrix damage parameter (D) is defined as [14],

$$D \equiv \frac{E-E^*}{E^*} = B\frac{R}{d}, \qquad (2)$$

where E is the elastic modulus of the composite, E* is Young's modulus of the composite with matrix cracks obtained from the reloading stress–strain curve, and B is a constant for particular composite. As shown in Eq. (2), the matrix damage parameter is inversely proportional to matrix crack spacing. Therefore, the interfacial sliding stress can be predicted using the interfacial sliding stress parameter obtained for the same matrix damage parameter.

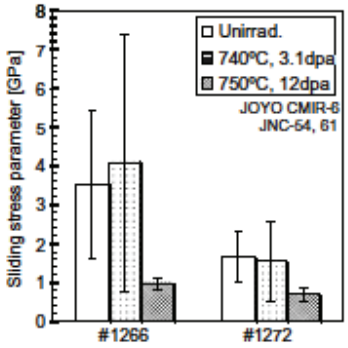

Fig. 5. Interfacial sliding stress parameters compared at similar matrix damage parameters for composite samples before and after neutron irradiation. #1266; TySA (2D)/PyC/FCVI, #1272; HNLS (2D)/PyC/FCVI. Error bars show standard deviation.

Fig. 5 exhibits the interfacial sliding stress parameter at approximately the same matrix damage parameter (D ffi 0.2). For both composites, the interfacial sliding stress parameter remained nearly constant after irradiation up to 3.1 dpa at 740 C, while the parameter decreased after irradiation up to 12 dpa at 750 °C. According to the work by Bokros et al. [19,20], the interfacial PyC is expected to shrink in both the a and c axis directions after neutron irradiation up to 2–3 × 10^{25} n/m^2 in the range of 520–690 °C.

However, it began to swell significantly in the c axis direction over ~10 × 10^{25} n/m^2 irradiation. This result might be correlated with the analysis of data in this study, but the details are unclear. Therefore, further research and SEM observations of crack propagation and TEM observation of the PyC interphase itself are required in order to understand the behavior of the interphase after neutron irradiation. Residual stress between the fiber and matrix may affect the tensile behavior of SiC/SiC composites, so the misfit stress rT was also estimated by hysteresis loop analysis. The conversion of misfit stress to residual stress components was carried out by the method discussed elsewhere [14]. At high peak stresses, the misfit stress was influenced by fiber roughness due to the damage of the PyC interphase during the test. Therefore, the misfit stress at a peak stress of 125–175 MPa was used for this evaluation. The result is: rT = +9 ± 6 MPa (unirradiated), +3 ± 3 MPa (3.1 dpa at 740 _C), +6 ± 2 MPa (12 dpa at 750 _C) for TySA composites, and +9 ± 5 MPa, +6 ± 5 MPa, +5 ± 3 MPa for HNLS composites. From these results, it appears that the misfit stress may not affect the tensile behavior of either composites under these irradiation conditions.

Ⅴ. Summary

In order to identify the effects of neutron irradiation on tensile properties of advanced SiC/SiC composites (Tyranno-SA3rd (2D)/PyC/FCVI and Hi-Nicalon Type-S (2D)/PyC/FCVI), unloading/ reloading cyclic tensile tests were conducted and hysteresis loop analysis was applied. Neutron fluence and irradiation temperature were 3.1×10^{25} n/m^2 (E > 0.1 MeV) and 1.2×10^{26} n/m^2 at 740−750 ^{o}C. The following results were obtained:

1. Both composites exhibited excellent irradiation resistance to changes in ultimate tensile strength and proportional limit stress. A slight reduction of elastic modulus was observed after irradiation.
2. Hysteresis loop analysis indicated that the sliding stress at fiber/matrix interfaces remained almost unchanged after irradiation to 3.1×10^{25} n/m^2 at 740 ^{o}C, whereas it was significantly reduced by 12×10^{25} n/m^2 at 750 ^{o}C for both composites.

Acknowledgements

This work was performed as a part of a corroboration at the Irradiation Experimental Facility, Institute for Materials Research, Tohoku University, Japan. Materials were supplied as part of the DOE/MEXT JUPITER-II Collaboration for Development of Advanced Blanket Performance under Irradiation and System Integration.

References

[1] Y. Katoh, L.L. Snead, C.H. Henager Jr., A. Hasegawa, A.Kohyama, B. Riccardi, H. Hegeman, J. Nucl. Mater., in press, doi:10.1016/j.jnucmat.2007.03.032.
[2] L.L. Snead, M.C. Osborne, R.A. Lowden, J. Strizak, R.J.Shinavski, K.L. More, W.S. Eatherly, J. Bailey, A.M. Williams, J. Nucl. Mater. 253 (1998) 20.
[3] G.W. Hollenberg, C.H. Henager Jr., G.E. Youngblood, D.J.Trimble, S.A. Simonson, G.A. Newsome, E. Lewis, J. Nucl.Mater. 219 (1995) 70.
[4] A.J. Frias Rebelo, H.W. Scholz, H. Kolbe, G.P. Tartagalia,P. Fenici, J. Nucl. Mater. 258−263 (1998) 1582.
[5] L.L. Snead, Y. Katoh, A. Kohyama, J.L. Bailey, N.L. Vaughn, R.A. Lowden, J. Nucl. Mater. 283−287 (2000) 551.
[6] T. Hinoki, L.L. Snead, Y. Katoh, A. Hasegawa, T. Nozawa,A. Kohyama, J. Nucl. Mater. 283−287 (2002) 1157.
[7] T. Nozawa, K. Ozawa, S. Kondo, T. Hinoki, L.L. Snead, A.Kohyama, J. ASTM Int. 2 (2005) 12884-1.
[8] K. Ozawa, T. Hinoki, T. Nozawa, Y. Katoh, Y. Maki, S.Kondo, S. Ikeda, A. Kohyama, Mater. Trans. 47 (2006) 207.
[9] Y. Katoh, T. Nozawa, L.L. Snead, T. Hinoki, J. Nucl. Mater., in press, doi:10.1016/j.jnucmat.2007.03.083.
[10] Y. Katoh, T. Nozawa, L.L. Snead, J. Am. Ceram. Soc. 88(2005) 3088.
[11] Y. Katoh, L.L. Snead, T. Hinoki, A. Kohyama, N. Igawa, T.Taguchi, Mater. Trans. 46 (2005) 527.
[12] T. Nozawa, Y. Katoh, A. Kohyama, E. Lara-Curzio, Ceram.Eng. Sci. Proc. 24 (2003) 415.
[13] T. Nozawa, E. Lara-Curzio, Y. Katoh, A. Kohyama, Ceram.Trans. 144 (2002) 245.
[14] E. Vagaggini, J.-M. Domergue, A.G. Evans, J. Am. Ceram.Soc. 78 (1995) 2709.
[15] A.G. Evans, J.-M. Domergue, E. Vagaggini, J. Am. Ceram.Soc. 77 (1994) 1425.
[16] J.-M. Domergue, E. Vagaggini, A.G. Evans, J. Am. Ceram.Soc. 78 (1995) 2721.
[17] J.-M. Domergue, F.E. Heredia, A.G. Evans, J. Am. Ceram.Soc. 79 (1996) 161.
[18] J.W. Hutchinson, H. Jensen, Mech. Mater. 9 (1990) 139.
[19] J.C. Bokros, G.L. Gthrie, R.W. Dunlap, A.S. Schwartz, J.Nucl. Mater. 31 (1969) 25.
[20] CEGA, Report CEGA-002820, Rev 1, July 1993.

Current status and critical issues for development of SiC composites for fusion applications

Y. Katoh [a,*], L.L. Snead [a], C.H. Henager Jr. [b], A. Hasegawa [c],
A. Kohyama [d], B. Riccardi [e], H. Hegeman [f]

a Oak Ridge National Laboratory, Materials Science and Technology Division, P.O. Box 2008, MS-6138, Oak Ridge, TN 37831-6138, USA
b Pacific Northwest National Laboratory, P.O. Box 999, Richland, WA 99352, USA
c Department of Quantum Science and Energy Engineering, Tohoku University, Sendai 980-8579, Japan
d Institute of Advanced Energy, Kyoto University, Kyoto 611-0011, Japan
e EFDA CSU Garching, Boltzmannstr. 2, 85748 Garching bei M€unchen, Germany
f NRG, P.O. Box 25, 1755 ZG Petten, The Netherlands

Silicon carbide (SiC)-based ceramic composites have been studied for fusion applications for more than a decade. The potential for these materials have been widely discussed and is now understood to be (1) the ability to operate in temperature regimes much higher than for metallic alloys, (2) an inherent low level of long-lived radioisotopes that reduces the radiological burden of the structure, and (3) perceived tolerance against neutron irradiation up to high temperatures. This paper reviews the recent progress in development, characterization, and irradiation effect studies for SiC composites for fusion energy applications. It also makes the case that SiC composites are progressing from the stage of potential viability and proof-of-principle to one where they are ready for system demonstration, i.e., for flow channel inserts in Pb–Li blankets. Finally, remaining general and specific technical issues for SiC composite development for fusion applications are identified.

Ⅰ.Introduction

Silicon carbide (SiC) is a unique heat-resistant material that exhibits several attractive properties such as high strength at elevated temperatures in excess of 1500 ºC, general chemical inertness, low specific mass, and low coefficient of thermal expansion. Continuous SiC fiber-reinforced SiC-matrix composites (SiC/SiC) are ceramic composites designed to have a pseudo-ductile and predictable fracture mode and tailorable physical and mechanical properties while taking advantage of most of the inherent merits of monolithic SiC. SiC/SiC have been studied and developed for decades because they are promising materials for high temperature applications such as gas turbines and aerospace propulsion systems. For fusion and advanced fission energy applications, additional interest in SiC and SiC/SiC comes from the excellent irradiation performance, which was demonstrated during early studies on chemically vapor deposited (CVD) SiC for fission fuel coatings [1,2]. Furthermore, safety features arising from the inherent low activation/low decay heat properties [3,4] and low tritium permeability [5] for SiC have been demonstrated.

Recent development of SiC/SiC in the fusion materials community has been intended to address the key feasibility issues when using an essentially new class of materials [6–10]. Benefiting from nonnuclear programs that pursued issues such as manufacturing technology, testing development, and to a limited extent how to design structures from these materials, the fusion community was able to focus on fusion-specific issues. For this reason, the majority of resources in fusion materials programs have addressed the fundamental performance of SiC composites under irradiation along with simulation to define the effects of transmuted helium. Additionally, fusion specific design issues such as the need to develop a leak-tight component, the need for joining the materials with low-activation agents, and issues regarding coolant compatibility have been addressed during the last decade.

In this paper, the recent status for application development and the design requirements for using SiC/SiC in fusion and advanced fission energy systems are first reviewed briefly. The case is made that SiC/SiC development has progressed from the stage of potential viability and proof-of-principle to one where they are ready for system demonstration. In the following sections, recent progress in research and development of SiC/SiC in fusion materials and related programs, namely development of materials, joining, characterization, and irradiation effects studies, is overviewed. Finally, identification of the remaining critical issues, both for general fusion applications and specific to individual target systems, is attempted.

Ⅱ. Status of application development and design Requirements

Ⅱ.A.Proposed power reactor blanket concepts

Utilization of SiC/SiC for structural components in fusion power reactor blankets was proposed in the early

1990s [11−13]. Reasons for the proposed employment of SiC/SiC were the anticipated attractive energy cost competitiveness and favorable social receptivity associated with the high operating temperature and low activation. The proposed designs were based on self-cooled lead−lithium (SCLL) or helium-cooled ceramic breeder (HCCB) concepts. The latest SCLL conceptual designs, EU Power Plant Conceptual Study (PPCS) Model D [14] and the US ARIES-AT [15], assume the lowest/highest operating temperatures for SiC/SiC structures of ~700/~1000 ºC yielding a power conversion efficiency of _60% for the blanket circuit. For the HCCB concept, the Japanese DREAM assumes the inlet/outlet helium coolant temperatures of ~600/~900 ºC with a gross thermal efficiency of ~50% [13]. In Table 1, key properties assumed for SiC/SiC when used in structural or the flow channel insert (FCI) application are summarized and compared with typical values for two resently-available promising materials (2D and 3D CVI and NITE). General reviews of issues regarding blanket designs using SiC/SiC are given elsewhere [16,17]. Many of the assumed basic requirements are already satisfied or advanced to a substantial extent so that the design could rather be adjusted. Discussion of some of the individual properties will be provided in the later sections.

Table 1
Key properties for SiC/SiC assumed in blanket designs and typical values for CVI and NITE composites

Key properties (Unit)	Structure	FCI	2D CVI	3D CVI	NITE
Thermal conductivity, thru-thickness (W/m K)					
Non-irradiated, 500 °C	≳ 20	<2	~15	25–40	15–40
Non-irradiated, 1000 °C	≳ 20	n/a	~10	20–30	10–30
Irradiated, 500 °C	≳ 20	<2	2–3	5–8	–
Irradiated, 1000 °C	≳ 20	n/a	4–6	12–18	–
Electrical conductivity, thru-thickness (S/m)					
Non-irradiated, 500–1000 °C	≲500	≲100	0.1–1000	–	–
Irradiated, 500–1000 °C	≲500	≲100	–	–	–
Tensile properties, in-plane					
Ultimate tensile stress, 500–1000 °C (MPa)	300	n/s	250–350	100–200	300–400
Matrix cracking stress, 500–1000 °C (MPa)	n/s	≳ 100	~150	–	200–250
Modulus, 500–1000 °C (GPa)	200–300	200–300	~250	~200	300–400

n/a: Not applicable; n/s: Not specified; –: Data not available.

Ⅱ.B. Flow channel insert application

The use of SiC/SiC as the insert for a lead−lithium flow channel was proposed initially in the EU advanced lead−lithium blanket concept [18] and the US ARIES-ST blanket design [19]. In this application, an FCI serves as an electrical and thermal insulator in order to mitigate the MHD pressure drop and to allow a significantly higher coolant outlet temperature compared to the temperature limit for the metallic duct structure. The dual-cooled lead−lithium blanket concept (DCLL) has been adopted for the proposed US test blanket module (TBM) and Chinese late-stage TBM to be inserted in the International Thermonuclear Experimental Reactor (ITER) [20]. The design inlet/outlet lead− lithium temperatures for the EU PPCS Model C DCLL blanket are 480/700 _C. This outlet temperature of 700 _C approximately corresponds to the inside temperatures for the FCI, whereas the outside temperature will be [500 ºC [21].

Ⅱ.C. Interaction with fission material programs

Programs considering potential utilization of SiC/SiC for core and/or in-vessel components in advanced fission energy systems have been initiated during the last few years. These programs are associated with the effort for Generation IV (Gen IV) Nuclear Power Plants, which is internationally coordinated by the Generation IV International Forum (GIF). In the US, the use of SiC/SiC is considered as an option for control rod sleeves in a very high temperature reactor (VHTR)/next generation nuclear power (NGNP). This option is based primarily on the promise of SiC/SiC demonstrated by the fusion materials program [22].

The US NGNP composite program assumes the fundamental viability of chemically vapor infiltrated (CVI) SiC/SiC in a fission neutron environment, and focuses on (1) confirmative feasibility issues which include irradiation effects and fabrication of desired shapes and sizes, (2) key technical issues governing the life-time envelope such as time-dependent fracture and

irradiation creep, and (3) providing support to test standards and design code development in the frameworks of ASTM International, International Organization for Standardization (ISO), and American Society of Mechanical Engineers (ASME). Similar efforts are on-going or planned in several countries including France and Japan. A common feature in these programs is that addressing the application-specific issues is targeted based on the perceived potential of SiC/SiC as a radiation-resistant high-temperature nuclear material.

SiC and SiC/SiC are also being considered as the primary candidate materials for fuel cladding and core structures in a gas-cooled fast reactor (GFR), which is one of the six Gen IV concepts. The GFR concept features a fast-neutron spectrum, a helium cooled reactor and a closed fuel cycle [23]. General feasibility issues still exist for SiC/SiC used in a GFR application, i.e., the effect of very high fluence neutron irradiation at temperatures ranging to largely beyond 1000°C, as well as issues which overlap those for fusion power reactor applications.

Ⅲ. Status of material development and Characterization

Ⅲ.A. CVI composites

For nuclear environments, SiC/SiC made from stoichiometric, high purity, and fully crystalline SiC fibers and matrices are preferred for the harshest conditions [24]. This is because of the demonstrated radiation instability of common matrix second phases such as metallic silicon in the reaction-bonded matrices [25], sintering agent represented by boron in hot-pressed SiC [26], and the amorphous Si−C−O commonly obtained through preceramic polymer routes [27]. Therefore, CVI, which essentially imparts CVD-SiC into a SiC fiber fabric, is an obvious selection of the matrix densification technique for fusion reference grade SiC/SiC [28,29].

Early Generation III (near-stoichiometric and crystalline) SiC fiber, CVI-SiC matrix composites were produced in US − Japan collaboration in 1998 and subjected to a neutron irradiation campaign [30]. Hi-NicalonTM Type S (‘Nicalon-S’ hereafter) and TyrannoTM-SA fibers were used and various fiber − matrix interfacial phases (‘interphases’ hereafter) including pyrolytic carbon (PyC) and SiC-based interphases, were examined. Uni-directional (UD) reinforcement architecture was employed for investigation of fundamental aspects of interfacial properties and irradiation effects. Non-irradiated and low dose (_1 × 10^{25} n/m^2, E > 0.1 MeV, the same shall apply hearafter) irradiation experiments demonstrated the promise of PyC and multilayered (ML) (PyC/SiC)n interphases [30 − 32]. The results for higher dose irradiation are discussed later in this review.

Optimum interphase structure and configurations for the advanced CVI composites were then explored. Nicalon-S and Tyranno-SA Grade-3 (SA3) composites with various PyC and ML interphases were fabricated using the forced-flow CVI (F-CVI) technique and evaluated [33−35]. The important finding was the general lack of sensitivity of mechanical properties on PyC interphase thickness for the both SiC fiber composites [34,35]. As seen in Fig. 1, the SA3 composites lacked the steep strength drop at very thin interphase, which is commonly observed for SiC/SiC with older generation fibers. These results show that the interphase can be designed for the optimum radiation and environmental compatibility without compromising the fast fracture strength.

For blanket materials, a high through-thickness thermal conductivity is required to reduce thermal stress. To identify the practical limit and to explore the possibility of further improvement of SiC/SiC thermal conductivity, CVI composites with threedimensional (3D) fabric architectures with various through-thickness (z) fiber fractions were recently produced and evaluated. A study on orthogonal 3D CVI composites with SA3 reinforcement [36] demonstrated that the presence of z-tows enables higher through-thickness conductivity, because the matrix shells around the tows carry a major fraction of heat. The maximum of the thermal stress figure of merit appeared to occur at relatively small z-fiber fractions [36−38]. Model-based predictive capability for temperature-dependent conductivity of 2D and 3D CVI SiC/SiC has been demonstrated [36,39]. Irradiated thermal conductivity of SiC/SiC willbe limited by the irradiation defect accumulation, which is determined primarily by the irradiation temperature [40,41]. Raising thermal conductivity beyond such limits obviously requires incorporation of very high thermal conductivity media [42]. To examine this possibility, 2D and 3D CVI SiC/SiC ’ s supplemented with pitch-based P-120S graphite fibers were produced and evaluated. These ‘hybrid fabric’ composites demonstrated limited promise, since the CTE (coefficient of thermal expansion) mismatch introduced fine micro-cracks in the SiC matrices surrounding the graphite fibers [43]. The concept requires an improved architectural design, perhaps properly adjusting the hybrid fabric configurations so that the matrix micro-cracking can be suppressed.In the EU program, manufacturing and extensive characterization of commercial grade 2D and 3D SA3, CVI SiC matrix composites has been pursued [44,45]. The composites were made with a singlelayered PyC interphase of _80 nm-thickness and were optimized mainly for thermal conductivity.

The 3D composites demonstrated reasonable through-thickness thermal conductivity (reaching ~18 W/m K at 1000 °C) [45]. Low cycle fatigueproperties were

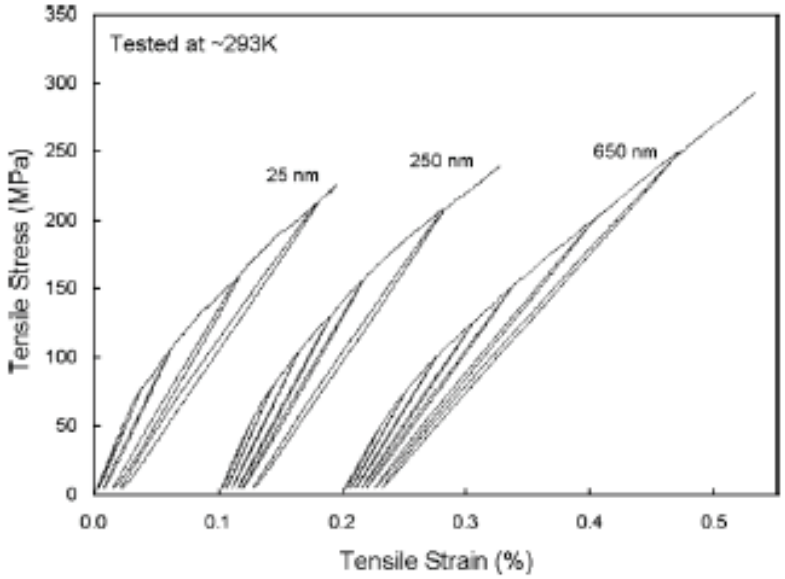

Fig. 1. The influence of carbon interphase thickness (shown in data labels) on tensile properties of TyrannoTM-SA3 CVI SiC/SiC. The similarity of the stress−strain curves indicate a general insensitivity of composite strength on interphase thickness.

investigated by 4-point flexural tests and showed satisfactory results at RT and 1000 °C in argon. The creep behavior, investigated by constant stress rupture test in a flexural configuration, exhibited a short lifetime at high stress with runouts only at approximately half of the room temperature proportional limit stress [44]. The high temperature test results suggest the necessity of further R&D on fiber−matrix interphase and oxidative protection at elevated temperatures.

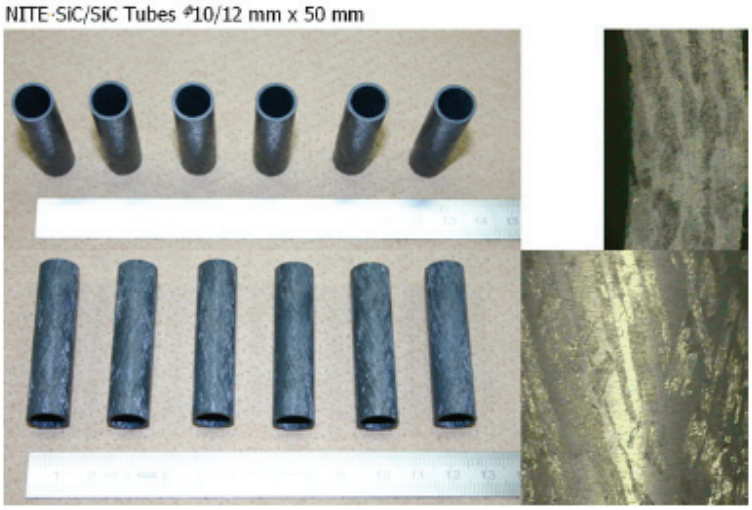

Fig. 2. Small diameter tubes of third generation pilot commercial grade (PG3) NITE SiC/SiC produced through the pseudo-isostatic hotpress technique.

Ⅲ.B. NITE composites

The nano-infiltration and transient eutecticphase (NITE) process was developed by employing a liquid phase sintering (LPS) method utilizing a small amount of oxide additives. The development and fundamental characterization of the early NITE SiC/SiC are summarized elsewhere [46,47]. Based on achievement by the laboratory grade development, pilot commercial grade (PG) production was recently initiated [48]. During the PG productions, several process improvements were achieved. Near net-shaping techniques for NITE SiC/SiC have also been improved [48]. Small diameter (10 mm ID) tubes were successfully fabricated with the fiber angle of $\pm 15^{o}$ and $\pm 30^{o}$ (Fig. 2). The highest density of the tubes was 3.02 g/cm3, which is close to 3.08 g/cm3 attained for the PG3 plates. The average diametral ring compression strength was 108 MPa. Also 200 mm diameter GFR fuel compartment cylinders were produced with a wall thickness of 3 mm. These cylinders were successfully engineered to possess 5−40% through-wall porosity.

A limited neutron irradiation data has been acquired for NITE SiC/SiC. The PG1 composite was irradiated in high flux isotope reactor (HFIR) at Oak Ridge National Laboratory (ORNL) to 4.2×10^{25} n/m^2 at 1000 ^{o}C. The observed mechanical and dimensional stability suggested decent irradiation tolerance of the matrix material [49]. Also, flexural strength of the NITE matrix material, in the form of a monolithic ceramic, was statistically evaluated after irradiation to 6×10^{24} n/m^2 at 750 ^{o}C in Japan Materials Test Reactor (JMTR), and exhibited no major strength degradation [49]. Remaining critical issues in the NITE SiC/SiC development include improved control of matrix quality, stability of the matrix second phases at high temperatures, creep and oxidative resistance associated with the potentially enhanced oxygen transport due to the sintering additives, and radiation stability to higher doses.

Ⅲ.C. Other matrix densification processes

Other matrix densification techniques historically considered for nuclear applications are polymer impregnation and pyrolysis (PIP) and variations of direct conversion processes represented by melt infiltration (MI). Either technique is not presently attracting much attention for nuclear applications due to the recognized significant challenges [50,51]. However, for PIP, it was suggested that enhanced matrix crystallization and improved stoichiometry could be attained using a very high temperature treatment and novel polymer precursors [50,52]. Primary issue identified for high-crystallinity PIP composites was a loss of matrix integrity due to severe micro-cracking [53].

This problem may possibly be overcome by employing precursors which shrink two-dimensionally into films surrounding fibers, instead of being severely cracked three-dimensionally upon ceramization.

As for the MI, a fine-tuned ‘reaction-sintering (RS)’ technique was developed to produce monolithic SiC with a minimal amount of unreacted silicon finely distributed as a scattered second phase [54]. The problem for conventional MI-SiC was its high temperature and irradiation instability due to the networked silicon [51]. A Nicalon-S composite with the fine-tuned RS matrix was produced and irradiated in HFIR. The composite, irradiated to 7.7×10^{25} n/m^2 at 800 ^{o}C, exhibited flexural strength of 244 ± 18 MPa, which was ~23% reduction from its non-irradiated value of 316 ± 22 MPa. These results imply further reduction of unreacted silicon and microstructural control are required to improve the irradiation stability of RS SiC/SiC.

Ⅲ.D. Advanced characterization and interphase design

For the advanced characterization of the fiber/matrix interfacial properties, a modified non-linear shear−lag model was developed [55]. Combined with the single fiber push-out experiment, the model was applied to determine the interfacial properties of Nicalon-S CVI composites with PyC and ML interphases. Neutron irradiation effects were investigated in detail. No systematic changes of the interfacial shear properties for the PyC interphase were found, in contrast, a decreased frictional stress was confirmed for the ML interphase. However, sufficient friction after irradiation to 7.7×10^{25} n/m^2 at 800 ^{o}C was retained, thus demonstrating relatively good radiation stability for this ML composite. Furthermore, a significant reduction in interfacial friction caused the modification of interfacial crack path. Knowledge obtained through these characterization works will be useful for designing radiationresistant interphases.

Ⅲ.E. Slow crack growth

Understanding and predicting time-dependent deformation processes, both thermal and radiation-induced, is an important consideration for structural materials. These time-dependent processes typically occur by slow crack growth in SiC/SiC. The matrix cracks propagate due to the time-dependent elongation of crack-bridging fibers because the fibers carry the highest stresses as they bridge across cracks. Previous studies have indicated that bridged matrix cracks grow via fiber creep processes [56,57]. This is true for composite specimens when creep of the SiC matrix can be ignored. Other time-dependent deformation behaviors result when environmental interactions with the fiber/matrix interface dominate [58]. Introduction of improved SiC fibers has

resulted in SiC/SiC with increased slow crack growth resistance.

Accordingly, SiC/SiC with Nicalon-S fibers were tested in bending as single-edge notched bars or as compact tension specimens [59]. Several constant stress, 4-point bend tests were performed to induce slow crack growth in unirradiated materials in high purity argon (Fig. 3). The sample tested at 1300 ^{o}C failed during the test but the other specimens were removed intact from the test. Optical microscopy indicated that the cracks were growing under a Mode-I crack opening mode and can be considered as classic examples of bridged cracks. Based on the similar response of the composite to single fiber thermal creep, it was concluded that slow crack growth of SiC/SiC made with Nicalon-S fiber is controlled by fiber creep in bridged cracks. Although Nicalon-S fiber is more thermal creep resistant compared to the previous generation SiC fibers, an upper temperature limit for its longterm use in a composite material subjected to moderate stresses is still <1300 ^{o}C. Importantly, further tests will be needed to include radiation-induced fiber creep together with any other environmental effects. Efforts are currently underway to model slow crack growth behavior for these other conditions.

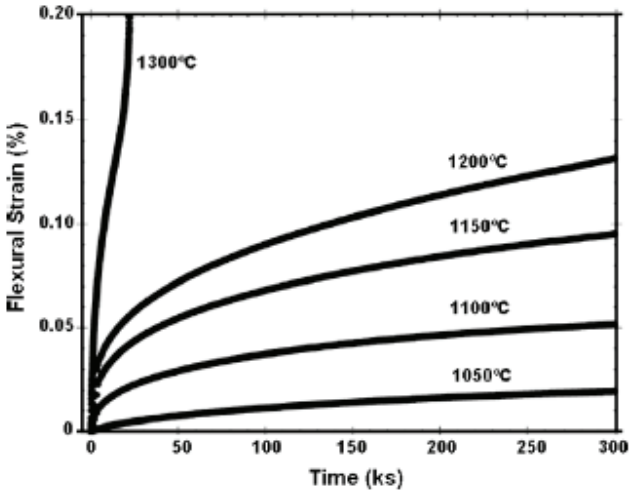

Fig. 3. Slow crack growth data for Hi-NicalonTM Type-S CVI SiC/SiC as a function of test temperature in argon under a constant applied stress of 260 MPa.

Ⅲ.F. Joining

A reliable technique of joining must be developed to use SiC/SiC as a primary structure. Joining technologies, including those through the preceramic polymer, direct reaction, and eutectic alloy routes, were overviewed previously [9]. Although recent efforts on joining development for fusion applications are rather limited, steady progress has been achieved. For instance, considering the polymer route, application of polyhydromethylsiloxane (PHMS) was shown to provide a flexible polymer chemistry and high ceramic yield [60]. Initial work demonstrated that PHMS systems with appropriate filler materials for joining SiC, particularly as a field repair technology, were viable. The NITE SiC/SiC matrix processing technique was also applied for SiC joining [61]. The ‘NITE Joint’ demonstrated tensile strengths in excess of 200 MPa, however, the joining process requires pressurization at high temperatures in a controlled environment. In addition, mechanical fastening of NITE SiC/SiC using screw-threaded tubes and manifolds was successfully demonstrated.

Ⅲ.G. Pb−Li Compatibility

To compliment prior SiC/Pb−17Li compatibility work [62,63], a series of static capsule tests was performed on high-purity CVD b-SiC specimens by Pint et al. [64]. Studying monolithic SiC avoids SiC/SiC composites processing issues, such as fiber interfaces and porosity. Initial 1000 h exposures at 800 ^{o}C and 1100 ^{o}C showed no mass change and no increase in the Si content (30 ppma detection limit) of the Pb−Li. Subsequent experiments were conducted at longer times and higher temperatures. After 5000 h at 800 _C, no increase in the Si content was measured. However, after 2000 h at 1100 ^{o}C and 1000 h at 1200 ^{o}C, increased levels of Si were detected in the Pb−Li (185 and 370 ppma, respectively) [65]. Based on these results, the maximum use temperature of SiC composites in Pb−Li appears to be [1100 ^{o}C. To fully determine the compatibility of these materials, future work will need to include testing in a flowing system with a thermal gradient.

Ⅲ.H. Hermetic behavior

Hermeticity is a major issue for first wall and blanket structure applications that require a pressure boundary and/or gas or fluid containment. A hermetic seal coating likely will be required for such applications, because the matrix micro-cracks, existing more or less in the as-fabricated CVI, PIP or MI SiC/SiC, cause unacceptable gas leak rates for the high pressure helium containment. For the PG3 NITE SiC/SiC, helium gas permeability was recently measured to be on the order of 10^{-10} m^2/s at room temperature [66]. It remained on the same order after unloading from tensile loading in excess of the matrix cracking stress, which indicates that the closed matrix micro-cracks do not significantly deteriorate hermeticity in this order. The helium permeability for the matrix micro-cracked PG3 NITE SiC/SiC was >3 orders smaller than that for typical as-produced MI SiC/SiC.

Ⅳ. Irradiation effects studies

IV.A.Radiation damage processes and microstructures

Substantial progress has been achieved in understanding the irradiation-induced microstructural evolution in b-SiC at elevated temperatures by neutron and self ion irradiations. The evolutions of various radiation defects (including tiny clusters, dislocation loops, network dislocations, and cavities) were mapped as a function of irradiation temperature and fluence [67]. The formation of black spot defects and small dislocation loops were shown to dominate at relatively low temperatures ([800°C], whereas these defects grow into Frank faulted loops and finally develop into dislocation networks at a higher temperature (1400°C). This radiation damage process is similar to that for FCC metals with low stacking fault energy [68]. During self ion irradiation, cavity formation on grain boundaries and stacking faults was observed at >1000 °C and became very significant at >1400 °C [69].

Ⅳ.B. Strength of composites

The effect of neutron irradiation on strength of SiC/SiC has long been evaluated by flexural tests due to the lack of more relevant test techniques [30,70]. Primarily for studying the neutron irradiation effects, small specimen test techniques (SSTT's) for room and elevated temperature tensile properties [71], in-plane shear strength [72], and transthickness tensile strength [73] have been developed in fusion SiC/SiC programs. Reliable tensile properties were obtained using specimens with typical dimensions of $40 \times 4 \times 2$ mm^3 whereas the conventional tensile tests typically require >10 times larger specimen volume. Tensile tests are preferred over flexural tests because they provide more design-relevant property data as well as additional information such as ultimate tensile stress (UTS), strain at load maximum and fracture, interfacial friction, and residual stress [74].

Several Nicalon-S, PyC interphase, UD CVI composites irradiated in HFIR and JMTR were evaluated using the developed tensile test [32,75]. In the HFIR experiment, strength retention of Nicalon-S CVI composites after neutron irradiation to 7.7×10^{25} n/m^2 at 800 °C was confirmed. The flexural tests only indicated a general lack of either the composite proportional limit stress (PLS) or the severe fiber tensile strength reduction, whereas the tensile tests reveal more detailed information such as the fact that the composite UTS slightly increases while other properties such as PLS and modulus do not significantly degrade after irradiation. Moreover, the detailed analysis on the loading－unloading behavior provides insight into the interfacial shear properties and the residual stress. The results for an identical material irradiated in JMTR to at 1-2 $\times 10^{25}$ n/m^2 at 800 and 1000 °C indicated similar tensile properties as that for a higher dose and 800 °C [32]. The major differences observed in non-linear behavior are due to the mitigation of residual stress by irradiation creep. Several 2D Nicalon-S and SA3, PyC interphase, CVI composites were irradiated in JOYO fast breeder reactor (Japan Atomic Energy Agency, Oarai, Japan) up to a relatively high dose of 1.2×10^{26} n/m^2 at 750 °C [76]. In Fig. 4, representative stress−strain curves are shown. The test results indicated no statistically significant changes in tensile properties for composites with either type of fibers, which confirms that SA3 composites also are radiation-stable. Up to this dose range, tensile hysteresis analysis and fractography implied no major degradation in interfacial frictional stress. However, as a major degradation of graphite strength is expected to take place at about this dose level, irradiation to even higher doses will be essential to determine the very high dose effect on the composite strength.

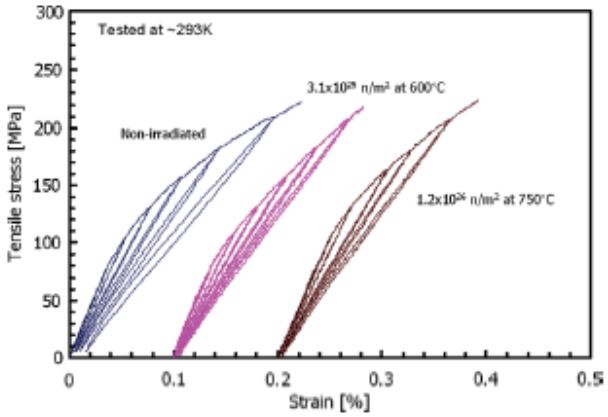

Fig. 4. Tensile stress−strain relationships for 2D TyrannoTM-SA3 CVI SiC/SiC non-irradiated and irradiated to 1.5 × 10^{26} n/m^2 (E > 0.1 MeV) at 750 °C.

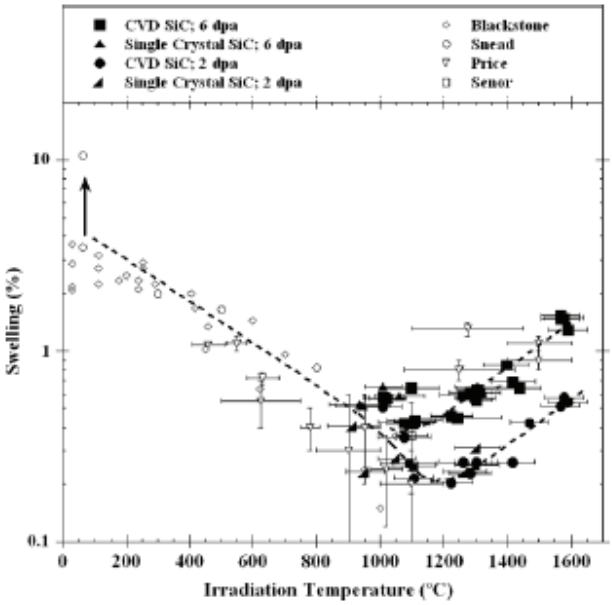

Fig. 5. Volumetric swelling of fission reactor irradiated high-purity SiC to 1600 °C.

Ⅳ.C. Swelling and thermal conductivity

Past examinations of SiC swelling for irradiation temperatures >1000 °C are limited and suffered from the technical difficulty of determining irradiation temperature [77 − 79]. Recent detailed work by Snead et al. [80] examined swelling in high purity CVD and monocrystalline SiC over the 900−1600 °C irradiation temperature range for doses up to ~1 × 10^{26} n/m^2. Fig. 5 shows the swelling results from this study along with various historical data. Of note is that the swelling at 1100−1300 °C appears not to saturate, increasing from ~0.2% to ~0.5% as the dose increases from 2 to 6 × 10^{25} n/m^2. Moreover, swelling is seen to increase with increasing irradiation temperature for T J 1100 °C. At ~6 × 10^{25} n/m^2 the maximum swelling is ~1.5% at ~1580 °C. The peak temperature for void swelling may be at or above 1580 °C. In the same paper, the authors correlate new data on swelling with the room temperature thermal conductivity for SiC irradiated at high temperatures as well as for material irradiated in the 200−800 °C range. As the irradiation temperature increases above 1000 °C, the as irradiated conductivity also increases. The non-irradiated room temperature thermal conductivity ~330 W/m K decreased to ~25 W/m K for CVD SiC irradiated at _800 °C to saturation. For CVD SiC irradiated at ~1595 °C, the thermal conductivity was ~110 W/m K. The thermal conductivity and swelling data for CVD SiC irradiated from 200 to 1600 °C were examined using the thermal defect resistance approach [40]. A clear, linear

correlation is observed between the swelling and the thermal defect resistance in the irradiation temperature range from 200 to 800 °C. This clear correlation between the defect swelling (generally attributed to point defects and small clusters at these low temperatures) and the vacancy defects (which dominate the phonon scattering) suggests that the room temperature thermal conductivity can be estimated from a simple swelling measurement. The linear relationship between the thermal defect resistance and swelling breaks down for irradiation temperatures >1200 °C, which indicates that void swelling becomes dominant and that these defects are less effective as phonon scatters. The capability of predicting anisotropic thermal conductivity for SiC/SiC composite with any given reinforcement architecture was developed based on the thermal defect resistance model [40] and constitutive models of the composites' transport properties [81,82]. The comprehensive models are able to predict the composites' thermal conductivity at various combinations of irradiation temperature, dose, and test temperature, with appropriately calibrated thermal resistance data for as-grown and irradiation-induced defects [36]. Meanwhile, further understanding of the physics of production, accumulation, and phonon-interaction of irradiation defects in SiC would greatly improve the quality of models.

Ⅳ.D. Irradiation creep

For estimating the neutron irradiation creep of SiC and SiC/SiC, bend stress relaxation (BSR) technique was applied [83] to an irradiation experiment. In this experiment, thin strip samples were bent at constant strain and irradiated in HFIR and JMTR at 400−1030 °C [84]. Irradiation creep strain at <0.7 dpa exhibited only a weak dependence on irradiation temperature. However, the creep strain dependence on fluence was non-linear due to the early domination of the initial transient creep, and a transition in creep behavior was likely between ~950 and ~1080 °C. Steady-state irradiation creep compliances of CVD SiC at doses >0.7 dpa were estimated to be $2.7(\pm2.6) \times 10^{-7}$ and $1.5(\pm0.8) \times 10^{-6}$ (MPa dpa)~1 at ~600 – ~950 °C and ~1080 °C, respectively, whereas linear-averaged creep compliances of $1-2 \times 10^{-6}$ (MPa dpa) were obtained for doses of 0.6 – 0.7 dpa at all temperatures. The larger irradiation creep compliances previously reported are attributed to the domination by transient creep component [85]. This work is ongoing, and further results will be presented as they become available.

Ⅴ. Other critical issues

Ⅴ.A. FCI-specific issues

For flow channel insert (FCI), low electrical and thermal conductivities are the primary requirements to lower MHD pressure drop and to maintain modest temperature at the ferritic steel/Pb – Li boundary [86]. However, optimum ranges for electrical and thermal conductivities are not only dependent on various blanket design parameters but also inter-related each other. For example, some preliminary evaluation suggest upper limits for electrical and thermal conductivity of ~100 S/m and <2 W/m K, respectively, for the 5 mm-thick FCI wall in US DCLL TBM [87]. Likewise, irradiation effects on the transport properties must be considered. Other issues for SiC/SiC FCI include: (1) chemical compatibility with lead−lithium in a flow system with strong temperature gradients, (2) hermeticity against lead−lithium, and (3) secondary stresses due to thermal expansion and differential swelling in the presence of strong trans-thickness temperature gradient [20]. Requirement for SiC/SiC for FCI application and typical values for presently available composites are summarized in Table 1. For the FCI application beyond ITER TBM, major technical issues added will be related with high fluence neutron loading and higher operating temperatures.

Ⅴ.B. He/H effects in irradiated SiC

Relatively extensive production of helium and hydrogen occurs in SiC as a result of nuclear trans-mutation due to fusion neutrons. Calculation by Sawan and El-Guebaly indicates production ratios of 80 – 170 appmHe/dpa and 30 – 70 appmH/dpa at the FW peak radiation regions for various blanket concepts [88]. The helium effect is important because helium interacts with the radiation defects and impurities, and consequently, may alter various irradiation effects on physical or mechanical properties.

Helium/hydrogen effects have been studied mostly by means of dual/triple beam ion irradiation experiments and TEM. Helium effect on swelling was reported [89], and later the enhanced void production in the presence of helium was confirmed [69]. In fact, bubble production in dual/triple-ion irradiated SiC was confirmed at >1000 °C, whereas temperature of >1300 °C was required to produce voids in irradiated, nearly helium-free SiC. Little difference between Si/He dual-beam and Si/He/H triple-beam has been observed [90]. Recently, interesting dislocation−helium interactions were examined by a dual-ion experiment. The presence of helium promotes Frank loop production and dislocations network development, which in turn promotes long-range transport of helium

along the dislocation network at 1400 ^{o}C [68]. Although much progress has been made, because in SiC the production of helium and hydrogen in the fusion environment is considerable, further investigations of helium/hydrogen effects are needed.

Ⅴ.C. Solid transmutation, burn-out/burn-in

In SiC-based materials, transmutations other than helium/hydrogen production also are remaining as major issues for fusion (e.g., non-stoichiometric burn-out of SiC and burn-in of impurities including Al, Mg, Li, Be, and P [9,88]). A small amount of impurity burn-in may cause a drastic change in electrical resistivity, hence a major consideration for the FCI application. Accumulation of burn-out and impurity burn-in may cause significant changes in other critical properties; e.g., solid solution Al is known to degrade oxygen corrosion resistance of SiC. General issues related with the solid transmutation were briefly overviewed previously [9]. A most appropriate tool for studying transmutation would be a 14 MeV neutron source with sufficient dose. However, fundamental understanding may also be acquired by ion implantation experiments.

Ⅵ. Conclusions

The recent status and the critical issues for SiC/SiC research and development for fusion applications, such as for use as a blanket structure in a fusion power reactor and also for relatively nearterm application in ITER TBM, were reviewed. Advanced (Generation III) SiC fiber, CVI SiC matrix composites have been evaluated as the current reference materials. Various interphase configurations and reinforcement architectures have been studied for improved radiation stability, strength, and thermal conductivity. Advanced characterization tests, including fiber/matrix interfacial friction and time-dependent deformation, have been developed. Baseline property characterization and low dose irradiation studies were completed for PG3 NITE SiC/SiC, as a promising alternate material. Some of the previously identified critical issues for SiC/SiC for fusion applications were addressed. Importantly, after tensile evaluation of CVI composites, no significant degradation of strength properties was observed for composites up to a relatively high dose of 1.2×10^{26} n/m^2. However, potentially significant void swelling in CVD SiC at >~1100 ^{o}C was implied. On the other hand, encouraging irradiation creep resistance at 600−1100 ^{o}C was indicated. Models for prediction of the thermal conductivity for irradiated CVI SiC/SiC have been developed. Also, understanding of the fundamental radiation damage processes and microstructural evolution in high purity SiC has been advanced substantially. However, further work will be required for a definitive understanding of irradiation-effects for various forms of SiC and SiC/SiC and the operating physical mechanisms. Nuclear transmutation remains as a critical issue. Finally, issues with respect to specific applications, such as for an FCI, were introduced, and other issues will arise as specific designs are developed.

References

[1] R.J. Price, J. Nucl. Mater. 33 (1969) 17.
[2] R.J. Price, Nucl. Technol. 35 (1977) 320.
[3] H.L. Heinisch, Fusion Mater., DOE/ER-0313/18, 1995, 91−96.
[4] T. Noda, M. Fujita, H. Araki, A. Kohyama, Fusion Eng. Des. 61&62 (2002) 711.
[5] R.A. Causey, W.R. Wampler, J. Nucl. Mater. 220−222 (1995) 823.
[6] L.L. Snead, R.H. Jones, A. Kohyama, P. Fenici, J. Nucl.Mater. 233−237 (1996) 26.
[7] P. Fenici, A.J. Frias Rebelo, R.H. Jones, A. Kohyama, L.L.Snead, J. Nucl. Mater. 258−263 (1998) 215.
[8] A. Hasegawa, A. Kohyama, R.H. Jones, L.L. Snead, B. Riccardi, P. Fenici, J. Nucl. Mater. 283−287 (2000) 128.
[9] R.H. Jones, L. Giancarli, A. Hasegawa, Y. Katoh, A. Kohyama, B. Riccardi, L.L. Snead, W.J. Weber, J. Nucl. Mater. 307 (2002) 1057.
[10] B. Riccardi, L. Giancarli, A. Hasegawa, Y. Katoh, A. Kohyama, R.H. Jones, L.L. Snead, J. Nucl. Mater. 329−333(2004) 56.
[11] S. Sharafat, F. Najmabadi, C.P.C. Wong, T.A. Team, Fusion Eng. Des. 18 (1991) 215.
[12] A.S. Perez Ramirez, A. Caso, L. Giancarli, N. Le Bars, G.
Chaumat, J.F. Salavy, J. Szczepanski, J. Nucl. Mater. 233−237 (1996) 1257.
[13] S. Nishio, S. Ueda, I. Aoki, R. Kurihara, T. Kuroda, H.Miura, T. Kunugi, Y. Seki, T. Nagashima, M. Ohta, J. Adachi, S. Yamazaki, I. Kawaguchi, T. Hashimoto, K. Shinya, Y. Murakami, H. Takase, T. Nakamura, Fusion Eng. Des. 41 (1998) 357.
[14] D. Maisonnier, I. Cook, P. Sardain, R. Andreani, L. Di Pace, R. Forrest, L. Giancarli, S. Hermsmeyer, P. Norajitra, N. Taylor, D. Ward, EFDA-RP-RE-5.0, European Fusion Development Agreement, 2005.
[15] A.R. Raffray, L. El-Guevaly, S. Gordeev, S. Malang, E.Mogahed, F. Najmabadi, I. Sviatoslavsky, D.-K. Sze, M.S.Tillack, X. Wang, A. Team, Fusion Eng. Des. 58&59 (2001)549.
[16] A.R. Raffray, R. Jones, G. Aiello, M. Billone, L. Giancarli,H. Golfier, A. Hasegawa, Y. Katoh, A. Kohyama, S. Nishio,B. Riccardi, M.S. Tillack, Fusion

Eng. Des. 55 (2001) 55.
[17] L. Giancarli, H. Golfier, S. Nishio, A.R. Raffray, C.P.C.Wong, R. Yamada, Fusion Eng. Des. 61&62 (2002) 307.
[18] P. Norajitra, L. Buhler, U. Fischer, K. Kleefeldt, S. Malang,G. Reimann, H. Schnauder, L. Giancarli, H. Golfier, Y.Poitevin, J.F. Salavy, Fusion Eng. Des. 58&59 (2001) 629.
[19] D.-K. Sze, M.S. Tillack, L. El-Guevaly, Fusion Eng. Des. 48(2000) 371.
[20] C.P.C. Wong, V. Chernov, A. Kimura, Y. Katoh, N.B.Morley, T. Muroga, K.W. Song, Y.C. Wu, M. Zmitko, J.Nucl. Mater., in press, doi:10.1016/j.jnucmat.2007.03.241.
[21] P. Norajitra, L. Buehler, U. Fischer, S. Gordeev, S. Malang,G. Reimann, Fusion Eng. Des. 69 (2003) 669.
[22] G.O. Hayner, E.L. Shaber, R.E. Mizia, R.L. Bratton, W.K.Sowder, R.N. Wright, W.E. Windes, T.C. Totemeier, K.A.Moore, W.R. Corwin, T.D. Burchell, J.M. Corum, J.W.Klett, R.K. Nanstad, L.L. Snead, P.L. Rittenhouse, R.W.Swindeman, D.F. Wilson, T.E. McGreevy, R.H. Jones, F.Gardner, INEEL/EXT-04-02347, Idaho National Engineeringand Environmental Laboratory, 2004.
[23] M. Konomura, T. Mizuno, T. Saigusa, Y. Ohkubo, A promising gas-cooled fast reactor concept and its R&D plan,GLOBAL 2003, New Orleans, 2003.
[24] Y. Katoh, A. Kohyama, T. Hinoki, L.L. Snead, Fusion Sci.Technol. 44 (2003) 155.
[25] R.J. Price, G.R. Hopkins, J. Nucl. Mater. 108&109 (1982)732.
[26] A.M. Carey, F.J. Pineau, C.W. Lee, J.C. Corelli, J. Nucl.Mater. 103&104 (1981) 789.
[27] L.L. Snead, S.J. Zinkle, D. Steiner, J. Nucl. Mater. 191−194(1992) 560.
[28] L.L. Snead, O.J. Schwarz, J. Nucl. Mater. 219 (1995) 3.
[29] R. Naslain, Compos. Sci. Technol. 64 (2004) 155.
[30] L.L. Snead, Y. Katoh, A. Kohyama, J.L. Bailey, N.L. Vaughn, R.A. Lowden, J. Nucl. Mater. 283−287 (2000) 551.
[31] T. Hinoki, Y. Katoh, A. Kohyama, Mater. Trans. 43 (2002)617.
[32] T. Nozawa, K. Ozawa, S. Kondo, T. Hinoki, Y. Katoh, L.L.Snead, A. Kohyama, J. ASTM Int. 2 (2005) 12884-1.
[33] N. Igawa, T. Taguchi, L.L. Snead, Y. Katoh, S. Jitsukawa,A. Kohyama, J.C. McLaughlin, J. Nucl. Mater. 307 (2002)1205.
[34] Y. Katoh, T. Nozawa, L.L. Snead, J. Am. Ceram. Soc. 88(2005) 3088.
[35] Y. Katoh, L.L. Snead, T. Nozawa, T. Hinoki, A. Kohyama,N. Igawa, T. Taguchi, Mater. Trans. 46 (2005) 527.
[36] Y. Katoh, T. Nozawa, L.L. Snead, T. Hinoki, A. Kohyama,Fusion Eng. Des. 81 (2006) 937.
[37] R. Yamada, N. Igawa, T. Taguchi, J. Nucl. Mater. 329−333(2004) 554.
[38] S.J. Zinkle, N.M. Ghoniem, Fusion Eng. Des. 51&52 (2000)55.
[39] G.E. Youngblood, D.J. Senor, R.H. Jones, S. Graham, Compos. Sci. Technol. 62 (2002) 1127.
[40] L.L. Snead, S.J. Zinkle, D.P. White, J. Nucl. Mater. 340(2005) 187.
[41] L.L. Snead, J. Nucl. Mater. 329−333 (2004) 524.
[42] L.L. Snead, M. Balden, R.A. Causey, H. Atsumi, J. Nucl.Mater. 307−311 (2002) 1200.
[43] T. Nozawa, Y. Katoh, L.L. Snead, T. Hinoki, A. Kohyama,Ceram. Eng. and Sci. Proc. 26 (2005) 311.
[44] B. Riccardi, E. Trentini, M. Labanti, M. Leuchs, S. Roccella,E. Visca, J. Nucl. Mater., in press, doi:10.1016/j.jnucmat.2007.03.098.
[45] J.B.J. Hegeman, M. Jong, P. ten Pierick, D.S. d' Hulst, J.G.van der Laan, J. Nucl. Mater., these Proceedings.
[46] Y. Katoh, S.M. Dong, A. Kohyama, Fusion Eng. Des. 61−62 (2002) 723.
[47] S.M. Dong, Y. Katoh, A. Kohyama, J. Am. Ceram. Soc. 86(2003) 26.
[48] A. Kohyama, T. Hinoki, J.S. Park, M. Sato, J. Nucl. Mater.,these Proceedings.
[49] T. Hinoki, A. Kohyama, Y. Katoh, K. Ozawa, T. Nozawa,J. Nucl. Mater., these proceedings.
[50] Y. Katoh, M. Kotani, H. Kishimoto, W. Yang, A. Kohyama,J. Nucl. Mater. 289 (2001) 42.
[51] R.B. Matthews, J. Nucl. Mater. 51 (1974) 203.
[52] J.B.J. Hegeman, J.G. van der Laan, M. van Kranenburg, M.Jong, D.S. d' Hulst, P. ten Pierick, Fusion Eng. Des. 75−79(2005) 789.
[53] M. Kotani, Y. Katoh, A. Kohyama, M. Narisawa, J. Ceram.Soc. Jpn. 111 (2003) 300.
[54] S.P. Lee, J.O. Jin, J.S. Park, A. Kohyama, Y. Katoh, H.K.Yoon, D.S. Bae, I.S.Kim, J.Nucl.Mater. 329−333 (2004) 534.
[55] T. Nozawa, Y. Katoh, L.L. Snead, J. Nucl. Mater., in press,doi:10.1016/j.jnucmat.2007.03.096.
[56] C.H. Henager, C.A. Lewinsohn, R.H. Jones, Acta Mater. 49(2001) 3727.
[57] C.H. Henager, R.G. Hoagland, Acta Mater. 49 (2001) 3739.
[58] R.H. Jones, C.H. Henager, J. Eur. Ceram. Soc. 25 (2005)1717.
[59] C.H. Henager, Ceram. Eng. Sci. Proc. 27 (2006).
[60] C.H. Henager, Y. Shin, R.H. Jones, Y. Blum, L.A. Giannuzzi,S.M. Schwarz, in: The Sixth IEA International Workshop on SiC/SiC Ceramic Composites for Fusion Applications, Boston, Massachusetts, USA, 46−62, 2004.
[61] T. Hinoki, N. Eiza, S.J. Son, K. Shimoda, J.K. Lee, A.Kohyama, Ceram. Eng. Sci. Proc. 26 (2005) 399.
[62] H. Kleykamp, J. Nucl. Mater. 321 (2003) 170.
[63] F. Barbier, P. Deloffre, A. Terlain, J. Nucl. Mater. 307−311(2002) 1351.

[64] B.A. Pint, L.D. Chitwood, J.R. DiStefano, Fusion Mater.,DOE/ER-0313-35, 2003, 13−17.
[65] B.A. Pint, J.L. Moser, P.F. Tortorelli, J. Nucl. Mater., inpress, doi:10.1016/j.jnucmat.2007.03.206.
[66] T. Hino, E. Hayashishita, A. Kohyama, Y. Yamauchi, Y.Hirohata, J. Nucl. Mater., in press, doi:10.1016/j.jnucmat.2007.03.089.
[67] Y. Katoh, N. Hashimoto, S. Kondo, L.L. Snead, A. Kohyama, J. Nucl. Mater. 351 (2006) 228.
[68] S. Kondo, K.H. Park, Y. Katoh, A. Kohyama, Fusion Sci.Technol. 44 (2003) 181.
[69] S. Kondo, T. Hinoki, A. Kohyama, Mater. Trans. 46 (2005)1923.
[70] G.W. Hollenberg, C.H. Henager, G.E. Youngblood, D.J.Trimble, S.A. Simonson, G.A. Newsome, E. Lewis, J. Nucl.Mater. 219 (1995) 70.
[71] T. Nozawa, Y. Katoh, A. Kohyama, Mater. Trans. 46 (2005)543.
[72] T. Nozawa, Y. Katoh, A. Kohyama, E. Lara-CurzioAdvancesin Ceramic Matrix Composites VIII: CeramicTransactions, vol. 139, The American Ceramic Society,Westerville, OH, 2002, p. 127.
[73] T. Hinoki, Y. Maki, A. Kohyama, E. Lara-Curzio, L.L.Snead, Ceram. Eng. Sci. Proc. 25 (2004) 65.
[74] A.G. Evans, J.-M. Domergue, E. Vagaggini, J. Am. Ceram.Soc. 77 (1994) 1425.
[75] Y. Katoh, T. Nozawa, L.L. Snead, T. Hinoki, J. Nucl. Mater., in press, doi:10.1016/j.jnucmat.2007.03.083.
[76] K. Ozawa, T. Nozawa, Y. Katoh, T. Hinoki, A. Kohyama,J. Nucl. Mater., in press, oi:10.1016/j.jnucmat.2007.03.033.
[77] R.J. Price, J. Nucl. Mater. 33 (1969) 17.
[78] R.J. Price, J. Nucl. Mater. 48 (1973) 47.
[79] D.J. Senor, G.E. Youngblood, L.R. Greenwood, D.V. Archer, D.L. Alexander, M.C. Chen, G.A. Newsome, J. Nucl. Mater. 317 (2003) 145.
[80] L.L. Snead, Y. Katoh, S. Connery, J. Nucl. Mater., in press,doi:10.1016/j.jnucmat.2007.03.097.
[81] G.E. Youngblood, D.J. Senor, R.H. Jones, Fusion Sci. Technol. 45 (2004) 583.
[82] T. Ishikawa, K. Bansaku, N. Watanabe, Y. Nomura, M.Shibuya, T. Hirokawa, Compos. Sci. Technol. 58 (1998) 51.
[83] G.N. Morscher, J.A. DiCarlo, J. Am. Ceram. Soc. 75 (1992)136.
[84] Y. Katoh, L.L. Snead, T. Hinoki, S. Kondo, A. Kohyama, J.Nucl. Mater., in press, doi:10.1016/j.jnucmat.2007.03.086.
[85] R. Scholz, R. Mueller, D. Lesueur, J. Nucl. Mater. 307−311(2002) 1183.
[86] M. Abdou, D.-K. Sze, C. Wong, M. Sawan, A. Ying, N.B.Morley, S. Malang, Fusion Sci. Technol. 47 (2005) 475.
[87] S. Smolentsev, N.B. Morley, M. Abdou, Fusion Sci. Technol.50 (2006) 107.
[88] M. Sawan, L. El-Guevaly, in: Fifth International EnergyAgency Workshop on SiC/SiC Ceramic Composites forFusion Energy Application, San Diego, California, USA,43−48, 2002.
[89] Y. Katoh, H. Kishimoto, A. Kohyama, J. Nucl. Mater. 307(2002) 1221.
[90] T. Taguchi, N. Igawa, S. Miwa, E. Wakai, S. Jitsukawa, L.L.Snead, A. Hasegawa, J. Nucl. Mater. 335 (2004) 508.Y. Katoh et al. / Journal of Nuclear Materials 367−370 (2007) 659−671 671

Evaluation of Fiber/Matrix Interfacial Strength of Neutron Irradiated SiC/SiC Composites Using Hysteresis Loop Analysis of Tensile Test

K. Ozawa[1], T. Hinoki[2], T. Nozawa[3], Y. Katoh[3], Y. Maki[1], S. Kondo[1], S. Ikeda[1], A. Kohyama[2]

[1] *Graduate School of Energy Science, Kyoto University, Gokasho Uji, Kyoto 611-0011, Japan, kazumi@iae.kyoto-u.ac.jp, y-maki@iae.kyoto-u.ac.jp, sosuke@iae.kyoto-u.ac.jp, s-ikeda@iae.kyoto-u.ac.jp*
[2] *Institute of Advanced Energy, Kyoto University, Gokasho Uji, Kyoto 611-0011, Japan, hinoki@iae.kyoto-u.ac.jp, kohyama@iae.kyoto-u.ac.jp*
[3] *Metals and Ceramics Division, Oak Ridge National Laboratory, Oak Ridge, TN 37831-6151, USA, katohy@ornl.gov, nozawat@ornl.gov*

Advanced SiC/SiC composites composed of highly-crystalline and near-stoichiometric SiC fibers, SiC matrix by CVI method, and PyC interphase were irradiated up to 1.0×10^{25} n/m^2 (E > 0.1 MeV, ~1 dpa) at 1273 K. Unload / reload cyclic tensile test and hysteresis loop analysis were carried out in order to identify neutron irradiation effects on interfacial properties of advanced SiC/SiC. The composites exhibited good irradiation resistance in ultimate tensile strength (~10% increase), but there were slight reduction of elastic modulus and proportional limit stress (PLS) (~10%). Wider hysteresis loops and lower gradient of the curves beyond PLS from the strain-stress curves, and longer pullouts of fiber from the SEM observation were observed, which imply weaker F/M interactions after neutron irradiation. From the hysteresis loop analysis, degradation of interfacial sliding stress and negative increment of misfit stress after neutron irradiation were obtained.

I. INTRODUCTION

Silicon carbide (SiC) and its composites (SiC/SiC) are attractive structural materials for fusion reactors and gas fast reactors because of their superior mechanical properties at high temperature and good irradiation resistance [1]. The mechanical properties of SiC/SiC composites after irradiation depend on the properties of their constituents, especially fiber/matrix (F / M) interphase [2-6]. SiC/SiC composites reinforced with less crystalline and non-stoichiometric SiC fibers have shown the interfacial debonding due to mismatch of swelling behavior of the fiber and β-SiC matrix after neutron irradiation. In contrast, due to highly crystalline and near stoichiometric SiC fibers, advanced SiC/SiC composites have exhibited excellent irradiation stability in ultimate bend/tensile strength [6, 7].

In our previous work [8], tensile, flexural and inter-laminar shear properties of advanced SiC/SiC composites with various interfaces (pyrolitic carbon (PyC), multilayered SiC/PyC (ML) and pseudo-porous SiC) after neutron irradiation up to 1×10^{25} n/m^2 at mainly 1023 K was examined. Advanced SiC/SiC composites exhibited good irradiation resistance in ultimate bend / tensile strength, but the result of a slight loss of proportional limit stress (PLS) in the monotonic tensile test and ~40% degradation of inter-laminar shear strength in the double notched specimen (DNS) test suggested degradation of F / M interphase. However, irradiation effects on F / M interphase remain uncertain because it is well known that PLS depends on various constituent properties of composites and inter-laminar shear strength also might be dependent on size, geometry and distribution of pores. Therefore, irradiation effects on the interfacial role became one of the most important issues to be discussed.

The main purpose of this study is to identify neutron irradiation effects on interfacial properties of advanced SiC/SiC composites. For this purpose, we applied unloading / reloading tensile test and hysteresis loop analysis.

II. EXPERIMENTAL PROCEDURE

II.A. Materials

Unidirectional (UD) SiC/SiC composites were prepared by isothermal chemical vapor infiltration (I-CVI) process at Hyper-Therm High-Temperature Composites, Inc.. They were composed of Hi-Nicalon^{TM} Type-S fibers as reinforcements with single pyrolytic carbon (PyC). The thickness of PyC coating was 520, 720 nm (PyC520, PyC720), the density of SiC/SiC was 2.58 Mg/m^3, and the fiber volume fraction was 29 %. Materials fabrication is detailed elsewhere [9, 10].

II.B. Neutron Irradiation

Neutron irradiation was performed in the Japan Materials Testing Reactor (JMTR) at Oarai, Japan. Neutron fluence and temperature were 1.0×10^{25} n/m^2 (E>0.1MeV, correspond to 1dpa) and 1273K, respectively.

II.C. Tensile Test

Tensile tests were carried out in accordance with ASTM C 1275 at room temperature by using a face-

loaded miniature specimen developed in previous works [11, 12]. The size of tensile test specimens was 4×1.5×50 mm except unirradiated PyC720. First, 1.0 mm-thick aluminum tabs were attached on both ends of rectangular specimens. Second, a couple of 6.0 mm-length gauges were adhered in the center of gauge sections on both sides. Prepared specimens were mounted in the test flame by connection of wedge-type grips gripping system was kept in the plastic bags during the test. Tensile tests were conducted under the displacement control of 0.5 mm/min. The detailed tensile setup is in [8], and more details are discussed elsewhere [11, 12]. In addition, the size of unirradiated PyC720 was 2×1.5×50 mm, and detailed procedures of the tensile test of unirradiated PyC720 were given elsewhere [2, 9].

II.D. Microstructural Observations

After the tests, the fractured surfaces of tensile specimens were observed by scanning electron microscopy (SEM).

III. RESULTS

Typical tensile stress / strain curves of PyC520 after neutron irradiation were shown in Fig. 1. Initial linear region and non-linear behavior beyond it during tensile loading were observed in all composites; ~ 435 MPa of ultimate tensile stress (UTS) with ~ 235 MPa of proportional limit stress (PLS) and ~ 319 GPa of elastic modulus, i.e. unirradiated composites, fractured at lower stress ~365 MPa of UTS with ~268 MPa of PLS and ~365 GPa of elastic modulus. As shown in Fig. 1, wider maximum hysteresis loop width and larger permanent strain after neutron irradiation were observed.

Table 1 exhibits the summary of unirradiated and irradiated tensile properties in PLS, UTS and elastic modulus after the test. PyC520 and PyC720 exhibited almost same behavior. Hence they are lumped together as PyC in this study, since SiC/SiC with >400nm-thick PyC showed almost same behavior in bend test [13].

Fig. 2 shows the relative tensile properties after neutron irradiation. PyC composites exhibited good irradiation resistance in UTS (~30% increase), but a slight loss of both elastic modulus (~10%) and PLS (~10%) were observed after neutron irradiation up to 1 dpa at 1273 K.

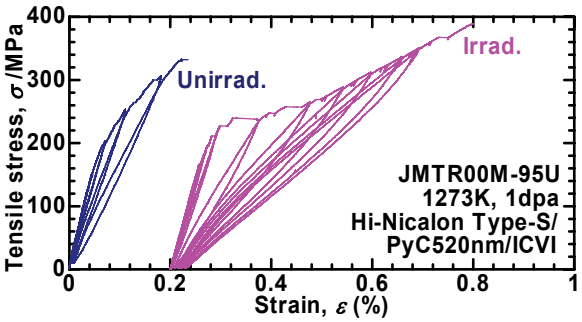

Fig. 1 Representative stress / strain curves and hysteresis loops for Hi-Nicalon™ Type-S / 520 nm-PyC / I-CVI composites after neutron irradiation up to 1 dpa at 1273 K.

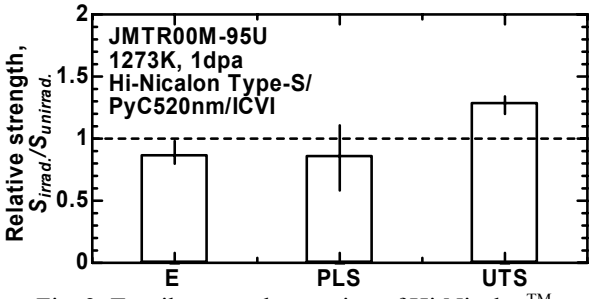

Fig. 2 Tensile strength retention of Hi-Nicalon™ Type-S / 520 nm-PyC / I-CVI composites after neutron irradiation up to 1 dpa at 1273 K.

Fig. 3 exhibits the typical fractured surfaces by SEM observation of the unirradiated and irradiated composites. Longer fiber pullouts were observed in the irradiated composites (0~287 μm, 94 μm in average), comparing with the unirradiated composites (0~121 μm, 46 μm in average). In addition, some regions of the fractured surfaces in the unirradiated composites were flat with no

Table 1 Summary of unirradiated and irradiated tensile properties. Averages and standard deviations were shown. PyC means PyC520 and PyC720. The parentheses in Number of test indicate the number of tests fractured successfully.

Specimen	Irradiation condition	*E*/GPa	*PLS*/MPa	*UTS*/MPa	Number of test
PyC520	Unirrad.	314.9±31.3	150.1±3.7	349.1±16.1	2 (2)
PyC520	1273K, 1dpa	296.8±16.3	175.5±45.6	409.2±19.6	3 (2)
PyC720	Unirrad.	329.1±33.2	236.9±16.3	287.4±37.3	5 (5)
PyC720	1273K, 1dpa	266.1±5.8	189.4±33.9	435.5±0.0	3 (1)
PyC	Unirrad.	325.0±33.3	212.1±41.6	325.0±42.9	7 (7)
PyC	1273K, 1dpa	281.4±19.6	182.4±40.8	418.0±20.2	7 (3)

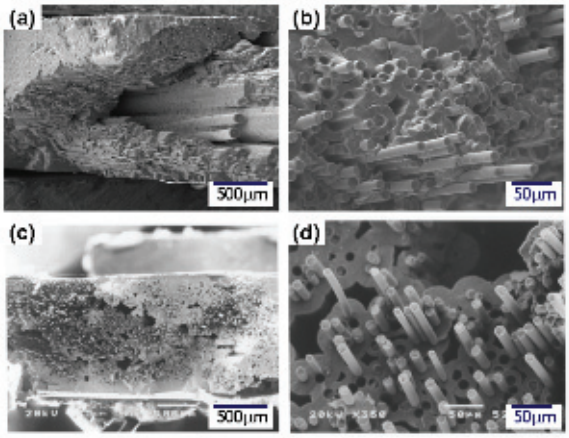

Fig. 3 Typical tensile fracture micrographs before and after neutron irradiation up to 1 dpa at 1273 K; (a), (b) unirradiated, (c), (d) irradiated.

pullouts.

IV. DISCUSSION

IV.A. Neutron Irradiation Effects on Tensile Elastic Modulus

The slight loss of tensile elastic modulus after neutron irradiation at 1273 K was similar to the decrease irradiated at 1073 K [8]. According to previous reports, moduli of Hi-Nicalon^{TM} Type-S single fiber by tensile test [14] and CVD-SiC by nano-indentation techniques [15, 16], decreased ~ 10% at 1dpa, and kept this level up to at least 10 dpa in the temperature range from 423 to 823 K. At 1023 to 1273 K, elastic modulus exhibited nearly no reduction at least up to 3 dpa, following 10 % decrease at ~ 8dpa. Therefore, the small amount of degradation in elastic modulus of advanced SiC/SiC after neutron irradiation might be occurred.

IV.B. Neutron Irradiation Effects on PLS

Generally, proportional limit stress, i.e. matrix cracking stress (σ_{mc}), is closely dependent on interfacial properties and moduli of fiber and matrix and misfit stress [17, 18],

$$\sigma_{mc} = E\left[\frac{6\tau\Gamma_m E_m f^2 E_f}{(1-f)E_m^2 RE}\right]^{1/3} - \sigma^T \qquad (1)$$

where σ^T is the misfit stress, Γ_m is the matrix fracture energy, E_f is the Young's modulus of fiber, E_m is that of matrix, E is that of composites, τ is the interfacial sliding stress, f is the fiber volume fraction, and R is the fiber radius, respectively. As discussed in Section IV.A., the irradiation-induced change of elastic moduli of highly crystalline SiC matrix and fiber should be minor at 1273 K up to 1 dpa.

Wider hysteresis loop width and lower gradient of the curves beyond PLS (Fig. 1), and longer fiber pullouts (Fig. 3) imply the degradation of interfacial properties. In order for further investigation of interfacial properties, the method of unloading / reloading hysteresis loop analysis methodology proposed by Vagaggini, Domergue, and Evans was applied [18-20]. In this analysis, inelastic strain index, which is important for estimating the interfacial property, and Young's modulus of material with matrix cracks were obtained from the reciprocal moduli during reloading tensile-strain curves from different peak stress (σ_p: the transition stress from reloading to unloading). The detailed method for unidirectional composites is given in elsewhere [18].

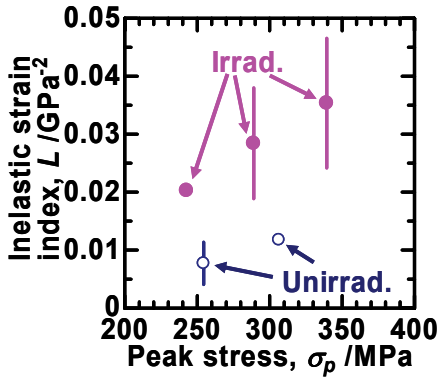

Fig. 4 Inelastic strain index of Hi-Nicalon^{TM} Type-S / 520 nm-PyC / I-CVI composites after neutron irradiation up to 1 dpa at 1273 K as a function of peak stress σ_p.

Figure 4 exhibits the inelastic strain index (***L***) of advanced SiC/SiC composites after neutron irradiation, which is given by,

$$\boldsymbol{L} = \frac{b_2(1-a_1 f)^2}{4f^2\tau E_m}\frac{R}{\bar{d}} \qquad (2)$$

with $\bar{d}$ being the matrix crack spacing, and a_1, b_2 the Hutchinson and Jensen parameters [21]. As defined in Eq. (2), ***L*** is dependent on interfacial stress and mean matrix crack spacing. Unfortunately, as the mean matrix crack spacing was not measured in individual tested samples, the saturated matrix crack spacing ($\bar{d}_s$) was determined by the crack spacing at fiber bundles of the fractured surfaces by SEM observation, in accordance with the matrix damage parameter (***D***) which is defined as,

$$E/E^* - 1 = \boldsymbol{B}R/\bar{d} \equiv \boldsymbol{D} \qquad (3)$$

where B is a constant for a particular composite (fixed f and E_f/E_m) and E^* is the Young's modulus of the composite with matrix cracks, respectively. As shown in Eq. (3), ***D*** is in inversely proportion to matrix crack spacing, and is almost saturated around 300 MPa of peak stress (Fig. 5), so we applied the saturated matrix crack spacing from the SEM observation (58 μm, 23 μm) to Eq. (2) at 306 MPa for the unirradiated specimens and 289 MPa for the irradiated. As a result, each interfacial sliding stresses was obtained ($\tau_{unirrad.}$=35 MPa, $\tau_{irrad.}$=21 MPa). Actually, about 40% degradation of the interfacial sliding stress after neutron irradiation up to 1 dpa at 1273 K was confirmed.

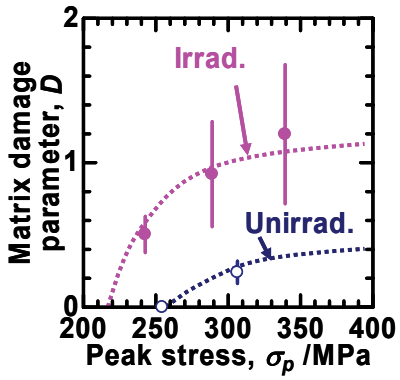

Fig. 5 Matrix damage parameter of Hi-Nicalon™ Type-S / 520 nm-PyC / I-CVI composites after neutron irradiation up to 1 dpa at 1273 K as a function of peak stress σ_p.

As shown in Eq. (1), PLS also depends on misfit stress, which correlates with residual stress in composites. Figure 6 exhibits the misfit stress for large debond energy as a function of peak stress using the following method in Ref. [20]. The conversion of misfit stress to residual stress components is provided elsewhere [18]. Negative increment of misfit stress was detected after neutron irradiation; was in range of +80~-10 MPa, -4 MPa in average at the highest peak stress, and was -60~-230 MPa, -150 MPa, respectively.

This result indicates that slight difference of swelling between each constituent (fiber and PyC interphase, matrix and PyC) might affect the residual stress in PyC interphase and cause the degradation of the interfacial property, ignoring the influence of interphase thickness and roughness of fiber. Or it is also considered that the degradation might be caused by volumetric change of PyC interphase itself. According to Kaae [22], low density isotropic PyC shrinks and has anisotropy in volumetric change after neutron irradiation up to 1 dpa. Therefore, further researches about swelling behaviors of SiC constituents (fiber, matrix) and PyC interphase after irradiation are required respectively in order to clarify the detailed mechanism of the degradation.

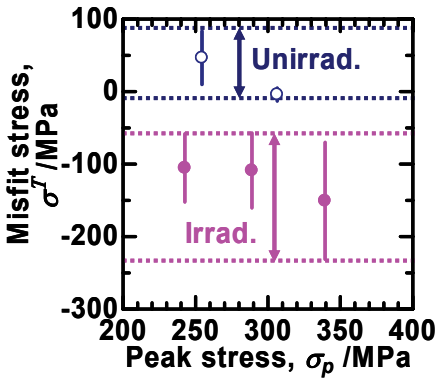

Fig. 6 Misfit stress of Hi-Nicalon™ Type-S / 520 nm-PyC / I-CVI composites after neutron irradiation up to 1 dpa at 1273 K as a function of peak stress σ_p.

IV.C. Neutron Irradiation Effects on UTS

It is well known that degradation of interphase affects composite maximum strength in unidirectional composites [23],

$$\sigma_u = f\sigma_c\left(\frac{2}{m+2}\right)^{\frac{1}{m+1}}\left(\frac{m+1}{m+2}\right) \quad (4)$$

$$\sigma_c = \left(\frac{\sigma_0^m \tau L_0}{R}\right) \quad (5)$$

where σ_u is the ultimate tensile strength, σ_c is the characteristic strength, σ_0 is the Weibull mean strength, m is the shape parameter, and L_0 is the gauge length, respectively. In this study, there was up to 30 % increment in UTS after neutron irradiation regardless of the decrease of interfacial sliding stress as discussed in Section IV.B.. However, low fluence neutron irradiation probably caused moderate degradation in interfacial properties of PyC layer, resulting in the fullest potential of fiber strength. Most cracks emerged in matrix penetrated into fibers through the strong-bonded F / M interface for the unirradiated samples. (The result of SEM observation showed that some regions of the fractured surfaces in unirradiated composites were flat with no pullouts.) This indicates that the maximum strength of composites significantly depends on the performance of intact fibers. There have no degradation in β-SiC [24, 25]) and Hi-Nicalon™ Type-S fiber [14]) and primary role of interphase is to control the fracture behaviors (brittle or quasi-ductile). From these aspects, it can be concluded that the major achievements to provide good irradiation tolerances of UTS.

IV. CONCLUSIONS

In order to identify neutron irradiation effects on interfacial properties of advanced SiC/SiC composites, unload / reload cyclic tensile test and hysteresis loop analysis were carried out. The advanced SiC/SiC composites exhibited good irradiation resistance in UTS (~ 30% increase), but a slight reduction of PLS was obtained. Wider hysteresis loops and lower gradient of the curves beyond PLS from the strain-stress curves, and longer fiber pullouts from the SEM observation were observed, which imply weaker F/M interactions. Additionally, from the hysteresis loop analysis, degradation of interfacial sliding stress was detected. Therefore it is considered that a slight reduction of PLS might be caused by the degradation of interfacial sliding stress.

ACKNOWLEDGMENTS

This work was performed as a part of corroboration works at Irradiation Experimental Facility, Institute for Materials Research, Tohoku University, Japan. Materials were supplied in the DOE/MEXT JUPITER-II Collaboration for Development of Advanced Blanket Performance under Irradiation and System Integration.

REFERENCES

[1] A.R. Raffray, R. Jones, G. Aiello, M. Billone, L. Giancarli, H. Golfier, A. Hasegawa, Y. Katoh, A. Kohyama, S. Nishio, B. Riccardi and M.S. Tillack: Fusion Eng. Des. 55 (2001) 55–95.
[2] T. Hinoki, doctoral thesis, Kyoto University, (2001).
[3] L.L. Snead, M.C. Osborne, R.A. Lowden, J. Strizak, R.J. Shinavski, K.L. More, W.S. Eatherly, J. Bailey and A.M. Williams: J. Nucl. Mater. 253 (1998) 20-30.
[4] G.W. Hollenberg, C.H. Henager, Jr., G.E. Youngblood, D.J. Trimble, S.A. Simonson, G.A. Newsome and E. Lewis: J. Nucl. Mater. 219 (1995) 70-86.
[5] A.J. Frias Rebelo, H.W. Scholz, H. Kolbe, G.P. Tartagalia and P. Fenici: J. Nucl. Mater. 258-263 (1998) 1582-1588.
[6] L.L. Snead, Y. Katoh, A. Kohyama, J.L. Bailey, N.L. Vaughn and R.A. Lowden: J. Nucl. Mater. 283-287 (2000) 551-555.
[7] T. Hinoki, L.L. Snead, Y. Katoh, A. Hasegawa, T. Nozawa and A. Kohyama: J. Nucl. Mater. 283-287 (2002) 1157-1162.
[8] T. Nozawa, K. Ozawa, S. Kondo, T. Hinoki, Y. Katoh, L.L. Snead and A. Kohyama: J. ASTM Int. 2 (2005) 215-227.
[9] T. Hinoki, L.L. Snead, E. Lara-Curzio, Y. Katoh and A. Kohyama: DOE/ER-0313/29 (2000) pp.74-84.
[10] T. Hinoki, Y. Katoh, L.L. Snead, E. Lara-Curzio, Y.S. Park and A. Kohyama: Proc. 4th, IEA workshop on SiC/SiC Ceramic Matrix Composites for Fusion Structural Applications, Oct., 2000, Frascati, Italy (2000) pp. 132-142.
[11] T. Nozawa, Y. Katoh, A. Kohyama, E. Lara-Curzio: Ceram. Eng. and Sci. Proc., 24 (2003) 415-420.
[12] T. Nozawa, E. Lara-Curzio, Y. Katoh, A. Kohyama: Advanced SiC/SiC composites: Developments and Aplications in Energy Systems, Ceram. Trans., 144 (2002) 245-252.
[13] W. Yang, doctoral thesis, Kyoto University, (2001).
[14] T. Nozawa, T. Hinoki, Y. Katoh, and A. Kohyama: J. Nucl. Mater. 307-311 (2002) 1173-1177.
[15] M.C. Osborne, J.C. Hay, L.L. Snead and D. Steiner: J. Am. Ceram. Soc. 82 (1999) 2490-2496.
[16] R.J. Price: Nucl. Tech. 35 (1977) 320-336.
[17] A.G. Evans F.W. Zok: J. Mater. Sci. 29 (1994) 3857-3896.
[18] E. Vagaggini, J.M. Domergue and A.G. Evans: J. Am. Ceram. Soc. 78 (1995) 2709-2720.
[19] A.G. Evans, J.-M. Domergue, and E. Vagaggini: J. Am. Ceram. Soc. 77 (1994) 1425-1435.
[20] J.-M. Domergue, E. Vagaggini and A.G. Evans: J. Am. Ceram. Soc. 78 (1995) 2721-2731.
[21] J.W. Hutchinson and H. Jensen: Mech. Mater. 9 (1990) 139-163.
[22] J.L. Kaae: Nucl. Technol. 35 (1977) 359-367.
[23] W.A. Curtin: J. Am. Ceram. Soc. 74 (1991) 2837-2845.
[24] R.J. Price: J. Nucl. Mater. 33 (1969) 17-22.
[25] R.J. Price and G.R. Hopkins: J. Nucl. Mater. 108-109 (1982) 732-738.

Mechanical Properties of Advanced SiC/SiC composites after Neutron Irradiation

K. Ozawa[1], Y. Katoh[2], T. Nozawa[2], T. Hinoki[3], A. Kohyama[3]

[1] *Graduate School of Energy Science, Kyoto University, Gokasho Uji, Kyoto 611-0011, Japan, kazumi@iae.kyoto-u.ac.jp*
[2] *Metals and Ceramics Division, Oak Ridge National Laboratory, Oak Ridge, TN 37831-6151, USA, katohy@ornl.gov, nozawat@ornl.gov*
[3] *Institute of Advanced Energy, Kyoto University, Gokasho Uji, Kyoto 611-0011, Japan, hinoki@iae.kyoto-u.ac.jp, kohyama@iae.kyoto-u.ac.jp*

The neutron irradiation effect on tensile properties in advanced 2D-SiC/SiC composites were evaluated. The composites used were composed of a SiC matrix obtained by FCVI process and either Tyranno-SA 3rd grade (TySA) or Hi-Nicalon Type-S fiber with singly-layered PyC. Neutron irradiation fluence and temperature were 3.1×10^{25}n/m^2 (E>0.1MeV) at 740°C and 1.2×10^{26}n/m^2 at 750°C, respectively. Tensile properties were evaluated by unloading/reloading cyclic tensile test, and hysteresis loop analysis was applied in order to predict interfacial properties. Both composites exhibited excellent irradiation resistance in ultimate and proportional limit tensile stresses. From the hysteresis loop analysis, the level of interfacial sliding stress was decreased significantly after irradiation to 1.2×10^{26}n/m^2 at 750°C.

I. INTRODUCTION

Silicon carbide (SiC) continuous fiber-reinforced SiC matrix composites (SiC/SiC composites) are attractive structural materials for fusion reactors and advanced fission reactors because of their superior mechanical properties at high temperatures [1]. The mechanical properties of SiC/SiC composites after irradiation is determined by the properties of their constituents, especially fiber/matrix (F/M) interphase in case of composites with high modulus matrix. In earlier studies, SiC/SiC composites reinforced with nano-crystalline and non-stoichiometric SiC fibers have shown interfacial debonding due primary to fiber contraction, which caused severe degradation in flexural strength [2-5]. In recent studies, however, advanced SiC/SiC composites appeared to retain ultimate flexural strength due to improved irradiation stability of the high crystallinity and near-stoichiometric SiC fibers [5, 6].

For composites with highly irradiation-resistant matrices and fibers, irradiation effects on F/M interfacial properties has become one of the most important issues to be investigated., However, it is difficult to use the simple flexural testing to develop an understanding of irradiation effects on interfacial properties, because it is hard to analyze the data due to mixed failure modes. Simple failure modes, such as are obtained in tensile tests enable the fracture behavior of SiC/SiC composites after irradiation to be understood more precisely. Recent studies have employed tests yielding simple failure modes to evaluate interfacial properties [7-9].

The main purpose of this work is to identify neutron irradiation effects on tensile and interfacial properties of advanced SiC/SiC composites reinforced with two commercially available, high crystallinity, near-stoichiometric SiC fibers. For this purpose, tensile properties were evaluated in an unloading/reloading cyclic tensile test and hysteresis loop analysis method was applied in order to predict interfacial properties.

II. EXPERIMENTAL PROCEDURE

The composites used in this study were produced thorough a forced-flow thermal gradient chemical vapor infiltration (FCVI) process developed at Oak Ridge National Laboratory. Either Tyranno^{TM}-SA 3rd grade (hereafter TySA) or Hi-Nicalon^{TM} Type-S (hereafter HNLS) fibers were used as reinforcements. These were plain-woven in a [0°/90°] orientation and held tightly in a graphite fixture for interphase deposition and subsequent matrix dentification. F/M interphase was singly-layered pyrolytic carbon (PyC) and the thickness was 20~60nm. The density of the composites was 2.3-2.7 g/cm3, and the fiber volume fraction and porosity were ~38% and 17-25%, respectively. More detailed information about the materials fabrication is given elsewhere [10, 11].

Neutron irradiation was performed in JOYO, fast spectrum reactor at Oarai, Japan, in JNC-54 and -61 capsules as part of the CMIR-6 irradiation campaign. Neutron fluence and nominal irradiation temperature were 3.1×10^{25}n/m^2 (E>0.1MeV) at 600°C and 1.2×10^{26}n/m^2 at 750°C. And equivalence of one displacement per atom (dpa) = 1×10^{25}n/m^2 (E>0.1MeV) is assumed. The irradiation temperature was passively controlled by a fixed composition gas gap technique. An estimation of the actual specimen temperature during irradiation has not been made available.

Tensile tests were conducted in accordance with ASTM C1275 at room temperature under the crosshead displacement control of 0.5mm/min by using a face-loaded miniature specimen developed previously [12, 13]. The gauge dimensions were 3×1.5×15mm and the specimen machining involved surface grinding into fabric layers [10]. A 1.0mm-thick aluminum tab was attached to each end of rectangular specimens, and a pair of 6.0mm-length strain gauges were adhered in the center of gauge sections on both sides. Specimens were mounted in the test flame by connection of wedge-type gripping system that was kept in the plastic bags during the test. Successful tests typically retained intact tab adhesion to the samples. In order to avoid fractional bending during the tests, the both side of wedge was fixed at 60kN·m equally using a torque driver. The detailed tensile setup is given elsewhere [7].

After the tensile tests, the fractured surfaces of the specimens were observed using optical microscope and scanning electron microscope (SEM).

III. RESULTS

Fig. 1 exhibits the typical tensile stress-strain curves of TySA and HNLS composites after neutron irradiation. The composites in all conditions exhibited quasi-ductile behaviors. There was an initial steeper linear region in the stress-strain curve, with a second, nearly linear region at higher strains during tensile loading with multiple unloading/reloading sequences. The initial linear protion corresponds to the linear elastic deformation of the composites, whereas the second linear protion corresponds to a process of progressive development and opening of the multiple matrix micro-cracks.

Table I lists a summary of unirradiated and irradiated tensile properties: proportional limit stress (PLS), ultimate tensile strength (UTS) and elastic modulus (E) obtained from the tensile tests, and Fig. 2 shows the tensile properties after neutron irradiation. Both composites exhibited excellent irradiation resistance. Almost no degradation in PLS and UTS was occurred under both

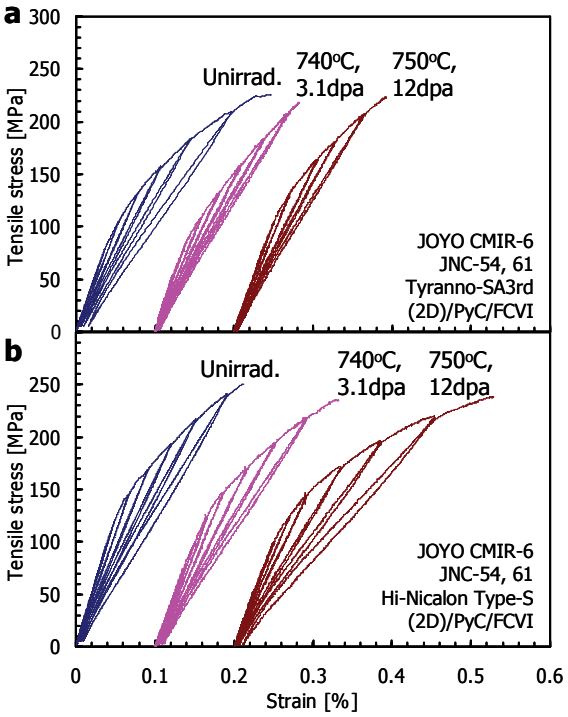

Fig. 1. Representative tensile stress-strain curves and hysteresis loops for (a) TySA (2D)/PyC/FCVI, (b) HNLS (2D)/PyC/FCVI composites after neutron irradiation.

irradiation conditions, and an increase of about 50% was measured in PLS of TySA composites irradiated to 12dpa at 750°C. In elastic modulus, a 15~20% decrease was obtained for both composites.

Fig. 3 exhibits the maximum hysteresis loop width at each peak stress where σ_p is the transition stress from reloading to unloading. For both composites, hysteresis loop width after irradiation up to 3.1dpa at 740°C became narrower than that of unirradiated one. After neutron irradiation to 12dpa, 750°C, the width of TySA composites remained narrower, while that of HNLS exhibited almost the same behavior as the unirradiated

Table I. Summary of unirradiated and irradiated tensile properties. Numbers in parenthesis show standard deviations. #1266, TySA (2D)/PyC/FCVI; #1272, HNLS (2D)/PyC/FCVI; E, tensile elastic modulus; PLS, proportional limit stress; UTS, ultimate tensile strength.

ID	Irradiation condition	E [GPa]	PLS [MPa]	UTS [MPa]	Number of test
#1266	Unirrad.	257 (32)	76 (31)	218 (18)	6
	740°C, 3.1dpa	216 (11)	80 (9)	241 (30)	3
	750°C, 12dpa	198 (19)	112 (12)	209 (11)	3
#1272	Unirrad.	253 (25)	98 (17)	227 (27)	10
	740°C, 3.1dpa	222 (33)	107 (9)	210 (18)	3
	750°C, 12dpa	200 (5)	100 (18)	220 (16)	4

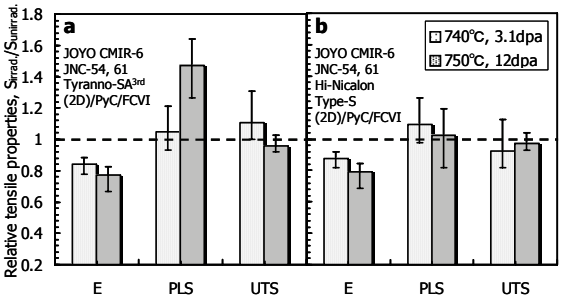

Fig. 2. Ratio of irradiated to unirradiated tensile properties of (a) TySA (2D)/PyC/FCVI, (b) HNLS (2D)/PyC/FCVI composites after neutron irradiation. Error bars show maximum and minimum.

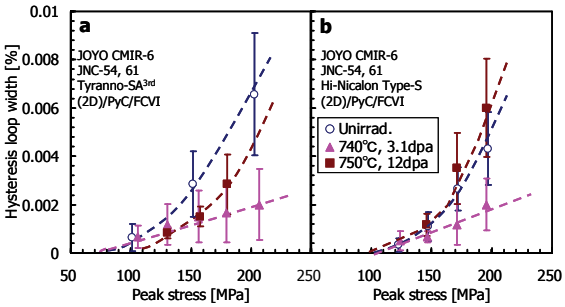

Fig. 3. Hysteresis loop width plotted against peak stress; (a) TySA (2D)/PyC/FCVI, (b) HNLS (2D)/PyC/FCVI composites. Error bars show standard deviation.

material.

Fig. 4 exhibits the typical fracture surfaces of the composites by SEM. No significant change of fiber-pull outs was observed for both composites after irradiation. Fiber pull-outs in TySA composites were shorter than that in HNLS composites under all conditions.

IV. DISCUSSION

Both composites irradiated to 3.1dpa at 740°C exhibited narrower hysteresis loop widths, a slightly steeper slope in the second linear portion of the curve and nearly unchanged fiber pull-out length, all of which imply retaining or increasing of interfacial sliding stress.

For further investigation of interfacial properties, the method of unloading/reloading hysteresis loop analysis methodology proposed by Vagaggini, Domergue and Evance was applied [14-17]. In this analysis, inelastic strain index, which is the most important for estimating interfacial property, and Young's modulus of the material with matrix cracks were obtained from values of the inverse tangent moduli of reloading tensile stress-strain curves at different peak stress. A detailed description for 2D composites is found elsewhere [17].

The maximum hysteresis loop width (δ_{max}) of before and after irradiation is dependent on both interfacial sliding stress (τ) and mean matrix crack spacing ($\overline{d}$). The composites in all conditions met large debond energy condition. For this condition, the maximum hysteresis loop width (δ_{max}) is given by [14, 17],

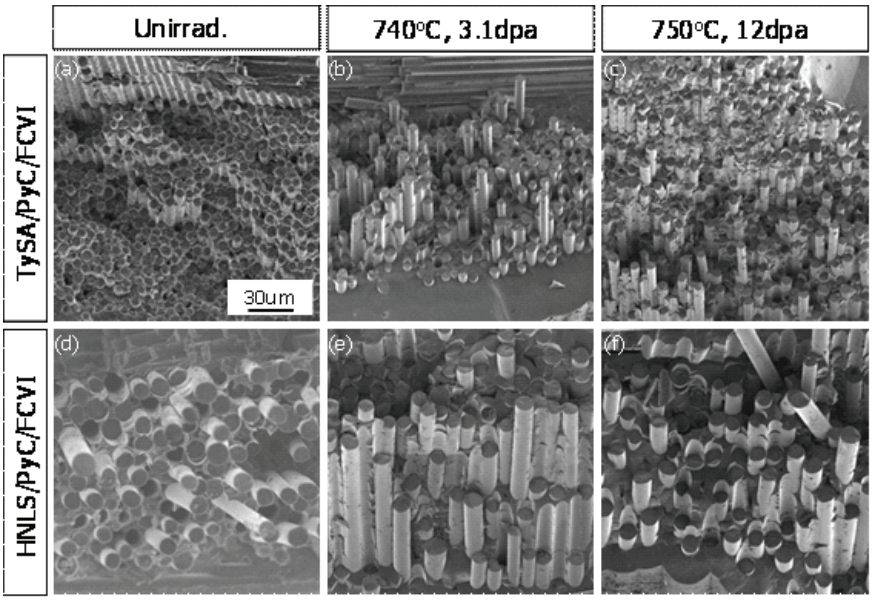

Fig. 4. Typical fracture surfaces of unirradiated and neutron-irradiated specimens; (a) unirradiated, (b) 740°C, 3.1dpa and (c) 750°C, 12dpa for TySA (2D)/PyC/FCVI, and (d) unirradiated, (e) 740°C, 3.1dpa and (f) 750°C, 12dpa for HNLS (2D)/PyC/FCVI.

$$\delta_{\max} = 4\lambda\sigma_p^2\left(1-\frac{\sigma_i}{\sigma_p}\right)^2 = \frac{b_2(1-a_1 f)^2}{f^2\tau E_m}\frac{R}{\bar{d}}\sigma_p^2\left(1-\frac{\sigma_i}{\sigma_p}\right)^2 \quad (1)$$
$$, for\ \sigma_i/\sigma_p \cong 0.85$$

where λ is inelastic strain index, σ_i is 'debond' stress [14], E_m is Young's modulus of matrix, R is fiber radius, f is fiber volume fraction, and a_1 and b_1 the Hutchinson-Jensen parameters [18]. All parameters except interfacial sliding stress and mean matrix crack spacing remain almost unchanged during irradiation.

Unfortunately, the mean matrix crack spacing was not measured, so the interfacial sliding stress parameter $\tau' = \tau \cdot \bar{d}/R$ obtained from inelastic strain index was used for this analysis. Thus, the evaluation of interfacial sliding stress parameter at the same matrix crack spacing (i.e. same matrix damage level) is required. The matrix damage parameter (D) is defined as [14],

$$D \equiv \frac{E-E^*}{E^*} = B\frac{R}{\bar{d}} \quad (2)$$

where E is elastic modulus of the composite, E^* is Young's modulus of the composite with matrix cracks obtained from the reloading stress-strain curve, and B is a constant for particular composite. As shown in Eq. (2), the matrix damage parameter is inversely proportional to matrix crack spacing. Therefore, the interfacial sliding stress can be predicted using the interfacial sliding stress parameter obtained for the same matrix damage parameter.

Fig. 5 exhibits the interfacial sliding stress parameter at approximately the same matrix damage parameter (D≅0.2). For both composites, the interfacial sliding stress parameter remained nearly constant after irradiation up to 3.1dpa at 740°C, while the parameter decreased after irradiation up to 12dpa at 750°C.

According to the work by Bokros et al. [19,20], the interfacial PyC is expected to shrink in both the a and c axis directions after neutron irradiation up to 2-3×10^{25} n/m^2 in the range of 520-690°C. However, it began to swell significantly in the c axis direction over ~10×10^{25} n/m^2 irradiation. This result might be correlated with the result of the analysis of data in this study, but the details are unclear. Therefore, further research and SEM observations of crack propagation and TEM observation of the PyC interphase itself are required in order to understand the behavior of the interphase after neutron irradiation.

Residual stress between the fiber and matrix may affect the tensile behavior of SiC/SiC composites, so the misfit stress σ^T was also estimated by hysteresis loop analysis. The conversion of misfit stress to residual stress components was carried out by the method discussed

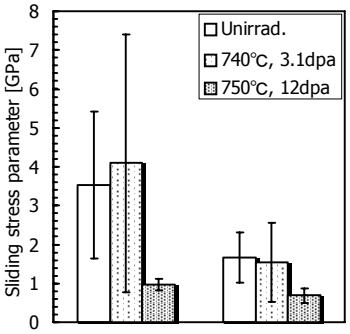

Fig. 5. Interfacial sliding stress parameters compared at similar matrix damage parameters for composite samples before and after neutron irradiation. #1266; TySA (2D)/PyC/FCVI, #1272; HNLS (2D)/PyC/FCVI. Error bars show standard deviation.

elsewhere [14]. At high peak stress, misfit stress was influenced by fiber roughness due to the damage of the PyC interphase during the test. Therefore, the misfit stress at a peak stress of 125-175 MPa was used for this evaluation. The result is: σ^T=+9±6MPa (unirradiated), +3±3MPa (3.1dpa at 740°C), +6±2MPa (12dpa at 750°C) for TySA composites, and +9±5MPa, +6±5MPa, +5±3MPa for HNLS composites. From these results, it appears that the misfit stress may not affect the tensile behavior of either composite under these irradiation conditions.

IV. SUMMARY

In order to identify the effects of neutron irradiation on tensile properties of advanced SiC/SiC composites (Tyranno-SA3rd (2D)/PyC/FCVI and Hi-Nicalon Type-S (2D)/PyC/FCVI), unloading/reloading cyclic tensile test was conducted and hysteresis loop analysis was applied. Neutron fluence and irradiation temperature were 3.1×10^{25}n/m^2 (E>0.1MeV) at 740°C and 1.2×10^{26}n/m^2 at 750°C. The following results were obtained:

1. Both composites exhibited excellent irradiation resistance to changes in ultimate tensile strength and proportional limit stress. And slight reduction of elastic modulus was observed after irradiation.
2. Hysteresis loop analysis indicated that the sliding stress at fiber/matrix interfaces remained almost unchanged after irradiation to 3.1×10^{25}n/m^2 at 740°C, whereas it was significantly reduced by 1.2×10^{26}n/m^2 at 750°C for both composites.

ACKNOWLEDGMENTS

This work was performed as a part of corroboration at Irradiation Experimental Facility, Institute for Materials Research, Tohoku University, Japan. Materials were

supplied as part of the DOE/MEXT JUPITER-II Collaboration for Development of Advanced Blanket Performance under Irradiation and System Integration.

REFERENCES

[1] Y. Katoh, et al..
[2] L.L. Snead, M.C. Osborne, R.A. Lowden, J. Strizak, R.J. Shinavski, K.L. More, W.S.Eatherly, J. Bailey and A.M. Williams, J. Nucl. Mater. 253 (1998) 20-30.
[3] G.W. Hollenberg, C.H. Henager, Jr., G.E. Youngblood, D.J. Trimble, S.A. Simonson, G.A. Newsome and E. Lewis, J. Nucl. Mater. 219 (1995) 70-86.
[4] A.J. Frias Rebelo, H.W. Scholz, H. Kolbe, G.P. Tartagalia and P. Fenici, J. Nucl. Mater. 258-263 (1998) 1582-1588.
[5] L.L. Snead, Y. Katoh, A. Kohyama, J.L. Bailey, N.L. Vaughn and R.A. Lowden, J. Nucl. Mater. 283-287 (2000) 551-555.
[6] T. Hinoki, L.L. Snead, Y. Katoh, A. Hasegawa, T. Nozawa and A. Kohyama, J. Nucl. Mater. 283-287 (2002) 1157-1162.
[7] T. Nozawa, K. Ozawa, S. Kondo, T. Hinoki, L.L. Snead and A. Kohyama, J. ASTM Int. 2 (2005) 12884-1-13.
[8] K. Ozawa, T. Hinoki, T. Nozawa, Y. Katoh, Y. Maki, S. Kondo, S. Ikeda and A. Kohyama, Mater. Trans. .
[9] Y. Katoh, T. Nozawa, L.L. Snead and T. Hinoki, J. Nucl. Mater..
[10] Y. Katoh, T. Nozawa and L.L. Snead, J. Am. Ceram. Soc. 88 (2005) 3088-3095.
[11] Y. Katoh, L.L. Snead, T. Hinoki, A. Kohyama, N. Igawa and T. Taguchi, Mater. Trans..
[12] T. Nozawa, Y. Katoh, A. Kohyama, E. Lara-Curzio, Ceramic Engineering and Science Proceedings, Vol. 24 (2003) pp. 415-420.
[13] T. Nozawa, E. Lara-Curzio, Y. Katoh, A. Kohyama, Advanced SiC/SiC composites: Developments and Applications in Energy Systems, Ceramic Transactions, Vol. 144 (2002) pp. 245-252.
[14] E. Vagaggini, J.-M. Domergue and A.G. Evans, J. Am. Ceram. Soc. 78 (1995) 2709-2720.
[15] A.G. Evans, J.-M. Domergue and E. Vagaggini, J. Am. Ceram. Soc. 77 (1994) 1425-1435.
[16] J.-M. Domergue, E. Vagaggini and A.G. Evans, J. Am. Ceram. Soc. 78 (1995) 2721-2731.
[17] J.-M. Domergue, F.E. Heredia and A.G. Evans, J. Am. Ceram. Soc. 79 (1996) 161-170.
[18] J.W. Hutchinson and H. Jensen, Mech. Mater. 9 (1990) 139-163.
[19] J.C. Bokros, G.L. Gthrie, R.W. Dunlap and A.S. Schwartz, J. Nucl. Mater. 31 (1969) 25-47.
[20] CEGA, Report CEGA-002820, Rev 1 (July 1993).

INNOVATIVE LIQUID BREEDER BLANKET DESIGN ACTIVITIES IN JAPAN

Akio Sagara[1], Teruya Tanaka[1], Takeo Muroga[1],
Hidetoshi Hashizume[2], Tomoaki Kunugi[3], Satoshi Fukada[4], Akihiko Shimizu[4]

[1]*National Institute for Fusion Science, Toki, 509-5292, Japan, sagara.akio@nifs.ac.jp*
[2]*Tohoku University, Sendai, 980-8579, Japan, hidetoshi.hasizume@qse.tohoku.ac.jp*
[3]*Kyoto University, Kyoto, 606-8501, Japan, kunugi@nucleng.kyoto-u.ac.jp*
[4]*Kyushu University, Fukuoka 812-8581, Japan, sfukada@nucl.kyushu-u.ac.jp, shimizu@ence.kyushu-u.ac.jp*

In order to clarify key engineering issues and to enhance key R&D activities for D-T fusion blankets, many design activities on innovative liquid blanket systems are on going as collaboration studies in Japan. Recently an improved long-life Flibe blanket has been proposed, and the self-cooled Li/V blanket design has started. For Flibe systems, much progress has been made on tritium permeation barrier, energy conversion system, free surface designs, and thermofluid loop experiments. For Li/V systems, evaluation studies have proceeded on Be-free nuclear properties and allowable crack fraction on multi-layered MHD insulation coatings.

I. INTRODUCTION

After selecting the molten-salt Flibe blanket in the LHD-type helical reactor FFHR in 1995[1], intensive design studies on Flibe blanket have been continued and expanded into wide R&D areas, including materials compatibility, tritium disengager systems, thermofluid and MHD effects, and energy conversion systems, in the NIFS collaborations as summarized in Fig.1 under the Fusion Research Network[2] in Japan Universities. And then, these activities have been expanded into international research programs such as JUPITER-II (2001-2006)[3].

The main purposes of these design activities are to clarify key engineering issues and to enhance key R&D activities required for advanced system integration of D-T power plants. Recently an improved long-life Flibe blanket has been proposed, and self-cooled Be-free liquid blanket designs such as Li/V have been started, based on intensive R&D works and results. This paper mainly focuses on these liquid blanket designs and related R&D activities in Japan.

II. FLIBE BLANKET DESIGN ACTIVITIES

II.A Long-life blanket designs

New design approaches are proposed for the Flibe / RAFS (reduced activation ferritic steel) blanket in FFHR to solve the major issues of blanket space limitation and replacement difficulty. For the neutron wall loading of 1.5MW/m^2 as adopted so far in FFHR designs, an innovative concept of replacement-free blankets is possible in the reactor life of 30 years, using carbon armor tiles as ISSEC (Internal Spectral Shifter and Energy Converter), in which, however, the tritium breeding and tile cooling were key issues[4].

Figure 2 shows the new proposal of our STB (Spectral-shifter and Tritium breeder Blanket) of flibe in the limited thickness of about 1m, where the Be_2C layer in C and the flibe zone are optimized. Comparing with the original blanket[1] without ISSEC, the MCNP-4C calculations using JENDL3.2 nuclear data show that in this STB the flux of fast neutrons (> 0.1MeV) at the first wall of JLF-1 (RAF) is reduced to 1.3x10^{18}/m^{2}s, which is about 140dpa in 30 years and 1/3 of the original flux as shown in Fig.3. At the same time the local TBR higher than 1.2 is obtained as

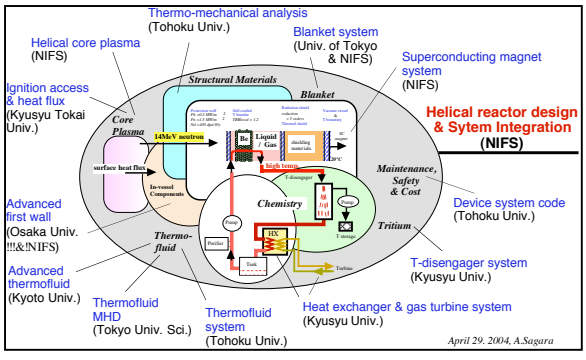

Fig.1 Reactor design activities in the NIFS collaboration.

shown in Fig.4, and the fast neutron fluence to SC magnets is one order reduced to $5x10^{22}n/m^2$, which is sufficient to keep Tc/Tc_0 >0.9 for Nb_3Sn, for instance.

According to a preliminary thermal analysis, the surface temperature of the carbon armor is about 1600°C under conditions of nuclear heating, an effective thermal conductivity of 100W/m/K for C-Be_2C-C bonded armors of 16cm thickness and heat transfer coefficient of $6000W/m^2/K$ for the mechanical contact under a normal bolted pressure using a super-graphite sheet[5] between the armor and the first wall of JLF-1. These conditions are not yet fully available, due to dimensional changes and degradation of thermal properties of carbon under neutron irradiations. Those are key R&D issues including thermal stress in tiles. Fortunately the tritium inventory trapped in carbon is negligible at such high temperatures.

II.B Tritium recovery systems

Because of low hydrogen-isotope solubility in Flibe, tritium recovery is very easy. At the same time, however, tritium leak due to permeation through the recovery system is a crucial problem. In the FFHR with 1GWth fusion power, the tritium generation rate is 1.8MCi/day and the Flibe flow rate is $2.3m^3/s$ for the in-out temperature difference of 100°C. Then, for the condition of the tritium concentration at the outlet to be $5x10^{-4}$wppm (1kPa), the tritium recovery system needs to recover almost all tritium in one cycle using such as a vacuum disengager or a He-Flibe counter-current flow extractor in order to decrease tritium leak from the heat exchanger. The overall tritium recovery ratio was assumed to be 99%.

The permeation leak rate through the duct with thickness of 3mm is about 1kCi/day. In order to reduce the leak rate below 10Ci/day, a double tube concept has been proposed in FFHR as shown in Fig.5. The leak rate is lowered down to 1Ci/day when the duct tube (~$100m^2$) is covered with a tritium barrier. For this barrier, a small part of Flibe is branched off at the heat exchanger outlet and made flow in the reversible direction. When tritium is generated in Flibe, the tritium pressure becomes considerably high, because of the low Henrry's solubility constant under a given tritium concentration. On the other hand, when tritium is not generated in Flibe, i.e., out-of-vessel Flibe, the tritium permeability through well-Redox-controlled Flibe becomes low because of the low solubility[6, 7]. Consequently, Flibe can be used as a permeation barrier[8]. Alternatively the conventional concept to flow He sweeping gas in the double tube is also feasible as the barrier with a flow rate around 220cc/s.

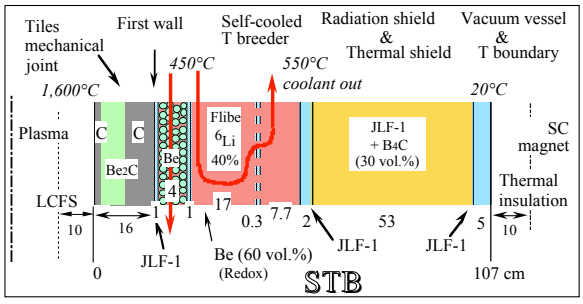

Fig.2 Radial build of STB Flibe blanket for FFHR2.

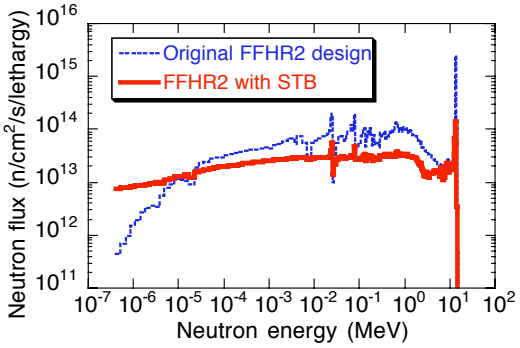

Fig.3 Neutron spectra at the first wall calculated for FFHR2 Flibe blanket with and without STB.

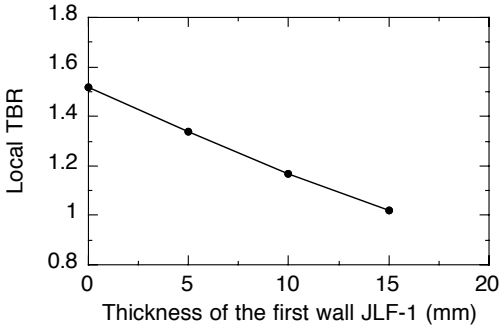

Fig.4 Local TBR in the STB Flibe blanket as a function of the thickness of the first wall.

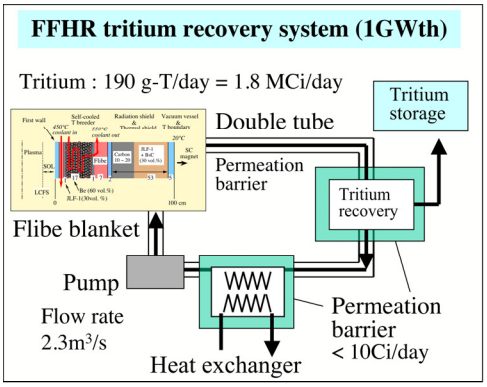

Fig.5 Schematic illustration of tritium recovery system for the Flibe blanket in FFHR2.

The most serious problem left on tritium safety is permeation leak through the heat exchanger to the secondary He loop, and its rate is estimated 18kCi/day assuming heat exchanger surfaces of several thousands m^2. With use of a high-pressure helium turbine system and good thermal conductivity tube, the area can be cut down. At all rates, tritium in Flibe coming out of tritium recovery system permeates through the heat exchanger walls if an effective tritium permeation barrier is not developed. Therefore, the tritium has to be recovered from the secondary He loop. Catalytic oxidation or Pd permeation method will be used for the tritium recovery in a similar way to the tritium recovery from the He purge gas in the solid blanket system.

II.C Energy conversion systems

The in/out operation temperature of Flibe in FFHR blanket design is 450˚C and 550˚C, respectively, where 45mol% BeF_2 is selected instead of peritectic Flibe (33mol%BeF_2) in order to keep the temperature margin at about 420°C, because the two times increase of viscosity ν does affect the pressure drop by only $\nu^{0.25}$. For this condition, a closed helium gas turbine cycle with three-stage compression-expansion as illustrated in Fig.6[9, 10] was newly proposed and the attainable thermal efficiency was estimated. It consists of one pre-cooler, two inter-coolers, one regenerative heat exchanger, one main heat exchanger, two reheaters as well as three compressors and expanders. The heat rejecting temperature was fixed at 30˚C and the compression and expansion ratios for each of the three stages were assumed to be equal. The maximum thermal efficiency was found to be 37% for compression ratio of 1.5, which can favorably be compared with standard thermal efficiency of conventional nuclear power plants.

However, the problem lies in the pressure drop ratio. In the above estimation, the relative pressure drop through whole cycle path was fixed at 0.1. Although it is a typical value in conventional gas turbine cycles, the present multi-stage cycle contains total 7 heat exchangers in the operating flow path. As the pressure drop ratio increases, the attainable thermal efficiency decreases rapidly. Therefore the layout of energy conversion devices is a key design issue for realizing such multi-stage compression-expansion gas turbine cycle.

Another problem may be a leakage of tritium-containing helium gas through the shaft bearing. It will give rise to the necessity of containing whole system in a large vessel, as in the design of modular type HTGR power plant.

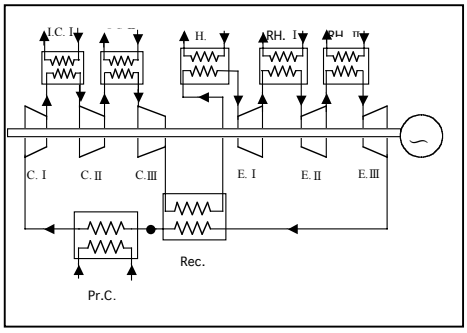

Fig.6 Proposed He gas turbine cycle with three-stage compression-expansion system.

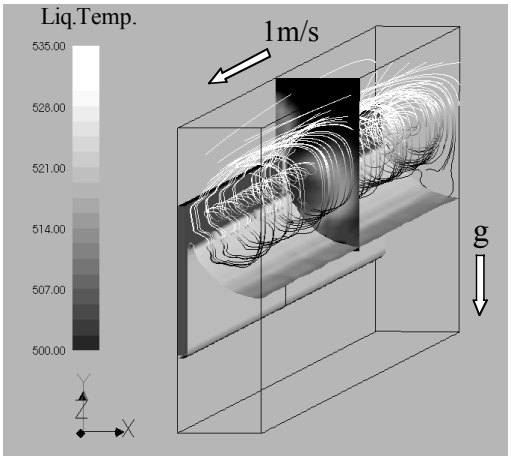

Fig.7 Result of the numerical simulation for free surface flow and liquid temperature profile under the surface heat flux of 0.1MW/m^2.

II.D Innovative free surface wall

In general, a high Prandtl number (Pr = ν /*a*, here ν is viscosity and *a* is thermal diffusivity) fluid like Flibe (Pr = ~30) has relatively lower heat transport capability than that of liquid metal (Pr = ~0.03 for Li), because of its very low thermal diffusivity and low thermal mixing feature due to thinner thermal boundary layer at an interfacial region. Therefore, in particular, the design feasibility of the first wall for Flibe blanket is one of the key issues.

As for the application of free surface concept to the FFHR design, it is necessary to consider the helical configuration, that is, at a certain position the free surface would be at the ceiling. In this case, the liquid might be falling down into the plasma. Therefore an innovative free surface design KSF wall (Kunugi-Sagara type Free surface wall) has been proposed, where many micro grooves are made on the first wall as a flow passage to use capillary force to withstand the gravity force[11, 12]. The higher velocity of

coolant to withstand the higher heat load from plasma and the lower vaporization from the coolant free surface would be necessary. In this sense, this innovative cooling concept (KSF) consists of two flow passages: the main coolant flow passage between blanket wall and the groove structures for maintaining the higher coolant velocity along the first wall/blanket structure, and the flow passages in the micro-grooves for reducing the free surface temperature due to the secondary flow convection: the enhancement of the thermal mixing near the free surface. The mean coolant flow velocity in the main passage was assumed 1m/s. However, the mean velocity in the grooves might be very small because of the large friction loss.

Advanced numerical simulation has explored that, as shown in Fig.7, a pair of symmetrical spiral flows is formed in a half of 1.2mm groove due to the flow induced by the surface tension, the shear force from the main stream and the buoyancy force. In case of the vertical and bottom wall configurations, both cases show the spiral flows as the same as Fig.7. So, the same heat transfer performance can be expected for both configurations. The most attractive result is that this spiral flow enhances heat transfer efficiency, where the local heat transfer coefficient evaluated at the groove side wall drastically increases about four times higher magnitude, however the pressure loss was not increased much because of the low flow velocity in the grooves.

II.E Thermofluid R&D activities

As for conventional closed-surface systems, heat-transfer enhancement for such high Prandtl-number fluid as Flibe has been performed using HTS (Heat Transfer Salt with low melting point of 142°C) in a large molten salt circulating experimental device "TNT loop" (Tohoku-NIFS Thermofluid loop) shown in Fig.8[9, 13, 14]. At the test section, a packed-bed tube is employed as the enhancer for molten salt flow activity.

In Fig.9, the results obtained with HTS is converted to the case of Flibe at the same inlet condition of Pr=28.5 where Tin=200^{o}C for HTS and 536^{o}C for Flibe. At this conversion, the temperature difference between the flow bulk and the wall temperature ΔT=100^{o}C and 25^{o}C are assumed, and the linear approximation is employed. It is found that the minimum allowable flow rate to cool 1 [MW/m^2] is about 60 [liter/min] under the condition that the copper bed (D/4: a quarter of the tube diameter D) is used and ΔT is 100^{o}C. This flow rate is lower than that of the turbulent heat transfer (100[litter/min]). This means that MHD effects including electro-chemical activities are preferably lowered.

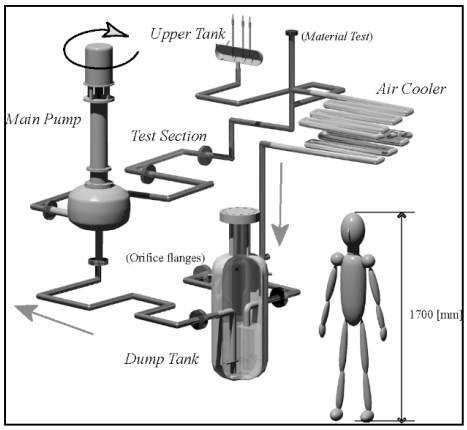

Fig.8 3D image of the TNT loop, which has the total capacity of 0.1m^3 and can be operated at 600°C.

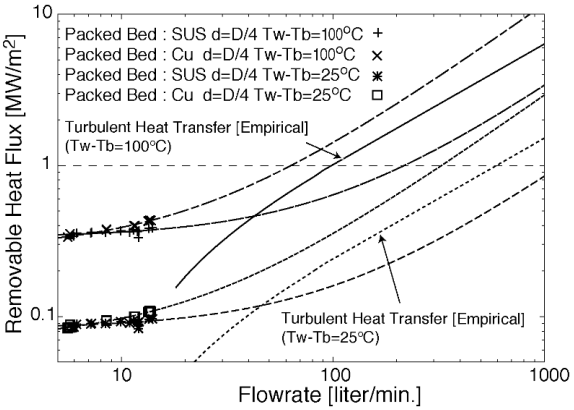

Fig.9 Flibe flow rate to remove the heat flux on packed-bed tubes in comparison with a strait tube.

The pressure drop induced in the packed-bed tube has to be quantitatively evaluated for a detailed reactor design. However, since there must be a lot of out-of-vessel tubes with many elbows, the total pressure drop may be lower for a low flow rate in case of packed bed comparing with the case of turbulent flow. And then the pumping power (pressure drop x volumetric flow rate) is beneficially lowered.

III. LI/V BLANKET DESIGN ACTIVITIES

III.A Self-cooled Be-free Li/V blanket

Based on intensive R&D progress on in-situ MHD coatings of Er_2O_3[15] and high purity V fabrication[16], self-cooled Li/V blanket designs have started[17, 18]. In particular, the Be-free Li/V concept has some attractiveness such as a simplified blanket structure, free from Be resource limitations, and with no concern for safe handling and neutron-irradiation

effects on solid Be. Moreover, vanadium alloy as the structure material enables high operation temperature up to ~750^{o} C, leading a high thermal efficiency. On the other hand, the nuclear shielding property becomes poor without Be.

Figure 10 shows a simple model of Be-free Li/V blanket as an alternative for FFHR2[18], where the total blanket thickness is expanded from 90 cm of the original design to 120 cm as a modified design. Under the condition of fixed blanket space of 120 cm, balance of the tritium production and the shielding performance was examined by changing the thickness of the breeder channels as shown in Fig.11. Performances of Flibe/V and Flibe/JLF-1 blankets adopting the same geometrical model of Fig. 10, which also do not use additional solid Be, are plotted in the figure for comparison. TBR of Li/V is higher than 1.3 at about 50 cm with an acceptable shielding efficiency for super-conducting magnets.

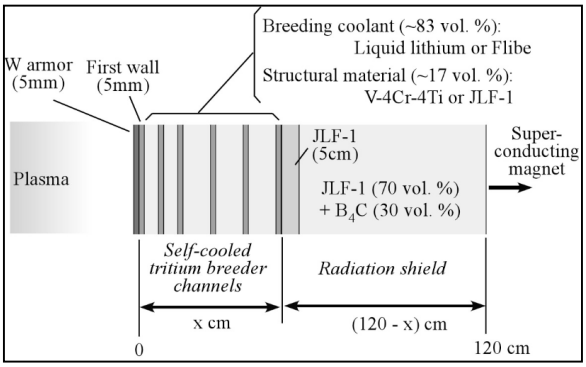

Fig.10 Geometrical model of self-cooled liquid blanket system for nuclear calculation

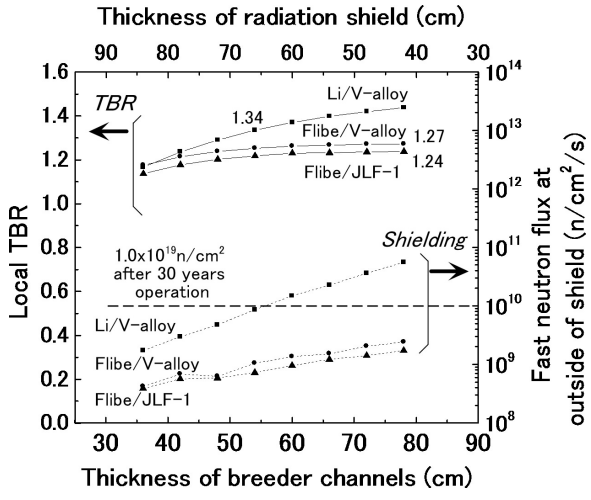

Fig.11 Local TBR and neutron shielding performance calculated for the Li/V blanket with 6Li enrichment of 35%.

III.B Evaluation of MHD pressure drop

Reduction of MHD pressure drop is one of critical issues in self-cooled lithium blanket systems. For this purpose, some concepts are proposed where insulating material is coated on the inside wall of metal channel. In these concepts, however, cracking in the insulator layer might become fatal to increase the MHD pressure drop drastically. In order to avoid this fatal failure, three-layered wall is proposed as schematically shown in Fig.12, where the inner thin vanadium layer helps prevent permeation of lithium into a crack in the insulating layer[19]. By expanding the theoretical models proposed in references[20, 21] to treat the inner wall thickness explicitly in the circuit theory, the following equations are obtained,

$$-\frac{dp}{dz} = \frac{b}{a}\frac{1}{R}\bar{u}B^2 \qquad (1)$$

$$R = \frac{b}{\sigma_{Li}a} + R(n)$$

$$R_y(i) = \frac{t_i}{2a\sigma_i} + \frac{t_{i+1}}{2a\sigma_{i+1}} \quad (1 \le i \le n-1)$$

$$R_y(n) = \frac{t_n}{2a\sigma_n}$$

$$R_p(i) = \frac{1}{\sigma_i}\left(\frac{a}{3t_i} + \frac{b}{t_i} + 1\right) \quad (1 \le i \le n-1)$$

$$R_p(n) = \frac{1}{\sigma_n}\left(\frac{1}{\frac{3t_n}{a} + \frac{3b\sigma_{Li}}{a\sigma_n\sqrt{Ha}}} + \frac{1}{\frac{t_n}{b} + \frac{a\sigma_{Li}}{b\sigma_n Ha}} + 1\right)$$

$$R(i) = R_y(i) + \frac{1}{\frac{1}{R(i-1)} + \frac{1}{R_p(i)}}$$

Here σ and Ha corresponds to electric conductivity and Hartmann number, respectively. The outermost and innermost layers are expressed by i=1 and i=n, respectively. In the equations, the Hartmann and M-shape layers at the boundary of Li are also treated as conducting walls. The performance required to the second layer as insulator is evaluated to be

$$\frac{1}{\sigma_2}\frac{t_2}{a} >> \frac{1}{\sigma_3}\left(\frac{1}{\frac{3t_3}{a} + \frac{3b\sigma_{Li}}{a\sigma_3\sqrt{Ha}}} + \frac{1}{\frac{t_3}{b} + \frac{a\sigma_{Li}}{b\sigma_3 Ha}} + 1\right) \qquad (2)$$

In this study, the following parameters are chosen; a=b=5cm, t_1=5mm, t_2=10μm[22] and t_3=10-25μm. Two-dimensional FEM analysis is also performed to evaluate effect of inner metal wall thickness on the MHD pressure drop[23]. Figure 13 shows the results of both numerical and theoretical calculations. Extremely good agreement can be seen between the results. From equation (2), the performance required to the insulator is calculated as follows;

$$\frac{\sigma_2}{\sigma_3} = \frac{\sigma_{insulator}}{\sigma_V} << 0.5 \times 10^{-7} - 1.0 \times 10^{-7}$$

The results clearly indicate that the ratio less than 10^{-9} is enough as complete insulator. The pressure drop *dp/dz* depends on the inner metal wall thickness *t*, flow velocity, and *B* field as follows

$$\frac{dp}{dz} \propto t_{inner\ wall} \times velocity \times B^{\alpha} \ (\alpha = 1.75 - 1.88 < 2)$$

where the reason of $\alpha<2$ is that the thickness of Hartmann and M-shape layers depends on the magnetic field itself.

IV. CONCLUSION

Liquid blanket researches in Japan have been widely expanded into key activities, and much progress has been made in the past decade. Furthermore the network research activities have matured, including international collaborations. Based on those activities, the next steps will be as follows: (1) System integration modeling, (2) Liquid loop experiments for each key issue, (3) Irradiation loop experiments in a hot cell, (4) Blanket system fabrication and operation tests in such devices as ITER[24].

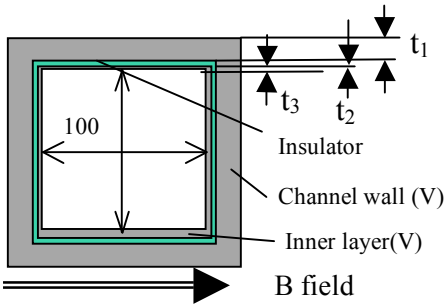

Fig.12 Three layered model to evaluate MHD effects.

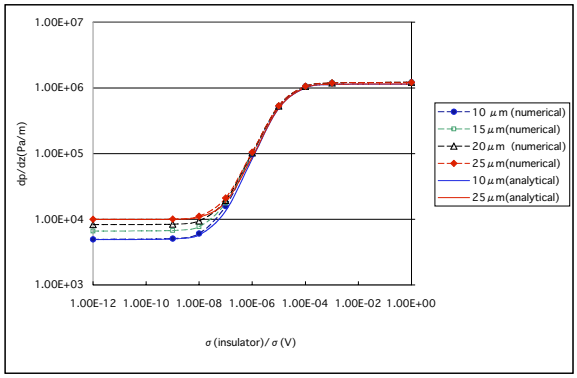

Fig.13 Pressure drop as a function of electro-conductivity ratio σ(insulator)/σ(vanadium), where Li velocity = 0.5m/s and B=5T.

REFERENCES

[1] A.Sagara et al., Fusion Eng. Des. 29 (1995) 51.
[2] A.Sagara, ANS-FED Newsletter - June 2004, http://fed.ans.org/
[3] K.Abe et al., JUPITER-II
[4] R.W.Conn, G.L.Kulchinski et al., Nucl. Technology, 26 (1975) 125.
[5] Y.Kubota et al., Fusion Eng. Des. 56-57(2001)205.
[6] R.A. Anderl, et al., J. Nucl. Mater., 329-333 (2004) 1327.
[7] D. K. Sze, M. Sawan, E. T. Cheng, Fus. Sci. Technol., 39 (2001) 789.
[8] S. Fukada et al., Proc. tritium 2004 (2004) .

[9] A.Sagara et al., Fusion Eng. Des. 49-50 (2000)661.
[10] A.Shimizu et al., NIFS Report, (2002) 272.
[11] A.Sagara et al., Fusion Technology, 39 (2001) 753.
[12] T.Kunugi et al., FED 65 (2003) 381.
[13] S.Toda et al., Fusion Eng. Des. 63/64 (2002) 405.
[14] S. Chiba et al., in these proceedings.
[15] Z.Yao et al., to be published in Proc. 23rd SOFT.
[16] T.Nagasaka et al., in these proceedings.
[17] T.Muroga et al., in these proceedings.
[18] T.Tanaka et al., in these proceedings.
[19] D. Smith et al., ANL/FPP/TM-122, 1984.
[20] K. Miyazaki et al., Fusion Technology 10(1984) 830.
[21] T. Q. Hua et al., Fusion Eng. Des. 27 (1995)696.
[22] D.L.Smith et al. J. Nucl. Mater. 307-311 (2002) 1314.
[23] H.Hashizume et al., ISEM 2003, Versailles.
[24] M.Enoeda et al., in these proceedings.

Neutronics investigation of advanced self-cooled liquid blanket systems in helical reactor

T. Tanaka[1], A. Sagara[1], T. Muroga[1] and M.Z. Youssef[2]

[1] National Institute for Fusion Science, Toki, Gifu 509-5292, Japan
[2] University of California, Los Angeles, CA 90095, USA

Neutronics investigations have been conducted in the design activity of the helical-type reactor Force Free Helical Reactor (FFHR2) adopting Flibe-cooled and Li-cooled advanced liquid blanket systems. In this study, comprehensive investigations and geometry modifications related to the tritium breeding ratios (TBRs), neutron shielding performance and neutron wall loading on the first walls in FFHR2 have been performed by improving the three-dimensional (3D) neutronics calculation system developed for non-axisymmetric helical designs. The total TBRs obtained after modifying the blanket dimensions indicated that all the advanced blanket systems proposed for FFHR2 would achieve adequate tritium self-sufficiency by dimension adjustment and optimization of structures in the breeder layers. However, it appeared that the most important neutronics issue in the present helical blanket configuration was suppression of neutron streaming through the divertor pumping areas and reflection from support structures for protection of poloidal and helical coils. Evaluation of neutron wall loading on the first walls indicated that the peaking factor would be moderated as low as 1.2 by the toroidal and helical effect of the helical-shaped plasma distribution in the helical reactor.

1. Introduction

The collaborative design activity of the helical-type power reactor Force Free Helical Reactor (FFHR2) has been conducted by the National Institute for Fusion Science (NIFS) and universities [1]. In the activity, the neutronics performance has been studied as one of the important issues for deciding the reactor parameters and improving the performance by design modification. Advanced self-cooled liquid blanket systems with Flibe or Li coolant have been studied for FFHR2 to achieve high-performance power generation. So far, the fundamental neutronics potentials for the proposed blanket concepts have been studied by neutron transport calculations with 1D [1, 2] or a simple torus geometry [3, 4].

For progress in the reactor design, evaluation of neutronics performance with 3D geometry data was required to simulate the neutron transport in complicated non-axisymmetric helical systems. The effort to import 3D geometry data from the CAD system into neutronics calculations was made by each neutronics group in Japan, US,EUand China for high accuracy evaluation [5–8]. However, the approach with CAD data has been considered unsuitable for the conceptual design activity of FFHR2, since it would require a long time for preparation, correction and modification of geometry data. Therefore, development of a 3D neutron transport calculation system has been started focusing on the quick generation of 3D geometry data of helical structures and feedback to the design modification and optimization [9, 10].

Progress in those previous works is summarized as (1) the start of development of a new3D neutronics calculation system for helical reactor design and (2) preliminary evaluation of tritium breeding ratios (TBRs) for Flibe+Be/JLF-1 and Li/Valloy blanket systems in 3D geometry and modification of blanket configuration to enhance TBRs. However, issues that remain are (1) TBR evaluation for the multi-layered new helical spectral-shifter and tritium breeding blanket (STB) concept, (2) more accurate evaluation of neutron streaming and reflection in the reactor including vacuum vessels, support structures, cryostat, etc, (3) evaluation of 3D neutron shielding performance especially for superconducting coils and (4) introduction of a helical-shaped plasma core regarding density and temperature distributions to evaluate peaking factors of neutron wall loading on the first walls.

In this study, evaluations for the remaining issues (1)–(4) have been performed and, based on those results, modifications of the helical blanket systems have been discussed. Details of the neutronics methodology and the present neutronics investigations in the FFHR2 design activity are described below.

2. Advanced Liquid-Cooled Blanket Systems for FFHR

Figure 1 shows the drawing of FFHR2m1, which is the present version of the FFHR2 design. The major radius of the torus is 14.0m and the plasma radius is 1.73 m [10]. The structures of the blanket systems proposed for FFHR2 are shown in figure 2. The design activity has originally been conducted with the selfcooled Flibe+Be/JLF-1 (reduced activation ferritic/martensitic steel) blanket system (figure 2(a)) for attractive merits on safety aspects, low MHD resistance, etc. Recently, the Flibe-cooled STB concept employing thick carbon armour (figure 2(b)) has been proposed for the FFHR2m1 design to avoid critical neutron damage on the first wall [11]. In this concept, the replacement-free blanket would be achieved during the reactor lifetime of ~30 years by reducing irradiation damage on the first wall of ferritic steel. In addition to the original Flibe-cooled systems,

Li/V-alloy (vanadium alloy) and Flibe/V-alloy blanket concepts without solid Be multiplier (figure 2(c)) also have been studied as alternatives for high-temperature operation [3, 4]. Neutronics properties of the candidate blanket systems have been investigated by using the Monte-Carlo neutron transport code MCNP-5 [12] and nuclear library JENDL-3.2 [13] for a simple torus geometry as shown in figure 2. In the reactor design activity, the blanket space of 1.2 m and the neutron wall loading of 1.5 MWm^{-2} (~5 × 10^{14} n cm^{-2}s^{-1}) have been

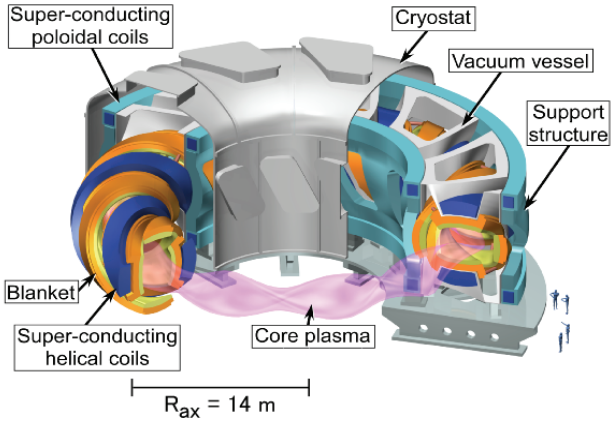

Figure 1. Helical-type power reactor FFHR2m1.

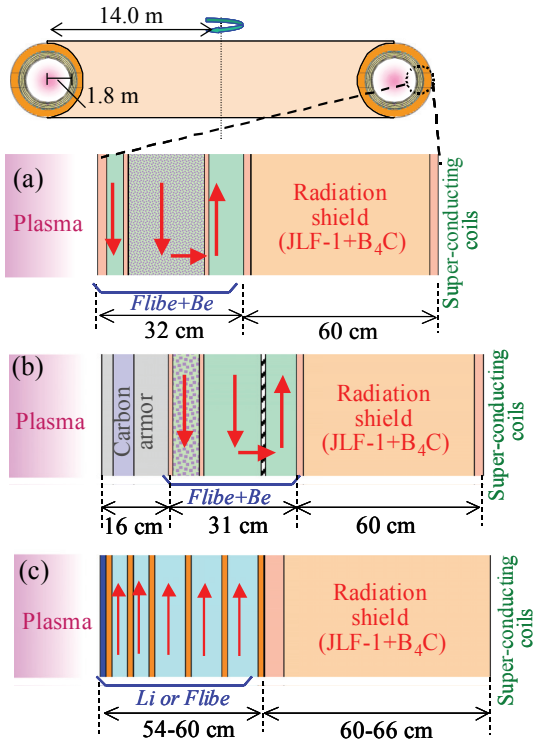

Figure 2. Structures of advanced liquid blanket systems proposed for FFHR2m. (*a*) Flibe+Be/JLF-1 (*b*) Flibe cooled STB and (*c*) Li/V-alloy, Flibe/V-alloy blanket systems.

set as parameters related to neutronics investigations. After optimization of material composition and thickness for the breeder and shielding layers, both requirements on the local TBR ~1.2–1.3 and the neutron shielding performance (<1.0×10^{10} n cm^{-2}s^{-1} for fast neutrons (>0.1 MeV) at superconducting magnet system) are satisfied in all of the blanket systems with the combination of a breeder layer of 30–60 cm and a radiation shield of ~60 cm.

3. The 3-D Neutronics Calculation System

Since the original FFHR2 design has adopted the helical divertor system, the DT core plasma is covered with four separated blanket layers running helically in the toroidal direction as shown in figure 3(a). For neutronics evaluation in the helical reactor, neutron transport in the helical blanket components, streaming through the divertor pumping areas and reflection from the components such as support structures, vacuum vessels and cryostat are important factors to be simulated with 3D geometry data. For the conceptual design activity of the helical reactor, development of a 3D neutronics calculation system has been conducted focusing on the quick feedback between neutronics evaluation and design modification [9].

Input data for the calculation system are prepared by dividing the cross-section of blanket components and helical coils into quadrangular meshes on design drawing as shown in figure 3(a). From the coordinates of each quadrangular mesh, a computer program written for this system calculates the vertices of the 3D helical structure according to the numerical equations defining all the helical structures of FFHR2 [14]. Figure 3(b) shows a model of 3D geometry data for the original blanket configuration of FFHR2m1. The geometry data are converted to an input file for the MCNP5 Monte-Carlo neutron transport code with the computer program. The full torus geometry data of the helical components shown in figure 3(b) consist of ~3,000 cells for the transport code. The number of cells could be decreased to ~500 in the 72° model by using the periodic boundary function of the MCNP code. Details of the 3D neutronics calculation method have been described in our previous paper [9].

The 3D neutronics calculation system has been improved for comprehensive neutronics investigations in this study. In the Monte-Carlo transport calculations, definition of void areas, i.e. vacuum areas, is a difficult issue for simulation of complicated 3D geometry as pointed out also in other calculation systems [5]. For the input of complicated geometry data without the limitation from the MCNP code [9], vacuum areas were divided into small sections in these calculations (section 4.1). A function for simulation of non-helical toroidal structures such as poloidal coils, support structures, vacuum vessel and cryostat has been installed for evaluation of neutron shielding performance in the helical reactor (section 4.2).

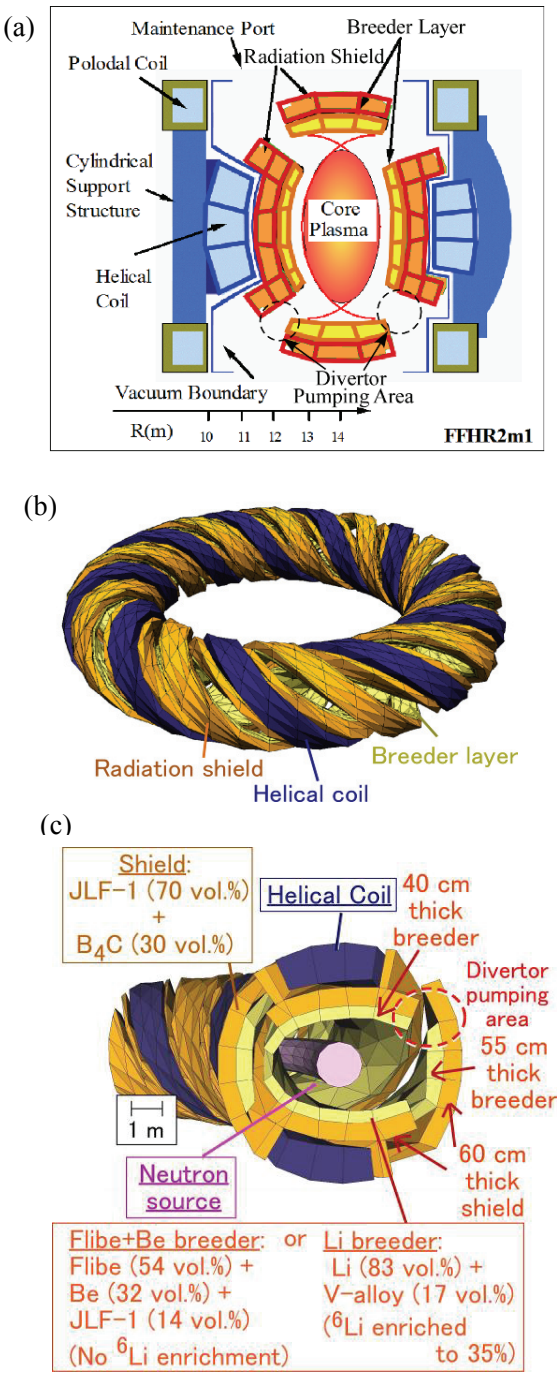

Figure 3. Making of 3D geometry data for present neutronics evaluations: (*a*) Division of cross-section of helical blanket components into quadrangular meshes. (*b*) Example of 3D geometry of helical blanket system. Vertices are calculated according to the numerical equations defining all the helical structures of FFHR2 [9, 10]. (*c*) Cross-section of Flibe+Be/JLF-1 and Li/V-alloy blanket geometry modified for improvement of tritium breeding [9].

Calculated neutron fluxes and neutron currents on components were extracted from an output file of the MCNP code with a post-process program also written for the present system and 3D distributions of the results have been drawn with visualization software for the understanding of the shielding performance (section 4.2) and neutron wall loading on the first walls (section 4.3).

4. Neutronics Performance of Helical Blanket System and Discussions

4.1. Tritium Breeding Ability

Tritium breeding abilities in the Flibe+Be/JLF-1 and Li/Valloy blanket systems have been evaluated using the 3D calculation system in our previous study [9]. The TBRs calculated for the original blanket configuration shown in figure 3(a) were 0.82 (Flibe+Be/JLF-1) and 0.81 (Li/V-alloy). The results indicated that the effective coverage was 60–70 % due to the wide opening at the divertor pumping areas. In order to enhance the tritium breeding ability and shielding efficiency, the dimensions of blanket components have been modified by expanding the edges as shown in figure 3(c). The effective coverage increased to ~80% and the total TBRs in the Flibe+Be/JLF-1 and Li/V-alloy blanket systems were 1.09 and 0.99, respectively. A uniform torus-shaped neutron source 1.5m in diameter was assumed in the investigation. In this study, the TBR of the Flibe/V-alloy blanket system, in which the volume ratios of Flibe and V-alloy are the same as the Li/V-alloy blanket, was also evaluated and was 0.97 for the modified configuration.

In the TBR evaluations described above, the breeder layer was simplified to a uniform mixture of a breeding material, neutron multiplier and structural material. From the results of transport calculations using a simple torus geometry shown in figure 2, it was confirmed that the simplification gives lower TBRs by ~0.3% (Li/V-alloy blanket) and ~4% (Flibe+Be/JLF-1 blanket) compared with the geometry simulating the material distribution in the breeder layer. In contrast to the three blanket systems, simulation of multilayered structure was necessary for the TBR evaluation of the helical STB concept [11]. Since the neutron energy from the core plasma is dramatically attenuated with a thick carbon armour, the position and thickness of the carbon and Be_2C layers affect the TBR sensitively. In previous calculations, the shape of a vacuum area has been defined by simply subtracting all the blanket component cells from a large calculation area with a Boolean command of the MCNP5 code as shown in figure 4(a) [9]. Therefore, the increase in the number of the component cells directly expanded the data length for defining the vacuum area and the data length exceeded the capacity of the MCNP5 code. For the input of the complicated multilayered structures of the STB concept, the calculation system has been modified to divide a vacuum area into small sections as shown in figure 4(b). The division of a vacuum area into smaller sections suppressed the data length for defining each vacuum area

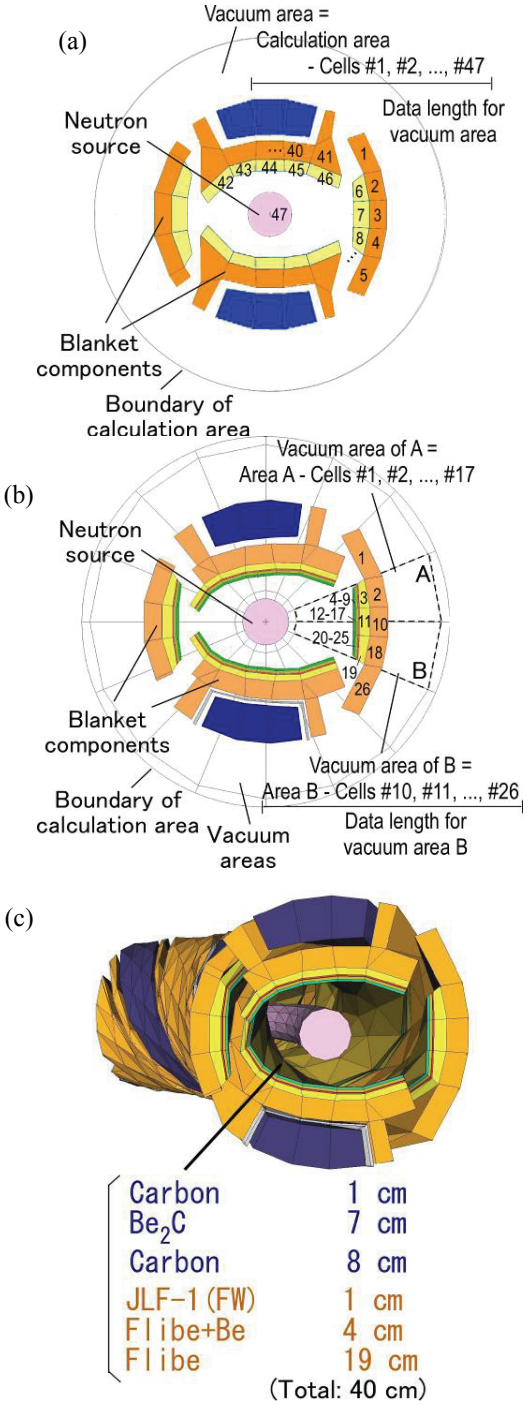

Figure 4. (*a*) Definition of vacuum area in precious calculations [9]. (*b*) Division of vacuum areas to prepare complicated geometry input data for the MCNP code. (*c*) Cross-section of 3D geometry for Flibe-cooled STB concept.

and avoided the limitation in the previous system. By increasing the number of cells defining the blanket structures to ~1,900 (72° model) as shown in figure 4(c), the TBR of the STB concept has been evaluated for the

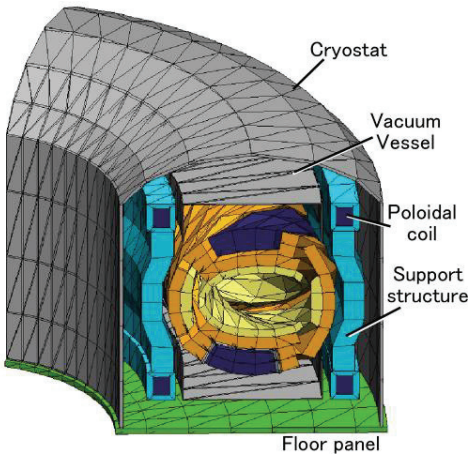

Figure 5. Calculation geometry for investigation of neutron shielding performance.

modified blanket configuration. In our previous optimization of the layer thickness and material compositions using the simple torus model [11], the thickness for the JLF-1 first wall was set to 1 cm. However, the total TBR calculated for the present 3D geometry was 0.91 due to the drastic absorption of thermal neutrons by the JLF-1 first wall. The relation between the local TBR and the first wall thickness evaluated with the simple torus model [11] indicated that the value of the TBR would be improved drastically by reducing the first wall thickness in the design effort. The total TBR of 1.0 was obtained for the 3D geometry with the first wall of 5mm thickness.

4.2 Shielding Performance

Issues of neutron shielding in helical reactors have been discussed in previous neutronics studies for the Heliotron-H reactor design [15, 16]. The importance of shielding for neutrons flowing in the tangential direction of the torus has been pointed out based on neutron transport calculations with a coarse 3D geometry due to a lower computer ability at that time. In this investigation for the FFHR2 design, neutron streaming through the openings of the divertor pumping areas is the main feature to be simulated with the 3D neutronics calculation system. The target of the neutron shielding performance in the FFHR2 design is to suppress the fast neutron flux (> 0.1 MeV) lower than 1.0×10^{10} n $cm^{-2}s^{-1}$ at the super-conducting coil system to avoid critical damage during the 30 years operation [17]. The shielding ability of the helical blanket system against neutrons from the core plasma is evaluated with the geometry shown in figure 5 for the Flibe+Be/JLF-1 blanket system. The intensity of the neutron source was fixed to 6.6×10^{20} n s^{-1} for the 360° full torus geometry, which gives the averaged neutron wall loading of 1.5 MWm^{-2} in the simple torus geometry shown in figure 2. The distribution of fast neutron fluxes

on the structure surfaces were investigated by 3D visualized drawing of the calculated results.

The results indicated the inhomogeneous distribution of fast neutron flux on the helical coil surfaces. Although neutron shielding for the helical coils might be considered adequate on the vertical cross-section of design drawing shown in figure 3(a), the maximum value was ~9×10^{11} n $cm^{-2}s^{-1}$ at the inner side of the torus in the initial design. From the horizontal cross-section of the blanket system shown in figure 6, it has been understood that direct neutrons from the core plasma (arrow (A)) were hitting the thin side shield of ~30 cm thickness. By increasing the thickness of the side shield to ~50 cm and expanding the breeder layers to shield the side surfaces from the direct neutrons, the fast neutron flux on the helical coils at the inner side of the torus could be suppressed to ~3×10^{10} n $cm^{-2}s^{-1}$. Previous neutronics investigations using the simple torus geometry indicated that the fast neutron flux would be reduced by a factor of ~3 by increasing the ratio of B_4C in the shield layer [4]. The improvement in the shielding ability has also been evaluated for the 3D geometry by increasing the B_4C ratio in the shielding layers to 60 vol.%. It was confirmed that the value of the fast neutron flux could be suppressed to ~1×10^{10} n cm^{-2} s^{-1}.

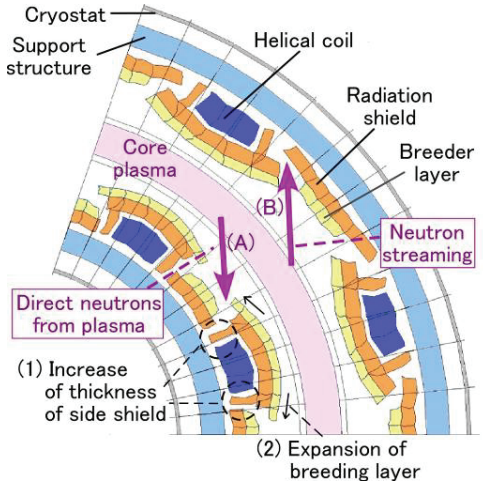

Figure 6. Horizontal cross-section of blanket system and modification of shielding performance against direct neutrons from core plasma.

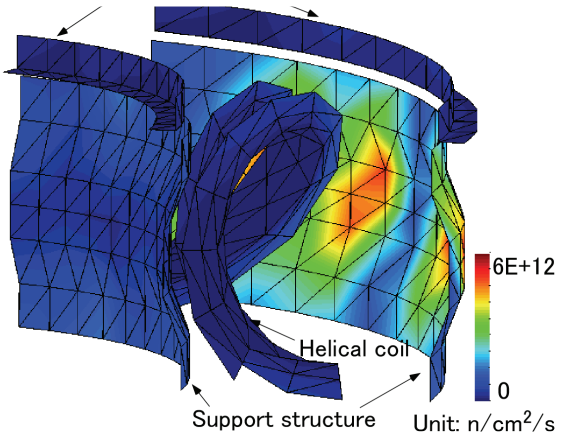

Figure 7. Distribution of fast neutron flux on helical coil, poloidal coils and support structures.

Another issue in the shielding performance is neutron streaming through the divertor pumping areas outside of the torus (arrow (B)). An example of 3D distribution of fast neutron fluxes on the structures is shown in figure 7. In the figure, the fast neutron fluxes on the upper poloidal coils, one of the helical coils and the support structures are extracted and drawn. The gradation of colour is by a smoothing function of the visualization software. The distribution indicated that the fast neutron flux was extremely high on the outer side support structure due to neutron streaming through the divertor pumping areas. The maximum fast neutron flux on the poloidal coils was 1.7×10^{11} n $cm^{-2}s^{-1}$ and exceeded the design target also due to neutron streaming. In addition, the maximum fast neutron flux on the helical coil increased to 1.1×10^{12} n $cm^{-2}s^{-1}$ near the outer support structure. From the comparison with the fast neutron flux of ~3×10^{10} n $cm^{-2}s^{-1}$ obtained for the geometry without the support structure, this is considered to be due to reflection of neutrons from the support structures. By taking into account that the large openings of the support structures for blanket maintenance (figure 1) have not been simulated in the present 3D geometry data, the neutron reflection from the support structures would be lower in the actual reactor geometry. However, the values of fast neutron flux indicate the necessity of drastic enhancement of the shielding ability to reduce the reflection. This is the most important key issue in the present reactor design, and the detailed design modification has been discussed [18] and will be presented elsewhere.

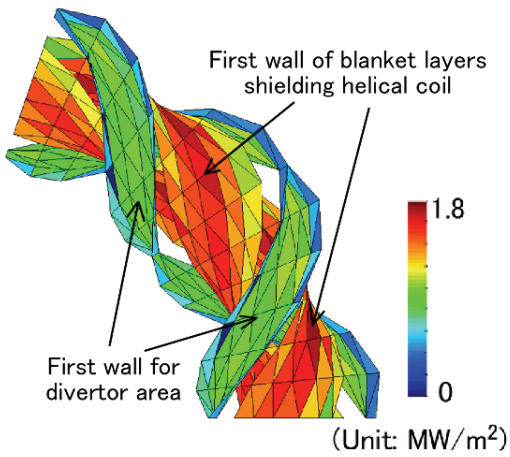

Figure 8. Top view of calculated neutron wall loading distribution (72° of the torus).

4.3 Toroidal and helical effect on neutron wall loading

While the averaged plasma radius has been assumed to be 1.73 m in the design parameters of FFHR2m1 [10], the shortest distance between the toroidal axis and the first wall is 1.45 m in the actual helical blanket configuration. The distribution of the neutron wall loading on the first wall was calculated to evaluate the maximum value in the 3D geometry. Since it has been considered that the neutron wall loading distribution would be affected by the plasma distribution shown in figure 1, the evaluation was performed by assuming helically rotating plasma distribution with an elliptical cross-section. The plasma distribution was simulated by adding a FORTRAN code to a source file of MCNP5, i.e. 'source.f' defining neutron source positions, directions and energies and by recompiling. The assumed long radius and short radius of the plasma cross-section were 2.4 m and 1.5 m, respectively. The second order distribution was assumed for the ion density and temperature in the plasma. The intensity of the neutron source in this investigation was also fixed to 6.6×10^{20} n s^{-1} for the 360° full torus geometry, which gives the averaged neutron wall loading of 1.5 MWm^{-2} in the simple torus geometry shown in figure 2. From the results shown in figure 8, the maximum neutron wall loading has been estimated to be 1.8 MWm^{-2}. Since the maximum neutron wall loading of 2.0 MWm^{-2} was obtained for the uniform torus-shaped neutron source shown in figures 3(c), the comparison of the results indicated that the peaking factor of the neutron wall loading on the first wall would be moderated by plasma distribution in the helical reactor. A more detailed investigation of the relation between the plasma distribution and neutron wall loading distribution is one of the important neutronics studies in the future. The simulation of the helical-shaped plasma increased the total TBR slightly by ~2 % for the Flibe+Be/JLF-1 blanket system compared with the evaluation with the uniform torus-shaped neutron source.

4.4 Improvement of calculation system

A quick feedback between the investigation of the neutronics performance in the helical blanket system and the design modification was performed effectively by using the current 3D neutronics calculation system. In the system, the helical and non-helical toroidal structures of the reactor components could be simulated from the input of small size data, which are the coordinates of the quadrangular meshes generated on the cross-section drawings of the components. However, the investigation of the shielding performance indicates the importance of simulating the maintenance ports on the support structures, divertor pumping ports on the shielding layers etc in further neutronics studies. The addition of the function for importing CAD data is planned for the detailed simulation of the ports. The target of the present development of the 3D neutronics calculation system is to understand the neutron flow in the reactor system by meshing the vacuum areas around structures similarly to the reactor components and by 3D visualization of neutron flux distribution.

5. Conclusion

Neutronics investigations have been conducted in the design activities of the helical-type power reactor FFHR2 by constructing the 3D neutronics calculation system for non-axisymmetrical helical designs. In this study, more accurate evaluations of tritium breeding abilities, neutron shielding performances and neutron wall loading distribution in the helical blanket systems have been performed by newly introducing the methods for complicated 3D geometry data generation and simulation of helical-shaped core plasma distribution. The new functions for 3D visualization of neutronics parameters have been successfully used for finding out the key points in enhancing the neutron shielding performance and also for understanding the positions on the first walls with maximum neutron wall loading.

The total TBR of the Flibe/V-alloy system has been evaluated to be 0.97 with 3D blanket geometry data. The TBR for the Flibe-cooled STB system employing a thick carbon armour was investigated by simulating the multilayered blanket geometry. The results indicate that the STB system would achieve the TBR>1.0 in FFHR2 by reducing the thickness of the JLF-1 firstwall in the design effort. Therefore, including the results evaluated previously for Flibe+Be/JLF-1 (TBR : 1.09) and Li/V-alloy (TBR : 0.99) blanket systems, all four types of advanced liquid-cooled blanket systems would achieve the total TBR>1.0 by further design modification such as optimization of reflectors and dimension adjustment. In the investigation of neutron shielding performance, neutron streaming and reflection in the reactor have been evaluated by including the geometry of the vacuum vessels, support structures, cryostat, etc. The maximum fast neutron fluxes on the helical and poloidal coil surfaces significantly exceeded the design target especially at the outer side of the torus. The neutron flux distribution on the components indicated that the suppression of neutron streaming through the divertor pumping areas and reflection from the support structures is the most important neutronics issue in this design to be improved by drastic modification of the shield configuration. In the evaluation of neutron wall loading on the first walls, it appeared that the peaking factor of distribution in the reactor is moderated as low as 1.2 by the toroidal and helical effect of the helical-shaped core plasma distribution.

After this fundamental investigation of the neutronics performance, this study for the FFHR2 design will proceed in optimizing in accordance with improvement in

other aspects such as plasma distribution, divertor system, superconducting coil system.

ACKNOWLEDGMENTS

The author would like to express his gratitude to Prof. Nobuaki Noda of National Institute for Fusion Science for encouraging the present study. This work has been conducted under the research program of National Institute for Fusion Science NIFS06UCFF004 and the Japan-US collaborative program JUPITER-II task 3-1.

REFERENCES

[1] SAGARA, A., et al., Blanket and Divertor Design for Force Free Helical Reactor (FFHR), Fusion Engineering and Design, 29 (1995) 51-56.

[2] YAMANISHI, H., et al., Design studies on nuclear properties on the Flibe blanket for helical-type fusion reactor FFHR, Fusion Engineering and Design 41 (1998) 583-588.

[3] TANAKA, T., et al., Tritium self-sufficiency and neutron shielding performance of self-cooled liquid blanket system for helical reactor, Fusion Science and Technology 47 (2005) 530-534.

[4] MUROGA, T., et al., Blanket neutronics of Li/vanadium-alloy and Flibe/vanadium-alloy systems for FFHR, Fusion Engineering and Design, 81 (2006) 1203-1209.

[5] SATO, S., et al., Development of CAD/MCNP interface program prototype for fusion reactor nuclear analysis, Fusion Engineering and Design 81 (2006) 2767-2772.

[6] WANG, M., et al., Three-dimensional modeling of complex fusion device using CAD-MCNPX interface, Fusion Science and Technology 47 (2005) 1079-1083.

[7] TSIGE-TAMIRAT, H., et al., Automatic generation of a JET 3D neutronics model from CAD geometry data for Monte Carlo calculations, 75-79 (2005) 891-895.

[8] LIU, X.P., Development and application of MCNP auto-modeling tool: Mcam 3.0, Fusion Engineering and Design 75-59 (2005) 1275-1279.

[9] TANAKA, T., et al., Development of three-dimensional neutronics calculation system for design studies on helical reactor FFHR, Fusion Engineering and Design 81 (2006) 2761-2766.

[10] SAGARA, A., et al., Conceptual design activities and key issues on LHD-type reactor FFHR, Fusion Engineering and Design 81 (2006) 2703-2712.

[11] SAGARA, A., et al., Improved structure and long-life blanket concepts for heliotron reactors, Nuclear Fusion 45 (2005) 258-263.

[12] BRIESMESTER, J.F., MCNP-A general Monte Carlo n-particle transport code, LA-12625-M, 2000.

[13] NAKAGAWA, T., et al., Japanese evaluated nuclear data library version 3 revision-2: JENDL-3.2", Journal of Nuclear Science and Technology 32 (1995) 1259-1271.

[14] YAMAZAKI, K., et al., Plasma transport simulation modeling for helical confinement systems, Nuclear Fusion 32 (1992) 633-644.

[15] NAKANISHI, H., et al., Neutron streaming analysis for helical geometry system, Heliotrion-H fusion power reactor, Journal of Nuclear Science and Technology 23 (1986) 287-299.

[16] HASEGAWA, H., et al., Helical geometry effect on tritium breeding in Heliotron fusion reactor blanket, Nuclear Science and Engineering 86 (1984) 405-409.

[17] OKADA, T., et al., Irradiation effect of superconductors for fusion application, Proceedings of the 6th Japan-US Workshop on High-Field Superconducting Materials and Standard Procedures for High-Field Superconducting Materials Testing, Boulder, Colorado, Feb 22-24,1989.

[18] SAGARA, A., et al., Optimization studies on conceptual designs of LHD-type reactor FFHR, Presented at 17th ANS Topical Meeting on the Technology of Fusion Energy, Nov.13-15, 2006, Albuquerque, NM, USA.

TRITIUM CONTROL FOR FLIBE/V-ALLOY BLANKET SYSTEM

T. Muroga[1], T. Tanaka[1], Zaixin Li[2], A. Sagara[1] and Dai-Kai Sze[3]

[1]*National Institute for Fusion Science, Toki, Gifu 509-5292 Japan, muroga@nifs.ac.jp, teru@nifs.ac.jp,sagara.akio@lhd.nifs.ac.jp*
[2]*The Graduate University for Advanced Studies, Toki, Gifu 509-5292 Japan, li.zaixin@nifs.ac.jp*
[3] *University of California at San Diego, La Jolla, CA 92093-0417, USA, sze@fusion.ucsd.edu*

One of the critical issues of Flibe/V-alloy blanket with REDOX control by Be is a large tritium inventory in V-alloy structures. Among the possible solutions to this issue would be to control REDOX not by Be but by addition of MoF_6 or WF_6 enhancing the reaction from T_2 to TF. The present study investigated feasibility of this procedure by thermodynamic and neutronics calculations. Using the blanket dimensions of Force Free Helical Reactor (FFHR), tritium inventory in V-alloy structure and Flibe were estimated based on the calculated equilibrium partial pressures of T_2 and TF in various cases of REDOX control by MoF_6 or WF_6. Also carried out were neutronics examinations for the impact of Mo or W doping in the blanket. The results showed that the tritium inventory in the blanket area would be less than 100g at the TF level of 0.1 and 1 ppm in Flibe with addition of WF_6 and MoF_6, respectively. WF_6 doping is far more advantageous than MoF_6 doping for low activation purposes.

I. INTRODUCTION

Flibe is one of the attractive liquid breeder materials because of its low chemical reactivity, very low MHD pressure drop and relatively high tritium recovery capability. In contrast to standard FFHR blanket design using Reduced Activation Ferritic/Martensitic Steel (RAFM),[1] the use of vanadium alloys (V-4Cr-4Ti) increased the maximum operation temperature and ΔT of the coolant Flibe in the blanket, which is significantly beneficial for reducing viscosity of the fluid and enhancing thermal efficiency of the plant.[2]

However, combination of high partial pressure of T_2 in Flibe and high tritium solubility of V-alloy structure would result in large tritium inventory in the blanket structural components. As a potential solution to this issue, it was proposed to dope MoF_6 or WF_6 into Flibe for corrosion protection of the wall surfaces by precipitation of Mo or W, and for reduction of the tritium inventory by enhancing the chemical reaction from T_2 to TF which is more soluble in Flibe.[3]

Fig. 1 is a schematic illustration of the REDOX control by WF_6 doping into Flibe. The reaction of the doped WF_6 with T_2 results in extremely biased equilibrium of TF over T_2. The resulting TF and W will be recovered out of the blanket. At the wall surface, the reaction of WF_6 with V results in dissolution of V into Flibe, because the resulting VF_4 and VF_5 are volatile, and plating of the wall surface with W at the initial operation period. The W plating is thought to be effective as a corrosion barrier for the wall according to free energies.[3] In addition, the plating has a self-healing capability.

This concept is quite attractive because of (1) enhanced operation temperature by the use of V-alloys, (2) suppressed wall corrosion by protective Mo or W plating, and (3) reduced T inventory in V-alloy structures by reduced partial pressure of T_2. This is one of the few self-cooled liquid breeder blanket concepts not requiring either MHD insulator or tritium barrier coatings which are recognized as key feasibility issues for the most liquid breeder blanket concepts. Among the issues of the concept is recovery of tritium in the form of TF and Mo or W out of the blanket.

The quantitative examination of this concept has been, however, quite limited. Especially it is necessary to evaluate the feasibility of the concept from the tritium management viewpoint. The present study investigated possible tritium management scenario by quantitative thermodynamic calculations. Also carried out was neutron transport and activation calculations for evaluating nuclear properties of the blanket including continuous WF_6 or MoF_6 doping. Comparisons were made between WF_6 and MoF_6 doping with respect to the tritium managements and the nuclear properties.

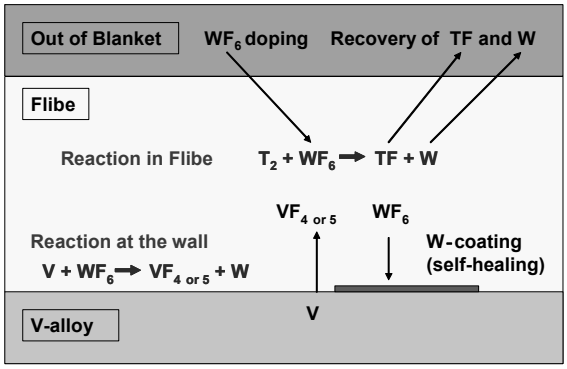

Fig. 1 Schematic illustration of REDOX control of Flibe by doping WF_6.

II. THERMODYNAMICS CALCULATION OF TRITIUM INVENTORY

II.A. Procedure

The reaction of WF_6 with T_2 is given as follows.

$$1/6\ WF_6 + 1/2\ T_2 = 1/6\ W + TF \qquad (1)$$

For this reaction, the chemical equilibrium equation at temperature T is given by

$$\Delta G_f^o = -RT\ ln\ P_{TF}/P_{WF6}^{1/6}P_{T2}^{1/2} \qquad (2)$$

where ΔG_f^o, R, P_{TF}, P_{WF6} and P_{T2} are the difference in the free energy for fluoride formation, gas constant, partial pressure of TF, WF_6 and T_2, respectively. In deriving the relation between P_{TF} and P_{T2}, P_{WF6} needs to be known. In this calculation it is assumed that the solubility of WF_6 in flibe is so high that solution of 1 mol-ppm WF_6 into Flibe at 1 atm results in P_{WF6} of 10^{-6} atm. Because P_{WF6} contributes to the relation between P_{TF} and P_{T2} only by 1/6 power as seen in eq. (2), the impact of the solubility of WF_6 in Flibe is small as will be shown in the results.

Calculation was carried out at 1000K, where ΔG_f^o for WF_6 to TF and MoF_6 to TF was assumed to be 10.6 and 16.0 kcal/mol, respectively.[4] The Sievert's constant for V-4Cr-4Ti at 1000K was assumed to be 0.05/atm$^{1/2}$ based on the recent hydrogen data.[5]

For evaluation of tritium inventory in the V-4Cr-4Ti, the blanket structure of FFHR-FV[6] was assumed, where the breeding blanket is composed of 700 tons of V-4Cr-4Ti structure, 1140 tons of Flibe, and neutron/thermal shield.

II.B. Results and Discussion

Fig. 2 shows partial pressure and tritium molar fraction of TF and T_2 in various levels of MoF_6 or WF_6 doping into Flibe. The conversion from partial pressure to tritium molar fraction for TF and T_2 were derived using the solubility of D_2 and DF,[7-9] respectively, and Henry's law. In the figure, tritium inventory in V-4Cr-4Ti structure and in Flibe were also indicated assuming FFHR-FV blanket structure. It should be noted that the tritium inventory in V-4Cr-4Ti structure and in Flibe are dominated by the partial pressure of T_2 and concentration of TF in Flibe, respectively.

Fig. 2 indicates that the solution level of MoF_6 or WF_6 should not influence strongly the results. The doping of MoF_6 results in partial pressure of T_2 three orders of magnitude lower than that of WF_6.

The level of TF in Flibe is a key parameter for the tritium management in the system. The tritium inventories in 700 tons of V-4Cr-4Ti structure and 1140 tons of Flibe in the blanket area were compared in Fig. 3 as a function

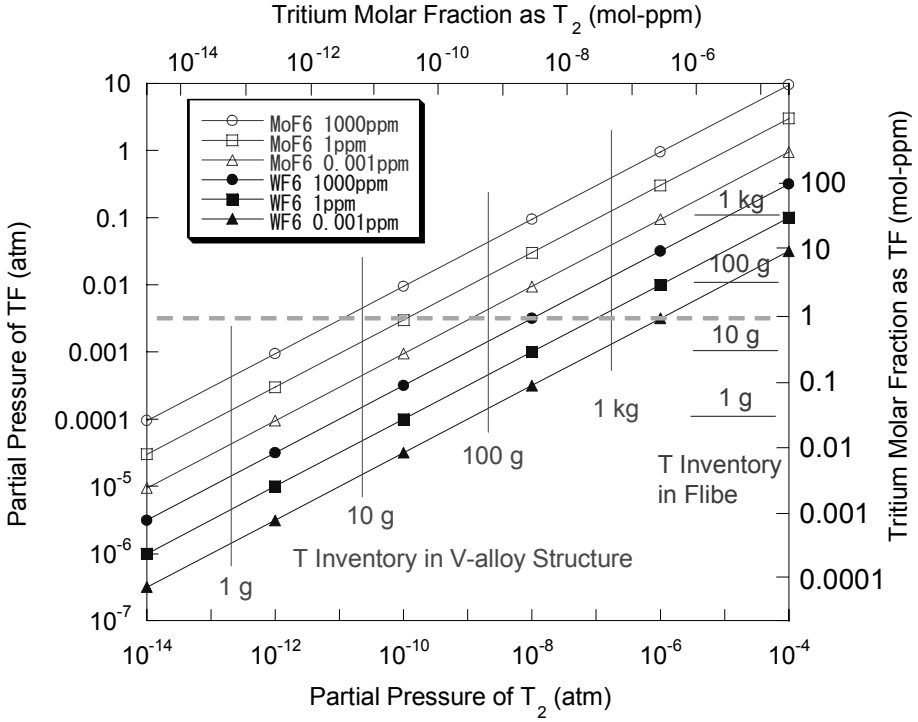

Fig. 2 Partial pressure and tritium molar fraction of TF and T_2 in Flibe for various levels of MoF_6 or WF_6 doping into Flibe at 1000K. Tritium inventory in V-4Cr-4Ti structure and in Flibe were also indicated assuming FFHR-FV blanket structure.

of the tritium molar fraction as TF in Flibe in two cases of MoF_6 and WF_6 doping.

The tritium inventory in Flibe is a unique function of the molar fraction of TF in Flibe because majority of the tritium in Flibe is in solution as TF in the case of REDOX control either by MoF_6 or WF_6 doping. On the other hand, the tritium inventory in V-4Cr-4Ti structure is quite different between the two types of doping. Interestingly, the tritium inventory in Flibe and in V-4Cr-4Ti structure is close with each other in the case of MoF_6 doping. The tritium inventory in V-4Cr-4Ti structure is about 30 times larger in the case of WF_6 doping.

Assuming the guideline of the total tritium inventory in the blanket area of 100g, the acceptable maximum level of TF in Flibe can be estimated to be ~3 ppm and ~0.1 ppm for MoF_6 and WF_6 doping, respectively. According to the previous analysis of tritium management, in which tritium level in Flibe was designed to be ~0.1 ppm,[3,10] the WF_6 doping seems to be feasible for the tritium management.

It should be noted that if REDOX control by Be is carried out enhancing the reaction from TF to T_2, the expected tritium inventory in V-4Cr-4Ti structure in the case of 1 mol-ppm tritium in Flibe would be ~130kg.

III. NEUTRONICS CALCULATION OF BLANKET PROPERTIES IN THE CASE OF MoF_6 or WF_6 DOPING

III.A. Procedure

Neutronics characterization was carried out for the blanket in the simple torus structure of FFHR-FV with the neutron wall loading of 1.5 MW/m^2. The procedure for the calculation was shown in the previous paper.[2]

Assuming the reactor power of 3 GWth, the reaction of the transmutant tritium with MoF_6 and WF_6 results in the precipitation of 2.7 kg of Mo and 5.1 kg of W per day, respectively. They would be removed from Flibe out of the blanket area by cold traps or other recovery systems. In this calculation, two cases, no recovery and 99% recovery, were assumed for the Mo or W precipitates. The impurities in V-4Cr-4Ti or Flibe were not considered in the calculation.

III.B. Results and Discussion

The dose rate of the blanket as a function of the cooling time after 30 years' operation is given in Fig. 4. The blanket without any precipitation of Mo or W can satisfy the hands-on recycle limit after 100 years' cooling. In the case of MoF_6 doping, Mo precipitation results in the radiation level where recycling is almost unfeasible if any recovery is not carried out. 99 % recovery of Mo precipitates results in potential recycling in some shielded conditions. In the case of WF_6 doping, the hands-on recycling limit is fulfilled only after several hundreds of years without any recovery. In contrast, the hands-on recycle limit is satisfied after 100 years' cooling with 99% recovery, which is similar to the case without any precipitates.

Therefore, the doping of WF_6 has a large advantage over that of MoF_6 with respect to the induced radioactivity and recycling capability.

Fig. 5 compares the local Tritium Breeding Ratio

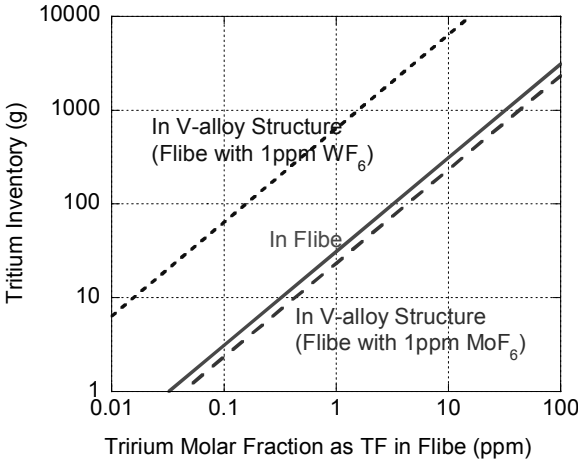

Fig. 3 The tritium inventories in V-4Cr-4Ti structure and Flibe in the blanket area as a function of the tritium molar fraction as TF in Flibe in two cases of MoF_6 and WF_6 doping at 1000K. The blanket structure of FFHR-FV[6] was assumed, which is composed of 700 ton of V-4Cr-4Ti structure and 1140 ton of Flibe.

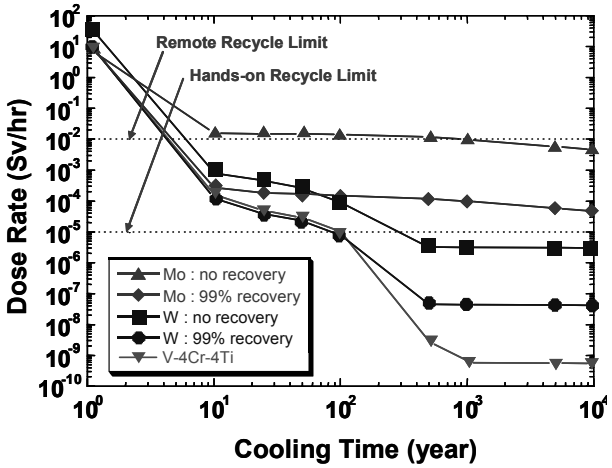

Fig. 4 Dose rate of the blanket as a function of the cooling time after 30 years' operation. The blanket parameter of FFHR-FV[6] was used. Two cases of no recovery and 99% recovery of Mo or W precipitates were assumed. The recycle limits[11] are also indicated.

(TBR) as a function of the operation years. Initial TBR of 1.261 continues to decrease with accumulation of Mo or W in the blanket. However, since the change in TBR is only ~0.01 after 30 years' operation in maximum case, the influence of Mo or W precipitation to TBR is thought to be negligible.

Fig, 6 shows the transmutation products in Mo and W during the operation. Mo and W coatings, once formed during the initial operation, will change into Mo-Nb-Tc-Ru alloy and W-Ta-Re-Os alloy coating during the succeeding operation, respectively. The chemical change in the coating could influence the corrosion protection ability.

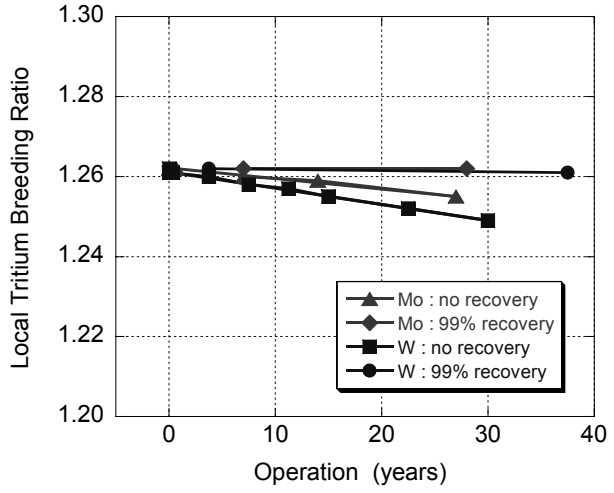

Fig. 5 Local Tritium Breeding Ratio (TBR) as a function of the operation time. Two cases of no recovery and 99% recovery of Mo or W precipitates were assumed.

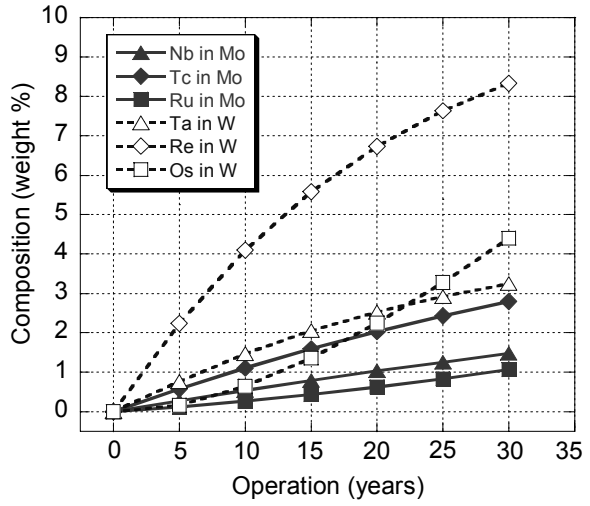

Fig. 6 Compositional change of Mo and Nb in the blanket during the operation.

Some prediction of the stability of the alloy is possible according to the thermodynamic data. Fig. 7 shows the free energies for fluoride formation for the relevant elements derived from MALT-2 database.[12] Higher free energies for RuF_5 and ReF_6 than those of MoF_6 , WF_6 and HF suggests that Ru and Re are stable in Flibe. Nb and Ta may be unstable in Flibe. Considering relatively high production rate, Ta in W could degrade the stability of the coating. The thermodynamic data for Tc and Os were not available in MALT-2 database. However, since Fig. 7 show that stability increases with the change of the element group from V-A, VI-A, VII-A and VIII, Tc (group VII-A) and Os (group VIII) are expected to have high stability in Flibe.

IV. CONCLUSIONS

1. Because of extremely large tritium inventory in structural materials, REDOX control using Be cannot be applied to V-alloy/Flibe blanket system.
2. REDOX control to enhance TF production by doping MoF_6 or WF_6 can reduce the tritium inventory and leakage by large decrease in partial pressure of T_2.
3. The reaction of MoF_6 or WF_6 with wall material (V-alloy) would form corrosion-protective Mo or W coating on the wall in the initial operation period. The coating could have self-healing capability.
4. MoF_6 doping is more effective in reducing the tritium inventory. However, WF_6 doping is still feasible if TF level of ~0.1 ppm in Flibe can be designed in the blanket region. The tritium inventory in the blanket area would be less than 100g at the TF level of 1 and 0.1 ppm in Flibe with addition of MoF_6 and WF_6, respectively.
5. WF_6 doping is far more advantageous than MoF_6

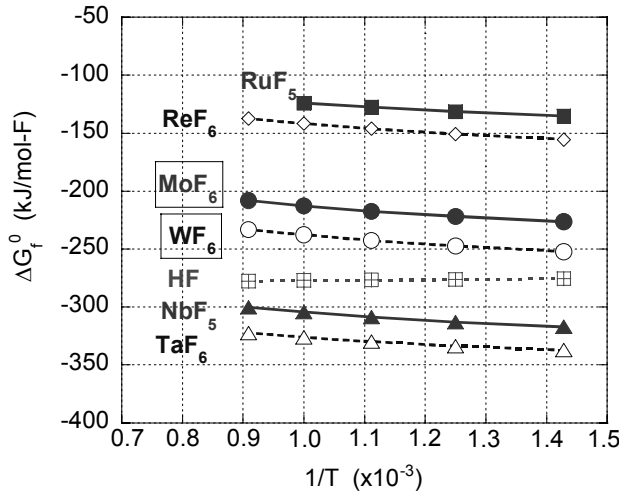

Fig. 7 Free energies for fluoride formation.[12]

doping for low activation purposes.
6. Impact of precipitation of Mo or W in blanket on Tritium Breeding Ratio will be negligible.
7. Transmutation products of Ta in W and Nb in Mo may degrade the stability of W and Mo coating in Flibe, respectively.
8. Among the issues of the concept are recoveries of tritium in the form of TF and Mo or W out of the blanket.

ACKNOWLEDGMENTS

The authors should like to thank Professors S. Fukada of Kyushu University for valuable suggestions. This work was supported by Japan-US Fusion Cooperation Program (JUPITER-II) and NIFS Budget Code NIFS06UCFF004.

REFERENCES

1. A. SAGARA, H. YAMANISHI, S. IMAGAWA, T. MUROGA, T. UDA, T. NODA, et al. "Design and development of the Flibe blanket for helical-type fusion reactor FFHR," *Fusion Engineering and Design*, **49-50**, 661 (2000).
2. T. MUROGA, T. TANAKA and A. SAGARA, "Blanket neutronics of Li/vanadium-alloy and Flibe/vanadium-alloy systems for FFHR," *Fusion Engineering and Design*, **81**, 1203 (2006).
3. D.K. SZE "IPFR, Integrated pool fusion reactor concept," *Fusion Technology*, **10**, 875 (1986).
4. W.R. GRIMS and S. CANTOR, "Molten salts as blanket fluids in controlled fusion reactors", in *The Chemistry of Fusion Technology*, D. M. Gruen, Ed. Plenum Press, 161 (1971).
5. R.E. BUXBAUM, D.L. SMITH and J.H. PARK, "Hydrogen solubility in V-4Cr-4Ti alloy," *J. Nucl. Mater.,* **307-311,** 576 (2002).
6. T. TANAKA, T. MUROGA and A. SAGARA, "Tritium self-sufficiency and neutron shielding performance of self-cooled liquid blanket system for helical reactor," *Fusion Science and Technology,* **47**, 530 (2005).
7. A. P. MALINAUSKAS and D. M. RICHARDSON, "The solubilities of hydrogen, deuterium, and helium in Molten Li_2BeF_4," *Industrial Engineering Chemistry of Fundamentals*, **13**, 242 (1974)
8. P. E. FIELD and J. H. SHAFFER, "The solubilities of hydrogen fluoride and deuterium fluoride in molten flourides," *Journal of Physical Chemistry*, **71**, 3218 (1967).
9. S. FUKADA, R. A. ANDERL, A. SAGARA and M. NISHIKAWA, "Diffusion coefficient of tritium through molten salt Flibe and rate of tritium leak from fusion reactor system," *Fusion Science and Technology*, **48**, 666 (2005).
10. S. FUKADA, M. NISHIKAWA, A. SAGARA and T. TERAI, "Mass-transport properties to estimate rates of tritium recovery from Flibe blanket" *Fusion Science and Technology*, **41**, 1054 (2002).
11. T.J. DOLAN, G.J. BUTTERWORTH, "Vanadium recycling" *Fusion Technology* **26** 1014 (1994).
12. MALT2, Version 1.06 – The Japan Society of Calorimetry and Thermal Analysis

MD and KMC modeling of the growth and shrinkage mechanisms of helium-vacancy clusters in Fe

K. Morishita [1], R. Sugano [1], B.D. Wirth [2]

[1] *Institute of Advanced Energy, Kyoto University, Uji, Kyoto 611-0011, Japan, morishita@iae.kyoto-u.ac.jp, r-sugano@iae.kyoto-u.ac.jp*
[2] *University of California at Berkeley, CA 94720-1730, USA, bdwirth@nuc.berkeley.edu*

A multiscale modeling approach, which is based on atomistic simulations, was applied to investigate the growth and shrinkage mechanisms of helium-vacancy (He-V) clusters in Fe. Firstly, a molecular dynamics (MD) technique with empirical interatomic potentials was used to determine energies for the formation and dissociation of clusters as a function of their size and He density. Both the number of He atoms and vacancies in a cluster ranged from 0 to 20. The dissociation energy of clusters showed a strong dependence on the He density, rather than the cluster size, indicating that the growth and shrinkage of clusters strongly depend on the He density. Secondly, these dissociation energies were employed in a kinetic Monte-Carlo (KMC) simulation, to explore long-time cluster behavior. The KMC simulation indicated that He can stabilize He-V clusters by suppressing thermal vacancy emission and by promoting thermal self-interstitial Fe atom emission. A preliminary KMC simulation to investigate the migration behavior of He-V clusters is also presented.

I. INTRODUCTION

During the operation of fusion reactors, He is directly implanted or generated internally by (n, α) nuclear transmutation reactions in materials, concurrently with energetic displacement damage. High He concentrations and the formation of He bubbles in materials are known to enhance void swelling, cause intergranular embrittlement, and produce surface roughening and blistering. This degradation results from the fact that He is insoluble and therefore tends to precipitate into vacancy clusters or voids in materials.

Trinkaus has classified helium-vacancy (He-V) clusters and He bubbles into three characteristic size classes: atomistic bubble nucleus, nonideal gas bubbles and ideal gas bubbles [1]. The lowest size class is usually indicated by He_nV_m clusters, which may play an important role in the nucleation of He bubbles. However, a physically precise description of bubble nucleation and the transformation of clusters into bubbles have not yet been obtained. The objective of the present study is to provide an appropriate model for nucleation and growth of He bubbles by using a multiscale modeling approach, where the advantages of various simulation techniques are utilized to understand the physical phenomena that take place at a wide variety of time and length scales. As a first step toward the establishment of the model, molecular dynamics (MD) was employed to investigate the energetics of He-V clusters in Fe, and then, a kinetic Monte-Carlo (KMC) technique was applied to understand the thermal stability and migration behavior of the clusters. To validate the computational results, the calculated energies were directly compared with experimental measurements using thermal He desorption spectrometry (THDS).

II. MD CALCULATION OF FORMATION ENRERGIES

In order to evaluate the formation energies of defect clusters in Fe, the empirical interatomic potentials developed by Ackland et al. [2], Wilson and Johnson [3], and Beck [4] were employed to describe interactions between Fe-Fe, Fe-He and He-He, respectively. The Beck potential was modified to smoothly connect with the Ziegler-Biersack-Littmark (ZBL) potential [5] that is appropriate at short atomic separation. Computational box size was 10 *a* x 10 *a* x 10 *a*, where *a* is the lattice constant of Fe. Periodic boundary conditions were applied. Details of the calculation method are described in ref. [6].

The formation energies of vacancy clusters (void) and self-interstitial atom (SIA) clusters in bcc Fe were calculated as a function of cluster size and shape, and the size dependence of the lowest formation energies are well described by the following equations, respectively:

$$E_f(V_k) = 2.7906k^{2/3} - 0.75526k^{1/3}, \quad (1)$$

$$E_f(I_k) = 1.1392k + 4.7035k^{1/2}, \quad (2)$$

where $E_f(V_k)$ is the formation energy of the cluster of *k* vacancies, and $E_f(I_k)$ is the formation energy of the cluster of *k* SIAs. The cluster size, *k*, investigated here ranged up to 76 and 25 for the vacancy and SIA clusters, respectively. The vacancy cluster formation energy agrees very well with a continuum level equation describing void surface energy, down to as small as one vacancy [7]. The binding energy of the vacancy and SIA clusters was defined as follows:

$$E_b(j_k)=E_f(j_1)+E_f(j_{k-1})-E_f(j_k), \quad (3)$$

where *j* is V or I. Both the binding energies defined in this way show an increasing function of cluster size. In addition, as shown in Fig. 1 of ref. [6], the binding energy of SIA clusters is greater than that of vacancy clusters at any size, indicating that a vacancy cluster is thermally less stable than an SIA cluster. In fact, even for larger size, the binding energy of vacancy clusters does not take more than about 1.2 eV, while the binding energy of SIA clusters is greater than 2.0 eV even for 4 SIAs. However, when He atoms are introduced into vacancy clusters, the binding state of the clusters is dramatically changed, as mentioned in the next section.

The formation energy of a He-V cluster that contains *n* He atoms and *m* vacancies was defined as follows:

$$E_f(He_nV_m)=E_{tot}(He_nV_m)-\{n\varepsilon_{He}+(N-m)\varepsilon_{Fe}\} \quad (4)$$

where $E_{tot}(He_nV_m)$ is the calculated total energy of a computational cell containing a He_nV_m cluster, ε_{Fe} is the cohesive energy of a perfect bcc Fe crystal, and ε_{He} is the cohesive energy of a perfect fcc He crystal. ε_{Fe} and ε_{He} was calculated to be –4.316 eV/atom and –0.00714 eV/atom, respectively. *N* denotes the number of perfect bcc lattice sites in the computational cell and therefore (*N*–*m*) is the number of Fe atoms in the cell. From the formation energy obtained here [7], the binding energies of various point defects to a He_nV_m cluster were calculated, where *n* and *m* ranged from 0 to 20. The binding energy of a vacancy, an interstitial He atom, and a self-interstitial Fe atom to He_nV_m clusters was calculated according to the following equations, respectively:

$$E_b(V)=E_f(V)+E_f(He_nV_{m-1})-E_f(He_nV_m), \quad (5)$$
$$E_b(He)=E_f(He)+E_f(He_{n-1}V_m)-E_f(He_nV_m), \quad (6)$$
$$E_b(I)=E_f(I)+E_f(He_nV_{m+1})-E_f(He_nV_m). \quad (7)$$

The formation energy of an isolated vacancy ($E_f(V)$), an interstitial He atom ($E_f(He)$) and an isolated self-interstitial atom (SIA) ($E_f(I)$) in bcc Fe was calculated to be 1.70, 5.25 and 4.88 eV, respectively. The binding energy defined in this way exactly equals the difference in total energy before and after the interaction between such a point defect and a He-V cluster. For example, from eqs. (4) and (5), the vacancy binding energy is rewritten by

$$E_b(V)=\{E_{tot}(V)+E_{tot}(He_nV_{m-1})\}-\{E_{tot}(perfect)+E_{tot}(He_nV_m)\}, \quad (8)$$

where $E_{tot}(perfect)$ is the total energy of a perfect crystal containing *N* Fe atoms which can be expressed as $N\varepsilon_{Fe}$, and $E_{tot}(V)$ is the total energy of a crystal containing an isolated vacancy with (*N*–1) Fe atoms. Thus, eq. (8) shows a difference in total energy between the crystal of 2*N* lattice sites containing a He_nV_m cluster and the same size of a crystal containing both a He_nV_{m-1} cluster and an isolated vacancy.

Extension of eq. (7) provides the definition of the binding energy of an SIA cluster to He_nV_m clusters, as follows:

$$E_b(I_k)=E_f(I_k)+E_f(He_nV_{m+k})-E_f(He_nV_m), \quad (9)$$

where $E_f(I_k)$ is the formation energy of the cluster of *k* SIAs, which can be fitted to eq. (2).

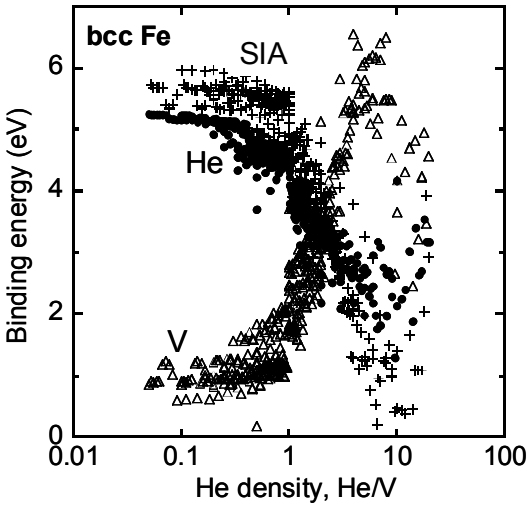

Fig. 1 The binding energy of a vacancy, an interstitial He atom, and an SIA to He-V clusters in bcc Fe as a function of the He density of clusters. All the binding energies strongly depend on the He density, rather than cluster size.

III. BINDING ENERGY OF He-V CLUSTERS

Fig. 1 shows a plot of the binding energies versus the He density of clusters in bcc Fe. The He density was defined as the helium-to-vacancy ratio of clusters, which was the number of He atoms divided by the number of vacancies in the cluster. Namely, the He density of a He_nV_m cluster was provided by *n*/*m*. As shown in the figure, the binding energies primarily depend on the He density. The cluster size dependence of the binding energies is relatively small, except for He_nV_1 clusters, where the binding energies of a vacancy and an SIA are somewhat greater and the binding energy of an interstitial He atom is somewhat lower to the He_nV_1 clusters than to He_nV_m clusters.

Except for the extremely high He density regime (> 6 He/V), the binding energy of a vacancy to He-V clusters gradually increases with increasing He density, which is consistent with the conclusion provided by Adams et al.

[8]. The calculated binding energy of a vacancy to high-density He-V clusters surprisingly exceeds 6 eV, implying that, at any temperature, a vacancy cannot be detrapped from the cluster. Such a high binding energy is inconsistent with the report for He in Ni [9], where Sharafat et al. have extrapolated and evaluated the binding energy of a vacancy to small He-V clusters, from the rather macroscopic point of view. This inconsistency may result from the fact that their estimation was only based on force balance between bubble surface tension and gas pressure, and moreover, the gas pressure was evaluated using the He equation of state (EOS) where only He-He interaction was considered. For such small clusters as investigated here (the number of He and vacancies ranged from 0 to 20), the interaction of He atoms with surrounding metal atoms is more important than the interaction between He-He in the cluster and therefore the metal-He interaction cannot be ignored. Our atomistic calculations giving such high values of the vacancy binding energy may indicate that there is a difficulty in determining the energies of small clusters from the macroscopic point of view. A physical description connecting our atomistic evaluation for smaller clusters and their macroscopic evaluation for larger clusters is beyond the scope of the present work, but it is very important and should be done in the future.

The configuration of He atoms in a He-V cluster strongly depends on the He density of the cluster. When the helium-to-vacancy ratio is approximately 1, the He atoms have bcc configuration, coherent with matrix Fe lattice atoms. On the other hand, when the ratio is greater than approximately 6, they have close-packed configuration in the cluster, and, in this case, the collective motion of He atoms in the cluster produces bubble pressure large enough to push a Fe atom off from its normal site and spontaneously creates additional vacancies and associated SIAs, thereby lowering the He density. These results indicate that the maximum He-to-vacancy ratio is about 6. The SIAs produced in high He density clusters were bound to the cluster, and moreover, the SIAs agglomerated on the same side of the cluster rather than uniformly distributed over the cluster surface, which is consistent with Wilson's observations [10]. This athermal behavior may effectively increase the number of vacancies in the cluster, and therefore, reduce the actual He density of the cluster. This may reflect the vacancy binding energy curve in Fig. 1, where the dependence of the binding energy on the He density changes when the ratio is greater than about 6. For example, as shown in Fig. 1, the binding energy of a vacancy to clusters of He-to-vacancy ratio 10 is approximately the same as that of ratio 3, indicating that the He density of the clusters is effectively reduced from 10 to 3 because of athermal vacancy creation.

The employed interatomic potentials used in this study show that the repulsive interaction between Fe-He is much greater than the relatively weak He-He interaction of a closed shell noble gas. It results in the energetically favorable He clustering in Fe through a decrease in the number of high energy, repulsive Fe-He interactions. This is a possible reason why He atoms make a cluster in Fe, though the cohesive energy of He atoms is negligibly small (ε_{He}=–0.00714 eV/atom for fcc He). In the same way, He atoms prefer to be bound to vacancies for further reduction in the number of the Fe-He interactions. In fact, He atoms are strongly trapped by vacancies and vacancy clusters, and namely, the binding energy of an interstitial He atom to nearly empty voids is very high. Fig. 1 also shows the binding energies of an interstitial He atom to He-V clusters as a function of the He density. The binding energy of an interstitial He atom to He-V clusters decreases from approximately the same value as interstitial He formation energy (E_f(He) = 5.25 eV) at 0 He/V to the value slightly smaller than 2 eV at 6 He/V, followed by an increase at ratios greater than 6. The change in the dependence of the energies on the He density at greater than 6 He/V may be because of the 'athermal SIA production and associated effective decrease in the He density', which is the same reason for the change of the dependence of vacancy binding energy on the He density, as mentioned above. The decreasing and increasing behavior of the He binding energy is qualitatively consistent with the results of He in Ni reported by Wilson et al [10].

Fig. 1 also shows the binding energy of an SIA to He-V clusters as a function of the He density. Similar to the density dependence of the He binding energy, the binding energy of an SIA to He-V clusters also decreases from the value close to the Frenkel pair formation energy (E_f(V)+E_f(I)=1.70+4.88=6.58 eV) at 0 He/V, to nearly zero eV at 6 He/V, followed by an increase with increasing the He density. The density dependence of the SIA binding energy is also qualitatively consistent with Wilson's calculations [10]. It should be noted here that the SIA binding energy is almost zero at high densities. The cluster is fully occupied by 6 He atoms per a vacancy and therefore additional incoming SIAs are prevented from recombining with vacancies.

The binding energies obtained above clearly show some of the He effects on the thermal stability of He-V clusters in Fe during and after irradiation. One is the impact on the binding energy of a vacancy to He-V clusters, where the vacancy binding energy increases with the He density. The second is the impact on the binding energy of an SIA to He-V clusters, where the SIA binding energy decreases with the He density. Both effects will stabilize He-V clusters. In order to profoundly understand He effects, the binding energies of He-V clusters were compared with those of copper-vacancy (Cu-V) clusters in Fe [6], where a Cu atom is usually a substitutional impurity in Fe. It should be noted that the notation of a Cu_nV_m cluster and the definition of the Cu density of the

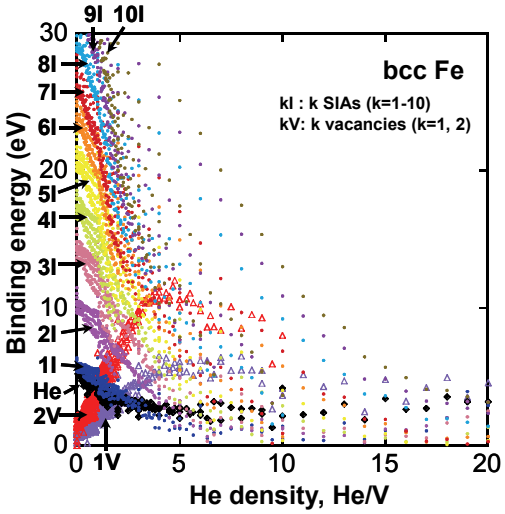

Fig. 2 The binding energy of an SIA cluster to He-V clusters in bcc Fe as a function of the He density of He-V clusters. The SIA cluster binding energy for the He-V clusters of high He density is significantly low.

cluster, n/m, were, on purpose, set to be the same as those for He-V clusters, though such notation is not usual for substitutional impurities. In Cu-V clusters, the athermal production of SIAs takes place at copper-to-vacancy ratios greater than 1, which may reflect the fact that an effective pair potential value of the employed Fe-Fe potential is lower than that of FeCu at the atomic separations expected here. The critical value of 1 for Cu-V clusters may correspond to the critical value of 6 for He-V clusters, and the difference in the critical values may be explained by the difference in the size of the impurities in Fe. In the case of He-V clusters, the gradual but significant changes in the binding energies of a vacancy and an SIA to the clusters were observed for the He density up to the critical value, while such drastic changes were not observed for Cu-V clusters. Thus, the drastic changes in binding energies are one of the characteristic features of He effects in Fe. Further investigation of binding states for other impurity-vacancy clusters in Fe is interesting and it may be required as a reference to understand the He effects more deeply.

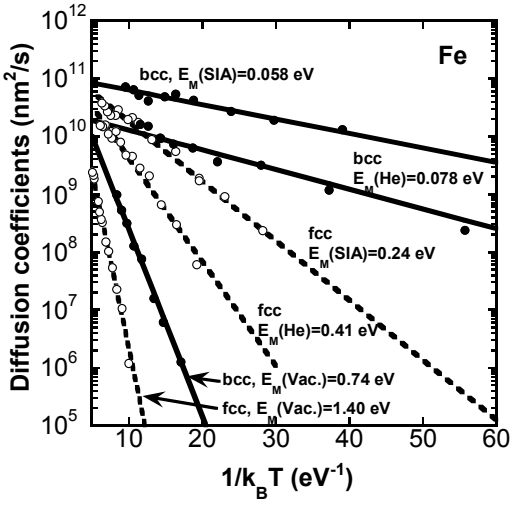

Fig. 3 The Arrhenius plot of diffusion coefficients of a vacancy, an interstitial He atom and an SIA in bcc and fcc Fe. The diffusion coefficients were calculated from the trajectories of the point defects during 1 – 100 ns at various temperatures. The slope of the plot provides the migration energy of the point defects.

Fig. 2 shows the binding energy of an SIA cluster to He-V clusters as a function of the He density, which was calculated using eq. (9). The binding energy primarily depends on the He density rather than cluster size, but there is also the difference of the density dependence between He_nV_1 clusters and He_nV_m ($m\neq1$) clusters. Interesting is the relatively higher density regime, where the binding energy of an SIA cluster to He-V clusters is very small, indicating that the emission of an SIA cluster from the clusters, i.e., 'loop punching [11] ', can take place even at relatively lower temperatures.

IV. DISSOCIATION ENERGY OF He-V CLUSTERS

The frequency of dissociation of a defect *j* from a He-V cluster is usually described by the following equation [15, 16]:

$$\nu(j)=\nu_0 \exp(-E_D(j)/kT), \quad (10)$$

where *j* denotes a defect that dissociates from a He-V cluster, i.e., j=V, He, SIA, SIA cluster, etc. ν_0 is the attempt frequency that is usually assumed to be 10^{13} s^{-1}, k is the Boltzman constant, and T is temperature. $E_D(j)$ is the dissociation energy that is defined as follows [6, 16, 17]:

$$E_D(j) = E_b(j) + E_m(j), \quad (11)$$

where $E_b(j)$ is the binding energy of point defect *j* to a He-V cluster. $E_m(j)$ is the activation energy for migration of point defect *j*. These were calculated to be 0.74, 0.078 and 0.058 eV for *j*=V, He, SIA in bcc Fe, respectively, where the migration energies were obtained by the slope of the Arrhenius plot of diffusion coefficients calculated from the trajectories of the defects during 1 – 100 ns at various temperatures, as shown in Fig. 3.

Fig. 4 shows the dissociation energies of a vacancy, an interstitial He atom and an SIA from He-V clusters as a function of the He density of clusters. The figure provides a deep insight into the growth and shrinkage behavior of He-V clusters in Fe during post-He-irradiation annealing,

from the viewpoint of energetics. At a particular annealing temperature, it is generally expected that, if the activation energy for a certain dissociation process is lower than kT, then the dissociation process can take place. When temperature gradually increases during post-irradiation annealing, firstly, at lower temperatures, thermal SIA emission can take place from clusters of high He density, and then, at higher temperatures, He can dissociate from clusters of higher He density, as well as thermal vacancy emission from the clusters of lower He density. It is interesting to note that, when thermal SIA emission takes place from a He-V cluster, the He density of the cluster decreases because of an increase in the number of vacancies. In the same way, when He dissociation takes place, the He density is decreased by a decrease in the number of He atoms in the cluster. Moreover, when thermal vacancy emission takes place, the He density increases due to a decrease in the number of vacancies in the cluster. Consequently, the He density of stable He-V clusters is given by the region below each curve in Fig. 4. For example, when the annealing temperature corresponds to the dissociation energy of 2 eV, the He density of stable clusters lies roughly from 0.7 to 4. At higher temperature, the lowest limit of the He density gradually increases and the highest limit gradually decreases. Finally, when the temperature corresponds to about 3.6 eV, the He density of stable clusters can only be 1.8, at which all the dissociation energy curves intersect in the figure. Furthermore, when the temperature increases more, the He density of clusters is still about 1.8. In this way, dissociation of a vacancy, He and an SIA from He-V clusters strongly depend on the He density of the cluster and the He density of stable He-V clusters can be determined by annealing temperature. It should be noted that the picture of dissociation processes discussed above does not include the effect of thermal vacancies nor other incoming defects.

V. EXPERIMENTAL VALIDATION

The calculated dissociation energy of an interstitial He atom from He-V clusters was directly compared with the experimental measurements of thermal He desorption spectrometry (THDS), where He atoms desorbed from Fe samples were detected as a function of annealing temperatures by a quadruple mass analyzer (QMA) during post-irradiation annealing at the constant temperature ramping rate of 1 K/s. All He atoms implanted were retained in the as-irradiated samples and all the He atoms were desorbed during the post-irradiation annealing. Details of the experiments are described in ref. [12-14]. The THDS spectra roughly indicated that He atoms are dissociated from the surface at lower temperatures, from He-V clusters at intermediate temperatures (700 – 1200 K), and from bubbles (i.e., bubble migration) at higher temperatures.

When the temperature ramping rate is assumed to be 1 K/s that is the same as our experimental condition and the attempt frequency is assumed to be 10^{13} s^{-1}, the first-order reaction model [18] provides the calculated relationship between annealing temperature, T, in K and dissociation energies, E_D, in eV as E_D=0.0029T [6, 15]. This is an

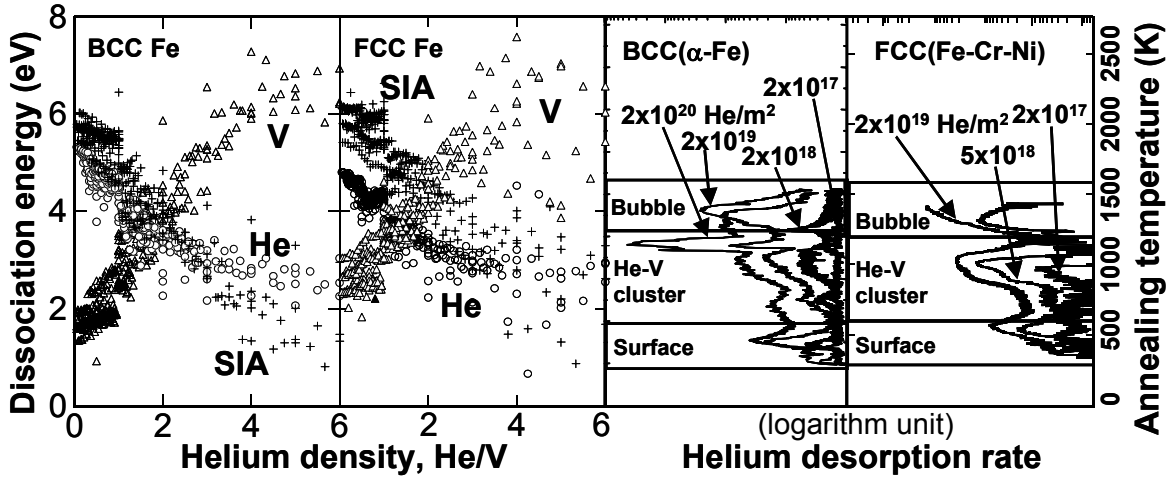

Fig. 4 The calculated dissociation energies of a vacancy, an interstitial He atom and an SIA from He-V clusters in bcc and fcc Fe as a function of the He density of clusters. The calculated energies can be compared with experimental He desorption spectra obtained during the post-He-irradiation annealing at the linear ramping rate of temperature, 1 K/s. The relationship between the calculated dissociation energy and the annealing temperature is described by E_D=0.0029T, where E_D is dissociation energy in eV and T is annealing temperature in K.

equation describing the relationship between the present calculations and our experiments. Fig. 4 also shows a comparison between the calculated dissociation energy curves and the experimental THDS spectra. The ordinate in the figure of the energy curves corresponds to that in the figure of the THDS spectra through the relationship described above. From the dissociation energy curves, He atoms can be detrapped from stable He-V clusters at temperatures approximately from 700 to 1200 K, which is consistent with experimental observation. However, there is a problem with the comparison, because a phase transformation from bcc to fcc takes place in pure Fe at 1183 K. Therefore, the dissociation energies of He-V clusters in fcc Fe were also calculated using the same potential set as used in the calculations for bcc Fe. Although the Ackland potential for Fe-Fe interaction was developed so as to fit bcc Fe [2], it also reproduces the lattice constant of fcc Fe very well (the calculated lattice constant of fcc Fe is 0.3680 nm). In addition, the elastic constants for fcc Fe were calculated to be C_{11}=187, C_{12}=122 and C_{44}=98 GPa at 0 K, which are consistent with the experimental elastic constants of C_{11}=154, C_{12}=122 and C_{44}=77 GPa at 1428 K [19]. Since Fe-He and He-He interactions were described by purely pairwise interatomic potentials [3, 4] and atom-atom separation is the most important parameter for energy evaluations, it may not be unreasonable that the potential set is also useful for evaluation of He-V clusters in fcc Fe. The dissociation energies for He-V clusters in fcc Fe is also plotted in Fig. 4. The dependence of the energies for fcc Fe on the He density is similar to the case for bcc Fe, but the magnitude of the dissociation energy of an interstitial He atom from He-V clusters in fcc Fe is somewhat smaller than that in bcc Fe. This may indicate that, when the phase transformation takes place from bcc to fcc, the He binding strength of the clusters suddenly decreases, resulting in dissociation of excess He. In fact, a burst of He desorption from α-Fe was experimentally observed at around the phase transformation temperature, at which the He desorption peak is so sharp that the usual first-order dissociation model cannot explain the peak. Such a peak is not observed in an fcc Fe (Fe-Cr-Ni alloy), where no phase transformation takes place. Thus, our calculations indicate athermal He desorption at the phase transformation temperature, which is consistent with experimental observations. Helium desorption accompanied with the phase transformation was also discussed in ref. [14] purely from an experimental point of view.

VI. LIFETIME OF He-V CLUSTERS

An MD simulation technique is a useful tool for physical description of the static and dynamic behaviors of nano-scale defects in materials. However, the simulation time is limited within about 1 μs even when using recent high performance computers. The lifetime of He-V clusters may depend on their size and He density and temperature, and it could be, in many cases, beyond the limitation. Therefore, a kinetic Monte-Carlo (KMC) technique was employed to evaluate the lifetime of He-V clusters, where only phenomenological 'known' events are considered. The KMC simulation includes the events of dissociation of a vacancy, an interstitial He atom and an SIA from He-V clusters, but, at present, for simplicity, it does not include the dissociation of an SIA cluster. The occurrence probabilities of the events were assumed to be proportional to eq. (10). Only the vacancies, He atoms and Fe atoms located at cluster-matrix interface were assumed to be the candidates for dissociation. Energetics associated with these events was described by the MD results mentioned above. The time step employed in the calculations is $\Delta t = -\log(R)/\Sigma\nu_i$, where R is random number from 0 to 1 and ν_i is the occurrence probability of an event *i* [20].

Fig. 5 is the time evolution of the size of a He-V cluster in bcc Fe as a function of its initial He density, where cluster size is defined as the number of vacancies in the cluster, independent on the number of He atoms. Initial cluster size is 20 and temperature is fixed at 600 K. Without He atoms, cluster size rapidly decreases and the cluster is completely collapsed within 10^2 s due to thermal vacancy emission. However, when the initial He density increases, cluster lifetime dramatically increases. In addition, when the initial He density is greater than 2, the cluster size increases initially due to thermal SIA emission. Thus, the time development of cluster size, or cluster lifetime, strongly depends on the initial He density.

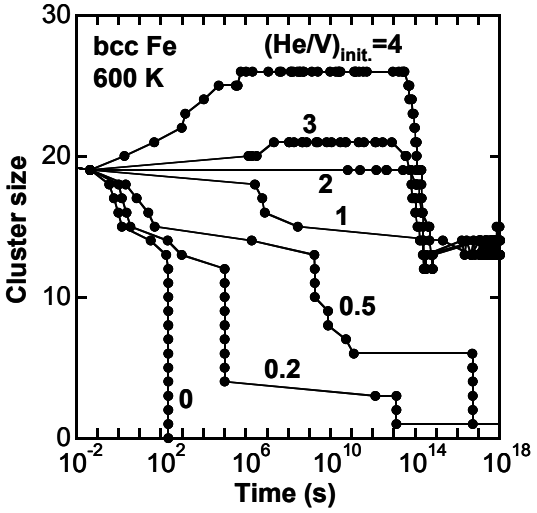

Fig. 5 The time evolution of the size of He-V clusters in bcc Fe as a function of the initial He density of clusters. Initial cluster size is 20 vacancies and temperature is 600 K.

It is noted that the cluster lifetime evaluated here shows the thermal stability of an isolated He-V cluster solely as the general nature of the cluster. Namely, it does not include the effect of incoming defects produced by irradiation. Such an effect may be significant, but introduction of the effect has no general results because how frequently the radiation-induced defects come to He-V clusters strongly depends on irradiation condition and microstructures such as dislocations, grain boundaries, etc. Evaluation of cluster lifetime for the individual specific irradiation and microstructure conditions is beyond the scope of the present paper.

VII. He-V CLUSTER MIGRATION

The migration behavior of He-V clusters in bcc Fe was investigated by KMC calculations, where the effect of thermal vacancies and the diffusion of Fe atoms on the cluster surface were included as well as the dissociation events mentioned above. The thermal vacancy effect and the surface migration of Fe atoms are described by the following equations, respectively:

$$\nu = \nu_0 \exp[-(E_f(V)+E_m(V))/kT], \quad (12)$$

$$\nu = \nu_0 \exp[-(E_M+\Delta E)/kT]. \quad (13)$$

where $E_f(V)$ is vacancy formation energy and $E_m(V)$ is vacancy migration energy. The vacancy formation and migration energies are 1.70 eV and 0.74 eV obtained by MD calculations, respectively. The present model description of the surface Fe atom diffusion was similar to the work by Huang et al [21]. Both E_M and ΔE were assumed to be a function of the He density and the coordination number, where the coordination number is defined as the number of Fe atoms within the first nearest neighbor distance from the Fe atom in considering. ΔE is the difference between the potential energies of a Fe atom at positions before and after a possible jump. The atom potential energy was obtained by MD calculations as a function of the coordination number and the He density. On the other hand, E_M is temporarily assumed to be the same as the migration energy of a Fe atom on a flat free surface (without He). Details of the simulation methods and further work will be reported elsewhere [22].

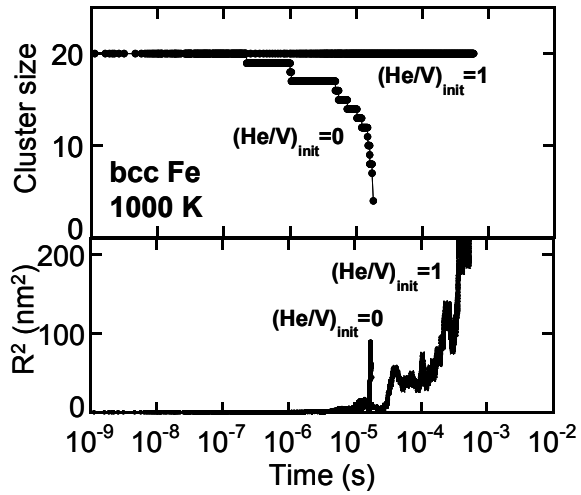

Fig. 6 The time development of the size and squared diffusion distance of He-V clusters in bcc Fe as a function of the He density. Initial cluster size is 20 vacancies and temperature is 1000 K.

Inclusion of the effects of Fe atom migration on the cluster surface and the existence of thermal vacancies into the KMC model provides an insight into the migration behavior of He-V clusters. The Arrhenius plot of diffusion coefficients of He-V clusters shows that the activation energy of He-V cluster migration is approximately the same as the migration energy of Fe atoms on the cluster surface, $E_M+\Delta E$. When 0.5-0.7 eV was used as E_M, the migration energy of a $He_{20}V_{20}$ cluster is approximately 0.89 eV [22]. It may indicate that cluster migration is dominated by the surface diffusion of Fe atoms, rather than by volume diffusion due to the effect of thermal vacancies. It should be noted that the prefactor of cluster diffusion coefficients is five orders of magnitude lower than that of usual point defect migration.

Fig. 6 shows the time development of the size and squared diffusion distance of clusters, as a function of the He density. Initial cluster size is 20, and temperature is fixed at 1000 K. When the He density is zero, cluster size gradually decreases with time due to thermal vacancy emission and cluster mobility increases with decreasing the size. On the other hand, when the He density is 1, cluster size does not change during the simulation time, and therefore, longer distance migration is available during longer cluster lifetime. Thus, cluster migration depends on the size and lifetime of clusters, both of which strongly depend on the He density.

VIII. SUMMARY

The growth and shrinkage behaviors of He-V clusters in Fe were investigated by a multiscale modeling approach using MD and KMC techniques. He atoms in a He-V cluster can stabilize the cluster by suppressing vacancy emission and by promoting SIA emission, resulting in a drastic increase in the lifetime of the cluster. The thermal emission of a vacancy, an interstitial He atom and an SIA from He-V clusters greatly depend on the He density of clusters, rather than the cluster size. The preliminary KMC calculations were also performed to investigate the migration behavior of He-V clusters. The diffusion of a He-V cluster depends on the size and lifetime of the cluster, and therefore depends on the He density.

REFERENCES

[1] H. Trinkaus, Radiat. Effects, 78 (1983) 189.
[2] G.J. Ackland, D.J. Bacon, A.F. Calder, and T. Harry, Philos. Mag., A75 (1997) 713.
[3] W.D. Wilson, R.D. Johnson, 'Rare Gases in Metals', in Interatomic potentials and simulation of lattice defects, (Ed. by P.C. Gehlen, J.R. Beeler, Jr., and R.I. Jaffee), Plenum (1972) p. 375.
[4] D.E. Beck, Mol. Phys., 14 (1968) 311.
[5] J.P. Biersack and J.F. Ziegler, Nucl. Instrum. Meth., 194 (1982) 93.
[6] K. Morishita, R. Sugano, B.D. Wirth, T. Diaz de la Rubia, Nucl. Instrum. Meth., B, in press.
[7] Kazunori Morishita, Brian D. Wirth, Tomas Diaz de la Rubia and Akihiko Kimura, in: Proc. 4th Pacific Rim International Conference on Advanced Materials and Processing (PRICM4), Hawaii, USA 2001, The Japan Institute of Metals, p. 1383.
[8] J. B. Adams, W. G. Wolfer, J. Nucl. Mater., 166 (1989) 235.
[9] S. Sharafat, N. M. Ghoniem, J. Nucl. Mater., 122 & 123 (1984) 531.
[10] W. D. Wilson, C. L. Bisson, M. I. Baskes, Phys. Rev., B 24 (1981) 5616.
[11] J.H. Evans, A. van Veen, L.M. Caspers, Radiat. Effects, 78 (1983) 105.
[12] Kazunori Morishita, Ryuichiro Sugano, Hirotomo Iwakiri, Naoaki Yoshida and Akihiko Kimura, in: Proc. 4th Pacific Rim International Conference on Advanced Materials and Processing (PRICM4), Hawaii, USA 2001, The Japan Institute of Metals, p. 1395.
[13] R. Sugano, K. Morishita, H. Iwakiri, N. Yoshida, J. Nucl. Mater., 307-311 (2003) 941.
[14] R. Sugano, K. Morishita, A. Kimura, in: Proc. 15th Topical Meeting on the Technology of Fusion Energy (TOFE-15), Washington D. C., USA 2002, American Nuclear Society (ANS), to be published.
[15] W. D. Wilson, M. I. Baskes, C. L. Bisson, Phys. Rev. B 13 (1976) 2470.
[16] K. Morishita, R. Sugano, B. D. Wirth, in: Proc. 15th Topical Meeting on the Technology of Fusion Energy (TOFE-15), Washington D. C., USA 2002, American Nuclear Society (ANS), to be published.
[17] N. M. Ghoniem, S. Sharafat, J. M. Williams, L. K. Mansur, J. Nucl. Mater., 117 (1983) 96.
[18] A.V. Fedorov, 'Evolution of point defect clusters during ion irradiation and thermal annealing', PhD thesis, Delft University of Technology, (2000) p. 25.
[19] J. Zarestky, C. Stassis, Phys. Rev. B 35 (1987) 4500.
[20] C. C. Battaile, D. J. Srolovitz, and J. E. Butler, J. Appl. Phys., 82 (1997) 6293.
[21] H. Huang, G. H. Gilmer, T. Diaz de la Rubia, J. Appl. Phys., 84 (1998) 3636.
[22] K. Morishita, R. Sugano, Nucl. Instrum. Meth. B 255 (2007) 52; K. Morishita, Phil. Mag. 87 (2007) 1139.

Nucleation path of helium bubbles in metals during irradiation

Kazunori Morishita

Institute of Advanced Energy, Kyoto University, Uji, Kyoto 611-0011, Japan
morishita@iae.kyoto-u.ac.jp

Thermodynamical formalization is made for description of the nucleation and growth of helium bubbles in metals during irradiation. The proposed formalization is available for evaluating both microstructural changes in fusion first wall materials where helium is produced by (n, α) nuclear transmutation reactions, and those in fusion divertor materials where helium particles with low energy are directly implanted. Calculated nucleation barrier is significantly reduced by the presence of helium, showing that a helium bubble with an appropriate number of helium atoms depending on bubble size can nucleate without any large nucleation barriers, even at a condition where an empty void has very large nucleation barrier without helium. With the proposed thermodynamical formalization, the nucleation and growth process of helium bubbles in iron during irradiation is simulated by the kinetic Monte-Carlo (KMC) technique. It shows the nucleation path of a helium bubble on the (N_{He}, N_V) space as functions of temperatures and the concentration of helium in the matrix, where N_{He} and N_V are the numbers of helium atoms and vacancies contained in the helium bubble, respectively. Bubble growth rates depend on the nucleation path and suggest that two different mechanisms operate for bubble growth: one is controlled by vacancy diffusion and the other is controlled by interstitial helium diffusion.

I. INTRODUCTION

Significant efforts toward modelling the nucleation and growth of helium bubbles in irradiated metals were made a few decades ago. Katz and Wiedersich [1] and Russell [2] separately used the classical nucleation theory to provide the homogeneous nucleation rate of empty voids (without helium) when vacancies and self-interstitial atoms (SIAs) are supersaturated in metals. Later, the effect of helium on bubble formation was introduced into the model and the nucleation rate of helium bubbles was derived [3-5]. In addition, Mansur and Coghlan [6] provided the size dependence of bubble growth rates as a function of helium pressures in a bubble using the rates of vacancy absorption, vacancy emission and SIA absorption by the helium bubble, and they applied it to simultaneous rate theory equations describing defect interactions in metals during irradiation. Their efforts succeeded to explain experimental observations such as the bimodal size distribution of helium bubbles and the shift of temperatures at which void swelling occurs. This model is well established and can be applied enough to bubble formation, where helium is created by (n, α) nuclear transmutation reactions in metals and hence the concentration of helium in the matrix is relatively low.

On the other hand, the theoretical treatment of the nucleation and growth of highly-pressurized helium bubbles has been developed separately from the above. This has been usually employed to interpret the experiments of direct low energy helium implantation. When the concentration of helium in the matrix is considerably high, such an experimental observation [7, 8] should be taken into account that helium bubbles can form even at low temperatures where vacancies cannot migrate. In this condition, the so-called SIA emission and SIA loop punching have been considered as possible mechanisms to understand the growth of helium bubbles, which are not included in the model above. The SIA emission and SIA loop punching were essentially regarded as athermal, mechanical processes, and criteria for the mechanisms to operate were usually given by the minimum pressure of helium in a bubble. Glasgow and Wolfer [9] derived the minimum pressure for the SIA emission under an assumption that the ratio of the number of helium atoms to the number of vacancies contained in a helium bubble (i.e., helium-to-vacancy ratio *or* helium density) remains constant. It was approximately in good agreement with an expression made by Trinkaus [10]. The minimum pressure for the SIA loop punching was provided by Greenwood, Foreman and Rimmer [11], Trinkaus [10], and Glasgow and Wolfer [9] under an assumption that the energy of an SIA loop at a distance far from a helium bubble must be equal to the work expended by helium within the growing bubble. The minimum pressure for the loop punching was furthermore improved by additional consideration of an energy barrier due to elastic interactions between an SIA loop and a helium bubble [12, 13].

Recently, we performed both atomistic calculations using empirical interatomic potentials [14-17] and analytical evaluation based on the continuum model approach with the linear elasticity theory and the equation of states (EOS) for helium [18], to evaluate the formation and binding energies of helium bubbles in iron. It was found that the binding energy significantly depends on the helium density of bubbles rather than bubble size. When

the helium density increases, both the binding energies of an SIA and an SIA loop to a helium bubble significantly decrease to very low positive values. This fact practically indicates that an SIA and an SIA loop have enough possibilities to be emitted thermally from a highly-pressurized helium bubble at finite temperatures, before the athermal mechanisms mentioned above begin to work.

In the present study, the SIA emission was treated as a thermal process, similar to the vacancy emission. And unified formalization was constructed for description of the nucleation and growth of helium bubbles, available for both the regimes of high and low helium pressures. This treatment is quite reasonable when one considers the symmetric behaviour of interactions in metals between vacancies and SIAs. Based on such formalization, the nucleation path of helium bubbles in bcc iron during irradiation was investigated by the kinetic Monte-Carlo simulation technique for a wide range of concentrations of helium in the matrix.

II. NUCLEATION ENERGY OF He-BUBBLES

A helium bubble is a three-dimensional void containing helium atoms, which is sometimes called a helium cavity or a helium-vacancy cluster depending on its size and helium pressure. It is usually regarded as an agglomeration of helium atoms and vacancies than would normally be in a solution in materials during irradiation. However, in the present study, a helium bubble is regarded as an agglomeration of helium atoms, vacancies and SIAs, because SIAs also play an important role, in a negative sense, on the formation of helium bubbles in materials during irradiation. If n helium atoms, m vacancies and l SIAs agglomerate into a single helium bubble that is composed of N_{He} helium atoms and N_{V} vacancies, one should have the relation: $n = N_{\mathrm{He}}$ and $m - l = N_{\mathrm{V}}$. It is noted that m should be greater than l because N_{V} is a positive number. These relations are allusively based on the fact that, when an SIA is absorbed by a helium bubble, it is spontaneously recombined with a vacancy at the bubble-matrix interface. This definition is very useful when one considers interaction between a helium bubble and an SIA, as described in the next section. A similar definition can also be applied to mobile SIA loops if interaction between a helium bubble and an SIA loop is considered, although the interaction between them is neglected here for simplicity.

Within the framework of the classical nucleation theory [19], the nucleation of a helium bubble is generally discussed in terms of the nucleation energy that is defined as a free energy difference between the state of point defects (interstitial helium, vacancies and SIAs) in a solution in metals and that of their agglomeration into a single helium bubble, and given by

$$\Delta g = V\Delta G_{\mathrm{V}} + S\sigma + G_{\mathrm{el}}, \qquad (1)$$

where ΔG_{V} is the volume-dependent term of the free energy change, σ is the surface tension of the helium bubble, G_{el} is the elastic energy of the matrix due to the formation of the helium bubble, V is bubble volume, and S is the surface area of the helium bubble. σ is often assumed to be the same as the surface (interface) free energy. Note that, Δg is identical to the total binding free energy of helium bubbles defined in our previous work [18].

Consider the formation free energy of a helium bubble $G_{\mathrm{bubble}}^{\mathrm{F}}$, which is the free energy change of a system when a helium bubble is introduced into a perfect crystal. This energy gives the binding free energy of point defects to a helium bubble that is derived in an analytical form in the next section. When the formation free energy of a helium bubble $G_{\mathrm{bubble}}^{\mathrm{F}}$ is used, equation (1) is rewritten by

$$\Delta g = G_{\mathrm{bubble}}^{\mathrm{F}} - n\mu_{\mathrm{He}}^{\mathrm{matrix}} - m\mu_{\mathrm{V}}^{\mathrm{matrix}} - l\mu_{\mathrm{SIA}}^{\mathrm{matrix}}, \qquad (2)$$

where $\mu_{\mathrm{k}}^{\mathrm{matrix}} = E_k^{\mathrm{F}} + k_{\mathrm{B}}T\ln C_k^{\mathrm{matrix}}$ is the chemical potential of the type k point defect in the matrix. E_k^{F} and C_k^{matrix} are the formation energy and concentration of the type k point defect in the matrix, respectively, T is the temperature, and k_{B} is the Boltzmann constant.

Following the work done by Trinkaus [10], the formation free energy of a helium bubble $G_{\mathrm{bubble}}^{\mathrm{F}}$ is provided by the sum of the helium bulk free energy $G_{\mathrm{He}}^{\mathrm{Bulk}}$, the helium surface free energy $G_{\mathrm{He}}^{\mathrm{Surface}}$, the metal surface free energy $G_{\mathrm{Metal}}^{\mathrm{Surface}}$, the metal-helium interface free energy $G_{\mathrm{He\text{-}Metal}}^{\mathrm{Interface}}$, and the relaxation free energy G_{Relax}. Considering the fact that the temperature dependence of these terms basically originates from the equation of state for helium [18], one may find that $G_{\mathrm{bubble}}^{\mathrm{F}}$ is almost independent on temperatures at least when the helium pressure is relatively high, because the contribution of a temperature-independent term in the virial equation for pressures [20] to the total pressure is obviously more dominant at high pressures than that of a temperature-dependent term. Besides, when the pressure is low, a main contribution to $G_{\mathrm{bubble}}^{\mathrm{F}}$ is $G_{\mathrm{Metal}}^{\mathrm{Surface}}$ and hence $G_{\mathrm{bubble}}^{\mathrm{F}}$ is considered to be independent on temperatures. After all, it is considered at any pressure regimes that $G_{\mathrm{bubble}}^{\mathrm{F}}$ is almost independent on temperatures. This fact implies that $G_{\mathrm{bubble}}^{\mathrm{F}}$ can be evaluated by the molecular dynamics and molecular static calculation techniques, which only provide internal energy.

The formation energy of helium bubbles $E_{\mathrm{bubble}}^{\mathrm{F}}$ ($\approx G_{\mathrm{bubble}}^{\mathrm{F}}$) was evaluated using the molecular dynamics and static calculations, where a system containing a helium bubble was at first fully relaxed at finite temperature, followed by a quench to obtain the energy of the system at 0 K. Empirical interatomic potentials employed were Ackland *et al*. [21], Wilson-Johnson [22] and ZBL-Beck [23, 24] for describing Fe-Fe, Fe-He and

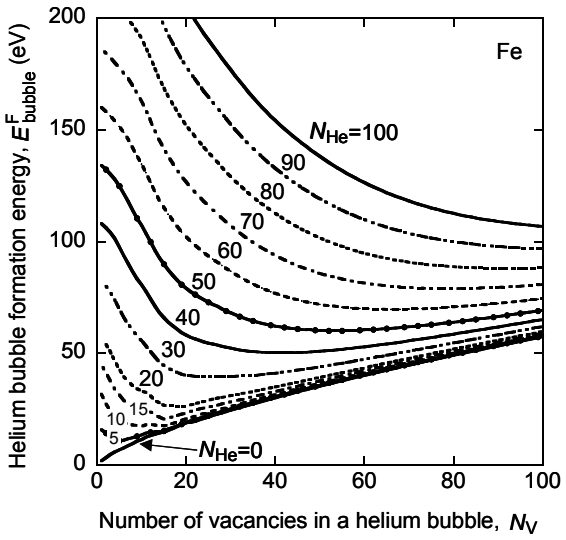

Figure 1 The formation energy of a He bubble in Fe as a function of the number of He atoms contained in the bubble. For He bubbles with both the numbers of He atoms and vacancies less than or equal to 20, the formation energies were calculated by the molecular dynamics and static calculation [14] with empirical interatomic potentials, while for the other bubbles, the energies were obtained by simple extrapolations. See text for more details. It is found that, for a given number of He atoms, the lowest energy configuration has one vacancy per He atom.

He-He interactions, respectively. Both the numbers of helium atoms and vacancies investigated ranged from 0 to 20. Details of the calculations have been described elsewhere [14-17]. In the present study, we have extended both the maximum numbers of helium atoms and vacancies contained in a helium bubble up to 100. However, additional evaluation of the formation energy was done by simple extrapolations of the data obtained from the above atomistic calculation, so that the binding energy of point defects to a helium bubble showed the same function of He/V ratios as the previous one, because those binding energies can approximately be regarded as the function of the ratios only [14-17]. The resultant formation energy of helium bubbles in iron is plotted in figure 1.

Validation of interatomic potential functions is always put in question, whenever empirical interatomic potentials are used. The present study is such the case. Recently, it has been reported that density functional theory (DFT) calculations [25, 26] showed somewhat different properties, such as the stable configuration of an interstitial helium atom and the dissociation energy of substitutional helium, from the present Wilson-Johnson pairwise potential (PP) [22]. The DFT method is generally believed to provide more reliable description of interaction between atoms. However, one should take care of the fact that the method has still a disadvantage; namely, the upper limits of computational box size available for calculations are relatively low. This disadvantage may lead to a problem especially when a highly-pressurized helium bubble is evaluated, where a large computational box is required by the presence of significant lattice relaxation around the bubble. Fortunately, as pointed out in [25], the interstitial helium migration energy obtained by the DFT is very low and it is consistent with that obtained by the present potential. Besides, more importantly, the binding energy of point defects to a helium bubble shows a qualitative similar tendency against the He/V ratio between the two methods. These facts may indicate that, at least, the *qualitative* picture of the nucleation and growth process of helium bubbles can appropriately be obtained by the present potentials.

When the formation free energy of a helium bubble thus defined is used, the chemical potential of point defects in a helium bubble is described as follows:

$$\mu_{\mathrm{He}}^{\mathrm{bubble}} = \partial G_{\mathrm{bubble}}^{\mathrm{F}} / \partial n = \partial G_{\mathrm{bubble}}^{\mathrm{F}} / \partial N_{\mathrm{He}},$$
$$\mu_{\mathrm{V}}^{\mathrm{bubble}} = \partial G_{\mathrm{bubble}}^{\mathrm{F}} / \partial m = \partial G_{\mathrm{bubble}}^{\mathrm{F}} / \partial N_{\mathrm{V}},$$
$$\mu_{\mathrm{SIA}}^{\mathrm{bubble}} = \partial G_{\mathrm{bubble}}^{\mathrm{F}} / \partial l = -\partial G_{\mathrm{bubble}}^{\mathrm{F}} / \partial N_{\mathrm{V}},$$

where the relations $n = N_{\mathrm{He}}$ and $m - l = N_{\mathrm{V}}$ was used for the second equal sign of the respective equations. It should be noted here that an SIA in a helium bubble indicates a metal atom at the bubble-matrix interface. This interpretation seems to be somewhat artificial; however, it is not only very useful from the viewpoint of mathematics, but also consistent with actual physical meanings. In fact, from these equations, one may find

$$\mu_{\mathrm{V}}^{\mathrm{bubble}} = -\mu_{\mathrm{SIA}}^{\mathrm{bubble}}, \tag{3}$$

which reasonably indicates that the work done to introduce a vacancy into a helium bubble is equivalent with the work done to remove an SIA from the bubble. This equation is always correct as long as an SIA in a helium bubble is spontaneously recombined with a vacancy at the bubble-matrix interface.

Consider the equilibrium condition as a special case. When a helium bubble is equilibrated with point defects in the matrix, the chemical potential of the type k point defect in a helium bubble should be equal to that in the matrix, i.e., $\mu_k^{\mathrm{matrix}} = \mu_k^{\mathrm{bubble}}$. This condition is replaced by $\mu_{\mathrm{V}}^{\mathrm{matrix}} = -\mu_{\mathrm{SIA}}^{\mathrm{matrix}}$, if equation (3) is applied. And eventually, equation (2) is rewritten by

$$\Delta g = \Delta H - T\Delta S, \tag{4a}$$
$$\Delta H = E_{\mathrm{bubble}}^{\mathrm{F}} - N_{\mathrm{He}} E_{\mathrm{He}}^{\mathrm{F}} - N_{\mathrm{V}} E_{\mathrm{V}}^{\mathrm{F}}, \tag{4b}$$
$$\Delta S = k_{\mathrm{B}} (N_{\mathrm{He}} \ln C_{\mathrm{He}}^{\mathrm{matrix}} + N_{\mathrm{V}} \ln C_{\mathrm{V}}^{\mathrm{matrix}}), \tag{4c}$$

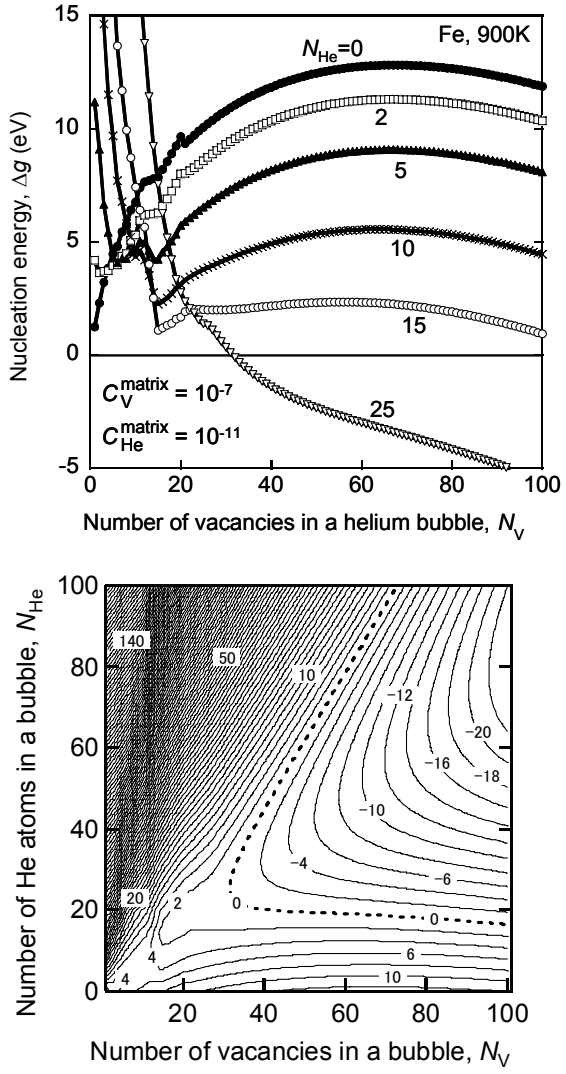

Figure 2 The nucleation energy of a He bubble in Fe as a function of the number of He atoms contained in the bubble (a) and the contour plot representation (b). The concentrations of vacancies and He atoms were fixed at 10^{-7} and 10^{-11}, respectively. Temperature was 900 K. An empty void cannot nucleate at this condition; however, the nucleation barrier is significantly reduced by the presence of He.

where ΔH is what is called the total binding energy of helium bubbles in [27]. These equations clearly indicate that the nucleation energy Δg increases with increasing temperatures and decreases with increasing the concentrations of helium and vacancies in the matrix. In addition, when the chemical potential of a helium bubble is introduced as follows:

$$\mu_{\text{bubble}} = n\mu_{\text{He}}^{\text{bubble}} + m\mu_{\text{v}}^{\text{bubble}} + l\mu_{\text{SIA}}^{\text{bubble}} = G_{\text{bubble}}^{\text{F}} + k_{\text{B}}T\ln C_{\text{bubble}},$$

the global equilibrium condition can be described by $\mu_{\text{bubble}} - N_{\text{He}}\mu_{\text{He}}^{\text{matrix}} - N_{\text{V}}\mu_{\text{V}}^{\text{matrix}}=0$. Therefore, the equilibrium concentration of helium bubbles is given by $C_{\text{bubble}}=\exp(-\Delta g/k_{\text{B}}T)$, showing that the equilibrium concentration decreases with increasing the nucleation energy, as indicated by the classical nucleation theory [19].

Figure 2(a) shows an example of the size dependence of the nucleation energy of a helium bubble in iron as a function of the number of helium atoms contained in the bubble. These were evaluated by equations (4a)-(4c). The concentrations of vacancies and helium atoms were fixed at 10^{-7} and 10^{-11}, respectively, and temperature was 900 K. Figure 2(b) is the contour plot of figure 2(a). It is shown in figure 2(a) that the size of the critical nucleus of an empty void (without helium) is about 70 vacancies and corresponding nucleation barrier is as high as 13 eV. It indicates that an empty void can not nucleate at this condition, because the temperature is too high for the nucleus to be stable and the concentration of vacancies in the matrix is too low to be supplied enough to the nucleation. However, as shown in the figure, when the number of helium atoms contained in the bubble increases, the nucleation barrier is significantly reduced. It may reflect the fact that the formation energy of isolated helium atoms in the matrix is so high that they prefer to agglomerate into a cluster. The figure also shows that the nucleation energy is dramatically increased at relatively smaller bubble size with increasing the number of helium atoms in the bubble. It indicates that helium bubbles with quite high He/V ratios are difficult to nucleate. Thus, it may suggest that a helium bubble with an appropriate number of helium atoms depending on bubble size can nucleate without any large energy barrier. Figures 3(a) and 3(b) show another example, where $C_{\text{V}}^{\text{matrix}}=5\times10^{-4}$, $C_{\text{He}}^{\text{matrix}}=5\times10^{-8}$ and T=1000K. The nucleation energy values are smaller than the previous case because of higher concentration of vacancies in the matrix; however, what the figures imply is qualitatively the same as the above. Thus, it is found that helium plays an effective role on promoting bubble nucleation.

III. BINDING FREE ENERGY OF He-BUBBLES

The fluxes of mobile defects to and from a helium bubble are important factors, which determine the growth and shrinkage rates of the bubble. According to the work done by Wolfer *et al*. [28, 29], the net flux of the type k mobile defect to an isotropic spherical helium bubble with radius R is given by

$$J_k^{\text{net}} = J_k^{\text{in}} - J_k^{\text{out}}, \quad (5a)$$
$$J_k^{\text{in}} = (4\pi RZ_kD_k/\Omega)C_k^{\text{matrix}}(\infty), \quad (5b)$$
$$J_k^{\text{out}} = (4\pi RZ_kD_k/\Omega)C_k^{\text{matrix}}(R)\exp(E_k^{\text{int}}(R)/k_{\text{B}}T), \quad (5c)$$

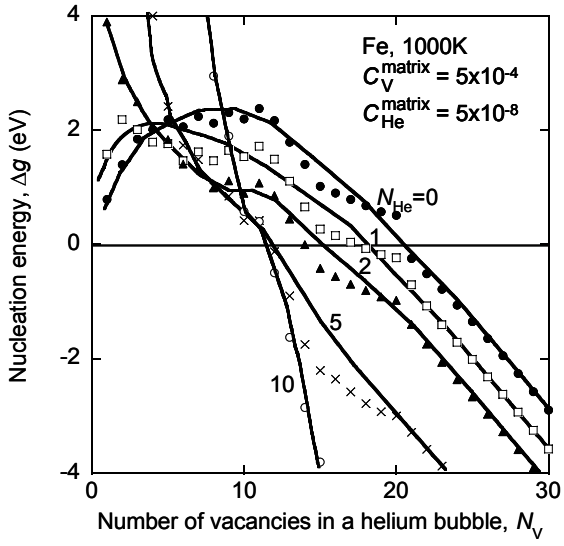

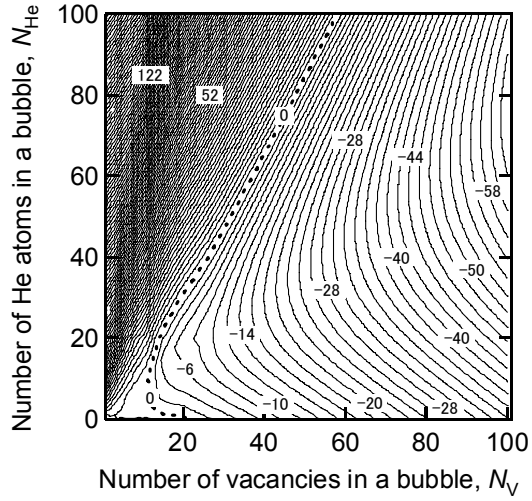

Figure 3 contained in the bubble (a) and the contour plot representation (b). The conditions are indicated in the figure.

where Ω is the atomic volume, D_k is the diffusion coefficient of the type k mobile defect in the unstrained matrix, $C_k^{matrix}(r)$ is the concentration of the type k mobile defect in the matrix at a distance r from the bubble centre, $E_k^{int}(r)$ is the interaction energy due to the elastic interaction between the type k mobile defect at r and the helium bubble, and Z_k is the capture efficiency (the bias factor) of the helium bubble for the type k mobile defect. The equations are obtained by solving the steady-state diffusion equation, where the flux of mobile defects has a spherical symmetry with respect to the bubble centre. The fluxes J_k^{in} and J_k^{out} of the type k mobile defect thus defined are both positive values, and they correspond to an inflow rate to the helium bubble and an outflow rate from the helium bubble, respectively.

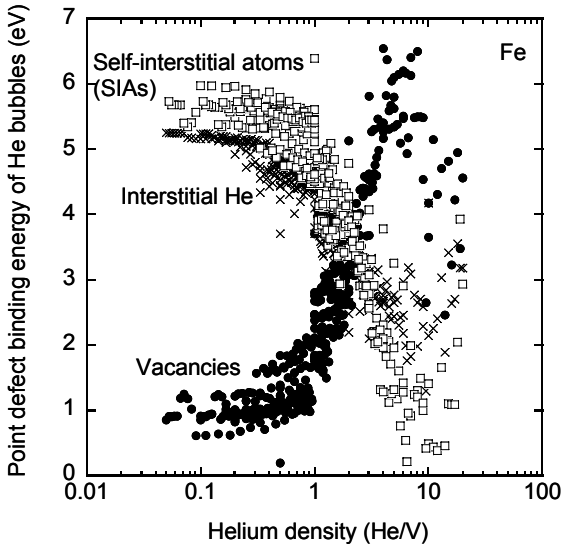

Figure 4 The binding energies of point defects to a He bubble in Fe, which were calculated by the molecular dynamics and static calculations [14-17] with empirical interatomic potentials. The numbers of He atoms and vacancies investigated were both less than or equal to 20. The binding energies significantly depend on the He density of bubbles, rather than bubble size.

The emission rate J_k^{out} is usually given under an assumption of local thermodynamic equilibrium condition, where a helium bubble is equilibrium with the type k mobile defect at R, i.e., $\mu_k^{bubble} = \mu_k^{matrix}(R)$. With this equation, equation (5c) is replaced by

$$J_k^{out} = (4\pi R Z_k D_k/\Omega)\exp(-G_k^{bind}/k_B T), \quad (5d)$$

where

$$G_k^{bind} = E_k^F - \mu_k^{bubble} \quad (6)$$

is the binding free energy of the type k mobile defect to a helium bubble. This indicates the free energy change when the type k mobile defect is removed from a helium bubble and immediately placed in an unstrained matrix. When the binding free energy defined here is used, the above local equilibrium condition is rewritten by

$$G_k^{bind} + E_k^{int}(R) = -k_B T \ln C_k^{matrix}(R), \quad (7a)$$

or, if the interaction energy is neglected,

$$G_k^{bind} = -k_B T \ln C_k^{matrix}(R). \quad (7b)$$

It indicates that a decrease in the configurational entropy, $\Delta S_k^{config.} = -k_B \ln C_k^{matrix}(R)$ due to absorption of the type k mobile defect at R by a helium bubble is compensated by

an energy gain due to the absorption described by $G_k^{bind} + E_k^{int}(R)$ in equation (7a), and G_k^{bind} in equation (7b).

Figure 4 shows the binding energy of point defects to a helium bubble in iron as a function of He/V ratios, which was calculated by our previous atomistic calculations [14-17]. As shown in the figure, the binding energy significantly depends on He/V ratios rather than bubble size [14-17]. These significant but gradual changes in the binding energy against He/V ratios are a characteristic of helium bubbles, and such changes are not observed in the case of copper-vacancy clusters in iron as discussed in [15], where copper is a substitutional impurity in the metal. When He/V ratios are less than 1, the binding energy of point defects to a helium bubble is almost constant. When He/V ratios are greater than 1 and less than 6, the vacancy binding energy is an increasing function, and the SIA and helium binding energies are decreasing functions of the ratios. Moreover, when He/V ratios are greater than 6, the binding energies show opposite tendencies against the ratios. Changes in the tendencies against the ratios are mainly due to the effect of lattice relaxation around the bubble. At higher He/V ratios than 6, metal atoms at the bubble-matrix interface showed significant displacements from their original lattice sites. These significant atomic displacements result in producing additional space for helium atoms, leading to a reduction in actual helium density in a helium bubble. Let us imagine the helium bubble of a very high He/V ratio with the significant atomic displacement of metal atoms at the interface, and one can easily understand that a helium bubble is regarded as an agglomeration of helium atoms, vacancies and SIAs as mentioned in the previous section.

The dependence of the binding energy of point defects to a helium bubble on He/V ratios is consistent with the analytical expression of the binding free energy obtained by the continuum model approach [18], except the range of very high He/V ratios where the linear elasticity theory employed by the analytical expression is not applicable. As is easily expected from the temperature independence of the formation free energy of helium bubbles discussed above, the binding free energy obtained by the continuum model approach [18] actually showed almost independent on temperatures. It is therefore considered that the binding energy evaluated at 0 K by our atomistic calculations can be applied at any temperatures.

It is obviously indicated in figure 4 that the vacancy and SIA binding energies have a trade-off relation with each other and the sum of those energies seems to always be a constant. It is well consistent with the relation of $G_V^{bind} + G_{SIA}^{bind} = E_V^F + E_{SIA}^F$ (=*const.*) that is simply obtained from equations (3) and (6). Within the continuum model approach [18], the analytical expression of the pressure at $G_V^{bind} = G_{SIA}^{bind}$ is simply given by $p=2\gamma/R + (E_{SIA}^F - E_V^F)/2\Omega$ if the elastic free energy is neglected, where γ is the surface free energy. Since E_{SIA}^F is generally higher than E_V^F in metals, such critical pressure is always higher than the equilibrium pressure by $(E_{SIA}^F - E_V^F)/2\Omega$. The corresponding He/V ratio to the critical pressure is evaluated to be 1.8 from the figure.

When a He/V ratio is much higher than 1.8, the SIA binding energy takes a very low positive value, while the vacancy binding energy is as high as 6 eV. In this condition, J_V^{out} evaluated by equations (5d) can be neglected but J_{SIA}^{out} takes a finite, significant value. It suggests that the SIAs can be emitted even when $G_{SIA}^{bind} > 0$. Similar things can be said regarding the SIA loop punching. When He/V ratios are very high, the binding energy of an SIA loop to a helium bubble G_{loop}^{bind} takes a very low positive value as shown in Fig. 2 of [16], and therefore, the SIA loop punching can also occur even at $G_{loop}^{bind} > 0$. These positive values of the binding energies (G_{SIA}^{bind} and G_{loop}^{bind}) at high He/V ratios are consistent with the earlier atomistic calculation work of Wilson *et al*. [30] for multiple helium-filled vacancies and for helium clusters (without vacancy).

Strictly speaking, the present treatment regarding the SIA emission described by equations (5d) and (6) is definitely different from the earlier athermal treatment for the SIA emission [10], where the threshold pressure is given by $G_{SIA}^{bind} = 0$. The present treatment is also different from the earlier athermal treatment for the SIA loop punching, where the threshold pressure is given by $G_{loop}^{bind} = 0$ [10-12], or more precisely, given by $G_{loop}^{bind} + E_{loop}^{int}(R) = 0$ [13]. A difference of the present treatment from the earlier works is an introduction of the configurational entropy. Namely, from equations (7a) and (7b), the present treatment considers the threshold events using the equations: $G_k^{bind} + E_k^{int}(R) - T\Delta S_k^{config.} = 0$, or if the interaction energy is neglected, $G_k^{bind} - T\Delta S_k^{config.} = 0$, where k denotes an SIA or an SIA loop. Namely, the binding energy G_k^{bind} for the latter case, or $G_k^{bind} + E_k^{int}(R)$ for the former case, can take a positive value for the threshold, by the amount of a reduction in the free energy that corresponds to a positive configurational entropy change, if T is finite. These treatments are not unreasonable, because the vacancy emission have been conventionally treated by equations (5d) and (6) as a usual manner [6]. Rather, the present treatment is considered to be more appropriate from the viewpoint of the symmetric behaviour of vacancies and SIAs in materials.

IV. NUCLEATION AND GROWTH OF He-BUBBLES DURING IRRADIATION

The nucleation and growth process of an isolated single helium bubble in bcc iron was investigated by the kinetic Monte-Carlo (KMC) simulation technique. Events employed in the simulation were the absorption and emission of a vacancy, an SIA and interstitial helium by a single helium bubble, while an event associated with SIA

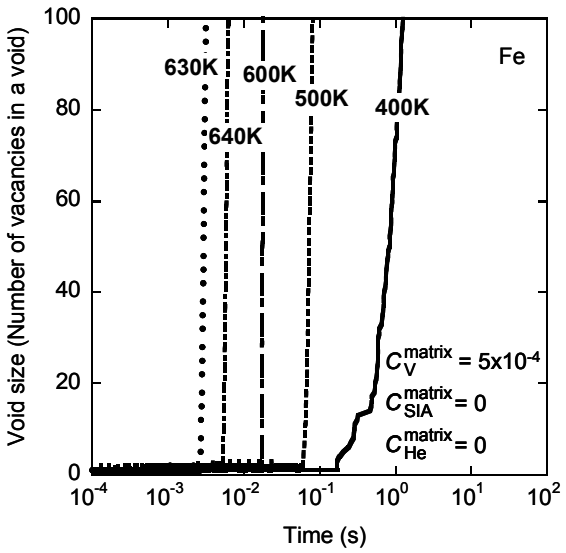

Figure 5 Temperature dependence of the time evolution of void size calculated by the KMC technique. The concentration of vacancies in the Fe matrix was fixed at 5×10^{-4}, and the concentrations of SIAs and He are both 0. Note that, simulated time period available with this technique is much greater than the normal molecular dynamics technique. After some incubation time, which depends on temperatures, an empty void suddenly begins to grow. At higher temperatures than 640 K, an empty void was not observed to grow within the simulation time.

loops or substitutional helium was neglected here for simplicity. The events employed here were thus limited, but the essence of bubble nucleation and growth may be fully described by those events, as discussed in the following.

The occurrence probability of the events for absorption and emission was respectively given by equations (5b) and (5d) that were given in the unit of per second. It was assumed that the interaction energy was neglected and therefore the capture efficiency was fixed at 1 for any events. Prior to the simulation, all possible events and their occurrence probabilities were listed in a table. And then, one event was selected by the random number generator. Once a particular event was chosen, the defect information was accordingly modified and the table of all possible events and their probabilities was updated. Time step for real time evolution was calculated with the following formula [31]: $\Delta t=-\log L/\Sigma\nu_i$, where L was a random number uniformly distributed between 0 and 1 and ν_i was the occurrence probability of the type i event. Vacancies, iron atoms and helium atoms at the bubble-matrix interface were regarded as candidates for the possible event of emission of point defects. A migration energy employed here for describing the diffusion coefficient of point defects in the matrix was 0.74, 0.058 and 0.078 eV for a vacancy, an SIA and interstitial helium, respectively [16].

The concentration of point defects at a distance R from the bubble centre was simply given by the combination (N_{He}, N_V) of a helium bubble as discussed in the previous section, whereas the concentration of point defects far from the helium bubble $C_k^{matrix}(\infty)$ can not be determined only by the character of the helium bubble. $C_k^{matrix}(\infty)$ is generally time dependent and therefore it is usually obtained by solving simultaneous rate theory equations describing a wide variety of defect interactions occurred in materials during irradiation such as production, migration, clustering and annihilation to various sinks. In the present study, $C_k^{matrix}(\infty)$ was regarded as a constant input parameter.

The initial configuration of a helium bubble was assumed to be a single vacancy. When a single vacancy was annihilated by an SIA during the simulation, an additional vacancy was prepared as a new candidate and the simulation was continued. Hence, when the occurrence probability of SIA absorption by a vacancy was relatively high, bubble size was almost kept at NV=1 during the simulation.

Table 1 Nucleation energy and corresponding critical size for empty voids in bcc Fe at various temperatures. Vacancy concentration is fixed at 5×10^{-4}. There are neither helium atoms nor SIAs in the system.

Temp. (K)	400	500	600	630	640	650
Nucleation energy (eV)	0.33	0.47	0.65	0.71	0.73	0.75
Critical size (No. of vacancies)	2	2	3	3	3	3

IV.A. TIME DEVELOPMENT OF BUBBLE GROWTH

Figure 5 is the time evolution of void size as a function of temperatures, which was calculated by the KMC technique, where there were only vacancies in the system and their concentration was 5×10-4. Temperatures ranged from 400 K to 640 K. As shown in the figure, there is the incubation period, followed by sudden growth of an empty void. During the incubation period, growth to a vacancy cluster with a few vacancies and its shrinkage to a single vacancy is alternately occurred, where the attempt of a nucleus to be beyond a critical size are repeatedly made. Nucleation energies and corresponding critical nucleus size at this condition were calculated using equation 2 and listed in table 1. The incubation period decreases with increasing temperatures at below 630 K, because vacancy mobility increases with increasing temperatures. However, when the temperature is greater than 630 K, the incubation period exhibits an

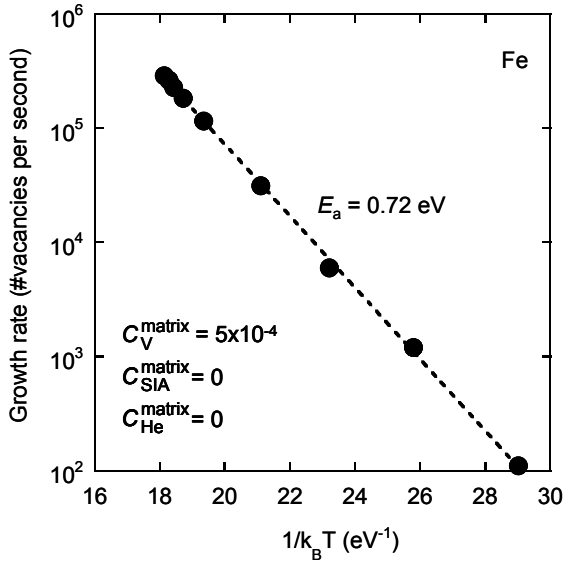

Figure 6 The Arrhenius plot of growth rates of empty voids in Fe. The slope of the line is 0.72 eV, which is in good agreement with the vacancy migration energy employed as an input parameter (0.74 eV). It reasonably indicates that the growth of empty voids is controlled by vacancy diffusion.

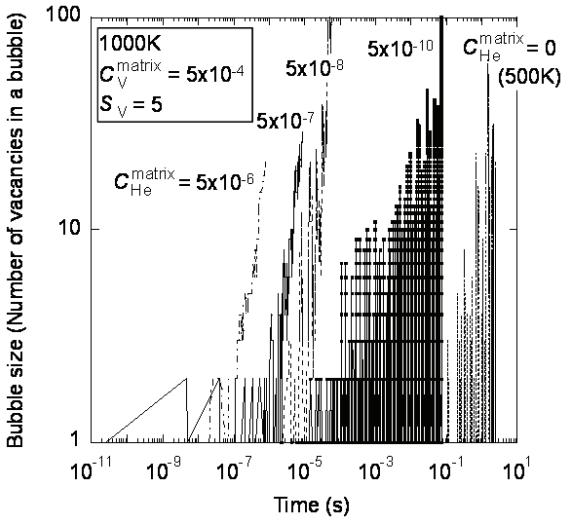

Figure 7 The time evolution of bubble size as a function of the concentration of He in the Fe matrix. Temperature was 500 K for an empty void and 1000 K for the others. The concentration of vacancies in the matrix was fixed at 5×10^{-4}, and the vacancy supersaturation was five. When the concentration of He in the matrix increases, incubation periods for bubble growth decrease. The shrinkage process of bubbles is significantly suppressed by the presence of He.

increasing function of temperatures. At 650 K or higher temperatures, the nucleation of empty voids was not observed at all during the present simulation of ~107 time steps. An increase in the incubation period at higher temperatures than 630 K is probably because of the thermal instability of void nuclei. These results may indicate that the so-called stage V temperature of iron represented by the present interatomic potential is approximately 650 K.

Figure 5 also shows that, after the incubation period, voids can grow without any significant shrinkage at this condition. From the slope of the growth curve after the incubation period in this figure, void growth rates were obtained in the unit of the number of vacancies per second. The growth rates depend on temperatures and exhibit the Arrhenius behaviour as shown in figure 6. The slope of the Arrhenius plot is 0.72 eV, which is in good agreement with the vacancy migration energy employed as an input parameter. It reasonably indicates that the growth of empty voids is controlled by vacancy diffusion.

When SIAs were additionally introduced into the system, the shrinkage of an empty void was observed to be more significant than the previous case, as shown in figure 7. Here, the temperature was 500K, the matrix vacancy concentration was fixed at 5×10-4, and the effective vacancy supersaturation was five. Note that, the effective vacancy supersaturation is defined by $S_V=(D_VC_V^{matrix}-D_{SIA}C_{SIA}^{matrix})/D_VC_V^{eq.}$ with the equilibrium vacancy concentration $C_V^{eq.}=\exp(-E_V^F/k_BT)$. The concentration of SIAs in the matrix was fixed so as to produce a given value of the effective vacancy supersaturation. When the temperature was increased to 1000 K, an empty void was not observed to nucleate at all during the present simulation, where a void nucleus was annihilated by an SIA in addition to its thermal instability at this high temperature.

However, when helium was introduced into the system, helium bubbles were observed to nucleate even at a high temperature of 1000 K. Figure 7 also shows the time evolution of bubble size at 1000 K as a function of the concentration of helium in the matrix. Even at such a high temperature, helium bubbles can nucleate and their growth rates are greater than those of an empty void. Additionally, the incubation period is significantly decreased. An increase in the growth rate and a decrease in the incubation period are more significant at higher concentration of helium in the matrix. Moreover, the shrinkage becomes less frequent when the helium concentration is higher.

IV.B. BUBBLE NUCLEATION PATH IN (NHe, NV) SPACE

Figures 8(a) and 8(b) are the mechanism map for bubble formation that we introduced in the previous work [18]. Here, the concentration of vacancies in the matrix

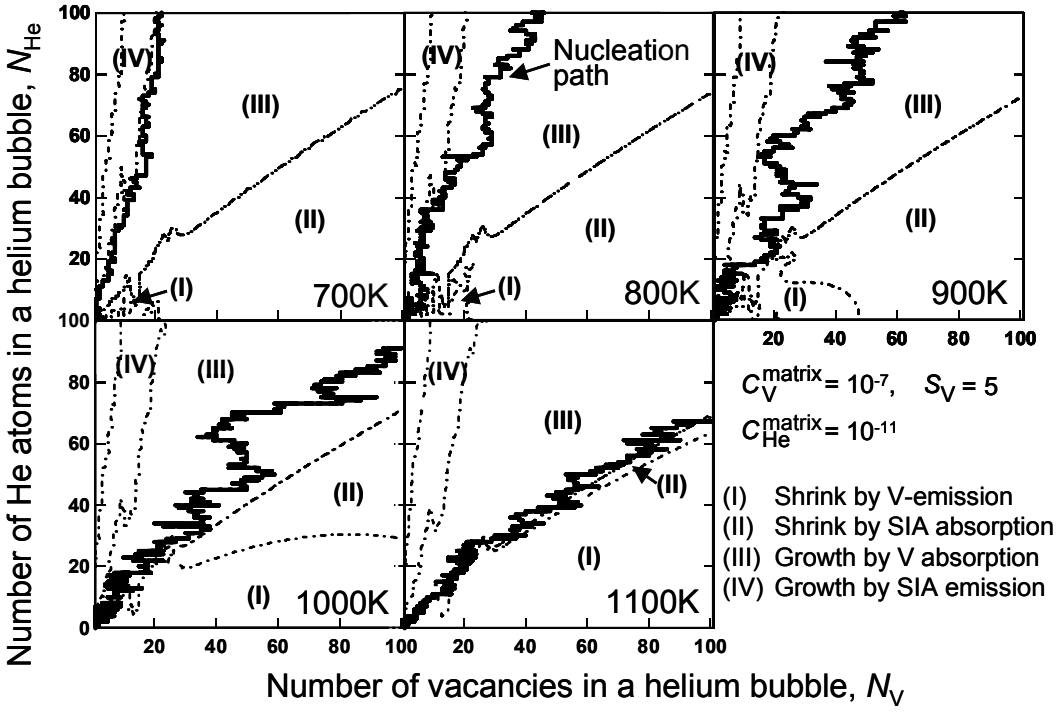

Figure 8(a) Mechanism maps for bubble formation in Fe as a function of temperatures. The concentrations of vacancies and interstitial He atoms in the matrix were 10^{-7} and 10^{-11}, respectively. The vacancy supersaturation was fixed at five. The nucleation paths for He bubbles in Fe are also indicated on the maps. The average He/V ratio of a growing He bubble decreases with increasing temperatures.

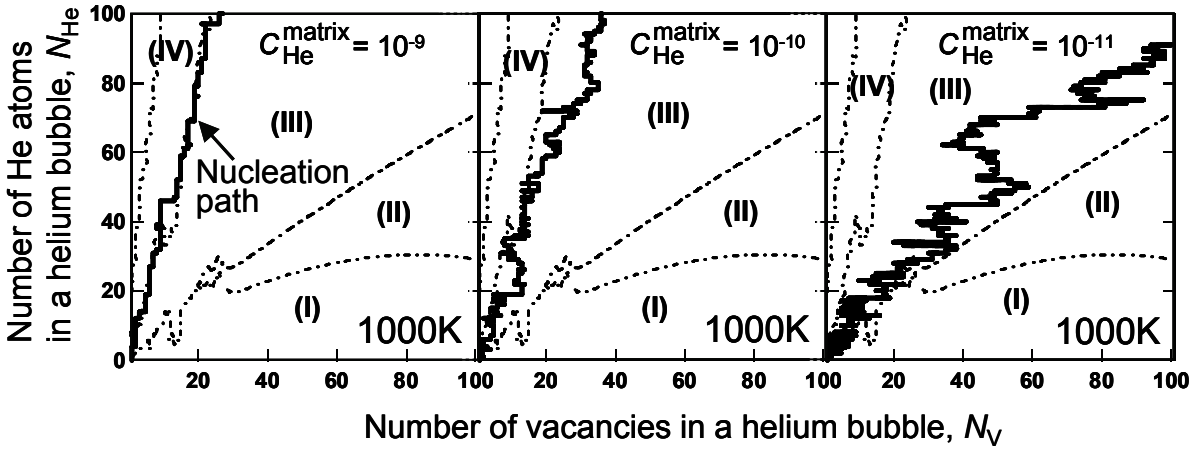

Figure 8(b) Mechanism maps for bubble formation in Fe as a function of the matrix He concentration. The concentration of vacancies in the matrix was fixed at 10^{-7}. The vacancy supersaturation was five. Temperature was 1000 K. The nucleation paths for He bubbles in Fe are also indicated on the maps. The average He/V ratio of a growing He bubble reasonably shows an increasing function of the matrix He concentration.

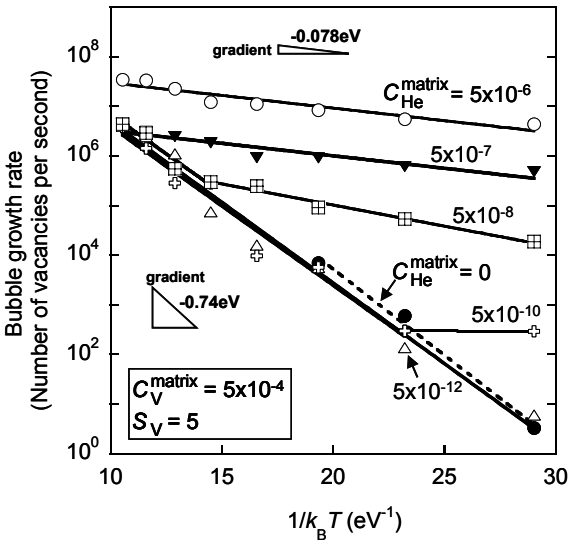

Figure 9 The Arrhenius plot of growth rates of He bubbles in Fe. The slope of the lines indicates either 0.74 eV or 0.078 eV. The former is the vacancy migration energy and the latter is the interstitial He migration energy. The figure indicates that the growth of He bubbles is controlled by vacancy diffusion when the concentration of He in the matrix is relatively low and the temperature is relatively high; otherwise, it is controlled by interstitial He diffusion. Since the interstitial He migration energy is very low, the interstitial He diffusion controlled growth is almost independent on temperatures.

was fixed at 10^{-7} and the effective vacancy supersaturation S_v was five. Temperature and the concentration of helium in the matrix were used as variable parameters in figures 8(a) and 8(b), respectively. The mechanism map describes bubble growth and shrinkage on the (N_{He}, N_V) space as shown in the figures, which is simply determined by the magnitude of point defect fluxes (J_k^{in} and J_k^{out}). Note that, a movement in right and left hand directions in the space indicates bubble growth and shrinkage, respectively. In these examples, an investigation of the most significant event of point defects to occur for bubble formation divided the (N_{He}, N_V) space into the following four regions: the region of bubble shrinkage due to vacancy emission, that of bubble shrinkage due to SIA absorption, that of bubble growth due to vacancy absorption, and that of bubble growth due to SIA emission. There exists the region of helium absorption but there is no region of helium emission in the space at this condition. Thus, the mechanism map provides the nucleation path of helium bubbles on the (NHe, NV) space deterministically. On the other hand, the present KMC simulation also provides the nucleation path of He bubbles, which is depicted on the mechanism map as shown in the figures. The KMC results are roughly consistent with what the mechanism map may indicate; however, there partly observed some inconsistencies between them. For example, bubble shrinkage is clearly observed even in the growth region on the mechanism map. This inconsistent behaviour is temporarily and caused by the stochastic fluctuation of point defect fluxes. The KMC nucleation path in the figures shows that the average He/V ratio of the growing helium bubbles decreases with increasing temperatures, suggesting that higher pressurized helium bubbles will form at lower temperatures. Besides, the figures also show that higher pressurized helium bubbles will form when the concentration of helium in the matrix is higher.

IV.C. Bubble growth rates

Bubble growth rates were obtained from the time evolution of helium bubble size after the incubation period in the same way as described in section 4.1. The concentration of vacancies in the matrix was fixed at 5×10-4, and the vacancy supersaturation was five. Figure 9 shows the Arrhenius plot of the bubble growth rates as a function the concentration of helium in the matrix. As shown in the figure, the growth rates obviously indicate two different activation energies: approximately one is 0.74 eV and the other is 0.078 eV.

When there is no helium in the matrix, the slope of the Arrhenius plot is the same as the vacancy migration energy (0.74 eV), as indicated by the dotted line in the figure. This is the same as the case of figure 6. It indicates that the growth of empty voids is also controlled by vacancy diffusion, regardless of the existence of SIAs in the matrix. Likewise, it was also observed that there exists a maximum temperature limit (~650 K), at above which empty voids cannot nucleate during the simulation because empty voids are thermally unstable at such higher temperatures.

When helium is introduced into the system, helium bubbles can nucleate even at greater than 650 K and therefore the growth rates can be defined at such very high temperatures. When the concentration of helium in the matrix is relatively low, the slope of the Arrhenius plot in the figure is identical to the vacancy migration energy. It indicates that the growth of helium bubbles is still controlled by vacancy diffusion. In this case, the Arrhenius plots of the growth rate of helium bubbles are almost overlapped with that of empty voids. Thus, when the matrix helium concentration is relatively low, the role of helium on bubble formation is only to raise the maximum temperature limit.

When the concentration of helium in the matrix becomes higher, bubble growth rates are significantly enhanced as shown in the figure, where the growth mechanism of helium bubbles is obviously different from the above. It was found from comparisons with the mechanism map that the enhanced growth rates are

strongly associated with nucleation paths along the region of the SIA emission, which is roughly represented by He/V≥6 on the mechanism map. Activation energy for bubble growth in this case is almost identical to the interstitial helium migration energy (0.078 eV). It suggests that bubble growth is controlled by interstitial helium diffusion. Since the interstitial helium migration energy is quite low, bubble growth by this mechanism is almost independent on temperatures. Namely, helium bubbles nucleate as if athermal process is working. This mechanism may work more significantly when the concentration of helium in the matrix is higher. When the concentration of helium in the matrix is intermediate, the mechanism works only when the temperature is relatively low. Since vacancy migration is not always required for bubble growth by this mechanism, helium bubbles can nucleate even at low temperatures where vacancies cannot migrate.

Interactions between an SIA loop and a helium bubble were neglected here for simplicity. If such interactions are included in the present KMC model, bubble growth due to the SIA loop punching is also considered to be controlled by interstitial helium diffusion, because the primary origin for dissociation of an SIA loop from a helium bubble (i.e., the SIA loop punching) is an increase in He/V ratios that leads to significant reduction in binding energy between them [16]. Therefore, bubble formation by this mechanism may also be almost independent on temperatures and may occur even at low temperature where vacancies cannot migrate. This is consistent with experiments [7, 8].

Another candidate for mobile defects that may contribute to bubble nucleation and growth but were neglected here is a substitutional helium atom. The migration of a substitutional helium atom is mainly controlled by vacancy migration, because the energy for transferring a helium atom at a substitutional position to a nearest neighboring vacancy is extremely small (about 0.015 eV [14]). Besides, when a substitutional helium atom is absorbed by a helium bubble, the trajectory of the growing bubble on the (N_{He}, N_V) space is highly expected to be along the straight line of N_{He}=N_V on the space because the He/V ratio of a substitutional helium atom is 1. This trajectory is far from the region of SIA emission on the mechanism map and therefore the SIA emission is not expected to occur by absorption of substitutional helium. Thus, it is reasonably considered that the growth rate of helium bubbles by the contribution of substitutional helium shows similar behaviour to the above case of interstitial helium with relatively low concentration, where bubble growth is controlled by vacancy diffusion.

V. CONCLUSION

Thermodynamical formalization was made for modelling the nucleation and growth of helium bubbles in metals during irradiation, which is applicable, independently on the concentrations of helium in the matrix. This is definitely different from the earlier theoretical treatments. With the present formalization, the nucleation and growth process of helium bubbles in iron was simulated by the kinetic Monte-Carlo technique, where a vacancy, an SIA and an interstitial helium atom were regarded as the compositions of helium bubbles. The nucleation path of helium bubbles were obtained on the (N_{He}, N_V) space as functions of temperatures and the concentration of helium in the matrix. Besides, two different activation energies for bubble growth were clearly shown, indicating that there are two different mechanisms for bubble growth: one is controlled by vacancy diffusion and another is controlled by interstitial helium diffusion. The interstitial helium diffusion controlled growth is associated with the SIA emission, where the formation of helium bubbles is almost independent on temperatures and helium bubbles can form even at low temperatures where vacancies cannot migrate. The present theoretical treatment is applicable to simultaneous rate theory equations describing various defect interactions to understand microstructural evolution in materials under more realistic conditions.

ACKNOWLEDGEMENT

The author would like to express his thanks to Drs. B.D. Wirth, T. Diaz de la Rubia, W.G. Wolfer, T. Okita, A. Kubota and M.P. Surh for valuable discussion and encouragement during his visit to Lawrence Livermore National Laboratory. The author would also like to thank Dr. R. Sugano for various assistances. This work was supported in part by the Japan-US joint research programs (JUPITER & JUPITER-II projects).

REFERENCES

[1] J.L. Katz and H.J. Wiedersich, J. Chem. Phys., **55**, 1414 (1971).
[2] K.G. Russell, Acta Metal., **19**, 753 (1971).
[3] K.G. Russell, Acta Metal., **20**, 899 (1972).
[4] K.G. Russell, J. Nucl. Mater., **61**, 330 (1976).
[5] K.G. Russell, Acta Metal., **26**, 1615 (1978).
[6] L.K. Mansur and W.A. Coghlan, J. Nucl. Mater., **119**, 1 (1983).
[7] J.H. Evans, A. van Veen and L.M. Caspers, Radiat. Effects, **78**, 105 (1983).
[8] H. Iwakiri, K. Yasunaga, K. Morishita, N. Yoshida, J. Nucl. Mater. **283-287**, 1134 (2000).
[9] B.B. Glasgow and W.G. Wolfer, 'Comparison of Mechanisms for Cavity Growth by Athermal and

Thermal Processes', UWFDM-544, University of Wisconsin (1983).
[10] H. Trinkaus, Radiat. Effects, **78**, 189 (1983).
[11] G.W. Greenwood, A.J.E. Foreman and D.E. Rimmer, J. Nucl. Mater., **1**, 305 (1959).
[12] H. Trinkaus and W.G. Wolfer, J. Nucl. Mater., **122&123**, 552 (1984).
[13] W.G. Wolfer, Phil. Mag., **58**, 285 (1988).
[14] K. Morishita, B.D. Wirth, T. Diaz de la Rubia, A. Kimura, 'Effects of Helium on Radiation Damage Processes in Iron', in '*Proc. Fourth Pacific Rim Int. Conf. on Advanced Materials and Processing (PRICM4)*', edited by S. Hanada, Z. Zhong, S.W. Nam and R.N. Wright, (The Japan Institute of Metals, 2001), p. 1383.
[15] K. Morishita, R. Sugano, B.D. Wirth and T. Diaz de la Rubia, Nucl. Instrum. and Meth., B **202**, 76 (2003).
[16] K. Morishita, R. Sugano and B.D. Wirth, J. Nucl. Mater., **323**, 243 (2003).
[17] K. Morishita and R. Sugano, B.D. Wirth, Fusion Sci. & Tech., **44**, (2) 441 (2003).
[18] K. Morishita and R. Sugano, J. Nucl. Mater. **353**, 52 (2006).
[19] K.F. Kelton, 'Crystal Nucleation in Liquids and Glasses', in 'Solid State Physics', Vol. **45**, edited by H. Ehrenreich and D. Turnbull, (Academic Press, San Diego, 1991), p. 75.
[20] Daan Frenkel and Berend Smit, '*Understanding Molecular Simulation from Algorithms to Applications*', Academic Press, New York, 1996, 444 pages, hardback (ISBN 0-12-267370-0).
[21] G.J. Ackland, D.J. Bacon, A.F. Calder, T. Harry, Phil. Mag. A **75**, 713 (1997).
[22] W.D. Wilson and R.D. Johnson, 'Rare gases in metals', in '*Interatomic Potentials and Simulation of Lattice Defects*', edited by P.C. Gehlen, J.R. Beeler Jr., R.I. Jaffee, (Plenum, 1972) p. 375.
[23] J.P. Biersack and J.F. Ziegler, Nucl. Instrum. and Meth., **194**, 93 (1982).
[24] D.E. Beck, Mol. Phys., **14**, 311 (1968).
[25] C.C. Fu and F. Willaime, Phys. Rev. B **72**, 064117 (2005).
[26] T. Seletskaia, Y. Osetsky, R.E. Stoller and G.M. Stocks, Phys. Rev. Lett. 94, 046403 (2005).
[27] J.B. Adams and W.G. Wolfer, J. Nucl. Mater. **166**, 235 (1989).
[28] W.G. Wolfer and M. Ashkin, J. Appl. Phys., **46**, 547 (1975).
[29] W.G. Wolfer, 'Segregation of Point Defects by Internal Stress Fields', in '*Proc. of International Conference on Fundamental Aspects of Radiation Damage in Metals*', edited by M.T. Robinson and F.W. Young, Jr., (Gatlinburg, Tennessee, 1975), CONF-751006-P2, p. 812.
[30] W.D. Wilson, C.L. Bisson and M.I. Baskes, Phys. Rev. B **24**, 5616 (1981).
[31] K.A. Fichthorn, W.H. Weinberg, J. Chem. Phys., **95**, 1090 (1991).

Task 2-1

(1) Optimization and characterization of chemical vapor infiltrated SiC/SiC Composites
(2) Tensile strength of chemical vapor infiltrated advanced SiC fiber composites at elevated temperatures
(3) Tensile and thermal properties of chemically vapor-infiltrated silicon carbide composites of various high-modulus fiber reinforcements

Task 2-2

(1) Impact of material system thermomechanics and thermofluid performance on He-cooled ceramic breeder blanket designs with SiCf/SiC
(2) Experimental study of the interaction of ceramic breeder pebble beds with structural materials under thermo-mechanical loads
(3) Numerical characterization of thermo-mechanical performance of breeder pebble beds

Task 2-3

(1) The effect of high dose/high temperature irradiation on high purity fibers and their silicon carbide composites
(2) Neutron irradiation effects on high-crystallinity and near-stoichiometry SiC fibers and their composites
(3) Effect of He pre-implantation and neutron irradiation on mechanical properties of SiC/SiC composite
(4) Mechanical properties of advanced SiC/SiC composites after neutron Irradiation
(5) Current status and critical issues for development of SiC composites for fusion applications
(6) Evaluation of Fiber/Matrix Interfacial Strength of Neutron Irradiated SiC/SiC Composites
(7) Mechanical properties of advanced SiC/SiC composites after neutron Irradiation

Task 3-1

(1) Innovative liquid breeder blanket design activities in Japan
(2) Neutronics investigation of advanced self-cooled liquid blanket systems in helical reactor
(3) Tritium control for Flibe/V-alloy blanket system

Task 3-2

(1) MD and KMC modeling of the growth and shrinkage mechanisms of helium-vacancy clusters in Fe
(2) Nucleation path of helium bubbles in metals during irradiation

5. List of publications

Task 1-1A　Flibe Handling/Tritium Chemistry

[1] Sagara, A., Yamanishi H., Uda T., Motojima, O., Kunigi, T., Matsumoto, Y., Wu, Y., Matsui, H., Takahasi, T., Yamamoto, T., Toda, S., Mitarai, O., Satake, S., Terai, T., Tanaka, S., Fukada, S., Nishikawa, M., Shimizu, A., Yoshida, N.,"Studies on Flibe Blanket Designs in Helical Reactor FFHR", Fusion Technology, Vol.39, 2001, pp.753-757

[2] Terai, T., Suzuki, A., Tanaka, S., "Tritium Release from Li2BeF4 Molten Salt Breeder under Neutron Irradiation at Elevated Temperature", Fusion Technology, Vol.39, 2001, pp.768-772

[3] Terai, T., Nishimura, H., Yamaguchi, K., Yamawaki, M., Suzuki, A., Muroga, T., Sagara, A. and Motojima, O., "Compatibility of Structural Materials with Li2BeF4 Molten Salt Breeder", Fusion Technology, Vol.39, 2001, pp.784-788

[4] Nishimura, H., Suzuki, A., Terai, T., Yamawaki, M., Tanaka, S., Sagara A., and Motojima, O, "Chemical Behavior of Li2BeF4 Molten Salt as a Liquid Tritium Breeder", Fusion Engineering and Design, Vols.58-59, 2001, pp.667-672

[5] Petti, D.A., Anderl, R.A., Smolik, G.R., Sze, D.-K., Terai T. and Tanaka, S., "JUPITER-II Flibe Tritium Chemistry and Safety Experimental Program", Fusion Science and Technology, Vol.41, 2002, pp.807-811

[6] Fukada, S., Nishikawa, M., Sagara A. and Terai, T., "Mass-Transport Properties to Estimate Rates of Tritium Recovery from FLIBE Blanket", Fusion Science and Technology, Vol.41, 2002, pp.1054-1058

[7] Fukada, S. Anderl, R.A., Hatano, Y., Schuetz, S.T., Pawelko, R.J., Petti, D.A., Smolik, G.R., Terai, T., Nishikawa, M., Tanaka S. and Sagara, A., "Initial Studies of Tritium Behavior in Flibe and Flibe-facing Material", Fusion Engineering and Design, Vols.61-62, 2002, pp.783-788

[8] Nishimura, H., Terai, T., Yamawaki, M., Tanaka, S., Sagara A. and Motojima, O., "Compatibility of Ferritic Steels with Li2BeF4 Molten Salt Breeder", Journal of Nuclear materials Vols.307-311, 2002, pp.1355-1359

[9] Fukada, S., Anderl, R.A., Pawelko, R.J., Smolik, G.R., Schultz, S.T., O'Brien, J.E., Nishimura, H., Hatano, Y., Terai, T., Petti, D.A., Sze, D.-K. and Tanaka, S., "FLIBE-D2 Permeation Experiment and Analysis", Fusion Engineering and Technology Vol.44, 2003, pp.410-414

[10] Smolik, G., Pawelko, R., Morimoto, Y., Okuno, K., Anderl, R., Petti, D.A. and Terai, T., "Mobilization Measurements from Flibe under Argon and Air Flow", Journal of Nuclear Materials Vols.329-333, 2004, pp.1322-1326

[11] Anderl, R.A., Fukada, S., Smolik, G.R., Pawelko, R.J., Schuetz, S.T., Sharpe, J.P., Merrill, B.J., Petti, D.A., Nishimura, H., Terai T. and Tanaka, S., "Deuterium/tritium Behavior in Flibe and Flibe-facing Materials", Journal of Nuclear Materials, Vols.329-333, 2004, pp.1327-1331

[12] Fukada, S., Morisaki, A., Sagara A. and Terai, T., "Control of Tritium in FFHR-2 Self-cooled Flibe Blanket", Fusion Engineering and Design Vol.81, 2006, pp.477-483

[13] Fukada, S., Morisaki, A., Hydrogen permeability through a mixed molten salt of LiF, NaF and KF (Flinak) as a heat-transfer fluid, Journal of Nuclear Materials, 358 (2006) 235-242.

[14] Simpson, M.F., Smolik, G.R., Sharpe, J.P., Anderl, R.A., Petti, D.A., Hatano, Y., Hara, M., Oya, Y., Fukada, S., Tanaka, S., Terai T., and Sze, D.-K, "Quantitative Measurement of Beryllium-controlled Redox of Hydrogen Fluoride in Molten Flibe ", Fusion Engineering and Design Vol.81, 2006, pp.541-547

[15] Hara, M., Hatano, Y., Simpson, M.F., Smolik, G.R., Sharpe, J.P., Oya, Y., Okuno, K., Nishikawa, M., Terai, T., Tanaka, S., Anderl, R.A., Petti D.A. and Sze, D.-K. “Interactions between Molten Flibe and Metallic Be”, Fusion Engineering and Design Vol.81, 2006, pp.561-566

[16] Klix, A., Suzuki A. and Terai, T., “Study of Tritium Migration in Liquid Li2BeF4 with Ab initio Molecular Dynamics”, Fusion Engineering and Design Vol.81, 2006, pp.713-717

[17] Kimura, A., Kasada, R., Kohyama, A., Konishi, S., Enoeda, M., Akiba, M., Jitsukawa, S., Ukai, S., Terai T. and Sagara, A., “Ferritic Steel-blanket Systems Integration R&D-Compatibility Assessment ”, Fusion Engineering and Design Vol.81, 2006, pp.909-916

[18] Sagara, A., Imagawa, S., Tanaka, T., Muroga, T., Kubota, Y., Dolan, T., Hashizume, H., Kunugi, T., Fukada, S., Shimizu, A., Terai T. and Mitarai, O., “Carbon Tiles as Spectral-shifter for Long-life Liquid Blanket in LHD-type Reactor FFHR ”, Fusion Engineering and Design Vol.81, 2006, pp.1299-1304

[19] Petti, D.A., Smolik, G.R., Simpson, M.F., Sharpe, J.P., Anderl, R.A., Fukada, S., Hatano, Y., Hara, M., Oya, Y., Terai, T., Sze, D.-K. and Tanaka, S., “JUPITER-II Molten Salt Flibe Research: An Update on Tritium, Mobilization and Redox Chemistry Experiments”, Fusion Engineering and Design Vol.81, 2006, pp.1439-1449

[20] Fukada, S., Simpson, M.F., Anderl, R.A., Sharpe, J.P., Katayama, K., Smolik, G.R., Oya, Y., Terai, T., Okuno, K., Hara, M., Petti, D.A., Tanaka, S., Sze, D.-K. and Sagara, A., “Reaction Rate of Beryllium with Fluorine Ion for Flibe Redox Control”, Journal of Nuclear Materials Vols.367-370, 2007, pp.1190-1196

[21] Calderoni, P., Sharpe, J.P., Hara M. and Oya, Y., “Measurement of tritium permeation in flibe”, submitted to Fusion Engineering and Design.

Task 1-1B Thermofluid Characteristics of Flibe Simulant

[1] Chiba, S., Toda, S., Yuki, K. and Sagara, A., “Heat Transfer Enhancement for a Molten Salt FLiBe Channel,” Fusion Technology, Vol. 39, 2001, pp. 779-783.

[2] Sagara, A., Yamanishi, H., Uda, T., Motojima, O., Mitarai, O., Kunugi, T., Matsumoto, Y., Satake, S., Wu, Y., Terai, T., Tanaka, S., Matsui, H., Takahashi, S., Yamamoto, T., Toda, S., Fukada, S., Nishikawa, M., Shimizu, A. and Yoshida, N., “Studies in Flibe Blanket Designs in Helical Reactor FFHR,” Fusion Technology, Vol. 39, 2001, pp. 753-757.

[3] Kunugi, T., Satake, S. and Sagara, A., “Direct Numerical Simulation of Turbulent Free-Surface High Prandtl Number Fluid Flows in Fusion Reactors,” Nuclear Instruments and Methods in Physics Research A, Vol. 464, 2001, pp. 165-171.

[4] Smolentsev, S., Abdou, M. A., Kunugi ,T., Morley, N. B., Satake, S. and Ying, A., “Modeling of Liquid Walls in Apex Study,” International Journal of Applied Electro-Magnetics and Mechanics, Vol. 13, 2001/2002, pp. 373-379.

[5] Satake, S., Kunugi, T. and Smolentsev, S., “Advances in Direct Numerical Simulation for MHD Modeling of Free Surface Flows,” Fusion Engineering Design, Vols. 61-62, 2002, pp. 95-102.

[6] Freeze, B., Dagher, M., Sketchley, T., Morley, N. B., Smolentsev, S. and Abdou, M. A., “FLIHY experimental facilities for studying open channel turbulent flows and heat transfer,” Fusion Engineering Design, Vols. 63-64, 2002, pp. 391-395.

[7] Smolentsev, S., Freeze, B., Morley, N. B. and Abdou, M. A., “Experimental study of turbulent supercritical open channel water flow as applied to the CLiFF concept,” Fusion Engineering Design, Vols. 63-64, 2002, pp. 397-403.

[8] Toda, S., Chiba, S., Yuki, K., Omae, M. and Sagara, S., “Experimental research on molten salt thermofluid technology using a high-temperature molten salt loop applied for a fusion reactor flibe blanket,” Fusion Engineering Design, Vols. 63-64, 2002, pp. 405-409.

[9] Kunugi, T. and Satake, S., “Approaches of Fusion Science to Global Warming from the Perspective of Thermofluid Research,” Fusion Engineering Design, Vols. 63-64, 2002, pp. 665-672.

[10] Smolentsev, S., Abdou, M. A., Morley, N. B., Ying, A. and Kunugi, T., “Application of the "k-□" model to open channel flows in a magnetic field,” International Journal of Engineering Science, Vol. 40, 2002, pp. 693-711.

[11] Freeze, B., Smolentsev, S., Morley, N. B. and Abdou, M. A., “Characterization of the Effect of Froude Number on Surface Waves and Heat Transfer in Inclined Turbulent Open Channel Water Flows,” International Journal of Heat and Mass Transfer, Vol. 46, 2002, pp. 3765-3775.

[12] Satake, S., Kunugi, T. and Smolentsev, S., “DNS of Turbulent Pipe Flow in a Transverse Magnetic Field,” Journal of Turbulence, Vol. 3, 2002, pp. 020 (http://jot.iop.org/).

[13] Satake, S., Kunugi, T. and Smolentsev, S., “Direct numerical simulation of MHD turbulent free surface flow,” Transaction JSME, Vol. 68, 2002, pp. 755-760.

[14] Smolentsev, S., Morley, N. B., Freeze, B., Miraghaie, R., Nave, J. C., Banerjee, S., Ying, A. and Abdou, M. A., “Thermofluid Modeling and Experiments for Free Surface Flows of Low-Conductivity Fluid in Fusion Systems,” Fusion Engineering Design, Vol. 72, 2004, pp. 63-81.

[15] Chiba, S., Omae, M., Yuki, K., Hashizume, H., Toda, S. and Sagara, A., “Experimental research on heat transfer enhancement for high Prandtl-number fluid,” Fusion Science and Technology, Vol. 47, 2005, pp. 569-573.

[16] Morley, N. B., Malang, S. and Kirillov, I., “Thermofluid Magnetohydrodynamic Issues for

Liquid Breeders," Fusion Science and Technology, Vol. 47, 2005, pp. 488-501.

[17] Okumura, M., Yuki, K., Hashizume, H. and Sagara, A., "Evaluation of Flow Structure in Packed-Bed Tube by Visualization Experiment," Fusion Science and Technology, Vol. 47, 2005, pp. 1089-1093.

[18] Sagara, A., Tanaka, T., Muroga, T., Hashizume, H., Kunugi, T., Fukada, S. and Shimizu, A., "Innovative liquid breeder blanket design activities in Japan," Fusion Science and Technology, Vol. 47, 2005, pp. 524-529.

[19] Smolentsev, S., Miraghaie, R. and Abdou, M. A., "MHD Effects on Heat Transfer in a Molten Salt Blanket," Fusion Science and Technology, Vol. 47, 2005, pp. 559-563.

[20] Smolentsev, S.,and Miraghaie, R., "Study of a Free Surface in Open-Channel Water Flows in the Regime from weak to strong Turbulence," International Journal of Multiphase Flow, Vol. 31, 2005, pp. 921-939.

[21] Abdou, M. A., Morley, N. B., Ying, A., Smolentsev, S. and Calderoni, P., "Overview of fusion blanket R&D in the US over the last decade," Nuclear Engineering and Technology, Vol. 37, 2005, pp. 401-422.

[22] Li, F-Ch., Kunugi, T. and Serizawa, A., "MHD effect on flow structures and heat transfer characteristics of liquid metal-gas annular flow in a vertical pipe," International Journal of Heat and Mass Transfer, Vol. 48, 2005/2006, pp. 2571-2581.

[23] Morley, N. B., Abdou, M. A., Anderson, M., Calderoni, P., Kurtz, R. J., Nygren, R., Raffray, R., Sawan, M., Sharpe, P., Smolentsev, S., Willms, S. and Ying, A, "Overview of Fusion Nuclear Technology in the US," Fusion Engineering Design, Vol. 81, 2006, pp. 33-43.

[24] Satake, S., Kunugi, T., Naito, N. and Sagara, A., "Direct numerical simulation of MHD flow with electrically conducting wall," Fusion Engineering Design, Vol. 81, 2006, pp. 367-374.

[25] Chiba, S., Yuki, K., Hashizume, H., Toda, S. and Sagara, A., "Numerical research on heat transfer enhancement for high Prandtl-number fluid," Fusion Engineering Design, Vol. 81, 2006, pp. 513-517.

[26] Satake, M., Yuki, K., Chiba, S. and Hashizume, H., "Numerical analysis of MHD flow structure behind a square rod," Fusion Engineering Design, Vol. 81, 2006, pp. 525-532.

[27] Takeuchi, J., Satake, S., Miraghaie, R., Yuki, K., Yokomine, T., Kunugi, T., Morley, N. B. and Abdou M. A., "Study of heat transfer enhancement / suppression for molten salt flows in a large diameter circular pipe: Part one – Benchmarking," Fusion Engineering Design, Vol. 81, 2006, pp. 601-606.

[28] Satake, S., Kunugi. T., Takase, K. and Ose, Y., "Direct numerical simulation of turbulent channel flow under a uniform magnetic field for large-scale structures at high Reynolds number," Physics of Fluids, Vol. 18, 2006, 125106.

[29] Nakaharai, H., Takeuchi, J., Yokomine, T., Kunugi, T., Satake, S., Morley, N. B. and Abdou, M. A., "The influence of a magnetic field on turbulent heat transfer of high Prandtl number fluid," Experimental Thermal and Fluid Science, Vol. 32, 2007, pp. 23-28.

[30] Takeuchi, J., Satake, S., Kunugi, T., Yokomine, T., Morley, N. B., and Abdou, M. A.,"Development of PIV technique under magnetic fields and measurement of turbulent pipe flow of FLIBE simulant fluid," Fusion Science and Technology, Vol. 52, 2007, pp. 860-864.

[31] Nakaharai, H., Takami, S., Yokomine, T., Ebara, S., Shimizu, A., "Numerical study of heat transfer characteristics in a tube with regularly spaced twisted tape," Fusion Science and Technology, Vol. 52, 2007, pp. 855-859.

[32] Yokomine, T., Takeuchi, J., Nakaharai, H., Satake, S., Kunugi, T., Morley, N. B., Abdou, M. A., “Experimental investigation of turbulent heat transfer of high Prandtl number fluid flow under strong magnetic field,” Fusion Science and Technology, Vol. 52, 2007, pp. 625-629.

[33] Satoh, T., Yuki, K., Chiba, S., Hashizume, H. and Sagara, S. “Heat Transfer Performance for High Prandtl and High Temperature Molten Salt Flow in Sphere-Packed Pipes”, Vol. 52, 2007, pp. 618-624.

[34] Seto, N., Yuki, K., Hashizume, H., Sagara, A., ”Heat transfer and pressure drop correlations of sphere-packed pipes for a wide range of Re and Pr”, Fusion Engineering and Design, submitted.

[35] Yamagishi, A., Yuki, K., Hashizume, H., Kunugi, T. and Sagara, A., ”Heat transfer enhancement of a circular pipe flow using nano-porous layer”, Fusion Engineering and Design, submitted.

[36] Takeuchi, J., Satake, S., Kunugi, T., Yokomine, T., Morley, N. B.and Abdou, M.A., “Experimental study on MHD effects on turbulent flow of FLIBE stimulant fluid in a circular pipe”, Fusion Engineering and Design, submitted.

[37] Yokomine, T., Takeuchi, J., Nakaharai, H., Satake, S., Kunugi, Morley, N. B. and Abdou, M. A.,“Experimental study of MHD effects on heat transfer characteristics on turbulent pipe flow of FLIBE stimulant fluid”, Fusion Engineering and Design, submitted.

[38] Yamamoto, Y., Kunugi, T. and Satake, S.“DNS and k-epsilon model simulation of MHD turbulent channel flows with heat transfer,” Fusion Engineering and Design, submitted.

Task 1-2A MHD coating for V/Li systems

[1] Fujiwara, M., Natesan, K., Satou, M., Hasegawa, A., and Abe, K. “Effects of doping elements on oxidation properties of V-Cr-Ti type alloys in several environments” Journal of Nuclear Materials, 307-311 (2002) 601-604.

[2] Pint, B.A., DeVan, J.H. and DiStefano, J.R., "Temperature Limits on Compatibility of Insulating Ceramics in Lithium," Journal of Nuclear Materials, 307-311 (2002) 1344-50.

[3] Suzuki, A., Koch, F., Maier, H., Nishimura, H., and Muroga, T., “Fabrication of ceramics coatings on NIFS-HEAT by arc-source plasma-assisted deposition method for fusion blanket application” Journal of Plasma Fusion Research SERIES, Vol. 5 (2002) pp.551~555.

[4] Sakurai, T., Yoneoka, T., Tanaka, S., Suzuki, A., Muroga, T., “Control of nitrogen concentration in liquid lithium by hot trapping” Fusion Engineering and Design, Vol. 61-62 (2002) pp.763~768.

[5] Smith, D.L., Konys, J., Muroga T. and Evitkhin, V., “Development of coating for fusion power applications”, Journal of Nuclear Materials, Vol. 307-311 (2002) pp.1314~1322.

[6] Sakurai, T. Yoneoka, T., Tanaka, S., Suzuki, A. and Muroga, T., “Control of the nitrogen concentration in liquid lithium by the hot trap method”, Journal of Nuclear Materials, 307-311 (2002) 1380~1384.

[7] Pint, B.A., DiStefano J.R. and Tortorelli, P.F., "High Temperature Compatibility Issues for Fusion Reactor Structural Materials," Fusion Science and Technology, 44, (2003) 433-40.

[8] Suzuki, A., Muroga, T., Pint, B.A., Yoneoka, T., Tanaka, S., “Corrosion behaviour of AlN for self-cooled Li/V blanket application” Fusion Engineering and Design, 69 (2003) 397~/401.

[9] Pint, B.A., Tortorelli, P.F., Jankowski, A.,J. Hayes, J., Muroga, T., Suzuki,A., Yeliseyeva. O.I., and Chernov, V.M., "Recent progress in the development of electrically insulating coatings for a liquid lithium blanket" Journal of Nuclear Materials, 329-333 (2004) 119-124.

[10] Tanaka, T., Suzuki, A., Muroga, T., Sato, F., Iida T. and Nishitani T., “Radiation induced conductivity of ceramic coating materials under 14 MeV neutron irradiation”, Journal of Nuclear Materials, 329-333 (2004) 1434-1437.

[11] Yao, Z., Suzuki, A., Muroga T. and Katahira, K., “Chemical formation of erbium oxide layer on V–4Cr–4Ti during exposure to liquid lithium doped with erbium” Journal of Nuclear Materials, 329-333（2004）1414-1418

[12] Pint, B.A., More, K.L., Meyer, H.M. and DiStefano, J.R. “Recent Progress Addressing Compatibility Issues Relevant to Fusion Environments,” Fusion Science and Technology, 47 (2005) 851-855.

[13] Suzuki, A., Muroga, T., Yoneoka, T., Tanaka, S., “Compatibility of compound oxides with liquid lithium for fusion reactor blanket application”, Journal of Physics and Chemistry of Solids 66, (2005) 690-693.

[14] Tanaka, T., Shikama, T., Narui, M., Tsuchiya, B., Suzuki A. and Muroga T., “Evaluation of insulating property of ceramic materials for V/Li blanket system under fission reactor irradiation”, Fusion Engineering and Design, 75-79 (2005) 933-937

[15] Sawada, A., Suzuki, A., Maier, H., Koch, F., Terai T. and Muroga T., “Fabrication of yttrium oxide and erbium oxide coatings by PVD methods”, Fusion Engineering and Design, 75-79 (2005) 737-740.

[16] Yao, Z., Suzuki, A., Muroga, T., Katahira, K., “In situ formation and chemical stability of Er2O3 coating on V-4Cr-4Ti in liquid lithium” Fusion Engineering and Design 75-79 (2005)

1015-1019

[17] Nagasaka, T., Muroga, T., Li, M., Hoelzer, D.T., Zinkle, S.J., Grossbeck, M.L., and Matsui, H., "Tensile property of low activation vanadium alloy after liquid lithium exposure", Fusion Engineering and Design, 81 (2006) 307-313

[18] Jankowski, A. F., Saw, C. K., Ferreira, J. L., Harper, J. S., Hayes J. P. and Pint, B. A., "Morphology, Microstructure and Residual Stress in EB-PVD Erbia Coatings," Journal of Materials Science, 42 (2006) 5722-5727.

[19] Pint, B. A., Moser, J. L. and Tortorelli, P. F., "Liquid Metal Compatibility Issues for Test Blanket Modules," Fusion Engineering and Design, 81 (2006) 901-908.

[20] Yao, Z., Suzuki, A., Muroga T. and Nagasaka T., "Structural stability and self-healing capability of Er2O3 in situ coating on V–4Cr–4Ti in liquid lithium", Fusion Engineering and Design, 81 (2006) 2887-2892.

[21] Tanaka, T., Nagayasu, R., Sato, F., Muroga, T., Ikeda, T. and Iida, T., "Comparison of electrical properties of ceramic insulators under gamma ray and ion irradiation" Fusion Engineering and Design, 81(2006) 1027-1031

[22] Yao, Z., Suzuki, A., Muroga, T., Yeliseyeva O. and Nagasaka, T., "The in situ growth of Er2O3 coatings on V–4Cr–4Ti in liquid lithium", Fusion Engineering and Design, 81(2006) 951-956

[23] Muroga, L., Chen, J.M., Chernov, V.M., Fukumoto, K., Hoelzer, D.T., Kurtz, R.J., Nagasaka, T., Pint, B.A., Satou, M., Suzuki A., and Watanabe, H., "Review of advances in development of vanadium alloys and MHD insulator coatings", Journal of Nuclear Materials, Volumes 367-370(2007) 780-787.

[24] Li, M, Nagasaka, T, Hoelzer, DT, Grossbeck, ML, Zinkle, SJ, Muroga, T, Fukumoto, K, Matsui, H, and Narui, M, "Biaxial thermal creep of two heats of V-4Cr-4Ti at 700 and 800 °C in a liquid lithium environment," Journal of Nuclear Materials, Volumes 367-370 (2007) 788-793.

[25] Pint, B. A., Moser, J. L., Jankowski, A. and Hayes, J., "Compatibility of Multi-Layer, Electrically Insulating Coatings For the Vanadium-Lithium Blanket," Journal of Nuclear Materials, 367-370 (2007) 1165-1169.

[26] Nagura, M., Kondoh, M., Suzuki, A., Muroga T., and Terai, T., "Experimental Study on Corrosion of Ceramic materials in National Convection Lithium Loop" Fusion Science and Technology, 52 (2007) 625-629.

[27] Tanaka, T., Nagayasu, R., Sawada, A., Ikeda, T., Sato, F., Suzuki, A., Muroga T. and Iida T. "Electrical insulating property of ceramic coating materials in radiation and high-temperature environment", Journal of Nuclear Materials, 367-370 (2007) 1155-1159.

[28] Pint, B. A., Pawel, S. J., Howell, M., Moser, J. L., Garner, G. W., Santella, M. L., Tortorelli, P. F., Wiffen, F. W. and DiStefano, J. R., "Initial Characterization of V-4Cr-4Ti and MHD Coatings Exposed to Flowing Li," submitted to Journal of Nuclear Materials.

[29] Hishinuma, Y., Tanaka, T., Nagasaka, T., Muroga, T., Tasaki, Y and Yoshizawa, S. "Er2O3 coating on V and V-4Cr-4Ti alloy through MOCVD process for advanced liquid breeder blankets", submitted to Journal of Nuclear Materials.

Task 1-2B Vanadium Alloy Capsule Irradiation

[1] Nagasaka, T., Heo, N. J., Muroga T., and Imamura, M. "Examination of fabrication process parameters for improvement of low-activation vanadium alloys", Fusion Engineering and Design, Vols. 61-62, 2002, pp. 757-762

[2] Heo, N. J., Nagasaka, T. ,Muroga, T., Nishimura, A., Shinozaki K., and Takeshita, N., "Metallurgical and mechanical properties of laser weldment for low activation V-4Cr-4Ti alloy", Fusion Engineering and Design, Vols. 61-62, 2002, pp. 749-755

[3] Nishimura, A., Nagasaka T., and Muroga, T., "Fracture toughness of high-purity V-4Cr-4Ti alloy (NIFS-HEAT-2) at room temperature", Journal of Nuclear Materials, Vols. 307-311, 2002, pp. 571-575

[4] Watanabe, H., Suda, M., Muroga, T., and Yoshida, N., "Oxide formation of a purified V-4Cr-4Ti alloy during heat treatment and ion irradiation", Journal of Nuclear Materials, Vols. 307-311, 2002, pp. 408-412

[5] Grossbeck, M. L., King, J. F., Nagasaka T., and David, S. A., "Gas tungsten arc welding of vanadium alloys with impurity control", Journal of Nuclear Materials, Vols. 307-311, 2002, pp. 1590-1594

[6] Heo, N. J., Nagasaka, T., Muroga, T., and Matsui, H., "Effect of impurity levels on precipitation behavior in the low-activation V-4Cr-4Ti alloys", Journal of Nuclear Materials, Vols. 307-311, 2002, pp. 620-624

[7] Chuto, T., Satou, M., Hasegawa, A., Abe, K., Nagasaka T., and Muroga, T., "Fabrication using a levitation melting method of V-4Cr-4Ti-Si-Al-Y alloys and their mechanical properties", Journal of Nuclear Materials, Vols. 307-311, 2002, pp. 555-559

[8] Nagasaka, T., Muroga, T., Grossbeck, M. L., and Yamamoto, T., "Effects of post-weld heat treatment conditions on hardness, microstructures and impact properties of vanadium alloys", Journal of Nuclear Materials, Vols. 307-311, 2002, pp. 1595-1599

[9] Nagasaka, T., Muroga, T.,, Wu, W.C., Xu, Z.Y., and Imamura, M., "Low Activation Characteristics of Several Heats of V-4Cr-4Ti Ingot", Journal of Plasma and Fusion Research SERIES, Vol. 5, 2002, pp. 545-550.

[10] Gelles, DS, "Microstructural examination of irradiated and unirradiated V-4Cr-4Ti pressurized creep tubes," Journal of Nuclear Materials, Volumes 307-311 (2002) 393-397.

[11] Toloczko, MB, Kurtz, RJ, Hasegawa, A, and Abe, K, "Shear punch tests performed using a new low compliance test fixture," Journal of Nuclear Materials, Volumes 307-311 (2002) 1619-1623.

[12] Hoelzer, DT and Rowcliffe, AF, "Investigating solute interactions in V-4Cr-4Ti based on tensile deformation behavior of vanadium," Journal of Nuclear Materials, Volumes 307-311 (2002) 596-600.

[13] Odette, GR, He, MY, Donahue, EG, Spatig, P, and Yamamoto, T, "Modeling the multiscale mechanics of flow localization-ductility loss in irradiation damaged bcc alloys," Journal of Nuclear Materials, Volumes 307-311 (2002) 171-178.

[14] Lucas, GE, Odette, GR, Sokolov, M, Spatig, P, Yamamoto, T, Jung, P, "Recent progress in small specimen test technology," Journal of Nuclear Materials, Volumes 307-311 (2002) 1600-1608.

[15] Odette, GR, He, M, Gragg, D, Klingensmith, D, Lucas, GE, "Some recent innovations in small specimen testing," Journal of Nuclear Materials, Volumes 307-311 (2002) 1643-1648.

[16] Zinkle, SJ, Hashimoto, N, Hoelzer, DT, Qualls, AL, Muroga, T, and Singh, BN, "Effect of

periodic temperature variations on the microstructure of neutron-irradiated metals," Journal of Nuclear Materials, Volumes 307-311 (2002) 192-196.

[17] Nagasaka, T., Muroga, T., and Iikubo, T., "Development of tubing technique for high-purity low activation vanadium alloys", Fusion Science and Technology, Vol. 44 (2003) 465-469.

[18] Heo, N., Nagasaka, T., Muroga, T., Nishimura, A., Shinozaki, K., Watanabe, H., "Mechanical properties of laser weldment of V-4Cr-4Ti alloy", Fusion Science and Technology, 44 (2003) 470-474.

[19] Fukumoto, K., Matsui, H., Narui, M., Nagasaka, T., Muroga, T., "Manufacturing pressurized creep tubes from highly purified V-4Cr-4Ti alloys, NIFS-Heat2", Journal of Nuclear Materials, Volume 335 (2004) 103-107

[20] Koyama, M., Fukumoto, K., Matsui, H., "Effects of purity on high temperature mechanicalproperties of vanadium alloys", Journal of Nuclear Materials, Volume 329-333 (2004) 442-446

[21] Fukumoto, K., Matsui, H., Muroga, T., Zinkle, S. J., Hoelzer, D. T., Snead, L. L., "Varying temperature effects on mechanical properties of vanadium alloys during neutron irradiation", Journal of Nuclear Materials, Volume 329-333 (2004) 472-476

[22] Sugiyama, M., Fukumoto, K., Matsui, H., "Dislocation channel formation process in V－Cr－Ti alloys irradiated below 300° C", Journal of Nuclear Materials, Volume 329-333 (2004) 467-471

[23] Chuto, T., Satou, M., Hasegawa, A., Abe, K., Muroga T., and Yamamoto, N., "Effects of small amount of additional elements on control of interstitial impurities and mechanical properties of V-4Cr-4Ti-Si-Al-Y", Journal of Nuclear Materials 326 (2004) 1-8

[24] Chuto. T,, Satou, M., Hasegawa, A., Abe, K., Muroga, T., and Yamamoto, N., "Changes in mechanical properties of high-purity V-4Cr-4Ti-Si, Al, Y alloys after neutron irradiation at relatively low temperatures", ASTM Special Technical Publications STP 1447 (2004) pp.693-701.

[25] Kurtz, R.J, Abe, K., Chernov, V.M., Hoelzer, D.T., Matsui, H., Muroga, T., and Odette, G.R. "Recent progress on development of vanadium alloys for fusion," Journal of Nuclear Materials, Volumes 329-333 (2004) 47-55.

[26] Watanabe, H., Nagamine M., Yamasaki, K., Yoshida, N., Nagasaka, T., Muroga, T., Shinozaki, K., "Effects of Ion Irradiation on Yag Laser Welded V-4Cr-4Ti Alloy" Journal of Plasma Fusion Res, Vol.80, No.10 (2004) 889-894

[27] Muroga, T., Nagasaka, T., Nishimura A., and Chen, J.M., "Improvement of Vanadium Alloys by Precipitate Control for Structural Component of Fusion Reactors", Materials Science Forum 475-479 (2005) 1449-1454.

[28] Muroga, T., "Vanadium Alloys for Fusion Blanket Applications", Materials Transactions 46 (2005) 405-411.

[29] Nagasaka, T. Muroga, T., Watanabe, H., Yamasaki, K., Heo, N-J., Shinozaki K., and Narui M.,, "Recovery of hardness, impact properties and microstructure of neutron-irradiated weld joint of a fusion candidate vanadium alloys" Materials Transactions 46 (2005) 498-502.

[30] Nagasaka, T., Muroga, T., Noda, N., Kawamura M., and Ise, H., "Tungsten Coating on Low Activation Vanadium Alloy by Plasma Spray Process" Fusion Science and Technology 47 (2005) 876-880.

[31] Lee, CY, Donahue, EG, and Odette, GR, "Verification of mechanical properties of a V-4CR-4TI alloy using finite element method," Advances in Fracture and Strength, Pts 1-4, Key Engineering Materials (2005) 1013-1018.

[32] Watanabe, H., Nagamine, M., Yamasaki, A., Yoshida, N., Nagasaka, T., Muroga, T., "The microstructure of laser welded V-4Cr-4Ti alloy after ion irradiation", Materials Science Forum Volumes 475-479(2005) 1491-1496

[33] Fukumoto, K., Takahashi, S., Kurtz, R.J., Smith, D.L., and Matsui, H. "Microstructural examination of V-(Fe or Cr)-Ti alloys after thermal-creep or irradiation-creep tests" Journal of Nuclear Materials, Volume 341 (2005) 83-89

[34] Fukumoto, K., Takahashi, K., Anma, Y., Matsui, H., "Effect of Impurities on Microstructural Evolution and Deformation Process of Ion-Irradiated V-Cr-Ti alloys", Materials Transactions, Volume 46 (2005) 503-510

[35] Kurishita, H., Kuwabara, T., Hasegawa, M., Kobayashi, S., and Nakai, K., "Microstructural control to improve the resistance to radiation embrittlement in vanadium" Journal of Nuclear Materials, Volume 343 (2005) 318-324.

[36] Nagasaka, T., Muroga, T., Li, M., Hoelzer, D.T., Zinkle, S.J., Grossbeck, M.L., and Matsui, H. "Tensile property of low activation vanadium alloy after liquid lithium exposure" Fusion Engineering and Design, 81 (2006) 307-313

[37] Nagasaka, T. Muroga, T., Fukumoto, K., Watanabe, H., Grossbeck, M.L., and Chen, J.M., "Development of fabrication technology for low activation vanadium alloys as fusion blanket structural materials" Nucl. Fusion 46 No 5 (2006) 618-625

[38] Muroga, L., Chen, J.M., Chernov, V.M., Fukumoto, K., Hoelzer, D.T., Kurtz, R.J., Nagasaka, T., Pint, B.A., Satou, M., Suzuki A., and Watanabe, H. "Review of advances in development of vanadium alloys and MHD insulator coatings" Journal of Nuclear Materials, Volumes 367-370(2007) 780-787

[39] Li, M., Nagasaka, T., Hoelzer, D.T., Grossbeck, M.L., Zinkle, S.J., Muroga, T., Fukumoto, K., Matsui, H., and Narui, M., "Biaxial thermal creep of two heats of V-4Cr-4Ti at 700 and 800 °C in a liquid lithium environment" Journal of Nuclear Materials, Volumes 367-370 (2007) 788-793

[40] Fukumoto, K., Nagasaka, T., Muroga, T., Nita, N., Matsui, H., "Creep mechanism of highly purified V–4Cr–4Ti alloys during thermal creep in a vacuum", Journal of Nuclear Materials, Volume 367-370 (2007) 834-838

[41] Fukumoto, K., Sugiyama, M., Matsui, H., "Features of dislocation channeling in neutron-irradiated V–(Fe, Cr)–Ti alloy ", Journal of Nuclear Materials, Volume 367-370 (2007) 829-833

[42] Watanabe, H., Yamasaki, K., Higashizima, A., Yoshida, N., Nagasaka, T., Muroga, T., "The microstructure of laser welded V-4Cr-4Ti alloy after neutron irradiation", Journal of Nuclear Materials, Volumes 367-370(2007) 794-799

[43] Li, M., Nagasaka, T., Hoelzer, D.T., Grossbeck, M.L., Zinkle, S.J., Muroga, T., Fukumoto, K., Matsui, H., and Narui, M., "Biaxial thermal creep of two heats of V-4Cr-4Ti at 700 and 800 °C in a liquid lithium environment," Journal of Nuclear Materials, Volumes 367-370 (2007) 788-793.

[44] Rowcliffe, A.F., Hoelzer, D.T., Kurtz, R.J., and Young, C.M., "Oxidation behavior of a V-4Cr-4Ti alloy during the commercial processing of thin-wall tubing," Journal of Nuclear Materials, Volumes 367-370 (2007) 839-843.

[45] Gelles, D.S., Toloczko, M.B., and Kurtz, R.J., "Thermal creep mechanisms in V-4Cr-4Ti pressurized tube specimens," Journal of Nuclear Materials, Volumes 367-370 (2007) 869-875.

[46] Toloczko, M.B., Fryd, M.M., and Kurtz, R.J., "Effect of neutron irradiation on the compression properties of two heats of V-4Cr-4Ti," Journal of Nuclear Materials, submitted.

[47] Li, M., Hoelzer, D.T., Grossbeck M.L., Rowcliffe, A.F., Zinkle, S.J., and Kurtz, R.J., "Irradiation creep of the US Heat 832665 of V-4Cr-4Ti," Journal of Nuclear Materials, submitted.

[48] Muroga, T., Nagasaka, T., Li, Y., and Chen, J.M., "Microstructure of Creep-deformed V-4Cr-4Ti Strengthened by Precipitation and Cold Rolling" Journal of Nuclear Materials, submitted.

[49] Watanabe, H., Higashizima. A., Yoshida, N., Nagasaka. T., Muroga, T., "The Microstructure of Laser Welded Y Doped V-4Cr-4Ti Alloys after Ion Irradiation" Journal of Nuclear Materials, submitted.

[50] Watanabe, H., Yamasaki, M., Higashizima. A., Yoshida, N., Nagasaka, T., Muroga, T., Shinozaki, K., "The Effects of Postwelding Heat Treatment on Microstructural Evolution of Yag Laser Welded V-4Cr-4Ti Alloy" Journal of Plasma Fusion Res, submitted

Task 2-1 SiC/SiC Fundamentals and Material Processing

[1] Y. Katoh, T. Nozawa, L.L. Snead, T. Hinoki and A. Kohyama, Fusion Engineering and Design 81 (2006) 937-944.

[2] Katoh, Y., Nozawa, T.,& Snead, L.L., Mechanical properties of thin pyrolitic carbon interphase SiC-Matrix composites reinforced with near-stoichiometric SiC fibers, J. Am. Ceram. Soc. 88 (2005) 3088-3095.

[3] Katoh Y., Snead, L.L., Nozawa, T., Hinoki, T., Kohyama, A., Igawa, N.,& Taguchi, T., Mechanical properties of chemically vapor-infiltrated silicon carbide structural composites with thin carbon interphases for fusion and advanced fission applications, Mater. Trans. 46 (2005) 527-535.

[4] Nozawa, T., Katoh, Y.,& Kohyama, A., Evaluation of tensile properties of SiC/SiC composites with miniaturized specimens, Mater. Trans. 46 (2005) 543-551.

[5] Igawa, N., Taguchi, T., Nozawa, T., Snead, L.L., Hinoki, T., McLaughl, J.C., Katoh, Y., Jitsukawa, S.,& Kohyama, A., Fabrication of SiC fiber reinforced SiC composite by chemical vapor infiltration for excellent mechanical properties, Journal of Physics and Chemistry of Solids 66 (2005) 551-554.

[6] Nozawa, T., Katoh, Y., Snead, L.L., Hinoki, T.,& Kohyama, A., Tensile and thermal properties of chemically vapor-infiltrated silicon carbide composites with various high-modulus fiber reinforcements, Ceram. Eng. and Sci. Proc. 26 (2005) 311-318.

[7] Katoh, Y., Nozawa, T., Kotani, M., Ozawa, K.,& Kohyama, A., Microstructures and flexural properties of high temperature-pyrolyzed PIP-SiC/SiC composites, Key Eng. Mater. 287 (2005) 346-351.

[8] Taguchi, T., Nozawa, T., Igawa, N., Katoh, Y., Jitsukawa, S., Kohyama, A., Hinoki, T.,& Snead, L.L., Fabrication of advanced SiC fiber/F-CVI SiC matrix composites with SiC/C multi-layer interphase, J. Nucl. Mater. 329-33 (2004) 572-576.,

[9] Nozawa, T., Ozawa, K., Katoh, Y.,& Kohyama, A., Effect of heat treatment on microstructure and mechanical properties of stoichiometric SiC/SiC composites, Mater. Trans. 45 (2004) 307-310.

[10] Katoh, Y., Lowden, R.A., Yang, W., Nozawa, T., Hinoki, T.,& Kohyama, A., Fast Fracture Properties of Thin Interphase Silicon Carbide Composites, in: M. Singh, R.J. Kerans, E. Lara-Curzio, R. Naslain (Eds.), High Temperature Ceramic Matrix Composites 5, The American Ceramic Society, Westerville, OH,2004, pp. 169-174.

[11] Y. Katoh, A. Kohyama, T. Nozawa and M. Sato, Journal of Nuclear Materials 329-33 (2004) 587-591.

[12] S.J. Son, K.H. Park, Y. Katoh and A. Kohyama, Journal of Nuclear Materials 329-33 (2004) 1549-1552.

[13] T. Nozawa, K. Ozawa, Y. Katoh and A. Kohyama, Materials Transactions 45 (2004) 307-310.

[14] Nozawa, T., Katoh, Y.,& Kohyama, A., Lara-Curzi E.., Specimen Size Effect on the Tensile and Shear Properties of the High-Crystalline and High-Dense SiC/SiC Composites, Ceram. Eng. and Sci. Proc. 24 (2003) 415-420.

[15] Y. Katoh, A. Kohyama, T. Hinoki and L.L. Snead, Fusion Science and Technology 44 (2003) 155-162.

[16] W. Yang, A. Kohyama, Y.T. Katoh, H. Araki, J.N. Yu and T. Noda, Journal of the American Ceramic Society 86 (2003) 851-856.

[17] S.M. Dong, Y. Katoh and A. Kohyama, Journal of the European Ceramic Society 23 (2003)

1223-1231.

[18] T. Hino, T. Jinushi, Y. Hirohata, M. Hashiba, Y. Yamauchi, Y. Katoh and A. Kohyama, Fusion Science and Technology 43 (2003) 184-190.

[19] J.S. Park, Y. Katoh and A. Kohyama, Ceramic Engineering and Science Proceedings 24 (2003) 421-426.

[20] Igawa, N., Taguchi, T., Snead, L.L., Katoh ,Y., Jitsukawa, S., Kohyama, A.,& McLaughl, J.C., Optimizing the fabrication process for superior mechanical properties in the FCVISiC matrix/stoichiometric SiC fiber composite system, J. Nucl. Mater. 307 (2002) 1205-1209.

[21] Nozawa, T., Katoh ,Y., Kohyama, A.,& Lara-Curzi, E., Specimen Size Effect on the In-Plane Shear Properties of SiC/SiC Composites, in: J.P. Singh, N.P. Bansal, M. Singh (Eds.), Advances in Ceramic Matrix Composites VIII: Ceramic Transactions, Vol. 139, vol. 139, The American Ceramic Society, Westerville, OH,2002, pp. 127-138.

[22] Nozawa, T., Hinoki, T., Katoh, Y., Kohyama, A.,& Lara-Curzi, E.(Eds.), Specimen Size Effects on the Tensile Properties of 2D/3D SiC/SiC Composites, ASTM International, West Conshohocken, PA,2002.

[23] W. Yang, A. Kohyama, T. Noda, Y. Katoh, T. Hinoki, H. Araki and J. Yu, Journal of Nuclear Materials 307 (2002) 1088-1092.

[24] K. Hironaka, T. Nozawa, T. Hinoki, N. Igawa, Y. Katoh, L.L. Snead and A. Kohyama, Journal of Nuclear Materials 307 (2002) 1093-1097.

[25] Y. Hirohata, T. Jinushi, Y. Yamauchi, M. Hashiba, T. Hino, Y. Katoh and A. Kohyama, Fusion Engineering and Design 61-2 (2002) 699-704.

[26] Y. Katoh, S.M. Dong and A. Kohyama, Fusion Engineering and Design 61-2 (2002) 723-731.

[27] J.S. Park, Y. Katoh, A. Kohyama, S.P. Lee and H.K. Yoon, Fusion Engineering and Design 61-2 (2002) 733-738.

[28] T. Nozawa, Y. Katoh, A. Kohyama and E. Lara-Curzio. in Fifth International Energy Agency Workshop on SiC/SiC Ceramic Composites for Fusion Energy Application (Jones, R.H., Kohyama, A. and Riccardi, B., eds.), pp. 74-86, San Diego, California, USA 2002.

[29] W. Yang, H. Araki, T. Noda, Q. Hu, H. Suzuki, Y. Katoh and A. Kohyama, Ceramic Transactions 144 (2002) 273-280.

[30] J.S. Park, Y. Katoh, A. Kohyama and H.K. Yoon, Ceramic Transactions 144 (2002) 263-272.

[31] T. Nozawa, K. Hironaka, Y. Katoh, A. Kohyama, T. Taguchi, S. Jitsukawa and L.L. Snead, Ceramic Transactions 144 (2002) 245-252.

[32] Y. Katoh, S.M. Dong and A. Kohyama, Ceramic Transactions 144 (2002) 77-86.

[33] T. Taguchi, N. Igawa, S. Jitsukawa, T. Nozawa, Y. Katoh, A. Kohyama, L.L. Snead and J.C. McLaughlin, Ceramic Transactions 144 (2002).

[34] T. Hinoki, L.L. Snead, T. Taguchi, N. Igawa, W. Yang, T. Nozawa, Y. Katoh and A. Kohyama, Ceramic Transactions 144 (2002) 55-67.

[35] J.S. Park, Y. Katoh and A. Kohyama, Ceramic Engineering and Science Proceedings 23 (2002) 469-476.

[36] K. Hironaka, T. Nozawa, T. Hinoki, Y. Katoh, A. Kohyama, T. Taguchi, N. Igawa and L.L. Snead, Ceramic Engineering and Science Proceedings 23 (2002) 403-410.

[37] Y. Katoh, A. Kohyama, S.M. Dong, T. Hinoki and J.J. Kai, Ceramic Engineering and Science Proceedings 23 (2002) 363-370.

[38] M. Hashiba, J. Jinushi, Y. Yamauchi, Y. Hirohata, T. Hino, Y. Katoh and A. Kohyama, Journal of Vacuum Society Japan 45 (2002) 145-148.

[39] L.L. Snead, T. Hinoki, Y. Katoh, T. Taguchi, R.H. Jones, A. Kohyama and N. Igawa. in CIMTEC 2002 - 10th International Ceramics Congress and 3rd Forum on New Materials, Florence, Italy 2002.

Task 2-2 SiC System Thermomechanics

[1] Ying, A., Yokomine, T. Shimizu, A., Abdou, M., Kohyama, A., "Impact of Material System Thermomechanics Performance on He-Cooled Ceramic Breeder Blanket Designs with SiCf/Sic" Journal of Nuclear Materials, 329-333(Part 2):1605 - 1609 (August 2004)

[2] G. R. Longhurst, L. L. Snead, & A. Abou-Sena, "The Status of Beryllium Research for Fusion in the United States", *Proceedings of the 6th IEA International Workshop on Beryllium Technology for Fusion*, Miyazaki, Japan, March 2004.

[3] An, Z., Ying, A., Abdou, M., "Experimental and numerical study of ceramic breeder pebble bed thermal deformation behavior" Fusion Science & Technology, 47(4):1101 - 1105 (May 2005)

[4] Abou-Sena, A., Ying, A., Abdou, M., "Effective thermal conductivity of lithium ceramic pebble beds for fusion blankets: a review" Fusion Science & Technology, 47(4):1094 - 1100 (May 2005)

[5] Z. An, A. Ying, M. Abdou, "Experimental and numerical study on the thermomechanical properties of ceramic pebble bed structure" Proc. 2005 Joint ASME/ASCE/SES Conference on Mechanics and Materials (McMat2005), Baton Rouge, LA (06/01/2005)

[6] Z. An, A. Ying and M. Abdou, “Thermo-mechanical analysis of ITER test unit cell under pulse operation,” Proceedings of 21st IEEE/NPSS Symposium on Fusion Engineering 2005, Oct. 2005

[7] Ali Abou-Sena, Alice Ying, & Mohamed Abdou, "Experimental Measurements of the Effective Thermal Conductivity of a Lithium Titanate (Li_2TiO_3) Pebbles-Packed Beds", *Journal of Materials Processing Technology*, Vol.181, pp.206-212, January 2006.

[8] Calderoni, P., Ying, A., Sketchley, T., Abdou, M., "Experimental Study of the Interaction of Ceramic Breeder Pebble Beds with Structural Materials under Thermo-Mechanical Loads" Fusion Engineering & Design, 81(1-7):607 - 612 (February 2006)

[9] An, Z., Ying, A., Abdou, M., "Numerical characterization of thermo-mechanical performance of breeder pebble beds" Proceedings of the 12th International Conference on Fusion Reactor Materials (ICFRM-12), to be published in Journal of Nuclear Materials (2006)

Task 2-3 SiC Capsule Irradiation

[1] Hinoki, T., Snead, L.L., Katoh, Y., Hasegawa, A., Nozawa, T.,& Kohyama, A., The effect of high dose/high temperature irradiation on high purity fibers and their silicon carbide composites, J. Nucl. Mater. 307 (2002) 1157-1162.

[2] Nozawa, T., Hinoki, T., Katoh, Y.,& Kohyama, A., Effects of fibers and fabrication processes on mechanical properties of neutron irradiated SiC/SiC composites, J. Nucl. Mater. 307 (2002) 1173-1177.

[3] Hinoki, T., Katoh, Y.,& Kohyama, A., Effect of fiber properties on neutron irradiated SiC/SiC composites, Mater. Trans. 43 (2002) 617-621.

[4] H. Kishimoto, Y. Katoh and A. Kohyama, Journal of Nuclear Materials 307 (2002) 1130-1134.

[5] K.H. Park, Y. Katoh, H. Kishimoto and A. Kohyama, Journal of Nuclear Materials 307 (2002) 1187-1190.

[6] Y. Katoh, H. Kishimoto and A. Kohyama, Journal of Nuclear Materials 307 (2002) 1221-1226.

[7] Y. Katoh, H. Kishimoto and A. Kohyama, Materials Transactions 43 (2002) 612-616.

[8] L.L. Snead, T. Hinoki and Y. Katoh. in Fusion Materials, pp. 49-57 2002.

[9] Y. Katoh, A. Kohyama, L.L. Snead, T. Hinoki and A. Hasegawa. in 19th IAEA Fusion Energy Conference, Vol. IAEA-CN-94 pp. FT/P1-03 2002.

[10] S. Nogamia, A. Hasegawa, L. L. Snead. [Journal of Nuclear Materials, 307-311 (2), (2002), 1163-1167]

[11] A. Hasegawa , S. Nogami, T. Aizawa, K. Katou and K. Abe. [Journal of Nuclear Materials, 307-311 (2), (2002), 1152-1156]

[12] S. Nogami , S. Ohtsuka, M. B. Toloczko, A. Hasegawa and K. Abe [Journal of Nuclear Materials, 307-311 (2), (2002), 1178-1182]

[13] Y. Katoh, M. Ando and A. Kohyama, Journal of Nuclear Materials 323 (2003) 251-262.K.H. Park, S. Kondo, Y. Katoh and A. Kohyama, Fusion Science and Technology 44 (2003) 455-459.

[14] S. Kondo, K.H. Park, Y. Katoh and A. Kohyama, Fusion Science and Technology 44 (2003) 181-185.

[15] A.Hasegawa, S.Nogami, S.Miwa, K.Abe, T.Taguchi, N.Igawa [Fusion Science and Technology, 44 (1), (2003), 175-180]

[16] Nogami, S., Hasegawa, Snead, L.L., Jones, R.H. & Abe, K., Effect of He pre-implantation and neutron irradiation on mechanical properties of SiC/SiC composite, Journal of Nuclear Materials 329–333 (2004) 577–581

[17] Nozawa, T., Hinoki, T., Snead, L.L., Katoh, Y.,& Kohyama, A., Neutron irradiation effects on high-crystallinity and near-stoichiometry SiC fibers and their composites, J. Nucl. Mater. 329-33 (2004) 544-548.

[18] Nogami, S., Miwa, M., Hasegawa, A., & Abe, K., Mechanical and Structural Property Change of Monolithic SiC and Advanced SiC/SiC Composites due to Low Temperature He+-ion Irradiation and Post-irradiation High Temperature Annealing[American Society for Testing and Materials (ASTM) STP 1447,1447,(2004),655-669]

[19] Hasegawa, A., Miwa, S., Nogami, S., Taniguchi, A., Taguchi, T., & Abe,K., Study of hydrogen effects on microstructural development of SiC base materials under simultaneous

irradiation with He- and Si-ion irradiation conditions[J. Nuclear Materials, 329-333,(2004),582-586]

[20] Miwa, S., Hasegawa, A., Taguchi,T., Igawa, N., & Abe, K., Cavity Formation in a SiC/SiC Composites under Simutaneous Irradiation of Hydrogen, Helium and Silicon Ions [Materials Transactions,46(3),(2005),536-542]

[21] Nozawa, T., Ozawa, K., Kondo, S., Hinoki, T., Katoh, Y., Snead, L.L.,& Kohyama, A., Tensile, Flexural, and Shear Properties of Neutron Irradiated SiC/SiC Composites with Different Fiber-Matrix Interfaces, J. ASTM Int. 2 (2005) 12884-12881-12813.

[22] Katoh, Y.,& Snead, L.L., Bend stress relaxation creep of CVD silicon carbide, Ceram. Eng. and Sci. Proc. 26 (2005) 265-272.

[23] Katoh, Y.,& Snead, L.L., Mechanical Properties of Cubic Silicon Carbide after Neutron Irradiation at Elevated Temperatures, J. ASTM Int. 2 (2005) 12377-12371-12313.

[24] Kondo, S., Katoh, Y., Kishimoto, H., Hinoki, T.,& Kohyama, A., Swelling and Recovery Behavior in Silicon Carbide Irradiated at High Temperature, Proceedings of 2005 International Congress on Advances in Nuclear Power Plants (ICAPP-05),2005.

[25] S. Kondo, Y. Katoh, H. Kishimoto, T. Hinoki and A. Kohyama. in 2005 International Congress on Advances in Nuclear Power Plants (ICAPP-05), Seoul, Korea 2005.

[26] T. Hinoki and A. Kohyama, Annales de chimie science des matériaux, 30[6] (2005) 659-71.

[27] A. Kohyama, Materials Transactions, 46[3] (2005) 384-393.

[28] A. Kohyama, K. Abe, A. Kimura, T. Muroga and S. Jitsukawa, Fusion Science and Technology, 47[4] (2005) 836-843.

[29] K. Ozawa, S. Kondo, T. Hinoki, K. Jimbo and A. Kohyama, Fusion Science and Technology, 47[4] (2005) 871-75.

[30] H. Kishimoto, K. Ozawa, S. Kondo and A. Kohyama, Materials Transactions, 46 [8] (2005) 1923-1927.

[31] H. Kishimoto, T. Hinoki, K. Ozawa, K.-H. Park, S. Kondo and A. Kohyama, Ceramic Engineering and Science Proceedings, 26[8] (2005) 215-222.

[32] Katoh, Y., Nozawa, T., Snead, L.L., Hinoki, T.,& Kohyama, A., Property tailorability for advanced CVI silicon carbide composites for fusion, Fusion Eng. and Design 81 (2006) 937-944.

[33] Katoh, Y., Hashimoto, N., Kondo, S., Snead, L.L.,& Kohyama, A., Microstructural Development in Cubic Silicon Carbide during Irradiation at Elevated Temperatures, J. Nucl. Mater. 351 (2006) 228-240.

[34] Ozawa, K., Hinoki, T., Nozawa, T., Katoh, Y., Maki, Y., Kondo, S., Ikeda, S.,& Kohyama, A., Evaluation of Fiber/Matrix Interfacial Strength of Neutron Irradiated SiC/SiC Composites Using Hysteresis Loop Analysis of Tensile Test Mater. Trans. 47 (2006) 207-210.

[35] Katoh, Y., Snead, L.L., Nozawa, T.,& Windes, W.E., Morley N.B., Advanced Radiation-Resistant Ceramic Composites, Advances in Science and Technology 45 (2006) 1915-1924.

[36] Y. Katoh, N. Hashimoto, S. Kondo, L.L. Snead and A. Kohyama, Journal of Nuclear Materials 351 (2006) 228-240.

[37] K. Ozawa, T. Nozawa, T. Hinoki and A. Kohyama, Ceramic Engineering and Science Proceedings 27 (5) (2006) 157-167.

[38] Nogami, S., Murayama, T., Nagata, Y., & Hasegawa A., Compatibility between SiC and Li Ceramics for Solid Breeding Blanket System. ICFRM-13（2007）submitted.

[39] Nogami, S., Otake, N., Hasegawa, A., Katoh, Y., Yoshikawa, A., Satou, M., Oya, Y.,& Okuno, K., Oxidation behavior of SiC/SiC composites for helium cooled solid breeder. ISFNT-8（2007）submitted.

[40] Nozawa, T., Katoh, Y.,& Snead, L.L., The Effect of Neutron Irradiation on Interfacial Shear Properties of Multilayered Interphase SiC/SiC Composite, J. Nucl. Mater. 3670-370 (2007) 685-691.

[41] Katoh, Y., Nozawa, T., Snead, L.L.,& Hinoki, T., Effect of Neutron Irradiation on Tensile Properties of Unidirectional Silicon Carbide Composites, J. Nucl. Mater. 367-370 (2007) 774-779.

[42] Katoh, Y., Snead, L.L., Hinoki, T., Kondo, S.,& Kohyama, A., Irradiation Creep of Chemically Vapor Deposited Silicon Carbide as Estimated by Bend Stress Relaxation Method, J. Nucl. Mater. 367-370 (2007) 758-763.

[43] Ozawa, K., Nozawa, T., Katoh, Y., Hinoki, T.,& Kohyama, A.," Mechanical Properties and Microstructure of Advanced SiC/SiC composites after Neutron Irradiation", J. Nucl. Mater. 367-370 (2007) 713-718.

[44] Katoh, Y., Snead, L.L., Henager, C.H., Hasegawa, A., Kohyama, A., Riccardi, B.,& Hegema, J.B.J., Current status and critical issues for development of SiC composites for fusion applications, J. Nucl. Mater. 367-370 (2007) 659-671.

[45] Kondo, S., Katoh, Y.,& Kohyama, A., Stoichiometric constraint for dislocation loop growth in silicon carbide, Ceram. Eng. and Sci. Proc. submitted (2007).

[47] Nozawa, T., Katoh, Y.,& Snead, L.L., The Effects of Neutron Irradiation on the Interfacial Shear Strength of SiC/SiC Composites, 7th IEA Workshop on SiC/SiC for Fusion and 1st International Workshop on C&SiC Composites for Advanced Fission, Petten,2007, p. submitted.

Task 3-1 Design-based Integration Modeling

[1] Fukada, S., Nishikawa, M., Sagara, A., Terai, T., “Mass-Transport Properties to Estimate Rates of Tritium Recovery from Flibe Blanket”, Fusion Science & Technology, 41 (2002) 1054-1058.

[2] Hashizume, H., Usui, Y., Kitajima, S., Hida, T., Sagara, A., “Numerical analysis of MHD flow in remountable first wall”, Fusion Engineering and Design, 61-62 (2002) 251-254.

[3] Toda, S., Chiba, S., Yuki, K., Omae, M., Sagara, A., “Experimantal research on molten salt thermofluid technology using a high-temperature molten salt loop applied for a fusion reactor Flibe blanket”, Fusion Engineering and Design, 63-64 (2002) 405-409.

[4] Kunugi, T., Matsumoto, Y., Sagara, A., “A new cooling concept of free surface flow balanced with surface tension for FFHR”, Fusion Engineering and Design, Vol.65 (2003) pp.381-385.

[5] Hashizume, H., Usui, Y., Kitajima, S., Sagara, A., “New concept of the first wall to reduce MHD pressure drop”, International Journal of Applied Electromagnetics and Mechanics, Vol.19, No.1-4 (2004)pp.591-595.

[6] Sagara, A., Imagawa, S., Mitarai, O., Dolan, T., Tanaka, T., Kubota, Y., Yamazaki, K., Watanabe, K.Y., Mizuguchi, N., Muroga, T., Noda, N., Kaneko, O., Yamada, H., Ohyabu, N., Uda, T., Komori, A., Sudo, S., and Motojima, O., “Improved structure and long-life blanket concepts for heliotron reactors”, Nuclear Fusion, 45 (2005) 258-263.

[7] Sagara, A., Tanaka, T., Muroga, T., Hashizume, H., Kunugi, T., Fukada, S., Shimizu, A., “Innovative Liquid Breeder Blanket Design Activities in Japan”, Fusion Science and Technology, 47 (2005) pp.524-529.

[8] Okumura, M., Yuki, K., Hashizume, H., Sagara, A., “Evaluation of Flow Structure in Packed-Bed Tube by Visualization Experiment”, Fusion Science and Technology, 47 (2005) pp.1089-1093.

[9] Chiba, S., Omae, M., Yuki, K., Hashizume, H., Toda, S., Sagara, A., “Experimental Research on Heat Transfer Enhancement for High Prandtl-Number Fluid Experimental Research on Heat Transfer Enhancement for High Prandtl-Number Fluid”, Fusion Science and Technology, 47, No.4 (2005) pp.569-573.

[10] Tanaka, T., Muroga, T., Sagara, A., “Tritium Self-Sufficiency and Neutron Shielding Performance of Self-Cooled Liquid Blanket System for Helical Reactor”, Fusion Science and Technology, 47 (2005) pp.530-534.

[11] Fukada, S., Anderl, R.A., Sagara, A., Nishikawa, M., “Diffusion Coefficient of Tritium Through Molten Salt Flibe and Rate of Tritium Leak from Fusion Reactor System”, Fusion Science and Technology, 48 (2005) pp.666-669.

[12] Satake, S., Kunugi, T., Naito, N., Sagara, A., “Direct numerical simulation of MHD flow with electrically conducting wall”, Fusion Engineering and Design, 81(2006) 367-374.

[13] Fukada, S., Morisaki, A., Sagara, A., Terai, T., “Control of tritium in FFHR-2 self-cooled Flibe blanket”, Fusion Engineering and Design 81 (2006) 477–483.

[14] Chiba, S, Yuki, K., Hashizume, H., Toda, S., Sagara, A., “Numerical research on heat transfer enhancement for high Prandtl-number fluid”, Fusion Engineering and Design 81(2006) 513-517.

[15] Muroga, T., Tanaka, T., Sagara, A., “Blanket neutronics of Li/vanadium-alloy and Flibe/vanadium-alloy systems for FFHR”, Fusion Engineering and Design, 81(2006) 1203-1209.

[16] Sagara, A., Imagawa, S., Tanaka, T., Muroga, T., Kubota, Y., Dolan, T., Hashizume, H., Kunugi, T., Fukada, S., Shimizu, A., Terai, T., Mitarai, O., "Carbon tiles as spectral-shifter for long-life liquid blanket in LHD-type reactor FFHR", Fusion Engineering and Design 81 (2006) 1299–1304.

[17] Sagara, A., Mitarai, O., Imagawa, S., Morisaki, T., Tanaka, T., Mizuguchi, N., Dolan, T., Miyazawa, J., Takahata, K., Chikaraishi, H., Yamada, S., Seo, K., Sakamoto, R., Masuzaki, S., Muroga, T., Yamada, H., Fukada, S., Hashizume, H., Yamazaki, K., Mito, T., Kaneko, O., Mutoh, T., Ohyabu, N., Noda, N., Komori, A., Sudo, S., Motojima, O., and FFHR design group, "Conceptual design activities and key issues on LHD-type reactor FFHR", Fusion Engineering and Design 81 (2006) 2703–2712.

[18] Tanaka, T., Sagara, A., Muroga, T., Youssef, M.Z., "Development of three-dimensional neutronics calculation system for design studies on helical reactor FFHR", Fusion Engineering and Design 81 (2006) 2761–2766.

[19] Tanaka, T., Sagara, A., Muroga, T., Youssef, M.Z., "Neutronics Investigation of Advanced Self-Cooled Liquid Blanket Systems in Helical Reactor", 21th IAEA Fusion Energy Conf. Chengdu, 2006, to be published in Nuclear Fusion.

[20] Muroga, T., Tanaka, T., Li, Z., Sagara, A., and Sze, D.K., "Tritium control for Flibe/V-alloy blanket system", Fusion Science & Technology 52 (2007) 682-686.

[21] Satoh, T., Yuki, K., Chiba, S., Hashizume, H., Sagara, A., "Heat Transfer Performance for High Prandtl and High Temperature Molten Salt Flow in Sphere-Packed Pipes", Fusion Science & Technology 52 (2007) 618-624.

[22] Fukada, S., Katayama, K., Terai, T., Sagara, A., "Recovery of Tritium from Flibe Blanket in Fusion Reactor", Fusion Science & Technology 52 (2007) 677-681.

Task 3-2 Materials Modeling

[1] Morishita, K., Wirth, B.D., Diaz de la Rubia, T., Kimura, A., "Effects of Helium on Radiation Damage Processes in Iron", Proc. Fourth Pacific Rim Int. Conf. on Advanced Materials and Processing (PRICM4), (The Japan Institute of Metals, 2001) pp. 1383-1386.

[2] Morishita, K., Sugano, R., Iwakiri, H., Yoshida, N., Kimura, A., "Thermal helium desorption from α-Iron", Proc. Fourth Pacific Rim Int. Conf. on Advanced Materials and Processing (PRICM4), (The Japan Institute of Metals, 2001) pp. 1395-1398.

[3] Sugano, R., Morishita, K., Iwakiri, H., Yoshida, N., "Effects of dislocation on thermal helium desorption from iron and ferritic steel", Journal of Nuclear Materials 307-311 (2002) pp. 941-945.

[4] Iwakiri, H., Morishita, K., Yoshida, N., "Effects of helium bombardment on the deuterium behavior in tungsten", Journal of Nuclear Materials 307-311 (2002) pp. 135-138.

[5] Morishita, K., Sugano, R., Wirth B.D., Diaz de la Rubia, T., "Thermal stability of helium-vacancy clusters in iron", Nuclear Instruments and Methods in Physics Research Section B, 202 (2003) pp. 76-81.

[6] Morishita, K., Sugano, R., Wirth, B.D., "MD and KMC modeling of the formation and migration of He-V clusters in Fe", Journal of Nuclear Materials 323 (2003) pp. 243-250.

[7] Morishita, K., Sugano, R., Wirth, B.D., "Thermal stability of helium-vacancy clusters and bubble formation", Fusion Science Technology, Vol. 44 (2) (2003) pp. 441-445.

[8] Sugano, R., Morishita, K., Kimura, A., "Helium accumulation behavior in iron based model alloys", Fusion Science Technology, Vol. 44 (2) (2003) pp. 446-449.

[9] Sugano, R., Morishita, K., Kimura, A., Iwakiri, H., Yoshida, N., "Microstructural evolution in Fe and Fe-Cr model alloys after He+ ion irradiations", Journal of Nuclear Materials, 329-333 (2004) pp. 942-946.

[10] Morishita, K., Sugano, R., "Atomistic Modeling of Helium Bubble Formation in Fe during Irradiation", Conference proceedings of Second International Conference on Multiscale Materials Modeling (MMM-II), UCLA, Los Angeles, CA, USA, 2004, pp. 525-527.

[11] Satou, M., Komatsu, N., Sawada, T., Abe, K., "Calculation of electronic structure at bonding interface between vanadium and oxide ceramics for insulator coating applications", Journal of Nuclear Materials, Volumes 329-333, Pages 1571-1574, 2004

[12] Satou, M., Abe, K., Kioussis, N., Ghoniem, N., "Ideal Interfacial Strength Between Vanadium and Oxide Ceramics", Second International Conference on Multiscale Materials Modeling Proceedings (2004), 135-137.

[13] Okita, T., Wolfer, W.G., Garner, F.A., Sekimura, N., "Effects of titanium additions to austenitic ternary alloys on microstructural evolution and void swelling", Philosophical Magazine vol. 85 No.18/21 (2005) 2033.

[14] Morishita, K., Sugano, R., "Mechanism map for nucleation and growth of helium bubbles in metals", Journal of Nuclear Materials, 353 (2006) pp. 52-65.

[15] Morishita, K., Sugano, R., "Modeling of Helium Bubble Migration in bcc Fe", Nuclear Instruments and Methods in Physics Research Section B 255 (2007) pp. 52-56.

[16] Watanabe, Y., Iwakiri, H., Yoshida, N., Morishita, K., Kohyama, A., "Formation of interstitial loops in tungsten under helium ion irradiation: Rate theory modeling and experiment", Nuclear Instruments and Methods in Physics Research Section B 255 (2007) pp. 32-36.

[17] Morishita, K., ”Atomistic evaluation of the point defect capture efficiency of He-V clusters in α-Fe”, Nuclear Instruments and Methods in Physics Research Section B 255 (2007) pp. 41-46.

[18] Morishita, K., “Nucleation path of helium bubbles in metals during irradiation”, Philosophical Magazine 87 (2007) pp. 1139-1158.

[19] Morishita, K., Watanabe, Y., Kohyama, A., Heinisch, H.L., Gao, F., “Nucleation and growth of vacancy clusters in β-SiC during irradiation”, submitted to Journal of Nuclear Materials.

[20] Watanabe, Y., Morishita, K., Kohyama, A., “Rate theory of defect accumulation in β-SiC under irradiation”, submitted to Journal of Nuclear Materials.

[21] Iwakiri, H., Tani, M., Hamaguchi, D., Morishita, K., Yoshida, N., “Radiation Damage and Deuterium Trapping in Deuterium Ion Irradiated Ferritic Steel”, submitted to Journal of Nuclear Materials.

[22] Wirth, B.D., Caturla, M.J., Fu, C.C., Kimura, A., Kurtz, R.J., Morishita, K., Odette, G.R., Xu, D., Yamamoto, T., “Assessment of He migration and trapping interactions in Ferritic Alloys”, submitted to Journal of Nuclear Materials.

[23] Okita, T., Sekimura, N., “The interaction between an edge dislocation and a loop in BCC systems”, Submitted to Journal of Nuclear Materials

[24] Okita, T., Sato, T., Sekimura, N., Iwai, T., Garner, F.A., “The Synergistic Influence of Temperature and Displacement Rate on Microstructural Evolution of Ion-Irradiated Model Austenitic Alloy Fe-15Cr-16Ni”, to be published in Journal of Nuclear Materials

[25] Sekimura, N., Okita, T., Garner, F.A., “The synergetic effects of the dose rate and the addition of minor elements to the austenitic ternary alloys in fast neutron irradiation”, Submitted to Journal of Nuclear Materials.

[26] Okita, T., Fujita, S., Kuramoto, E., Garner, F.A., Sekimura, N., “Interaction between line dislocation and prismatic dislocation loops in FCC metals”, to be submitted to Philosophical Magazine A.

[27] Okita, T., Sekimura, N., Iwai, T., Garner, F.A., “The use of both neutron and ion irradiation to show the microstructural origins of strong flux-sensitivity of void swelling in model Fe-Cr-Ni alloy”, Proceedings of the influence of atomic displacement rate on radiation-induced ageing of power reactor components: Experimental and modeling, on CD with no pages.

[28] Okita, T., Sekimura, N., “Effects of Dose Rate on Radiation Hardening in Fe and Fe-Cu-Ni Model Alloys under Heavy Ion and Fast Neutron Irradiation”, Proceedings of the influence of atomic displacement rate on radiation-induced ageing of power reactor components: Experimental and modeling, on CD with no pages.

[29] Morishita, K., Okita, T., Sekimura, N., “Modeling of the formation of He-V clusters in Fe”, Proceedings of the 1st International Workshop on Integration of modeling, database and inspection techniques to evaluate the material behavior under irradiation.

[30] Garner, F.A., Okita, T., Sekimura, N., Isobe, Y., “Void swelling of austenitic internal components of PWRs and VVERS, and its possible impact on plant life extension”, Proceedings of the 1st International Workshop on Integration of modeling, database and inspection techniques to evaluate the material behavior under irradiation.

[31] Garner, F.A., Isobe, Y., Okita, T., Sekimura, N., ”Emerging topics in LWR austenitic internals”, Proceedings of the 1st International Workshop on Integration of modeling, database and inspection techniques to evaluate the material behavior under irradiation.

[32] Garner, F.A., Toloczko, M.B., Isobe, Y., Okita, T., Sekimura, N., “Irradiation creep and

creep-swelling relationship for BWRs and PWRs", Proceedings of the 1st International Workshop on Integration of modeling, database and inspection techniques to evaluate the material behavior under irradiation.

[33] Isobe, Y., Sagisaka, M., Okita, T., Garner, F.A., "Non-destructive measurement for swelling in austenitic alloys", Proceedings of the 1st International Workshop on Integration of modeling, database and inspection techniques to evaluate the material behavior under irradiation.

[34] Sharafat, S., Hu, Q., Ghoniem, N., " HEROS: A Spatial and Temporal Helium Bubble Evolution and Resolution Code," submitted to J. Nucl. Mater. , 2007

[35] Hu, Q., Sharafat, S., Ghoniem, N., "Modeling Space-Time Dependent Helium Bubble Evolution in Tungsten Armor Under IFE Conditions," Fusion Science & Technology, 52 [3] (2007) 574-578.

6. List of academic degrees					
Task	Degree obtained in (Month/Year)	Degree (B,M,D)	Name	University	Title of theThesis
1-1-A	9/2004	D	Yi Kang	U. Tokyo	Hydrogen isotope behaviors in Lithium-tin alloy as a potential liquid breeder or coolant for fusion reactor
1-1-A	3/2005	M	Tomohiro	Kyushu U.	Study on tritium behavior in fusion reactor blanket
1-1-A	3/2005	M	Hiroki Takada	Kyushu U.	Study of solid blanket breeder with catalytic performance
1-1-A	3/2005	B	Naoya Yamashita	Kyushu U.	Behavior of hydrogen isotopes in liquid blanket
1-1-A	3/2005	B	Kazuo Nakashima	Kyushu U.	Effects of water vapor on tritium release from fusion reactor blanket
1-1-A	3/2006	B	Manabu Nishijima	Kyushu U.	Tritium recovery from molten salt blanket of fusion reactor
1-1-A	3/2006	B	Takumi Chikada	U. Tokyo	Study on Self-healing of MHD Coatings at Fusion Reactor Liquid Metal Blanket
1-1-A	3/2006	M	Takaaki Sato	U. Tokyo	Tritium release behavior from CTR solid breeder
1-1-A	3/2006	M	Mika	Kyushu U.	Study on tritium behavior in liquid lithium blanket
1-1-A	3/2006	M	Tokoaki Ishisaka	Kyushu U.	Study of tritium release from solid breeder of fusion reactor
1-1-A	3/2006	D	Toshiharu Takeishi	Kyushu U.	Study on control of surface contamination with tritium
1-1-A	3/2007	M	Juro Yagi	U. of Tokyo	Purification of molten Li by recovery of nonmetallic
1-1-A	3/2007	M	Akio Morisaki	Kyushu U.	Behavior of hydrogen isotopes in molten salt blanket
1-1-A	3/2007	B	Yuki Edao	Kyushu U.	Behavior of tritium in liquid blanket
1-1A	3/2007	B	Kazuki Suematsu	Kyushu U.	Effects of water vapor on tritium release from solid breeder blanket
1-1-A	9/2007	M	Tomoyoshi Yakata	U. of Tokyo	Tritium production and release behavior in Flibe molten salt under neutron irradiation at high temperature
1-1-A	9/2007	D	Tomohiro Kinjo	Kyushu U.	Study on tritium release behavior from solid breeder materials of D-T fusion reactor
1-1-A	3/2008(expected)	M	Yasushi	Kyushu U.	Tritum recovery for liquid breeder of fusion reactor
1-1-A	3/2008(expected)	M	Takanori Koyama	Kyushu U.	Effects of surface water on grain in tritium breeder
1-1-A	3/2008(expected)	M	Takumi Chikada	U. of Tokyo	Characterization of Erbium Oxide Coatings for Hydrogen Permeation Barrier
1-1-A	3/2008(expected)	M	Masaru Nagura	U. of Tokyo	Corrosion behavior of insulating materials for CTR lithium blanket under static and flowing conditions
1-1-B	3/2002	D	Chiba, S.	Tohoku	Study on the improvement of thermofluid characteristics with optimization of flow field for high Prandtl-number
1-1-B	2003	D	Freeze, B. A.	UCLA	Wave structure and scalar transport at the free surface of turbulent flow on an inclined place
1-1-B	3/2005	M	Tabata, T.	Kyushu	Numerical simulation on high Prandtl number fluid flowing in pipe with twisted tape insert by means of BFC-LES
1-1-B	12/2006	M	Takeuchi, J.	UCLA	Fully developed turbulent pipe flow: comparison of particle image velocimetry data to direct numerical simulation at two different Reynolds numbers
1-1-B	12/2007	D	Nakaharai, H.	Kyushu	Study on thermofluid characteristics of high Prandtl number fluid under magnetic filed for design of liquid blanket of
1-1-B	3/2008	M	Takami, S.	Kyushu	Numerical simulation of effect of magnetic field on thermofluid charactersitics of liquid metal by Larghe Eddy
1-1-B	2008(Expected)	D	Takeuchi, J.	UCLA	Experimental Investigation of Magnetohydrodynamic Turbulent Pipe Flow and Heat Transfer of Aqueous
1-2-A	3/2003	M	Akihiko SAWADA	U. Tokyo	Research on insulator coatings for structural material of nuclear fusion reactor by physical vapor deposition
1-2-A	3/2005	B	Takayuki KOMATSU	Tohoku U	First principles calculation for ideal adhesive strength of vanadium alloy/oxide ceramics interface
1-2-A	3/2005	M	Tomoyo SAWADA	Tohoku U	Study of yttrium oxide coating on vanadium alloys by DC sputter
1-2-A	9/2005	D	Zhenyu YAO	Graduate U. Adv. Study	Development of insulating coating on vanadium alloys for liquid lithium blanket of fusion reactors

1-2-A	3/2006	B	Takashi YAMAKAW	Tohoku U	Preparation of yttrium oxide coating by DC sputter
1-2-A	3/2006	B	Takumi CHIKADA	U. Tokyo	Study on self-healing of MHD coatings for fusion reactor liquid metal blanket
1-2-A	3/2006	M	Michito KAKIE	Tohoku U	First principles calculation for interface between oxide ceramics and metals
1-2-A	3/2006	M	Takuya HANDA	U. Tokyo	Fabrication of erbium oxide coatings as hydrogen permeation barrier
1-2-A	3/2006	D	Akihiko SAWADA	U. Tokyo	Research on insulator coatings for structural material of nuclear fusion reactorby physical vapor deposition
1-2-A	3/2008(expected)	M	Takumi CHIKADA	U. Tokyo	Characterization of erbium oxide coatings for hydrogen permeation barrier
1-2-A	3/2008(expected)	M	Masaru NAGURA	U. Tokyo	Corrosion behavior of insulating material for liquid lithium blanket in the static and flowing condition
1-2-A	3/2008(expected)	M	Takashi YAMAKAW	Tohoku U	Evaluation of adhesive strength of yttrium oxide coating layer on vanadium alloys
1-2-B	3/2003	B	Akio IWAHORI	Nagoya Ins. Tech.	Mechanical property change of fusion candidate vanadium alloys by impurity dissolution and precipitation
1-2-B	3/2003	M	Masanosuke NAGAMINE	Kyushu U	Microstructure of Yag laser weled V-4Cr-4Ti alloys
1-2-B	9/2003	D	Nam-Jin HEO	Graduate U. Adv. Study	Impurity behavior and weld joint properties of low activation vanadium alloys for fusion reactor
1-2-B	3/2004	M	Masanori MATOBA	Tohoku U	Formation of oxide layer on vanadium alloy in high-temperature environment
1-2-B	3/2004	M	Kazutaka SAKAI	Tohoku U	Effects of heat-treatment conditions on microstructure of high chromium vanadium base alloys
1-2-B	3/2005	B	Takeshi HINO	Tohoku U	Mechanical properies of vanadium alloy prepared by levitation method and their effects of yttrium addtion
1-2-B	3/2005	M	Kazuhiro YAMASAKI	Kyushu U	Ion irradiation on Yag laser weled V-4Cr-4Ti alloys
1-2-B	3/2006	B	Shimon OCHI	Tohoku U	Study on adhesive properties of surface oxide layer on vanadium alloys
1-2-B	3/2006	M	Daisuke TANIGUCHI	Tohoku U	Effects of surface oxdation layer on mechanical properties of V-Cr-Ti alloy with yttrium addition
1-2-B	3/2007	B	Takashi SATO	Tohoku U	Study on improvement of high-temperature strength of vanadium alloy bu means of microstructure controlling
1-2-B	3/2007	B	Shinji Kuritani	U. Fukui	Creep deformation of highly purified V-4Cr-4Ti alloys using pressurized creep tube
1-2-B	3/2007	M	Takeshi HINO	Tohoku U	Improvement on mechanical properties of vanadium alloys by means of yttrium additions for nuclear fusion
1-2-B	3/2007	M	Akira HIGASHIZIM	Kyushu U	Effects of Y additons on welded V-4Cr-4Ti alloys
2-1	3/2002	M	Keisuke Hironaka	Kyoto University	Research of Mecanical Strength on SiC Fiber Reinforced SiC Matrix Composites
2-1	3/2002	D	Masaki Kotani	Kyoto University	Reserach of Processing of SiC Fiber Reinforced SiC Matrix Composites
2-1	3/2002	D	Wen Yang	Kyoto University	Development of CVI Process and Property Evaluation of CVI-SiC/SiC Composites
2-1	3/2003	D	Joon-Soo Park	Kyoto University	Evaluation Methods for Fracture Resistance of Ceramic Matrix Composites
2-1	9/2003	D	Takashi Nozawa	Kyoto University	Study of Mechanical Properties of SiC/SiC Composites
2-1	3/2004	M	Masao Eto	Kyoto University	Research of Densification Prodcedure of SiC in NITE Method
2-1	3/2005	D	Jae-Kwang Lee	Kyoto University	A Study on Fabrication and Joining of SiC/SiC Composite Materials by Liquid Phase Sintering Method
2-1	3/2005	M	Kazuya Shimoda	Kyoto University	Research and development of SiC/SiC composites using SiCultrafine powder
2-1	3/2005	M	Yuichi Maki	Kyoto University	Research of Mechanical Property Orientation of SiC/SiC Composites
2-1	3/2004	M	Shunji Nakajima	Tohoku Universituy	Effects of Insert Metal of Joining between SiC and Tungsten

2-1	9/2005	D	Jianjun Sha	Kyoto University	Performance of SiC-based Fibers under Severe Environments and Its Mechanistic Analysis
2-1	9/2005	D	Soo-Jung Son	Kyoto University	Research of Tungsten Coating on SiC and SiC/SiC Composites
2-1	9/2005	D	Yong-Seong Lee	Kyoto University	Research of SiC/SiC Composites as Thermally Functional or High Temperature Structural Materials
2-1	10/2005	D	Zuhair S.Khan	Kyoto University	Development of Environmental Barrier Coatings(EBCs) on SiC and SiC Composites for Advenced Energy Generation
2-1	3/2006	M	Nobuhiko Eiza	Kyoto University	Research of High Strength Joining of SiC and SiC/SiC Composites using Applied NITE Method
2-1	3/2007	M	Kazuoki Toyoshima	Kyoto University	Research og Fracture og High Performance SiC/SiC Composites
2-1	11/2007	D	Yi-Hyun Park	Kyoto University	Study on High Performance Multifunctional Porous SiC Ceramics
2-2	3/2002	B	KENJI Matsuo	Kyushu Univ.	Porosity estimation of pebble bed layer by water dipping tomography
2-2	3/2004	M	KENJI Matsuo	Kyushu Univ.	Thermo-fluid analysis of solid blanket pebble layer by use of lattice Boltzmann method
2-2	3/2008	M (expected)	Nobuyuki Ohtake	Tohoku Universituy	Effects of interface on Oxidation Behavior of Advanced SiC/SiC Composites
2-3	3/2002	D	Masaki Kotani	Kyoto University	Reserach of Processing of SiC Fiber Reinforced SiC Matrix Composites
2-3	3/2002	D	Hirotatsu Kishimoto	Kyoto University	Research of Radiation Effects on SiC Materials
2-3	3/2003	D	Shuhei Nogami	Tohoku University	Effects of Transmutation Helim and Displacement Damage on Mechanical Properties of SiC/SiC Copmosites for Fusion
2-3	3/2003	D	Joon-Soo Park	Kyoto University	Evaluation Methods for Fracture Resistance of Ceramic Matrix Composites
2-3	3/2003	D	Shuhei Nogami	Tohoku University	Effects of Transmutation Helim and Displacement Damage on Mechanical Properties of SiC/SiC Copmosites for Fusion
2-3	9/2003	D	Takashi Nozawa	Kyoto University	Study of Mechanical Properties of SiC/SiC Composites
2-3 &2-1	9/2003	D	Takashi Nozawa	Kyoto University	Study of Mechanical Properties of SiC/SiC Composites
2-3 & 2-1	3/2004	M	Shunji Nakajima	Tohoku University	Effects of Insert Metal of Joining between SiC and Tungsten
2-3	3/2004	M	Shuhei Miwa	Tohoku University	Study of Cavity Formation Behavior of SiC/SiC Composites by Triple-ion Beam Irradiation
2-3	3/2004	M	S.Miwa	Tohoku University	Study of Cavity Formation Behavior of SiC/SiC Composites by Triple-ion Beam Irradiation
2-3	9/2004	D	Kyeong-Hwan Park	Kyoto University	Effects of Ion Irradiation on β-SiC for Advanced Nuclear Energy Systems
2-3	3/2006	D	Sosuke Kondo	Kyoto University	Irradiation Effects on Microstructure Development of SiC
2-2 & 2-3	3/2005	M	Takahide Murayama	Tohoku University	Study of Compatibility between SiC and Solid Breeding Materials for Fusion Reactor
2-3	3/2006	D	Sosuke Kondo	Kyoto University	Irradiation Effects on Microstructure Development of SiC